FOREWORD

A wide variety of atomic, molecular, radiative and plasma-wall interaction processes involving a mixture of atoms, ions and molecules occur in the plasmas produced in nuclear fusion experiments. In the low-temperature divertor and near-wall region, molecules and molecular ions are formed. The plasma particles react with electrons and with each other. Plasma modelling requires cross-sections and rate coefficients for all these processes, and in addition spectral signatures to support interpretation of data from fusion experiments.

The mission of the International Atomic Energy Agency Nuclear Data Section (NDS) in the area of atomic and molecular data is to enhance the competencies of Member States in their research into nuclear fusion through the provision of internationally recommended atomic, molecular, plasma-material interaction and material properties databases. One mechanism by which the IAEA pursues this mission is the Coordinated Research Project (CRP). The present volume of *Atomic and Plasma-Material Interaction Data for Fusion* contains contributions from participants in the CRP "Atomic and Molecular Data for Plasma Modelling" (2004-2008). This CRP was concerned with data for processes in the near-wall and divertor plasma and plasma-wall interaction in fusion experiments, with focus on cross-sections for molecular reactions. Participants in the CRP came from 14 different institutes, many with strong ties to fusion plasma modelling and experiment. D. Humbert of the Nuclear Data Section was scientific secretary of the CRP.

Participants' contributions for this volume were collected and refereed after the conclusion of the CRP. The IAEA takes this opportunity to thank the CRP participants for their dedicated efforts during the CRP and for their contribution to this volume.

Contents

INTRODUCTION AND SUMMARY

This volume of Atomic and Plasma-Material Interaction Data for Fusion contains contributions from participants in the IAEA Coordinated Research Project (CRP) "Atomic and Molecular Data for Plasma Modelling" (2004-2008). It is extremely complex to understand the plasmas produced in the edge region of nuclear fusion reactors since a mixture of atoms, ions and molecules from a variety of species interacts not only with electrons but also with each other. The interactions include electron and proton impact excitation and ionization, charge exchange, radiative and di-electronic recombination with atoms and molecules as well as dissociation of molecules. The vibrational and rotational states of molecules significantly add to the complexity of the modelling. While the numerical simulations of such plasmas require a comprehensive set of interaction data, there are still a large number of interaction data missing.

The Atomic and Molecular (A+M) Subcommittee of the International Fusion Research Council (IFRC) noted this issue and recommended a CRP on the establishment of databases for plasma edge plasmas. Researchers from 14 institutes in the field of atomic, molecular physics and plasma modelling and experiment participated in the CRP. Participants attended three Research Coordination Meeting (RCM) at which progress was reviewed and future research plans were formulated. These meetings took place on 26-28 September 2005, 18-20 June 2007, and 17-19 November 2008. Summary Reports of these RCMs were produced in the INDC(NDS) series and are available through the A+M Data Unit web pages under http://www-amdis.iaea.org/publications/INDC/ (Reports. 0482, 0515, 0544).

The CRP focused on the collection, evaluation and generation of new data for surface processes and volume processes in the near-wall and divertor plasma and plasma-wall interaction in fusion experiments with emphasis on the formation of molecules and the interaction of molecules with the various plasma constituents. In this volume, the data are presented for cross-sections, rate coefficients, branching ratios, and kinetic energies from various sources for hydrides and isotopes and the estimates of vibrational relaxation times in the hydride complexes. Further considered are the data for methane family with all the break-up products and the data from acetylene, BeH_y and their isotopomers as well as their ions. Information on surface interactions, such as sticking and generation of hydride species is included. The results from this CRP have been implemented in the on-line cross-section database and analysis tool HYDKIN (http://www.eirene.de/eigen/) and the IAEA A+M PSI database ALADDIN (http://www-amdis.iaea.org/ALADDIN/).

At the conclusion of the CRP, participants identified many important issues for both surface and volume processes and recommended close collaboration for further work. For surface processes, two important issues were recognized:

- The effect of molecular vibrational distributions in surface processes is not known, and it is difficult to address experimentally.
- The form of beryllium which leaves the surface is not known.

For the volume processes, the following areas were recognized for further inverstigation:

- A full quantal test of $H^+ \leftrightarrow$ hydrocarbon collisions with Langevin rates is of high interest, particularly at energies below 2 eV.
- There is a need for complete deuterium databases and reliable vibrationally-resolved cross-sections for H and H_2 collisions.
- Vibrational effects in electron-C_2 collisions are important.
- Vibrationally-resolved electron impact electronic excitation cross-sections are needed for BeH/BeD/BeT, CH/CD, BH/BD.
- The data for BeH/BeD need further investigation for emission spectra.
- Electron impact electronic excitation (both dissociative and non-dissociative) cross-sections are needed for hydrocarbons as well as photon emission.

Many of these issues are being pursued in on-going and future CRPs of the IAEA Atomic and Molecular Data Unit:

- "Data for Surface Composition Dynamics Relevant to Erosion Processes" (2007-2011)
- "Characterization of Size, Composition and Origins of Dust in Fusion Devices" (2008-2012)
- "Light Element Atom, Molecule and Radical Behaviour in the Divertor and Edge Plasma Regions" (2009-2013)
- "Atomic and Molecular Data for State-Resolved Modelling of Hydrogen and Helium and Their Isotopes in Fusion Plasma" (2011-2014).
- "Erosion and tritium retention for beryllium plasma-facing materials" (tentatively 2012-)

These CRPs are expected to enable generation, evaluation and compilation of more comprehensive data sets for plasma modelling for the edge region of nuclear fusion reactors.

ELECTRON-IMPACT DISSOCIATION OF HYDROCARBON MOLECULAR IONS

M. E. BANNISTER, D. R. SCHULTZ

Physics Division, Oak Ridge National Laboratory,
Oak Ridge, TN 37831-6372, USA

Abstract

Absolute cross-sections for electron-impact dissociation of CH_x^+ (x=1,2,3) producing CH_y^+ (y=0,1,2) fragment ions were measured in the 3-100 eV range using a crossed electron-ion beams technique with total uncertainties of about 11% near the cross-section peaks. For CH^+ dissociation, although the measured energy dependence agrees well with two sets of storage ring measurements, the magnitude of the present results lies about 15% to 25% lower at the cross-section peak near 40 eV. For dissociation of CH_2^+, the cross-sections are nearly identical for energies above 15 eV, but they are dramatically different at lower energies. The CH^+ channel exhibits a strong peak rising from an observed threshold of about 6 eV; the C^+ channel is relatively flat down to the lowest measured energy. For dissociation of CH_3^+ and CD_3^+, good agreement is found with other results reported for the CH^+ fragment, but some differences are found for the CD_2^+ and C^+ fragments. A pilot study has also been undertaken to assess the feasibility of applying a molecular dynamics approach to treat the full range of electron-hydrocarbon dissociation processes, especially for energies above a few eV, in order to provide an overarching theoretical model that can be readily applied. Comparison with the experimental data for CH^+ shows favourable agreement.

1. INTRODUCTION

The chemistry, particle and energy balance, and neutral transport of low-temperature plasmas are greatly influenced by collisions of electrons with molecular ions. In particular, hydrocarbon ions are found in the divertor and edge plasmas of fusion devices that use graphite for plasma-facing components [1] and may contribute to detachment of divertor plasmas through molecule assisted recombination [2]. They are also important in the plasma processing of diamond films [3,4] and in the chemistry of diffuse interstellar and planetary clouds [5]. Hence, modelling and diagnosing these varied plasma environments require accurate, reliable cross-sections for interactions of these molecular ions with electrons, atoms, and photons.

Published results on the structural, reactive, and spectroscopic properties of hydrocarbons are sparse, but several investigations have been performed [6-19]. In 2000 and 2002, collections of data on interactions of hydrocarbons with hydrogen and with electrons were made available by Alman and Ruzic [20] and by Janev and Reiter [21,22], for the CH_n and the C_mH_n families and their ions, respectively. Subsequently, new investigations based either on the improved understanding of the physical mechanisms governing those processes or on entirely new experimental methods have been performed, mostly investigating the fragmentation of the molecules via the dissociative recombination (DR) process. DR involves the efficient capture of a low energy electron ($\leq$ 1 eV) by the molecular ion which then stabilizes its excess energy by dissociating into neutral fragments. Two recent reviews of measurements of DR of hydrocarbon ions at ion storage rings have been reported by Viggiano *et al.* [23] and by Mitchell *et al.* [24]. Very few experiments have focused on the dissociative excitation (DE) and the dissociative ionization (DI) processes, which differ from DR in that charged fragments are produced in the reaction and are more efficient at higher electron energies ($\geq$ 10 eV); these studies have been mostly limited to the detection of light fragment ions from the reaction [13,14,19,25-27].

The production of CH_y^+ fragment ions by electron-impact dissociation of CH_x^+ ions can occur by a number of different channels, as illustrated for the case of CH^+ ions:

$$e + CH^+ \rightarrow e + C^+ + H \tag{1}$$
$$\rightarrow CH^{**} \rightarrow e + C^+ + H \tag{2}$$
$$\rightarrow e + C^+ + H^+ + e \tag{3}$$
$$\rightarrow CH^{**} \rightarrow C^+ + H^- \tag{4}$$

The first process, direct dissociative excitation (DDE), involves a vertical transition from the initial state of CH^+ to a dissociative excited state. The second process, resonant dissociative recombination (RDE), proceeds through the resonant capture of the incident electron to a Rydberg state of the neutral molecule CH^{**} which then decays by ejecting an electron and dissociating. Hereafter, we will refer to the first two processes together as simply dissociative excitation (DE). Dissociative ionization (DI), the third process, is similar to DDE but ends in a dissociative state with two ion fragments. The last process producing C^+ fragments, resonant ion pair (RIP) formation, is expected to be negligible compared to the DE and DI contributions, based on RIP measurements on other systems [28-30].

The electron-impact dissociation of CH^+ and CD^+ in the DE and DI channels has been investigated previously using several techniques. Amitay *et al.* [31] measured the production of C^+ ions up to 40 eV at the Heidelberg Test Storage Ring (TSR), but their results had total absolute uncertainties of about 50% due to difficulties measuring the ion current circulating in the storage ring. Forck [32] investigated the dissociation of CD^+ at TSR, measuring cross-sections for production of C^+ ions as well as C and D neutrals, also with total uncertainties of about 50%. Djurić *et al.* [33] measured the sum of DE and DI for the H^+/D^+ production channel using a crossed-beams technique; below the DI threshold where DE provides the only energetically allowed channel, their results for the production of D^+ were in excellent agreement with those of Forck [32] for the production of C neutrals. Recently, Lecointre *et al.* [34] published crossed-beams measurements for the production of C^+ from the DE and DI of CD^+.

The electron-impact dissociation of CH_2^+/CD_2^+ in the light-ion-fragment DE channels has been investigated previously using two different techniques. Djurić *et al.* [35] measured the sum of DE and DI for the D^+ production channel using a crossed-beams technique. Larson *et al.* [36] investigated the same light ion fragment DE channels in CH_2^+ at the CRYRING heavy ion storage ring, although they directly detected the corresponding neutral products CH and (C + H) with solid-state surface-barrier detectors. The agreement between the two sets of measurements for the light-ion-fragment channels is excellent, suggesting that the DI contributions are small for energies measured in the CRYRING experiment (up to 55 eV). However, there have been no published measurements for dissociation of CH_2^+ producing the heavy ion fragments CH^+ and C^+.

To the authors' knowledge there has been no data reported in studying the heavy ion fragments from the DE and DI reactions of CH_3^+ or CD_3^+. To date, only some preliminary results have been presented at conferences [27,37]. Djurić *et al.* [35] reported cross-sections for production of D^+ and D_2^+ fragment ions from the DE and DI of CD_3^+.

Janev and Reiter [21,22] have recently published a review of data for collisions of simple hydrocarbon ions and neutrals with electrons and protons, including empirical formulae for electron-impact DE and DI of CH_x^+. Information about the thresholds and average kinetic energies of release (KERs) for these processes are summarized in Table 1. D_0 corresponds to the dissociation energy limit. For a given reaction channel, D_0 is estimated using the energy released in the production of ground-state fragments from dissociative recombination of CH_x^+ ion [36,38,39] and the ionization potential energies of C, CH, CH_2, H, and H_2 neutral fragments [40]. In contrast, E_{th} corresponds to the threshold energy for a vertical transition from the CH_x^+ ground state to the appropriate dissociative state for the given final products (also in their ground states); the values of E_{th} are averaged over the Franck-Condon region of the vibrational ground state of CH_x^+ and are from the work of Janev and Reiter [21].

Resonant ion pair (RIP) formation also produces ion fragments, but for the energy range of the present measurements, the contribution of this process is expected to be negligible [28-30].

The measurements [41-43] reported here are absolute total cross-sections for the production of CH_y^+ (y=0,1,2) ions by electron-impact on CH_x^+ (x=1,2,3). The measurements were performed using the ORNL electron-ion crossed beams apparatus [44,45] with CH_x^+ ions produced in a Caprice electron-cyclotron-resonance (ECR) ion source. We note that all of the pathways through which a given CH_y^+ fragment ion can be produced from dissociation of a given CH_x^+ target ion by impact of electrons cannot be resolved in the present study. Hence, the measurements reported here represent the contributions summed over all of the possible reaction channels. In the present measurements coincidentally ejected light-mass fragments (H, H^+, H_2, or H_2^+) are not detected; the absolute cross-sections for these channels measured with a similar apparatus have been reported elsewhere [33,35]. The measured cross-sections are compared to published results of other experiments [31-34] where they exist. The experimental data for CH^+ are also compared to results from a molecular dynamics plus energy deposition model presented in this paper (see section 3 for a description). In the absence of other experimental or theoretical data, the present results are compared with the empirical fits of Janev and Reiter [21, 46].

TABLE 1. ENERGIES FOR ELECTRON-IMPACT DISSOCIATION CHANNELS OF CH_x^+ (x=1,2,3) IONS PRODUCING CH_y^+ (y=0,1,2) FRAGMENT IONS (*Vertical transition threshold energies E_{th} are taken from Ref. [21] where available and are given in eV for CH_x^+ ions in the v=0 ground state. The dissociation limit energies D_0 are estimated from dissociative recombination measurements of Refs. [36,38,39] and ionization energies of neutral fragments given by Ref. [40]. The kinetic energies of release (KER) are from Ref. [21]. Resonant ion pair formation processes are not included; see text for an explanation*)

Parent	Products	E_{th}(eV)	D_0(eV)	KER(eV)
Dissociative excitation				
CH^+	$C^+ + H$	6.50	4.08	2.50
CH_2^+	$CH^+ + H$	6.08	4.84	1.40
	$C^+ + H_2$	5.62	4.46	1.30
	$C^+ + 2H$	11.52	8.96	2.66
CH_3^+	$CH_2^+ + H$	7.03	5.40	1.62
	$CH^+ + H_2$	7.22	5.44	1.67
	$CH^+ + 2H$	–	9.94	–
	$C^+ + H_2 + H$	12.65	9.66	2.92
	$C^+ + 3H$	–	14.16	–
Dissociative ionization				
CH^+	$C^+ + H^+$	29.00	17.68	11.78
CH_2^+	$CH^+ + H^+$	30.41	18.44	11.78
	$C^+ + H_2^+$	–	19.89	
	$C^+ + H^+ + H$	34.15	22.56	11.78
CH_3^+	$CH_2^+ + H^+$	30.81	19.00	11.78
	$CH^+ + H_2^+$	–	20.87	–
	$CH^+ + H^+ + H$	35.94	23.54	11.78
	$C^+ + H^+ + H_2$	35.09	23.26	11.78
	$C^+ + H_2^+ + H$	–	25.09	–
	$C^+ + H^+ + 2H$	–	27.76	–

2. EXPERIMENT

The electron-ion crossed beams apparatus used for the present study has been described in detail previously [44,45], but issues specific to measurements of cross-sections for dissociation of molecular ions will be discussed below. The apparatus is shown schematically in Figure 1.
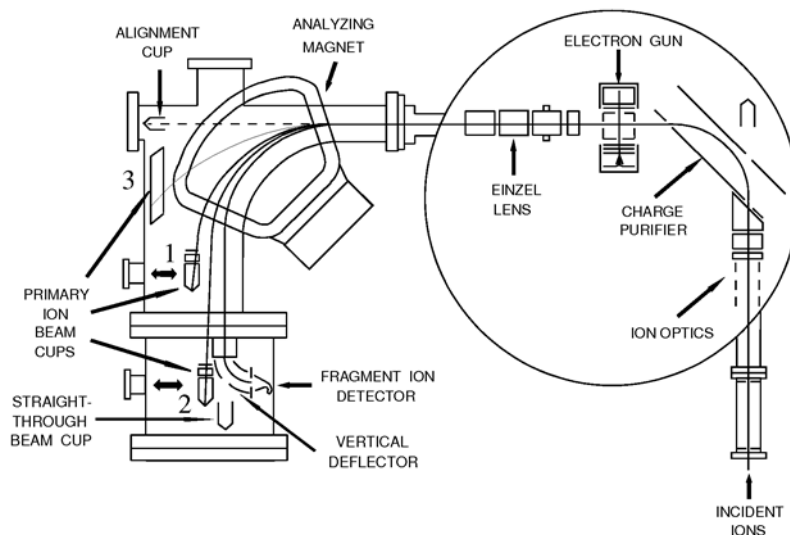

FIG. 1. Electron-ion crossed-beams experimental apparatus. The fragment ion detector and vertical deflector are rotated 90° to the plane of the figure.

2.1. Ion and electron beams

The parent ions are produced in the ORNL Caprice ECR ion source [47] fed by methane gas (CH_4 or CD_4) and then extracted and accelerated to 10 keV. The source is typically operated with 1-2 Watts of microwave power and a gas pressure of approximately $4-8 \times 10^{-7}$ Torr in the ECR region. This typically gives 30-50 µA CH_x^+ ion beam current after leaving the magnetic mass selector. The primary ions are collected in a Faraday cup, with typical currents of 30-90 nA.

Since the lifetimes of electronic and ro-vibronic excited states of CH_x^+ [38,48,49] are much longer than the 1 µs flight time of the ions from the ECR source to the collision volume, the excited state population of the target CH_x^+ ions is essentially preserved from the ion source. Even operating the source at minimal microwave power levels of a few watts and with source pressures of order 10^{-6} Torr, the electron temperature in the ECR discharge may be tens of eV or more, producing a sizable fraction of CH_x^+ ions in excited states. For CH^+ this includes higher vibrational levels of the $X^1\Sigma$ ground state and the $a^3\Pi$ metastable state. Because the $a^3\Pi$ state has a lifetime of approximately 7s [38], it was not feasible to measure the population of these ions in the beam extracted from the ECR source. For CH_2^+, there exists a metastable electronic state, CH_2^+ ($\tilde{a}^4A_2$), whose $v=0$ level lies about 3.7 eV above the ground state [50]. The presence of excited states has been found to have a significant effect on measured cross-sections for the dissociative recombination of CH^+ [38,51], although less dramatic influences are expected for DE and DI. We have no mechanisms for determining the fractions of low-lying excited states in the incident CH_2^+ ion beam, although whether these excited ions are present usually can be inferred from measurements below the lowest ground-state threshold.

Mass spectra of extracted CH^+ ions demonstrated that the only impurity ions in the analyzed beam were $^{13}C^+$ ions, comprising less than 1% of the extracted ions with $m/q=13$ as estimated from the $^{12}C^+$ peak and known natural abundances. Since $^{12}CH_2^+$ has a mass of 14 amu, $^{14}N^+$ ions extracted from

4

the ion source will not be separated and will be an impurity in our target beam. The fraction of N^+ ions in the beam is estimated from two sets of ionization data measured in the present study. First, using the crossed-beams apparatus, electron-impact ionization cross-sections were measured at 100 eV for m/q = 14 ions ($^{12}CH_2^+$ and N^+); both $^{12}CH_2^{2+}$ and N^{2+} product ions were detected by the CEM. The ion source was cleaned to remove essentially all traces of carbon-12. Second, the ionization cross-sections were measured for $^{13}CH_2^+$ using carbon-13 methane as the gas in the ECR ion source so that there would be no contamination from N^+ ions. Using the published cross-section for ionization of N^+ at 100 eV [52], we determined the fraction of N^+ ions in the m/q = 14 ion beam to be 4.8%. Since carbon-13 is only 1.1% of naturally occurring carbon, we estimate that the total amount of impurity ions in the $^{12}CH_2^+$ ion beam is less than 6%.

For the production of CH_3^+ ions, special care is taken to eliminate nitrogen from the feeding gas line of the ECR ion source since NH^+ ions, which have mass m=15 and electric charge q=1, would contaminate the ion beam. Furthermore, the methane used as the working gas is not 100% pure and may contain some impurities. Hence, contamination from $^{13}CH_2^+$ ions should be considered since, like NH^+, they have the same m/q ratio as the CH_3^+ target ion. In our study of the CH_2^+ ion fragmentation [42] we estimated the contribution of N^+ and $^{13}CH^+$ to be less than 6%, considering both nitrogen contamination of the source and the natural abundance of ^{13}C. In the present study, we expect a similar contribution, or even less, for the same reasons. Similarly, contamination from H_2O^+ must also be minimized since those ions have the same m/q ratio as CD_3^+. Analyzed ion spectra extracted from the CD_4 plasma showed a contamination of less than 5% for the CD_3^+ ion beam, as indicated by the population of OH^+ ions.

The ions are transported with magnetic and electrostatic optics from the ECR ion source to the crossed beams apparatus. Just before the collision volume the ions are deflected electrostatically through 90° in a charge purifier to eliminate any charge-exchange components in the beam. In the collision volume, the ion beam (1 mm diameter) interacts at a right angle with an electron beam formed by a magnetically-confined gun described below. Upon leaving this interaction region, the parent and fragment ions are separated by a double-focusing 90° sector analyzing magnet with a radius of curvature of 20 cm. This ensures that the collision volume is imaged at the throat of the fragment ion detector. The CH_y^+ fragment ions are deflected 90° by the magnet, then electrostatically deflected out of the magnetic dispersion plane and onto either a 1.0 cm diameter channel electron multiplier (CEM) or a 1.0 cm x 2.5 cm discrete dynode detector. The CH_x^+ primary ions are deflected less by the analyzing magnetic field and collected in one of three Faraday cups, depending on the mass ratio of the parent and fragment ions (see Figure 1).

The electron gun used for the present study is a magnetically-confined model described previously [44,53,54]. A magnetic field of 250 G confines the electrons and yields a uniform rectangular cross-section (approximately 2 mm wide by 10 mm high) over the 2 mm length of the interaction region. Spiralling of the electrons is minimized [54] by accelerating them in a uniform electric field through a series of apertures between the indirectly heated planar cathode and the collision volume. The electron collector is comprised of a stack of tantalum "razor blades" turned with the sharp edges facing the interaction region; this design helps prevent backscattered electrons from returning to the collision volume. The collector is also biased +300 V with a battery to minimize the escape of secondary electrons. Typical electron currents are 11 μA at 10 eV and 230 μA at 100 eV. The electrons are chopped at 1 kHz in order to separate the dissociation signal from the relatively larger background count rate associated with the ion beam. Measurements of excitation cross-sections using the configuration shown in Figure 1 [55] indicated that the net collision energy distribution is degraded from the 0.4 eV of the gun [53,54] to about 1.5 eV full-width-half-maximum as a result of field leakage into the collision region from the post-collision ion deflector plates.

The overlap of the ion and electron beams in the direction perpendicular to both beams (vertical direction) was measured with a slit probe moving through the center of the interaction region. Current

profiles of the ion and electrons, $I_i(z)$ and $I_e(z)$, were measured independently and numerical integration yielded the form factor F needed for determination of absolute cross-sections:

$$F = \frac{\int I_e(z)dz \int I_i(z)dz}{\int I_e(z)I_i(z)dz}. \tag{5}$$

2.2. Cross-section determination and uncertainties

The absolute cross-sections are determined [56] from measured quantities using

$$\sigma(E) = \frac{R}{I I_e} \frac{qe^2 v_i v_e}{\sqrt{v_i^2 + v_e^2}} \frac{F}{\varepsilon}, \tag{6}$$

where $\sigma(E)$ is the absolute cross-section at the center-of-mass electron-impact energy E, R is the CH_y^+ fragment signal rate, I_i and I_e are respectively the incident ion and electron currents, qe is the charge of the incident ions, v_i and v_e are the incident ion and electron velocities, F is the form factor that is determined from the two beam profiles, and ε is the detection efficiency for the product ions that we estimated to be 98% [57] for the channeltron and 90% for the discrete dynode detector.

TABLE 2. ABSOLUTE SYSTEMATIC UNCERTAINTIES AT A HIGH CONFIDENCE LEVEL EQUIVALENT TO 90%-CONFIDENCE FOR STATISTICAL UNCERTAINTIES

Source	Uncertainty (%)
Signal detection and pulse transmission	± 5
Fragment ion collection	± 4
Form factor	± 4
Ion current	± 6
Electron current	± 2
Ion velocity	± 1
Electron velocity	± 1
Quadrature sum	± 9.9

The systematic uncertainties in the experiment arise from a number of sources connected to the measurement of the quantities in Eq. (6) and are given at a level equivalent to 90%-confidence level for statistical uncertainties in Table 2. One contribution is from the detection of the CH_y^+ fragment ions (estimated at 5%); this includes detection efficiency ε, pulse signal discrimination, and dead times of the detector and signal processing electronics. The transmission and collection of the fragment ions contributes an estimated 4% and includes possible losses due to fragment ions in the tail of the KER distribution. These two uncertainties are connected to the measurement of the true signal rate (R/ε) in Eq. (6). The systematic uncertainty of measuring the absolute form factor F is estimated to be 4%. Other contributions are from determinations of the ion current (6% including beam impurities), electron current (2%), and the ion and electron velocities (1% each). The quadrature sum of all these contributions is ±9.9%. Combining this sum with the statistical uncertainties at a 90%-confidence level yields the total expanded uncertainties for the measurements, typically about 11% near the cross-section peak.

2.3. Diagnostics

Upon dissociation of a molecular ion, the fragments share KER that is the result of redistribution of the excess internal energy in the molecular ion after the collision with an electron.

Thus a given fragment will have a velocity that is the vector sum of that of the target ion and a velocity component due to its share of the KER. The maximum change in lab frame momentum occurs when the corresponding additional momentum is parallel or anti-parallel to the incident ion momentum. In this case the dispersion of the CH_y^+ fragment ion by the analyzing magnet causes a horizontal displacement Δx at the detector that is given by [41]

$$\Delta x = 4r_0 \left(\frac{\Delta E}{E_i} \frac{M-m}{m} \right)^{\frac{1}{2}}$$

(7)

where r_0 is the radius of curvature of the double-focusing analyzing magnet, M and m are the parent and fragment masses, respectively, ΔE is the KER, and E_i is the energy of the incident (parent) ion.

Measurements of the apparent dissociation cross-section at a center-of-mass energy of 100 eV as a function of the analyzing magnetic field are used to infer the maximum displacement Δx, from which one can determine an upper limit for the average KER for a dissociation process. Such measurements were performed using the 1.0 cm diameter CEM detector for the dissociation of CH^+ producing C^+ fragment ions, yielding an upper limit of 3.8 eV for the average KER, compared to the 2.5 eV value predicted by Janev and Reiter [21]. Similar measurements for the dissociation of CH_2^+ ions yielded upper limits of 2.1 eV and 2.5 eV for the CH^+ and C^+ fragment ion channels, respectively. Upper limits of 2.2 eV and 2.4 eV were measured for the KER for dissociation of CH_3^+ producing CH^+ and C^+ fragment ions, respectively. The $CD_3^+ \rightarrow CD_2^+$ dissociation measurements were performed only using the larger discrete dynode detector and, hence, no determination of KER was made.

The KER also causes angular spreading of the CH_y^+ fragment ions, but this is mostly compensated for by the double-focusing analyzer magnet. As demonstrated by trajectory modelling using the computer program SIMION [58], the spread of the fragment ions at the detector due to KER perpendicular to the target ion velocity is much smaller than that due to KER in the parallel direction. Note that angular effects of KER are sufficient, however, to cause significant loss of H^+ fragment ions, which are not collected in these experiments.

The high background count rates due to dissociation of the parent CH_x^+ ions on residual gas in the collision volume necessitated limiting the incident ion current. By measuring the apparent cross-section as a function of the total CEM count rate, it was found that full signal could be maintained with count rates of less than 70 kHz, but increasing it beyond 100 kHz caused a reduction of greater than 10% due to reduced gain of the CEM detector. The larger discrete dynode detector produces much faster output pulses and it was found that full signal collection could be maintained for total count rates above 1 MHz.

The position of the Faraday cup that collected the primary ion beam was optimized in each measurement to maintain the full current and signal while minimizing the ion background on the detector. Parameters for the electron chopping such as frequency, voltage, and delay times were also varied and found to have a negligible effect on the measured cross-sections.

3. THEORETICAL MODEL

The fully quantum mechanical treatment of electron-impact dissociative recombination, excitation, and ionization over a wide range of energies for all hydrocarbon ions and neutrals of interest in modelling the edge and divertor plasmas of present and next-step devices would be a daunting challenge. While fully quantum methods will undoubtedly provide the most accurate results for individual systems it is also desirable to determine if a simpler and widely applicable approach could be developed to describe this wide range of collisions and reaction channels. Therefore, we have undertaken a pilot study here in which we describe the electron-molecular ion collision e + CH^+ through a kind of molecular dynamics approach coupled with a model determining the fragmentation channel probability through binning of the energy deposition in the collision. This pilot study which

has included the least possible degree of sophistication will be followed up in future work by more complete treatment of the dynamics.

The present approach is based on the classical trajectory Monte Carlo (CTMC) method [59,60] originally develop to treat inelastic ion-atom collisions. In this method, in brief, an ion-atom collision is simulated by analyzing the result of a large number of trajectories chosen from an ensemble of projectile-target configurations, prepared in such a way that they mimic the initial quantum mechanical electronic position and momentum distributions as closely as possible. The subsequent motion of all the particles is then determined by solving classical mechanical equations of motion. At an asymptotic separation, the relative energies of the electron to each of the ionic centers is calculated to determine what transition has occurred - elastic scattering, excitation, charge transfer, or ionization. The classical orbital state of the electron can then be mapped to the corresponding quantum state using appropriate binning rules (e.g., [61]) yielding the quantum numbers n, l, etc. CTMC results are usually reasonable above a collision energy in which the projectile ion velocity is above 1 atomic unit and are generally progressively better for large quantum numbers.

CTMC has also been successfully applied to a number of electron-impact cases. For example, the total and multiply-differential cross-sections for ionization of H, H_2, and He by electron- and positron-impact were calculated and shown to be in quite reasonable agreement with experimental measurements [62] over a wide range of impact energies. Aspects of the total and differential cross-sections not in good agreement in these cases are mostly due to collisions with very small momentum transfers which are better described through quantum perturbation theory (i.e., the Born approximation) [63,64]. Another strenuous test of CTMC for ionization by electron-impact was recently made by comparing the most sophisticated contemporary method, the R-matrix with pseudostates approach, for e + H, Li^{2+}, and B^{4+} in the ground and excited states [65]. For example, significant utility of the CTMC method is its feasibility for systems in high levels of excitation where quantum methods require huge or intractably large close-coupling basis sets.

The total and differential cross-section for excitation in electron-impact of Ar^{7+} has also been calculated with the CTMC approach and shows substantial agreement with quantum mechanical results. Thus, while providing only an approximate treatment as compared to appropriate fully quantum mechanical methods, CTMC has been shown to be applicable to a variety of electron-atom, -ion, and -molecule cases. Here we have used the simplest possible model of the e + CH^+ system in order to test its applicability and to pave the way for more complete, molecular dynamics − like approaches.

In particular, we begin by considering the CH^+ target as a single nucleus with one active electron orbiting with a binding energy equal to the energy required to remove an electron (i.e., CH^+ → C^+ + H^+) selected from the microcanonical distribution as in typical applications of the CTMC method. Electrons of varying impact parameter are then impingent at a fixed kinetic energy within the range presently considered (1 to 1000 eV). After each trajectory, the binding energy of the electron that was initially in the target is computed in order to determine what, if any, reaction has occurred. Specifically, if the target electron and the impingent electron both have positive energy, dissociative ionization has occurred. If the impingent electron is free after the collision and the target electron's energy is greater than that required for dissociation (4.08 eV) then we count this trajectory as corresponding to dissociative excitation. Other channels possible include elastic scattering, electron exchange, or recombination where the target and projectile electrons are both bound to the target core after the collision. By binning each trajectory in this way to compute an impact parameter dependent reaction probability, the total cross-sections for DE and DI can be computed by integrating them over impact parameter. The results of this model are shown in Figure 3 and display reasonable agreement with experiment as described below.

We have also performed several tests of this model by making it more elaborate in incremental steps. For example, we have similar results when more than one active electron is included in the model (the so-called nCTMC method) or when the C and H nuclei are separated by a fixed distance

8

corresponding to their equilibrium internuclear distance in the ground state of CH^+ (~2.1 a.u.). Much more extensive exercise of these and other elaborations of the model will be described in forthcoming work. In these elaborations as well as the present, more simple model the reaction channel probabilities have been determined by comparing the binding energy before and after the collision in order to approximate the energy deposition to the electronic degree of freedom in the system. This energy deposition model is very much in the spirit of how autoionization has been calculated in the nCTMC method [66,67]. In this case, the sum of the binding energies of the n-electrons in the model are compared before and after the collision and if the energy deposited is great enough for an Auger to occur, one or more electrons are considered to have been ejected via autoionization.

4. RESULTS

4.1. Dissociation of CH^+

Absolute cross-sections for electron-impact dissociation of CH^+ ions producing the C^+ fragment for energies up to 100 eV are shown in Figure 2. The present measurements, the sum of the DE and DI channels, are indicated as filled circles and are shown with error bars representing the total absolute uncertainty at a 90%-confidence level. The histogram line represents the storage ring measurements of Amitay et al. [31] for production of C^+ ions. The open squares in Figure 2 represent the measurements of Lecointre et al. [34] for CD^+ dissociation yielding C^+ fragment ions. The dashed and solid curves represent the predictions of Janev and Reiter, from Ref. [21] and the HYDKIN database [46], respectively.

The experimental results of Lecointre et al. [34] are in excellent agreement with the present measurements up to 30 eV, then diverge at higher energies with a factor of two difference at 100 eV. For energies above 15 eV, the energy dependence of the storage ring measurements [31, 32] is similar to that of the present results, but the magnitudes of Forck [32] (not shown) and of Amitay et al. [31] lie about 15% and 25% above the present value for the peak of the cross-section near 40 eV. Considering the large total uncertainty of the earlier data, estimated at 50%, those data are in agreement with the present results. For energies less than 15 eV, however, the present cross-sections tend to remain high as one approaches the dissociation energy of 4.08 eV for ground-state ions, which is consistent with the presence of excited states in the CH^+ ion beam produced in the ECR ion source for our experiment. The ion source used at TSR for the work of Forck and Amitay et al. produced an estimated 60-70% of CH^+ ions in the $a^3\Pi$ metastable state, although after storing the ions for 10-20 s, the estimated population was only 5-10% of the total ion current during the cross-section measurements. The population of the $a^3\Pi$ metastable state could be much higher than 5-10% in the present experiment, and higher ro-vibrational levels within the $a^3\Pi$ state may also be populated.

The measured cross-section is non-zero below the thresholds for vertical transitions from the $X^1\Sigma$ ground and $a^3\Pi$ metastable states at 9.7 eV and 8.6 eV, respectively, suggesting that RDE plays a role in dissociation in the low-energy region. However, one should note that the vertical transition thresholds for the $X^1\Sigma$ and $a^3\Pi$ states will be lowered by the presence of ions in higher v levels. Another mechanism that may contribute at these energies is pre-dissociation through the $b^3\Sigma^-$ following a vertical transition from the $a^3\Pi$ state. The opening of this channel would occur at about 2-5 eV, depending on the ro-vibrational level of the initial $a^3\Pi$ state molecular ion [41].

The empirical cross-sections of Ref. [21] exceed the present data by a factor of 2-4 below 20 eV, suggesting they have overestimated the contribution of RDE for this collision system. Likewise, their sum of DE (DDE and RDE) plus DI exceeds the present measurements by a factor of almost two at 100 eV. However, the HYDKIN data [46] are in much better agreement with the present measurements, although the two sets of data diverge in the 20-50 eV range.

FIG. 2. Absolute cross-sections for the production of C^+ fragment ions by electron-impact dissociation of CH^+ ions as a function of center-of-mass energy. The filled circles are the present measurements with total absolute uncertainties at a 90% confidence level, the open squares and histogram line are the measurements of Refs. [34] and [31], respectively. The dashed curve represents the predictions of Ref. [21] and the solid curve presents the data found in the HYDKIN database [46].

FIG. 3. Absolute cross-sections for the sum of electron-impact dissociative excitation and dissociative ionization of CH^+ ions as a function of center-of-mass energy. The filled circles represent the sum the present measurements for DE+DI producing C^+ fragment ions and the measurements of Ref. [32] for DE producing H^+ fragment ions, both with total absolute uncertainties at a 90% confidence level. The solid and dashed curves represent the predictions of the present molecular dynamics model for DE+DI and DE, respectively.

10

Above the DI threshold of 29 eV [68] the present measurements are the sum of the DE and DI channels producing C^+ fragment ions, although no clear onset of the DI contribution can be seen in Figure 2 for any of the three experimental data sets.

The results of our pilot molecular dynamics plus energy deposition model for this system are shown in Figure 3 (for DE and the sum of DE and DI) along with the experimental results as described in the Figure caption. For about 10 eV and above the theoretical model yields good agreement with the measurements but drops significantly below them for lower energies due to the assumed significant population of metastable ions in the experiments. The theoretical data have been computed for impact energies up to 1000 eV.

4.2. Dissociation of CH_2^+

Absolute cross-sections for electron-impact dissociation of CH_2^+ ions producing the CH^+ and C^+ fragments for energies up to 100 eV are shown in Figs. 4 and 5, respectively. The present measurements, the sum of the DE and DI channels, are indicated as filled circles and are shown with error bars representing the total absolute uncertainty at a 90%-confidence level. Also shown in the figures are the semi-empirical predictions of Janev and Reiter: the solid curve represents data from the HYDKIN database [46] and the dashed curve represents the predictions of Ref. [21].

4.2.1. CH⁺ fragments

The cross-section for the production of CH^+ rises sharply from an observed threshold of about 6 eV (this value is consistent with the DDE threshold of Janev and Reiter [21] given in Table 1) and exhibits a strong peak in the 7-15 eV range, similar to that seen for the dissociation of DCO^+ [69]. For that ion, it was suggested that this peak feature is due to a series of strong vertical transitions to dissociative excited states. There are several bound excited states of CH_2^+ in this energy range (above the dissociation limit) from 1 $^2A_2$ at 6.92 eV to 2 $^2B_1$ at 13.9 eV, that are accessible via allowed transitions from the ground state. These bound states can then pre-dissociate through coupled repulsive states. This process is analogous to excitation-autoionization in electron-impact ionization of atomic ions.

The empirical cross-sections of Ref. [21] for the DDE and DI contributions are shown as the dashed curve in Figure 4. Because of a lack of experimental data for CH_2^+, they do not provide any cross-section estimates for the RDE process, which they refer to as Capture Assisted Dissociation (CAD). The portion of this curve above 50 eV exceeds the measurements by about 60%, suggesting that their empirical formula overestimates the contribution of DI. However, the DE cross-sections for this channel in the HYDKIN database [46] are in better agreement with the present experimental data, although there is a shift in the position of the low-energy peak. The HYDKIN DE cross-sections do not fall off as fast from the peak value as do the present measurements, differing by a factor of two around 30 eV. Above the DI threshold of 30.41 eV [21, 68] the present measurements are the sum of the DE and DI channels producing CH^+ fragment ions, although no clear onset of the DI contribution can be seen in Figure 4.
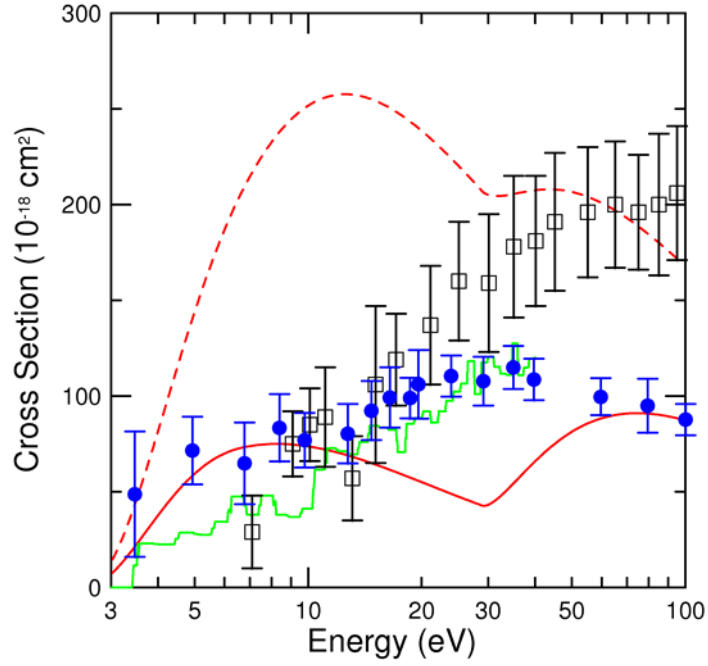
FIG. 4. Absolute cross-sections for the production of CH+ fragment ions by electron-impact dissociation of CH_2^+ ions as a function of center-of-mass energy. The filled circles are the present measurements with total absolute uncertainties at a 90% confidence level, while the dashed curve represents the predictions of Ref. [21] and the solid curve represents the data found in the HYDKIN database [46].
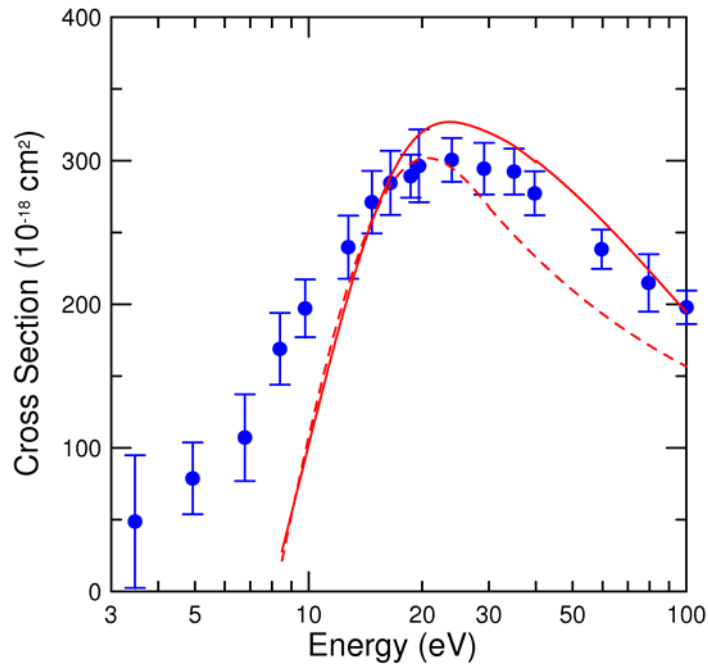

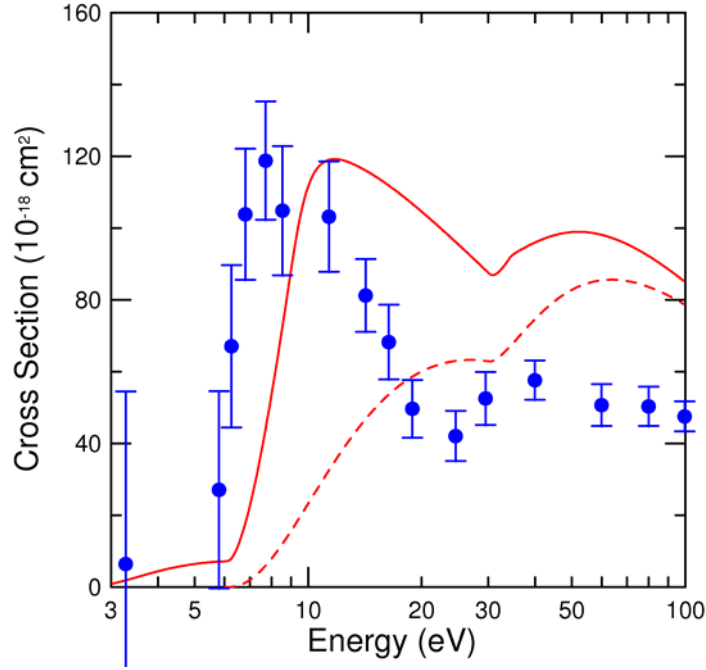FIG. 5. Absolute cross-sections for the production of C+ fragment ions by electron-impact dissociation of CH_2^+ ions as a function of center-of-mass energy. The filled circles are the present measurements with total absolute uncertainties at a 90% confidence level, while the dashed curve represents the predictions of Ref. [21] and the solid curve represents the data found in the HYDKIN database [46].
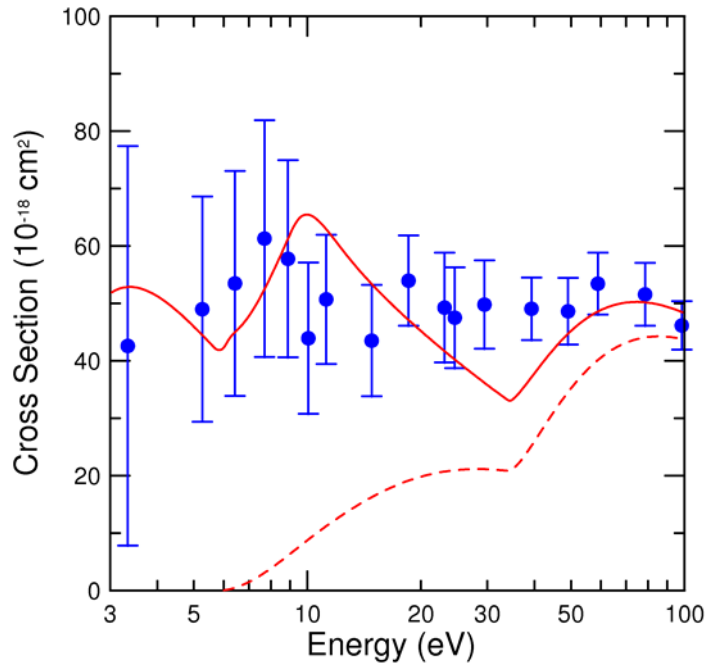
12

4.2.2. C+ fragments

In contrast to the results for the CH+ fragment channel, the cross-section for the C+ fragment channel is relatively flat over the entire energy range of the measurements with no observed threshold. There appears to be a small peak near 8 eV with the cross-section decreasing down to 3 eV, the lowest energy possible with the present electron gun. Extrapolation of this behavior yields a threshold of about 1 eV.

Also shown in Figure 5 are empirical cross-sections of Ref. [21] for the DDE + DI contributions; these are shown as the dashed curve. Their predictions clearly underestimate the experimental results, especially for energies below 50 eV. However, the updated data in the HYDKIN database [46] are in much better overall agreement with the present measurements. The HYDKIN cross-sections exhibit structure not seen in the experimental data, however the experimental uncertainties are large enough below 20 eV so as to obscure any structure in the cross-sections.

Above the lowest DI threshold of 31.5 eV the present measurements are the sum of the DE and DI channels producing C+ fragment ions, although only a slight increase in the cross-section is seen in this region in Figure 5.

It is interesting to note that the cross-sections for the C+ and CH+ channels are practically identical for energies in the 15-100 eV range, despite the dramatic differences in the two channels below 15 eV. For the CH+ channel, the cross-section shows strong DDE contributions just above a threshold of about 6 eV. The C+ channel, however, exhibits a low-energy dependence consistent with RDE contributions with a threshold of about 1 eV. Above 15 eV, both cross-sections appear to be dominated by direct processes, including DI since the lowest DI thresholds for the CH+ and C+ channels are close.

4.3. Dissociation of CH_3^+ and CD_3^+

Absolute measurements of the cross-sections for the production of CD_2^+, CH+ and C+ fragment ions from electron-impact dissociation of the CD_3^+ and CH_3^+ molecular ions are made over a collision energy range from threshold up to 100 eV. The results for the CD_2^+, CH+ and C+ channels are presented as filled circles in Figs. 6, 7, and 8, respectively, with the error bars corresponding to the absolute total expanded uncertainties at a 90%-confidence level. The cross-section data reported represent the sum of all processes through which CD_2^+, CH+, and C+ fragment ions can be produced from dissociation of CD_3^+ and CH_3^+ by electron-impact. These are compared to the empirical predictions of Janev and Reiter [21,46] for the dissociation channels of the CH_3^+ molecular ion as well as preliminary measurements [27,37] on dissociation of CD_3^+. The solid curves in Figs. 6-8 represent data for the sum of DE and DI from the HYDKIN database [46], while the dashed curves represent the DE+DI predictions given in Ref. [21].

4.3.1. CD_2^+ fragments

The measured cross-sections for the production of CD_2^+ fragment ions shown in Figure 6 exhibit two distinct sections, divided by the threshold for dissociative ionization. Below this threshold, only dissociative excitation contributes to the cross-section. The lowest energy measurements suggest a DE threshold of about 5 eV, consistent with the dissociation limit energy D_0 given in Table 1. The cross-section rises quickly to almost its maximum value by an energy equivalent to the vertical transition threshold, E_{th} and then exhibits a broad peak. Two possible explanations exist for this behavior: first, the RDE process contributes significant dissociation above D_0 or, second, excited states of the CD_3^+ target ion effectively lower the dissociation threshold. The $1^3A''$ and $1^3A'$ metastable electronic states lie 3.56 eV and 3.86 eV above the ground state, respectively [70]. The vertical transition threshold for

these states would be less than 3.5 eV; this is not consistent with the observed threshold behavior. However, ions in higher vibrational levels of the CD_3^+ ground electronic state could effectively lower the vertical transition threshold by at least 2 eV.

The CD_3^+ ion is a planar molecule [9] and has two bound electronic states that lie above the dissociation limit: $^1E''$ at 6.46 eV, $^1A_2''$ at 17.4 eV above the ground state [71]. Excitations to these allowed states, followed by pre-dissociation through coupled repulsive states, can enhance the DE cross-sections. The sharp rise from the observed threshold may be due in part to contributions from excitation to the $^1E''$ state; no obvious enhancement to the cross-section from excitations to the $^1A_2''$ state is seen.

The measured cross-sections increase for energies above the DI threshold, reaching values over 50×10^{-18} cm^2 for E $\geq$ 50 eV. Although the DI predictions of Janev and Reiter [21,46] are in good agreement with the experiment, their DDE predictions clearly overestimate the cross-section by factors of two to four. They provided no predictions for the RDE contribution that may be present just above threshold.

FIG. 6. *Absolute cross-sections for the production of CD_2^+ fragment ions by electron-impact dissociation of CD_3^+ ions as a function of center-of-mass energy. The filled circles are the present measurements with total absolute uncertainties at a 90% confidence level, while the dashed curve represents the predictions of Ref. [21] and the solid curve represents the data found in the HYDKIN database [46].*

FIG. 7. Absolute cross-sections for the production of CH^+ fragment ions by electron-impact dissociation of CH_3^+ ions as a function of center-of-mass energy. The filled circles are the present measurements with total absolute uncertainties at a 90% confidence level, while the dashed curve represents the predictions of Ref. [21] and the solid curve represents the data found in the HYDKIN database [46].

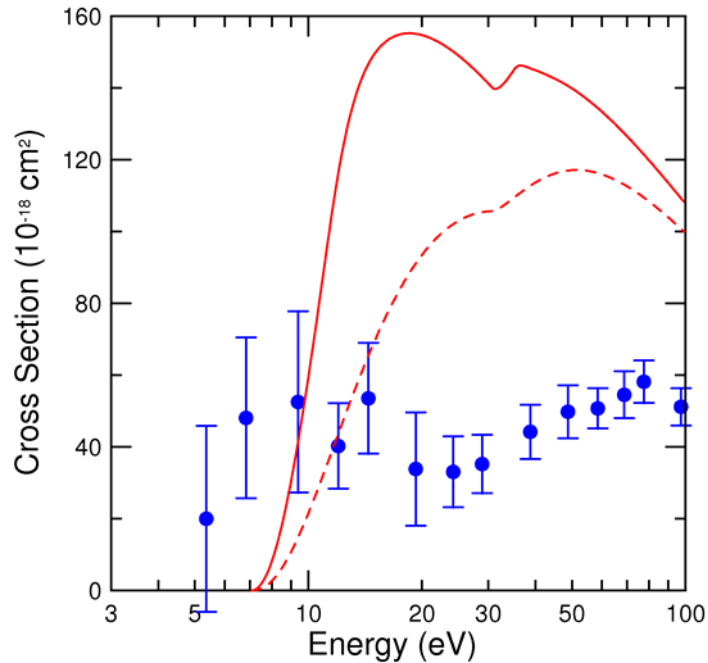FIG. 8. Absolute cross-sections for the production of C^+ fragment ions by electron-impact dissociation of CH_3^+ ions as a function of center-of-mass energy. The filled circles are the present measurements with total absolute uncertainties at a 90% confidence level, while the dashed curve represents the predictions of Ref. [21] and the solid curve represents the data found in the HYDKIN database [46].
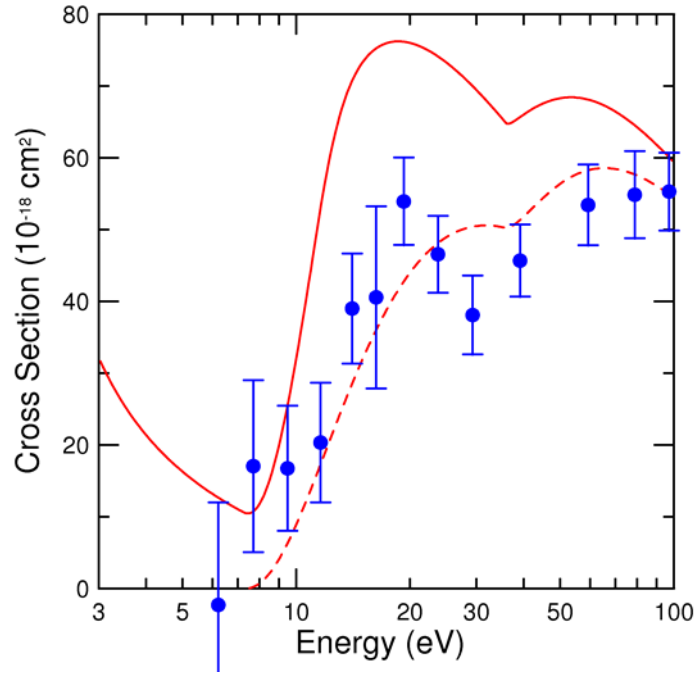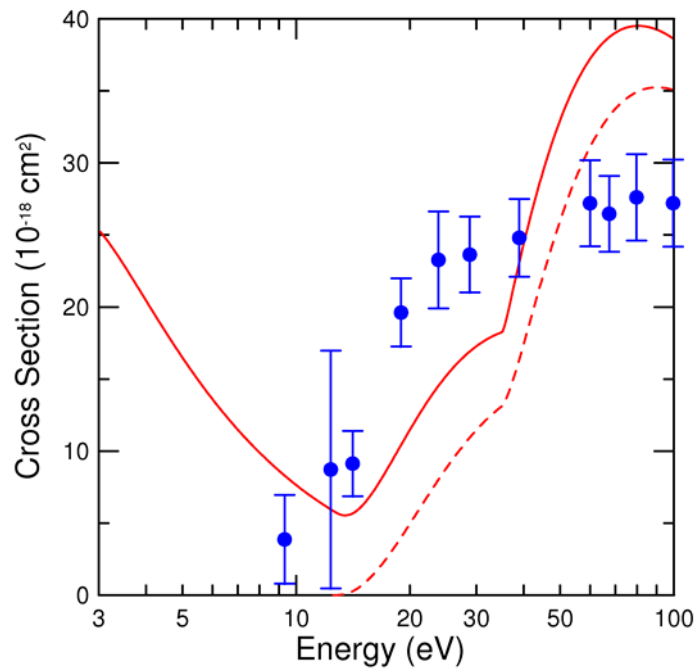
15

4.3.2. CH^+ fragments

The structure of the cross-sections we show in Figure 7 is similar to that observed in our previous measurements on dissociation of DCO^+ by electron-impact producing the CO^+ fragment [69]: a curve with three distinct sections. Rising from a threshold of $\approx 7 \pm 1$ eV, the CH^+ production cross-section peaks at about 20 eV before decreasing and then smoothly rising again above 30 eV.

The first section, which ranges from the observed threshold up to around 12 eV, is characterized by small magnitudes for the measured cross-sections, the maximum being approximately 17×10^{-18} cm^2. This small cross-section at the vertical transition threshold E_{th} indicates that the contribution of both excited states in the CH_3^+ target ions and the RDE process are minimal for this channel, as is any contribution from pre-dissociation through the $^1E^{''}$ state.

Above 12 eV, another rise of the DE cross-section coincides with the opening of the $CH^+ + 2H$ channel. At slightly higher energies, a peak appears in the DE cross-section, rising to a value of about 54×10^{-18} cm^2 near 20 eV. The sharpness of the peak suggests excitation to a single bound state, namely the $^1A_2^{''}$ state, followed by pre-dissociation.

The third region ranges from around 30 eV to 100 eV. The sudden change of slope of the cross-section curve observed at the beginning of this region indicates the opening of the first DI channel. As previously mentioned, our experiment cannot separate the contribution of this individual process to the measured signal. The sum of the DE and DI contributions then rises smoothly to a broad peak of about 54×10^{-18} cm^2.

The semi-empirical predictions of Janev and Reiter [21,46] for the production of CH^+ fragment ions are also shown in Figure 7. The DE+DI predictions of Ref. [21] are in excellent agreement with the experimental results and do not include any contributions of RDE. The cross-sections from the HYDKIN database [46], however, exceed the experimental results by about 50% near the DE peak around 20 eV, at least partly because of the included RDE contribution at the lowest energies. Their formulation does not account for the contribution of excitations to bound excited states followed by pre-dissociation, such as the contribution of the $^1A_2^{''}$ state evident for this channel.

4.3.3. C^+ fragments

The energy-dependent cross-sections for the production of C^+ fragments are shown in Figure 8 and, unlike the data observed for the production of CD_2^+ and CH^+, do not exhibit any noticeable structure. The cross-section is not zero below the predicted vertical transition threshold energy of the first DE process, 12.65 eV (see Table 1). The observed threshold, $\approx 9 \pm 1$ eV, is obtained by extrapolation of data below 14 eV. Nevertheless, the observed threshold energy is comparable to the dissociation energy limit of this channel. This may indicate that, as for the CD_2^+ channel, in the threshold region, C^+ is produced either through RDE mechanisms involving Rydberg states of CH_3^{**} or vertical transitions to repulsive states from higher vibrational levels of the ground state.

The cross-section is essentially featureless over the range of the present measurements, with only a slight inflection that is probably associated with the opening of the second DE channel, namely $C^+ + 3H$, with an expected vertical transition threshold of about 16 ± 1 eV, assuming a similar KER as for the lower DE channel (see Table 1). In addition, one cannot rule out a small contribution from excitation to the $^1A_2^{''}$ bound state at 17.4 eV followed by pre-dissociation. A slight increase in the dissociation cross-section is observed above the DI thresholds, although no clear onset of these contributions is seen in the measurements.

Figure 8 also shows the semi-empirical predictions of Janev and Reiter [21,46] for the production of C^+ fragment ions.. In contrast to the data for the other two fragment channels, their DI

predictions seem to overestimate the experimental data. Also, their predictions for DDE underestimate the measured cross-sections by about 20-40%. The HYDKIN cross-sections [46] also include RDE contributions at low energy, however the large uncertainties on the experimental cross-sections in this region prevent us from a definitive comparison.

It should be noted that measurements on electron-impact dissociation of CD_n^+ were also carried out at Louvain-la-Neuve and preliminary results for n=3 and n=4 presented at two conferences [27,37]. A comparison with the present results yields good agreement for the CH^+ channel, including the peak in the DE cross-section here attributed to excitation to the $^1A_2^{''}$ bound state at 17.4 eV followed by pre-dissociation. The overall agreement for the C^+ channel is fair. The shape and magnitude of their results for CD_2^+ channel differs greatly from the present results.

5. CONCLUSIONS

Absolute cross-sections for electron-impact dissociation of CH_x^+ (x=1,2,3) ions producing CH_y^+ (y=0,1,2) fragment ions have been measured with the ORNL crossed-beams apparatus with a total expanded uncertainty of approximately 11% near the peak for most of the dissociation channels.

In comparison with the present experimental results for dissociation of CH^+ producing C^+ ions, the storage ring measurements of Forck [32] and Amitay *et al.* [31] are about 15-25% higher than the present results, but the discrepancy is within the combined experimental uncertainties. The experimental cross-sections of Lecointre *et al.* [34] are in excellent agreement for energies below 30 eV, but diverge from the present data for energies above 30 eV, reaching a difference of a factor of two at 100 eV. The low-energy behavior of the present data suggests a significant population of target CH^+ ions in excited states, both electronic and vibrational, as expected for an ECR ion source.

Because no other experimental or theoretical data exist for the dissociation of CH_2^+ ions yielding CH^+ and C^+ fragments, the present results are compared with the empirical cross-sections of Janev and Reiter [21,46]. The agreement is very good for the C^+ fragment channel when using the latest data available in the HYDKIN database [46]; the agreement for the CH^+ is not as good, partly because of a strong peak observed just above threshold in the 7-15 eV range that is not reproduced very well by their formulas for RDE and DDE contributions.

The obtained results are compared to other available data from empirical predictions [21,46] and from electron-impact dissociation of CD_3^+ [27]. For the formation of CH^+ fragment from the dissociation of CH_3^+, good agreement is found between the present cross-sections and semi-empirical fits of Janev and Reiter [21,46] as well as with measurements reported on CD_3^+ [27], especially if one omits the RDE contributions given in the HYDKIN database [46]. However, such good agreement is not observed for the production of the CD_2^+ and C^+ fragments.

Future measurements on the dissociation of CH_x^+ ions must focus on the contributions of ro-vibrationally excited ions by reducing their population in the target ion beam by utilizing colder sources of ions and by storing the ions for times long enough for radiative relaxation. Only then can detailed comparisons be made between experiments and with both theoretical and semi-empirical predictions.

Finally, we find that the comparison between experimental data for CH^+ and our pilot molecular dynamics plus energy deposition model is good enough to encourage further work to develop and apply the molecular dynamics approach for electron – hydrocarbon ion systems and possibly for electron – hydrocarbon neutrals. The goal is to provide a relatively simple theoretical model that can be applied across a wide range of impact energies and systems.

REFERENCES

[1] TAWARA, H., in Atomic and Molecular Processes in Fusion Plasmas, (JANEV, R.K., Ed.) Plenum, New York (1995) 461-496.

[2] JANEV, R.K., KATO, T., WANG, J.G., Catalytic mechanism of divertor plasma recombination provided by hydrocarbon impurities, Phys. Plasmas **7** (2000) 4364.

[3] LUQUE, J., JUCHMANN, W., BRINKMAN, E.A., JEFFRIES, J.B., Excited state density distributions of H, C, C_2, and CH by spatially resolved optical emission in a diamond depositing dc-arcjet reactor, J. Vac. Sci. Technol. A **16** (1998) 397.

[4] ZHU, X.D., ZHAN, R.J., ZHOU, H.Y., WEN, X.H., LI, D., Optical properties of bias-induced CH_4–H_2 plasma for diamond film deposition , J. Vac. Sci. Technol. A **20** (2002) 941.

[5] DALGARNO, A., in Atomic Processes and Applications (BURKE, P.G., MOISEIWITSCH, B.L., Eds) North-Holland, Amsterdam (1976) 109-132.

[6] STANCU, G.D., RÖPCKE, J., DAVIES, P.B., Line strengths and transition dipole moment of the ν_2 fundamental band of the methyl radical, J. Chem. Phys. **122** (2005) 14306.

[7] YU, H.G., SEARS, T.J., Vibrational energy levels of methyl cation, J. Chem. Phys. **117** (2002) 666.

[8] FEUCHTGRUBER, H., HELMICH, F.P., VAN DISHOECK, E.F., WRIGHT, C.M., Detection of Interstellar CH_3^*, Astrophys. J. **535** (2000) L111.

[9] CROFTON, M.W., JAGOD, M.F., REHFUSS, B.D., KREINER, W.A., OKA, T., Infrared spectroscopy of carbo-ions. III. v3 band of methyl cation CH^{+3}, J. Chem. Phys. **88** (1988) 666.

[10] LIU, X., GROSS, R.L., SUITS, A.G., Heavy Electron Photoelectron Spectroscopy: Rotationally Resolved Ion Pair Imaging of CH^{3+} , Science **294** (2001) 2527.

[11] MARYNICK, D.S., DIXON, D.A., Electron affinity of the methyl radical: Structures of CH_3 and CH_3^-, Proc. Natl. Acad. Sct. **74** (1977) 410.

[12] CROFTON, M.W., KREINER, W.A., JAGOD, M.F., REHFUSS, B.D., OKA, T., Observation of the infrared spectrum of methyl cation CH_+^3, J. Chem. Phys. **83** (1985) 3702.

[13] HAYAKAWA, S., FENG, B., COOKS, R.G., Differentiation of isomeric $C_3H_4^+$ ions and T → V energy partitioning in surface-induced dissociation, Int. J. Mas. Spectrom. Ion Proc. **167** (1997) 525.

[14] CHUPKA, W.A., LIFSHITZ, C., Photoionization of the CF3 Free Radical, J., Chem. Phys. **48**, (1967) 1109.

[15] HOGNESS, T.R., KVALNES, H.M., The Ionization Processes in Methane Interpreted by the Mass Spectrograph, Phys. Rev. **32** (1928) 942.

[16] SMITH, L.G., Ionization and Dissociation of Polyatomic Molecules by Electron Impact. I. Methane, Phys. Rev. **51** (1937) 263.

[17] WEITZEL, K.M., et al., High-resolution pulsed field ionization photoelectron–photoion coincidence study of CH_4: Accurate 0 K dissociation threshold for CH_3^+, J. Chem. Phys. **111** (1999) 8267.

[18] HIPPLE, J.A., STEVENSON, D.P., Ionization and Dissociation by Electron Impact: The Methyl and Ethyl Radicals, Phys. Rev. **63** (1943) 121.

[19] ITZHAK, B., et al., Fragmentation of CH_4 caused by fast-proton impact, Phys. Rev. A **47** (1993) 3748.

[20] ALMAN, D.A., RUZIC, D.N., A hydrocarbon reaction model for low temperature hydrogen plasmas and an application to the Joint European Torus, Phys. Plasmas **7** (2000) 1421.

18

[21] JANEV, R.K., REITER, D., Collision processes of hydrocarbon species in hydrogen plasmas: I. The methane family, Report FZ-Jülich Jül 3966, pub. Feb. 2002, updated Dec. 2004 (Forschungszentrum-Jülich, Jülich, Germany), ISSN 0944- 2952. Copies may be ordered from Forschungszentrum Jülich GmbH, Zentralbibliothek, D-52435 Jülich, Bundesrepublik Deutschland.

[22] JANEV, R.K., REITER, D., Collision processes of CH_y and CH_y^+ hydrocarbons with plasma electrons and protons, Phys. Plasmas **9** (2002) 4071.

[23] VIGGIANO, A.A., EHLERDING, A., ARNOLD, S.T., LARSSON, M., Dissociative recombination of hydrocarbon ions, J. Phys. Conf. Ser. **4** (2005) 191.

[24] MITCHELL, J.B.A., et al., Branching ratios for the dissociative recombination of hydrocarbon ions, J. Phys. Conf. Ser. **4** (2005) 198.

[25] BELIĆ, D.S., JURETA, J.J., CHERKANI, H., DEFRANCE, P., in BPU-5 Fifth General Conference of the Balkan Physical Union, Vrnjačka Banja, Serbia and Montenegro (2003), 317.

[26] POPOVIĆ, D.B., DJURIĆ, N., HOLMBERG, K., NEAU, A., DUNN, G.H., Absolute cross-sections for H^+ formation from electron-impact dissociation of C_2H^+ and $C_2H_2^+$, Phys. Rev. A **64** (2001) 052709.

[27] LECOINTRE, J., HASSANI, H.C., JURETA, J.J., BELIĆ, D.S., DEFRANCE, P., in XXIV Conference on the Physics of Electronic and Atomic Collisions - ICPEAC, Rosario, Argentina (2005).

[28] ZONG, W., et al., Resonant Ion Pair Formation in Electron Collisions with Ground State Molecular Ions, Phys. Rev. Lett. **83** (1999) 951.

[29] LE PADELLEC, A., et al., Resonant ion-pair formation in the recombination of no+ with electrons: cross-section determination, Phys. Rev. A **64** (2001) 12702.

[30] DJURIĆ, N., et al., Resonant ion-pair formation and dissociative recombination in electron collisions with ground-state HF^+ ions, Phys. Rev. A **64** (2001) 22713.

[31] AMITAY, Z., et al., in Applications of Accelerators in Research and Industry (Duggan J.L., Morgan I.L. Eds), AIP Press, New York, (1997) 51.

[32] FORCK, P., Ph.D. thesis, Ruprech-Karls-Universität Heidelberg (1994).

[33] DJURIĆ, N., CHUNG, Y.-S., WALLBANK, B., DUNN, G.H., Measurement of light fragments in dissociative excitation of molecular ions: CD^+, Phys. Rev. A **56** (1997) 2887.

[34] LECOINTRE, J., et al., Absolute cross-sections and kinetic energy release distributions for electron impact ionization and dissociation of CD^+, J. Phys. B **40** (2007) 2201.

[35] DJURIĆ, N., ZHOU, S., DUNN, G.H., BANNISTER, M.E., Electron-impact dissociative excitation of CD_n^+ (n=2-5): Detection of light fragment ions D^+ and D_2^+, Phys. Rev. A **58** (1998) 304.

[36] LARSON, A., et al., Branching Fractions in Dissociative Recombination of CH_2^+, Astrophys. J. **505** (1998) 459.

[37] LECOINTRE, J., CHERKANI, H., JURETA, J.J., BELIĆ, D.S., DEFRANCE, P., in Proc. 22nd Symposium on Physics of Ionized Gases - SPIG, (National Park Tara, Bajna Bata, Serbia and Montenegro, 2004), (HADZIJEVSKI, L., Ed) Beograd, Vinca Institute of Nuclear Sciences, (2004) 63.

[38] AMITAY, Z., et al., Dissociative recombination of CH^+: Cross-section and final states, Phys. Rev. A **54** (1996) 4032.

[39] VEJBY-CHRISTENSEN, L., ANDERSEN, L.H., HEBER, O., KELLA, D., PEDERSEN, H.B., Complete Branching Ratios for the Dissociative Recombination of H_2O^+, H_3O^+, and CH_3^+, Astrophys. J. **483** (1997) 531.

[40] LIAS, S.G., "Ionization Energy Evaluation" in NIST Chemistry WebBook, NIST Standard Reference Database Number 69, (LINSTROM, P.J., MALLARD, W.G., Eds) June 2005, National Institute of Standards and Technology, Gaithersburg MD, 20899 (http://webbook.nist.gov).

[41] BANNISTER, M.E., et al., Electron-impact dissociation of CH^+ ions: Measurement of C^+ fragment ions, Phys. Rev. A **68** (2003) 042714.

[42] VANE, C.R., BAHATI, E.M., BANNISTER, M.E., THOMAS, R.D., Electron-impact dissociation of CH_2^+ ions: Measurement of CH^+ and C^+ fragment ions, Phys. Rev. A **75** (2007) 052715.

[43] BAHATI, E.M., et al., Electron-impact dissociation of CD_3^+ and CH_3^+ ions producing CD_2^+, CH^+, and C^+ fragment ions, Phys. Rev. A **79** (2009) 52703.

[44] GREGORY, D.C., MEYER, F.W., MÜLLER, A., DEFRANCE, P., Experimental cross-sections for electron-impact ionization of iron ions: Fe^{5+}, Fe^{6+}, and Fe^{9+}, Phys. Rev. A **34** (1986) 3657.

[45] BANNISTER, M.E., Absolute cross-sections for electron-impact single ionization of Ne^{q+} (q=2,4–6) ions, Phys. Rev. A **54** (1996) 1435.

[46] HYDKIN online database, http://www.eirene.de/eigen/index.html.

[47] MEYER, F.W., in Trapping Highly Charged Ions: Fundamentals and Applications, (GILLASPY, J., Ed) Nova Science Publishers, Huntington, New York (2001) 117.

[48] ORNELLAS, F.R., MACHADO, F.B.C., A theoretical study of the infrared transition matrix elements for the X $^1\Sigma+$ state of the CH^+ and CD^+ molecules J. Chem. Phys. **84** (1986) 1296.

[49] BEAR, A., Ph.D. thesis, Weizmann Institute of Science, Rehovot, Israel (2000).

[50] BRINKMANN, N.R., RICHARDSON, N.A., WESOLOWSKI, S.S., YAMAGUCHI, Y., SCHAEFER III, H.F., Characterization of the $\tilde{X}^2A_1$ and $\tilde{a}^4A_2$ electronic states of CH_2^+ Chem. Phys. Lett. **352** (2002) 505.

[51] MUL, P.M., MITCHELL, J.B.A., D'ANGELO, V.S., DEFRANCE, P., MCGOWAN, J.W., FROELICH, H.R., Merged electron-ion beam experiments. IV. Dissociative recombination for the methane group CH^+,...,CH^{5+}, J. Phys. B **14** (1981) 1353.

[52] YAMADA, I., et al., Electron Impact Ionization of C^+, N^+ and P^+ Ions, J. Phys. Soc. Japan **58** (1989) 1585.

[53] TAYLOR P.A., DUNN, G.H., Absolute cross-sections and polarization for electron-impact excitation of the K and H resonance lines of the Ca^+ ion, Phys. Rev. A **8** (1973) 2304.

[54] TAYLOR, P.A., DOLDER, K.T., KAUPPILA, W.E., DUNN, G.H., Measurement of spiraling in a magnetically confined electron beam for use in collision studies, Rev. Sci. Instrum. **45** (1974) 538.

[55] BELIĆ, D.S., FALK, R.A., DUNN, G.H., GREGORY, D., CISNEROS, C., CRANDALL, D.H., Bull. Am. Phys. Soc. **27** (1981) 49.

[56] See, for example, HARRISON, M.F.A., The determination of atomic collision cross-sections using crossed electron and ion beams (and some sources of error in such experiments), Brit. J. Appl. Phys. **17**(1966) 371.

[57] GREGORY, D.C., DITTNER, P.F., CRANDALL, D.H., Absolute-cross-section measurements for electron-impact ionization of triply charged inert-gas ions: Ne^{3+}, Ar^{3+}, Kr^{3+}, and Xe^{3+}, Phys. Rev. A **27** (1983) 724.

[58] SIMION 3D, Version 6.0, DAVID DAHL, INEL-95/0403 (1995).

[59] ABRINES, R., PERCIVAL, I.C., Classical theory of charge transfer and ionization of hydrogen atoms by protons, Proc. Phys. Soc. Lond. **88** (1966) 861.

[60] OLSON, R.E., SALOP, A., Charge-transfer and impact-ionization cross-sections for fully and partially stripped positive ions colliding with atomic hydrogen, Phys. Rev. A **16** (1977) 531.

[61] BECKER, R.L., MACKELLAR, A.D., Theoretical initial l dependence of ion-Rydberg-atom collision cross-sections, J. Phys. B **17** (1983) 3923.

[62] SCHULTZ, D.R., MENG, L., OLSON, R.E., Classical description and calculation of ionization in collisions of 100 eV electrons and positrons with He and H_2, J. Phys. B **25** (1992) 4601.

[63] SCHULTZ, D.R., OLSON, R.E., REINHOLD, C.O., GEALY, M.W., KERBY, G.W., HSU, Y-Y., RUDD, M.E., Ejected-electron spectra in proton-atomic hydrogen collisions, J. Phys. B **24** (1991) L599.

[64] REINHOLD, C.O., BURGDORFER, J., The classical limit of ionization in fast ion-atom collisions, J. Phys. B **26** (1993) 3101.

[65] GRIFFIN, D.C., et al., The validity of classical trajectory and perturbative quantal methods for electron-impact ionization from excited states in H-like ions , J. Phys. B **38** (2005) L199.

[66] OLSON, R.E., ULLRICH, J., SCHMIDT-BOCKING, H., Multiple-ionization collision dynamics, Phys. Rev. A **39** (1989) 5572.

[67] SCHULTZ, D.R., et al., Coincident charge state production in F^{6+}+Ne collisions, J. Phys. B **23** (1990) 3839.

[68] ROSENSTOCK, H. M., DRAXL, K., STEINER, B.M., HERRON, J.T., Energetics of gaseous ions, J. Chem. Phys. Ref. Data **6** (Suppl. 1) (1977) 1.

[69] BAHATI, E.M., THOMAS, R.D., VANE, C.R., BANNISTER, M.E., Electron-impact dissociation of $D^{13}CO^+$ molecular ions to $^{13}CO^+$ ions, J. Phys. B **38** (2005) 1645.

[70] XI, H.W., HUANG, M.-B., CHEN, B.-Z., LI, W.-Z., F-Loss and H-Loss Dissociations in Low-Lying Electronic States of the CH_3F^+ Ion Studied Using Multiconfiguration Second-Order Perturbation Theory, J. Phys. Chem. A **109** (2005) 9149.

[71] BLINT, R.J., MARSHALL, R.F., WATSON, W.D., Calculations of the lower electronic states of CH^{3+} - A postulated intermediate in interstellar reactions, Astrophys. J. **206** (1976) 627.

ASPECTS OF THE CONSTRUCTION OF POTENTIAL ENERGY SURFACES FOR REACTIVE DYNAMICS

B. J. BRAAMS

Department of Chemistry and Emerson Center for Scientific Computation, Emory University, Atlanta, GA 30322, USA

Abstract

The construction of full-dimensional fitted potential energy surfaces suitable for reaction dynamics simulations is discussed. We briefly review the use of polynomial basis functions that are invariant under the full molecular permutation symmetry group and describe our approach to sampling the configuration space.

1. INTRODUCTION

Graphite is almost universally used as a first-wall material in present tokamak experiments, and as a result hydrocarbon molecules are a common pollutant in tokamak edge plasma. They enter the plasma as CH_4, C_2H_4, or some other member of the C_mH_n family ($m \leq 3$ normally) and then undergo charge exchange, excitation, ionization, and breakup due to reactions with electrons and hydrogen ions; in the cold and dense divertor region also reactions with H, H_2, H_2^+ and negative ions are important. Modelling of the plasma and interpretation of measurements is critical for the final design of ITER and a future DEMO in view of the concern over tritium co-deposition with carbon on the first wall and in the divertor region. This modelling requires a comprehensive database of rate coefficients and cross-sections for these reactions. The present paper describes some key mathematical tools towards the construction of such a database.

The starting point for molecular dynamics studies of (plasma-)chemical reactions is the Born-Oppenheimer approximation according to which the nuclei of the system move in a force field for which the potential is obtained by solution of the electronic Schrödinger equation at the instantaneous nuclear configuration. In view of the computational cost of *ab initio* electronic structure calculations it is extremely attractive to perform the trajectory simulations with use of an analytical approximation to the potential energy. The potential energy surface is a function of all nuclear coordinates simultaneously and so, after taking into account invariance under translation and rotation, of $3N$-6 variables if there are N nuclei. In reactive dynamics chemical bonds are created and broken, possibly many times in a single trajectory, and a fitted potential energy surface must normally be full-dimensional and accurate over widely disparate regions of configuration space. Already for systems of 4 or 5 atoms this poses difficult problems of function fitting in many dimensions.

In recent years, in joint work with Joel Bowman of Emory University, we have developed an approach to constructing fitted potential energy surfaces (PESs) and dipole moment surfaces (DMSs) that relies on mathematical *Invariant Theory* and on computer algebra to construct a linear basis for the approximation space for expanding the PES or DMS. These surfaces have then been used in studies of chemical reactions, photodissociation and recombinative dissociation, and molecular spectroscopy. Systems for which full-dimensional potential energy surfaces were constructed, for the purpose of reactive dynamics or spectroscopic studies, include protonated methane, CH_5^+ [1], the vinyl cation, $C_2H_3^+$ [2], the water dimer, $(H_2O)_2$ [3], protonated dimer, $H_5O_2^+$ [4], and trimer, $(H_2O)_3$ [5], malonaldehyde, $H_4C_3O_2$ [6], and others. Very recently a start has been made to making these and other fitted potential energy surfaces available through a web interface [7].

Section 2 of this paper provides an overview of the mathematical aspects of our approach to fitting potential energy surfaces. In section 3 we describe the multiple ways by which we sample the high-dimensional configuration space. Section 4 provides some outstanding issues and a conclusion.

The present paper describes only our own work on potential energy surfaces (a broader review is in preparation). However, one important early body of work must be mentioned. In the late 1970s and 1980s John Murrell and coworkers [8] developed an approach to potential energy surfaces that, like our present approach, was based on permutationally invariant polynomials and a many-body expansion. Due to limitations of computer power their work was limited to 3- and 4-atom systems, and for whatever reason there was not over the subsequent years a steady development of that approach towards larger and more complicated systems. We provided a fresh start and developed the method to a level where it can be applied to systems of 7 and more atoms.

2. REPRESENTATION OF THE POTENTIAL

In our work the potential energy is represented via an expansion in basis functions, with the coefficients determined by solution of a least-squares system of equations for which *ab initio* electronic structure calculations provide the right hand side. The basis functions are defined globally as functions of all the internuclear distances and each basis function is invariant under the complete molecular permutation symmetry group. A full or a partial many-body expansion is incorporated in the model. The remainder of this section describes the common features of our potential energy surfaces.

Let us first establish some notation. We consider a molecular system composed of N atoms, indexed by $S=\{i:1\leq i\leq N\}$. The atoms are of K kinds, indexed by $\{k:1\leq k\leq K\}$, and we let S_k denote the index set for the atoms of the k-th kind; thus, $S=S_1\cup\ldots\cup S_K$ (disjoint union). Let n_k denote the number of atoms of the k-th kind, so $n_k=|S_k|$ and $N=n_1+\ldots+n_K$.

The geometry of the molecule is specified by $3N$ coordinates. We will normally use the letter X to denote a geometry, and then $x(i)$ denotes the coordinates (in R^3) of the i-th nucleus. The internuclear distances are denoted by $r(i,j)=\|x(i)-x(j)\|$ or collectively by r (so r has $N(N-1)/2$ components). If X is a geometry and if I is a subset of the indices, $I\subseteq S$, then X_I denotes the geometry of the subsystem containing just the nuclei indicated by the index set I. This subsystem contains $N'=|I|$ atoms and the composition is described by the numbers $n'_k=|I\cap S_k|$ ($1\leq k\leq K$), so $N'=n'_1+\ldots n'_K$. We use the notation $n'=\text{comp}(I)$ to denote this integer vector.

Generally speaking a many-body expansion of the potential energy $V(X)$ is a representation $V(X)=\sum_I F_I(X_I)$; a sum of functions of geometries of subsystems, and this sum might be truncated at some maximum value of $|I|$. Because of the required invariance under the molecular permutation symmetry group we let the functions F_I be the same for all index sets that have the same composition, comp(I), and so we write:

$$V(X) = \sum_I \tilde{V}_{comp(I)}(X_I)$$

or alternatively using a double sum:

$$V(X) = \sum_{n'\leq n}\sum_{comp(I)=n'}\tilde{V}_{n'}(X_I)$$

$\tilde{V}_{n'}$ is called an N'-body term where $N'=n'_1+\ldots+n'_K$. The structure of the individual functions $\tilde{V}_{n'}$ is yet to be described, but first a few comments are in order regarding the nature of the many-body expansion.

A true first-principles many-body expansion would be constructed sequentially: the one-body terms are free atom energies, the two-body terms are the two-body potentials shifted to vanish at dissociation, and generally a k-body potential must tend to 0 for any dissociation of the k-atom system, so whenever some internuclear distance in the k-atom system tends to infinity. Our many-body expansions are not obtained sequentially. Even when we use a full many-body expansion, including all terms up to the N-body ones, we fit all those terms simultaneously to one large dataset. (We only fix

the one-body terms in advance.) Moreover, in much of our work we only use a partial many-body expansion; for example, an expansion containing 2-body terms and a single N-body term. In this case the N-body term is not required to vanish at dissociation.

The many-body terms $V_n(X)$ are expressed ultimately as functions of the internuclear distances. This guarantees invariance under the point group operations: translation, rotation, and inversion. For a given geometry X let r denote the vector (or ordered sequence) of internuclear distances and define "Morse variables" $y=\exp(-r/\lambda)$ where λ is a parameter and the expression is understood component-wise. Also, let $rmsd(X)$ denote the root mean square internuclear distance within the cluster (of size k):

$$rmsd(X) = ((\sum_{i<j} r(i,j)^2)/(k(k-1)/2))^{1/2}$$

Then we use a representation that is a polynomial in the Morse variables times a damping function:

$$\tilde{V}_n(X) = P_n(y) * damp_n(rmsd(X))$$

The coefficients of the polynomial P_n are to be determined by least-squares fitting. (As said, fitted simultaneously with the coefficients of the polynomials for other terms in the many-body expansion.) Polynomial $P_n(y)$ is made explicitly invariant under the molecular permutation symmetry group for the composition n acting on the variable y, in a manner to be described below. For a proper many-body term the damping function $damp_n$ tends to 0 as $rmsd(X)$ tends to ∞. We choose a form that goes smoothly to 0 at a finite distance, a:

$$damp_n(s) = (\max(0,1-s/a))^3$$

(The exponent 3 is a bit arbitrary; we have used other values too.) For the two-body terms we include in the damping function also a factor $1/s$, so that the fitted potential energy may tend to infinity at small internuclear distance. The nonlinear parameter λ is given a value in the vicinity of 2 bohr, and the nonlinear parameter a is given a value in the vicinity of 8 bohr for a proper many-body term, but $a=\infty$ for the N-body term if we are not using a full many-body expansion (in which case $damp_n(s)=1$ for all s).

The polynomial $P_n(y)$ is explicitly invariant under the permutation symmetry group for molecules of composition n. This group is a direct product of symmetric groups, $G=Sym(n_1)*...*Sym(n_K)$, where $Sym(m)$ denotes the group of all permutations of the set $\{0,...,m-1\}$; the factor $Sym(n_k)$ acts on the indices of the atoms of the k-th kind. Group G acts on pairs of indices in the natural way, and hence on $R^{N(N-1)/2}$ by permutation of the basis. For element $\pi \in G$:

$$(\pi.y)(i,j) = y(\pi^{-1}i, \pi^{-1}j)$$

(It has to be π^{-1} on the right hand side to make the group composition law come out right).

In order to develop a compact representation of a basis for the vector space of invariant polynomials (up to some maximum total degree) we rely on computational invariant theory [9] and on the Magma computer algebra system [10]. The key elements are common to the theory of invariant polynomials for any finite group acting on any finite-dimensional real or complex vector space (and in further generality that won't concern us here). In mathematical language the fundamental property is that the algebra of invariant polynomials is finitely generated in the Cohen-Macaulay form of a free finite-dimensional module over a polynomial ring. [9, Ch. 3]. The generators of that polynomial ring are called primary invariants and the basis for the module is formed by what are called secondary invariants. What this means for our application is that, given the group G acting on the vector space

24

R^d, there exists a family of d invariant polynomials p_i ($1 \leq i \leq d$), called the primary invariant polynomials, and another family of invariant polynomials q_α, called the secondary invariant polynomials, such that every invariant polynomial f has a unique representation in the form

$$f(x) = \sum_\alpha poly_\alpha(p_1(x),...,p_d(x)) * q_\alpha(x)$$

Here, $poly_\alpha$ is an arbitrary polynomial, not restricted by symmetry considerations. The number of secondary invariant polynomials is finite and can be computed via the Molien series; [9, Ch. 3]. A small example that exhibits this structure clearly is the following: the vector space is R^2 on which acts the two-element group G that is generated by reflections, $(x,y) \rightarrow (-x,-y)$. We want to describe the polynomials of (x,y) that are invariant under G. Clearly a polynomial of (x,y) is invariant if and only if every non-zero monomial term, $c(i,j)x^i y^j$, is of even total degree. We may divide these non-zero terms into two classes, those for which i and j are both even and those for which i and j are both odd. Terms with i and j both even may be collected into a polynomial of x^2 and y^2, and terms with i and j both odd may be collected into xy times such a polynomial. An appropriate choice of primary and secondary invariants is therefore: $p_1(x,y)=x^2$, $p_2(x,y)=y^2$, $q_1(x,y)=1$, and $q_2(x,y)=xy$.

Further small examples can be worked out by hand, but already for the X_5 molecule (five identical atoms, whatever they be) the use of computer algebra is essential. We have used the Magma computer algebra system, which has excellent coverage in the area of representation theory, to develop the invariant polynomial approximation bases for almost all possible molecular symmetry groups of at most 10 atoms; all equal, all distinct, or anything in between. (The present exceptions are the X_6Y_4 system and systems that have 8 or more identical atoms.) The Magma output is converted into Fortran code and the result has been assembled into a large library of invariant polynomial basis routines. Although these codes have not been published, they have been quite widely shared already. Prospective users may contact the author.

3. SAMPLING THE CONFIGURATION SPACE

A fitted potential energy surface is constructed from a database of *ab initio* energies. The key tools for our sampling strategies are molecular dynamics (MD) and diffusion Monte Carlo (DMC) simulations and a broad search for configurations where the PES is stationary; therefore the sampling of configuration space alternates with the improvement of the fitted surface.

3.1. Start-up

The first step towards the construction of a surface for a new system is to sample very broadly the configuration space, and this may be done by molecular dynamics using whatever cheap potential energy method is at hand. We have used *ab initio* molecular dynamics based on the Hartree-Fock or a density functional theory (DFT) method on a minimal one-electron basis, but also a semi-empirical method or even a mechanical model is suitable. We have used even more haphazard techniques for initial sampling, then fitted a surface based on a minimal basis Hartree-Fock or DFT method, and then run molecular dynamics on that preliminary surface to get the first proper sample of configurations for our better *ab initio* calculations. In any case, as far as computer effort is concerned the start-up phase towards constructing a surface is trivial. The main concern is that the initial conditions for the MD runs ensure that all the relevant potential energy basins are visited.

3.2. Iterative improvement

We now describe the, sometimes arduous, process of improving a potential energy surface on the basis of a good, but still easily affordable, *ab initio* method. In our present work for first-row systems the selected method is most often DFT with use of the b3lyp functional, and using the aug-cc-pVTZ basis if there are not more than 2 heavies, else the cc-pVTZ basis.

Two natural methods to sample the configuration space are molecular dynamics and diffusion Monte Carlo. Molecular dynamics can be done at any energy (trajectories are terminated when the system dissociates), and DMC can be done at artificially reduced nuclear masses in order to sample higher-energy regions of the potential. The two techniques have different character as concerns the range of configurations visited, and neither one is adequate. Molecular dynamics, at some thermal range of energies, samples in essence a Boltzmann distribution for the potential, so a density proportional to $\exp(-\beta V(X))$. Diffusion Monte Carlo, without bias, samples the wavefunction. The difference is clear already for a simple two-atom bound system: molecular dynamics at high enough energy will visit geometries all the way to dissociation, but is not suitable for sampling the region of short-range repulsion, whereas DMC may visit high-energy regions at short internuclear distance but is not suitable for sampling configurations at large separations. The combination of the two techniques would be appropriate for a two-atom system, but of course, for those systems we can just lay down a one-dimensional grid of geometries.

The more interesting, and very common, situation is that of a multi-atom system for which there are several local minima, with barriers between them at energies in the vicinity of a dissociation barrier, and the application demands an accurate representation of the barriers in the fitted PES. Sampling the various basins is easy, and the problem is to have sampling methods that will provide good coverage of the barriers. To this end, straightforward molecular dynamics at any energy is quite unsuitable. At energies of physical interest an MD trajectory may spend several times 10^5 timesteps in one well and then cross the barrier in maybe 10-50 timesteps. And if one increases the energy to get more frequent barrier crossing the molecule typically just breaks apart first. Diffusion Monte Carlo at artificially reduced mass is more effective and we have used it extensively. However, molecular dynamics remains our basic sampling method and we apply it with various twists.

First and most elementary, when we sample from a molecular dynamics run then we subject the sampled configurations to a further perturbation, a random displacement in each nuclear coordinate drawn from a normal distribution with standard deviation up to about 0.1 bohr. Sometimes we also scale all the nuclear coordinates by a common factor less than 1; down to about 0.9.

Second, after sampling from an MD run we prune the sample by removing near-duplicate configurations. For this purpose we have designed tests for similarity that involve only permutationally invariant functions of internuclear distances, so we recognize similarity between configurations in arbitrary relative position and with arbitrary relabeling of nuclei. We expect that the sample from an MD run will have many similar configurations deep in the basins and not many similar ones near the top of barriers, and so this pruning should give better relative coverage of the barriers. The pruning involves a sequential pass through the sample, and before that pass we sort the sample in order of increasing norm of the gradient of the potential energy; this is meant to favor configurations near stationary points of the potential energy surface.

Third, we sometimes sample from MD simulations in which a critical part of the configuration is frozen. A typical situation involves a barrier for hydrogen migration, say from one C to another C in a larger molecule. The critical part is then a CCH triangle and we freeze it in the configuration of the saddle point, but the remainder of the molecule is left to go about its way in the MD. And again, after sampling from the MD we subject the configurations to random nuclear displacements.

Besides making use of diffusion Monte Carlo and molecular dynamics to sample configuration space quite broadly we focus attention on stationary configurations. This is done by quasi-Newton search for grad.V=0 on whatever is the current approximate potential energy surface. We use thousands of initial guesses, usually drawn from our total sample space with preference for configuration for which grad.V is close to 0. The quasi-Newton method involves computation of the gradient and hessian in cartesians, pseudo-inversion of the hessian (it has at least three zero singular values, associated with translation, and as convergence is approached two or three more zero singular values appear), a simple line search, and we give up if convergence isn't achieved within a rather small number of iterations. We don't particularly care to have a highly robust method here; if the search fails

to converge we just move on to the next initial guess. Converged configurations are saved, but configurations that are effectively duplicates of a previously found stationary configuration (up to point-group and permutation symmetries) are removed. Finally, for the purpose of further *ab initio* calculations, the collection of stationary points is replicated some number of times and each such configuration is subjected to a random perturbation of the nuclear coordinates similar to the one that we apply to an MD sample.

Coverage of configuration space is improved in a more or less automatic manner by another feature of our work. For any molecular system of interest, when we construct a PES at a not too expensive level of theory then we do it at the same time for several charge and spin states, and we use to some extent configurations sampled for one charge and spin state also for *ab initio* calculations for other states. An example where this improves coverage of an important barrier region is ethene, C_2H_4. In the neutral singlet state the global minimum is planar, D_{2h} geometry, and there is a high-lying saddle point in which one CH_2 group is twisted by 90 deg relative to the other. On the triplet surface, however, the roles are reversed. Likewise, in vinyl, C_2H_3, the methylcarbyne isomer, CH_3C, has on the doublet surface a shallow, high-lying local minimum that would not be well covered in routine MD or DMC sampling on that surface, but on the quartet surface and also on the negative ion triplet surface it belongs to deep well.

One more approach needs to be mentioned by which we improve our sample of configurations for *ab initio* calculations. Often we will construct two surfaces to fit the same dataset. The surfaces may differ in the degree of the polynomials used in the fit, or in one of the nonlinear scale parameters a and λ. We then run DMC or MD on one surface, sample from that run, and evaluate also the potential according to the other surface. Where the two surfaces differ by much there is probably a lack of coverage in the database, and we add configurations found that way to the *ab initio* sample.

3.3. Higher-accuracy ab initio calculations

Having obtained a satisfactory database and fitted potential energy surface for a level of *ab initio* that is not very expensive, we may now proceed to identify a relatively small subset of the database for which higher-quality and higher-cost *ab initio* calculations are to be carried out. A strategy that we used for the malonaldehyde surface is the following. Say that the fitted surface involves M free parameters (M is a few 1000 in our work). We select more or less randomly about $2M$ configurations from our database for the cheaper ab initio method. We then re-fit the surface, and look for configurations in the entire database for which the energy is an outlier relative to the refitted surface. Add a sample of those outliers, randomly removing some other configurations, and iterate the process a few times so that finally a sample of about $2M$ configurations gives a satisfactory refitted surface. That is then taken to be a good sample for expensive *ab initio* calculations.

Note that the higher accuracy *ab initio* calculations can be combined in various ways with lower accuracy calculations. We could use, for example, expensive coupled cluster calculations for function values and combine them with lower-cost DFT calculations for gradients, and give the gradient data not much weight in the least squares system.

Or we can use relatively few coefficients to fit the difference between the high-accuracy and the lower-accuracy *ab initio* data. We should be using those techniques, but in our work to-date we have always just spent the computer time to get a large enough database at whatever is finally our selected quality of *ab initio*.

4. CONCLUSION

The approach to fitted analytical potential energy surfaces described here, centered around a permutationally invariant polynomial expansion in functions of all the internuclear distances, has been very successful for systems of up to 7 atoms, and even larger systems (malonaldehyde, the water trimer) for which interest was focused on geometries at not too high energy. However, all this is

restricted to a single surface, normally the ground state surface at a particular charge and spin state. For charged systems the assumption that reaction dynamics takes place on a single surface is very often wrong. In particular, whenever charge exchange is of interest one is automatically dealing with two electronic surfaces, which may cross in a conical intersection. Therefore it is of great interest to develop the present methods further in order to fit a pair of electronic states, ideally in a global diabatic representation. Thus, a 2-by-2 real symmetric matrix function of the nuclear configuration must be fitted such that its eigenvalues are the two energies. The transformation properties of such a function under exchange of like nuclei are not obvious, and it isn't even clear that it should always be possible to define a smooth single-valued matrix function having the desired spectral property; perhaps one needs to look for a 3-by-3 matrix function for which the two lowest eigenvalues are the energies of the two intersecting states. This is a research subject.

ACKNOWLEDGEMENTS

REFERENCES

[1]   BROWN, A., MCCOY, A.B., BRAAMS, B.J., JIN, Z., BOWMAN, J.M.. Quantum and classical studies of vibrational motion of CH^{+5} on a global potential energy surface obtained from a novel *ab initio* direct dynamics approach, J. Chem. Phys. **121** (2004) 4105.

[2]   SHARMA, A.R., WU, J., BRAAMS, B.J., CARTER, S., SCHNEIDER, R., SHEPLER, B., BOWMAN, J.M., Potential energy surface and MULTIMODE vibrational analysis of $C_2H_3^+$. J. Chem. Phys. **125** (2006) 224306.

[3]   HUANG, X., BRAAMS, B.J. and BOWMAN, J.M., Ab initio potential energy and dipole moment surfaces of $(H_2O)_2$. J. Phys. Chem. **110** (2006) 445.

[4]   HUANG, X., BRAAMS, B.J., BOWMAN, J.M.. Ab initio potential energy and dipole moment surfaces for $H_5O_2^+$. J. Chem. Phys. **122**, (2005) 044308.

[5]   WANG, Y., CARTER, S., BRAAMS, B.J. and BOWMAN, J.M., MULTIMODE quantum calculations of intramolecular vibrational energies of the water dimer and trimer using ab initio-based potential energy surfaces, J. Chem. Phys. **128** (2008) 071101.

[6]   WANG, Y., BRAAMS, B.J., BOWMAN, J.M., CARTER, S., TEW, D.P., Full-dimensional quantum calculations of ground-state tunneling splitting of malonaldehyde using an accurate ab initio potential energy surface, J. Chem. Phys. **128** (2008) 224314.

[7]   OpenShell. Center for computational studies of electronic structure and spectroscopy of open-shell and electronically excited species. See: http://iopenshell.usc.edu/downloads/ezpes/.

[8]   MURRELL, J.N., CARTER, S., FARANTOS, S.C., HUXLEY, P. and VARANDAS, A.J.C., Molecular Potential Energy Functions, Wiley, New York (1984).

[9]   DERKSEN, H. and KEMPER, G., Computational Invariant Theory, Springer Verlag, Berlin, etc. (2002).

[10]   BOSMA, W., CANNON, J.J., Playoust, C., The Magma Algebra System I: The User Language. J. Symb. Comput. **24** (1997) 235. See also http://magma.maths.usyd.edu.au/magma/.

ELEMENTARY PROCESSES, THERMODYNAMICS AND TRANSPORT OF H$_2$ PLASMAS

M. CAPITELLI[a,b], D. BRUNO[b], C. CATALFAMO[a], R. CELIBERTO[c], G. COLONNA[b], M. C. COPPOLA[a], G. D'AMMANDO[a], O. DE PASCALE[b], P. DIOMEDE[a], F. ESPOSITO[b], C. GORSE[a,b], A. LARICCHIUTA[b], S. LONGO[a,b], F. TACCOGNA[b]

[a] Dipartimento di Chimica, Università di Bari, via
 Orabona 4, 70126 Bari (Italy)

[b] CNR IMIP Bari, via
 Amendola 122/D, 70126 Bari (Italy)

[c] Dipartimento di Ingegneria delle Acque e Chimica, Politecnico di Bari, via
 Orabona 4, 70126 Bari (Italy)

Abstract

Recent results by the plasma group in Bari are reviewed ranging from the derivation of elementary processes probability to the PIC/MC simulation of a negative ion source. State-resolved cross-section for selected processes in photon-H$_2$, e-H$_2$ and D+D$_2$ collisions are presented. The cut-off issue in the calculation of thermodynamic and transport properties of equilibrium atomic hydrogen plasmas is discussed considering different criteria. The radiative transport equation has been solved for an equilibrium hydrogen plasma. Finally results of the simulation of an RF-ICP negative ion source are reported.

1. INTRODUCTION

The theoretical description of plasma-chemical systems for predictive purposes is still a challenge, requiring an accurate information on the microscopic dynamics of elementary processes occurring in the plasma, a kinetic model consistently coupled with the Boltzmann equation for electrons, and transport modules.

In the last decades a great effort has been devoted in different laboratories to the theoretical investigation of non-equilibrium plasmas, focusing on hydrogen plasma relevant to fusion applications [1, 2, 3]. A consistent state-to-state kinetic approach has been developed for the simulation of the plasma, including all the relevant channels in the microscopic dynamics and accounting also for the role of energy stored in the internal degrees of freedom of chemical species. State-resolved cross-sections for electron-molecule and atom-molecule processes have been obtained in the framework of semi-classical impact parameter and quasi-classical trajectory methods respectively. Concerning electron-impact induced processes, results for direct dissociation and non-resonant vibrational excitation through radiative decay of H$_2$ low-lying Rydberg states are presented. QCT calculation already performed for hydrogen system have been extended to D-D$_2$ collisions, in the perspective of cross-section database completion. Moreover cross-sections for photodissociation processes initiated from vibrationally excited targets are critically reviewed and used to obtain a state-weighted global rate coefficient valuable in macroscopic approaches.

Thermodynamic and transport properties of hydrogen equilibrium plasma are also investigated. In the first case attention is paid to the energy levels to be inserted in the partition function, i.e. Coulomb against Debye-Hückel, while in the second the influence of appropriate transport cross-sections for electronically excited states on the transport coefficients is reported.

A module for 1D radiation transport in high temperature atomic hydrogen plasma has been implemented. The absorption and emission coefficients entering the radiative transport equation have been obtained generating a synthetic hydrogen spectrum, that is determined by elementary radiative processes and includes different line broadening factors.

Finally a PIC/MC code has been used for the 2D simulation of the extraction region of an RF-ICP negative ion source. The modeling includes also the effect of caesium adsorbed at the grid wall in increasing the H$^-$ density.

2. ELECTRON-MOLECULE COLLISION PROCESSES

Electron-impact dissociation represents one of the most efficient channels for atom formation and follows the transition to the continuum belonging to electronically excited states. The transition process to the pure repulsive $b\,^3\Sigma_u^+$ state has been deeply investigated by different groups, both experimentally [4, 5] and theoretically [6, 7, 8].

Different theoretical approaches (impact parameter, T-matrix) have been used to describe the dynamics with the inclusion of the effect of the energy stored in the internal degrees of freedom. In Figure 1 accurate results by Stibbe et al. [6] have been reported considering the dissociation initiated from vibrationally excited target molecules. The considered dipole-forbidden process is characterized by a near-threshold maximum, shifted to lower energies and enhanced in value for $\nu_i > 0$. In the same Figure classical Gryzinski cross-sections [8] and results obtained with the Kohn variational method by Rescigno and Schneider [7] are also reported. Unfortunately the Rescigno cross-sections do not sample the threshold energy region, but a common feature with Stibbe results is the large dependence of the maximum on the vibrational quantum number, not observed in the third set of results. Despite these differences a general agreement is found between the cross-sections estimated by the classical Gryzinski, widely used in the past, and by more accurate theoretical approaches, especially for $\nu=0$ case.
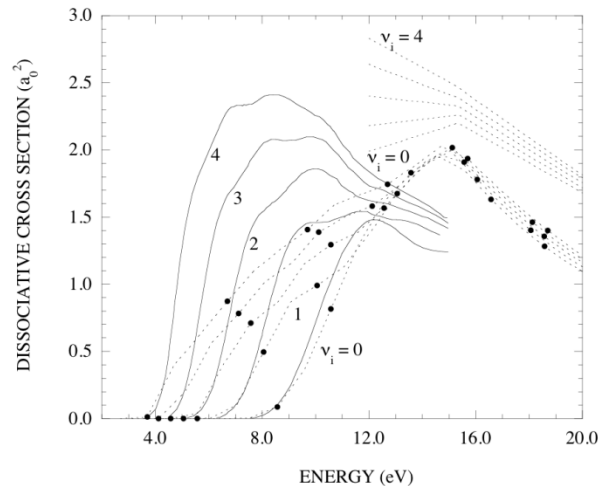
FIG. 1. Cross-section for H_2 direct dissociation through $b\,^3\Sigma_u^+$ state, as a function of impact energy, for different initial vibrational levels by different authors. (solid line)-Ref. [6] (dotted line)- Ref. [7] (close circle)-Ref. [8].

Also direct dissociation through the repulsive branch of singlet excited states could significantly contribute to the atomic budget. The dynamics of these dipole-allowed transitions has been widely studied in the framework of the impact-parameter method and results collected in a database of state-resolved cross-sections [8]. The energy profile is characterized by a threshold energy located at higher energies and by a broad maximum in the medium-energy region. Again the vibrational excitation acts enhancing the process probability, however the vibrational profile shows, in general, a strongly irregular behavior, closely following the Franck-Condon density factors. Considering electronic states progressively more excited (correlating with hydrogen atoms with the principal quantum number $n > 1$) the absolute cross-section value decreases with an inverse power-law.
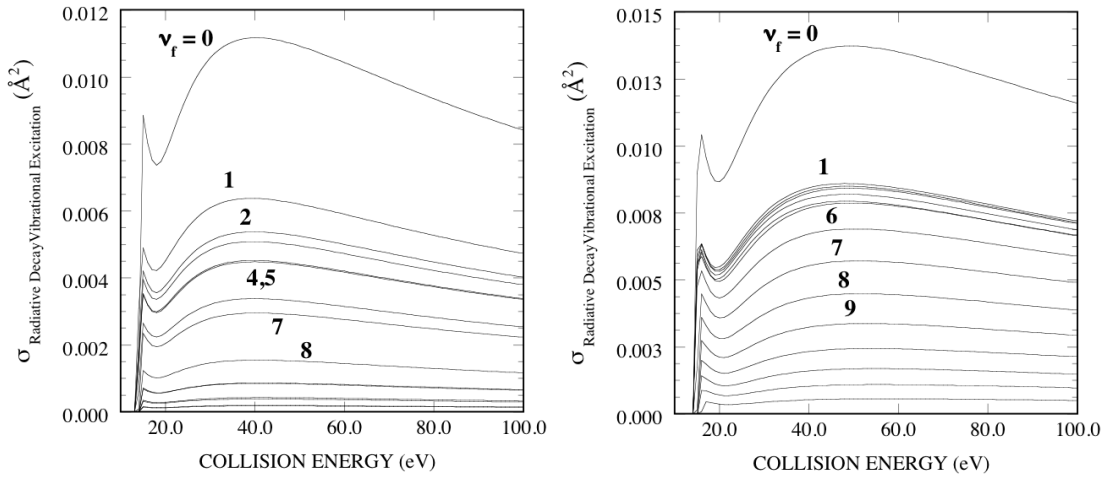
FIG. 2. Cross-section for the process $H_2(X^1\Sigma_g^+, \nu_i) + e \rightarrow H_2^* + e \rightarrow H_2(X^1\Sigma_g^+, \nu_f) + e + h\nu$ for $\nu_i=0$, as a function of energy, for different ν_f (left panel) $H_2^* = B' \, ^1\Sigma_u^+$ (right panel) $H_2^* = D \, ^1\Pi_u$.

The vibronic excitation to singlet electronic terms has been also studied in the frame of the semiclassical impact parameter method, representing the first step of the E-V mechanism for the efficient vibrational excitation of ground state molecules

$$H_2(X^1\Sigma_g^+, \nu_i) + e \rightarrow H_2^*(^1\Lambda_u, \nu') + e \rightarrow H_2(X^1\Sigma_g^+, \nu_f) + e + h\nu \qquad (1)$$

Radiative decay cross-sections have been firstly calculated for $\Lambda = B, B' \, ^1\Sigma_u^+ \, C, D \, ^1\Pi_u$ by Hiskes [9], estimating also the cascade 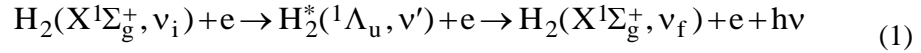contributions from highly excited states. Recently comprehensive calculations are reported in Ref. [10] for the low-lying Rydberg states belonging to the Σ and Π spectroscopic series ($B' \, ^1\Sigma_u^+$ and $D \, ^1\Pi_u$). Results have been obtained combining the excitation cross-section with the probability of spontaneous emission (Einstein coefficients), considering also the coupling to the continuum of the ground state, i.e. radiative decay processes leading to dissociation. In Figure 2 cross-sections for the process initiated from the $\nu=0$ vibrational and having as intermediate the $B' \, ^1\Sigma_u^+$ and $D \, ^1\Pi_u$ states level are shown as a function of collision energy for different final vibrational levels. The energy shape of the cross-section is dominated by the excitation function and, though the most favorable process still remain the decay back to the $\nu=0$ level, also higher levels are populated, leading to tails in the vibrational profile.

3. ATOM-MOLECULE COLLISION PROCESSES: D-D$_2$ SYSTEM

Calculations about D+D$_2$ collision process are in progress, therefore only partial results can be shown here. All the calculations have been performed by quasiclassical method on the BKMP2 PES [11]. In Figure 3 vibrational deactivation for the process: D+D$_2(\nu,j) \rightarrow$ D+D$_2(\nu_f, j_f)$, with ν, ν_f: initial and final vibrational quantum numbers, j, j_f: initial and final rotational quantum numbers, is shown as a function of initial vibrational quantum number at three temperatures (from higher to lower panel): T=300 K, 1 000 K, 5 000 K. The rate is the sum of non reactive and exchange rates. Only a relatively low number of initial vibrational states are available, covering the whole vibrational range.

As usual in our results, initial rotation is always included, explicitly taken into account in the original calculations, and considered in all the results by means of a rotational temperature taken equal to the translational one, only for simplicity of representation; for the same reason final rotation is summed up for each final vibrational state. Different curves in the Figure are referred to different quantum jumps: $\nu \rightarrow \nu-1$, $\nu \rightarrow \nu-2$, $\nu \rightarrow \nu-5$. The trends are similar for $\Delta\nu=2$ and $\Delta\nu=5$, with an ascending part up to a maximum, followed by a rapid rate decrease, with maximum position ranging

from ν =15 to ν =20. For Δν=1 there is a steep rising between ν =1 and ν =5, followed by a plateau, while for T=300 and 1 000K there is a decreasing part, for T=5 000K an increasing part due to the rate from the last vibrational state. Of course, these are partial results, and a complete analysis needs complete data.
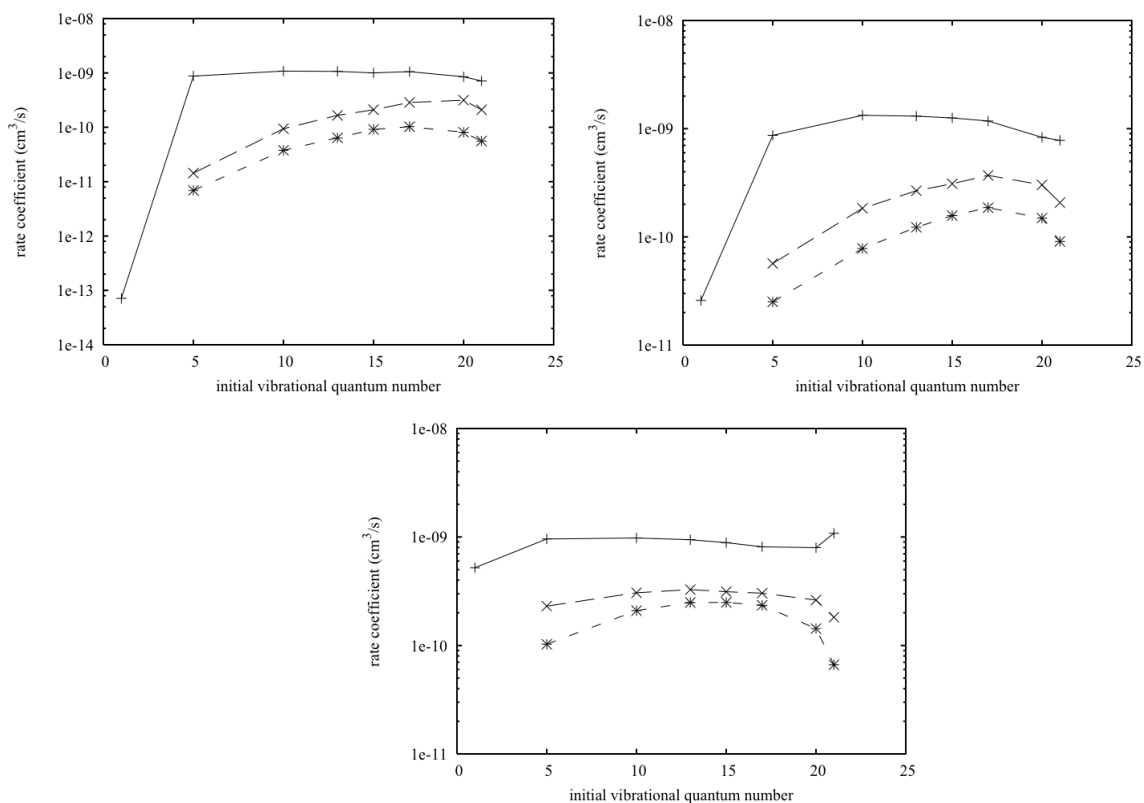
FIG. 3. Deuterium vibrational deactivation rate coefficients as a function of initial vibrational quantum number, at T=300 K (left higher panel), T=1 000 K (right higher panel), T=5 000 K (lower panel). (+) v→v-1, (×) v→v-2, (∗) v→v-5.

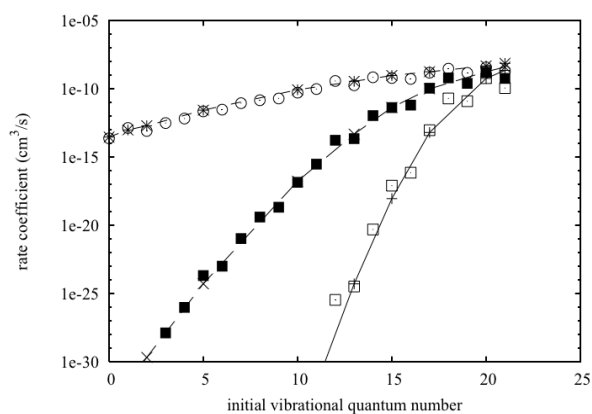FIG. 4. Deuterium dissociation rate coefficients as a function of initial vibrational quantum number at T=300 K (+), T=1 000 K (×), T=5 000 K (∗). Markers not connected by lines are results of hydrogen scaled results.
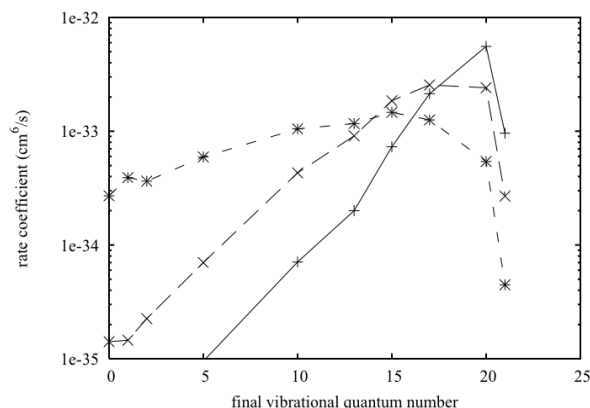
FIG. 5. Deuterium recombination rate coefficients as a function of final vibrational quantum number. at T=300 K (+), T=1 000 K (✕), T=5 000 K (∗).

The comparison with experimental data is limited, to our knowledge, to the results given in [12], relative to total rate (reactive plus non reactive) from v=1 to v=0 at 300 K. This value is actually an upper limit ($1×10^{-13}$ cm^3/s), which is perfectly compatible with our result ($7.15×10^{-14}$ cm^3/s), but one order of magnitude higher. Also in the case of monoquantum deactivation of H+H$_2$ on the same PES the comparison with experimental result shows a discrepancy in the same direction, with higher experimental value. It is not clear if this can be attributed to effects not correctly evaluated in the experimental setup or to deficiencies in the theoretical treatment (quasiclassical method, PES not completely adequate, non Born-Oppenheimer effects).

Concerning dissociation (D+D$_2$(v,j) →3D) the trends seem quite smooth, rapidly ascending with initial vibrational quantum number, as shown for T=300, 1 000 and 5 000 K in Figure 4, and it is quite unlikely that the general trend will be changed by further calculations. In the same Figure the markers not connected by lines show the results obtained with scaling of hydrogen results, as illustrated in Ref. [13]. The scaled results seem reasonable at all the conditions, but for low temperature data quite approximated.

Recombination of deuterium due to collisions of atoms: D+D+D→D$_2$(v,j)+D can be studied by direct recombination dynamics, or by orbiting resonance theory, or by inverting the dissociation data by means of detailed balance. The first and very interesting approach is actively studied at a theoretical level in our group in the context of quasiclassical calculations. The theory of orbiting resonance needs rate coefficients relative to the whole ro-vibrational ladder of states compatible with the D$_2$ potential used, and these calculations are not complete for deuterium, as already mentioned. The last possibility is the use of detailed balance applied to dissociation rates. In this case the problem is the high statistical errors of very low dissociation values (essentially obtained near energy thresholds): these values are not very important for application in models concerning dissociation, but when translated to recombination they produce values not very low (due to the compensation coming from the equilibrium constant at low temperature) with huge relative errors. Collisional recombination results obtained in this way are shown in Figure 5, at T=300, 1 000 and 5 000 K, as a function of final vibrational quantum number (on rotation results are summed up for each vibrational state). The general observation of the Figure shows a clear preference for higher vibrational states (except the last one) at all temperatures, but much more pronounced at low temperature. On the contrary, at high temperature recombination shows a smooth dependence on the final vibrational quantum number, if the last state is excluded.
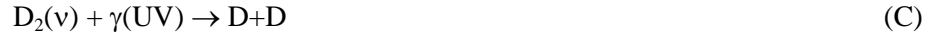
4. PHOTODISSOCIATION RATES FOR H$_2$ (WITH ISOTOPIC VARIANTS)

Interactions between photons and molecules play a very important role in plasma physics; in fact, a large ensemble of absorption or emission photonic processes can occur in ionized gases. The absorption of photon/s in molecule can provoke different fates for the molecule itself, depending on

the energy of the incident photon/s, and going from the growing up of internal energy to photoionization or photodissociation. Single or multi-photons absorption can occur.

A large ensemble of researches on this field of plasma physics is directly connected with the study of astrophysical environments. Indeed, the detection of molecules in the intergalactic medium and in other galaxies is performed through the emission and absorption spectra of molecules. Among them, molecular hydrogen represents the most abundant one (e.g. [14, 15]); moreover, the formation of more complex molecules in interstellar space is intimately connected to the presence of H_2 ([16]). In particular, the vibrational spectrum of H_2 is a widely used probe of the environments both in our and external galaxies.

In this section, the processes of photodissociation of $H_2(v)$, $HD(v)$ and $D_2(v)$ due to thermal photons (in the cosmological context, the ones belonging to the Cosmic Microwave Background) are investigated. These reactions consist in the absorption of photons and subsequent dissociation of the molecules:

$$H_2(v) + \gamma(UV) \rightarrow H+H \qquad\qquad (A)$$

$$HD(v) + \gamma(UV) \rightarrow H+D \qquad\qquad (B)$$

$$D_2(v) + \gamma(UV) \rightarrow D+D \qquad\qquad (C)$$

In (A)-(B)-(C) cases, the absorptions from all vibrational levels of the ground electronic state $^1\Sigma_u^+$ into the continua of the Lyman ($B\ ^1\Sigma_u^+$) and Werner ($C\ ^1\Pi_u$) systems are considered. These channels are responsible for the direct process of photodissociation, different from the so-called Solomon photodissociation, in which UV-photons absorptions into a vibrational level higher than the 14-th are followed by fluorescence to the vibrational continuum of the ground state. Calculations of the photodissociation rate coefficients are reported for vibrationally excited H_2 molecules and its isotopomers HD and D_2 as a function of the temperature T_g of the gas, considering thermal equilibrium between the different molecular degrees of freedom (electronic, vibrational and rotational). An analytic fit of the rate coefficients of these processes is provided and the effect of the inclusion of the vibrational states in these evaluations (as shown in [17] for the process of dissociative attachment of molecular hydrogen) is discussed.

Considering thermal equilibrium between the temperature connected with the internal degrees of freedom and the radiation, the photonic processes rate coefficient (see [18]) can be written as:

$$k_v = c \int_{\varepsilon_{th}}^{\infty} d\varepsilon\, f(\varepsilon)\, \sigma_v(\varepsilon) \qquad\qquad (2)$$

where c, $\sigma_v(\varepsilon)$ and $f(\varepsilon)$ represent the speed of light, the state-to-state photodissociation cross-sections and the density of photons, respectively. $f(\varepsilon)$ is written as:

$$f(\varepsilon) = \frac{8\pi\varepsilon^2}{(hc)^3} \frac{1}{e^{\varepsilon/KT}-1} \qquad\qquad (3)$$

with h and K representing Planck's constant and Boltzmann's constant, respectively. The total rate coefficient, defined as:

$$k_{tot} = \sum_v \chi_v k_v \qquad\qquad (4)$$

represents the rate coefficient of the process of photodissociation due to the contribution of all vibrational levels, with χ_v vibrational distribution function (sometimes known with the acronym *vdf*).

The range for the vibrational temperature is 1.4×10^3 K $< T_{vib} < 5.3 \times 10^4$ K: this applies to all the fits provided in the following. These processes, and the related rate coefficients, can be relevant to the formulation of a reaction network for recombining protium and deuterium plasmas in the divertor region of magnetic confinement devices. Chemical networks for recombining protium/deuterium ionized mixtures find applications in the study of early universe conditions [19] and HII regions and astrophysical shocks. Depending on the concept considered, they could also be relevant for beam neutralizer modelling in the context of neutral beam injection.

The photodissociation cross-sections $\sigma_v(\varepsilon)$ are taken from [20]. In the computation of these cross-sections, quantum [20] approaches are used. A Boltzmann vibrational distribution function is assumed, and the vibrational level energies have been taken from Wolniewicz [21].

A few cross-sections were lacking of data for the high energy range. These cross-sections were therefore extrapolated at high energy based on the trends of comparable processes reported in Table 1. The procedure is illustrated by Figure 6, where the extrapolated trends of a few cross-sections for the $D_2(v)$ Werner process are shown together with the one used as a reference for the trend, while for $v=5$ as shown the interpolation process was not requested while its trend appears to support the extrapolation process.
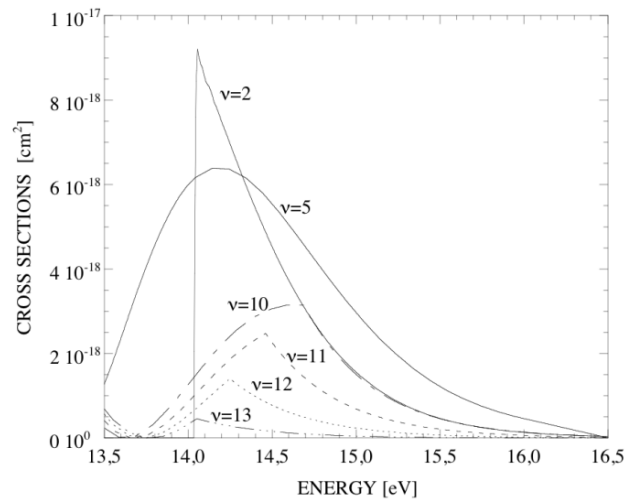
FIG. 6. High energy trends of selected cross-sections for the $D_2(v)$ Werner process (see text).

TABLE 1. DATA EXTRAPOLATION FOR HIGH-TEMPERATURE RANGE

$H_2(v)$ Lyman	$H_2(v)$ Werner
from $v =3$ for $v =9,10,11,12,13$	from $v =7$ for $v =8,9,10,11,12$
HD(v) Lyman	HD(v) Werner
from $v =2$ for $v =0$ from $v =5$ for $v =10,11,12,13,14$	from $v =5$ for $v =9,10,11,12$
$D_2(v)$ Lyman	$D_2(v)$ Werner
from $v =2$ for $v =11,12,13,14,15$	from $v =2$ for $v =10,11,12,13,14$

In Figs. 7(a) and (b) an example of global rate coefficients has been reported. Labels "$v = 0$" and "k_{tot}" stand for the contribution calculated considering all the molecules of the gas in the ground state and hypothesizing the Boltzmann distribution among vibrational levels, respectively. In Figs. 7a and b it has been also reported a comparison with the data used in recent cosmological calculations by

Schleicher et al. [22]: these authors also consider vibrational excitation under local equilibrium conditions, but for the indirect Solomon process of photodissociation: it is evident that the two processes are competitive. The effect of vibrational excitation is not so high here like that found for the process of dissociative attachment [17], since the cross-sections are not changing so dramatically with the vibrational quantum number, but it is still important. In all cases reported in the figures, it can be seen that the inclusion of the whole manifold of vibrational levels produces results which deviate sensibly from those obtained considering just the cross-section for $v=0$ in conjunction with the whole H_2, HD and D_2 populations from the more correct result for T_g over $\sim 10^4$ K. At this temperatures these molecule will be almost fully dissociated in most cases, but it must be remarked that there are fields, namely astrophysics, where it is important to determine accurately the kinetics even of a small fraction of H_2 molecules in essentially H plasma at high T. For technological plasma applications the work needs to be completed by determining the rates as function of both the radiation temperature and the vibrational temperature, and to consider deviations of the radiation field from the blackbody spectrum. In Figs. 7a and b it has been also reported a comparison with the data used in recent cosmological calculations by Schleicher et al. [22]: these authors also consider vibrational excitation under local equilibrium conditions, but for the indirect Solomon process of photodissociation: it is evident that the two processes are competitive.
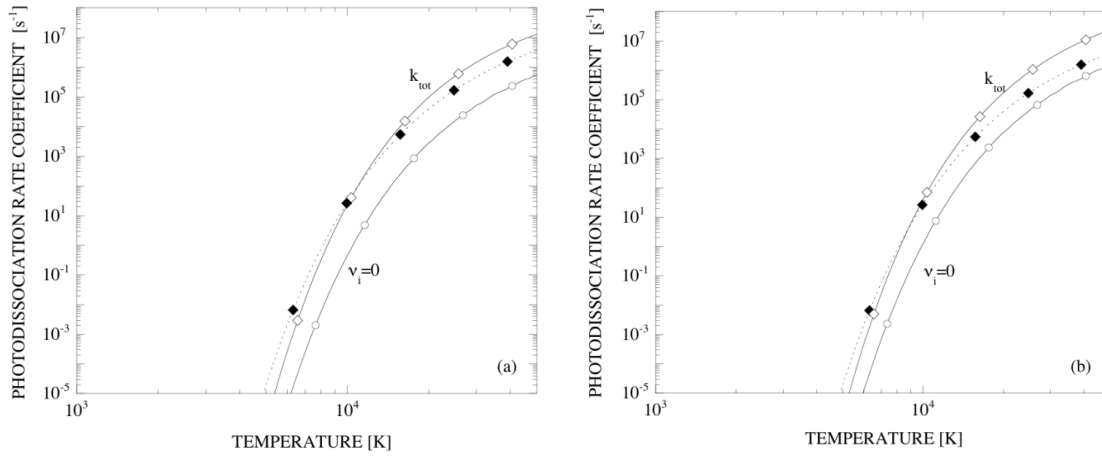
FIG. 7. *Photodissociation rate coefficients for $H_2(v)$ in Lyman (a) and Werner (b) systems. The contribution from all vibrational levels (open diamonds) and neglecting vibrational excitation (open circles) have been reported, compared with the rate coefficient in Ref. [22] (close diamonds).*

For future applications we report our calculated rate coefficients:

- Lyman

$$k_{tot} = 1.27 \times 10^8 \, T_g^{0.08365} e^{-159600 T_g} \text{ s}^{-1} \qquad H_2(v) \tag{5}$$

$$k_{tot} = 1.19 \times 10^7 \, T_g^{0.28013} e^{-145310 T_g} \text{ s}^{-1} \qquad HD(v) \tag{6}$$

$$k_{tot} = 8.01 \times 10^7 \, T_g^{0.11692} e^{-157380 T_g} \text{ s}^{-1} \qquad D_2(v) \tag{7}$$

- Werner

$$k_{tot} = 6.46 \times 10^8 \, e^{-165530 T_g} \text{ s}^{-1} \qquad H_2(v) \tag{8}$$

$$k_{tot} = 5.70 \times 10^8 \, e^{-157380 T_g} \text{ s}^{-1} \qquad HD(v) \tag{9}$$

$$k_{tot} = 5.72 \times 10^8 \, e^{-160600 T_g} \text{ s}^{-1} \qquad D_2(v) \tag{10}$$

5. THERMODYNAMIC PROPERTIES OF HYDROGEN PLASMA

Accurate approaches to determine thermodynamic properties of gases and plasma are based on the statistical thermodynamic, determining the relevant quantities starting from the internal partition function [23] for each species s

$$Q_s = \sum_{\ell=0}^{N_s} g_s e^{-\varepsilon_{s\ell}/T} \tag{11}$$

where the index ℓ refers to levels. For atomic species, the number of levels, N_s, must be limited by the cutoff to avoid the divergence of H partition function. The strong dependence of partition function and thermodynamic quantities on the cutoff criterion has been observed [24, 25]. In particular, use of Fermi's criterion, comparing Bohr's atomic radius with the mean interparticle distance, increases the importance of electronically excited states as compared with the Griem cut-off, based on the Debye-Hückel theory [26, 27]. The presence of charged particles induces non ideal behaviors to the gas and correction following the Debye-Hückel theory must be added to global properties.

The corrections to thermodynamic quantities are proportional to (see for example [23,28])

$$\Delta_{DH} = \frac{kT}{24\pi\lambda_D^3} \tag{12}$$

which depend on the plasma Debye lenght λ_D. To include these features in the equilibrium calculation, the cutoff must determined self-consistently with the electron density. However, the Griem cut-off criterion, as usually used, suffers of an important limitation: the energy levels considered in the partition function are those derived from the Schrödinger equation solved for the Coulomb potential. This is a strong approximation especially at high electron density when the Debye-Hückel potential predicts large variation in the H level energies as compared with those calculated using the unperturbed Coulomb potential. It must be also considered that the contribution of electronically excited states of atoms and atomic ions is often neglected [29] in calculating the thermodynamic properties of high temperature plasmas.

The influence of the selection of energy levels, Coulomb versus Debye-Hückel potential, in affecting the thermodynamic properties of single species and mixtures has been recently investigated [30] in a wide range of pressures (1-1000 atm) for (H, H$^+$, e) plasma, focusing mainly on the specific heat and on the isentropic coefficient. In particular we have compared three cases considering different excited state systems:

a. - with Debye-Hückel levels

b. - with Coulomb levels

c. - only ground state

The effect of the internal level structure becomes more relevant as the pressure increases. The small differences observed in Figure 8 for the total specific heat is due to the compensation of frozen and reactive contributions to the total specific heat. In fact, the frozen specific heat is positively affected by the presence of electronically excited states, the reverse being true for the reactive thermal conductivity, both these quantities depending on the concentration of atomic hydrogen (see Refs.[31, 32]).
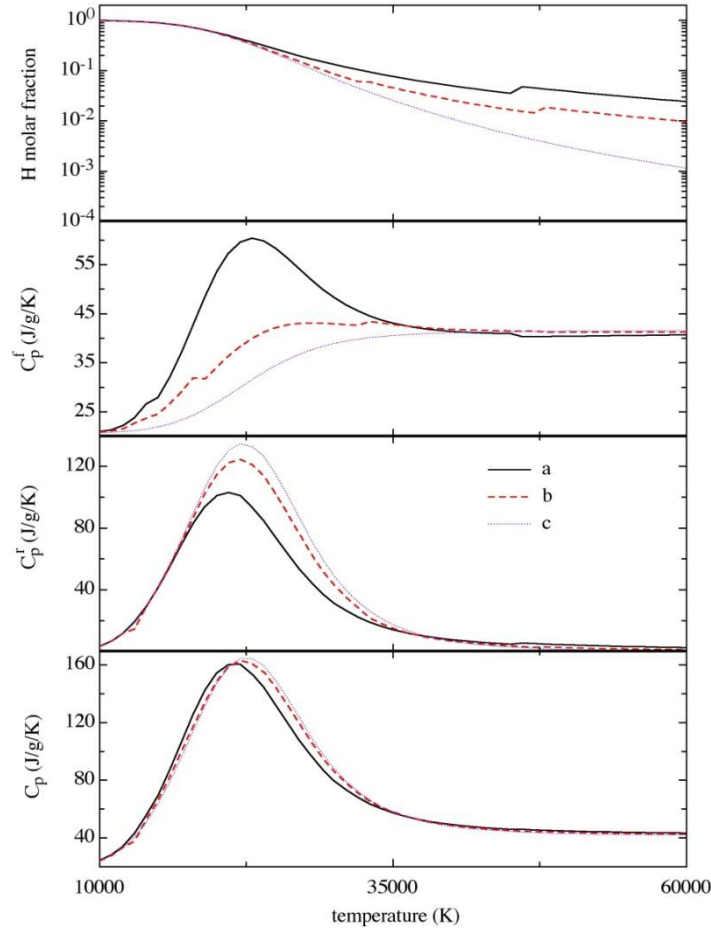
FIG. 8. Molar fraction of hydrogen atom and frozen (C_p^f), reactive (C_p^r) and total (C_p) specific heat of H, H^+, e mixture as a function of the gas temperature for pressure P=100 atm. (curves a) with Debye-Hückel levels, (curves b) with Coulomb levels, (curves c) only ground state.

6. TRANSPORT PROPERTIES OF HYDROGEN PLASMA: THE INFLUENCE OF ELECTRONICALLY EXCITED STATES

Three models (GS, CA, SSCP) have been extensively used by our group to calculate the atomic partition function and hence the composition and the thermodynamic properties of atomic hydrogen plasmas to be inserted in the Chapman-Enskog formulation of the transport coefficients [33]. The first method (GS) completely disregards the presence of electronically excited states by imposing an electronic partition function of atomic hydrogen equal to 2 i.e. to the degeneracy of the ground state. As a consequence internal energy and specific heat of atomic hydrogen are zero in this approximation. The confined atom (CA) approximation inserts in the electronic partition function of atomic hydrogen all levels whose Bohr radius does not exceed the inter-particle distance. This method can be considered well representative for describing high pressure-high temperature plasmas. Another method very often used in truncating the electronic partition function is the Griem method [23], essentially based on the Debye-Hückel theory of electrolytes i.e. on the static screening Coulomb potential (SSCP) model (see also section 5.). It is worth mentioning that the SSCP model, at variance from the other two, entails a pressure-dependent lowering of the ionization threshold. This has a deep influence on the equilibrium ionization degree, especially at large pressure where this effect becomes significant.

FIG. 9. Reactive thermal conductivity for equilibrium hydrogen plasma as a function of temperature for different pressure and for different cutoff. (continuous lines)-GS, (dashed lines)-CA, (dotted lines)-SSCP.

On the other hand electronically excited states (EES) present transport cross-sections which dramatically increase as a function of the principal quantum number n determining unusual effects in the transport equations. The effect of EES on the plasma transport coefficients is due to the large EES collision integrals. The largest increase pertains to H(n)-H$^+$ diffusion-type collision integrals and, to a minor extent, to H(n)-H$^+$ viscosity-type collision integrals, whereas H(n)-e show a smaller dependence on the principal quantum number n. The highest effect is therefore expected on the internal and reactive contributions while the translational thermal conductivity of heavy particles as well as the viscosity should be less affected. These effects are then modulated by differences in the atom concentration and in the number of allowed EES predicted by different models. The calculated coefficients are obtained in the framework of the Chapman-Enskog method; the first nonvanishing approximation in terms of Sonine polynomials [34,35] has been used to estimate the heavy particle contributions and the second for the electron component [36].

In Figure 9 we report the reactive thermal conductivity calculated by using different cutoff methods and appropriate EES cross-sections. We note that the cut-off criterion used in the calculation of equilibrium composition and of thermodynamic properties entering in the relevant equations determines strong differences in these transport coefficients. In particular the inclusion of the lowering of ionization potential in SSCP method is such to anticipate the maximum in the reactive thermal conductivity as compared with the corresponding results obtained with GS and CA methods. On the other hand GS and CA methods present maxima in the reactive thermal conductivity located approximately at the same temperature. Moreover the maximum occurring in the GS method is much higher than the corresponding maximum of the CA method. This is the consequence of the fact that the DH of the ionization reaction.

$$H(n) \Leftrightarrow H^+ + e$$
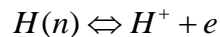
appearing in the reactive thermal conductivity is much higher in the GS method compared with the corresponding quantity obtained by the CA method. In the case of reactive thermal conductivity CA results are strongly affected by the insertion of abnormal cross-sections, while the SSCP results are slightly modified. This is indeed due to compensation effects rather than to an insensitivity of the transport coefficient on the abnormal cross-sections. In Figure 10 we show the internal thermal conductivity calculated by using abnormal cross-sections and according CA and SSCP methods (in the GS method this coefficient is zero for definition). Again the maximum in the SSCP method anticipates that one of CA method. It is also worth noting that the differences in the two methods increase with

pressure and that there are dramatic effects on the influence of the abnormal cross-sections in both the results coming from CA and SSCP methods.
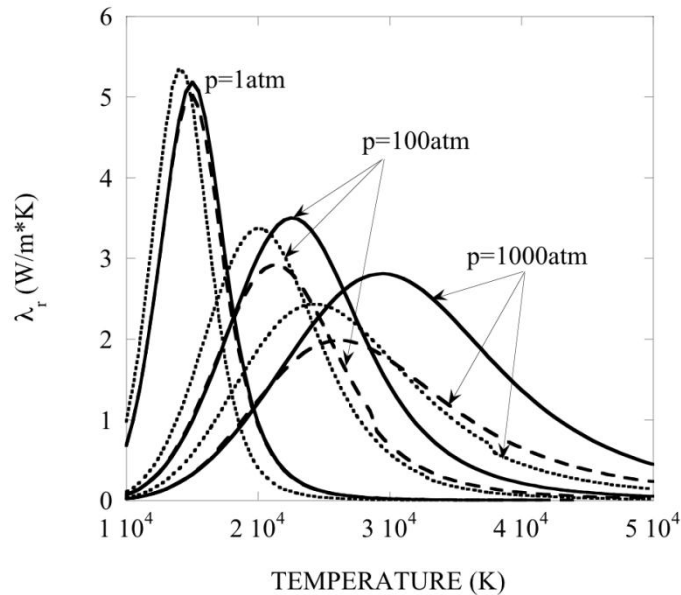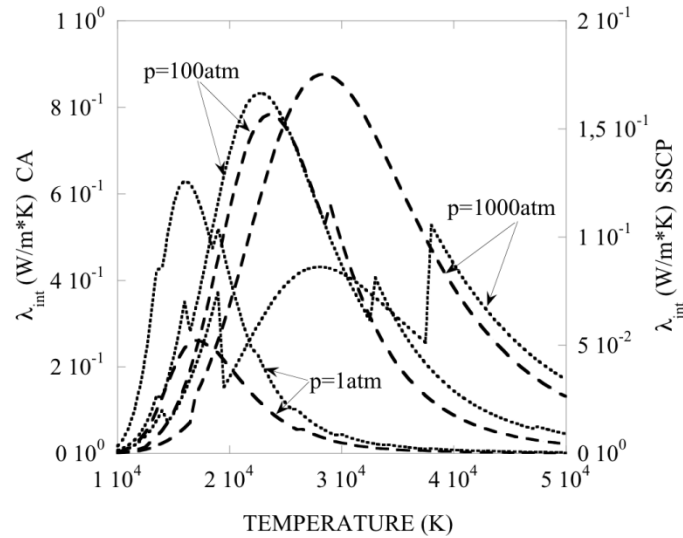

FIG. 10. Internal thermal conductivity for equilibrium hydrogen plasma as a function of temperature for different pressure and for different cut-off. (dashed lines)-CA, (dotted lines)-SSCP.

7. TRANSPORT OF RADIATION IN HYDROGEN PLASMA

Good understanding of the non-equilibrium properties of plasmas requires detailed treatment of the elementary mechanisms of radiation generation and radiation transport. These phenomena have been investigated in the relatively simple case of an high temperature atomic hydrogen plasma [37].

Generation of a synthetic spectrum of the hydrogen plasma requires a) calculation of the level populations and b) calculation of the relevant quantum-mechanical cross-sections for the important radiative mechanisms. The following elementary radiative processes have been considered for the H plasma

- absorption and emission due the transition of the optical electron between pairs of atomic levels (bound-bound transitions) which results in atomic lines

- radiation due to the transition of the optical electron from a bound state towards the continuum and the inverse process of electron capture of a free electron by the H^+ ion (bound-free transitions) which results in photoionization ad photorecombination edges

- radiation due to the acceleration of electrons in the electron field of H^+ ions (*bremsstrahlung*) which results in the continuum background.

Einstein coefficients for the bound-bound process, as well as photoionization cross-sections have been exactly computed using methods available in literature [38, 39]. The Bremsstrahlung and inverse Bremsstrahlung processes are also treated in a fully quantum mechanical framework by means of non-relativistic free-free Gaunt factors which have been calculated using a modified Karzas & Latter method [40, 41] using multiprecision arithmetic [42] in a very large range of electron and photon energies. The most important line broadening effects have been considered.
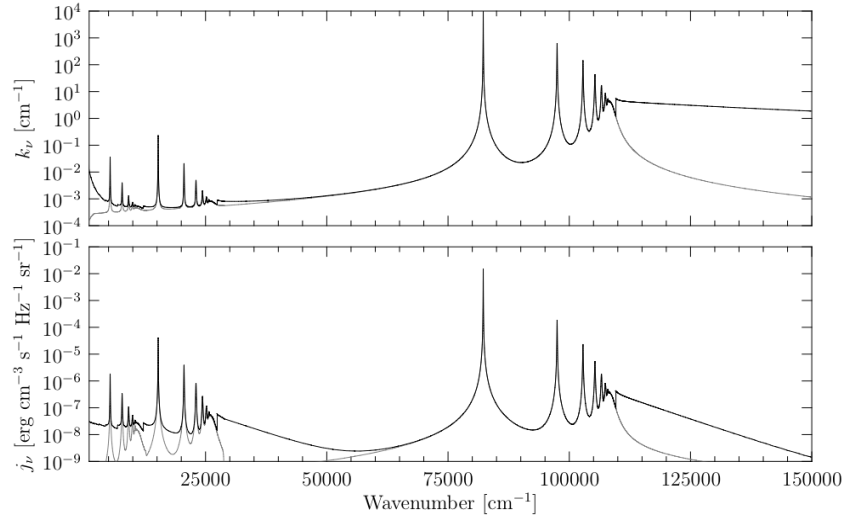
FIG. 11. Absorption, κ'_n, and emission, j_n , coefficients for the (H, H$^+$, e). Plasma at thermodynamic equilibrium, T=10 000 K, p=1 torr. (solid line) total spectrum, (gray-line) bound–bound contribution.
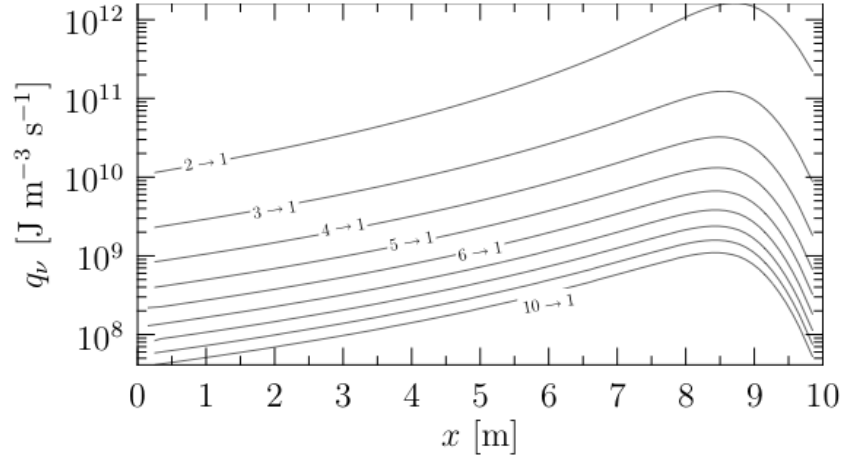
FIG. 12. Spectrally integrated divergence of the radiative heat flux integrated over the lines of the Lyman series.

Absorption and emission coefficients have been derived for both the equilibrium (Bolzmann for internal states, Maxwell-Boltzmann for the free electron EEDF) and non equilibrium cases. Ion Stark broadening [43] and electron Stark broadening [44, 45] are included using the semiclassical theory in which ions are considered quasi-static and electrons are treated with the impact approximation. The resonance broadening due to the impact of excited H atom with atoms in the ground state is taken from Griem [27]. Natural broadening and Doppler broadening effects have been included for completeness, even if their role is negligible except at very low pressure or very high temperature. The complete line shape function arising from all the broadening affects has been modeled using a Voigt line shape, using an high precision approximation to the Voigt function published by Wells [46]. A recent line shape sampling algorithm with guaranteed fractional accuracy has been adapted from literature and implemented in the code [47], in order to reduce the number of points of the spectral grid, which is especially important in radiation transport calculations. In Figure 11 the absorption and emission coefficients for equilibrium case and calculated according to the described model, have been reported considering the wavenumber range in which (from right to left) Lyman, Balmer and Pashen spectral series appear.

In order to estimate macroscopic quantities, such as the radiative heat flux and its divergence a radiative transfer module has been implemented, which solves the radiative transfer equation (RTE) using the optical spectral coefficients, κ'_ν and j_ν.

RTE has been solved in the 1D case with the short characteristics method using the optical depth as space variable. This method is based on the angular discretization of the RTE with the Gauss-Legendre quadrature nodes on [-1;1] and source function parabolically interpolated in space. In Figure 12 the spectrally integrated divergence of the radiative heat flux integrated over the lines of the Lyman series. The test case analyzes a simple case of 1D slab with a linear temperature gradient (left wall temperature: 50 000 K, right wall temperature: 10 000 K). The system pressure is 1 atm, the composition is the equilibrium one at the given temperature and pressure.

8. RF-ICP NEGATIVE ION SOURCE MODELING

The device modelled is the RF inductively coupled negative ion source [48]. It consists of three parts: the driver, where the RF is coupled to the plasma, the expansion region, where the plasma expands into the actual source body, and the extraction region. The latter two are separated by a magnetic field parallel the filter field. This field is necessary in order to keep the 'hot' electrons generated by the RF away from the extraction region. A typical space dependence of the B-field is reported in Figure 9 of Ref. [48] for the two cases of an operating Extraction Grid (EG) and a diagnostic flange.

The driver is mounted on the back of the source body. Caesium is delivered (with a rate of typically 10 mg h^{-1}) from an oven connected to the back flange of the source body. Inside this source, H$^-$ are produced in the volume through the electron dissociative attachment to vibration-excited molecules by two main mechanisms: in collisions with low energy electrons through the H_2^- resonance (e-V excitation) and by radiative decay from singlet states ($B\ ^1\Sigma_u^+$ and $C\ ^1\Pi_u$), excited by collisions of ground state molecules with energetic primary electrons (E-V excitation). Furthermore, in the caesium-seeded negative ion source, the negative ions are also produced by the conversion of protons and hydrogen atoms on the caesium-covered surface of the molybdenum plasma grid (PG) with a low work function. The contribution of the volume production process to the negative ion production is considered to be small, less than 10%, especially at the low operational gas pressure operation. In order to better understand the physics involved in this source, an ab-initio method is necessary. Here, we present a one-dimensional (1D) self-consistent Particle-In-Cell/Monte Carlo model [49, 50, 51] where the complete motion of electrons and ions (H$^+$, H_2^+ and H$^-$) is calculated in the self-consistent electric and applied magnetic fields by solving the equation of motion, including collisional effects via different Monte Carlo techniques, and using a spatial grid (cell size of the order of Debye length) for the potential calculation. The time step is set equal to the inverse plasma frequency. The injection conditions (particle density, temperature etc.) are those calculated for the extraction region in [50]. As for the B-field, we use the space dependence reported in the above cited reference by Speth et al. for the case of the diagnostic flange which corresponds to a peak value of about 4mT.

The region simulated starts 2 cm upstream from the extraction aperture of the PG. In this work a one-dimensional axial model is used, considering uniformity in x and y directions. Two different axial lines are simulated: line A ending on one hole (open boundary condition: $\partial \varphi / \partial z |_{PG} = 0$ a strong provisional assumption for the present case, to be emended in a model with higher dimensionality) and line B ending on the PG (fixed potential). In the volume, both charged-neutral particle and Coulomb collisions are implemented. When a charged particle hits the PG wall different processes are possible. Among them, the most important one concerning the effect of the caesiated surface is the formation of negative ions by electron capture from the wall [53] because they are directly related to the negative ion production. The H$^-$ yield can be expressed as a function of incident energy E$_{in}$ by the formula:

$$Y(E_{in}) = R_N \eta_0 \left(1 - \frac{E_{th}/R_E}{E_{in}} \right) \qquad (13)$$

where R_N and R_E are the particle and energy reflection coefficients, respectively, while η_0 is the height and E_{th} is the threshold energy for the electron transfer probability. H$^-$ are launched from the surface with energy of $R_E E_{in}$ and with a cosine angular distribution. Plasma-neutral interaction is very important and neutrals cannot be considered as a fixed background. Every 1000 PIC cycles (in order to allow the ion system to relax), the neutral module is called and the Direct Simulation Monte Carlo (DSMC) technique is used. The most important mechanism in the neutral module is the negative ion production from the caesiated PG by neutral impact. Two types of ion emission are considered: thermodynamic and non-thermodynamic equilibrium surface ionization [54]. In the first case, atoms impinging on the metal surface may be emitted as atoms or ions in subsequent evaporation processes after mean residence times long enough for the establishment of equilibrium. In this case, the probability of leaving the surface as a negative ion is given by the Langmuir-Saha relation:

$$Y = \left[1 + \frac{g_0}{g_-} e^{(\varphi - E_A)/kT_H} \right]^{-1} \qquad (14)$$

where E_A is the electron affinity, φ is the work function, g_0 and g_- are the degeneracy of atom and negative ion respectively. The second mechanism, called hot atom, is the result of the interaction of a fast particle with the surface and eq. (13) is used. Figure 13 shows the space dependence of the potential for the two different lines considered. The strong drop (-15V) in the closed line case is correlated to the grid charging.
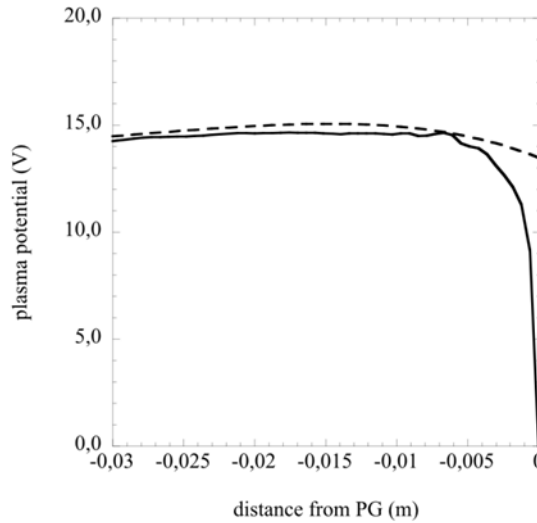
FIG. 13. Axial profiles of the plasma potential for the two different line considered: extraction hole (dashed line) and PG surface (full line). (B_{peak}=4 mT and φ_{PG}=0 V).
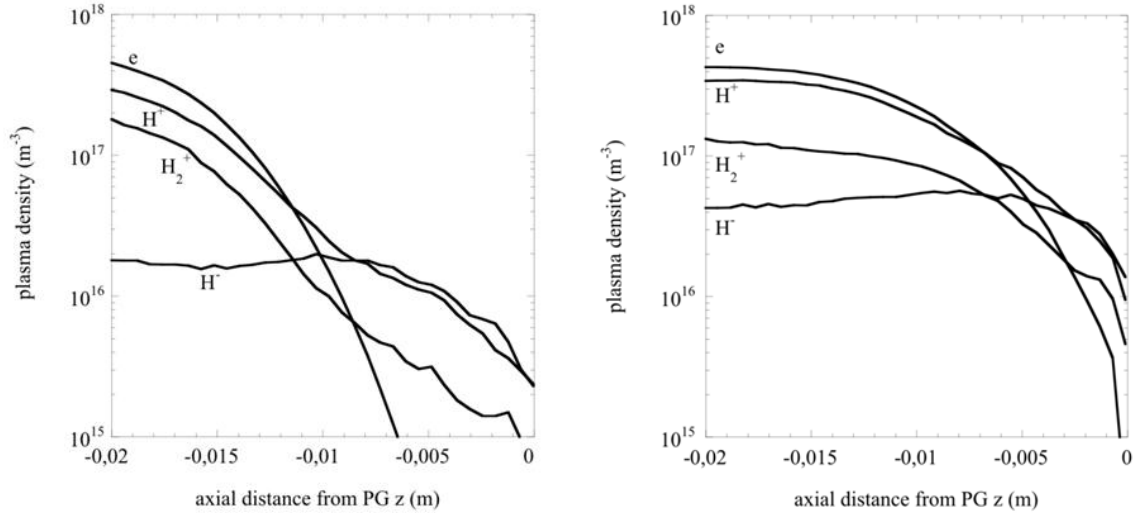
FIG. 14. Axial profiles of the plasma density for the two different line considered: (left panel) extraction hole (line A) and (right panel) PG surface (line B). (B_{peak}=4 mT and φ_{PG}=0 V.

Figs. 14(a-b) show the axial profiles of densities of charged particles for the case of PG bias φ_{PG}=0 V and for an extraction hole. The residual quantitative difference, albeit not big, in the particle densities on the left boundary of Figure 14 is a simulation artifact, which can be corrected by assuming an even larger domain with increase of the computational cost. However, the known phenomenology of discharge plasmas is retrieved: the plasma is neutral in the center (2 cm from the PG) while a charge region (the sheath) develops in contact to the grid. The most important effect is the contribution of surface processes to the negative ion production. The negative ion density near the wall increases by a factor of 5 in the case of the PG line. For this reason the plasma density near the grid increases also, reducing the insulating properties of the sheath and the sheath size as well.

9. CONCLUSIONS

Modeling of hydrogen plasmas for different technological applications, including fusion, needs extensive calculations of cross-sections for elementary processes as well as the application of kinetic tools to the description of the plasma as a whole. Different aspects, based on the work performed by our group, have been discussed in this paper. In particular vibrationally-resolved cross-sections involving electron-molecule and atom-molecule processes have been reported and used in a PIC-MCC description of a negative ion source for ITER. Radiation problems have been also reported including the dependence of photodissociation rates of H_2 on initial vibrational quantum number as well as new results for absorption and emission coefficients of an atomic hydrogen plasmas. Finally we discuss the dependence of thermodynamic and transport properties of LTE atomic hydrogen plasmas on the type of energy levels to be inserted in the partition function as well as the transport cross-sections of EES. The results reported emphasize the role of excited states in determining the properties of hydrogen plasmas in equilibrium and non-equilibrium conditions, indicating new trends towards a rigorous understanding of plasma properties.

ACKNOWLEDGMENTS

REFERENCES

[1] JANEV, R.K., REITER, D., SAMM, U., Collision process in low-temperature hydrogen plasmas, Berichte des Forschungszentrums, Jülich, Jül-4105 (2003).

[2] FRANZEN, P., et al., Progress of the development of the IPP RF negative ion source for the ITER neutral beam system, Nucl. Fusion **47** (2007) 264.

[3] CAPITELLI, M., et al. Vibrational kinetics, electron dynamics and elementary processes in H_2 and D_2 plasmas for negative ion production: modelling aspects, Nucl. Fusion **46** (2006) S260.

[4] HALL, R., ANDRIC, L., Electron impact excitation of H_2 (D_2). Resonance phenomena associated with the X $^2\Sigma_u^+$ and B $^2\Sigma_g^+$ states of H_2^- in the 10 eV region, J. Phys. B **17** (1984) 3815.

[5] KHAKOO., M. A., SEGURA, J., Differential cross-sections for the electron impact excitation of the $b^3\Sigma_u^+$ continuum of molecular hydrogen, J. Phys. B **27** (1994) 2355.

[6] STIBBE, D.T., TENNYSON, J., Near-threshold electron impact dissociation of H_2 within the adiabatic nuclei approximation, New J. Phys., **1** (1998) 2.

[7] RESCIGNO, T.N, SCHNEIDER, B.I., Electron-impact excitation of the b $^3\Sigma_u^+$ state of H^2 using the complex Kohn method: R dependence of the cross-section, J. Phys. B, **21** (1988) L691.

[8] CELIBERTO, R., et al., Cross-section data for electron-impact inelastic processes of vibrationally excited molecules of hydrogen and its isotopes, At. Data. Nucl. Data Tables **77** (2001) 1.

[9] HISKES, J.R., Cross-sections for the vibrational excitation of the H2 X $^1\Sigma_g^+$(v) levels generated by electron collisional excitation of the higher singlet states, J. Appl. Phys. **70** (1991) 3409.

[10] LARICCHIUTA, A., CELIBERTO, R., ESPOSITO, F., CAPITELLI, M., State-to-state cross-sections for H2 and its isotopic variants, Plasma Sources Sci. and Technol. **15** (2006) S62.

[11] BOOTHROYD, A.I., KEOGH, W.J., MARTIN, P.G., PETERSON, M.R., A refined H_3 potential energy surface, J. Chem. Phys. **104** (1996) 7139.

[12] GERSHENZON, Y.M., IVANOV, A.V., ROZENSHTEIN, V.B., UMANSKII, S.Y., High Energ. Chem. (Translated from Khim. Vys. Energ. **21** (1987) 387), **21** (1988) 323.

[13] CAPITELLI, M., et al., Elementary Processes, Transport and Kinetics of Molecular Plasmas, Atom. Plasma-Mater. Interact. Data Fusion, **14** (2008) 44.

[14] DALGARNO, A., Molecular processes in the early Universe, J. Phys.: Conf. Ser. 4 (2005) 10.

[15] ALEMAN, I., GRUENWALD, R., Molecular Hydrogen in the Ionized Region of Planetary Nebulae, Astrophys. J. **607** (2004) 865872.

[16] FLOWER, D.R., Atomic and molecular processes in interstellar shocks, J. Phys. B, **22** (1989) 2319.

[17] CAPITELLI, M., COPPOLA, C.M., DIOMEDE, P., LONGO, S., An evaluation of the effect of the dissociative attachment of vibrationally excited H_2 on primordial universe chemistry, Astron. Astrophys. **470** (2007) 811813.

[18] BLACK, J.H., DALGARNO, A., Models of interstellar clouds. I - The Zeta Ophiuchi cloud, Astrophys. J. Suppl. Ser. **34** (1977) 405.

[19] GALLI, D., PALLA, F., Astron. The chemistry of the early Universe, Astrophys. **335** (1998) 403.

[20] ALLISON, A.C., DALGARNO, A., Photodissociation of vibrationally excited H_2, HD, and D_2 by absorption into the continua of the Lyman and Werner systems , At. Data. Nucl. Data Tables, **1** (1969) 91.

[21] WOLNIEWICZ, L., The X $^1\Sigma_g^+$ state vibration-rotational energies of the H_2, HD, and D_2 molecules, J. Chem. Phys.**78** (1983) 6173.

[22] SCHLEICHER, D.R.G.,.et al., Effects of primordial chemistry on the cosmic microwave background, Astron. Astrophys. **490** (2008) 521.

[23] LANDAU, D., LIFSHITZ, E., Statistical Physics, Pergamon Press, Oxford (1986).

[24] PALMA, F.D., CASAVOLA, A.R., CAPITELLI, M., Influence of Electronic Excitation on the Thermodynamic Properties of Hydrogen Plasmas, J. Thermophys. Heat Tran. **20** (2006) 921.

[25] CAPITELLI, M., et al., Non-equilibrium plasma kinetics: a state-to-state approach, Plasma Sources Sci. Technol. **16** (2007) S30–S44.

[26] GRIEM, H.R., High-Density Corrections in Plasma Spectroscopy, Phys. Rev., **128** (1962) 997.

[27] GRIEM, H.R., Principles of Plasma Spectroscopy, Cambridge University Press, Cambridge (1997).

[28] D'ANGOLA, A., COLONNA, G., GORSE, C., CAPITELLI, M., Thermodynamic and transport properties in equilibrium air plasmas in a wide pressure and temperature range, Eur. Phys. J. D, **46** (2008) 129.

[29] BOULOS, M.I., FAUCHAIS, P., PFENDER, E., Thermal Plasmas: Fundamental and Applications, Plenum Press, New York (1994).

[30] CAPITELLI, M., GIORDANO, D., COLONNA, G., The role of Debye–Hückel electronic energy levels on the thermodynamic properties of hydrogen plasmas including isentropic coefficients, Phys. Plasmas, **15** (2008) 082115.

[31] CAPITELLI, M., FICOCELLI, E., The contribution of electronic excitation to the total specific heats of high temperature gases: a misinterpreted absence, J. Plasma Phys. **5** (1971) 115.

[32] CAPITELLI, M., BRUNO, D., COLONNA, G., CATALFAMO, C., LARICCHIUTA, A., Thermodynamics and transport properties of thermal plasmas: the role of electronic excitation, J. Phys. D, **42** (2009) 194005.

[33] BRUNO, D., CAPITELLI, M., CATALFAMO, C., LARICCHIUTA, A., Cutoff criteria of electronic partition functions and transport properties of atomic hydrogen thermal plasmas, Phys. Plasmas **15** (2008) 112306.

[34] BRUNO, D., LARICCHIUTA, A., CAPITELLI, M., CATALFAMO, C., Effect of electronic excited states on transport in magnetized hydrogen plasma, Phys. Plasmas **14** (2007) 022303.

[35] BRUNO, D., CAPITELLI, M., CATALFAMO, C., LARICCHIUTA, A., Transport of internal electronic energy in atomic hydrogen thermal plasmas, Phys. Plasmas **14** (2007) 072308.

[36] DEVOTO, R.S., Simplified Expressions for the Transport Properties of Ionized Monatomic Gases, Phys. of Fluids, **10** (1967) 2105.

[37] D'AMMANDO, G., PIETANZA, L.D., COLONNA, G., LONGO S., CAPITELLI, M., Modelling the spectral optical properties of atomic hydrogen plasmas, Spectrochim. Acta, Part B **65** (2010) 120.

[38] HEY, J.D., On the determination of radial matrix elements for high-n transitions in hydrogenic atoms and ions, J. Phys. B **39** (2006) 2641.

[39] STOREY, P.J., HUMMER, D.G., Fast computer evaluation of radiative properties of hydrogenic systems, Comput. Phys. Commun. **66** (1991) 129.

[40] KARZAS, W.J., LATTER, R., Electron Radiative Transitions in a Coulomb Field, Astrophys. J. Suppl. Ser. **6** (1961) 167.

[41] O'BRIEN, J., Transforms of the Hypergeometric Function that Allow for More Rapid Convergence in Calculations of Free-Free Gaunt Factors, Astrophys. J. **170** (1971) 613.

[42] PARI Group Bordeaux, PARI/GP version 2.4.2, available from http://pari.math.u-bordeaux.fr/, 2008.

[43] SOBEL'MAN, I.I., VAINSTHTEIN, L.A., YUKOV, E.A., Excitation of atoms and brodening of spectral lines, Springer-Verlag (1995).

[44] GRIEM, H.R., Stark Broadening by Electron and Ion Impacts of NA Hydrogen Lines of Large Principal Quantum Number, Astrophys. J., **148** (1967) 547.

[45] WATSON, J.K. G., Electron-impact broadening of radio recombination lines of atomic hydrogen for different Δn , J. Phys. B, **39** (2006) 1889.

[46] WELLS, R.J., Rapid approximation to the Voigt/Faddeeva function and its derivatives, J. Quant. Spec. Radiat. Transfer **62** (1999) 29.

[47] QUINE, B.M., DRUMMOND, J.R., GENSPECT: a line-by-line code with selectable interpolation error tolerance, J. Quant. Spec. Radiat. Transfer **74** (2002) 147.

[48] SPETH, E. et al., Overview of the RF source development programme at IPP Garching, Nucl. Fusion, **46** (2006) S220.

[49] TACCOGNA, F., SCHNEIDER, R., LONGO, S., CAPITELLI, M., Modeling of a negative ion source. I. Gas kinetics and dynamics in the expansion region, Phys. Plasmas **14** (2007) 073503.

[50] TACCOGNA, F., SCHNEIDER, R., LONGO, S., CAPITELLI, M., Modeling of a negative ion source. II. Plasma-gas coupling in the extraction region, Phys. Plasmas **15** (2008) 103502.

[51] TACCOGNA, F., LONGO, S., CAPITELLI, M., SCHNEIDER, R., Negative-Ion-Source Modeling: From Expansion to Extraction Region, IEEE Transactions on Plasma Science, **36** (2008) 1589.

[52] BIRDSALL, C.K., LANGDON, A.B., Plasma Physics via Computer Simulation, McGraw-Hill, New York (1985).

[53] SEIDL, M., CUI, H.L., ISENBERG, J.D., KWON, H.J., LEE, B.S., MELNYCHUK, S.T., Negative surface ionization of hydrogen atoms and molecules, J. Appl. Phys. **79** (1996) 2896.

[54] PELLETIER, J., POMOT, C., COCAGNE, J., Negative surface ionization: Intense halogen-ion source, J. Appl. Phys. **50** (1979) 4517.

VIBRATIONALLY STATE-SELECTIVE ELECTRON-MOLECULE COLLISION PROCESSES INVOLVING CH(v) AND THE H_2^- ($^2\Sigma_g^+$) RESONANCE

R. CELIBERTO[1], R. K. JANEV[2,3], D. REITER[3], J. M. WADEHRA[4], A. LARICCHIUTA[5]

[1]Department of Water Engineering and Chemistry,
 Polytechnic of Bari, 70125 Bari, Italy

[2]Macedonian Academy of Sciences and Arts,
 1000 Skopje, Macedonia

[3]Institute for Energy Research – Plasma Physics, Forschungszentrum – Juelich GmbH,
 52425 Juelich, Germany

[4]Physics Department, Wayne State University,
 Detroit, MI, 48202 USA

[5]Institute for Inorganic Methodologies and Plasmas,
 CNR, 70125 Bari, Italy

Abstract

We report on the results of cross-section calculations for the following three types of electron impact processes: 1) vibrational state-selective excitation of CH(X; v) to its first three electronically excited states CH(A; v'), CH(B; v') and CH(C; v'), 2) resonant vibrational excitation of $H_2(v)$ via its $H_2^-(^2\Sigma_g^+)$ resonance at 14 eV and 3) dissociative electron attachment on $H_2(v)$ via the same resonance producing H^- and H(n = 2). All these processes play an important role in the divertor plasmas of magnetic fusion devices.

1. INTRODUCTION

Atomic collision processes in fusion edge and divertor plasmas play an important role in resolving the impurity control and power exhaust issues that are critical for the successful operation of a magnetic fusion experiment. The power exhaust issue is further related to the outstanding problem of selection of adequate plasma facing materials on which severe requirements are imposed under reactor operation conditions. Atomic collision processes in the divertor of a fusion device determine the required plasma energy and momentum losses in order to bring the plasma power and particle fluxes on the plasma facing materials to acceptable levels. The quantitative information on the characteristics of these processes (cross-sections, rate coefficients, etc.) is obviously indispensable for modeling of divertor plasma properties (radiation and particle losses, neutral particle transport, etc) and its dynamics. This information, however, is equally necessary for the development of various plasma diagnostic methods and the interpretation of their results.

In the present article we report on the results of cross-section calculations for electron impact excitation of CH molecule in its ground and first five vibrationally excited states to the available vibrational states of the first three excited electronic doublet states and for the processes of resonant vibrational excitation (RVE) and dissociative electron attachment (DEA) to $H_2(X; v)$ involving the 14-eV resonance, $H_2^-(^2\Sigma_g^+)$. The vibrationally state-selective excitation of CH(v) plays a crucial role in the molecular divertor plasma diagnostics containing hydrocarbons [1, 2] and, in particular, for determination of chemical erosion fluxes entering the plasma from the graphite walls [3, 4]. The RVE and DEA processes involving vibrationally excited H_2 play also an important role in divertor plasma chemistry, particularly in the divertor plasma volume recombination, molecular dissociation and neutral particle transport [5, 6].

In presenting the results of our calculations, we shall keep the description of applied theoretical methods to a minimum and direct the reader to standard or specific references.

2. VIBRATIONALLY STATE-SELECTIVE EXCITATION OF CH

2.1. Computational method

We have studied the electron-impact excitation of CH to its lowest three excited doublet electronic states:

$$e + CH(X\,^2\Pi;\, v) \rightarrow CH(F;\, v'), \quad F = A^2\Delta, B^2\Sigma^-, C^2\Sigma^+ \tag{1}$$
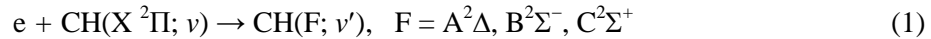
where v and v' denote the initial and final vibrational state, respectively. The previous studies of the above processes have been done only for the $v = v' = 0$ case and include the reaction rate calculations for excitation of $A^2\Delta$ [3] and $B^2\Sigma^-$ [4] states, performed by using the impact-parameter version of the Born approximation (BA) [7], and the R-Matrix (RM) cross-section calculations for all three final states [8] in the energy range below 10 eV. The BA formulation in [7] was done for the electron-ion (atom) case and for its use in the molecular case the required oscillator strength has to be taken from elsewhere. It is well known that BA is valid only for electron energies well above the reaction threshold (at least above 2-3 times of the threshold value) [9]. On the other hand, the RM method (implemented without pseudostates, as in Ref. [8]) provides good results only for energies below the ionization energy of the initial state.

In view of the need to have accurate cross-sections for processes (1) in the entire energy range of interest (from threshold to several hundreds eV) to fusion community, we have adopted in our work the following approach. We have first derived the cross-sections for the $v = v' = 0$ transitions of processes (1) by using the RM cross-sections of Ref. [8] available below 10 eV and smoothly connecting them with the quantal Born-Bethe (BB) cross-sections at energies above 18 – 20 eV. The BB cross-sections have been calculated by using the molecular form of BB approximation and the most accurate available electronic structure information (potential energy curves and transition dipole moments) for the ground and excited electronic states involved in processes (1) from Refs. [10] (for X and A states) and [11] (for B and C states). The transition matrix elements, involved in BB cross-section formula, were determined from the published dipole moments [10, 11] and by solving the Schrödinger equation for the nuclear motion in the adopted potentials [10, 11] of considered electronic states to determine their vibrational states. Hence, no use was made of Born-Oppenheimer approximation in determining the transition matrix elements. With the calculated vibrational wave functions and energies in the potential wells of the initial (X) and final (F) electronic state, it was also possible to calculate the transition matrix elements for all $(X;\, v) \rightarrow (F;\, v')$ transitions,

$$M_{Xv;Fv'} = \left\langle \chi_{Fv'} \left| D_{XF}(R) \right| \chi_{Xv} \right\rangle, \tag{2}$$

where $\chi_{\Lambda v}$ is the vibrational wave function of the level v in electronic state Λ, $D_{XF}(R)$ is the dipole moment between the states X and F and R is the internuclear distance in CH. The BB cross-section is given by the expression (in atomic units) [9, 11]

$$\sigma_{Xv;Fv'} = \frac{2\pi a_0^2}{3E} g \left| M_{Xv;Fv'} \right|^2 \ln\left(\frac{4EI_p}{\Delta E_{Fv';Xv}^2} \right), \tag{3}$$

where g is a statistical factor (equal to one for all processes in Eq. (1)), E is the electron energy, I_p (= 10.64 eV) is the ionization energy of CH, $\Delta E_{Fv';Xv} = E_{Fv'} - E_{Xv}$ is the transition energy and a_0 is the Bohr radius.

The BB cross-section is scalable with respect to reduced energy $\varepsilon = E / \Delta E_{Fv';Xv}$. If the cross-section $\sigma_{X0;F0}(\varepsilon)$ is known (as in our case, see the discussion above), then the BB cross-section for any $(X, v) \rightarrow (F, v')$ transition can be determined from the scaling relation

$$\sigma_{v,v'}(\varepsilon) = \frac{\Delta E_{0,0}}{\Delta E_{v,v'}} \frac{M_{v,v'}^2}{M_{0,0}^2} \sigma_{0,0}\left(\varepsilon \cdot \Delta E_{0,0}\right) , \tag{4}$$

where we have omitted the labels of electronic states for brevity. Although this scaling relation is, strictly speaking, valid only for reduced collision energies commensurate with the validity of Bethe-Born approximation, it can plausibly be assumed that when the cross-section $\sigma_{0,0}(\varepsilon)$ is determined with a higher accuracy (like in our case) that accuracy is approximately preserved in the scaled cross-sections as well. Eq. (4) was used in the present work for determining the cross-sections for the $(X, v) \rightarrow (F, v')$ transitions.

The scaling relation (4) translates also into a scaling relation for the excitation rate coefficients $K_{Xv;Fv'}(T)$ (Maxwellian average of Eq. (4)). The result is [12]:

$$K_{v,v'}(T) = \frac{\Delta E_{0,0}^{1/2}}{\Delta E_{v,v'}^{1/2}} \frac{M_{v,v'}^2}{M_{0,0}^2} K_{0,0}\left(T \cdot \frac{\Delta E_{0,0}}{\Delta E_{v,v'}}\right). \tag{5}$$

It should be mentioned that when solving the Schrödinger equation for the nuclear motion in the potentials of electronic states $X^2\Pi$, $A^2\Delta$, $B^2\Sigma^-$ and $C^2\Sigma^+$, we have found that these potentials support 15, 7, 1 and 3 vibrational levels, respectively, in accordance with previous calculations [10, 11]. However, except for the $v' = 0$ state of $A^2\Delta$, all these level are subject to predissociation (see, e.g., [12]). The ratio of radiative and predissociation decay rates depends on the rotational excitation within a given vibrational level, and for low rotational excitations the radiative decay is significantly faster than the predissociation decay only for the $v' = 1$ level of the A state and for the $v' = 0$ level of the C state. This circumstance has to be taken into account both in the hydrocarbon fragmentation modeling and in the CH-radiation based plasma spectroscopy.

2.2. Rate coefficients for vibrationally resolved excitation

The details of cross-section calculations for vibrationally resolved excitation transitions given by Eq. (1) are given in Ref. [12]. Here we present only the results for their rate coefficients.

The calculated rate coefficients for the $(X, 0) \rightarrow (F, 0)$ (F = A, B, C) in the temperature range 0.2 – 1500 eV can all be represented by the analytic fit

$$K_{0,0}(T) = \left(c_1 T^{-c_2} + c_3 + c_4 T + c_5 T^2\right)\exp\left(-c_6 / T\right) \; (cm^3 / s), \tag{6}$$

where T is plasma temperature in eV and c_i are the fitting coefficients given in Table 1.

TABLE 1. VALUES OF FITTING PARAMETERS C_I IN EQ. (6) FOR THE $(X, 0) \rightarrow (F, 0)$ TRANSITIONS (F = A, B, C)

Transition	c_1	c_2	c_3	c_4	c_5	c_6
X → A	-6.0857	0.15	16.204	$2.864 \cdot 10^{-3}$	$-7.3983 \cdot 10^{-7}$	3.0721
X → B	39.177	-0.03	-31.391	$3.4296 \cdot 10^{-4}$	$-8.0275 \cdot 10^{-8}$	3.3638
X → C	63.837	-0.03	-51.03	$4.7802 \cdot 10^{-4}$	$-1.1666 \cdot 10^{-7}$	4.224

For the calculation of $K_{0,v'}$ and $K_{v,v'}$ rate coefficients in the range $0.2\,\text{eV} \le T \cdot \Delta E_{0,0} / \Delta E_{v,v'} \le 1500\,\text{eV}$ one can use the scaling relation (5). The values of parameters $\Delta E_{v,v'}$ and $M_{v,v'}$ that appear in this equation can be found in Ref. [12] for all transitions from X($v = 0 - 4$) to A($v' = 0 - 4$), B($v' = 0$) and C($v' = 0 - 2$). It should be mentioned that the squared matrix elements $M_{v,v'}$ decrease very sharply with increasing the difference $|v'-v|$: by one to two orders of magnitude for each increase of this difference by one. This is a consequence of the fact that the potential energy curves of considered excited electronic states have the same shape and equilibrium nuclear distance (to somewhat smaller extent for the state B however) making the overlap of nuclear wave functions for the $v = v'$ states very close to one and, consequently, for those with $v \ne v'$ very small. This is, of course, reflected also in the magnitudes of the corresponding cross-sections and rate coefficients.

In Figures 1 – 5 we show the rate coefficients (in the temperature range 1 – 100 eV) for the transitions X($v = 0$) $\rightarrow$ A($v' = 0 - 4$), X($v = 0 - 4$) $\rightarrow$ A($v' = v$), X($v = 0 - 4$) $\rightarrow$ B($v' = 0$), X($v = 0$) $\rightarrow$ C($v' = 0 - 2$) and X($v = 0 - 2$) $\rightarrow$ C($v' = v$). The drastic decrease of rate coefficients with the increase of the difference $|v'-v|$ is obvious from the figures 1, 3 and 4.

The uncertainties of calculated rate coefficients have several sources: the basic cross-sections for the $0 \rightarrow 0$ transitions used in the present approach (the RM data of Ref. [8] and their interpolation to the region of validity of BB approximation), the input data for the BB calculations (potential energy curves of all considered electronic states and their coupling dipole moments) and the analytic fit of calculated rate coefficients. For the $v, v' \ne 0$ transitions, also the scaling relation (5) is a source of uncertainty. In the temperature range 1 – 100 eV, the fit (6) represents the calculated $K_{0,0}$ (T) data with an accuracy of about 1%, but outside this range its accuracy decreases to about 10% at the end points of the interval 0.2 – 1500 eV. The potential energy curves of the X and A states and the transition dipole moment D_{XA}(R) have a claimed accuracy of 5% [10], but the accuracy of the B and C potential curves and of the dipole moments D_{XB}(R) and D_{XC}(R) is lower, but better than 10% and 15%, respectively [11]. Analyzing the other uncertainty sources one can assess that in the temperature range 0.5 – 1000 eV the accuracy of the rate coefficients for $0 \rightarrow 0$ transitions may be in the range 15-20%, while for the $v \rightarrow v'$ transitions ($v, v' \ne 0$) it may be in the range 20-30%.

3. ELECTRON - H$_2$ COLLISION PROCESSES INVOLVING THE 14 eV - $^2\Sigma_g^+$ RESONANCE OF H$_2$

3.1. General considerations and theoretical model

The most effective mechanism for vibrational excitation of hydrogen molecule by electron impact is the so-called resonance mechanism, whereby the electron is temporarily captured (attached) to one of the resonant (autoionizing) states of H$_2$ and after its release (autode-tachment) the molecule is left in a vibrational state higher than the one it was before the collision. The resonant vibrational excitation (RVE) has already been studied for the two lowest resonances of H$_2$ appearing at ≈ 3.75 eV and ≈ 10 eV above the ground state energy, respectively. If the autodetachment is not completed during the time when the potential energy curves of these resonant states intersect the potential energy curve of the ground electronic state of H$_2$, then the temporarily formed negative H$_2^-$ ion dissociates to H$^-$ + H(1s) products. This dissociative electron attachment (DEA) process is also the main mechanism for H$^-$ formation in low-temperature plasmas, particularly when H$_2$ is vibrationally excited. Resonance states of H$_2$ have been experimentally observed also in the energy region around 14 eV above the H$_2$ ground-state energy level by observing DEA H$^-$ production [13, 14] and in the RVE differential cross-sections [15, 16]. Extensive R-matrix calculations, performed recently [17, 18], have confirmed the existence of several resonances in this energy region and provided information about their energies and widths for internuclear distances up to 4 a_0. Among these resonances the one having $^2\Sigma_g^+$ symmetry and energy threshold of 13.922 eV seems to be responsible for the observed resonance peak of DEA cross-section at 14 eV and has a system of vibrational levels (see [17]) in agreement with that observed experimentally [15, 16]. In order to shed more light on the dynamics of RVE and DEA processes in the e + H$_2$ system in the energy region around 14 eV, we have performed cross-section calculations for the these processes assuming that the resonant state is indeed the H$_2^-$($^2\Sigma_g^+$) state, i.e.,

$$e + H_2(v_i = 0) \rightarrow H_2^- \left({}^2\Sigma_g^+ \right) \rightarrow e' + H_2(v_f = 0 - 14), \quad (RVE) \tag{7}$$

$$e + H_2(v_i) \rightarrow H_2^- \left({}^2\Sigma_g^+ \right) \rightarrow H^-(1s^2) + H(n = 2), \quad (DEA) . \tag{8}$$

For the cross-section calculation of above processes we have adopted the local complex-potential (LCP) approximation [19, 20]. The use of LCP approximation for these calculations can be justified since the 14 eV $^2\Sigma_g^+$ resonance is a Feshbach type resonance. Below we shall give the basic computational formulae and some of the results of our calculations. The details of the calculations can be found in Ref. [21] for RVE and Ref. [22] for DEA.

3.2. Resonant vibrational excitation

The differential cross-section for the RVE process can be expressed, in an approximate form, as a product of an angular part, $g_{\bar{l}}(\vartheta)$, where ϑ is the scattering angle, times an energy-dependent term $\sigma_{v_i,v_f}^{res}(E)$. Explicitly [21]

$$\left(\frac{d\sigma^{res}}{d\Omega} \right)_{v_i \rightarrow v_f} = \sigma_{v_i,v_f}^{res}(E) \cdot g_{\bar{l}}(\vartheta) \tag{9}$$

.

The angular factor is defined in terms of Legendre polynomials, P_L, as $4\pi \cdot g_{\bar{l}}(\vartheta) = \sum_{L=0}^{2\bar{l}} A_L P_L(\cos \vartheta)$, where the coefficients A_L are given in Ref. [21]. The incident electron angular momentum quantum number $\bar{l}$ is associated, in the collision process, with the main entrance channel represented by the $\bar{l} - $th partial wave. Its value has been determined from the experimental analysis of Refs. [15, 16], in which the d nature ($\bar{l} = 2$) of the incident wave has been established. The energy-dependent term can be written as

$$\sigma_{v_i,v_f}^{res}(E) = \frac{4m^2\pi^3}{\hbar^4} \frac{k_f}{k_i} \left| \int dR \chi_{v_f J}^*(R) \cdot V_{\bar{l}}^*(k_f, R) \cdot \xi_i(R) \right|^2 \tag{10}$$

where m is the electron mass and k_i and k_f are the electron momentum before and after the collision, respectively. $\chi_{v_f J}^*(R)$ represents the vibrational wave function, depending on the internuclear distance R and associated with the rovibrational level (v_f, J) of the target molecule after the autodetachment process. $\xi_i(R)$ is the complex nuclear wave function of the resonant state and $V_{\bar{l}}^*(k_f, R)$ is the matrix element describing the resonant coupling between the $^2\Sigma_g^+$ bound electronic state and its energy continuum spectrum [21]. It is associated to the so-called energy width $\Gamma(R)$ of the resonant state through the relation $\Gamma(R) = 2\pi \left(mk_f / \hbar^2 \right)^{1/2} \times \left| V_{\bar{l}}^*(k_f, R) \right|^2$ and can be obtained by chemical structure calculations. Finally, the $\xi_i(R)$ resonant wave function can be calculated by solving the scattering equation which, in the LCP approximation, takes the form

$$\left[-\frac{\hbar^2}{2M} \frac{d^2}{dR^2} + \frac{\hbar^2 J(J+1)}{2MR^2} + V^-(R) - i\frac{\pi}{2}\Gamma(R) - E \right] \xi_i(R) = \left[\frac{\Gamma(R)}{2\pi} \right]^{1/2} \chi_{v_i J}(R) \tag{11}$$

.

Here M is the reduced nuclear mass, $V^-(R)$ is the potential energy of the resonant electronic state of the negative molecular ion, and $\chi_{v_i J}(R)$ is the target wave function of the (v_i, J) rovibrational level before the collision.

In Figures 6-8 the calculated $v_i \to v_f$ RVE differential cross-sections are shown as function of incident energy, for the $0 \to 1$-9 excitations, compared with the experimental values of Comer and Read [15]. The scattering angle ϑ has been set to 85°.

The agreement between the two sets of data, for $v_f > 2$, is quite satisfactory, particularly if we keep in mind that no empirical parameters have been introduced in the theoretical model. This successful comparison confirms the role of the resonant $^2\Sigma_g^+$ Rydberg state in the electron-impact vibrational excitations in the region of 10 - 14 eV observed experimentally.

The large discrepancy between theory and experiment, observed in figures 6 (a) and (b), is not due to the breakdown of theoretical model but can be interpreted as a background contribution to the cross-section coming from the direct vibrational excitation, not considered in the present calculations, which, as it is well known, is quite strong for excitations to the lower vibrational levels. For $v_f = 3$, in Figure 6 (c), in fact, the background is quite reduced.
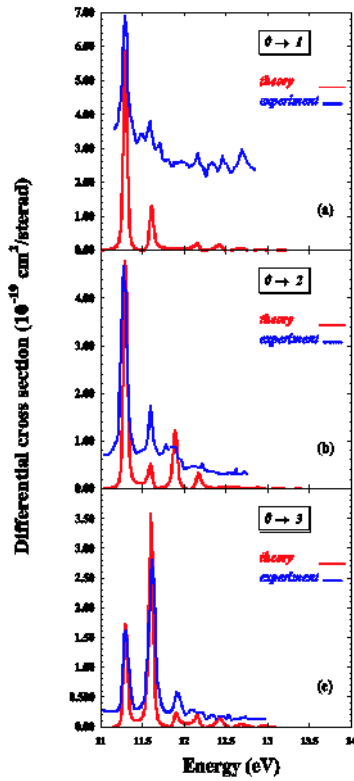
FIG. 6. RVE cross sections for the $0 \to vf = 1$-3 excitation.
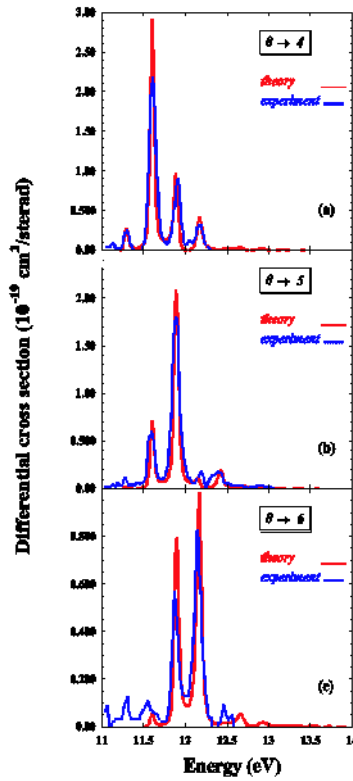
FIG. 7. RVE cross sections for the $0 \to v_f = 4$-6 excitation.
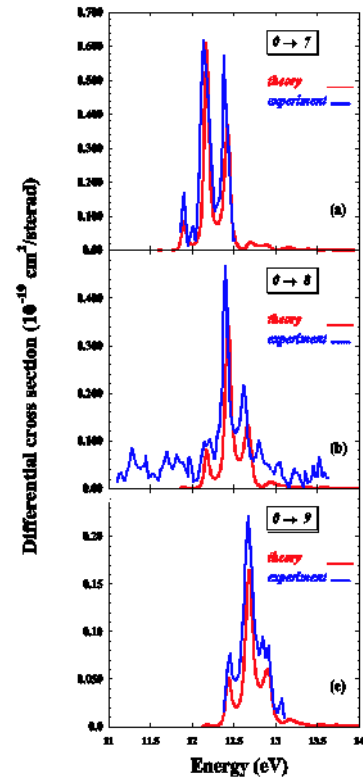
FIG. 8. RVE cross sections for the $0 \to vf = 7$-9 excitation.

3.3. Dissociative electron attachment

The DEA cross-sections can be written as [22]

$$\sigma(E) = 2\pi^2 \frac{m}{M} \frac{K}{k_i} \lim_{R \to \infty} |\xi(R)|^2$$

(12)

where K is the momentum of the outgoing negative ion produced in process (8). $\xi(R)$, already defined in the previous section, is obtained by solving Eq. (11) with the appropriate boundary conditions for a dissociative process.

In Figure 9 the DEA cross-section is shown as a function of collision energy for the process (8) where the molecule is initially in its lowest vibrational level, $v_i = 0$.
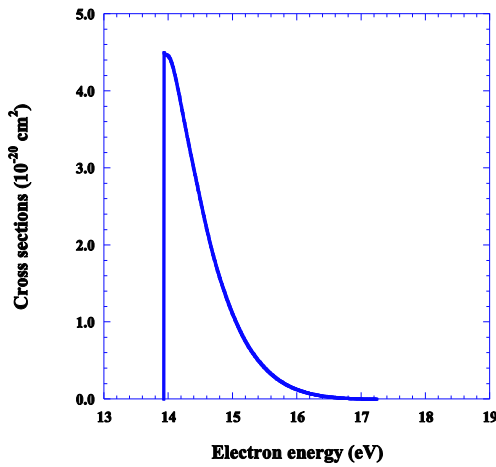
FIG. 9. DEA cross-sections as a function of the incident energy
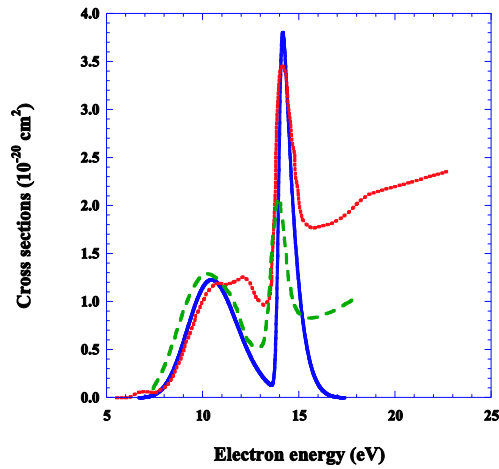
FIG. 10. Comparison between calculated (full curve) and measured cross-sections from refs. [13] (dotted curve) and [14] (dashed

The cross-section exhibits the typical onset behavior which characterize the DEA process occurring through bound electronic states of the intermediate resonant molecular ion. In order to compare this cross-section with the only available experimental measurements of Schultz [13] and Rapp et al. [14], we have summed the data of Figure 9 with the cross-section for the so-called 10 eV process occurring through the non-Rydberg repulsive state $^2\Sigma_g^+$ of the H_2^- ion, i.e.

$$e + H_2 \to H_2^-\left(^2\Sigma_g^+\right) \to H^-\left(1s^2\right) + H(1s)$$

(13)
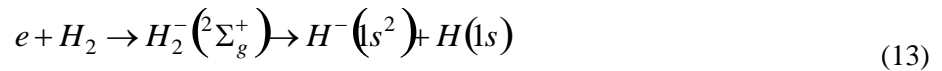
The cross-section for this DEA channel shows a broad peak at about 10 eV and has been obtained by Wadehra [23] by a semiempirical calculation performed in the frame of the LCP model.

The summed cross-sections for the DEA channels (8) and (13) have been convoluted with the instrumental resolution energy of 0.3 eV, as set in the Rapp et al. experiments [14]. The comparison between the theoretical and experimental cross-sections for the processes (8) and (13) is shown in Figure 10. The striking feature of this plot is the discrepancy, about a factor of 1.7, between the Schultz and Rapp et al. measurements, of the highest peak occurring at energy of about 14 eV, very

close to dissociation threshold energy of 13.922 eV of the $^2\Sigma_g^+$ Rydberg state. This disagreement is well known in literature and has never received an explanation. Our cross-sections seem to be in fairly good agreement with the Schultz results. However, some limitations in the input data of the theoretical model, prevents us from any definitive conclusion. The restricted range of internuclear distances for the potential curve and widths of the $^2\Sigma_g^+$ Rydberg state, as provided in Ref. [17], does not allow in fact the possibility of an unambiguous extrapolation of these quantities in the region of large R, and this might cause some uncertainty in the determination of the asymptotic value of the $\xi(R)$ wave function on which, according to Eq. (12), the DEA cross-section directly depends.

Above 14 eV other processes, not considered in the present theoretical calculations, can contribute, as suggested in Ref. [14], to the observed cross-sections, and may determine the rising portion of the experimental curves in this energy region.
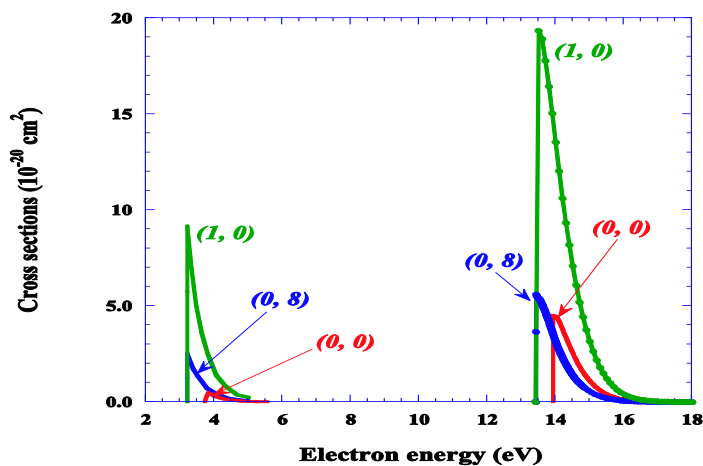
FIG. 11. Comparison between DEA cross-sections occurring through the $^2\Sigma_u^+$ ground state (left) and the $^2\Sigma_g^+$ Rydberg state (right) of the H_2^- ion. (see text).
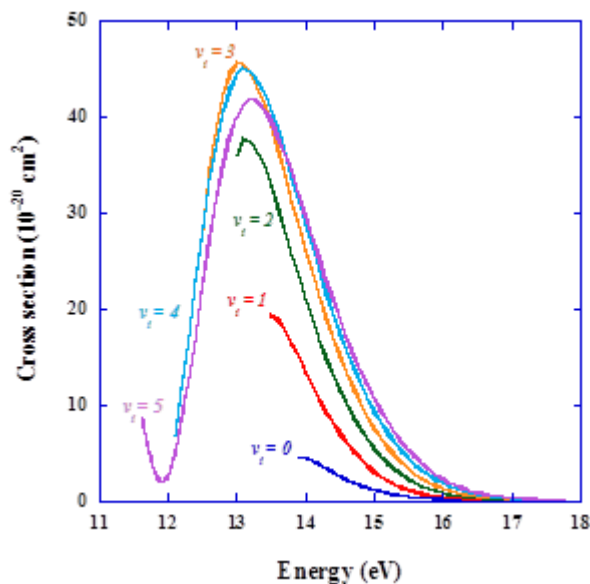
FIG. 12. DEA cross-sections for process (8) where v_i = 0-5.

It is well known since the early calculations of Wadehra and Bardsley [24] on the dissociative attachment process involving the $^2\Sigma_u^+$ ground state of the H_2^- ion that the cross-section strongly increases with the rovibrational excitation of the target molecule. In order to investigate this effect in the present case, we have calculated the cross-sections for the process (8) in two different rovibrational situations, namely $(v_i, J) = (1, 0)$ and $(v_i, J) = (0, 8)$. The obtained results are shown in Figure 11 (right side) where they are also compared with the corresponding DEA cross-sections for the $^2\Sigma_u^+$ ground state recently calculated by Horáček et al. [25] (left side). As expected, the DEA cross-sections increase with increasing the initial rovibrational energy of the molecule, particularly its vibrational excitation. The DEA cross-section enhancement due to the initial state vibrational excitation in the case of 14 eV H_2 resonance appears to be much stronger than in the case of 3.75 eV H_2 resonance (see Figure 11). This circumstance makes the 14 eV DEA process of particular importance for the negative H^- ion sources.

The increase in cross-section with the vibrational quantum number, however, is not regular, as can be seen in Figure 12 where the uncovoluted DEA cross-sections for process (8) for the first several vibrational levels of the neutral hydrogen molecule are shown. The $v_i > 0$ cross-sections shown in the Figure should be considered as preliminary results. They have been obtained again in the LCP approximation by making use of the same potential energy and widths of the $v_i = 0$ case. The enhancement of the cross-section with the vibrational excitation is observed for the first few v_i values, while for $v_i > 3$ the regular increase is interrupted and an unexpected threshold behavior, characterized by an oscillating structure which starts to appear for $v_i = 2$, becomes more and more evident for $v_i = 3$ to 5. Comparison of these curves, however, with those shown in Figure 2 of Ref. [25] for DEA from the $^2\Sigma_u^+$ resonant state, shows that a similar behavior is observed also in this latter case, although shifted to higher v_i values. A regular and strong increase of the cross-sections in Figure 2 of Ref. [25], in fact, is shown up to $v_i = 8$, but for higher v_i the curves follow a reversed trend and are characterized by the appearance of a maximum just above the threshold, quite similar to that of $v_i = 2$ and 3 curves in Figure 12.

Our first investigations seem to suggest that the observed cross-section behavior is mainly determined by the shape of the vibrational wave functions of the neutral H_2 molecule, and this could justify the cross-section oscillations. However, before reaching a conclusion, it will be necessary to extend the calculations to the higher vibrational levels and probably get a deeper insight also on the mathematical aspects of the model to completely rationalize the observed phenomena.

4. CONCLUSIONS

In this article we have presented the rate coefficients $K_{v_i, v_f}(T)$ for the electron-impact induced vibrational state-selective transitions from the $X^2\Pi$ ground state of the CH molecule to the $A^2\Delta$, $B^2\Sigma^-$ and $C^2\Sigma^+$ excited electronic states. The calculations have been performed on the basis of accurate R-matrix cross-sections available up to 10 eV and their extrapolation (above 20 eV) by the Born-Bethe cross-sections. The final results have been expressed in form of analytical fits for $K_{0,0}(T)$ and a scaling relation for $v_i, v_f > 0$. The same quantities have also been stored in the IAEA database in form of numerical data.

Cross-sections for electron-impact resonant collisions have been reported for vibrational excitation and dissociative electron attachment processes starting from the lowest vibrational level of the neutral H_2 molecule, and involving the $^2\Sigma_g^+$ resonant Rydberg state of the intermediate molecular ion H_2^-. Finally, preliminary calculations for dissociative attachment, involving the same H_2^- resonant state but starting from vibrationally excited hydrogen molecules, have been also presented and briefly discussed.

REFERENCES

[1]   POSPIESZCZYK, A., et al., Impurity sources in TEXTOR, J. Nucl. Mater. **145 -147** (1987) 574.

[2]   ISLER, R.C. et al., Spectroscopic determinations of carbon fluxes, sources, and shielding in the DIII-D divertors, Phys. Plasmas **8** (2001) 4470.

[3]   BEHRINGER, K.,Measurement of CH_4/CD_4 fluxes and of chemical carbon erosion from CH/CD band emission, J. Nucl. Mater. **176-177** (1990) 606.

[4]   FANTZ, U., et al., Correlation of the intensity ratio of C_2/CH molecular bands with the flux ratio of C_2H_y/CH_4 particles, J. Nucl. Mater. **337-339** (2005) 1087.

[5]   JANEV, R.K., Alternative Mechanisms for Divertor Plasma Recombination, Physica Scripta T**96** (2002) 94.

[6]   REITER, D., et al., in Atomic and Molecular Data and Their Applications (KATO, T., FUNABA, H., KATO, D., Eds) AIP Conf. Proceedings Series, **771** (2006) 3.

[7]   BURGESS, A., SUMMERS, H.P., The recombination and level populations of ions. I - Hydrogen and hydrogenic ions, Mon. Not. R. Astr. Soc. **174** (1976) 345.

[8]   BALUJA, K.L. MSEZANE, A.Z., Electron collisions with methylidyne (CH) radical using the R-matrix method, J. Phys. B **34** (2001) 3157.

[9]   INOKUTI, M., Inelastic Collisions of Fast Charged Particles with Atoms and Molecules—The Bethe Theory Revisited, Rev. Mod. Phys., **43** (1971) 297.

[10]   LARSSON M., SIEGBAHN, P.E.M., A theoretical study of the radiative lifetime of the CH A $^2\Delta$ state, J. Chem. Phys. **79** (1983) 2270.

[11]   DISHOECK, E.F., Photodissociation processes in the CH molecule, J. Chem. Phys. **86** (1986) 196.

[12]   CELIBERTO, R., JANEV, R.K., REITER, D., Basic molecular processes for hydrocarbon spectroscopy in fusion edge plasmas: vibrationally state-selective excitation of A $^2\Delta$, B $^2\Sigma^-$ and C $^2\Sigma^+$ states of CH by electron impact, Plasma Phys. Control. Fusion **51** (2009) 085012.

[13]   SCHULTZ, G., Formation of H$^-$ Ions by Electron Impact on H_2, Phys. Rev. **113** (1959) 816.

[14]   RAPP, D., SHARP, T.E., BRIGLIA, D.D., Large Isotope Effect in the Formation of H$^-$ or D$^-$ by Electron Impact on H_2, HD, and D_2, Phys. Rev. Lett. **14** (1965) 533.

[15]   COMER. J. READ, F.H., Potential curves and symmetries of some resonant states of H_2^-, J. Phys. B **4** (1971) 368.

[16]   JOYEZ, G., COMER, J., READ, F.H., Resonant rotational excitation of H_2 by electron impact, J. Phys. B **6** (1973) 2427.

[17]   STIBBE, D.T., TENNYSON, J., Electron- scattering resonances as a function of bond length, J. Phys. B **31** (1998) 815.

[18]   STIBBE, D.T., TENNYSON, J., Ab Initio Calculations of Vibrationally Resolved Resonances in Electron Collisions with H_2, HD, and D_2, Phys. Rev. Lett. **79** (1997) 4116.

[19]   BARDSLEY, J.N., Configuration interaction in the continuum states of molecules, J. Phys. B **1** (1968) 349.

[20]   ATEMS, D.E., WADEHRA, J.M., Nonlocal effects in dissociative electron attachment to H_2, Phys. Rev. A **42** (1990) 5201.

[21]   CELIBERTO, R., JANEV, R.K., WADEHRA, J.M., LARICCHIUTA, A., Cross-sections for 11−14-eV e-H_2 resonant collisions: Vibrational excitation, Phys. Rev. A **77** (2008) 012714

[22]   CELIBERTO, R., JANEV, R.K., WADEHRA, J.M., LARICCHIUTA, A., Cross-sections for 14-eV e-H_2 resonant collisions: Dissociative electron attachment, Phys. Rev. A. **80** (2009) 012712

[23]   WADEHRA, J.M., Rates of dissociative attachment of electrons to excited H_2 and D_2, Appl. Phys. Lett., **35** (1979) 917.

[24]   WADEHRA, J. M., BARDSLEY, J. N., Vibrational- and Rotational-State Dependence of Dissociative Attachment in e-H_2 Collisions, Phys. Rev. Lett. **41** (1978) 1795.

[25]   HORÁČEK, J., ČÍŽEK, M., HOUFEK, K., KOLORENČ, P., DOMCKE, W., Dissociative electron attachment and vibrational excitation of H2 by low-energy electrons: Calculations based on an improved nonlocal resonance model, Phys. Rev. A **70** (2004) 052712.

ABSOLUTE CROSS-SECTIONS AND KINETIC ENERGY RELEASE DISTRIBUTIONS FOR ELECTRON-IMPACT IONIZATION AND DISSOCIATION OF CD_n^+ (n=1-4)

P. DEFRANCE[1], J. LECOINTRE[2], R.K. JANEV[3,4]

[1]Université Catholique de Louvain, Département de Physique, Unité PAMO,
 Chemin du Cyclotron 2, B-1348 Louvain-la-Neuve, Belgium

[2]Durham University, Department of Chemistry,
South Road, Durham DH1 3LE, United-Kingdom.

[3]Institut für Plasmaphysik, Forschungszentrum Jülich Gmbh, EURATOM Association,
Trilateral Euregio Cluster, D-52425 Jülich, Germany

[4]Macedonian Academy of Sciences and Arts,
1000 Skopje, The Former Yugoslav Republic of Macedonia

Abstract

Absolute cross-sections for electron impact dissociative excitation and ionization of CD_n^+(n=1-4) leading to the formation of ionic products (CD_n^{2+}, D^+, D_2^+, C^+, CD^+, CD_2^+, CD_3^+) are reported in the energy range from their respective thresholds to 2.5 keV. The animated crossed-beams method is used. Around the maximum, all these cross-sections are found to range from 3×10^{-17} cm^2 to 20×10^{-17} cm^2, except for CD_n^{2+} and D_2^+, which are lower than 1.7×10^{-17} cm^2. Kinetic energy release distributions are deduced from the analysis of ionic product velocity distributions, which are obtained for each ionic fragment, at selected electron energies. KERDs are seen to extend from 0 to a maximum of 13 eV both for both for the light and the heavy ion fragments. The comparison of the present energy thresholds and kinetic energy release with available published data allows the identification of initial or intermediate states contributing to the observed processes. Individual contributions for dissociative excitation and dissociative ionization are determined for each singly-charged product, which are of significant interest in fusion plasma edge modelling and diagnostics. A complete database including cross-sections and energies is compiled for dissociative excitation and ionization of CD_n^+ions with n= 1–4, for use in fusion application.

1. INTRODUCTION

Electron impact experiments on the deuterated methane family members have been performed in our laboratory by means of a crossed electron-ion beam set-up. Each possible singly-charged ionic fragment has been detected separately and cross-sections for its production have been determined from their respective thresholds up to 2.5 keV. The absolute cross-sections and kinetic-energy-release distributions have recently been published for CD^+ and CD_4^+ [1, 2] and they are submitted for publication for $CD_2^+$and for CD_3^+ [3, 4] so that the CD_n^+ (n= 1–4) series is completed.

A comprehensive modelling of the hydrocarbon transport in tokamak divertors requires a complete set of cross-sections for all collision processes affecting the hydrocarbon fragmentation and chemistry. Among these molecular ions, the deuterated methane family (CD_n^+, n= 1–4) evidently plays a particular role. To get some more insight into the complexity of multispecies hydrocarbon plasmas, experimental electron-impact collisions with the deuterated methane family members CD_n^+ are being systematically investigated in our laboratory for n ranging from 1 to 4. Usually, for these experiments the deuterated target is chosen rather than the hydrogenated one, since the light D^+ fragment energy spread is lower in that case and consequently its collection is much easier than that of the H^+ fragments. Within the Born-Oppenheimer approximation and disregarding vibrational excitation, the energies as well as the lifetimes of the electronic states of the deuterated target are identical to those of the hydrogenated one.

The present paper reports on the available results regarding the production of the singly-charged ionic fragments from the (CD_n^+, n= 1–4) molecular ion. Following reactions are considered:

$$CD_n^+ + e^- \rightarrow CD_n^{+*} \rightarrow F_p^+ + \ldots \sigma_{np} \qquad (1)$$

with p= 1-6 for fragments $F_p^+ = D^+$, D_2^+/H_2^+, C^+, CD^+, CD_2^+, CD_3^+, CD_n^{2+} respectively. Reactions are noted in the synthetic form $F_p^+ = CD_n^+$ throughout this paper.

TABLE 1. LIST OF CROSS-SECTIONS (σ_{np}) MEASURED FOR THE CD_n^+ (n= 1– 4) TARGETS

p =	1	2	3	4	5	6	-
Target	D^+	D_2^+	C^+	CD^+	CD_2^+	CD_3^+	CD_n^{2+}
CD^+	σ_{11}	-	σ_{13}	-	-	-	-
CD_2^+	σ_{21}	σ_{22}	σ_{23}	σ_{24}	-	-	σ_2^{SI}
CD_3^+	σ_{31}	σ_{32}	σ_{33}	σ_{34}	σ_{35}	-	-
CD_4^+	σ_{41}	σ_{42}	σ_{43}	σ_{44}	σ_{45}	σ_{46}	σ_4^{SI}

Singly-charged ions are produced both by dissociative excitation (DE) and by dissociative ionization (DI) processes, so that, in the experiment, the ion production measurements correspond to the sum of the DE and the DI signals:

$$\sigma_{np} = \sigma_{np}^{DE} + \sigma_{np}^{DI} \qquad (2)$$

where σ_{np}^{DE} and σ_{np}^{DI} stand for the excitation and ionization contributions, respectively. Note that for technical and experimental reasons, the CH_3^+ target has been used for some reactions instead of CD_3^+.

A specific procedure has been developed to separate the DE and DI contributions to the total cross-section for each particular fragment [1] so that absolute cross-sections are reported separately for DE and for DI from the threshold up to 2.5 keV. Dissociative excitation can occur via direct (DDE) and via indirect (IDE) channels. Indirect dissociative excitation channels can be predissociative DE (PDE) or resonant DE (RDE) ones.

Doubly-charged molecular ions CD_n^{2+} result from single ionization (SI) of the molecular target. They have been observed only for n = 2 and n = 4, the corresponding reactions are labelled as σ_2^{SI} and σ_4^{SI}. Otherwise, CD_n^{2+} ions are formed in excited states, which preferentially dissociate to the singly-charged ion pair above the ionization threshold. A specific method for analysis of fragment velocity distributions is used to determine the kinetic energy released to dissociation products so that kinetic-energy-release distributions (KERDs) are determined for each ionic fragment, at selected electron energies.

The potential energy curves or surfaces relevant for the present discussion are well known for CH^+ and for CH_4^+ only, while for CH_2^+ and for CH_3^+, detailed information is not available. The reader may refer to the above-mentioned papers and reference therein for the description of ion structures. It is worth mentioning that metastable excited bound state may be formed in the ion source. Some of these states (electronically or vibrationally excited) have lifetimes which allow them to survive until ions reach the collision region, so that they may affect the experiment, in particular in the threshold energy region. This is the case for CD^+ and for CH_4^+.

Janev and Reiter (JR) [5] have developed a semi-empirical model to evaluate cross-sections for electron-impact ionization and dissociation of hydrocarbon anions. Cross-sections for one electron

ejection from all the orbitals of molecular ions are calculated both by the Binary-Encounter-Bethe (BEB) [6] and by the Deutsch-Märk (DM) [7] theoretical models.

In sections 2 and 3, the experimental set-up and the data analysis method are described for the estimation of absolute cross-sections and of kinetic-energy-release distributions. Section 4 is devoted to the description and the discussion of the results. The present work provides a database for the collisional processes mentioned in Table 1 which include cross-sections, thresholds and kinetic energies presented in a convenient form for their application in plasma physics. Present data have been fitted with the appropriate formulae whose estimated parameters are presented and discussed in the companion paper [8].

2. APPARATUS AND EXPERIMENTAL METHOD

The animated crossed electron-ion beam method is applied in present experiment [9]. The apparatus and the experimental method have been previously described in detail [2, 10]. The molecular ion beam of well-defined energy (a few keV) interacts at right angles with an electron beam whose energy is tuned from a few electron volts up to 2.5 keV. Product ions are separated from the primary ion beam by using a double focusing 90° magnetic analyser. Product ions are further deflected by a 90° electrostatic spherical deflector and directed onto the channeltron detector.

In the animated beam method [9], the electron beam is swept across the ion beam in a linear motion at a constant speed u. The total number of events K produced during one complete electron beam movement is related to the measured cross-section σ_m by

$$\sigma_m = \frac{uK}{I_e I_i \gamma} \frac{v_e v_i q_i e^2}{(v_e^2 + v_i^2)^{1/2}}$$

(3)

In this expression, γ is the detector efficiency, I_e and I_i, e and $q_i e$, v_e and v_i, are the electron and ion beam current intensities, the charges and velocities of electrons and ions, respectively. Assuming $m_i \gg m_e$, the interaction energy E (eV) is given by:

$$E = V_e + \frac{m_e}{m_i} \left(q_i V_i - V_e \right)$$

(4)

where V_e and V_i, m_e and m_i are the acceleration voltages and masses of electrons and target ions, respectively.

Due to the transfer of internal potential energy, dissociation fragments exhibit both a broad velocity and a broad angular distribution in the laboratory frame. The angular acceptance of the magnet analyser allows the total transmission of the angular distribution of product fragments emitted at a given velocity v in the laboratory frame. In order to put the cross-section on absolute scale, the velocity distribution is computed and the total cross-section σ is obtained by integrating this distribution over the entire velocity range. Finally, the total kinetic-energy-release distribution (KERD), for the investigated fragment, is expressed in terms of the velocity distribution by

$$\frac{d\sigma\left(E_{KER}\right)}{dE_{KER}} = \frac{-2\mu v_c}{m^2 \left(1 - \varepsilon/2\right)} \frac{d}{dv}\left(\frac{1}{v}\frac{d\sigma(v)}{dv}\right)$$

(5)

where m is the fragment ion mass, μ is the reduced mass of the fragments, v_c represents the centre-of-mass velocity and ε expresses the anisotropy factor. This quantity characterizes the angular distribution of dissociation products with respect to the velocity of the incident electron, due to the initial orientation of the molecular axis [10]. E_{KER} represents the sum of the kinetic energy released to

the dissociation fragments. By assuming the fragmentation of the target to be binary only and by applying the momentum conservation, this sum is given by

$$E_{KER} = \frac{m^2 w^2}{2\mu}$$

(6)

where w represents the fragment velocity in the centre of mass frame.

3. SEPARATION OF DE AND DI CONTRIBUTIONS AND DATA ANALYSIS

The light ionic products (D_2^+ and D^+) of reactions typically form two velocity distributions [2] whose shapes depend on the various E_{KERs} involved. At low energies, only DE is observed and the spectrum is narrow, what corresponds to low E_{KERs}. Above the ionization threshold, the spectrum becomes broader because of the Coulomb repulsion experienced by DI fragments. The DI signal is isolated by integrating the outer part of the spectrum and absolute values of DE cross-sections (σ_{np}^{DE}) are obtained by subtracting the DI contribution (σ_{np}^{DI}) from the total absolute cross-section σ_{np} for each fragment.

Moreover, the cross-section energy dependence also shows distinct contributions and this may help to check above findings. In absence of detailed information about the potential energy surfaces of excited states (CD_n^{+*}) and doubly excited states of (CD_n^{**}) (as well as of the corresponding couplings), it is not possible to obtain an unambiguous identification of the contribution of the different excitation channels to the total excitation cross-section. However, the thresholds of indirect processes are generally lower than those for the DDE channels. Moreover, as the indirect DE channels do not involve only (if at all, like in the RDE) dipole couplings but also additional couplings (as the non-adiabatic coupling in the case of PDE, or coupling with the ionization continuum in the case of RDE), the high-energy dependence of their cross-sections should be sharper than that for the DDE channels, governed dominantly by dipole electron transitions. Therefore, if both direct and indirect DE channels significantly contribute to the total DE cross-section, their contributions should produce a distinct structure in the total cross-section. Both the DDE and the DI contribution can be represented over the whole energy range by the expression

$$\sigma(E) = a \times \left(1 - \frac{E_{th}}{E}\right)^b \times \left(\frac{1}{E}\right) \times \ln\left(e + c \times E\right) \times 10^{-17} cm^2$$

(7)

where E is the electron energy, e is the Euler's number. a, b and c are fitting parameters and E_{th} is the estimated threshold energy for the particular considered process. The analytic form (7) has the usual Born-Bethe cross-section form for dipole allowed transitions, appropriately corrected in the threshold energy region, alike the one used by Janev and Reiter [5]. Although equation (7) only requires three adjustable parameters, it provides physically adequate representation of the cross-section behaviour both for DDE and DI processes together in both the threshold and high-energy regions [10]. The total excitation contribution $\sigma_{DE}(E)$ is obtained by subtracting the estimated DI component from the measured total absolute cross-section. The contribution of indirect DE channels can conveniently be represented in the form

$$\sigma_{DE1}(E) = a \times \left(1 - \frac{E_{th}}{E}\right)^b \times \left(\frac{1}{E}\right)^c \times 10^{-17} cm^2$$

(8)

where a, b and c are fitting parameters.

In DE reactions producing a given fragment, one generally observe two distinct structures in its total cross-section, the low-energy one (DE_1) can be attributed to some IDE process, while the one occurring at higher energies (DE_2) can be attributed to a DDE process. The thresholds for these two

DE processes, as well as those for other DDE reactions producing other ion products are determined from the experimental results. The root-mean-square (rms) deviation for these evaluations is estimated to be of the order of 10%.

For heavy carbonated (C^+, CD^+, CD_2^+, CD_3^+) fragments, velocity distributions are generally narrower. They do not show well-separated contributions allowing any separation of the two dissociative processes. Therefore, DE and DI contributions are isolated from the total absolute cross-section by using another procedure based on the kinetic-energy-release distributions and the thermochemical dissociation limits [5]. In most of the KERDs, the DI contribution can be isolated as it corresponds to a broad maximum at the high-energy side of the considered distribution. Knowing E_{th}^{DI} and a few values σ_{DI}, for which the KERD were measured, the shape of the DI absolute cross-section $\sigma_{DI}(E)$ is reconstructed

We should note that for a given ion production resulting from DE or DI, there may be more than one channel contributing to the cross-section, because neutral or ionic molecular products may dissociate. As an example, for CD_3^+, two DDE channels are forming CD^+ (σ_{34}^{DE}): $CD^+ + D_2$ and $CD^+ + 2D$ and two others are forming C^+ (σ_{33}^{DE}): $C^+ + D_2 + D$ and $C^+ + 3D$. These neutral particle channels have different (sometimes drastically) energy thresholds and the channel with the smallest dissociation limit usually gives the dominant contribution to the DE or DI cross-section.

The typical working conditions in our experiments were: ion current 3–10 nA, electron current 0.5–2.5 mA, electron beam sweeping speed 3.75 m/s. The number of events per sweep ranged from 0.05–1, depending on the fragment.

The total uncertainty (90 % confidence limit) is obtained as the square root of the quadratic sum of the statistical and systematic uncertainties [10]. For most of the investigated cross-sections, it is found to be less than 10 % at the cross-section maximum. Uncertainties associated with the separation or fitting procedures are estimated to be 10 % so that the total uncertainty (90% confidence limit) is found to be in range 15-20 %. The absolute cross-sections values are listed in paper [1-4] together with the associated total uncertainties.

4. TOTAL CROSS-SECTIONS

Absolute total cross-sections have been measured [1-4] in the energy range from their respective thresholds to 2.5 keV for production of singly-charged ionic (atomic and molecular) fragments from the CD_n^+ (n= 1–4) molecular ion (see Eq. (1)) for fragments F_p^+= D^+, D_2^+/H_2^+, C^+, CD^+, CD_2^+, CD_3^+, CD_n^{2+}, respectively, with p= 1-6. They are shown in figures 1 to 4 for n= 1–4, respectively. On these figures, error bars intentionally correspond to one standard deviation only and not the commonly used 90% confidence limit, in order to help distinguish between all different sets of data. This representation allows a global overview of all the present results and to compare their respective magnitude.

Present results are found to be in fair agreement with other available experimental results, which were obtained in crossed beams experiments or in merging beam experiments held at the storage rings [11], except for the low energy results (up to 80 eV) obtained for D^+/CD_n^+ [12] which are substantially (a factor of two) larger than present ones. To summarize these results, the cross-sections values at the maximum are given in Table 2, for each target and for each singly charged fragment, as well as for the doubly charged molecular ions which were observed for n = 2 and 4 only. The maximum of these cross-sections is reached at electron energies which are all in the range 75-115 eV. This maximum almost corresponds to the maximum of the DI cross-sections (see discussion below).

62
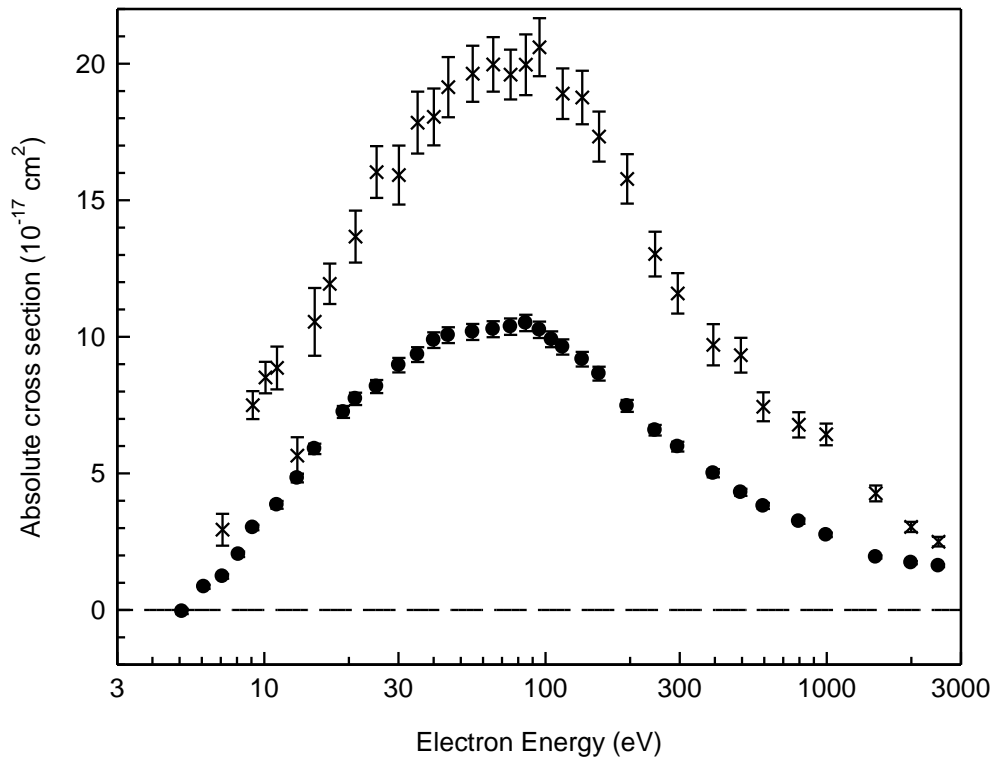
FIG. 1. *Absolute* cross-sections *for the production of* D^+ *($\bullet$, σ_{11}) and C^+ ($\times$, σ_{13}) versus electron energy.*
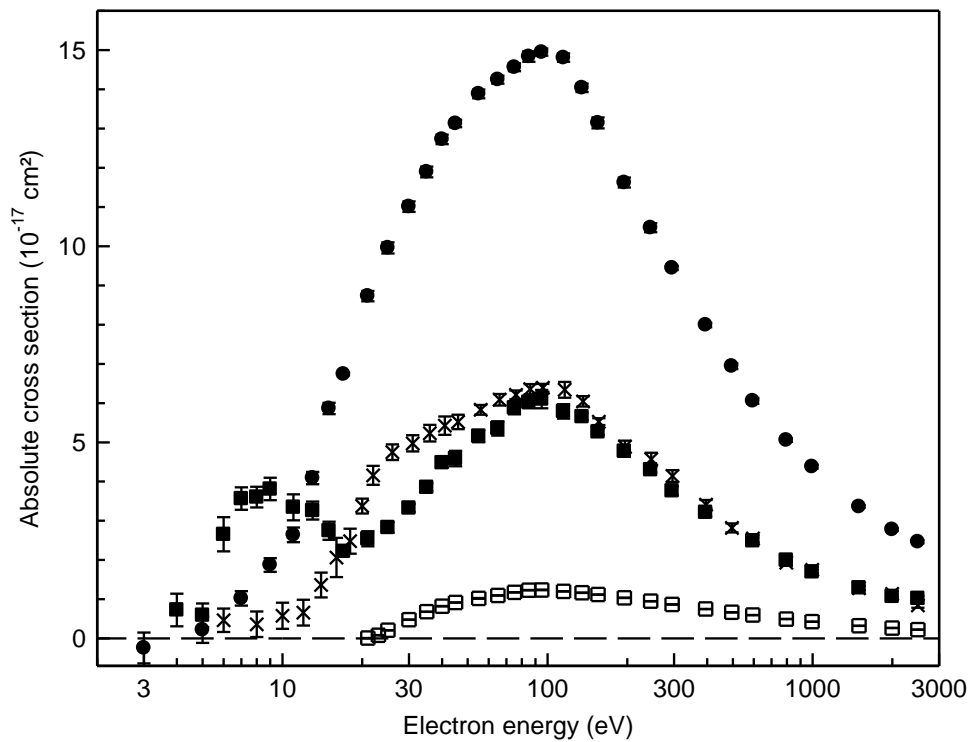
FIG. 2. *Absolute cross-sections versus the electron energy for electron-impact on* CD_2^+, *for the production of:* D^+ *(σ_{21} $\bullet$), C^+ (σ_{23} $\times$) CD^+ (σ_{24} $\blacksquare$), and CD_2^+ (σ_{2I} $\square$).*
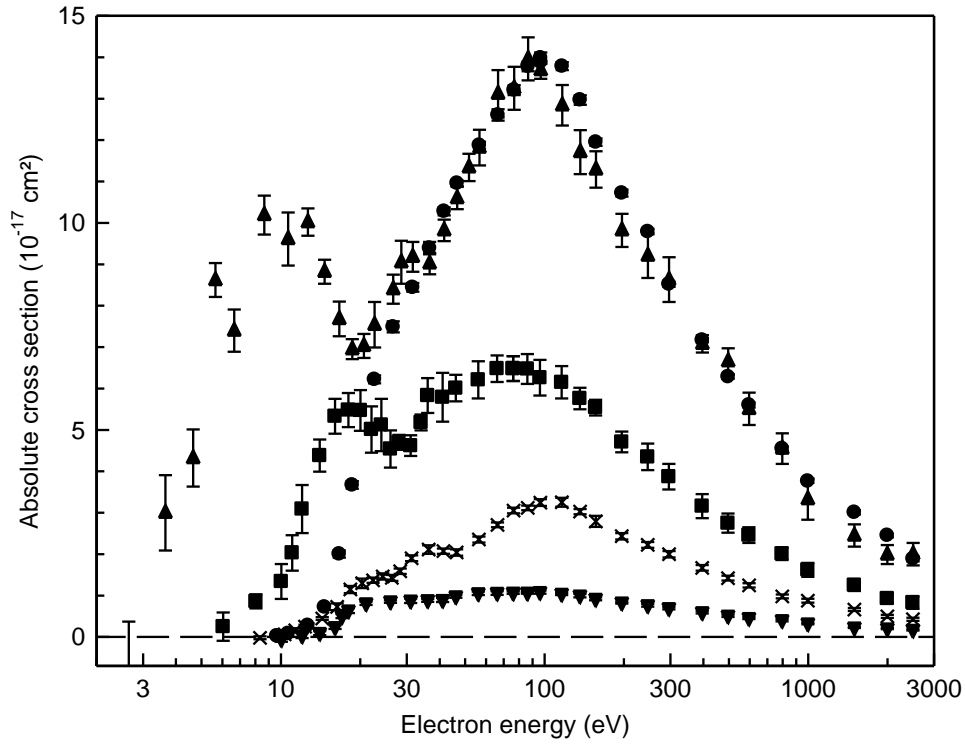
FIG. 3. Absolute cross-sections versus the electron energy for electron-impact on $CD_3^+/(CH_3^+)$ for the production of: D^+ (σ_{31} ●), H_2^+ (σ_{32} ▼), C^+ (σ_{33} ×), CH^+ (σ_{34} ■) and CD_2^+ (σ_{35} ▲).
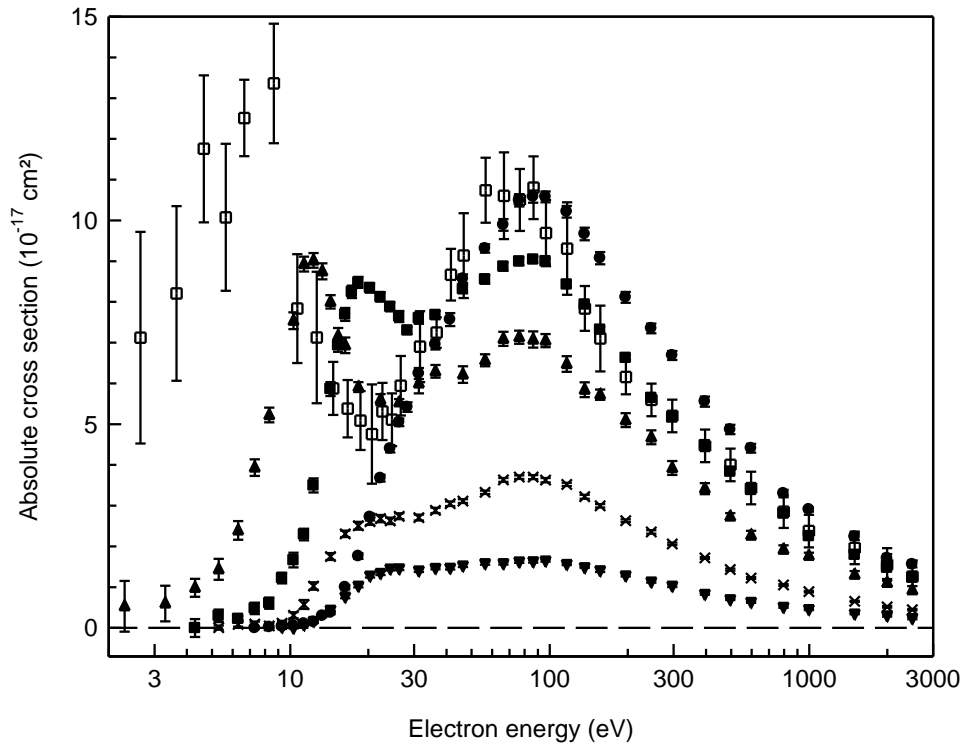
FIG. 4. Absolute total cross-sections for electron impact upon CD_4^+, versus the electron energy for: D^+ (σ_{41}; ●), D_2^+ (σ_{42}; ▼), C^+ (σ_{43}; ×), CD^+ (σ_{44}; ■), CD_2^+ (σ_{45}; ▲) and CD_3^+ (σ_{46}; □).

TABLE 2 MAXIMUM CROSS-SECTION

p =	1	2	3	4	5	6	7
Target	D^+	D_2^+	C^+	CD^+	CD_2^+	CD_3^+	CD_n^{2+}
CD^+	10.5±1	-	20.6±3.7	-	-	-	-
CD_2^+	14.9±1.4	0.26±0.04	6.4±0.7	6.1±0.7	-	-	1.24±0.11
CD_3^+	14.0±1.3	1.1±0.1	3.3±0.3	6.5±0.7	14.0±1	-	-
CD_4^+	10.6±1	1.7±0.2	3.7±0.4	9.0±0.8	7.1±0.8	10.8±1.5	0.038±0.002

Most of the investigated reactions have cross-section maxima in the range $3\text{--}15\times10^{-17}$ cm^2. The production of molecular hydrogen or deuterium (H_2^+ or D_2^+) fragments is very weak, though it is seen to rise from 0.26 to 1.7×10^{-17} cm^2 with increasing n. Some other fragments have been also studied: C^{2+}/CD^+, C^{3+}/CD^+ and D_3^+/CD_4^+ However, their corresponding maximum cross-sections were found to be very small (1.2×10^{-17} cm^2, 3.3×10^{-19} cm^2 and 8×10^{-20} cm^2, respectively) and we do not include them in the present discussion.

As described above, different procedures have been developed in order to determine separately the DE and the DI contributions, based on velocity distributions or on cross-sections shape. Results, which were obtained for all investigated reactions, are described in detail in the referenced papers and they are summarized in the companion paper [8], together with the analytic fits of the cross-sections. The present work provides an almost complete set of data which can be implemented in the model in order to improve it by systematic inclusion of experimental results, which are undoubtedly more realistic than the semi-empirical ones.

5. DE AND DI ENERGY THRESHOLDS

Threshold energies were estimated by extrapolation and analysis of experimental data in the low energy region. They are listed in Table 3, together with their uncertainties for all the DE, DI and SI processes.

TABLE 3. DE, DI AND SI EXPERIMENTAL ENERGY THRESHOLDS

Target	Process	D^+	D_2^+	C^+	CD^+	CD_2^+	CD_3^+	CD_n^{2+}
	p =	1	2	3	4	5	6	7
CD^+	DE	5.1 ± 0.5	-	5.5 ± 1.0	-	-	-	-
(m: $a^3\Pi$)	DI	22.1 ± 0.5	-	22.1 ± 0.5	-	-	-	-
CD_2^+	DE	4.0 ± 0.5 9.0 ± 1.0	7.0 ± 1.0	9.5 ± 1.0	4.5 ± 1.0 9.5 ± 1.0	-	-	-
	DI	23.0 ± 1.0	26.0 ± 1.0	25.5 ± 1.0	25.0 ± 1.0	-	-	21.0 ± 0.5
CD_3^+	DE	10.0 ± 0.5 13.0 ± 1.0	11.0 ± 0.5	9.5 ± 1.0 15.0 ± 1.0	6.0 ± 1.0 7.0 ± 1.0	2.5 ± 1.0 10.0 ± 1.0	-	-
	DI	24.6 ± 1.0	28.0 ± 1.0	29.4 ± 1.0	29.2 ± 1.0	25.5 ± 1.0	-	-
CD_4^+	DE	7.5 ± 0.5 11.5 ± 1.0	9.5 ± 0.5 17.0 ± 1.0	9.0 ± 1.0 16.5 ± 1.0	8.0 ± 1.0 12.5 ± 1.0	4.5 ± 1.0 8.2 ± 1.0	2.5 ± 1.0 17.5 ± 1.0	-
(m: v)	DI	26.5 ± 1.0	28.5 ± 1.0	$30.0 \pm 1.$	29.0 ± 1.0	24.7 ± 1.0	19.2 ± 1.0	22 ± 1

For CD^+, the lowest threshold energy leading to the $C(^3P)+D^+$ dissociation limit was calculated to be 6.5 eV from the ground state $X^1\Sigma^+$ [12]. The present D^+ production threshold (5.1 ± 0.5 eV), is found to be in good agreement with the theoretically predicted one (5.3 eV), assuming a shift (1.2 eV) due to the presence of the $a^3\Pi$ metastable state in the primary beam. For C^+/CD^+, the present value of 5.5 eV, agrees both with the upper Test Storage Ring (TSR) [18] result and with the theoretical threshold leading to the $C^+(^2P)+D(^2S)$ dissociation limit (5.6 eV from the ground state $X^1\Sigma^+$ [13]. A contribution from the $a^3\Pi$ metastable state to this channel is probably excluded because it would shift the threshold down to 4.4 eV. Similar conclusions can be drawn for other targets, DE energy thresholds are generally found in good agreement with estimations or predictions assuming target ions to be in the ground state. Nevertheless, some reaction channels seem to be fed by possible metastable states, electronically or vibrationally excited. As it can be seen from table 3, even the lowest DE threshold energy is determined to be (2.5 ± 1.0) eV, for CD_3^+/CD_4^+, in good agreement with estimation of Rabalais et al [14] (2.19 eV). These figures are the lowest ones to be obtained in crossed beams experiments.

Reasonable agreement is observed for all the DE threshold energies. Present values are often found to be somewhat higher than the other experimental groups. For these targets cations, vibrational excitation and complicated interconnections among point-groups may evidently affect threshold values. In the present experiment, there is no way to estimate the population of vibrationally excited states of either parent or fragment ions.

As mentioned above, only CD_2^{2+} and CD_4^{2+} have been observed as doubly-charged molecular ions and the corresponding single ionization energy threshold for are observed to be in good agreement with theoretical or experimental values. In spite of the very weak CD_4^{2+} signal, starting at 22 eV, an even weaker signal extending down to 18 eV, indicates the presence of metastable states which are barely identified.

For the CD^+ target, present DI threshold energies obtained both for the $C^+ + D^+$ channel (22.1 ± 0.5) eV and for C^{2+} formation confirm the observation of the energy shift due to the presence of metastable states which could be the $a^3\Pi$ state or excited rovibrational levels of the $X^1\Sigma^+$ state with v<10. All these energies are in the range 22-30 eV, with the exception of 19.2 eV, obtained for

CD_3^+/CD_4^+. This unexpectedly low value could result from imperfect the separation procedure, the DE_2 channel being important, with a threshold of 17.5 eV, i.e. very close the DI one.

6. TOTAL EXCITATION AND IONIZATION CROSS-SECTIONS

Total ionization cross-sections are determined as the sum of the SI and the partial DI cross-sections for all the reaction channels:

$$\sigma_n^I = \sigma_n^{SI} + \frac{1}{2}\sum_p \sigma_{np}^{DI}$$

(9)

The factor 1/2 is introduced to avoid double-counting of ionic products resulting from the same DI event.

For CD^+, the measured maximum cross-section is slightly underestimated by the BEB [6] and DM [7] models (Figure 5). Both curves are in good agreement with present experimental results, for energies above about 150 eV, but at lower energies, the calculated cross-sections slightly underestimate the experimental data. As pointed out above, metastable states ($a^3\Pi$ or vibrationally excited states) could also contribute to the observed ionization signal and subsequently, they may partially account for the observed differences. For CD_4^+ (Figure 6a), the both the BEB and the DM models overestimate the experimental result, while, as expected, the semi-empirical Janev-Reiter (JR) model closely reproduces these results.
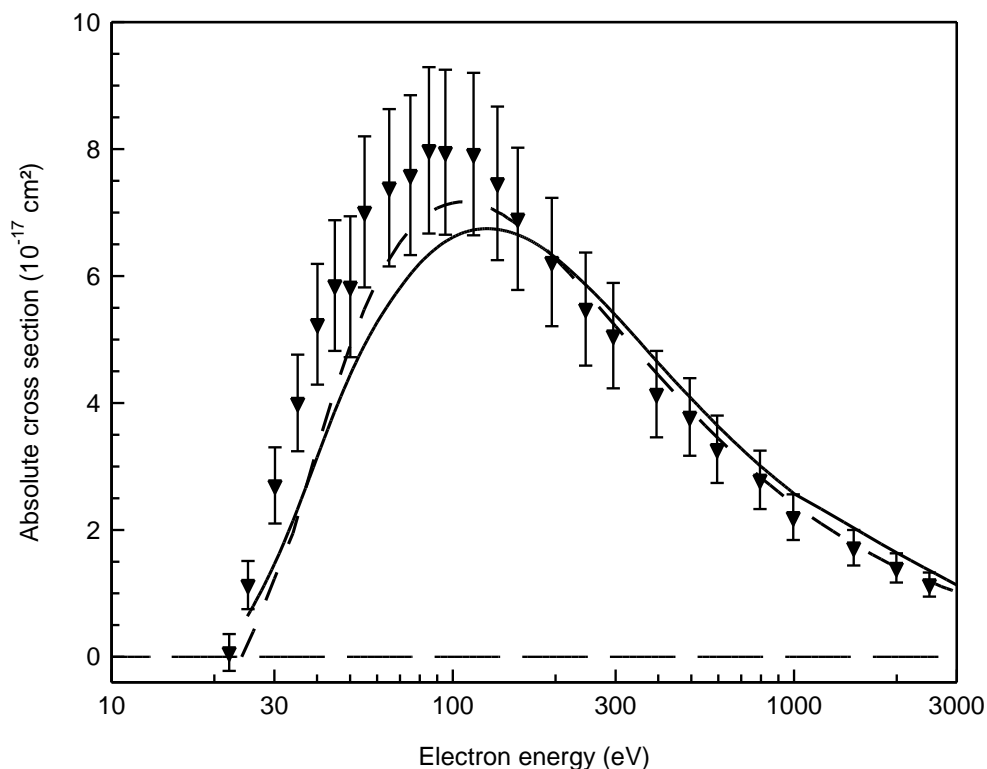
FIG. 5. Total ionization cross-sections (σ_I) for electron impact upon CD^+ versus electron energy: ▼, present measurements; ——, DM formalism [7]; — —, BEB model [6].
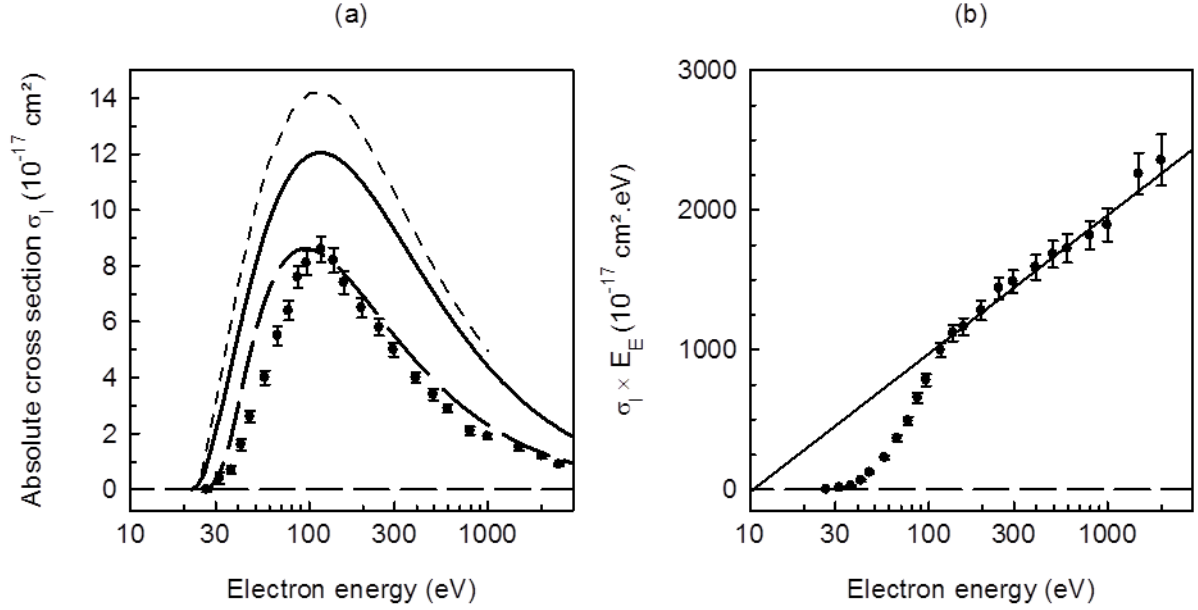
FIG. 6. (a) Total ionization cross-sections (σ_I) for electron impact upon CD_4^+ versus electron energy: (●) present measurements; (———) BEB formalism [6]; (− −) DM formalism [15] and (— —) semi-empirical model [5]. (b) Bethe-plot of the ionization cross-section (σ_I). The full line results from a linear fit using the Bethe-Born formula.

It is particularly interesting to check the energy dependence of both the excitation and the ionization cross-sections and, for this purpose, the Bethe-plot of data is remarkably powerful, as it indicates the general trends of high energy cross-sections. Figure 6b shows such a plot for data of Figure 6a. The linear dependence, observed above 100 eV, indicates that the cross-section can adequately be represented by the usual Bethe-Born formula [16]

$$\sigma = \frac{4\pi a_0^2 R}{E}\left[M^2 \ln\left(\frac{E}{R}\right) + \gamma\left(\frac{R}{E}\right) + C \right] \tag{10}$$

where a_0 is the first Bohr radius of atomic hydrogen, R is the Rydberg energy, γ and C are two constants characteristic of the target. The squared matrix element M^2 is obtained by integrating the generalized oscillator strength for the considered process, M_I^2 and M_E^2 for ionization and excitation, respectively. The second term into brackets $\gamma\left(\frac{R}{E}\right)$ becomes negligible in the high-energy region.

Similarly to ionization, total excitation cross-sections are determined as the sum of the partial DE and DI cross-sections for all the reaction channels:

$$\sigma_n^E = \sum_p \sigma_{np}^{DE} \tag{11}$$

The results are shown in the normal plot (Figure 7a) and in the Bethe-plot (Figure 7b), respectively. Figure 7a indicates the necessity to adapt the JR model to present data. No other data are presently available for electron impact excitation of presently investigated targets. Moreover, the excitation cross-section also exhibits the Bethe-Born energy dependence above 100eV. Figures 8a and 8b and Figures 9a and 9b show these data for CD_2^+ and CD_3^+, respectively.
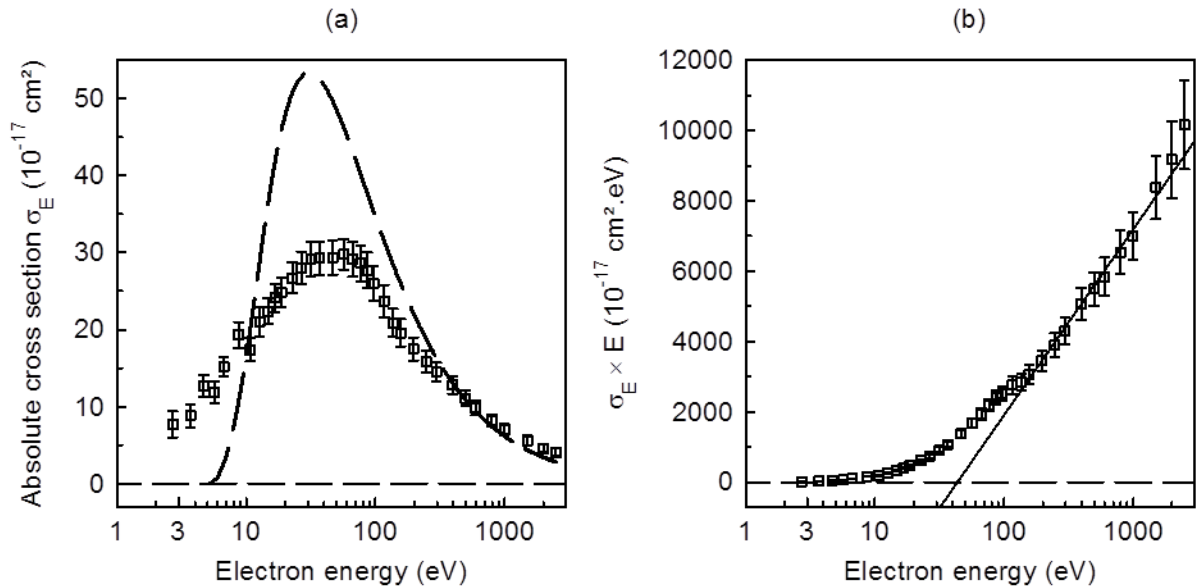
FIG. 7. (a) Total excitation cross-sections (σ_E) for electron impact upon CD_4^+ versus electron energy: (□) present measurements and (— —) semi-empirical model [5]. (b) Bethe-plot of the excitation cross-section (σ_E). The full line results from a linear fit using the Bethe-Born formula.
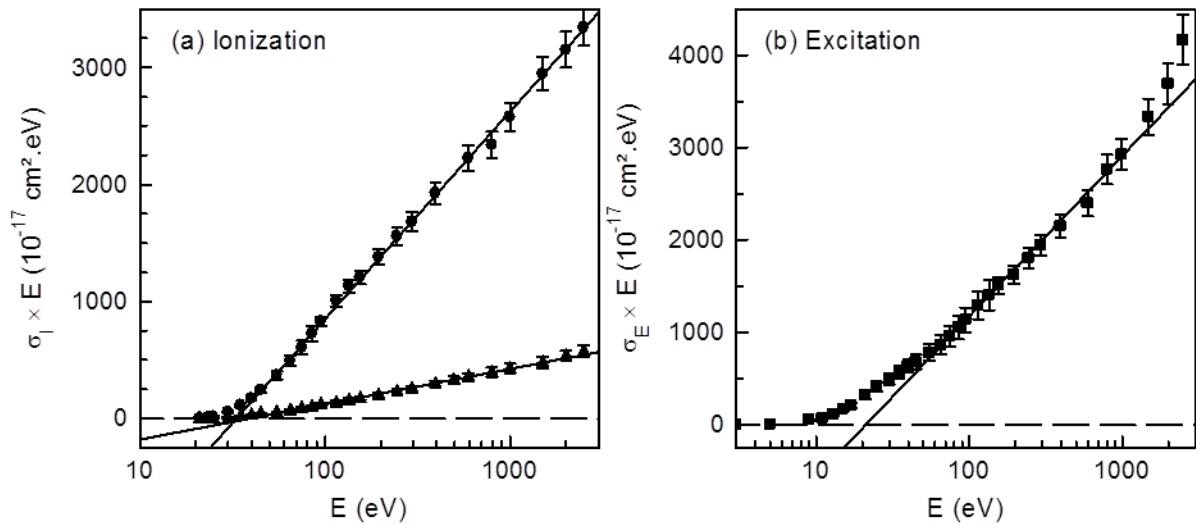
FIG. 8. Bethe-plot of the (a) total ionization cross-section (● σ_I) together with the single ionization cross-section (▲ σ_{SI}), and of the (b) total excitation cross-section (■ σ_E) of CD_2^+. Each full line results from a linear fit using the Bethe-Born formula.

For CD_2^+, single ionization cross-sections are also reported in Figure 8a, and one notices that the SI cross-section is a significant part of the total ionization cross-section. Moreover, in this case, the Bethe-Born high-energy behaviour is seen to extend well below the maximum cross-section, both for the total and for the SI cross-sections.
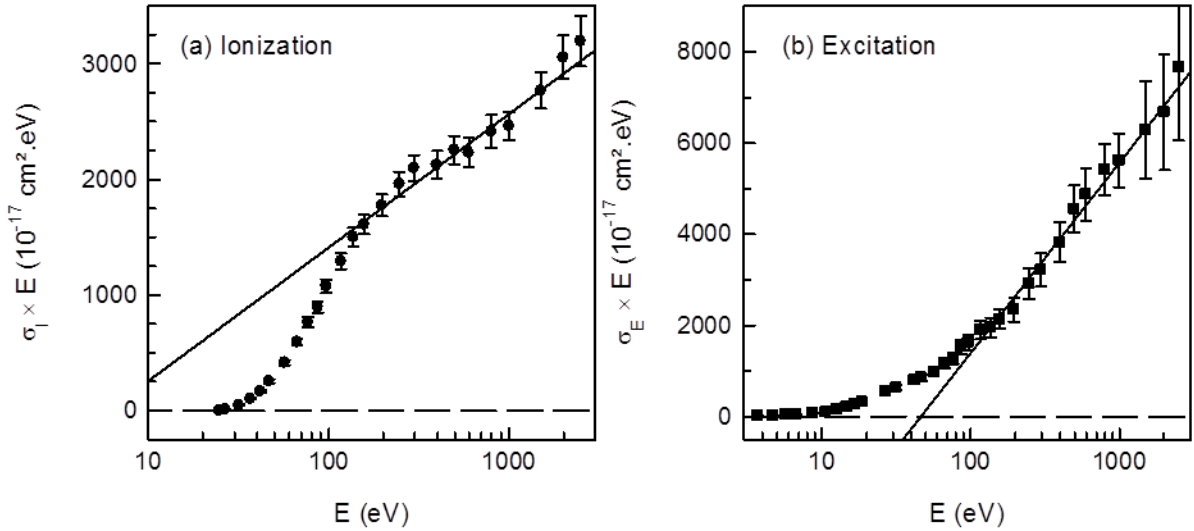
FIG. 9. Bethe-plot of the (a) total ionization cross-section ($\bullet$ σ_I) and of the (b) total excitation cross-section ($\blacksquare$ σ_E) of $CD_3^+/(CH_3^+)$. Each full line results from a linear fit using the Bethe-Born formula.

The total CD_4^+ ionization cross-section is unexpectedly of comparable magnitude to that of CD^+ [1, 2], in contrast to what was observed for the ionization cross-sections of the corresponding neutral hydrocarbons, CD and CD_4. For these targets, a monotonic increase among the CD_n (n=1–4) sequence is observed, in agreement with the empirical additivity rule which predicts the linearity of σ_I with the number of deuterium atoms in CD_n.

Ionization (σ_I) and excitation (σ_E) data are fitted to the asymptotic form of equation (10). The present values of M_I^2 and of M_E^2 are listed in table 4. They are calculated to be (1.05±0.05) and (4.0±0.1) for total ionization and total excitation of CD_3^+, respectively. M_I^2 is found to be larger than the one obtained for electron-impact upon CD_4^+, whereas M_E^2 is found to be smaller. The present value of M_I^2 is estimated to be (0.90±0.05) for total ionization of CD_4^+.

TABLE 4. PRESENT VALUES OF M_I^2 AND OF M_E^2 FOR TOTAL EXCITATION AND IONIZATION OF CD_n^+

Target	Excitation: M_E^2	Ionization: M_I^2
CD^+	2.5±0.1	1.37±0.05
CD_2^+	1.6±0.1	1.61±0.05
CD_3^+	4.0±0.1	1.05±0.05
CD_4^+	4.8±0.1	0.90±0.05

7. KINETIC ENERGY RELEASE DISTRIBUTIONS

Kinetic-energy-release distributions (KERDs) of dissociation fragments are determined according to the above-mentioned procedure (see above, equations (5) and (6)). It is worth reminding that E_{KER} is defined as the total kinetic energy released to dissociation fragments, assuming that only two fragments are emitted in the process. This means that E_{KER} directly reflects the energy difference between the dissociation limit and the intermediate state formed via a Franck-Condon transition. They are obtained at the selected incident electron energies where analyzer magnetic field scans have been performed, for each investigated reaction F_p^+/CD_n^+. As example, results obtained for CD_4^+ are shown in Figure 10 at the indicated electron energies.
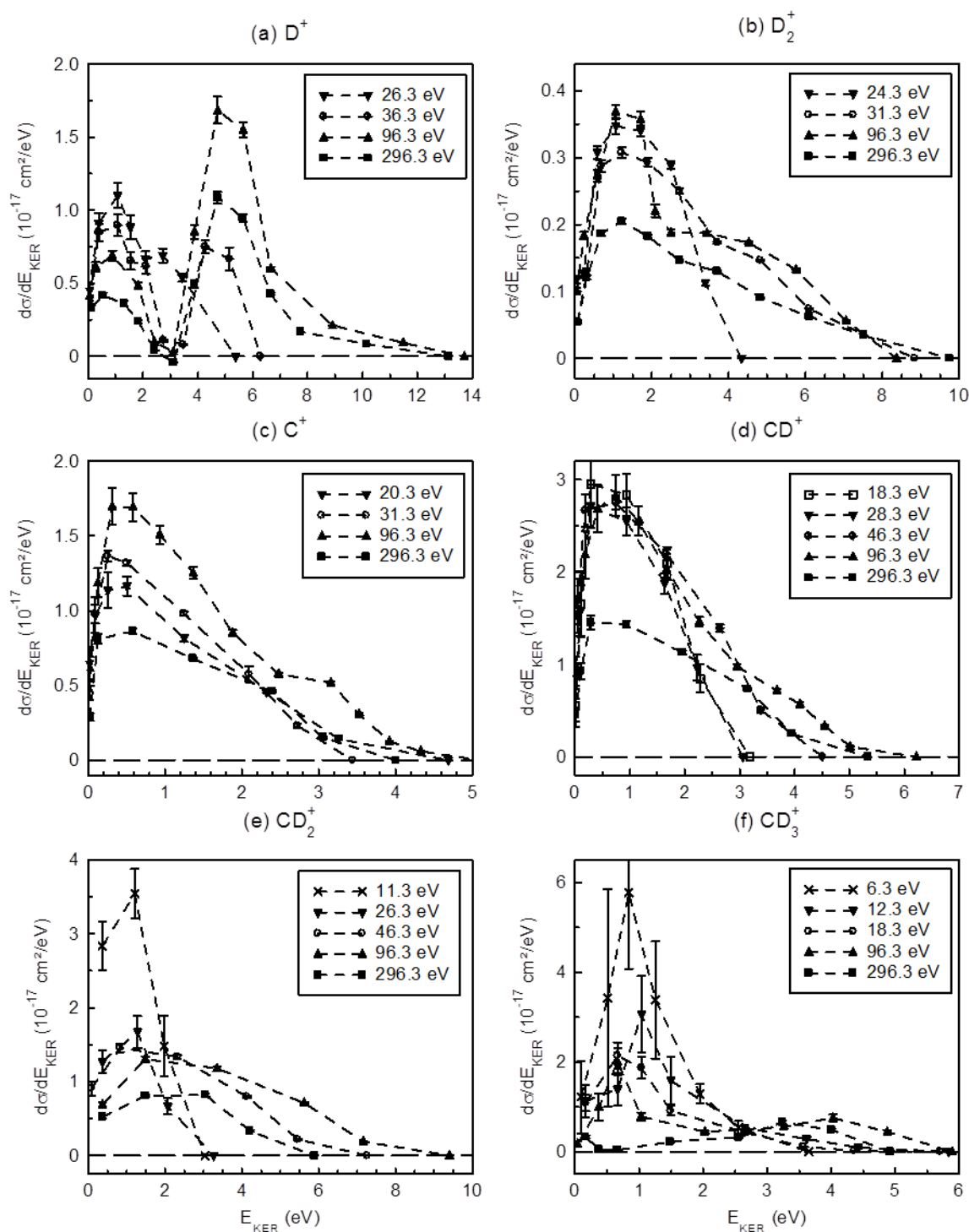
FIG. 10. Total kinetic energy release distributions for electron impact upon CD_4^+, for indicated electron energies for: (a) D^+, (b) D_2^+, (c) C^+, (d) CD^+, (e) CD_2^+ and (f) CD_3^+.

The KERDs for extreme fragments, the lightest and the heaviest ones, exhibit common features: for both of them two distinct contributions can be isolated, one ranges approximately from 0 to 2.5 eV and the other one from 2.5 to 9 eV. The low energy contribution may be attributed to DE and the high energy one to DI, as one can expect, because coulomb repulsion transfers the maximum kinetic energy to dissociation fragments. For other carbonated fragments, KERDs are smooth curves without clear apparent structure, meaning that the KERD for DE is overlapping with the DI one. The DE KERD is here only identified by observing the signal below the ionization threshold, where distributions are generally peaked in the low KER range, as DE dominates. Above the ionization threshold, dissociative contributions are barely isolated, excitation and ionization KERDs overlap. For higher incident electron energies, KERDs progressively enlarge from 3 to 15 eV, due to the opening of successive DI channels. Moreover, as already mentioned above, none of the dissociative processes is significantly dominant, even for high electron energies. Consequently, for many fragments, the DI and the DE contributions cannot be separated.

Mean kinetic-energy-release ($\overline{E_{KERs}}$) are deduced from the analysis of the observed KERDs below 40 eV for DE, and above 90 eV for DI (Table 5).

TABLE 5. DE AND DI EXPERIMENTAL MEAN $\overline{E_{KERs}}$

	p =	1	2	3	4	5	6
Target	Process	D^+	D_2^+	C^+	CD^+	CD_2^+	CD_3^+
CD^+	DE	3.8 ± 0.5	-	3.5 ± 0.5	-	-	-
(m: $a^3\Pi$)	DI	6 ± 1					-
CD_2^+	DE	2.1 ± 0.2	2.2 ± 0.2	1.0 ± 0.2	0.5 ± 0.1 1.5 ± 0.2	-	-
	DI	5.6 ± 0.2	5.0 ± 0.6	5.6 ± 0.2	3.9 ± 0.2		-
CD_3^+	DE	1.0 ± 0.2	1.3 ± 0.1	0.5 ± 0.1	1.5 ± 0.2	0.5 ± 0.1	-
	DI	5.6 ± 0.2	2.8 ± 0.2	1.5 ± 0.2	5.5 ± 0.2	6.0 ± 0.2	-
CD_4^+	DE	1.2 ± 0.2	1.4 ± 0.2	1.6 ± 0.3	0.8 ± 0.3	1.2 ± 0.2 1.4 ± 0.2	0.8 ± 0.2 1.0 ± 0.2
(m: v)	DI	5.0 ± 0.5	6.0 ± 0.6	6.2 ± 0.6	3.6 ± 0.5	4.2 ± 0.5	4.0 ± 0.5

Mean $\overline{E_{KER}}$ are found to be of the order of 0.5-2 eV for all investigated DE reactions, except for CD^+ where DE and DI are not distinguishable in the KERDs, In this case, the corresponding mean kinetic energy release ($\overline{E_{KER}} = 3.8 \pm 0.5$ eV) almost coincides with the E_{KERs} calculated for the transitions to $d^3\Pi$ and the $3^1\Sigma^+$ molecular states (3.6 and 3.7 eV, respectively). Consequently, the low energy KERD can be mainly attributed to these states, though the corresponding calculated threshold energies are higher than the observed ones.

For C^+/CD^+, the rather large background made it impossible to perform meaningful magnetic scans at low incident electron energies: the lowest one (E= 40.1 eV), is well above the DI threshold. This experimental value (3.5±0.5) agrees with the estimation of Bannister et al [17], who assigned the $\overline{E_{KER}}$ upper limit to be 3.8 eV, and with the evaluation of Janev and Reiter [5] who estimated (from the potential energy curves) the mean total kinetic energy to be 4.0 eV.

For CD_2^+, KERDs obtained for light D^+ fragments are broad as they extend up to 14 eV and, in contrast to what is observed for CD_n^+ (n= 3, 4) targets, no typical shape can be easily identified. Nonetheless, the excitation contribution can be isolated via the two reasonably sharp KERDs, measured at 15 eV and 35 eV, peaked at E_{KER}= 2.1 eV. The mean kinetic-energy-release value attributed to the ionization process is estimated to be 5.6 eV for the D^+ formation.

8. SUMMARY

Absolute cross-sections for electron impact dissociative excitation and ionization of CD_n^+ leading to the formation of ionic products (CD_n^{2+}, D^+, D_2^+, C^+, CD^+, CD_2^+, CD_3^+) are reported in the energy range from their respective thresholds to 2.5 keV. The animated crossed-beams method is used. The accuracy of presented cross-sections for electron impact processes is within 10–20%. The present article summarizes the experimental characterization of electron-impact ionization and dissociative processes of CD_n^+ ions (n= 1–4), that includes absolute cross-sections, energy thresholds and kinetic-energy-release values for the single ionization, dissociative excitation and dissociative ionization processes. The present results provide an insight in the dissociation dynamics of electron-impact dissociative processes of CD_n^+ ion. They should make a significant contribution to the enhancement of atomic and molecular databases for fusion energy research.

The cross-sections, threshold energies and kinetic energy distributions of charged products are observed to be comparable with data available in the literature. The present total ionization data are in good agreement with cross-sections calculated by means of both the BEB model [6] and the recently modified DM formalism [7]. The lack of accurate information on the potential energy surfaces of excited states of these ionic targets, of the doubly excited states of the parent neutral molecules and of doubly ionized molecular ions makes it very difficult to explain in detail observations. The present study shows that the mechanisms that determine the dissociation patterns of the methane molecular ion are complex, and no general rules can be applied to the whole range of states.

The results of the semi-empirical model of Janev and Reiter (JR) [5] often differ from the present absolute cross-sections. Present data for electron-impact on CD_n^+ should help refining the model.

REFERENCES

[1]   LECOINTRE, J., et al., Absolute cross-sections and kinetic energy release distributions for electron impact ionization and dissociation of CD^+, J. Phys. B: At. Mol. Opt. Phys. **40** (2007) 2201.
[2]   LECOINTRE, J., BELIC, D.S., JURETA, J.J., JANEV, R.K., DEFRANCE, P., Absolute cross-sections and kinetic energy release distributions for electron-impact ionization and dissociation of CD_4^+, Eur. Phys. J. D **50** (2008) 265.
[3]   LECOINTRE, J., BELIC, D.S., JURETA, J.J., JANEV, R.K., DEFRANCE, P., Absolute cross-sections and kinetic-energy-release distributions for electron-impact ionization and dissociation of CD_2^+, Eur. Phys. J. D **55** (2009) 557.
[4]   LECOINTRE, J., BELIC, D.S., JURETA, J.J., JANEV, R.K., DEFRANCE, P., Absolute cross-sections and kinetic-energy-release distributions for electron-impact ionization and dissociation of CD_3^+, Eur. Phys. J. D **55** (2009) 569.
[5]   JANEV, R.K., REITER, D., Collision processes of CH_y and CH_y^+ hydrocarbons with plasma electrons and protons, Phys. Plasmas **9** (2002) 4071; see also: *Berichte des Forschungszentrum Jülich* 3966 (2002) ISSN 0944-2952.
[6]   IRIKURA, K.K., KIM, Y.K., ALI, M.Z.J., Electron-Impact Total Ionization Cross-sections of Hydrocarbon Ions, Res. Natl. Stand. Technol. **107** (2002) 63.
[7]   LECOINTRE, J., et al., Absolute cross-sections and kinetic energy release for doubly and triply charged fragments produced by electron impact on CO^+, J. Phys. B: At. Mol. Opt. Phys. **40** (2007) 85.

[8]   JANEV, R.K., et al., Analytic representation of cross-sections for electron-impact dissociative excitation and ionization of CH_y^+ (y = 1 − 4) ions, Atom. Plasma-Mater. Interact. Data Fusion **16** (2009).

[9]   DEFRANCE, P., BROUILLARD, F., CLAEYS, W., VAN WASSENHOVE, G., Crossed beam measurement of absolute cross-sections: an alternative method and its application to the electron impact ionization of He^+, J. Phys. B: At. Mol. Opt. Phys. **14** (1981) 103.

[10]   LECOINTRE, J., BELIC, D.S., CHERKANI-HASSANI, H., JURETA, J.J., DEFRANCE, P., A crossed-beam experiment for electron impact ionization and dissociation of molecular ions: its application to CO^+, J. Phys. B: At. Mol. Opt. Phys. **39** (2006) 3275.

[11]   BANNISTER, M.E., SCHULTZ, D.R., Electron-impact dissociation of hydrocarbon molecular ions, Atom. Plasma-Mater. Interact. Data Fusion **16** (2009).

[12]   DJURIC, N., CHUNG, Y.S., WALLBANK, B., DUNN, G.H., Measurement of light fragments in dissociative excitation of molecular ions: CD^+, Phys. Rev. A **56** (1997) 2887.

[13]   GREEN, S., BAGUS, P.S., LIU, B., MCLEAN, A.D., YOSHIMINE, M., Calculated Potential-Energy Curves for CH^+, Phys. Rev. A **5** (1972) 1614.

[14]   RABALAIS, J.W., BERGMARK, T., WERNE, L.O., KARLSON, L., SIEGBAHN, K., The Jahn-Teller Effect in the Electron Spectrum of Methane, Phys. Scr. **3** (1971) 13.

[15]   BECKER, K., Stevens Institute of Technology, Hoboken, DEUTSCH, Ernst-Moritz-Arndt Universität, H., PROBST, M., MÄRK, T.D., Leopold Franzens Universität Innsbruck, personal communication to be published (2009).

[16]   INOKUTI, M., Inelastic Collisions of Fast Charged Particles with Atoms and Molecules—The Bethe Theory Revisited, Rev. Mod. Phys. **43** (1971) 297.

[17]   BANNISTER, M.E., et al., Electron-impact dissociation of CH^+ ions: Measurement of C+ fragment ions, Phys. Rev. A **68** (2003) 042714.

[18]   AMITAY Z., et al., in Applications of Accelerators in Research and Industry, (DUGGAN, J.L., MORGAN, I.L.), AIP Press, New-York (1997) 51.

FUNDAMENTAL DATA OF DIATOMIC MOLECULES RELEVANT FOR FUSION

U. FANTZ, D. WÜNDERLICH

Max-Planck-Institut für Plasmaphysik, EURATOM Association,
Boltzmannstr. 2, D-85748 Garching, Germany

Abstract

With the aim to provide a fundamental database for diatomic molecules which occur in fusion edge plasmas available data has been compiled and completed. Focus has been laid on hydrogen molecules and its coupling to the molecular ion, on hydrocarbons, in particular CH and C_2, and on BeH and BH, including their hydrogen isotopes. Starting from available potential curves and transition dipole moments Franck-Condon factors and vibrationally resolved transition probabilities have been calculated using the `TraDiMo` code. The flexible solver `Yacora` has been applied for vibrationally resolved collisional radiative modelling and dissociation modelling providing effective rate coefficients as a function of electron density and temperature. The influence of heavy particle collisions has been investigated. Missing electron impact excitation rate coefficients have been generated applying the semi-classical `IPProg` code to molecules

1. INTRODUCTION

The plasma edge of fusion devices is characterised by a cold temperature with respect to the hot core. Specifically in the divertor region the electron temperature is typically a few eV; in the detached plasma regime where volume recombination dominates even below one eV [1]. Since the edge plasma is in interaction with surfaces the plasma wall interaction is one of the key issues for a fusion device [2]. Molecules are produced at surfaces by recombining hydrogen particles and by chemical erosion processes. The survival probability of the molecules which are released from the surface, and thus their penetration depth, depends basically on electron density and temperature. In cold plasma regions molecules can undergo a variety of reactions, among them dissociation and dissociative ionization creating other molecular species.

The consequences are manifold and mentioned briefly here, whereas details can be found in ref. [3]. Due to close lying energy levels and high reaction rates in the low energy range, molecules can influence significantly the plasma energy balance. By creating new particles, for example vibrationally excited hydrogen molecules which are metastable, transport of these additional species have to be taken into account. In addition, the presence of molecular species may influence the interpretation of plasma edge diagnostics. One example is the determination of the recycling flux in which the dissociative excitation from the hydrogen molecule into excited states of atomic hydrogen influences the Balmer line emission. Others are the diagnostics and thus the quantification of the molecules itself [4].

Besides hydrogen molecules, which are created by the recycling process of hydrogen particles at the surface, the molecular species created by plasma wall interaction processes depends on the wall material. Common fusion devises operate with carbon (e.g. DIII-D, JT-60U, ASDEX Upgrade before turning to a fully tungsten machine) and with beryllium (JET). ITER will have a material mix of beryllium, tungsten and carbon.

In case of carbon hydrocarbons are released, whereas in case of beryllium beryllium-hydrides are formed. Due to the usage of boron as getter material for oxygen, boron hydrides are frequently observed after the boronization of the machine. Depending on the fuelling, i.e. hydrogen, deuterium, tritium the corresponding molecular isotopes have to be considered.

The relevance of individual processes among the manifold of molecular processes in the edge plasma depends on the plasma regime, i.e. whether the plasma is ionizing or recombining or in the

transition between both cases. In addition to the reactions relevant to electronic states of atoms and ions such as dissociation, ionization, recombination, charge exchange, etc. the vibrational and rotational excitation in the ground state and electronically excited states have to be taken into account for molecules. One approach to reduce the amount of data is the generation of effective rate coefficients [5].

In general, the available data base for molecules is scarce and even for one species, the simplest one, namely hydrogen, by far not complete and consistent.

The present contribution focuses on a fundamental and consistent data set for the diatomic molecules which occur in the plasma edge of fusion devices. Efforts are undertaken to compile and compare available data with the aim to generate a basis data set in which the gaps are filled with simple methods. Whenever possible, the calculated results are validated by experimental data.

Starting from available potential curves and dipole transition moments, which are based on the electronic wavefunctions, fundamental vibrationally resolved data are generated: Franck-Condon factors ($q_{v'v''}$) and transition probabilities ($A_{v'v''}$). Although rotational resolution might be desirable it has not been taken into account explicitly for the purpose of clarity; the data represent an average over rotational levels.

For modelling of population densities collisional radiative (CR) models are applied which are based on vibrationally resolved rate coefficients. Wherever needed, the latter are generated by using simple to use methods (the semi-classical impact parameter method for optically allowed and the Gryzinski method for optically forbidden transitions) to get an estimate. CR modelling results in effective rate coefficients and is important for analysing spectroscopic measurements to obtain plasma parameters such as electron density and temperature but also particle fluxes.

For modelling the break-up of a molecule and formation of radicals by collisions, dissociation models are used which calculate the corresponding particle densities. Here focus is laid on the comparison of available data sets taking into account also heavy particle collisions. No efforts are undertaken to generate dissociation rate coefficients or calculations of the particle chemistry.

Table 1 summarizes the data which has been compiled by the authors during the Co-ordinated Research Project "*Atomic and Molecular Data for Plasma Modelling*" organized by IAEA, Vienna. Part of the data have been made available by the respective webpage (http://www-amdis.iaea.org/) or can be sent upon request (email to: fantz@ipp.mpg.de). It is the intention of this paper to describe the data compilation and to present selected results.

TABLE 1. SCHEMATIC OVERVIEW OF DATA COMPILED FOR DIATOMIC MOLECULES WITH THE CORRESPONDING HYDROGEN ISOTOPES

	Hydrogen	Hydro-carbons	BeH	BH
$q_{v'v''}$ TraDiMo	✓	✓	✓	-
$A_{v'v''}$ TraDiMo	✓	✓	✓	-
$X_{em}^{v'v''}(T_e)$ IPProg	✓	✓	✓	✓
$n_p(T_e,n_e)$ CR model	✓	✓	-	-
$n(T_e,n_e)$ diss. model	✓	✓	-	-

2. FRANCK-CONDON FACTORS AND TRANSITION PROBABILITIES

The computer code `TraDiMo` (Transitions of Diatomic Molecules) has been used to calculate Franck Condon factors and vibrationally resolved transition probabilities on the basis of potential curves and electronic transition dipole moments by solving the Schrödinger equation in the Born-Oppenheimer approximation [6]. The usage of the respective reduced mass allows calculating data for all isotopes.

Throughout the paper the following notation is used: one prime (e.g. v') denotes the energetically higher lying level, two primes (v'') the lower level.

The Frank-Condon factors $q_{v'v''}^{p'p''}$ are given by the overlap integral of the two wavefunctions in the electronic levels p' and p'' with vibrational quantum number v' and v'', respectively

$$q_{v'v''}^{p'p''} = \left| \int_0^\infty \psi_{v'}^{*p'}(r)\,\psi_{v''}^{p''}(r)\,dr \right|^2 \tag{1}$$

Vibrationally resolved transition probabilities $A_{v'v''}^{p'p''}$ are obtained from

$$A_{v'v''}^{p'p''} = \frac{2 - \delta_{0,\Lambda'+\Lambda''}}{2 - \delta_{0,\Lambda'}} \frac{16}{3} \frac{\pi^3}{\varepsilon_0 h} \frac{1}{\lambda^3}$$
$$\times \left| \int_0^\infty \psi_{v'}^{*P'}(r)\,D_{el}(r)\,\psi_{v''}^{P''}(r)\,dr \right|^2 \tag{2}$$

in which $D_{el}(r)$ denotes the electronic transition dipole moment. The first term takes the statistical weights into account with Λ for the quantum number of the angular momentum of the electronic state.

For hydrogen and its isotopomeres a complete data set (up to the main quantum number n = 4 in the united atom notation) has been already generated including calculations of radiative lifetimes of the electronic states [6]. The numerical data have been made available by the IAEA Atomic and Nuclear Data Section and can be downloaded [7].

The data base for the Franck Condon factors has been extended by coupling the electronic states of the hydrogen molecule to the ground state of the molecular hydrogen ion. Hence, the vibrational population in the ground state of the molecular ion can be calculated from the population of the ground and excited states of the molecule using the Franck-Condon principle. This is of high relevance for the dissociative recombination process which depends strongly on the vibrational population. Figure 1 shows the Franck-Condon factors for the transition of the first electronically excited state of the molecule (B $^1\Sigma_u^+(v'')$) into the ground state of the molecular ion (X $^2\Sigma_g^+(v')$, v'=0, 1, and 2) for H_2, D_2 and T_2. The numerical data for this transition in H_2 is given in table 1 (Appendix). Data for the transition from the ground state of the molecule to the ground state of the molecular ion is given in table 2 (Appendix). The potential energy curve for the ground state of H_2^+ is taken from ref. [8]; data used for H_2 is listed in Ref. [6].
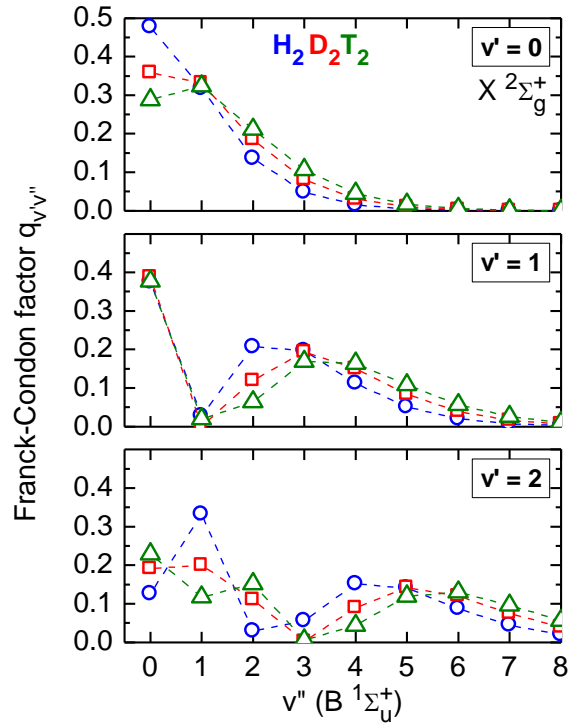
FIG. 1. Franck-Condon factors for the vibrational transitions from the first electronically excited state of H_2, D_2 and T_2 molecules (B, v''=0-8) to the ground state of the respective molecular ion (X, v'=0, 1, and 2).
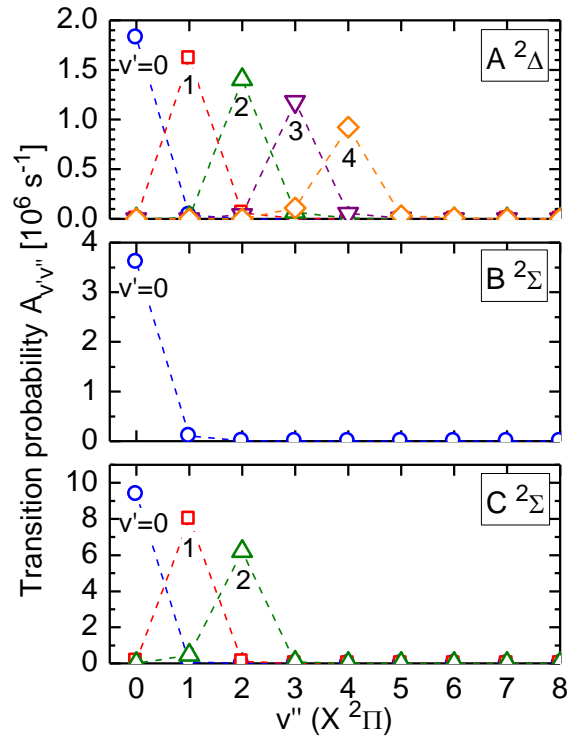
FIG. 2. Vibrationally resolved transition probabilities for the first electronic states into the ground state of CH: $A(v'$=0-4)$, $B(v'$=0)$ and $C(v'$=0-2)$ to $X(v''$=0-8)$.

In case of the hydrocarbons data has been generated for the CH and C_2 molecule. For CH transitions from the ground state $(X\ ^2\Pi)$ to the three first electronically excited states in the doublet system $(A\ ^2\Delta, B\ ^2\Sigma^-, C\ ^2\Sigma^+)$ have been considered using potential curves from [9] (for the X, A, and C-states) and [10] (for the B-state). The electronic transition dipole moments are taken from [9] (for the X – A and X – C transition) and [11] (for X – B transition). The radiation of the CH molecule is frequently used for the determination of hydrocarbon fluxes [12]. The $A\ ^2\Delta$ - $X\ ^2\Pi$ transition is the standard Gerö band, $B\ ^2\Sigma^-$ - $X\ ^2\Pi$ is occasionally measured, and the $C\ ^2\Sigma^+$ - $X\ ^2\Pi$ is detectable. For these transitions the transition probabilities are shown in Figure 2 for CH (numerical data is given in tables 3, 4, and 5 of the Appendix). Data for CD, CT are also calculated and available. Due to the shape of the potential curves only a few vibrational levels exists in the excited states, their lifetime is also strongly reduced by predissociation [11].

In general, it can be stated that the calculated values show deviations of less than 10% to values available in literature. For example, the transition probability for the v'=0 to v''=0 transition of the Gerö band is in agreement with other calculations [13] and with measurements of the lifetime of the A $^2\Delta$ (v'=0) state [14].

For the carbon molecule potential curves for the electronic states X, A, C, D in the singlet system and a, b, c, d in the triplet system are compiled from ref. [15]; for B and B' in the singlet system data from ref. [16] have been used. The ground state is the $X\ ^1\Sigma_g^+$ state; the a $^3\Pi_u$ state is a metastable state. Franck-Condon factors for transitions among these 10 levels have been calculated and are available now. Vibrationally resolved transition probabilities have been calculated for the optically allowed transitions using the corresponding electronic transition dipole moments: A – X [15], B – A [17], B' – A [17], C – A [18], D – X [18], b – a [15], d – a [15], d – c [15] and e – a [19]. The d $^3\Pi_g$ – a $^3\Pi_u$ transition is commonly known as the Swan transition and used for flux measurements of higher hydrocarbons (C_2 family) [12, 20]. The Mulliken transition $(D\ ^1\Sigma_u^+ - X\ ^1\Sigma_g^+)$ has the advantage of being a resonance transition but the radiation is in the near ultraviolet region and thus less accessible by the standard optical emission spectroscopy technique [20].

FIG. 3. *Vibrationally resolved transition probabilities for the first electronic state into the ground state of BeH, BeD and BeT: A(v'=0, 1, and 2) into X(v''=0-8).*

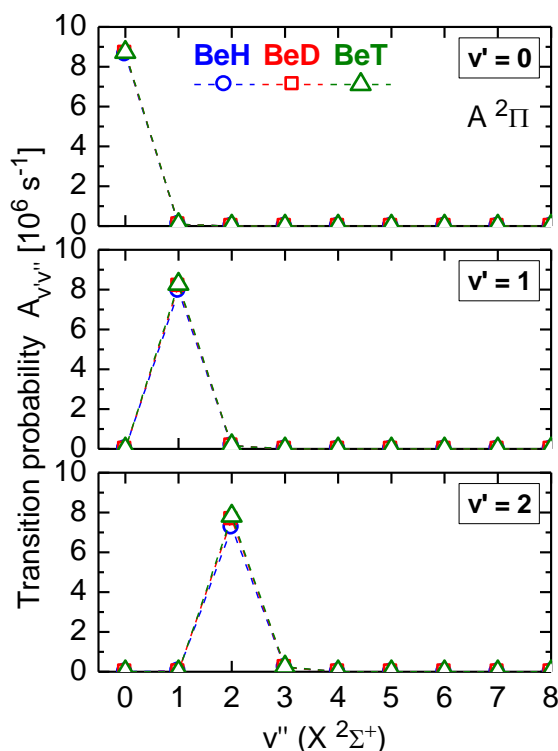In case of beryllium, data for the A $^2\Pi$ – X $^2\Sigma^+$ transition of the BeH, BeD and BeT molecules have been compiled. This transition is used for diagnostic purposes and is in particular a promising candidate for the detectability of the DT isotope ratio [21]. The transition probabilities are shown in Figure 3, tables 6, 7, and 8 of the Appendix give the numerical data. Potential curves and the electronic transition dipole moment are taken from [22].

The calculation of Franck-Condon factors and vibrationally resolved transition probabilities has been closed by calculation data for the transitions of the BH, BD and BT molecules among three electronic states: the ground state X $^1\Sigma^+$, and the two first excited states, the A $^1\Pi$ and B $^1\Sigma^+$ state using potential curves from ref. [23]. The electronic dipole transition moment for the A – X transition is taken from ref. [24]. Data has been generated for the two boron isotopes ^{10}B and ^{11}B, which occur with 20% and 80% abundance.

3. POPULATION AND DISSOCIATION MODELLING

3.1. General remarks

Modelling of population densities of particles in the excited states is of particular importance for the determination of plasma parameters from emission spectroscopy. Since edge plasmas are far from thermal equilibrium and since they cover a wide parameter range, corona modelling might also not be justified. Hence collisional radiative (CR) modelling is essential. CR modelling provides effective rate coefficients [5] which can be implemented in other plasma simulations. In addition, the effect of inelastic collisions for the plasma energy balance can be quantified. Transport of particles in these excited levels is negligible due to the very short lifetime. Exceptions are, of course, particles in metastable states. In contrast, radiation transport might play an import role as it has been identified for edge plasmas recently [25].

Dissociation and ionization modelling, i.e. calculation of particle densities, is of relevance for several applications such as: (i) quantification of particle fluxes from spectroscopic measurements, (ii) understanding of chemical erosion effects, e.g. the transport of impurities from plasma surface interaction, (iii) calculation of the particle balance for neutrals (pressure) and ions (ionization degree). An example in which such modelling and experimental results improve the understanding of the relevance of molecular processes in the plasma edge is the molecular assisted recombination [3]; it describes the influence of hydrogen molecules on the transition of an ionizing to recombining divertor plasma [26].

Preferentially one would like to have one complex model for the manifold of species on a time scale given by the short lifetime of the radiating particles. This, however, would require a presently non-feasible computing time. Therefore, the system is often been decoupled into a CR model describing the fast species without taking their transport into account and into dissociation and transport models for the slow species [27]. Besides collisions with electrons and protons, collisions among particles generated during the break-up of a molecule should be examined.

Due to the manifold of molecular species and due to the large number of vibrational energy levels a huge amount of data, i.e. rate coefficients, is required to build such models. This data can be compiled from literature and, wherever possible, should be compared among each other to identify the proper data set.

Apart from measurements, different methods are commonly applied to calculate rate coefficients for optical allowed and optical forbidden electron impact transitions. Simple methods such as the Born and Born-Bethe method [28], the Gryzinski method [29,30] and the semi-classical impact parameter method applied to atoms and ions [31,32] are easy-to-use. They describe their individual energy range properly and can give quite good estimates when nothing else is available. The semi-classical impact parameter method has been adapted to molecules by using a more sophisticated approach to satisfy the reciprocity and adjusting the cutoff to achieve Born approximation at high

energies [33]. A step further, for example, is the close coupling method [34] whereas R-matrix calculations [35,36] can be regarded as highly sophisticated and most precise in the low energy range which is of particular importance in cold plasmas.

Transition probabilities or oscillator strengths are a basis for calculating (electron impact) rate coefficients for optical allowed transitions. Thus, vibrationally resolved transition probabilities calculated for example with the TraDiMo code can be used directly to generate vibrationally resolved rate coefficients.

As mentioned before, focus is laid on compilation of data. If cross-sections or rate coefficients are not available, different simple-to-use methods are used for generation of consistent data, such as the semi-classical impact parameter method for excitation of optically allowed transitions, the Gryzinski method for optically forbidden transitions. Rate coefficients for de-excitation are given by detailed balancing.

The semi-classical impact parameter method for atoms and ions is described in [28]; the corresponding computer code is IPProg. In the past this code has been also applied to diatomic molecules for example to CH, C_2, (both in [20]) N_2^+ [37], and SiH [38].
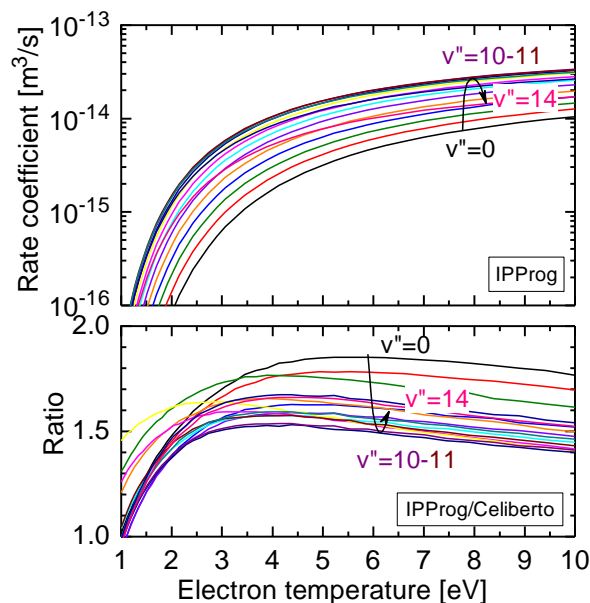
FIG. 4. Excitation rate coefficient for the X $^1\Sigma_g^+$ to B $^1\Sigma_u^+$ transition of the hydrogen molecule calculated with IPProg. Ratio of the rate coefficient from IPProg calculations to the rate coefficient calculated by Celiberto [39] using the semi-classical impact parameter method for molecules [33].

As an example Figure 4 shows vibrationally resolved rate coefficients for electron impact excitation from the ground state of molecular hydrogen X $^1\Sigma_g^+$ into the first electronically excited state in the singlet system, B $^1\Sigma_u^+$, calculated with IPProg using transition probabilities obtained with TraDiMo. The results are compared with more sophisticated calculations from Celiberto [39] which are based on the semi-classical impact parameter method for molecules [33]. The ratio of rate coefficients obtained from IPProg with data from Celiberto is also shown in Figure 4. The overall agreement is within a factor of two which is satisfying taking into account the precision expected and the effort to run IPProg. It should be mentioned again, that wherever available other more precise data is to be preferred.

For CR and dissociation modelling the system of coupled differential equations is solved using the flexible solver `Yacora` [40]. `Yacora` is capable to solve also a non-linear equation system, which allows implementing self-absorption due to optical thickness of emission lines and heavy particle collisions.

3.2. Hydrogen

One of the first CR models for H_2 and H was established by Sawada [41] and was soon extended [26]. Details of the model and further improvements are described in refs. [42,43,44], which also give some applications. Several other CR models for hydrogen are available, for example the ones of refs. [45- 50].

The latest version of the Sawada model has been adopted for `Yacora`, extending strongly the electronic and vibrational resolution. Different data sets have been implemented, for example, the most recent compilation for hydrogen, Janev et al. [51], is now implemented as an alternative.

In order to validate the model, calculated and experimentally determined population densities are compared. The latter are obtained from spectroscopic measurements in small laboratory plasmas operating in the low temperature region. Electron temperature and density are known from other independent diagnostic techniques such as Langmuir probes and emission from diagnostic gases (He, Ar).

In the case of atomic hydrogen, discrepancies of measured to calculated Balmer line emission, in particular H_γ, led to a modification of the respective rate coefficients which improved the agreement significantly [40].

In the case of the hydrogen molecule, population densities of several electronic states in the singlet and triplet system have been investigated. Measurements are carried out in ECR discharges in hydrogen and deuterium with variation of pressure and power. The Fulcher emission band (d $^3\Pi_u$ – a $^3\Sigma_u^+$) is easily accessible by diagnostics and is widely used. Therefore, the population density of the d $^3\Pi_u$ state has been chosen as a representative for the triplet system whereas for the singlet system the I $^1\Pi_g$ state has been selected.

Figure 5 compares measurements from different plasma discharges in hydrogen and deuterium with calculations of these two population densities normalised to the ground state density (n_0). In the calculations low and high quenching by heavy particle collisions has been taken into account using $n(H_2)= 5\times10^{19}$ m^{-3} with T_{vib} = 10000 K and $n(H_2)= 1.2\times10^{21}$ m^{-3} with T_{vib} = 3000 K, respectively at an electron density of 10^{17} m^{-3}. Low quenching results in an upper value for the density ratio, high quenching in a lower value. The calculations are performed using two different data sets: the most recent compilation by Janev et al. [51], exchanged by data implemented in the Sawada model [41], i.e. Miles data [52]. Cross-sections for electron impact induced transitions between the excited states in the singlet and in the triplet system are kept unchanged.

Obviously the singlet system is less sensitive on the implemented data whereas problems occur within the triplet system. (This is been seen also for other states than shown in Figure 4). As a tendency the original Miles/Sawada data fit best. It should be kept in mind that the population of states in the triplet system is influenced by the metastable v=0 level in the c $^3\Pi_u$ state [43,44]. Regarding the isotopes, no major effect can be seen in the measurements. For the calculations the hydrogen data is being used.
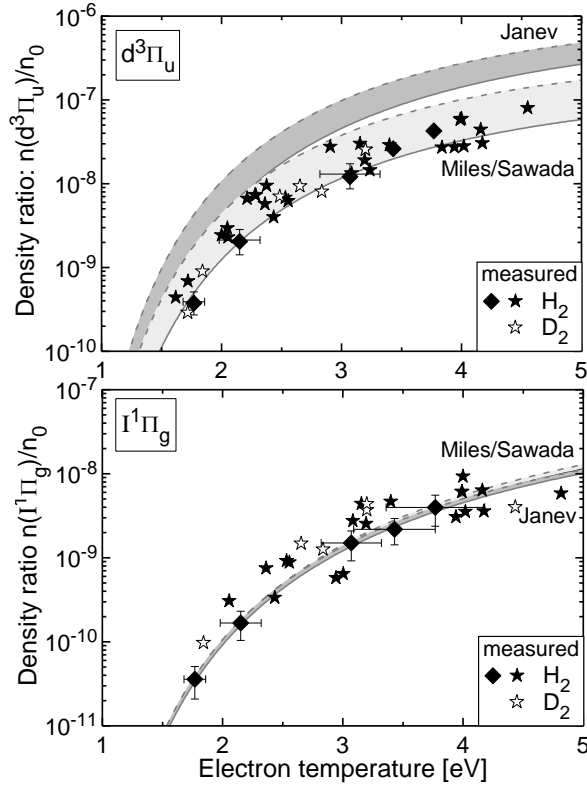
FIG. 5. Comparison of measured hydrogen density ratios in the singlet and triplet system with `Yacora` *CR model calculations for different input data sets (Janev [51] and Miles/Sawada [52]/[41]).*

It is difficult to adjust properly the calculated data to measurements without doing it in an arbitrary manner. This example emphasises the data needs, in particular for electron impact excitation of the H_2 molecule from the ground state into the electronic excited states of the triplet system, i.e. optically forbidden transitions. Desirable is also a complete and consistent vibrationally resolved data base for hydrogen and its isotopes, most important for D_2.

As in cold plasmas the hydrogen molecules contribute via the dissociative excitation to the population of the excited states of atomic hydrogen the molecular ions can contribute via the dissociative recombination channel. In addition, if the plasma contains negative hydrogen ions the contribution via the mutual neutralization process ($H^- + H_x^+ \rightarrow H^* + H$) might be of importance. The coupling of the CR model for atomic hydrogen to six different species (H, H_2, H^+, H_2^+, H_3^+, H^-) is introduced explicitly in refs. [40,53]. The contribution of negative ions has been quantified in ref. [53].

Next, the dissociative recombination has been investigated thoroughly since this process is of interest also for the molecular assisted recombination and, as mentioned above, might be an interface between the ionizing plasma into the fully recombining plasma. In comparison to radiative recombination and three-body recombination which occur typically at intermediate and high electron densities, respectively and at temperatures below 1 eV, dissociative recombination has an onset at a few eV at intermediate electron densities. Emphasis has been laid on the data evaluation, in particular on vibrationally resolved data.
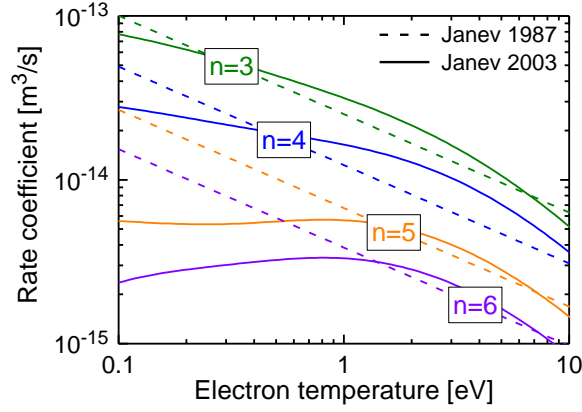
FIG. 6. Comparison of two data sets for the rate coefficient for dissociative recombination of the molecular ion H_2^+. The quantum numbers refer to the final state of atomic hydrogen.
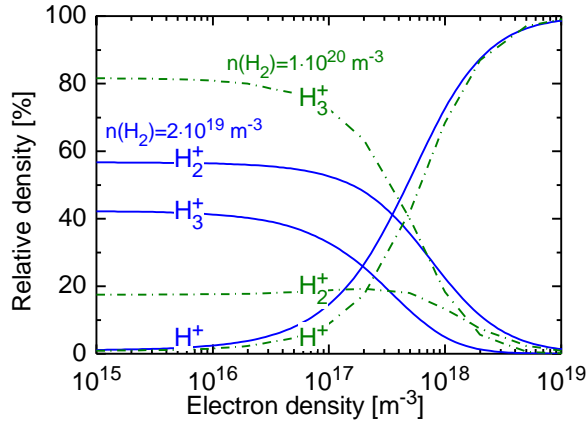
FIG. 7. Calculation of the hydrogen ion composition for two molecular hydrogen densities.

Figure 6 shows a comparison of data for dissociative recombination already compiled and (re-) evaluated by Janev. In Janev 1987 [54] only vibrational averaged data are available and a fixed branching ratio for the quantum number of the resulting excited hydrogen atom has been given. In Janev 2003 [51] the latest available data have been compiled, partly based on new measurements at the CRYRING accelerator facility of Sweden. This means vibrational scaling is now possible and improved data on the branching ratio is available. Rate coefficients shown in Figure 6 (full curves) have been calculated for a vibrational population of H_2^+ corresponding to a vibrational temperature of $T_{vib} = 7000$ K for H_2 in the ground state and being transferred using the Franck-Condon principle with the Franck Condon factors obtained from TraDiMo. A difference between the Janev 1987 and Janev 2003 data is clearly to be seen for the low temperature region, in particular the distribution among the different quantum numbers of the final state differs remarkably. First validations with experimental results from plasmas dominated by dissociative recombination indicate that a better agreement of measurements with CR models results can be observed by using Janev 2003 data instead of Janev 1987 data.

Regarding particle densities of the slow species, i.e. particles in the ground and metastable states, a dissociation model has been constructed on the basis of the Janev 2003 data [51]. Besides the degree of dissociation, the composition of the ion species H^+, H_2^+ and H_3^+ is of special interest. Studies are performed on the relevance of heavy particle collisions, in particular collisions of H_2 with H_2^+ forming H_3^+. The dependence of the densities of the ion species on the electron density is shown in

Figure 7 for two different molecular hydrogen densities. The calculation are carried out for a heavy particle temperature of $T_{gas} = T_{ion} = 1000$ K assuming full recombination of atomic hydrogen at surfaces ($\gamma = 1$). For the calculation, the electron temperature has been adjusted to fulfil quasineutrality; the atomic hydrogen density is a free parameter. As expected, in the high electron density range the H^+ species is dominant, independent on the molecular density due a high dissociation of the molecules. In the intermediate range, however, the composition depends strongly on electron density and on molecular density. Molecular ions dominate, which means dissociative recombination not only of H_2^+ but also of H_3^+ should be considered in modelling. Experimental validation of calculated positive ion distributions is presently undertaken in positive hydrogen ion sources.

3.3. CR modelling of CH and C_2

The quantification of hydrocarbon fluxes from surfaces is based on the measurement of the molecular band emission of CH (Gerö-band) and C_2 (Swan band) and the (inverse) photon efficiency [12, 20]. The latter describes the dissociation and ionization process per emitted photon. It makes use of results from dissociation modelling inclusive transport and the emission rate coefficient for the respective band emission. So far, the corona model has been assumed to calculate the emission rate coefficient. It is however not clear if, for molecules with relatively low excitation energies of less than five eV, CR modelling should be used to obtain effective rate coefficients which depend on electron temperature and density. (The influence of the dissociative excitation from the parent molecule, CH_4 in case of CH and C_2H_y in case of C_2, has been described and quantified in ref. [5,20]).

Thus, efforts are undertaken to construct CR models for CH and C_2, which in a first step needs a data compilation. Here the situation is rather poor: apart from the direct electron impact excitation rate coefficient into the excited state which is the upper level of the measured radiation, nothing is available. Even the available rate coefficients are based on calculations using the semi-classical method for atoms, which means IPProg. Consequently IPProg has been used together with the vibrationally resolved transition probabilities presented above to obtain rate coefficients for CR modelling.
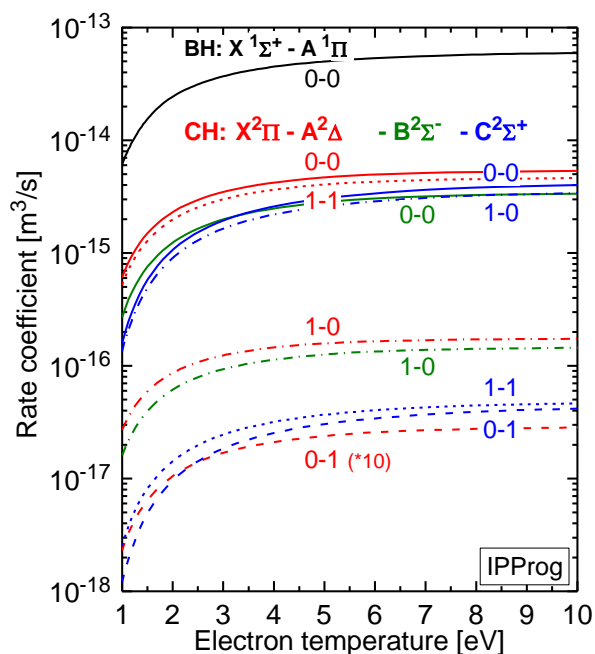
FIG. 8. Vibrationally resolved excitation rate coefficients calculated with IPProg for the ground state of CH into the first electronic states A, B and C as well as for BH the X to A, 0-0 transition.
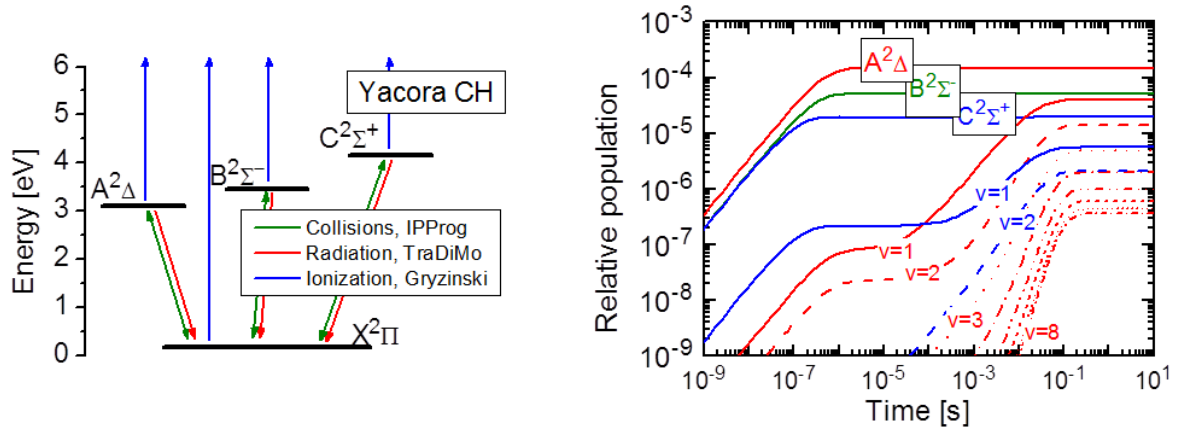
FIG. 9. Left: sketch of the levels used for the CR modelling of CH radiation. Right: equilibrium population density for different excites states of CH ($T_e = 3$ eV, $n_e = 10^{17}$ m^{-3}).

Examples of rate coefficients calculated with `IPProg` are shown in Figure 8 for some vibrational transitions of the first three excited states of CH. In addition, the rate coefficient for the X $^1\Sigma^+ -$ A $^1\Pi$, 0-0 transition of BH is shown, based on the transition probability of $A_{00}=1.98\times10^7$ s^{-1} which has been calculated with `TraDiMo`.

For the CR model of CH, the ground state, three electronically excited states (A, B, and C) and ionization are taken into account vibrationally resolved. Basically, electron impact excitation and de-excitation as well as spontaneous emission are considered. Ionization rate coefficients are obtained using the Gryzinski method. Figure 9 shows a sketch of the levels and processes considered and, as an example for the results, the density development with time for different electronic states and their vibrational levels. Equilibrium density is achieved on different time scales, i.e. vibrationally excited states need more time to achieve equilibrium due to the redistribution among vibrational levels.

In case of C_2 the same processes as for CH are considered. Noteworthy is the existence of a metastable state of C_2, namely the a $^3\Pi_u$ state. As already mentioned the Swan transition, i.e. the d $^3\Pi_g$ – a $^3\Pi_u$ transition is commonly used for flux measurements. In total, 10 electronic states are considered vibrationally resolved; the full energy term schema however is much more complex. The first four electronic states of the triplet system are implemented, which means six states in the singlet system are taken into account, one of them being the ground state.
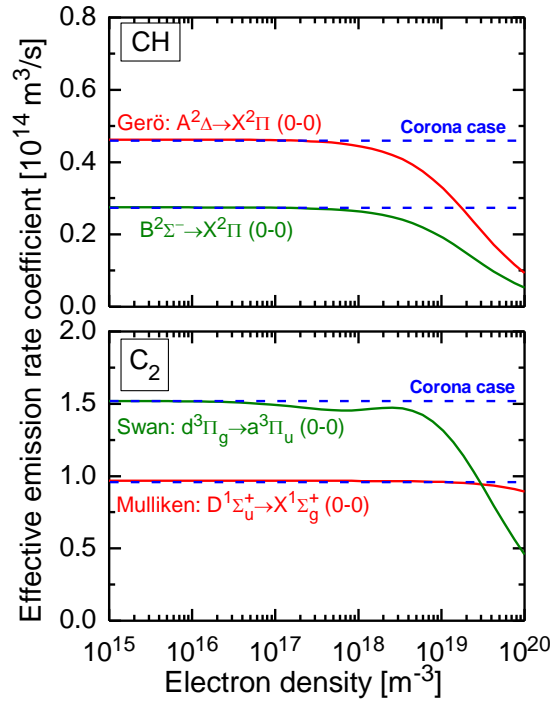
FIG. 10. Effective emission rate coefficients calculated with the CR model in comparison with the corona case for two transitions of the CH and the C_2 molecule at a fixed temperature of $T_e = 5\,eV$.

Figure 10 shows the effective emission rate coefficients for two transitions in CH and in C_2 calculated with the CR model for a fixed electron temperature. For comparison the emission rate coefficient from direct electron impact excitation (corona case) is plotted also. It can be seen that for high electron densities other processes become important, for example electron impact de-excitation, and the system approaches Boltzmann equilibrium. As expected, corona equilibrium can be applied at low electron densities. For electron densities of edge plasmas (10^{18} to 10^{19} m^{-3}) the transition from corona to Boltzmann is clearly taking place. Thus, by using the corona case (as done presently) the radiation is overestimated by roughly a factor of 1.5 for both relevant transitions (CH Gerö and C_2 Swan band) at electron densities of 10^{19} m^{-3} increasing to roughly a factor of three at 10^{20} m^{-3}. This demonstrates clearly that a CR model should be applied for the analysis of these molecular transitions.

3.4 Dissociation modelling of hydrocarbons

As the break-up of the hydrocarbons and their transport is widely used in edge modelling, for examples in B2-Eirene (SOLPS) [55], in the EDGE2D/NIMBUS code package [56] and in the ERO code [57], details of their break-up into different chains, the consequences of using different available compiled data sets and the influence of heavy particle collisions on the results is been studied using Yacora. Since most of the codes are originally based on Erhardt&Langer data [58] and are being replaced by the latest data compilation of Janev&Reiter [59] a comparison between these is of special interest. Heavy particle collisions are taken either from Brooks data [60] which has been added to some of the edge codes or from the comprehensive compilation by Tahara [61]. The flexibility of the solver Yacora turned out to be very useful for these studies.
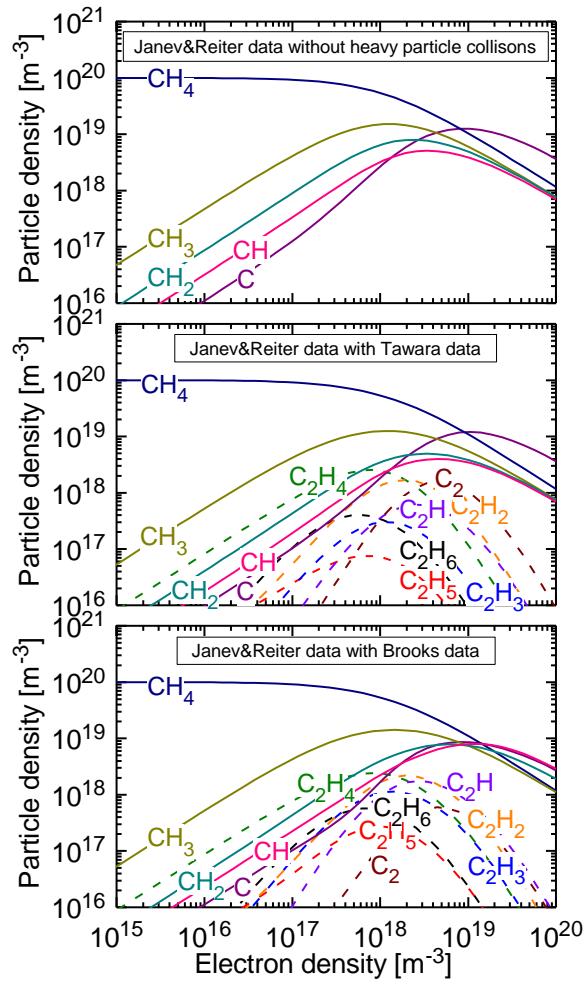
FIG. 11. Results from the `Yacora` *dissociation model for methane (T_e = 4 eV) using the different input data sets described in the text.*

      Figure 11 shows the neutral particle densities of the methane break-up at T_e = 4 eV (T_{heavy}= 500 K and diffusion for 1 Pa) as a function of electron density for different data sets. The comparison of results obtained with Janev&Reiter data without and with heavy particle collisions (Tawara data) shows the relevance of the C_2-family in the electron density range between 10^{17} to 10^{19} m^{-3}. Most important, C_2 molecules are formed only in a relevant amount if heavy particle collisions are taken into account. The comparison of results using Janev&Reiter and Tawara data with results using Erhardt&Langer and Brooks data show differences for several species, in particular for electron densities above 10^{17} m^{-3}. For example atomic carbon dominates in the first case whereas in the second case the carbon density is smaller and similar to the CH_2 and CH densities at high electron densities. In a similar manner molecular carbon dominates the C_2-family in the first case, whereas in the second case C_2H and C_2H_2 are most prominent. For better comparison, particle densities calculated based on these three data sets are plotted in Figure 12 for two electron densities.

88
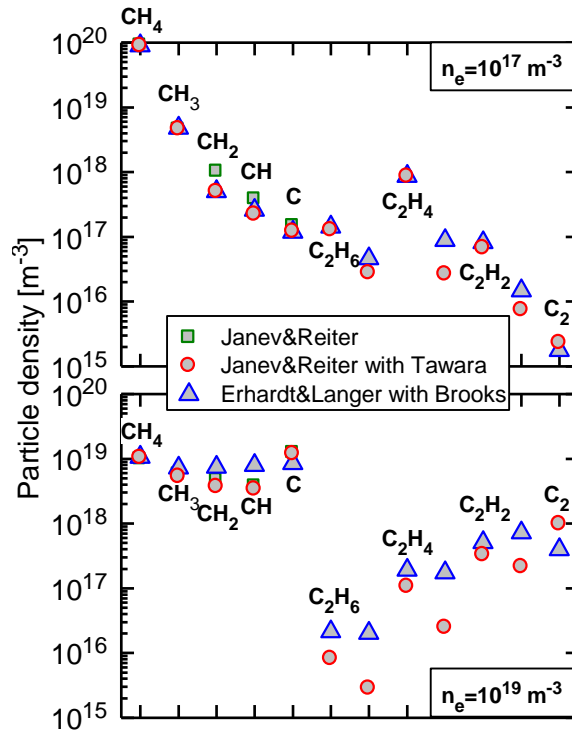
FIG. 12. Comparison of the results from the `Yacora` *dissociation model for methane (using the different input data sets described in the text) at two different electron densities for $T_e = 4$ eV.*

The change of the data set has direct consequences on the calculations of the (inverse) photon efficiencies in which the number of dissociation processes changes. The usage of CR modelling for the effective emission rate coefficient instead of using the corona model is another important factor. Systematic investigations on comparison calculations with measurements have been done in the past (see for example [12,62,63]) and should be repeated in order to resolve the discrepancies obtained so far. Any change in the (inverse) photon efficiencies has direct impact on the determination of the chemical erosion yields of carbon.

4. DATA NEEDS AND PROSPECTS

The data compilation described in the previous sections identified clearly the data needs in fundamental molecular data for fusion applications.

The availability of results from calculations of electronic wavefunctions (i.e. potential curves, electronic transitions dipole moments) is limited although these data are a basic outcome for much more complex systems. Consistent compilations for each of the molecules would allow calculating a consistent data set of Franck-Condon factors and vibrationally resolved transition probabilities. Preferably the data would be available electronically with good resolution in internuclear distance. These data would on one hand improve the analysis of emission spectra since diatomic molecules are easy accessible by optical diagnostic techniques. On the other hand many methods for calculating cross-sections for optically allowed transitions need these transition probabilities.

For CR modelling there is a strong need of vibrationally resolved electron impact cross-sections for optically allowed and optically forbidden transitions. Of particular importance is the reliability in the low energy region due to the low temperature in the plasma edge. Although data have been compiled and generated in the present report, it should be kept in mind that this is done within a simple approach giving estimates. There is a strong demand for the CH and C_2 molecule due to the

fact that the quantification of the chemical erosion yield of carbon in plasmas is based on the analysis of the emission of these molecules.

As the discrepancies between results from CR calculations for molecular hydrogen with results from measurements showed, the situation is still unsatisfying even for the simplest molecule, i.e. hydrogen. Consistent data for the isotopes, most important for deuterium would allow quantifying an isotope effect in the Fulcher radiation which is commonly used to measure the molecular hydrogen flux.

The role of hydrogen molecules to plasma recombination is still an open issue. Here, vibrationally resolved data sets for dissociative recombination of H_2^+ and H_3^+ (and the respective ions in deuterium) in an extended parameter range as available now would improve the present situation.

The relevance of data for BeH, BeD and BeT molecules has been already recognised for the interpretation of measurements at JET and will be of importance for ITER. Again improved data for electron impact cross-sections are most important.

The complex dissociation chain of hydrocarbon molecules and the efforts to reduce the discrepancies between measured data with results from calculations demonstrate the need of detailed investigations on identification of relevant processes and the corresponding rate coefficients. Since heavy particle collisions are of relevance special attention should be given to these data also.

5. SUMMARY

With respect to diatomic molecular data needs for fusion applications basic molecular data for H_2, CH, C_2, BeH, BH have been compiled and, whenever possible, validated by experiments. Attention has been given to make data available also for their isotopomeres with heavier hydrogen isotopes. This includes Franck-Condon factors and vibrationally resolved transition probabilities. CR modelling of molecular hydrogen provides effective rate coefficients. The importance of dissociative recombination of molecular hydrogen ions has been discussed. Vibrationally resolved rate coefficients for electron impact excitation have been generated based on the semi-classical impact parameter method. This allowed constructing CR models for CH and C_2. Systematic parameter variations showed that the effective rate coefficients from CR modelling should be used for determination of hydrocarbon fluxes in the cold divertor plasma. The importance of heavy particle collisions on dissociation modelling of hydrogen and hydrocarbons has been demonstrated in the parameter range relevant to these edge plasmas. General data needs have been identified and discussed within the relevance for present applications.

REFERENCES

[1]   STANGEBY, P.C., The Plasma Boundary of Magnetic Fusion Devices, Institute of Physics Publishing, Bristol (2000).
[2]   SAMM, U., Plasma Wall Interaction: Status and Data Need, Nuclear Fusion Research, Springer Series in Chem. Phys. **78**, (CLARK, R., REITER, D. Eds), Springer, Berlin Heidelberg (2005).
[3]   REITER, D., Fusion Reaction Plasma Edge Modelling Code, Nuclear Fusion Research, Springer Series in Chem. Phys. **78**, (CLARK, R., REITER, D. Eds), Springer, Berlin Heidelberg (2005).
[4]   FANTZ, U., Molecular Diagnostics of Cold Edge Plasmas, Nuclear Fusion Research, Springer Series in Chem. Phys. **78**, (CLARK, R., REITER, D. Eds), Springer, Berlin Heidelberg (2005).
[5]   FANTZ, U., WÜNDERLICH, D., Effective Rate Coefficients for Molecular Processes of Hydrogen and Hydrocarbons in Edge Plasmas, Atom. Plasma-Mater. Interact. Data Fusion **14** (2008).
[6]   FANTZ, U., WÜNDERLICH, D., Franck-Condon Factors, Transition Probabilities and Radiative Lifetimes for Hydrogen Molecules and Their Isotopomeres, Atomic Data and Nuclear Data Tables **92** (2006) 853.

[7] FANTZ, U., WÜNDERLICH, D., Franck–Condon Factors, Transition Probabilities and Radiative Lifetimes for Hydrogen Molecules and Their Isotopomeres, Report, **INDC(NDS)–457**, IAEA Vienna, 2004, http://www-amdis.iaea.org/data/INDC-457.

[8] DRESSLER, K., WOLNIEWICZ, L., Berichte der Bunsen-Gesellschaft für Physikalische Chemie, **99** (1995) 246.

[9] HETTEMA, H., YARKONY, D.R., On the radiative lifetime of the $(a\,^4\Sigma^-,v,N,Fi)$ levels of the CH radical: An ab initio treatment, J. Chem. Phys. **100** (1994) 8991.

[10] LIE, G.C., HINZE, J., LIU, B., Valence excited states of CH. I. Potential curves, J. Chem. Phys. **59** (1973) 1872.

[11] VAN DISHOECK, E.F., Photodissociation processes in the CH molecule, J. Chem. Phys. **86** (1987) 196.

[12] BRESZINSEK, S. et al. Hydrocarbon injection for quantification of chemical erosion yields in tokamaks, J. Nucl. Mater. **363-365** (2007) 1119.

[13] HINZE, J., LIE, G.C., LIU, B., Valence Excited States of CH. 111. Radiative Lifetimes, Astrophys. J. **196** (1975) 621.

[14] BAUER, W., ENGELHARDT, B., WIESEN, P., BECKER, K.H., Lifetime measurements of GeH and CH in the A 2Δ, $v'=0$ state by laser-induced fluorescence, Chem. Phys. Lett. **158** (1989) 321.

[15] KOKKIN, D.L., BACSKAY, G.B., SCHMIDT, T.W., Oscillator strengths and radiative lifetimes for C_2: Swan, Ballik-Ramsay, Phillips, and d $^3\Pi_g \leftarrow$ c $^3\Sigma_u^+$ systems, J. Chem. Phys. **126** (2007) 084302.

[16] ABRAMS, M.L., SHERILL, C.D., Full configuration interaction potential energy curves for the $X\,^1\Sigma_g^+$, B $^1\Delta_g$, and B$'\,^1\Sigma_g^+$ states of C_2: A challenge for approximate methods, J. Chem. Phys. **121** (2004) 9211.

[17] BRUNA, P.J., WRIGHT, J.S., Transition probabilities for the B$^1\Delta_g$-A$^1\Pi_u$ and B$'^1\Sigma_g^+$ -A$^1\Pi_u$ infrared bands of C_2. An ab initio study, Chem. Phys. **157** (1991) 111.

[18] CHABALOWSKI, C.F., PEYERIMHOFF, S.D., The Ballik-Ramsay, Mulliken, Deslandres-d'Azambuja and Phillips systems in C_2: a theoretical study of their electronic transition moments, Chem. Phys. **81** (1983) 57.

[19] CHABALOWSKI, C.F., BUENKER, R.J., PEYERIMHOFF, S.D., Theoretical study of the electronic transition moments for the d$^3\Pi_g$-a$^3\Pi_u$ (SWAN) and e$^3\Pi_g$-a$^3\Pi_u$ (Fox-Herzberg) bands in C_2, Chem. Phys. Lett. **83** (1981) 441.

[20] FANTZ, U., MEIR, S., ASDEX Upgrade TEAM, Correlation of the intensity ratio of C_2/CH molecular bands with the flux ratio of C_2H_y/CH_4 particles, J. Nucl. Mater. **337-339** (2005) 1087.

[21] DUXBURY, et al., Report **EFDA–JET–CP(04)03-54** (2004).

[22] PITARCH-RUIZ ,J., SANCHEZ-MARIN, J., VELASCO, A.M., MARTIN, I., Full configuration interaction calculation of BeH adiabatic states, J. Chem. Phys. **129** (2008) 054310.

[23] LUH, W.T., STWALLEY, W. C., The $X^1\Sigma^+$, $A^1\Pi$, and $B^1\Sigma^+$ potential energy curves and spectroscopy of BH, J. Molec. Spectr. **102** (1983) 212.

[24] CIMIRAGLIA, R., PERSICO M., On the $A^1\Pi$-$X^1\Sigma^+$ transition in BH: Λ-doubling and vibrational structure Ab initio calculations, J. Mol. Spectr. **87** (1981) 303.

[25] REITER, D., WIESEN, S., BORN, M., Towards radiation transport modelling in divertors with the EIRENE code, Plasma Phys. Control. Fusion **44** (2002) 1723.

[26] GREENLAND, P.T., REITER, D., *The Role of Molecular Hydrogen in Plasma Recombination*, Report **JUEL-3258** (1996).

[27] GREENLAND, P.T., Collisional-radiative models with molecules, Proc. R. Soc. Lond. A **457** (2001) 1821.

[28] BURGESS, A., TULLY, J.A., On the Bethe approximation, J. Phys. B. **11** (1978) 4271.

[29] GRYZINSKI, M., Classical Theory of Atomic Collisions. I. Theory of Inelastic Collisions, Phys. Rev. **138** (1965) A336.

[30] BAUER, E., BARTKY, C.D., Calculation of Inelastic Electron—Molecule Collision Cross-sections by Classical Methods, J. Chem. Phys. **43** (1965) 2466.

[31] SEATON, M.J., The Impact Parameter Method for Electron Excitation of Optically Allowed Atomic Transitions, Proc. Phys. Soc. 79 (1962) 1105.

[32] BURGESS, A., SUMMERS, H.P., The recombination and level populations of ions. I - Hydrogen and hydrogenic ions, Mon. Not. R. Astr. Soc. **174** (1976) 345.

[33] HAZI, A.U., Impact-parameter method for electronic excitation of molecules by electron impact, Phys. Rev. A **23** (1981) 2232.

[34] BRAY, I., STELBOVICS, A.T. Convergent close-coupling calculations of electron-hydrogen scattering, Phys. Rev. A **46** (1992) 6995.

[35] GILLAN, C.J., NAGY, O., BURKE, P.G., MORGAN, L.A., NOOBLE, C.J., Electron scattering by nitrogen molecules, J. Phys. B **20** (1987) 4583.

[36] MORGAN, L.A., in Computational Methods for Electron Molecule Collisions, (HUO, W.M., GIANTURCO, W.M., Eds.) Plenum: New York (1995).

[37] BEHRINGER, K., Diagnostics and modelling of ECRH microwave discharges, Plasma Phys. Control. Fusion **33** (1991) 997.

[38] FANTZ U., Spectroscopic diagnostics and modelling of silane microwave plasmas, Plasma Phys. Control. Fusion **40** (1998) 1035.

[39] CELIBERTO, R., et al., Cross-section data for electron-impact inelastic processes of vibrationally excited molecules of hydrogen and its isotopes, Atomic Data and Nuclear Data Tables **77** (2001) 161.

[40] WÜNDERLICH, D., DIETRICH, S., FANTZ, U., Application of a collisional radiative model to atomic hydrogen for diagnostic purposes, J. Quant. Spec. Radiat. Transfer **110** (2009) 62.

[41] SAWADA, K., FUJIMOTO, T., Effective ionization and dissociation rate coefficients of molecular hydrogen in plasma, J. Appl. Phys. **78** (1995) 2913.

[42] WÜNDERLICH, D., FANTZ, U., A Collisional-Radiative Model for H_2 and H, IPP Report, **IPP 10/18** (2001).

[43] FANTZ, U., Atomic and Molecular Emission Spectroscopy in Low Temperature Plasmas Containing Hydrogen and Deuterium, IPP Report, **IPP 10/21** (20021).

[44] FANTZ, U., Molecular Diagnostics of Fusion and Laboratory Plasmas, Aotmic and Molecular Data and their Applications, CP771, (KATO, T., FUNABA, H., KATO, D., Eds.) American Institute of Physics (2005).

[45] JOHNSON, L. C., HINNOV, E., Ionization, recombination, and population of excited levels in hydrogen plasmas, J. Quant. Spec. Radiat. Transfer **13** (1973) 333.

[46] SUMMERS, H.P., The ADAS User Manual, version2.6, http://adas.phys.strath.ac.uk

[47] COLONNA, G., PIETANZA, L.D., CAPITELLI, M., Coupled solution of a time-dependent collisional-radiative model and Boltzmann equation for atomic hydrogen plasmas: possible implications with LIBS plasmas, Spectrochimica Acta Part B: Atomic Spectroscopy **56** (2001) 587.

[48] PIGAROV, A.Yu., Collisional Radiative Kinetics of Molecular Assisted Recombination in Edge Plasmas, Phys. Scipta **T96** (2002) 16.

[49] PIGAROV, A.Yu., KRASHENINNIKOV, S.I., Application of the collisional-radiative, atomic-molecular model to the recombining divertor plasma, Phys. Lett. A **122** (1996) 251.

[50] HASSOUNI, K. GICQUEL, A., CAPITELLI, M ., Loureiro J., Chemical kinetics and energy transfer in moderate pressure H_2 plasmas used in diamond MPACVD processes, Plasma Sources Sci. Technol. **8** (1999) 494.

[51] JANEV, R.K., REITER, D., SAMM, U., Collision Processes in Low-Temperature Hydrogen Plasmas, Report **JUEL-4105** (2003).

[52] MILES, W.T., THOMPSON, R., GREEN, A.E.S., Electron-Impact Cross-sections and Energy Deposition in Molecular Hydrogen, J. Appl. Phys. **43** (1972) 678.

[53] FANTZ, U., WÜNDERLICH, D., A novel diagnostic technique for $H^-(D^-)$ densities in negative hydrogen ion sources, New J. Phys. **8** (2006) 301.

[54] JANEV, R.K., LANGER, W.D., EVANS, J.K., POST, D.E., Elementary Processes in Hydrogen-Helium Plasmas, Springer: Berlin Heidelberg (1987).

[55] SCHNEIDER, R., et al., Plasma Edge Physics with B2-Eirene, Contrib. Plasma Phys. **46** (2006) 3.

[56] SIMONINI, R., CORRIGAN, G., RADFORD, G., SPENCE, J., TARONI, A., Models and Numerics in the Multi-Fluid 2-D Edge Plasma Code EDGE2D/U, Contrib. Plasma Phys. **34** (1994) 368.

[57] KIRSCHNER, A., PHILIPPS, V., WINTER, J., KÖGLER, U., Simulation of the plasma-wall interaction in a tokamak with the Monte Carlo code ERO-TEXTOR, Nucl. Fusion **40** (2000) 989.

[58] ERHARDT, A.B., LANGER, W.D., Report **PPPL-2477** (1987).

[59] JANEV, R.K., REITER, D., Collision Processes of Hydrocarbon Species in Hydrogen Plasmas I and II, Report **JUEL-3966** and **JUEL-4005** (2002).

[60] BROOKS, J.N., WANG, Z., RUZIC, D.N. ALMAN, D., Report **ANL/FPP/TM-297** (1999).

[61] TAHARA, H., MINAMI, K., MURAI, A., YASUI, T., YOSHIKAWA, T., Diagnostic Experiment and Kinetic Model Analysis of Microwave CH_4/H_2 Plasmas for Deposition of Diamondlike Carbon Films, Jpn. J. Appl. Phys. **34** (1995) 1972.

[62] POSPIESZCZYK, A. et al., Determination of Rate Coefficients for Atoms and Molecules (Hydrocarbons and Hydrogen with its Isotopes) by Measurement and Modelling in the Boundary Plasma of TEXTOR, Atom. Plasma-Mater. Interact. Data Fusion **13**, IAEA Vienna (2007).

[63] DING, R., ERO Modelling of Hydrocarbon Transport and Spectroscopy in the Injection Experiments at TEXTOR, ADAS Workshop (2008).

TABLE 1. FRANCK-CONDON FACTORS $q_{v'v''}$ FOR THE TRANSITION FROM THE GROUND STATE X $^2\Sigma_g^+$ (v') OF H_2^+ INTO THE B $^1\Sigma_u^+$ (v") STATE OF H_2

v'	v"=0	v"=1	v"=2	v"=3	v"=4	v"=5	v"=6	v"=7	v"=8
0	0.4762400	0.3174600	0.1361400	0.0482210	0.0153990	0.0046410	0.0013546	0.0003875	0.0001093
1	0.3753900	0.0272540	0.2073000	0.1963900	0.1120200	0.0504680	0.0199860	0.0073338	0.0025644
2	0.1257900	0.3319100	0.0292780	0.0559300	0.1513500	0.1399600	0.0873950	0.0445160	0.0200910
3	0.0209760	0.2531300	0.1750100	0.1145500	0.0006820	0.0725980	0.1205700	0.1046400	0.0676970
4	0.0015635	0.0644080	0.3220500	0.0590940	0.1490500	0.0168460	0.0182590	0.0775430	0.0971870
5	0.0000320	0.0057597	0.1185500	0.3384100	0.0090116	0.1329600	0.0504680	0.0002797	0.0371820
6	0	0.0000908	0.0115660	0.1710500	0.3308400	0.0001053	0.0981030	0.0725120	0.0052489
7	0	0.0000015	0.0000853	0.0163030	0.2145300	0.3239600	0.0050103	0.0658330	0.0783870
8	0	0.0000001	0.0000108	0.0000039	0.0169350	0.2452600	0.3346800	0.0080479	0.0428720
9	0	0	0	0.0000362	0.0001818	0.0118380	0.2574100	0.3737200	0.0046342
10	0	0	0	0.0000006	0.0000529	0.0012664	0.0033561	0.2395500	0.4448600
11	0	0	0	0	0.0000080	0.0000110	0.0032878	0.0006281	0.1779200
12	0	0	0	0.0000001	0.0000003	0.0000251	0.0000919	0.0040537	0.0173070
13	0	0	0	0	0	0.0000047	0.0000129	0.0009265	0.0010364
14	0	0	0	0	0	0.0000003	0.0000159	0.0000494	0.0019808
15	0	0	0	0	0	0	0.0000055	0.0000012	0.0006841
16	0	0	0	0	0	0	0.0000014	0.0000069	0.0001523
17	0	0	0	0	0	0	0.0000003	0.0000041	0.0000260

v'	v"=9	v"=10	v"=11	v"=12	v"=13	v"=14	v"=15	v"=16	v"=17
0	0.0000308	0.0000088	0.0000026	0.0000008	0.0000002	0.0000001	0	0	0
1	0.0008696	0.0002900	0.0000960	0.0000315	0.0000102	0.0000032	0.0000009	0.0000003	0.0000001
2	0.0083955	0.0033368	0.0012830	0.0001822	0.0001783	0.0000653	0.0000237	0.0000086	0.0000031
3	0.0370790	0.0182750	0.0084064	0.0036986	0.0015800	0.0006604	0.0002715	0.0001105	0.0000449
4	0.0799310	0.0527110	0.0303470	0.0160030	0.0079679	0.0038137	0.0017723	0.0008059	0.0003617
5	0.0739110	0.0780690	0.0615880	0.0410110	0.0245390	0.0136730	0.0072446	0.0037017	0.0018459
6	0.0119790	0.0473270	0.0656720	0.0618190	0.0472380	0.0317670	0.0196180	0.0114110	0.0063652
7	0.0171090	0.0015868	0.0259860	0.0493730	0.0554480	0.0482550	0.0361480	0.0245250	0.0155310
8	0.0738960	0.0265390	0.0001395	0.0123480	0.0341760	0.0457520	0.0450080	0.0371650	0.0274110
9	0.0280910	0.0656910	0.0307000	0.0020553	0.0051090	0.0225160	0.0356950	0.0392140	0.0352900
10	0.0000063	0.0176880	0.0585570	0.0298640	0.0040004	0.0019265	0.0147070	0.0270740	0.0326890
11	0.5343800	0.0126170	0.0080113	0.0563120	0.0217740	0.0048254	0.0008003	0.0099499	0.0205750
12	0.0770350	0.5863500	0.0754380	0.0002914	0.0649100	0.0153950	0.0049173	0.0005989	0.0072195
13	0.0515730	0.0015176	0.4924000	0.2030300	0.0101700	0.0982160	0.0031658	0.0061970	0.0013091
14	0.0026837	0.0565130	0.0660340	0.2076900	0.2951100	0.0573510	0.1786400	0.0054183	0.0155010
15	0.0003214	0.0237430	0.0060522	0.2058600	0.0007522	0.1645200	0.0750500	0.2667900	0.0691600
16	0.0008409	0.0046420	0.0219650	0.0443970	0.0959160	0.1054200	0.0009946	0.0010386	0.1434800
17	0.0004472	0.0005167	0.0121730	0.0035595	0.0719380	0.0113080	0.0312020	0.0162330	0.0661680

TABLE 2. FRANCK-CONDON FACTORS $q_{v'v''}$ FOR THE TRANSITION FROM THE GROUND STATE X $^2\Sigma_g^+$ (v') OF H_2^+ INTO THE GROUND STATE X $^1\Sigma_g^+$ (v'') STATE OF H_2.

v'	v''=0	v''=1	v''=2	v''=3	v''=4	v''=5	v''=6	v''=7	v''=8
0	0.0911850	0.2779700	0.3367400	0.2092100	0.0710110	0.0127650	0.0010561	0.0000258	0
1	0.1605800	0.1700000	0.0027966	0.1365300	0.2916700	0.1849500	0.0486090	0.0048524	0.0000953
2	0.1742600	0.0369390	0.0692400	0.1177400	0.0020598	0.2065100	0.2757800	0.1052500	0.0120520
3	0.1521300	0.0000001	0.1068100	0.0035945	0.1091300	0.0424500	0.0815420	0.3107700	0.1728200
4	0.1190800	0.0169440	0.0657650	0.0246010	0.0678070	0.0247470	0.1068700	0.0106980	0.2986300
5	0.0875530	0.0417730	0.0207160	0.0611110	0.0056853	0.0781960	0.0017105	0.1095300	0.0020453
6	0.0619910	0.0563770	0.0013674	0.0595660	0.0068272	0.0480950	0.0300640	0.0343330	0.0690640
7	0.0431950	0.0596910	0.0021383	0.0373110	0.0297710	0.0090195	0.0557390	0.0006178	0.0622700
8	0.0299210	0.0556350	0.0106860	0.0161460	0.0408360	0.0004118	0.0383300	0.0247940	0.0101560
9	0.0207080	0.0480610	0.0190770	0.0040739	0.0369130	0.0099206	0.0132410	0.0390190	0.0017560
10	0.0143850	0.0396110	0.0242700	0.0001319	0.0262240	0.0200960	0.0011716	0.0312880	0.0163690
11	0.0100560	0.0316750	0.0260270	0.0007721	0.0156070	0.0241540	0.0008391	0.0167470	0.0253150
12	0.0070679	0.0247700	0.0251290	0.0029857	0.0079136	0.0226800	0.0049736	0.0060352	0.0236310
13	0.0049789	0.0189920	0.0225190	0.0050088	0.0033703	0.0183850	0.0086187	0.0011179	0.0168990
14	0.0034841	0.0142050	0.0189240	0.0060757	0.0011403	0.0134720	0.0100480	0.0000011	0.0101360
15	0.0023826	0.0102210	0.0148380	0.0060202	0.0002674	0.0091080	0.0093746	0.0003626	0.0053425
16	0.0015298	0.0068089	0.0105000	0.0049523	0.0000284	0.0056227	0.0072687	0.0007789	0.0025273
17	0.0007257	0.0033056	0.0052914	0.0027256	0	0.0025607	0.0038272	0.0006250	0.0009168

v'	v''=9	v''=10	v''=11	v''=12	v''=13	v''=14
0	0	0	0	0	0	0
1	0.0000008	0.0000001	0	0	0	0
2	0.0001340	0.0000121	0	0	0	0
3	0.0200180	0.0000222	0.0000505	0.0000032	0.0000001	0
4	0.2393500	0.0251380	0.0002769	0.0000527	0.0000241	0.0000055
5	0.2736800	0.2968300	0.0183580	0.0027234	0.0000606	0.0000007
6	0.0194580	0.2694300	0.3331300	0.0022416	0.0054754	0.0012892
7	0.0287530	0.0298710	0.3177300	0.3022400	0.0144260	0.0000043
8	0.0606170	0.0073281	0.0189800	0.4487200	0.1287900	0.0525470
9	0.0298800	0.0420830	0.0005963	0.0000702	0.5799300	0.0083108
10	0.0035652	0.0366180	0.0242330	0.0009200	0.0666000	0.2263900
11	0.0011307	0.0116550	0.0301780	0.0155650	0.0257140	0.2159500
12	0.0082447	0.0020591	0.0194700	0.0190890	0.0268640	0.1819600
13	0.0133700	0.0001673	0.0079839	0.0161490	0.0059538	0.1778800
14	0.0139050	0.0023750	0.0019054	0.0095075	0.0111100	0.0332110
15	0.0114420	0.0041969	0.0001194	0.0044343	0.0062874	0.0412430
16	0.0079021	0.0043045	0.0000594	0.0017540	0.0035437	0.0004411
17	0.0038186	0.0025810	0.0001656	0.0005245	0.0011827	0.0024699

TABLE 3 VIBRATIONALLY RESOLVED TRANSITION PROBABILITIES $A_{v'v''}$ FOR THE A $^2\Delta(v')$ - X $^2\Pi(v'')$ TRANSITION OF CH

v'	$v''=0$	$v''=1$	$v''=2$	$v''=3$	$v''=4$	$v''=5$	$v''=6$	$v''=7$	$v''=8$
0	1.8250e+06	3.7639e+04	1.2070e+03	4.5503e+01	2.7597e+00	2.4215e-01	8.9387e-03	8.8908e-05	6.3316e-04
1	1.4881e+03	1.6148e+06	6.1278e+04	3.3608e+03	1.6667e+02	1.0824e+01	1.0132e+00	7.7843e-02	2.2647e-03
2	5.8179e+02	1.1412e+04	1.4036e+06	6.6525e+04	5.7406e+03	3.6726e+02	2.7422e+01	2.6431e+00	3.4849e-01
3	1.3419e+01	1.3546e+03	4.2020e+04	1.1807e+06	5.4290e+04	7.5049e+03	5.7929e+02	5.5571e+01	6.2318e+00
4	1.8531e+00	2.0068e+02	9.8625e+02	1.1031e+05	9.2293e+05	3.1107e+04	8.3117e+03	6.4162e+02	7.0939e+01
5	1.9030e+00	1.9531e+00	8.4694e+02	2.5016e+02	2.2307e+05	5.9901e+05	8.5722e+03	7.9173e+03	4.9900e+02
6	3.4042e-01	1.5937e+00	1.2919e+02	1.0687e+03	1.8272e+04	3.2691e+05	2.4111e+05	1.3010e+02	6.1717e+03
7	1.3196e-02	1.4051e+00	1.2581e+01	6.0705e+02	4.8737e+02	8.8572e+01	2.3443e+05	2.9826e+04	8.1382e+01
8	2.3339e-04	4.1677e-01	1.0437e+00	1.5154e+02	1.3709e+00	1.6740e+04	7.7619e+04	2.4350e+04	8.4522e+01

v'	$v''=9$	$v''=10$	$v''=11$	$v''=12$	$v''=13$	$v''=14$	$v''=15$
0	2.9139e-01	3.7962e-05	5.0330e-07	0.0000e+00	0.0000e+00	0.0000e+00	0.0000e+00
1	3.9315e-01	5.4928e-04	1.2455e-01	1.0127e-05	2.9185e-07	5.8078e-10	0.0000e+00
2	5.3263e-02	3.4782e-03	1.5555e-04	7.0572e-04	3.8863e-04	1.1636e-04	2.5718e-05
3	6.4862e-01	8.8055e-02	2.1941e-02	5.2662e-03	4.4843e-04	2.4012e-05	1.4573e-04
4	1.2134e+01	1.9698e+00	1.7263e-01	6.6564e-03	1.8167e-03	3.2557e-03	2.9343e-03
5	5.9251e+01	9.9807e+00	3.0605e+00	1.1328e+00	2.2830e-01	8.5660e-03	2.2372e-03
6	1.6227e+02	4.3469e+01	1.0747e+01	1.2670e+00	2.0988e-02	3.5498e-01	3.7840e-01
7	2.8867e+03	8.1250e+00	1.1079e+01	2.1743e-01	2.3065e+01	7.1648e-01	2.3712e-02
8	7.2313e+02	1.4268e+02	3.2449e+00	3.8937e+01	4.3674e+01	8.8522e+01	3.1176e+01

TABLE 4. VIBRATIONALLY RESOLVED TRANSITION PROBABILITIES $A_{v'v''}$ FOR THE B $^2\Sigma^-(v')$ - X $^2\Pi(v'')$ TRANSITION OF CH

v'	$v''=0$	$v''=1$	$v''=2$	$v''=3$	$v''=4$	$v''=5$	$v''=6$	$v''=7$	$v''=8$
0	3.6096e+06	1.0283e+05	5.6030e+03	3.1974e+02	6.3284e+01	8.3520e-02	3.3934e-01	3.3394e-01	7.2834e-02

v'	$v''=9$	$v''=10$	$v''=11$	$v''=12$	$v''=13$	$v''=14$	$v''=15$
0	5.2110e-03	1.4265e-03	3.5846e-03	1.2570e-03	1.2587e-04	1.3079e-06	0.0000e+00

TABLE 5. VIBRATIONALLY RESOLVED TRANSITION PROBABILITIES $A_{v'v''}$ FOR THE C $^2\Sigma^+(v')$ - X $^2\Pi(v'')$ TRANSITION OF CH

v'	$v''=0$	$v''=1$	$v''=2$	$v''=3$	$v''=4$	$v''=5$	$v''=6$	$v''=7$	$v''=8$
0	9.3632e+06	7.7268e+04	9.5504e+02	2.5250e+01	2.9842e+00	2.2570e+00	9.6566e-01	1.4101e-01	5.3484e-04
1	1.3402e+05	8.0002e+06	1.1087e+05	3.0158e+03	1.7382e-02	1.0345e+01	8.7602e-01	3.3486e+00	7.9214e-01
2	9.0398e+01	4.5646e+05	6.2160e+06	7.5158e+04	1.4318e-03	2.9386e+02	1.4718e+02	2.0326e+01	2.4992e-01

v'	$v''=9$	$v''=10$	$v''=11$	$v''=12$	$v''=13$	$v''=14$	$v''=15$
0	1.0437e-02	1.5322e-02	1.1395e-02	5.7566e-03	2.0358e-03	5.0004e-04	8.1588e-05
1	2.6924e-03	5.2118e-02	9.0644e-03	6.0184e-06	3.4728e-04	9.3350e-06	9.9756e-05
2	1.1229e+01	2.4232e+00	1.9144e-03	4.8564e-01	3.9290e-01	1.0256e-01	7.5958e-03

TABLE 6. VIBRATIONALLY RESOLVED TRANSITION PROBABILITIES $A_{v'v''}$ FOR THE A $^2\Pi(v')$ - X $^2\Sigma^+(v'')$ TRANSITION OF BeH

v'	$v''=0$	$v''=1$	$v''=2$	$v''=3$	$v''=4$	$v''=5$	$v''=6$	$v''=7$	$v''=8$
0	8.6166e+06	8.5558e+04	1.2341e+03	1.9762e+01	3.0061e-02	3.0251e-02	5.4320e-02	1.3813e-02	2.5149e-03
1	2.0756e+04	7.9315e+06	1.6366e+05	3.6749e+03	8.4254e+01	2.8235e-01	2.6548e-01	2.6088e-01	7.4697e-02
2	2.9704e+00	5.3971e+04	7.2465e+06	2.3036e+05	7.0288e+03	2.2048e-02	1.9995e+00	5.5023e-01	5.4113e-01
3	5.1611e-01	1.4563e+00	1.0531e+05	6.5612e+06	2.8479e+05	1.1134e-04	4.8637e+02	1.1677e+01	8.4115e-02
4	7.4551e-01	1.8418e+00	1.8228e+01	1.8008e+05	5.8708e+06	3.2991e-05	1.6167e+01	1.0060e+03	5.2462e+01
5	7.6259e-01	7.8884e+00	3.8545e+00	2.5784e+02	2.7804e+05	5.1699e-06	3.7017e+05	2.2361e+04	1.9395e+03
6	2.1688e 01	5.5997e+00	2.4015e+01	1.0273e 01	1.2758e+03	3.9340e-05	4.4554e+06	4.0864e+05	3.0119e+04
7	5.0940e 01	2.9737e+00	1.4698e+01	2.8937e+01	1.4157e+01	4.4111e-03	5.1536e+05	3.7302e+06	4.4871e+05
8	5.5336e-01	2.0155e+00	4.5773e+00	1.9317e+01	7.7831e+00	6.0139e-01	1.2588e+04	6.2510e+05	2.9994e+06
9	2.3315e-01	8.3961e-01	1.9116e+00	1.2317e+00	1.3632e+01	7.8963e+00	3.8178e+01	3.0516e+01	6.8939e+05
10	7.4881e-02	1.5172e-01	5.1686e-01	4.8800e-01	2.6174e+00	1.6819e+00	9.6652e+01	7.0415e+01	6.1915e+04
11	2.8067e-02	2.3312e-03	1.7804e-03	1.3450e-02	5.3170e-03	1.0314e+00	1.1684e+01	1.9624e+02	1.8563e+03
12	7.4137e-03	1.8290e-02	1.5770e-01	4.0321e-01	5.2693e-01	6.4257e-04	7.2258e-01	9.5232e+01	4.2053e+01
13	1.2743e-04	4.8581e-02	3.1448e-01	7.1327e-01	1.0830e+00	4.5115e-01	1.4485e-01	2.6381e+01	1.4645e+02
14	1.0177e-03	4.8553e-02	2.6402e-01	5.8937e-01	9.4546e-01	6.5512e-01	1.3615e-01	6.9435e+00	7.9743e+01

v'	$v''=9$	$v''=10$	$v''=11$
0	9.3702e-04	2.8625e-04	4.5825e-05
1	1.7990e-02	5.0894e-03	1.1613e-03
2	1.7744e-01	4.2784e-02	8.4104e-03
3	4.8084e-01	2.1226e-01	5.6498e-02
4	1.2545e+00	2.8173e-02	6.3609e-02
5	1.8237e+02	1.6783e+01	1.5482e+00
6	3.4760e+03	5.2044e+02	8.4966e+01
7	4.0824e+04	5.8765e+03	1.1419e+03
8	4.9467e+05	5.8677e+04	9.3035e+03
9	2.2677e+06	5.4075e+05	8.7789e+04
10	6.6290e+05	1.5304e+06	4.9207e+05
11	9.9556e+04	5.0866e+05	7.2166e+05
12	9.3688e+03	1.1518e+05	2.2773e+05
13	4.9517e+02	2.1752e+04	6.7170e+04
14	2.8205e+00	4.0534e+03	1.8223e+04

TABLE 7. VIBRATIONALLY RESOLVED TRANSITION PROBABILITIES $A_{v'v''}$ FOR THE A $^2\Pi(v')$ - X $^2\Sigma^+(v'')$ TRANSITION OF BeD

v'	$v''=0$	$v''=1$	$v''=2$	$v''=3$	$v''=4$	$v''=5$	$v''=6$	$v''=7$	$v''=8$
0	8.6968e+06	8.6578e+04	1.2372e+03	1.8997e+01	6.4404e-02	3.7808e-03	6.2498e-02	1.4068e-02	8.2593e-03
1	6.0120e+03	8.1756e+06	1.6576e+05	3.7008e+03	7.6942e+01	1.9526e-01	3.2133e-01	4.1493e-01	1.4854e-01
2	5.5441e+01	1.6926e+04	7.6580e+06	2.3379e+05	6.9888e+03	1.7485e+02	1.7551e-01	1.5377e+00	1.1532e+00
3	2.0057e-04	1.7797e+02	3.5764e+04	7.1478e+06	2.8777e+05	1.0667e+04	3.2797e+02	7.4061e-01	2.5682e+00
4	7.9813e-03	7.5317e-03	2.5222e+02	6.6985e+04	6.6439e+06	3.2998e+05	1.4805e+04	5.8641e+02	5.4456e+00
5	2.2844e-01	2.7608e+00	8.1874e-01	2.1136e+02	1.1310e+05	6.1405e+06	3.6388e+05	1.9551e+04	1.0423e+03
6	2.8286e-03	3.5960e+00	1.7833e+01	2.1146e+00	1.1191e+02	1.7396e+05	5.6315e+06	3.9232e+05	2.4990e+04
7	6.7266e-01	1.9402e+00	1.3566e+01	4.1025e+01	3.1848e-01	1.1874e+01	2.4831e+05	5.1139e+06	4.1725e+05
8	7.3651e-01	2.8030e+00	7.2548e+00	2.5036e+01	5.1030e+01	2.9823e+01	7.0320e+01	3.3359e+05	4.5872e+06
9	1.8916e-01	1.4433e+00	4.4287e+00	8.3963e+00	2.9150e+01	3.3540e+01	1.6179e+02	7.4940e+02	4.2587e+05
10	1.0350e-01	3.8509e-01	1.1400e+00	3.8830e+00	7.3224e+00	2.4691e+01	4.2106e+00	4.2015e+02	3.1274e+03
11	6.6696e-02	1.1128e-01	6.8297e-02	4.7255e-01	1.3659e+00	4.1317e+00	1.4845e+01	1.5886e+01	6.9190e+02
12	4.9406e-04	5.9031e-01	3.7612e-02	1.4024e-01	2.5865e-02	2.9577e-02	1.7246e+00	2.9098e+00	1.4635e+02
13	1.1956e-01	2.3709e-01	3.4478e-01	7.7727e-01	1.1445e+00	1.0902e+00	4.2113e-01	3.2917e-01	4.1433e+00
14	2.1858e-01	6.4321e-01	8.4643e-01	1.4174e+00	2.3178e+00	3.0370e+00	3.3999e+00	1.4698e+00	3.0485e-01
15	2.2074e-01	7.5425e-01	1.1789e+00	2.0560e+00	3.0853e+00	4.2658e+00	5.9092e+00	5.7206e+00	2.1184e+00
16	1.3079e-01	5.9710e-01	1.1797e+00	2.3283e+00	3.4271e+00	1.7430e+00	6.7087e+00	8.4743e+00	5.7585e+00
17	6.5665e-02	3.9328e-01	9.7523e-01	2.0741e+00	3.2076e+00	1.5451e+00	6.2896e+00	8.6343e+00	8.1282e+00

v'	$v''=9$	$v''=10$	$v''=11$	$v''=12$	$v''=13$	$v''=14$	$v''=15$
0	8.4138e-03	1.9598e-03	2.8711e-05	1.9442e-05	1.1731e-05	7.7719e-06	6.9803e-06
1	6.3786e-02	1.9992e-02	1.6035e-03	3.5508e-05	2.2399e-04	2.1723e-04	1.6284e-04
2	3.8357e-01	1.2773e-01	2.6823e-02	7.7605e-04	1.0904e-03	2.3111e-03	1.8671e-03
3	2.1046e+00	5.5184e-01	1.2662e-01	1.7154e-02	4.4935e-04	7.1071e-03	7.1866e-03
4	2.1710e+00	1.9944e+00	6.2827e-01	1.0030e-01	1.2578e-03	8.8066e-03	1.4965e-02
5	2.6029e+01	2.9110e-01	1.3103e+00	3.7411e-01	4.0873e-02	8.0282e-04	1.6374e-02
6	1.7928e+03	8.9713e+01	1.3988e+00	1.4892e-01	8.2696e-02	2.1520e-03	7.4246e-03
7	3.1056e+04	2.9418e+03	2.4320e+02	1.5545e+01	7.5560e-01	7.4546e-02	3.5451e-02
8	1.1033e+05	3.7690e+04	4.5671e+03	5.6095e+02	6.5675e+01	8.5487e+00	1.5684e+00
9	1.0532e+06	1.6366e+05	1.5092e+04	6.7117e+03	1.1562e+03	2.0493e+02	4.0467e+01
10	5.1770e+05	3.5139e+06	4.9019e+05	5.4209e+04	9.5682e+03	2.1570e+03	5.1980e+02
11	9.1019e+03	5.9665e+05	2.9711e+06	5.2469e+05	6.7715e+04	1.3173e+04	3.4884e+03
12	7.2178e+02	2.1189e+04	6.4382e+05	2.4278e+06	5.7036e+05	9.0934e+04	1.8562e+04
13	4.4415e+02	3.3101e+02	4.0994e+04	6.3632e+05	1.8859e+06	6.0713e+05	1.3120e+05
14	6.0773e+01	8.0739e+02	9.2079e+00	6.5583e+04	5.5885e+05	1.3130e+06	5.6231e+05
15	7.2887e+00	2.3443e+02	9.0254e+02	1.3605e+03	8.5723e+04	3.9659e+05	6.8225e+05
16	3.2244e+00	4.7897e+01	5.2472e+02	4.2158e+02	5.8625e+03	8.4342e+04	1.8413e+05
17	4.1299e+00	1.1925e+01	1.7687e+02	6.4711e+02	2.6614e+00	1.1626e+04	4.9958e+04

TABLE 8. VIBRATIONALLY RESOLVED TRANSITION PROBABILITIES $A_{v'v''}$ FOR THE A $^2\Pi(v')$ - X $^2\Sigma^+(v'')$ TRANSITION OF BeT

v'	$v''-0$	$v''-1$	$v''-2$	$v''-3$	$v''-4$	$v''-5$	$v''-6$	$v''-7$	$v''-8$
0	8.7293e+06	8.7834e+04	1.2434e+03	1.8703e+01	1.4702e-01	3.0998e-04	3.3032e-02	1.0070e-02	1.6812e-02
1	2.0571e+03	8.2746e+06	1.6864e+05	3.7614e+03	7.8108e+01	4.0651e-01	2.2381e-01	3.6566e-01	1.7390e-01
2	8.2478e+01	6.5588e+03	7.8239e+06	2.3918e+05	7.1496e+03	1.7199e+02	1.4642e-01	1.3570e+00	1.4651e+00
3	1.6433e-02	2.9628e+02	1.5319e+04	7.3822e+06	2.9535e+05	1.0864e+04	2.9980e+02	9.1442e-02	3.6362e+00
4	5.2001e-02	3.1807e-01	5.1672e+02	3.1733e+04	6.9514e+06	3.3878e+05	1.4835e+04	4.8990e+02	7.9981e-01
5	4.2857e-02	8.6359e-01	7.5216e-02	6.1734e+02	5.8456e+04	6.5257e+06	3.7244e+05	1.9215e+04	8.0232e+02
6	2.1497e-02	2.0994e+00	1.2064e+01	2.3237e+00	6.1881e+02	9.6631e+04	6.1001e+06	3.9924e+05	2.4116e+04
7	6.4261e-01	9.7991e-01	1.0161e+01	3.5640e+01	1.5145e+00	5.3981e+02	1.4622e+05	5.6695e+06	4.2103e+05
8	5.6136e-01	2.9696e+00	6.6133e+00	2.3920e+01	6.1120e+01	2.5323e+00	3.8537e+02	2.0675e+05	5.2325e+06
9	1.3713e-01	1.5051e+00	4.4235e+00	1.0262e+01	3.4595e+01	6.6630e+01	5.0417e+01	1.5415e+02	2.7709e+05
10	1.5754e-01	3.9733e-01	1.5751e+00	6.0821e+00	1.0679e+01	3.7149e+01	4.7573e+01	2.1865e+02	1.0407e-02
11	7.2290e-02	1.8866e-01	4.2021e-01	9.6687e-01	4.1196e+00	8.7633e+00	3.3985e+01	1.3336e+01	5.6864e+02
12	2.4324e-02	3.1272e-04	7.6978e-03	4.7953e-04	1.9624e-01	1.8446e+00	5.3465e+00	2.3797e+01	2.7801e+00
13	2.0276e-01	3.5207e-01	2.8002e-01	2.3868e-01	3.5729e-01	5.8707e-02	1.7396e-01	2.2707e+00	9.6347e+00
14	1.8141e-01	6.5981e-01	8.9545e-01	9.7587e-01	1.1294e+00	1.5871e+00	1.2571e+00	2.9771e-01	7.5685e-01
15	6.8410e-02	4.6097e-01	1.1709e+00	1.8725e+00	2.2626e+00	3.0297e+00	4.0990e+00	3.9257e+00	2.0685e+00
16	2.3221e-02	2.2356e-01	1.0959e+00	1.9981e+00	3.3165e+00	4.4131e+00	5.6410e+00	7.6369e+00	7.9872e+00
17	1.7188e-02	1.4982e-01	8.6539e-01	1.5646e+00	3.3239e+00	5.2610e+00	6.6623e+00	8.9889e+00	1.1698e+01

v'	$v''-9$	$v''-10$	$v''-11$	$v''-12$	$v''-13$	$v''-14$	$v''-15$	$v''-16$	$v''-17$
0	1.4122e-02	2.3422e-03	9.4012e-05	2.6346e-06	2.2496e-05	1.2326e-04	1.3714e-04	6.5099e-05	1.8171e-05
1	9.5534e-02	2.9848e-02	3.9425e-03	2.3013e-04	9.4753e-05	7.6525e-04	1.0934e-03	7.6874e-04	3.6825e-04
2	4.7793e-01	2.1945e-01	5.9672e-02	1.1318e-03	1.7326e-03	2.3298e-03	2.8611e-03	3.3556e-03	2.7002e-03
3	2.8584e+00	8.1397e-01	2.8108e-01	5.3233e-02	5.7326e-05	9.7163e-03	1.3494e-02	1.3987e-02	1.1755e-02
4	5.0374e+00	3.8275e+00	1.0663e+00	2.5082e-01	1.5082e-02	1.2285e-02	3.5640e-02	3.8566e-02	3.2618e-02
5	5.9244e+00	3.9665e+00	3.7537e+00	9.3912e-01	1.4605e-01	1.3891e-04	5.9741e-02	9.4616e-02	8.0533e-02
6	1.3103e+03	2.7411e+01	1.1942e+00	2.3501e+00	6.1146e-01	4.0548e-02	3.4457e-02	1.4399e-01	1.6618e-01
7	2.9537e+01	2.0076e+03	8.7827e+01	2.9360e-01	5.9116e-01	1.7731e-01	1.6900e-03	1.2156e-01	2.1139e-01
8	4.3940e+05	3.5394e+04	3.2480e+03	2.2261e+02	9.2977e+00	1.0355e-01	2.3749e-02	9.7352e-02	1.8518e-01
9	4.7884e+06	4.5583e+05	4.1579e+04	4.8214e+03	4.8459e+02	4.1412e+01	3.7061e+00	8.0149e-01	4.3171e-01
10	3.5477e+05	4.3373e+06	4.7159e+05	4.7984e+04	6.8445e+03	9.4398e+02	1.2379e+02	1.8064e+01	4.0645e+00
11	3.6380e+02	4.3619e+05	3.8807e+06	4.8846e+05	5.4784e+04	9.3458e+03	1.7091e+03	3.0735e+02	6.1723e+01
12	1.0580e+03	2.1710e+03	5.1498e+05	3.4202e+06	5.0927e+05	6.2758e+04	1.2368e+04	2.8883e+03	6.9715e+02
13	8.2880e+01	1.5131e+03	6.9069e+03	5.8152e+05	2.9572e+06	5.3846e+05	7.4027e+04	1.5923e+04	4.5456e+03
14	1.0935e-01	3.3204e+02	1.6240e+03	1.6365e+04	6.2113e+05	2.4936e+06	5.8049e+05	9.2372e+04	2.0667e+04
15	5.1218e-03	1.5852e+01	7.8180e+02	1.1628e+04	3.1576e+04	6.1879e+05	2.0330e+06	6.2547e+05	1.2686e+05
16	3.7282e+00	1.6169e+00	1.0299e+02	1.3320e+03	3.2118e+04	5.0686e+04	5.6477e+05	1.5540e+06	6.4769e+05
17	1.0922e+01	4.7593e+00	1.2629e+01	3.2144e+02	1.6772e+03	6.8493e+01	6.8239e+04	4.4843e+05	1.0290e+06

EXCITED STATE FORMATION IN ELECTRON CAPTURE BY SLOW MULTIPLY CHARGED IONS

H.B. GILBODY, R.W. MCCULLOUGH, B. SEREDYUK, D.M. KEARNS

Department of Physics and Astronomy, Queen's University Belfast,
Belfast, United Kingdom

Abstract

Translational energy spectroscopy (TES) has been used to study one-electron capture by H and He-like ions of C, N and O in both H and H_2 at energies below 1 keV amu^{-1}. Similar measurements have been carried out for He^{2+} ions in the hydrocarbons CH_4, C_2H_4, C_2H_6 and H_2O at energies within the range 250 - 2000 eV amu^{-1}. One-electron capture by O^{6+} ions in H_2O, CO_2 and CH_4 and by C^{4+} ions in CH_4 have also been studied in the range 200 - 1500 eV amu^{-1}. The main excited product states have been identified, their relative importance assessed and, in some cases, cross-sections determined. In the molecular targets, contributions to one-electron capture from non-dissociative and dissociative mechanisms as well as from two-electron capture into autoionizing states has also been determined. In all cases, the highly selective nature of the electron capture process is confirmed even in the case of molecules with many possible fragmentation channels involving a wide range of energy defects. In the case of H, the main product channels are well predicted by reaction windows calculated using a Landau-Zener approach. However, the same approach applied to molecules, where both non-dissociative and dissociative mechanisms are significant, is found to be of limited use.

1. INTRODUCTION

A detailed understanding of one-electron capture processes of the type

$$X^{q+} + Y \rightarrow X^{(q-1)+}(n, l) + Y^+ (n', l')$$
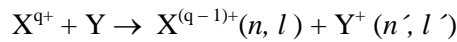
leading to product ions in specified excited states (n, l) is relevant to the accurate modelling and diagnostics of edge plasmas in fusion devices. At velocities v < 1 au, it is well known that, in processes with moderate exothermicity, electron capture may take place very effectively through a limited number of pseudocrossings of the adiabatic potential energy curves describing the initial and final molecular systems. In the case of collisions with molecules such as

$$X^{q+} + Y_iZ_j \rightarrow X^{(q-1)+} (n, l) + Y_iZ_j^+(\Sigma)$$
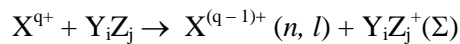
where $Y_iZ_j^+(\Sigma)$ includes all final bound or dissociative states, the electron capture process may still be highly selective. However, the relative importance of non-dissociative and dissociative mechanisms as well as the extent to which two-electron capture into autoionizing states contribute to the one-electron capture process is also of considerable interest.

The technique of translational energy spectroscopy (TES) can allow identification and a quantitative assessment of the main excited product channels as well as a useful insight into the mechanisms involved in the electron capture process. It is complementary to photon emission spectroscopy (PES). In the TES approach, the X^{q+} primary ion beam of well defined energy T_1 is passed through the target gas and the kinetic energy T_2 of the forward scattered $X^{(q-1)+}$ ions formed as products of single collisions is then measured. The difference in kinetic energy ΔT is then given by $\Delta T = T_2 - T_1 = \Delta E - \Delta K$ where ΔE is the energy defect for a particular product channel and ΔK is a small recoil correction. Provided that the ratio $\Delta E/T_1 \ll 1$ and the scattering is confined to small angles, the measured change in translational energy $\Delta T \approx \Delta E$. The relative importance of collision product channels characterised by particular values of ΔE may then be assessed from a careful analysis of the energy change spectra subject to the limitations of the available energy resolution.

In previous work in this laboratory [1] our TES studies of 0.5 – 2 keV amu^{-1} He^{2+} - H$_2$ collisions provided the first direct evidence of the great importance of highly selective dissociative excitation mechanisms in the one-electron capture process at low energies. Our subsequent TES studies [2] of one-electron capture by 0.2 – 1 keV amu^{-1} He^{2+} ions in CO have also confirmed the important role of processes involving selective electron capture with dissociation at low energies. In this review, we describe recent TES studies carried out in this laboratory [3, 4] of one-electron capture by H and He-like ions of C, N and O in both H and H$_2$ at energies below 1 keV amu^{-1}. We also present TES data [5, 6] for one-electron capture by He^{2+} ions in CH$_4$, C$_2$H$_4$, C$_2$H$_6$ and H$_2$O within the range 200 - 2000 eV amu^{-1}. The results of studies [7] of one-electron capture by 200 - 1500 eV amu^{-1} O^{6+} ions in H$_2$O, CO$_2$ and CH$_4$ and by C^{4+} ions in CH$_4$ are also described.

2. EXPERIMENTAL APPROACH

A detailed explanation of the apparatus and experimental approach has been given in our previous publications (see [3] and references therein) so that only a brief summary need be given here. A beam of the required primary ions, produced by an all-permanent magnet 10 GHz ECR ion source, was extracted into an accelerator beam line held at a potential - 4kV. This beam was then momentum analysed using a 90 degree double focusing magnet and passed through two hemispherical electrostatic analysers. The energy of the emergent beam was then adjusted to that required by passage through a cylindrical electrostatic lens system before entering a voltage-labelled target gas cell. The target gas of interest flowed into the cell at constant rate low enough to ensure single collision conditions. Our measurements in atomic hydrogen were carried out using our specially developed (Voulot *et al* 2001) aluminium target cell fed with highly dissociated hydrogen from a microwave-driven discharge source.

The forward-scattered ions produced by one-electron capture emerged from the cell (within an acceptance angle of ± 3 deg.) and were then energy analysed by a third hemispherical energy analyzer and recorded by a computer-controlled position sensitive detector. By scanning the retarding voltage, a translational energy spectrum of the product ions could be obtained while maintaining an energy resolution of about 1 eV. An analysis of the positions and magnitudes of the peaks in the observed spectra (using Peak-fit software) allow identification and determination of the relative importance of each product channel. In principle, cross-sections for each observed product channel can then be derived by normalising the sum of the relative yields to total one-electron capture cross-sections if reliable values are available.

Our TES measurements in atomic hydrogen followed the procedure described previously [8] in which the energy change spectra in pure atomic hydrogen were derived from the measured spectra in highly dissociated hydrogen by careful subtraction of the appropriate fraction of the molecular contribution. The accurate subtraction process was facilitated by the ability of the hydrogen source to be rapidly switched from highly dissociated hydrogen to pure H$_2$.

Energy defects for specific product channels were obtained by reference to the energy level tabulations of Bashkin and Stoner [9] and, in the case of H$_2$, the potential energy curves of Sharp [10]. Energy defects for product channels involving the more complex molecules were identified by reference to photoelectron spectroscopy data and we have that assumed Franck-Condon transitions are valid throughout. For CH$_4$ we used the data of Brundle *et al* [11], Dujardin *et al* [12] and Rabalais *et al* [13], for C$_2$H$_4$ the data of Pollard *et al* [14] , for C$_2$H$_6$ the data of Mackie *et al* [15], for H$_2$O the data of [J. E. Reutt et al, 16] and of Richardson [17] and for CO$_2$ the data of Cornaggia and Hering [18] and Masuoka *et al* [19].

3. RESULTS AND DISCUSSION

3.1. One-electron capture by H and He-like ions of O, N and C in collisions with H and H$_2$

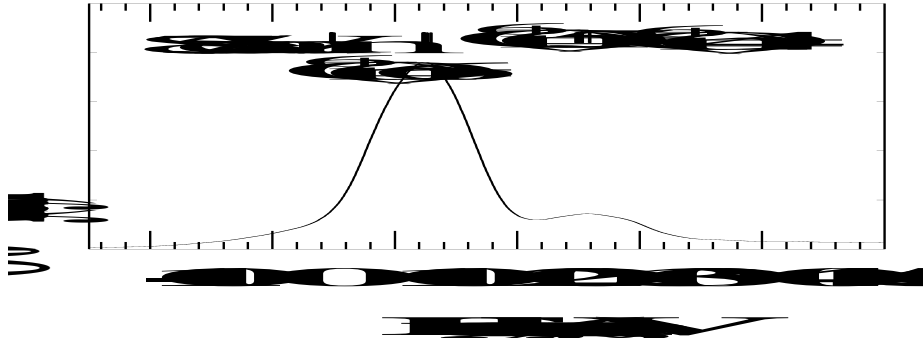### 3.1.1. One-electron capture by H-like ions of O, N and C in collisions with H atoms

FIG. 1. Energy change spectra for one-electron capture by O^{7+} ions in H (from [4]).

TES measurements for one-electron capture by O^{7+}, N^{6+} and C^{5+} ions in H have been carried out [4] for energies within the range 250 to 950 eV amu^{-1}. In Figure 1 the energy change spectrum obtained for O^{7+} ions in H at 875 eV amu^{-1} shows that capture occurs predominantly into the O^{6+}(n = 5) states according to

$$O^{7+}(1s)^2S + H(1s) \rightarrow O^{6+}(n = 5) + H^+ + (13.0 - 13.7)\ eV$$
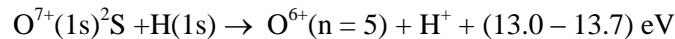
The smaller peak centred on an energy defect of about 27 eV corresponds to O^{6+}(n = 4) formation channels. There is also evidence of a very small contribution from O^{6+}(n = 6) formation channels. We have used a peak fitting deconvolution procedure to estimate from our measured spectra the relative contributions of the O^{6+}(n = 4), O^{6+}(n = 5) and O^{6+}(n = 6) formation channels to the total capture cross-section over the range 875 to 350 eV amu^{-1}. At 350 eV amu^{-1}, the O^{6+}(n = 4) contribution was found to have increased to about 94 % of the total.

Our energy change spectra [4] for one-electron capture by N^{6+} ions in H exhibit a similar pattern of behaviour. In this case, at the higher energies N^{5+}(n = 4) product channels are found to be dominant according to

$$N^{6+}(1s)\ ^2S + H(1s) \rightarrow N^{5+}(n = 4) + H^+ + (16.9 - 18.1)\ eV$$
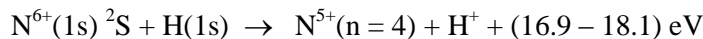
with a small contribution from n = 5 formation channels and even smaller contributions arising from N^{5+}(n = 6) and N^{5+}(n = 7) formation. However, as the energy decreases to 343 eV amu^{-1} it is found that N^{5+}(n = 4) product channels rapidly become the only significant contribution to the total capture cross-section.

Our measurements [4] for one-electron capture by C^{5+} ions in H within the range 833 − 250 eV amu^{-1}, also show that, at the lower energies, the energy change spectra are dominated by a single peak. This corresponds to capture into C^{4+}(n = 4) states through

$$C^{5+}(1s)^2S + H(1s) \rightarrow C^{4+}(n = 4) + H^+ + (6.8 - 8.7)\ eV$$
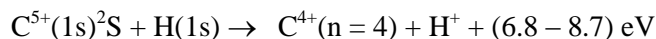
However, at higher energies and larger exothermicities, there is also a small contribution from C^{4+} (n = 3) product channels in addition to a very small C^{4+}(n = 5) contribution through slightly endothermic formation channels. Using our peak fitting deconvolution procedure, we estimate that, at 833 eV amu^{-1}, capture into n = 4, n = 3 and n = 5 states respectively account for about 83 %, 12 % and 5 % of total captures.

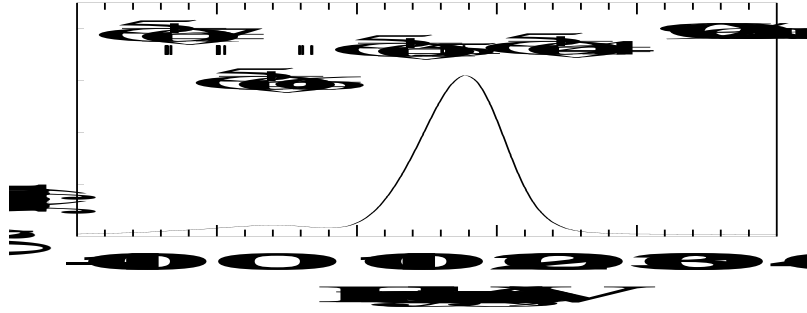*3.1.2. One-electron capture by He -like ions of O, N and C in collisions with H atoms*

FIG. 2. Energy change spectra for one-electron capture by O^{6+} ions in H (from [4]).

We have carried out TES measurements [3, 4] for one-electron capture by O^{6+}, N^{5+} and C^{4+} ions in H within the range 250 to 950 eV amu^{-1}. Figure 2 shows our observed energy change spectra for one electron capture by O^{6+} ions in H at 900 eV amu^{-1}.

It can be seen that capture occurs predominantly into O^{5+} (n = 4) states according to

$$O^{6+}(1s^2)\,^1S + H(1s) \rightarrow\ O^{5+}(n = 4) + H^+ + (17.0 - 18.8)\ eV$$
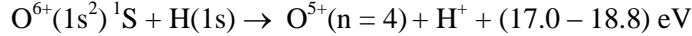
This observation is in agreement with the theoretical predictions of Hanssen *et al* [20]. At smaller energy defects the spectrum also exhibits a small broad peak indicating some contributions arising from O^{5+} (n = 5) capture

$$O^{6+}(1s^2)\,^1S + H(1s) \rightarrow\ O^{5+}(n = 5) + H^+ + (6.0 - 6.9)\ eV$$
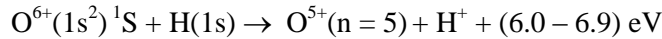
with the possibility of additional very small contributions from O^{5+} (n = 6) and O^{5+} (n = 7) capture channels. Only the single peak corresponding to O^{5+} (n = 4) formation could be detected at energies below 900 eV amu^{-1}. Measurements based on photon emission spectroscopy (PES) by the KVI group [21] carried out above our present high energy limit in the range 940 – 7500 eV amu^{-1} only recorded contributions from the O^{5+} (n = 4) sublevels.

Figure 3 shows our measured energy change spectra [3] for one-electron capture by N^{5+} ions in H at energies in the range from 857eV amu^{-1} down to 357eV amu^{-1}. These spectra show very clearly that capture into the n = 4 states of N^{4+} through

$$N^{5+}(1s^2)\,^1S + H(1s) \rightarrow\ N^{4+}(n = 4) + H^+ + (7.64 - 9.09)\ eV$$
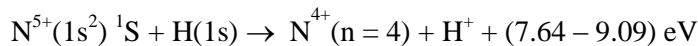
is dominant throughout the present energy range. A contribution from capture into the N^{4+}(n = 3) states through the more exothermic channels

$$N^{5+}(1s^2)\,^1S + H(1s) \rightarrow\ N^{4+}(n = 3) + H^+ + (24.21 - 27.72)\ eV$$
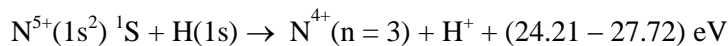
while negligible at 357eV amu⁻¹, can be seen to make an increasing contribution as the impact energy increases. The fraction of N^{4+} ions formed in the n = 4 and n = 3 states, as determined from an analysis of our TES spectra are summarised in Table 1.
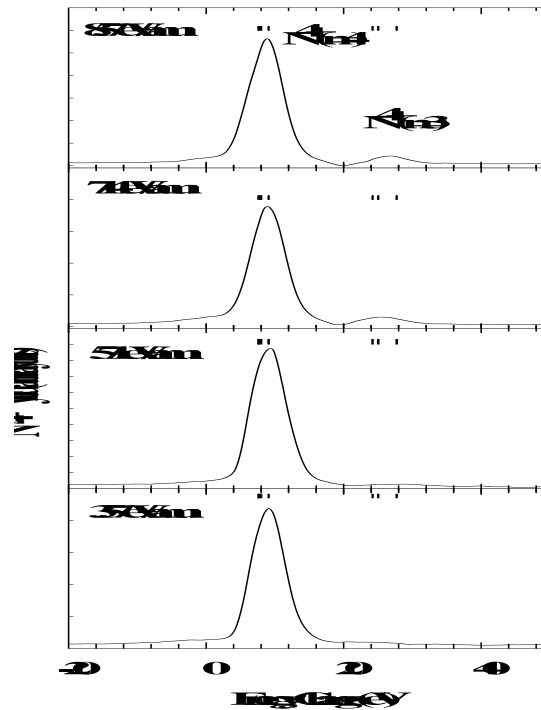

FIG. 3. Energy change spectra for one-electron capture in N^{5+} - H(1s) collisions in the range 357 - 857 eV amu⁻¹(from [3]).
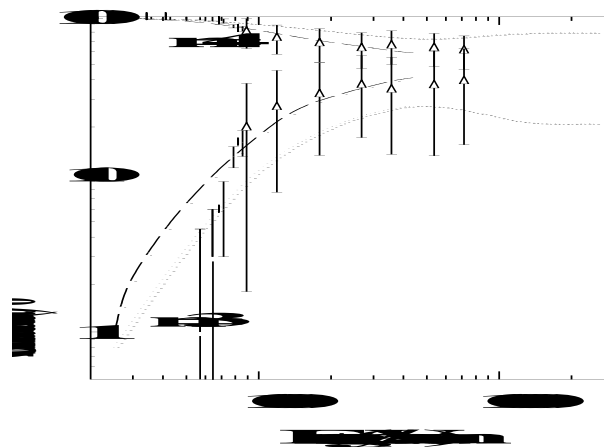

FIG. 4. One-electron capture into the n = 4 and n = 3 states of N^{4+} by N^{5+} ions in atomic hydrogen shown as a fraction of the total electron capture cross-section (from [3]). Experiment: ●, Our TES data [3] Δ, Dijkkamp et al [21] Theory: ——, Shimakura and Kimura [22] •••••• Bendahman et al [23].

TABLE 1. MEASURED FRACTIONS OF $N^{4+}(N = 3)$ AND $N^{4+}(N = 4)$ PRODUCT IONS FORMED THROUGH ONE-ELECTRON CAPTURE IN N^{5+} – H COLLISIONS (FROM [3])

Energy (eV/amu)	n = 4 (%)	n = 3 (%)
857	84 ± 3	16 ± 3
786	87 ± 2	13 ± 2
714	94 ± 3	6 ± 3
643	97 ± 3	3 ± 3
571	> 99	< 1
500	> 99	< 1
429	> 99	< 1
357	> 99	< 1
286	> 99	< 1
250	> 99	< 1
214	> 99	< 1

There have been numerous experimental measurements of the total cross-sections for one-electron capture in $N^{5+}(1s^2)^1S$ – H(1s) collisions using several different techniques over a wide energy range but results from different laboratories exhibit large discrepancies and are subject to large uncertainties in the present energy range (cf. data in paper by Havener *et al* [24]). For this reason, we have made no attempt to normalise our TES data to previously measured total cross-sections. In Figure 4 we show our measured yields of $N^{4+}(n = 4)$ and $N^{4+}(n = 3)$ product ions (expressed as a fraction of the total electron capture cross-section) compared with the higher energy PES measurements of Dijkkamp *et al* [21]. There is good general accord between the two sets of experimental data. Theoretical estimates of the N^{5+} - H(1s) one-electron capture process by Bendahman *et al* [23] based on a molecular orbital expansion method and by Shimakura and Kimura [22] based on both quantum mechanical and semiclassical molecular-orbital expansion methods are included in Figure 4. The theoretical values of Bendahman *et al* [23] can be seen to be in somewhat better accord with the low energy experimental values for n = 4 capture. In the case of n = 3 capture, neither theory satisfactorily describes the very rapid decrease in the product yields observed at low energies.

Our energy change spectra [4] for one-electron capture by C^{4+} ions in H exhibit a main peak main peak correlated with $C^{3+}(n = 3)$ formation through

$$C^{4+} (1s^2)\ ^1S + H(1s) \rightarrow\ C^{3+}(n = 3) + H^+ + (10.6 - 13.4)\ eV$$
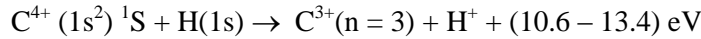
At 867 eV amu^{-1}, although incompletely resolved, the separate contributions to 3s and (3p+ 3d) formation can be discerned. A smaller peak observed in the 867 eV amu^{-1} spectrum corresponds to mainly $C^{3+}(n = 4)$ formation through the slightly exothermic channels

$$C^{4+} (1s^2)\ ^1S + H(1s) \rightarrow\ C^{3+}(n = 4) + H^+ + (0.01 - 1.1)\ eV$$
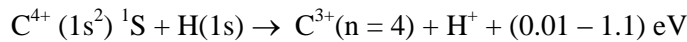
together with a possible very small contribution from endothermic $C^{3+}(n = 5)$ channels. At 333 eV amu^{-1}, only the peak corresponding to $C^{3+}(n = 3)$ formation is significant. Our TES data are in good accord with the PES measurements of Dijkkamp *et al* [21] in the overlapping range 830 – 6670 eV amu^{-1}. At 830 eV amu^{-1}, which is close to the highest energy we consider, $C^{3+}(n = 3)$ formation was found to account for about 95% of the total capture cross-section. Calculations carried out by Tseng and Lin [25] using a semi-classical AO close-coupling model are also in reasonable accord with our observations. Over the range 1000 – 200 eV amu^{-1} they predict that capture into n = 4 levels falls from 5.4% to about 2% of the total capture cross-section.

3.1.3. One-electron capture by H-like ions of O, N and C in collisions with H_2
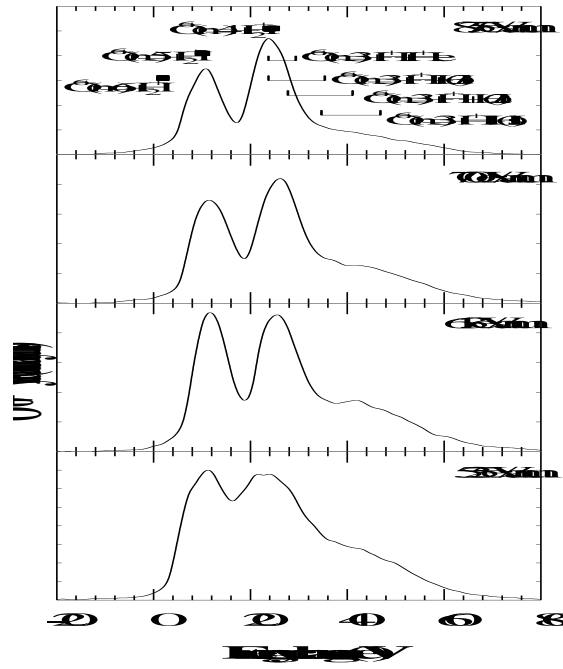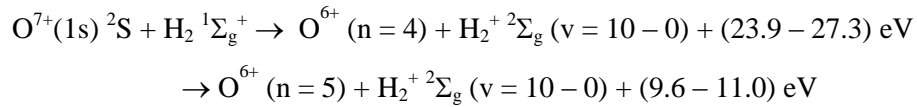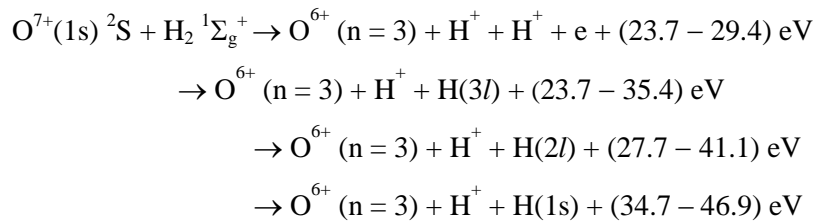
FIG. 5. Energy change spectra for one-electron capture by O^{7+} ions in H_2 (from [4]).

Figure 5 shows our observed energy change spectra [4] for one-electron capture by O^{7+} ions in H_2 at energies ranging from 525 to 875 eV amu^{-1}. These spectra exhibit a rich and interesting structure with evidence of important contributions to one-electron capture from a number of different collision mechanisms. The two well defined peaked centred on energy defects of about 24 and 6 eV correspond to $O^{6+}(n = 4)$ and $O^{6+}(n = 5)$ formation respectively through the non-dissociative processes

$$O^{7+}(1s)\ ^2S + H_2\ ^1\Sigma_g^+ \rightarrow\ O^{6+}\ (n = 4) + H_2^+\ ^2\Sigma_g\ (v = 10 - 0) + (23.9 - 27.3)\ eV$$

$$\rightarrow O^{6+}\ (n = 5) + H_2^+\ ^2\Sigma_g\ (v = 10 - 0) + (9.6 - 11.0)\ eV$$

with the latter becoming dominant at the lower energies considered. The broad peak at high exothermicities in the spectra is consistent with substantial contributions from unresolved dissociative $O^{6+}(n = 3)$ product channels which could include the following :

$$O^{7+}(1s)\ ^2S + H_2\ ^1\Sigma_g^+ \rightarrow O^{6+}\ (n = 3) + H^+ + H^+ + e + (23.7 - 29.4)\ eV$$

$$\rightarrow O^{6+}\ (n = 3) + H^+ + H(3l) + (23.7 - 35.4)\ eV$$

$$\rightarrow O^{6+}\ (n = 3) + H^+ + H(2l) + (27.7 - 41.1)\ eV$$

$$\rightarrow O^{6+}\ (n = 3) + H^+ + H(1s) + (34.7 - 46.9)\ eV$$
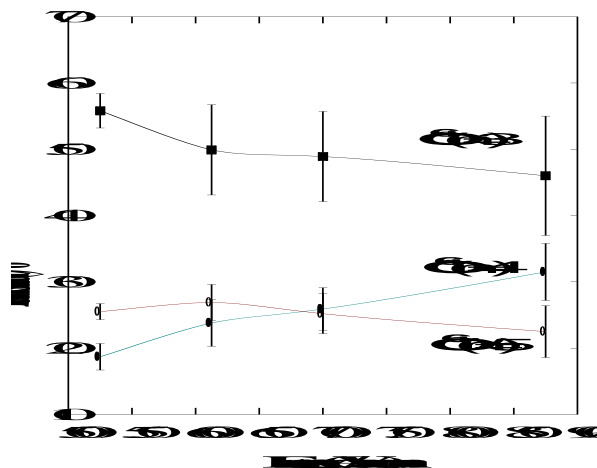
106

FIG. 6. Contributions from the $O^{6+}(n = 3)$, $O^{6+}(n = 4)$ and $O^{6+}(n = 5)$ product channels in one-electron capture by O^{7+} ions in H_2 (from [4]).
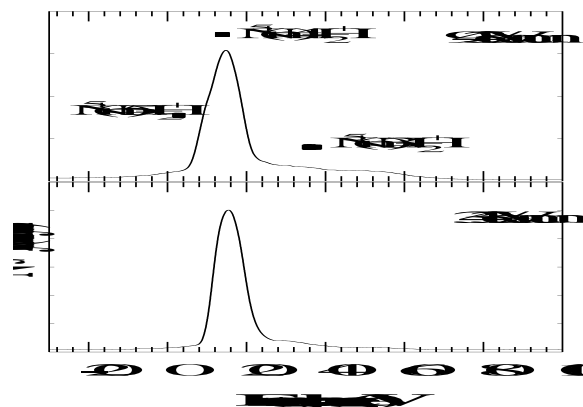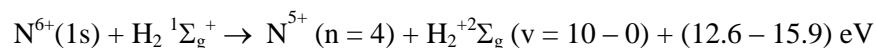

FIG. 7. Energy change spectra for one-electron capture by N^{6+} ions in H_2 (from [4]).

We have used a peak fitting procedure to obtain relative contributions (Figure 6) from $O^{6+}(n = 3)$, $O^{6+}(n = 4)$ and $O^{6+}(n = 5)$ product channels. The $O^{6+}(n = 3)$ contribution from dissociative electron capture channels can be seen to increase from about 46 % at 875 eV amu^{-1} to 56 % at 525 eV amu^{-1}.

Figure 7 shows energy change spectra for one-electron capture by N^{6+} ions in H_2 at the two energies 943 and 343 eV amu^{-1}. There is no evidence of dissociative electron capture. The spectra are dominated by a large peak corresponding to non-dissociative $N^{5+}(n = 4)$ formation channels:

$$N^{6+}(1s) + H_2\ {}^1\Sigma_g^+ \rightarrow N^{5+}(n = 4) + H_2^{+2}\Sigma_g\ (v = 10 - 0) + (12.6 - 15.9)\ eV$$

The broad highly exothermic peak in Figure 7 is consistent with $N^{5+}(n = 3)$ formation

$$N^{6+}(1s) + H_2\ {}^1\Sigma_g^+ \rightarrow N^{5+}(n = 3) + H_2^{+2}\Sigma_g\ (v = 10 - 0) + (36.4 - 41.5)\ eV$$
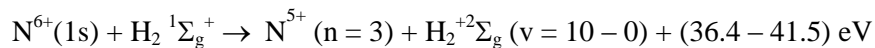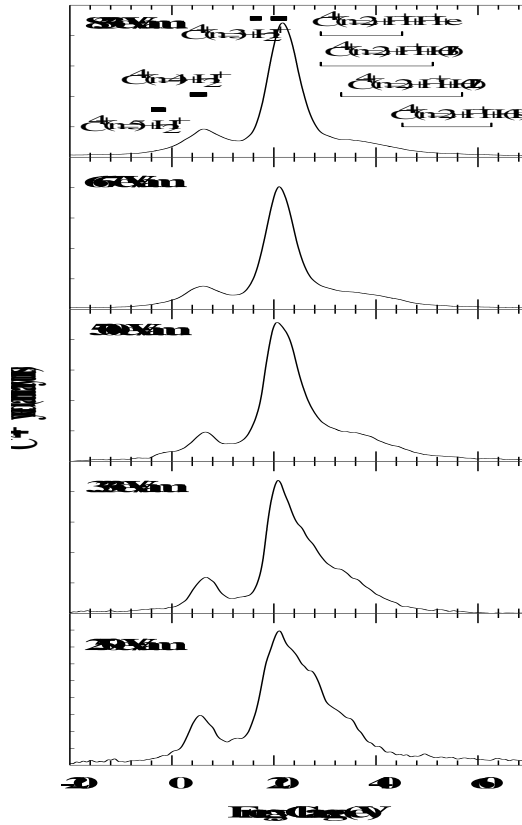
FIG. 8. Energy change spectra for one-electron capture by C^{5+} ions in H_2 (from [4]).

At still higher energy defects, there is an additional broad peak that appears to increase in relative importance with increasing energy. This cannot be correlated with any non-dissociative or dissociative one-electron capture channels and it seems likely that this peak arises through contributions from two-electron capture into autoionizing states of N^{4+}. Indeed, Bordenave-Montesquieu *et al* [26] have used electron emission spectroscopy to observe this mechanism in previous studies of the N^{6+} - H_2 system.

Figure 8 shows energy change spectra [4] for one-electron capture by $250 – 833$ eV amu^{-1} C^{5+} ions in H_2. The rich structure can be seen to involve contributions from more collision channels as the energy decreases. The main peak can be identified with the $C^{4+}(n = 3)$ formation channels

$$C^{5+}(1s)^2S + H_2\,^1\Sigma_g^+ \rightarrow C^{4+}(n = 3)\,^1S + H_2^+(v = 10 - 0) + (15.9 - 23.2)\text{ eV}$$
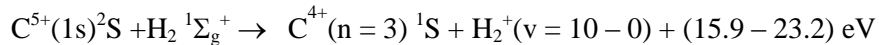
A second well defined peak centred on an energy defect about 6 eV is correlated with $C^{4+}(n = 4)$ formation through the channels

$$C^{5+}(1s)^2S + H_2\,^1\Sigma_g^+ \rightarrow C^{4+}(n = 4)\,^1S + H_2^+(v = 10 - 0) + (3.7 - 6.2)\text{ eV}$$
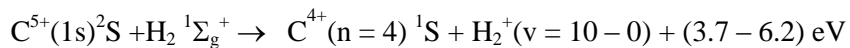
There is also evidence of small contributions to $C^{4+}(n = 5)$ states through the endothermic channels

$$C^{5+}(1s)^2S + H_2\,^1\Sigma_g^+ \rightarrow C^{4+}(n = 5)\,^1S + H_2^+(v = 10 - 0) - (1.3 - 3.9)\text{ eV}$$
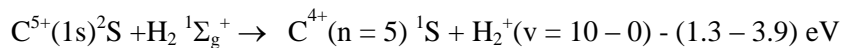
The spectra in Figure 8 also exhibit substantial contributions from channels involving dissociative one-electron capture mainly (as indicated) leading to C^{4+}(n = 2) formation with energy defects in the range 29 – 62.6 eV. These channels can be seen to increase in relative importance with decreasing impact energy. Although these highly exothermic channels are incompletely resolved, there is clear evidence, particularly at the lowest energy considered, of additional contributions in the energy defect range 20 - 24 eV that cannot be correlated with either dissociative or non-dissociative one-electron capture. Again, this indicates the possibility of significant contributions from a two-electron autoionizing capture mechanism. In fact, the presence of such a mechanism was inferred by Siraud *et al* [27] in their PES studies of one-electron capture by C^{5+} ions in H_2 in the range 830 – 7500 eV amu[-1].

3.1.4. One-electron capture by He-like ions of O, N and C in collisions with H_2

FIG. 9. Energy change spectra for one-electron capture by O^{6+} ions in H_2 (from [4]).

Our observed energy change spectra [4] for one-electron capture by O^{6+} ions in H_2 at 225 and 900 eV amu[-1] (Figure 9) exhibit a prominent peak corresponding to non-dissociative O^{5+}(n = 4) formation

$$O^{6+}\ (1s^2)\ ^1S + H_2\ ^1\Sigma_g^+ \rightarrow O^{5+}(n = 4) + H_2^+\ ^2\Sigma_g\ (v = 10 - 0) + (13.2 - 17.0\ eV)$$
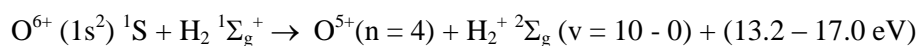
The slight broadening of this peak at the higher energy indicates a possible small contribution from the dissociative product channel

$$O^{6+}\ (1s^2)\ ^1S + H_2\ ^1\Sigma_g^+ \rightarrow O^{5+}(n = 3) + H^+ + H(1s) + (15.5 - 28.3\ eV)$$
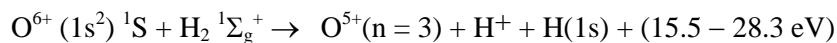
The non-dissociative O^{5+}(n = 3) formation process

$$O^{6+}\ (1s^2)\ ^1S + H_2\ ^1\Sigma_g^+ \rightarrow O^{5+}(n = 3) + H_2^+\ ^2\Sigma_g\ (v = 10 - 0) + (37.0 - 43.3)\ eV$$
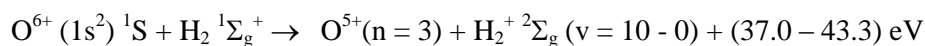
can be correlated with the second very minor peak observable in these spectra.
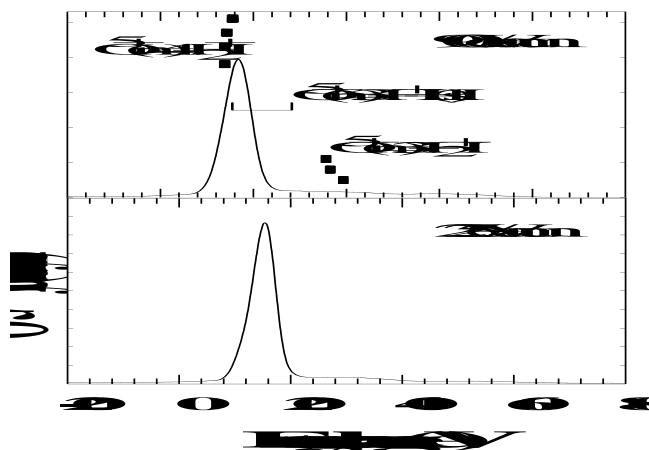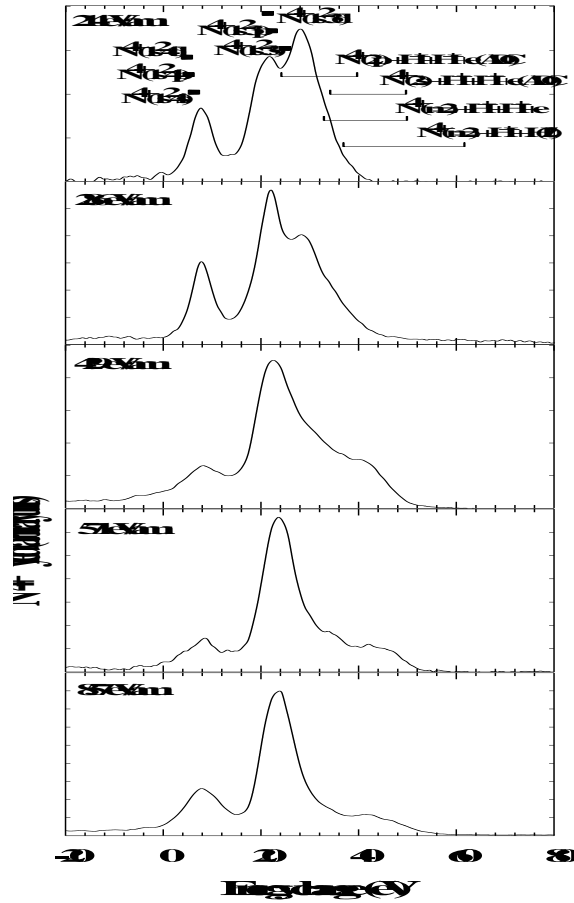
FIG. 10. Energy change spectra for one-electron capture by N^{5+} ions in H_2 (from [3]).

Figure 10 shows our measured energy change spectra [3] for N^{5+} ions in H_2 at energies between 857 eV amu^{-1} and 214 eV amu^{-1}. At the highest energy, three peaks centred on energy defects of about 8, 24 and 42 eV are apparent. The largest of these corresponds to the non-dissociative capture process

$$N^{5+}(1s^2)\ ^1S + H_2(^1\Sigma_g^+) \rightarrow N^{4+}(n = 3) + H_2^+(v = 10 - 0) + (20.4 - 25.9)\ eV$$
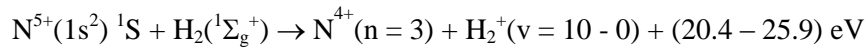
which involves $N^{4+}(n = 3)$ formation together with some evidence of vibrational excitation of the H_2^+ product ion. The second largest peak in the spectrum at 857 eV amu^{-1} can be identified with the $N^{4+}(n = 4)$ formation process

$$N^{5+}(1s^2)\ ^1S + H_2(^1\Sigma_g^+) \rightarrow N^{4+}(n = 4)) + H_2^+(v = 10 - 0) + (3.78 - 7.29)\ eV$$
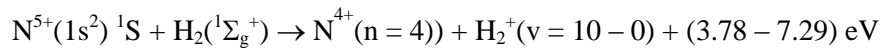
The third and most exothermic peak in the spectrum at 857 eV amu^{-1} contains contributions from a number of incompletely resolved processes leading to $N^{4+}(n = 2)$ production. The main contribution appears to be due to the dissociative electron capture process

$$N^{5+}(1s^2)\ ^1S + H_2(^1\Sigma_g^+) \rightarrow N^{4+}(n = 2) + H^+ + H(2l) + (36.87 - 61.61)\ eV$$
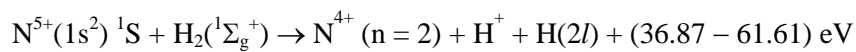
with contributions from the following dissociative transfer ionization process also likely

$$N^{5+}(1s^2)\ ^1S + H_2(^1\Sigma_g^+) \rightarrow N^{4+}(n = 2) + H^+ + H^+ + e + (34.15 - 49.66)\ eV$$

110
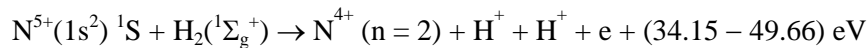
At impact energies below 857 eV amu^{-1}, the peaks in Figure 10 corresponding to N^{4+}(n = 3) and N^{4+}(n = 3) formation remain as major features of the energy change spectra. However, additional collision mechanisms leading to N^{4+}(n = 2) production become apparent. In particular, at our lowest energy of 214 eV amu^{-1}, the dominant peak (centred on an energy defect of about 28 eV) can be correlated with the autoionizing double capture channels

$$N^{5+}(1s^2)\ ^1S + H_2(^1\Sigma_g^+) \rightarrow N^{3+}(**) + H^+ + H^+$$
$$\rightarrow N^{4+}(1s^2 2p) + H^+ + H^+ + e + (24.15 - 39.66)\ eV$$
$$\rightarrow N^{4+}(1s^2 2s) + H^+ + H^+ + e + (34.15 - 49.66)\ eV$$
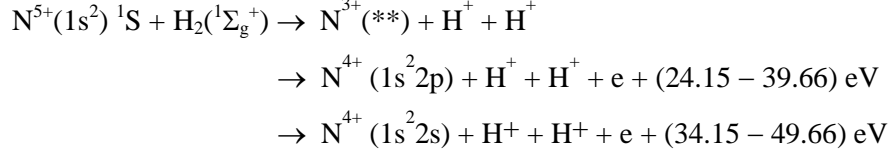
The N^{4+}(1s^{2}2p) channel appears to be dominant but the available energy resolution precludes a clear quantitative assessment.

TABLE 2. OBSERVED PRODUCT CHANNELS (FROM [3]) FOR ONE-ELECTRON CAPTURE IN N^{5+} - H$_2$ COLLISIONS

Product channels	Energy defects (eV)
Non-dissociative channels	
N^{4+}(1s^{2}3s) + H$_2^+$	23.86 (v = 10) – 25.91 (v = 0)
N^{4+}(1s^{2}3p) + H$_2^+$	21.17 (v = 10) – 23.22 (v = 0)
N^{4+}(1s^{2}3d) + H$_2^+$	20.35 (v = 10) – 22.40 (v = 0)
N^{4+}(1s^{2}4s) + H$_2^+$	5.23 (v = 10) – 7.29 (v = 0)
N^{4+}(1s^{2}4p) + H$_2^+$	4.14 (v = 10) – 6.19 (v = 0)
N^{4+}(1s^{2}4d) + H$_2^+$	3.80 (v = 10) – 5.85 (v = 0)
N^{4+}(1s^{2}4f) + H$_2^+$	3.78 (v = 10) – 5.83 (v = 0)
Dissociative channels	
N^{4+}(n = 2) + H$^+$ + H(2l)	36.87 – 61.61
N^{4+}(n = 2) + H$^+$ + H$^+$ + e	32.87 – 49.86
A*utoionizing* two-electron capture	
N^{3+}(**) + H$^+$ + H$^+$ →	
N^{4+}(1s^{2}2s) + H$^+$ + H$^+$ + e	34.15 – 49.66
N^{4+}(1s^{2}2p) + H+ + H+ + e	24.15 – 39.66

TABLE 3. MEASURED FRACTIONS OF N^{4+} PRODUCT IONS FORMED IN n = 2, n = 3 AND n = 4 STATES THROUGH ONE-ELECTRON CAPTURE IN N^{5+} - H$_2$ COLLISIONS (FROM [3])

Energy (eV/amu)	n = 2 (%)	n = 3 (%)	n = 4 (%)
857	16.9 ± 3.0	66.2 ±2.5	16.9 ± 4.0
786	19.0 ± 2.9	60.4 ± 2.4	20.6 ± 3.7
714	19.3 ± 3.0	61.5 ± 3.0	19.2 ± 4.1
643	25.8 ± 2.5	55.2 ± 3.0	19.0 ± 4.0
571	19.4 ± 2.7	67.3 ± 2.7	13.2 ± 5.4
500	26.6 ± 3.0	55.2 ± 3.0	18.3 ± 3.0
429	30.7 ± 3.0	53.8 ± 3.2	15.5 ± 2.7
357	37.9 ± 2.4	47.5 ± 3.7	14.6 ± 2.5
286	37.8 ± 3.2	43.1 ± 3.4	19.1 ± 2.5
250	59.0 ± 1.7	31.5 ± 3.8	9.5 ± 1.8
214	50.0 ± 1.8	33.0 ± 3.7	17.0 ± 2.6

The main observed product channels are summarised in Table 2 while in Table 3 we have estimated the fractions of N^{4+} ions formed in n = 2, n = 3 and n = 4 states through these collision mechanisms from an analysis of energy change spectra in the range 857 - 250 eV amu^{-1}.

TABLE 4. MEASURED TOTAL ONE-ELECTRON CAPTURE CROSS-SECTIONS AND DERIVED CROSS-SECTIONS FOR ONE-ELECTRON CAPTURE INTO N^{4+}(n = 2), N^{4+}(n = 3) AND N^{4+}(n = 4) STATES IN N^{5+} - H_2 COLLISIONS (FROM [3])

| Energy (eV/amu) | Cross-sections (cm$^2 \times 10^{-16}$) | | | |
	N^{4+}(n = 2)	N^{4+}(n = 3)	N^{4+}(n = 4)	Total
893	-	-	-	16.0 ± □ 4.8
857	2.3 ± 0.4	8.9 ±1.5	2.3 ± 0.4	13.5 ± 2.3
786	2.3 ± 0.4	7.3 ± 1.3	2.5 ± 0.5	12.0 ± □ 2.2
714	2.6 ± 0.6	8.1 ± 1.8	2.5 ± 0.6	13.2 ± □ 2.9
643	3.2 ± 0.6	6.8 ± 1.2	2.4 ± 0.4	12.4 ± 2.2
571	2.4 ± 0.3	8.4 ± 1.2	1.6 ± 0.2	12.4 ± 1.7
500	3.0 ± 0.7	6.3 ± 1.5	2.1 ± 0.5	11.4 ± 2.8
429	3.5 ± 0.6	6.1 ± 1.0	1.8 ± 0.3	11.3 ± 1.9
357	4.0 ± 1.0	5.0 ± 1.3	1.5 ± 0.4	10.9 ± 2.8
286	3.2 ± 0.4	3.7 ± 0.4	1.6 ± 0.2	8.1 ± 0.9
250	4.6 ± 0.8	2.5 ± 0.4	0.7 ± 0.1	7.8 ± 1.3
214	2.7 ± 1.5	1.8 ± 1.0	0.9 ± 0.5	5.3 ± 3.0

From Table 3 it will be seen that N^{4+}(n = 3) formation through the non-dissociative capture channel decreases from about 66 % at 857 eV amu^{-1} to 33 % at 214 eV amu^{-1} while N^{4+}(n = 4) formation through the same type of process changes little over the same energy range. N^{4+}(n = 2) production arises through several possible collision mechanisms and accounts for 16.9 % of the total at 857 eV amu^{-1} rising to 50 % at 214 eV amu^{-1}. While dissociative electron capture leading to N^{4+} (n = 2) production is clearly important at the higher energies, this is by no means a dominant process. The most surprising feature in the present data is the dominant role at the lower energies of the two-electron capture autoionizing mechanism leading to N^{4+}(n = 2) production.

There are large unexplained discrepancies between some of the previously measured low energy total one-electron capture cross-sections for N^{5+} in H_2. For this reason, we carried out measurements [3] of the total cross-section in the range 214 - 893 eV amu^{-1} using a simple beam attenuation technique. These values have been used with our TES data to obtain cross-sections (Table 4) for electron capture into the main excited product states of N^{4+}.

In Figure 11 our measured total one-electron capture cross-sections are shown together with those of Dijkkamp *et al* [21], with values measured by Okuno [28] and with results due to Panov *et al* [32] in overlapping energy ranges. It will be seen that , while our values are in reasonable accord with those of Dijkkamp *et al* [21] and confirm the downward trend with decreasing impact energy, they are greatly at variance with the low energy measurements of Okuno [28] based on attenuation using an octupole field guide which provide very large cross-sections that even exhibit a gradual increase towards the lowest energies. Included in Figure 2 are the results of calculations by Kumar and Saha [29] based on a semiclassical impact parameter close-coupling method, by Gargaud and McCarroll [30] based on a full quantal approach and by the Madrid group (Elizaga *et al* [31]) who used an *ab initio* approach. There are large unexplained discrepancies between these different calculations and between the experimental values.
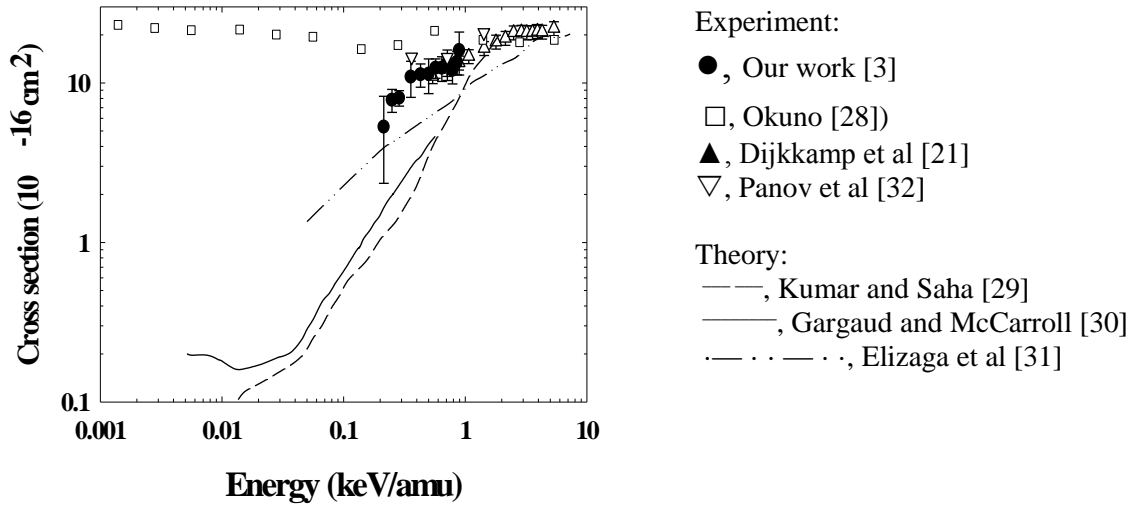
FIG. 11. *Total one-electron capture cross-sections for N^{5+} ions in H$_2$ (from [3]).*
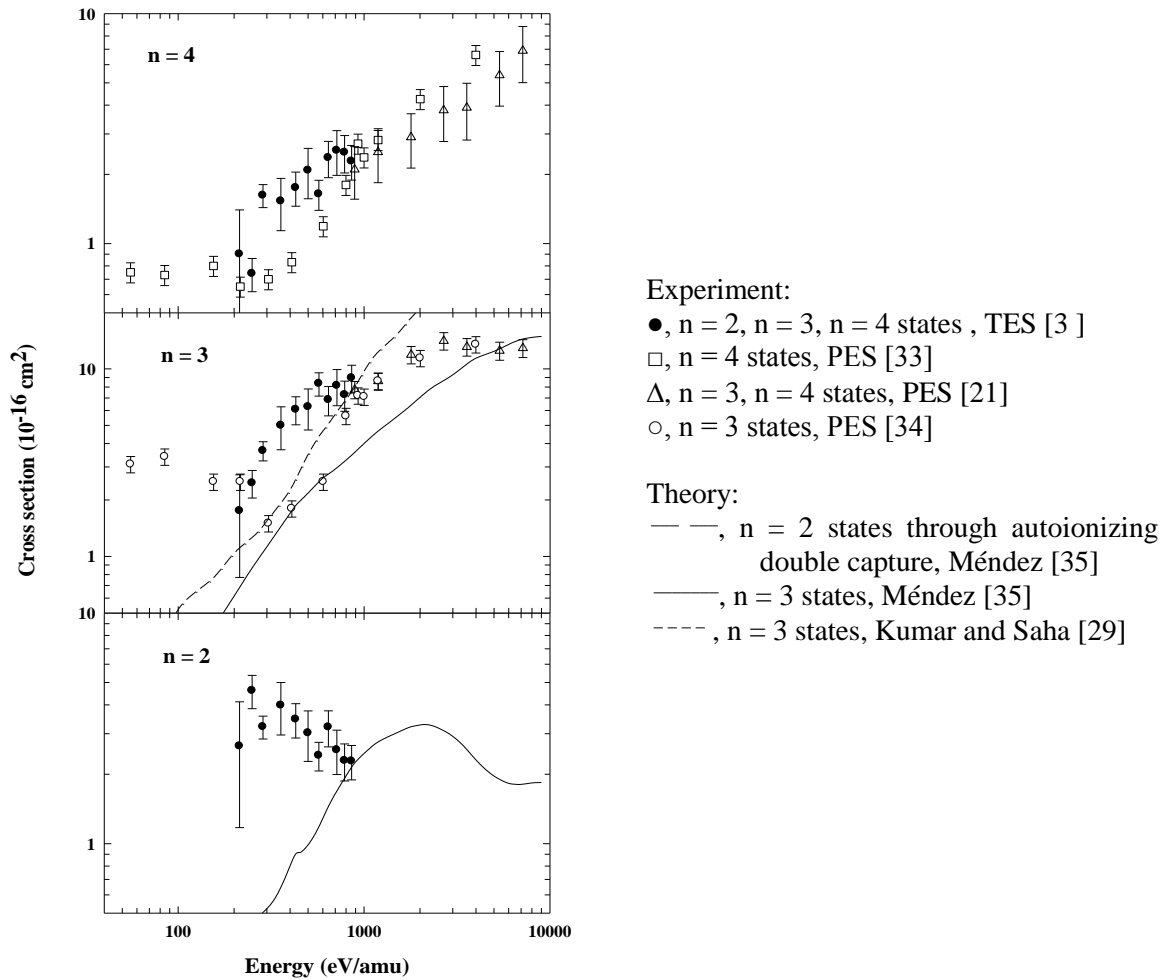

FIG. 12. *Cross-sections for selective one-electron capture into n = 2, 3 and 4 states of N^{4+} by N^{5+} ions in H$_2$ (from [3]).*
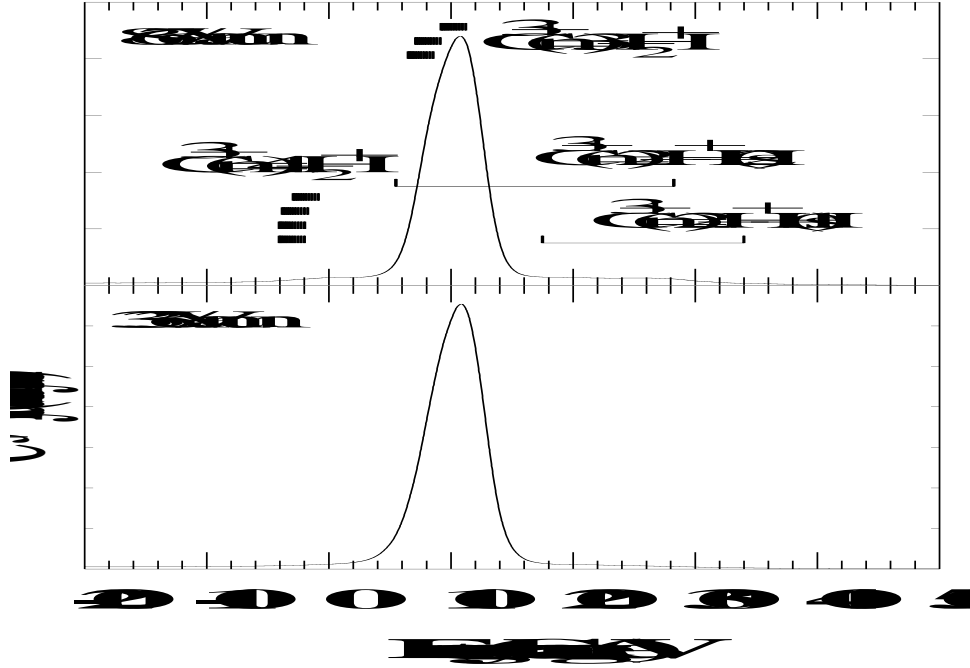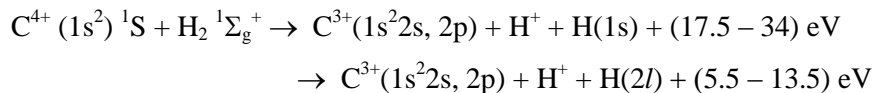
113

FIG. 13. Energy change spectra for one-electron capture by C^{4+} ions in H_2 (from [4]).

Cross-sections for $N^{4+}(n = 2)$, $N^{4+}(n = 3)$ and $N^{4+}(n = 4)$ formation in N^{5+} - H_2 collisions derived from our TES data are compared in Figure 12 with PES measurements [21,33,34] of the KVI Groningen group and some theoretical estimates. Unlike the PES data, our TES measurements have been able to record the substantial contribution of the $N^{4+}(n = 2)$ products to the total one-electron capture cross-section. The preliminary theoretical estimate by the Madrid group [35] of cross-sections for autoionizing double capture leading to $N^{4+}(n = 2)$ formation can be seen to be much smaller and in poor agreement with our measured cross-sections.

Our TES measurements [4] for one-electron capture by C^{4+} ions in H_2 within the range 214 – 857 eV amu^{-1} extend earlier measurements [36] in the overlapping range 333 – 1330 eV amu^{-1}. Figure 13 shows energy change spectra at 330 and 867 eV amu^{-1}. The large peak centred around an energy change of about 11 eV can correlated with the non-dissociative $C^{3+}(n = 3)$ formation channels

$$C^{4+} (1s^2)\ ^1S + H_2\ ^1\Sigma_g^+ \rightarrow\ C^{3+}(n = 3) + H_2^+\ ^2\Sigma_g\ (v = 10 - 0) + (6.6 - 11.4)\ eV$$
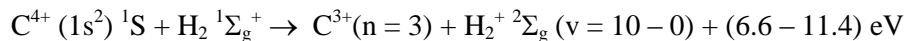
Product channels leading to $C^{3+}(n = 4)$ formation appear to be negligible. However, at large energy defects, the spectrum at 867 eV amu^{-1} exhibits a small broad peak consistent with $C^{3+}(n = 2)$ formation through the dissociative electron capture product channels

$$C^{4+} (1s^2)\ ^1S + H_2\ ^1\Sigma_g^+ \rightarrow\ C^{3+}(1s^22s, 2p) + H^+ + H(1s) + (17.5 - 34)\ eV$$

$$\rightarrow\ C^{3+}(1s^22s, 2p) + H^+ + H(2l) + (5.5 - 13.5)\ eV$$

This minor peak, which was unrecognised in our previous work [36], can be seen to be insignificant in the spectrum obtained at 330 eV amu^{-1}. The KVI group have carried out PES studies of the $C^{4+} + H_2$ system in the range 830 – 6670 eV amu^{-1} [21] and in the range 48 – 1330 eV amu^{-1} [37]. Their measurements confirm a dominant contribution from $C^{3+}(n = 3)$ product channels with a small $C^{3+}(n = 4)$ contribution decreasing with decreasing energy but they find no evidence of $C^{3+}(n = 2)$ formation. Kumar and Sahar [29] have used a semi-classical, impact parameter close-coupling MO

114

method in the range 10 – 2000 eV amu^{-1} to correctly predict that electron capture occurs mainly into C^{3+}(n = 3) levels, with C^{3+}(n = 4) formation becoming more likely with increasing energy.

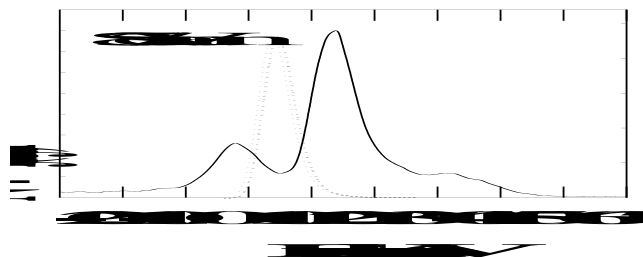*3.1.5. Product channel predictions based on Landau-Zener reaction windows*

FIG. 14. Energy change spectrum (from [4]) for one-electron capture by 857 eV amu^{-1} N^{5+} ions in H$_2$ compared with Landau-Zener reaction window (dotted line).

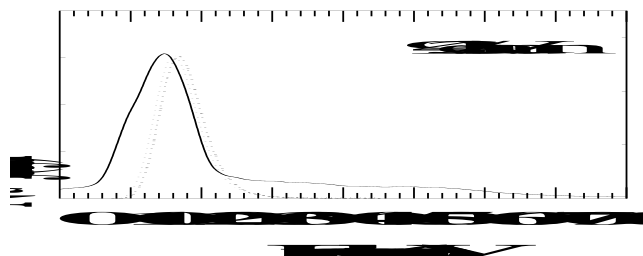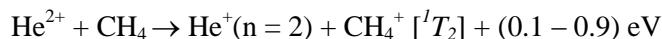FIG. 15. Energy change spectrum (from [4]) for one-electron capture by 943 eV amu^{-1} N^{6+} ions in H$_2$ compared with Landau-Zener reaction window (dotted line).

Detailed theoretical calculations for the cases studied have so far been rather limited. It is therefore useful to determine to what extent our TES measurements can be predicted in terms of reaction windows (cf Taulbjerg [38], Kimura *et al* [39]). This approach is based on the dependence of the single-crossing Landau-Zener cross-section σ_{LZ} on the crossing distance R$_c$ for a series of crossings in the range occupied by the observed energy change spectra and has been described in our previous work [40]. We determined reaction windows for the present cases by using the generalised expression of Kimura *et al* [39] to describe the nature and position of the adiabatic curves at the crossing point.

In Figure 14, we compare our calculated reaction window for one-electron capture by 857 eV amu^{-1} N^{5+} ions in H$_2$ with the our observed energy change spectrum [3]. In this case, the calculated reaction window is too narrow and falls between the two main peaks corresponding to N^{4+}(n = 3) and N^{4+}(n = 4) formation. However, in cases where the observed energy change spectrum is dominated by a single peak, the calculated reaction window provides a much better description of the collision. This is illustrated in Figure 15 which shows corresponding data for one-electron capture by 943 eV amu^{-1} N^{6+} ions in H$_2$. In this case, the calculated reaction window can be seen to accommodate most of the captures within the dominant observed peak corresponding to N^{4+}(n = 4) formation. Although the predictions of reaction windows are far from precise, when electron capture is highly selective (as in the case of electron capture in H at low energies), they can provide a useful indication of the dominant *n* channel. An alternative approach based on the classical overbarrier model in several different variants (cf Niehaus [41]) may also be used to predict the main product channels. However, we have found that, for the cases investigated, the use of reaction windows based on the Landau-Zener approach is rather more successful.

3.2. One-electron capture by He^{2+} ions in the hydrocarbons CH_4, C_2H_4 and C_2H_6

Figure 16 shows our observed energy change spectra [5] for one-electron capture by $300 - 2000$ eV amu^{-1} He^{2+} ions in CH_4. At 2000 eVamu^{-1}, the spectrum is dominated by the peak centred on an energy change of about 0.5 eV which (by reference to photoelectron spectroscopy data) appears to correspond mainly to the non-dissociative product channel

$$He^{2+} + CH_4 \rightarrow He^+(n = 2) + CH_4^+ \, [^1T_2] + (0.1 - 0.9) \text{ eV}$$

leading to $He^+(n = 2)$ formation. The spectra also indicate the presence of a much smaller non-dissociative contribution from the endothermic channel

$$He^{2+} + CH_4 \rightarrow He^+(n = 3) + CH_4^+ \, [^1T_2] - (6.7 - 7.5) \text{ eV}$$
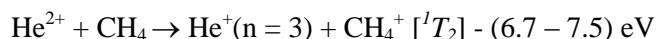
leading to $He^+(n = 3)$ formation.
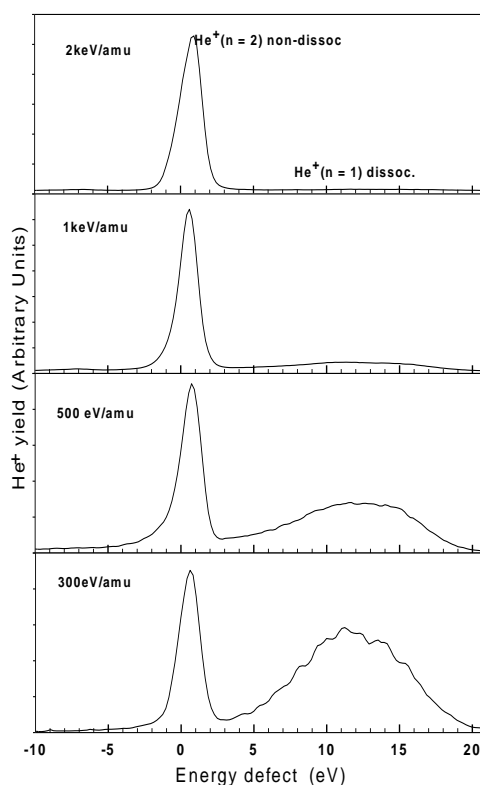
FIG. 16. Energy change spectra for one-electron capture by He^{2+} ions in CH_4 (from [5]).

The spectra in Figure 16 also show the presence of a broad peak centred on an energy change of about 12 eV. This peak, while small at 2000 eVamu^{-1}, becomes larger with decreasing energy and at 300 eVamu^{-1}, it provides the main contribution to the total captures. This broad peak comprises a number of possible product channels involving a variety of fragmentation modes

$$He^{2+} + CH_4 \rightarrow He^+(n = 1) + (CH_4^{2+} \Rightarrow \text{fragmentation}) + (3.3 - 21 \text{ eV})$$
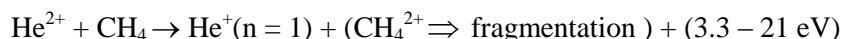
through transfer ionization accompanied by $He^+(n = 1)$ formation. The energy resolution available in our TES measurements is insufficient to distinguish between the many possible fragmentation modes. As in our previous studies of one-electron capture by He^{2+} ions in H_2 and CO [1, 2] , there is no evidence of contributions from autoionizing double capture. Overall, in spite of the many different product channels involving a wide range of energy defects ΔE, one-electron capture in He^{2+} - CH_4 can

be seen to be highly selective in the energy range considered with only He^+(n = 1, 2 and 3) formation observable.
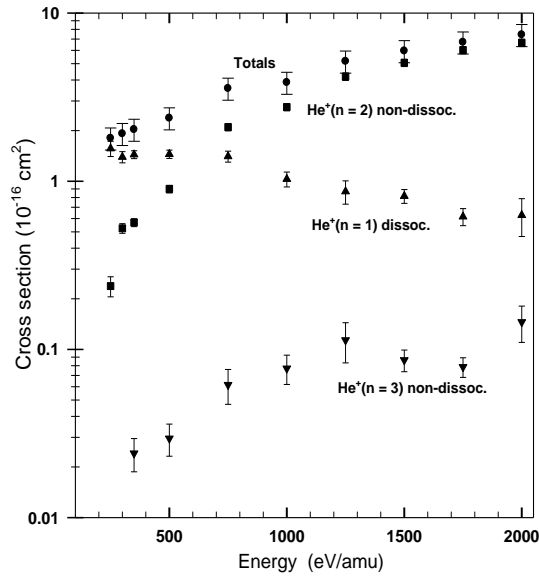
FIG. 17. Measured cross-sections for main product states of He^+ formed in one-electron capture by He^{2+} ions in CH_4 together with total one-electron capture cross-sections (from [5]).

TABLE 5. MEASURED CROSS-SECTIONS (IN UNITS OF 10^{-16} CM^2) FOR ONE-ELECTRON CAPTURE BY He^{2+} IONS IN CH_4 LEADING TO He^+(n = 1, 2 AND 3) FORMATION COMPARED WITH TOTAL ELECTRON CAPTURE CROSS-SECTIONS (FROM [5])

Energy (keVamu^{-1})	Totals	He^+(n = 1)	He^+(n = 2)	He^+(n = 3)
0.25	1.80 ± 0.27	1.56 ± 0.16	0.23 ± 0.03	
0.30	1.91 ± 0.28	1.39 ± 0.10	0.52 ± 0.03	
0.35	2.03 ± 0.30	1.44 ± 0.07	0.56 ± 0.03	0.02 ± 0.02
0.50	2.37 ± 0.35	1.44 ± 0.08	0.89 ± 0.04	0.03 ± 0.01
0.75	3.56 ± 0.53	1.40 ± 0.10	2.09 ± 0.10	0.06 ± 0.01
1.00	3.86 ± 0.57	1.02 ± 0.10	2.76 ± 0.13	0.07 ± 0.01
1.25	5.16 ± 0.77	0.86 ± 0.13	4.18 ± 0.21	0.11 ± 0.03
1.50	5.95 ± 0.89	0.81 ± 0.07	5.05 ± 0.25	0.08 ± 0.01
1.75	6.71 ± 1.00	0.61 ± 0.07	6.01 ± 0.30	0.07 ± 0.01
2.00	7.43 ± 1.11	0.62 ± 0.15	6.65 ± 0.33	0.14 ± 0.03

Figure 17 shows cross-sections for He^+(n = 1, 2 and 3) formation which have been derived [5] from the measured energy change spectra by normalization to total cross-sections for one-electron capture. These total cross-sections were measured using a simple attenuation technique in which we normalised our relative cross-sections to a value measured at 2 keV amu^{-1} by Hoekstra [42]. Our cross-sections necessarily include contributions from two-electron capture and therefore are strictly an upper limit to the true total one-electron capture cross-section. All our measured cross-sections for one-electron capture by He^{2+} ions in CH_4 are listed in Table 5.

FIG. 18. Energy change spectra for one-electron capture by He^{2+} ions in C_2H_4 (from [5]).

Figure 18 shows energy change spectra [5] for one-electron capture by $215 - 2000$ eVamu^{-1} He^{2+} ions in C_2H_4. At 215 eVamu^{-1} the main peak can be correlated with $He^+(n = 2)$ formation through one of the following possible dissociative channels

$$He^{2+} + C_2H_4 \rightarrow He^+(n = 2) + C_2H_4^+ [\tilde{A}^2B_2] \Rightarrow (C_2H_3^+, H) + 0.38 \text{ eV}$$

$$He^{2+} + C_2H_4 \rightarrow He^+(n = 2) + C_2H_4^+ [\tilde{A}^2B_2] \Rightarrow (C_2H_2^+, H_2) + 0.46 \text{ eV}$$
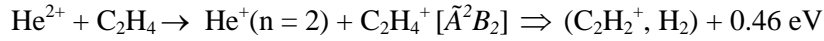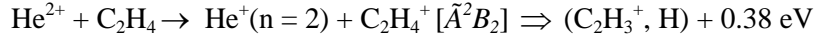
which our available energy resolution cannot separately distinguish. This peak can be seen to decrease in relative importance with increasing impact energy.

In the spectrum at 2000 eV amu^{-1} in Figure 18, the peak centred on an energy change of about 2.6 eV corresponding to the non-dissociative channel

$$He^{2+} + C_2H_4 \rightarrow He^+(n = 2) + C_2H_4^+ [\tilde{X}\ ^2B_3] + (2.4 - 2.9) \text{ eV}$$
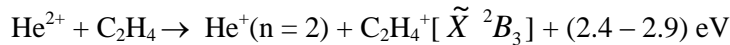
leading to $He^+(n = 2)$ formation can be seen to provide the main contribution to the total although this contribution becomes small at our lowest impact energy. Small endothermic contributions from the channel

$$He^{2+} + C_2H_4 \rightarrow He^+(n = 2) + C_2H_4^+ [\tilde{B}\ ^2A] - (1.9 - 1.2) \text{ eV}$$
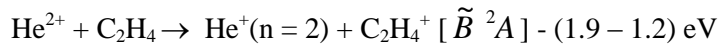
and, at the higher energies, from the channel

$$He^{2+} + C_2H_4 \rightarrow He^+(n = 3) + C_2H_4^+ [\tilde{X}\ ^2B_3] - (5.1 - 4.6) \text{ eV}$$
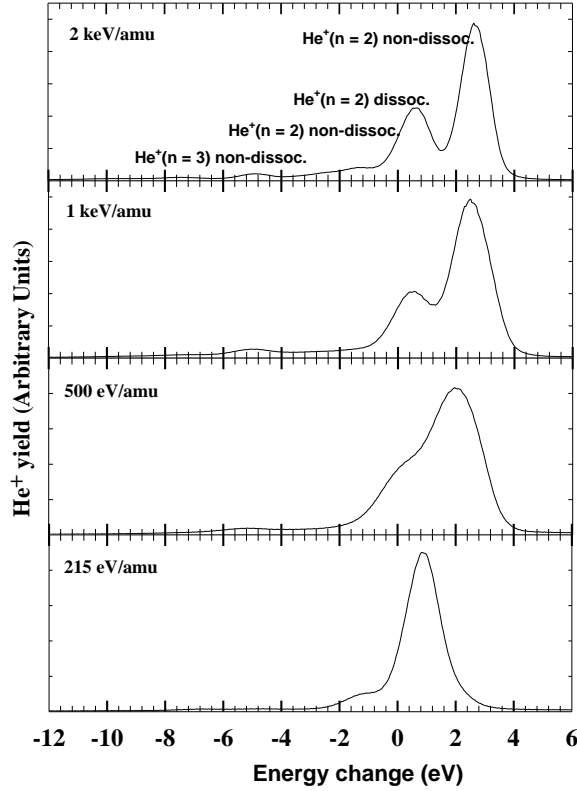
are also evident.

118
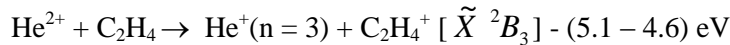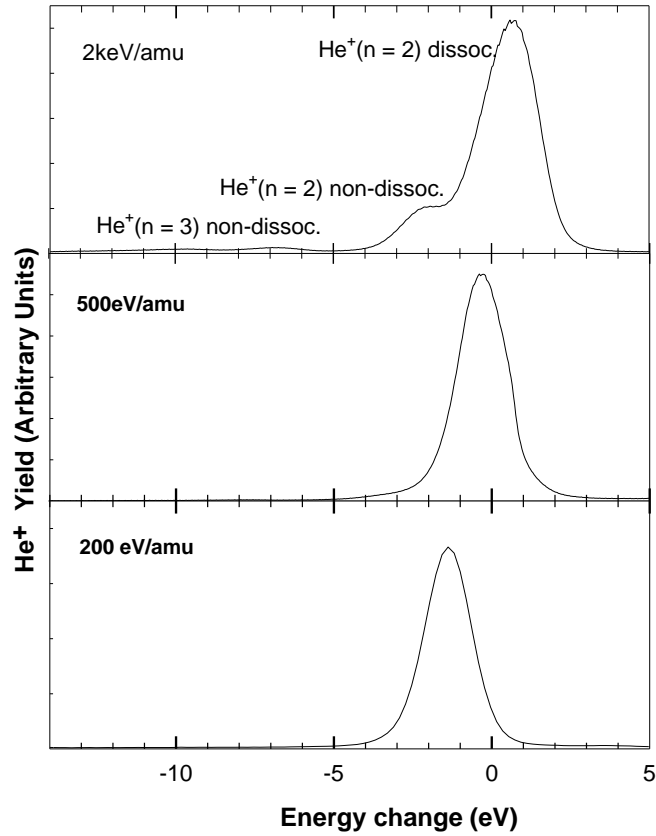
FIG. 19. Energy change spectra for one-electron capture by He^{2+} ions in C_2H_6 (from [5]).

TABLE 6. MEASURED RELATIVE CROSS-SECTIONS FOR ONE-ELECTRON CAPTURE BY He^{2+} IONS IN C_2H_4 LEADING TO $He^+(n = 2$ AND $3)$ FORMATION THROUGH BOTH DISSOCIATIVE AND NON-DISSOCIATIVE PROCESSES EXPRESSED AS A PERCENTAGE OF THE TOTAL CAPTURES
(from [5])

Energy, keVamu^{-1}	$He^+(n = 2)$ non-dissoc.	$He^+(n = 2)$ dissoc.	$He^+(n = 3)$ non-dissoc.
0.35	38.76 ± 1.93	53.94 ± 2.69	7.28 ± 0.36
0.50	44.30 ± 2.21	50.28 ± 2.51	5.40 ± 0.27
0.75	55.58 ± 2.77	36.85 ± 1.84	7.55 ± 0.37
1.00	61.89 ± 3.09	31.82 ± 1.59	6.28 ± 0.31
1.25	54.85 ± 2.74	36.97 ± 1.84	8.17 ± 0.40
1.50	52.43 ± 2.62	39.33 ± 1.96	8.22 ± 0.41
1.75	54.13 ± 2.70	38.74 ± 1.93	7.12 ± 0.35
2.00	56.00 ± 2.80	38.46 ± 1.92	5.52 ± 0.27

Total cross-sections for one-electron capture by He^{2+} ions in C_2H_4 in the energy range of our TES measurements are unavailable so in Table 6, we simply list the relative cross-sections for excited state formation derived from an analysis of the peaks in our energy change spectra. While both dissociative and non-dissociative capture both lead to $He^+(n = 2)$ formation, the dissociative capture process is clearly dominant at our lowest impact energy.

Figure 19 shows energy change spectra [5] for 200 – 2000 eV amu^{-1} He^{2+} ions in C_2H_6. In this case also, He$^+$(n = 2) formation is the dominant excited product. At the lowest energy, rather surprisingly, the spectrum is dominated by a single endothermic peak associated with the non-dissociative channel

$$He^{2+} + C_2H_6 \rightarrow He^+(n=2) + C_2H_6{}^+ [\,^2E_u\,] \text{ - } (2.6 - 1.8) \text{ eV}$$
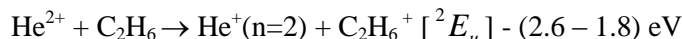
However, at the higher energies the spectra indicate increasing contributions from the channels

$$He^{2+} + C_2H_6 \rightarrow He^+(n = 2) + C_2H_6{}^+ [\,^2A_{1g}\,] \Rightarrow \text{(fragments)} + 0.1 \text{ eV}$$

$$He^{2+} + C_2H_6 \rightarrow He^+(n = 2) + C_2H_6{}^+ [\,^2E_g\,] \Rightarrow \text{(fragments)} + (0.4 - 1.1) \text{ eV}$$
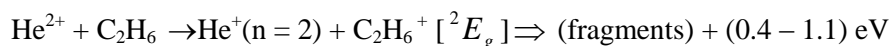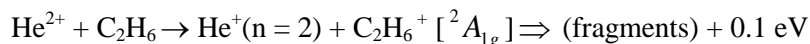
in which, according to the photoionization measurements of Mackie *et al* [15], the main break-up fragment is $C_2H_4{}^+$. At 2000 eVamu^{-1}, there is evidence of a small He$^+$(n = 3) contribution from the non-dissociative endothermic channel

$$He^{2+} + C_2H_6 \rightarrow He^+(n = 3) + C_2H_6{}^+[\,^2E_g\,] \text{ - } (7.3 - 6.5) \text{ eV}$$
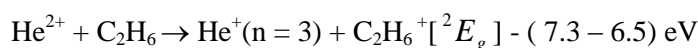
3.3. One-electron capture by He^{2+} ions in H_2O

Experimental data for one-electron capture by He^{2+} in H_2O have recently been obtained in a joint investigation [6] involving four different laboratories. Our TES measurements at QUB for one-electron capture by He^{2+} in H_2O in the energy range 250 – 2000 eV amu^{-1} complement TES studies by Abu-Haija *et al* [43] at Western Michigan University (WMU) in the range 25 – 375 eV amu^{-1}. In addition, measurements have been carried out by the KVI Institute based on photon emission spectroscopy (PES) in the range 1.5 and 12 keV amu^{-1} and by the Hahn-Meitner Institute (HMI) using fragment ion spectrometry (FIS) in the range 0.33 – 6.7 keV amu^{-1}
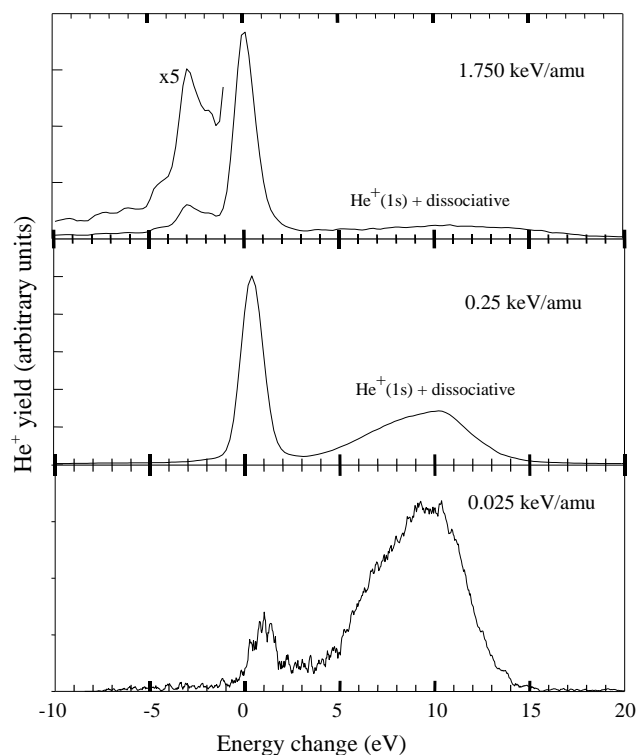
FIG. 20. *Energy change spectra for one electron capture by He^{2+} ions in H_2O (from [6]).*

TABLE 7. PRODUCT CHANNELS FOR ONE-ELECTRON CAPTURE BY HE^{2+} IONS IN H_2O (FROM [6])

Product channels	Energy defects (eV)
$He^+(n = 3) + H_2O^+ [\tilde{A}\ ^2A_1\ ]$	-7.79 – -10.61
$He^+(n = 3) + H_2O^+ [\tilde{X}\ ^2B_1\ ]$	-6.57 – -7.35
$He^+(n = 2) + H_2O^+ [\tilde{B}\ ^2B_2\ ] \Rightarrow OH^+,\ O^+$	-4.50 – -5.11
$He^+(n = 2) + H_2O^+ [\tilde{B}\ ^2B_2\ ]$	-3.57 – -6.39
$He^+(n = 2) + H_2O^+ [\tilde{A}\ ^2A_1\ ]$	-0.23 – -3.05
$He^+(n = 2) + H_2O^+ [\tilde{X}\ ^2B_1\ ]$	0.20 – 0.98
$He^+(n = 1) + H_2O^{2+} [\ ^3B_1\ ] + e$	17.90
$He^+(n = 1) + H_2O^{2+} [\ ^1A,\ ^1B\ ] + e$	12.40 – 14.40
$He^+(n = 1) + H_2O^{2+} [(2)\ ^1A_1] + e$	9.10

TABLE 8. CROSS-SECTIONS (IN UNITS OF 10^{-16} CM^2) FOR ONE-ELECTRON CAPTURE BY HE^{2+} IONS IN H_2O LEADING TO $HE^+(N = 1)$, $HE^+(N = 2)$ AND $HE^+(N = 3)$ FORMATION MEASURED USING THE TES AND PES TECHNIQUES (FROM [6])

Energy keV/amu	TES (n = 1) (WMU)	TES (n = 2) (WMU)	TES (n = 1) (QUB)	TES (n = 2) (QUB)	PES (2p - 1s) (KVI)	TES (n = 3) (QUB)	PES (3p - 1s) (KVI)
0.025	0.84 ± 0.13	0.10 ± 0.01					
0.050	1.40 ± 0.17	0.23 ± 0.03					
0.075	1.57 ± 0.18	0.41 ± 0.05					
0.100	1.94 ± 0.19	0.61 ± 0.07					
0.125	2.30 ± 0.24	0.88 ± 0.10					
0.150	2.40 ± 0.23	1.11 ± 0.11					
0.175	2.42 ± 0.23	1.28 ± 0.14					
0.200	2.26 ± 0.23	1.73 ± 0.19					
0.225	2.14 ± 0.20	2.00 ± 0.19					
0.250	1.99 ± 0.19	2.31 ± 0.23	2.56 ± 0.35	1.98 ± 0.31		0.04 ± 0.01	
0.275	1.96 ± 0.21	2.41 ± 0.27					
0.300	2.02 ± 0.23	2.67 ± 0.30					
0.325	2.08 ± 0.24	2.90 ± 0.38					
0.350	2.07 ± 0.28	3.05 ± 0.45	2.30 ± 0.25	2.92 ± 0.29		0.05 ± 0.01	
0.375	2.11 ± 0.29	3.31 ± 0.43					
0.500			2.03 ± 0.13	4.20 ± 0.30		0.06 ± 0.01	
0.750			2.45 ± 0.43	5.32 ± 0.53		0.12 ± 0.05	
1.000			2.80 ± 0.16	6.18 ± 0.45		0.19 ± 0.04	
1.250			2.69 ± 0.38	7.32 ± 0.58		0.21 ± 0.14	
1.500			3.45 ± 0.31	7.22 ± 0.64	6.43 ± 0.65	0.39 ± 0.15	0.04 ± 0.01
1.750			3.19 ± 0.13	8.15 ± 0.67	7.22 ± 0.52	0.43 ± 0.26	0.07 ± 0.01
2.000			3.24 ± 0.17	8.62 ± 0.62	7.32 ± 0.53	0.46 ± 0.02	0.07 ± 0.01
2.500					7.75 ± 0.78		0.07 ± 0.01
3.000					8.54 ± 0.61		0.10 ± 0.01
4.500					9.12 ± 0.92		0.14 ± 0.02
6.000					9.43 ± 0.28		0.18 ± 0.01
7.500					10.12 ± 1.02		0.29 ± 0.03
9.000					8.99 ± 0.91		0.29 ± 0.04
10.50					9.01 ± 0.91		0.39 ± 0.05
12.00					8.30 ± 0.84		0.50 ± 0.06

Three representative energy change spectra from the QUB and WMU laboratories are shown in Figure 20. The two main features evident in these spectra are sharp peaks in the energy change region below 3 eV and a broader peak in the region of $4 - 17$ eV. The peaks below 3 eV can be correlated with $He^+(n = 2) + H_2O^+$ and $He^+(n = 3) + H_2O^+$ product channels (see Table 7). The broad distribution above 4 eV corresponds to $He^+(n = 1)$ formation resulting from the decay of unstable H_2O^{2+} ions formed in doubly charged states via an Auger type process (see [17]). The spectra show that non-dissociative electron capture into the $He^+(n = 2)$ states is the dominant product channel above about 250 eV amu^{-1} while, at lower energies, dissociative transfer ionization leading to $He^+(n = 1)$ is the main mechanism.

The sum of the relative yields of the individual capture processes resulting in $He^+(n = 1)$, $He^+(n = 2)$ and $He^+(n = 3)$ formation identified in the QUB energy change spectra were normalized to total one-electron capture cross-sections of Greenwood $et~al$ [44]. The WMU data for $He^+(n = 1)$ and $He^+(n = 2)$ formation were determined from absolute measurements of the target pressures and detector efficiencies. These cross-sections are tabulated in Table 8 together with KVI data for HeII $(2p - 1s)$ and HeII $(3p - 1s)$ emissions measured by the KVI group using the PES approach.
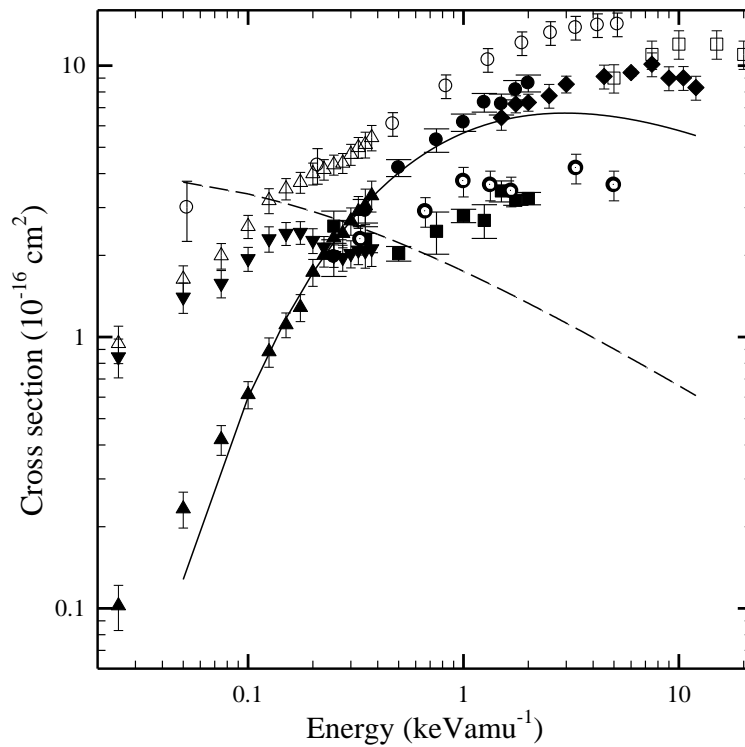
FIG. 21. Cross-sections for one electron capture by He^{2+} ions in H_2O (from [6]). Total cross-sections: open squares, Rudd et al [45]; open circles, Greenwood et al [44]; open triangles, sum of $He^+(n = 1)$ and $He^+(n = 2)$ from TES data [43]. Capture into $He^+(n = 2)$ states: closed circles, QUB; closed triangles, WMU. He II (2p-1s): closed diamonds, KVI. Capture into $He^+(n = 1)$ state: closed squares, QUB; inverted triangles, WMU. Transfer ionization leading to $He^+(n = 1)$: circles with cross hairs, HMI. Theory: solid line, $He^+(n = 2)$ formation; dashed line, $He^+(n = 1)$ formation, HMI.

In Figure 21 measured cross-sections for selective one-electron capture into the $He^+(n = 1)$ and $He^+(n = 2)$ states through the channels listed in Table 7 are shown together with known total cross-sections [44, 45]. Since capture into the n = 3 levels of He^+ is insignificant, the sum of $He^+(n = 1)$ and $He^+(n = 2)$ formation cross-sections derived from the low energy TES measurements can be compared with the total cross-sections of Greenwood $et~al$ [44]. The agreement can be seen to be very good except at energies below 0.2 keV amu^{-1}. It is also interesting to note that, in the energy region of

overlap, the ratio of the PES values for He II (2p-1s) emission to the TES cross-sections for $He^+(n = 2)$ formation is in accord with a statistical distribution of sublevels. There can be seen to be good agreement between the TES results from QUB and WMU groups in the energy range of overlap. Cross-sections for the transfer ionization product channel $He^+ + H_2O^{2+} + e$ determined by the HMI group from their FIS measurements also shown can be seen to be consistent with the TES data. The HMI group have also used Demkov and Landau-Zener models of charge transfer to calculate cross-sections for $He^+(n = 1)$ and $He^+(n = 2)$ formation which are in reasonable general accord (Figure 21) with experiment.

3.4. One-electron capture by O^{6+} ions in H_2O, CO_2 and CH_4 and C^{4+} ions in CH_4
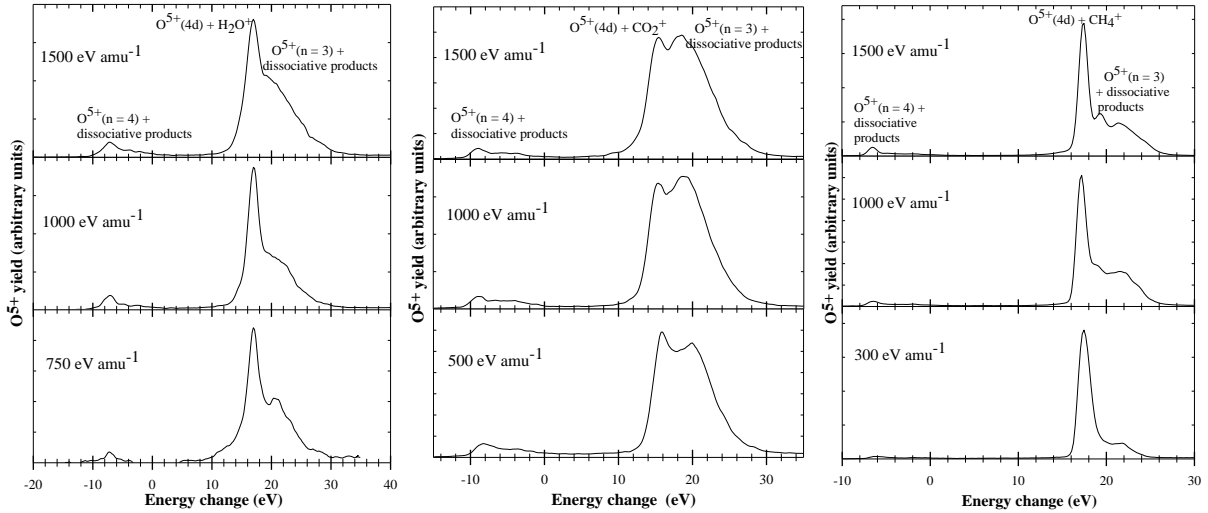
FIG. 22. Energy change spectra for one-electron capture by O^{6+} ions in H_2O, CO_2 and CH_4 (from [7]).

Our TES energy change spectra [7] for one-electron capture by slow O^{6+} ions in H_2O, CO_2 and CH_4 are shown in Figure 22. These exhibit similar patterns of behaviour. In each case, there is a large peak at moderate exothermicities corresponding to selective non-dissociative electron capture.

In the H_2O spectra this corresponds to O^{5+} (4d) formation process

$$O^{6+} (1s^2)^1S + H_2O \, [^1A_1] \rightarrow O^{5+} (1s^2 \, 4d) + H_2O^+ \left[\tilde{X}^2 B_1 \right] + (17.2 - 18) \text{ eV}$$
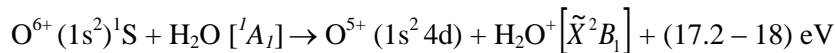
The corresponding peak in the CO_2 spectra is correlated with O^{5+} (4d) formation through

$$O^{6+} (1s^2)^1S + CO_2 [\, X^1\Sigma_g^+] \rightarrow O^{5+} (1s^2 \, 4d) + CO_2^+ \, [X \, ^2\Pi_g] + (16 - 16.9) \text{ eV}$$
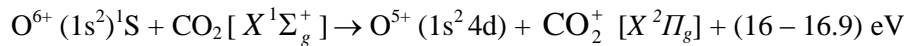
while in CH_4, the corresponding peak is consistent with the O^{5+} (4d) formation process

$$O^{6+} (1s^2)^1S + CH_4 [X \, ^1A_1] \rightarrow O^{5+} (1s^2 \, 4d) + CH_4^+ \, [^1T_2] + (17.1 - 17.9) \text{ eV}$$
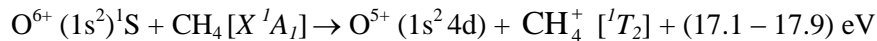
At higher exothermicities, all three spectra exhibit structure corresponding to contributions from dissociative channels involving a number of possible fragmentation modes which our TES measurements are unable to resolve. In the case of H_2O, this structure is correlated with $O^{5+}(n = 3)$ formation through dissociative transfer ionization

$$O^{6+} (1s^2)^1S + H_2O \, [^1A_1] \rightarrow O^{5+} (n = 3) + \{H_2O^{2+} \Rightarrow (OH^+, H^+) \, (H^+, H^+, O)\} + (17.9 - 22.3) \text{ eV}$$

123
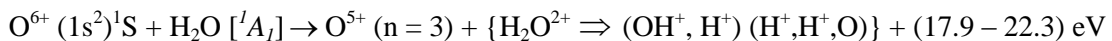
together with dissociative electron capture

$$O^{6+} (1s^2)^1S + H_2O\ [^1A_1] \rightarrow O^{5+}\ (n = 3) + \{H_2O^+ \Rightarrow (OH^+, O)\ (H^+, O_2)\ (O^+, H_2)\} + (21.4 - 31.0)\ eV$$
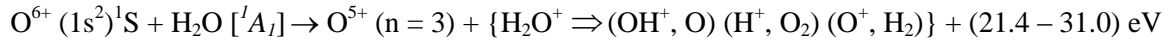
For O^{6+} in CO_2, the broad peak in the spectra at large exothermicities can also be correlated with channels corresponding to the O^{5+} (n = 3) formation through dissociative transfer ionization

$$O^{6+} (1s^2)^1S + CO_2\ [X\,^1\Sigma_g^+] \rightarrow O^{5+}\ (n = 3) + (CO_2^{2+} \Rightarrow O^+, CO^+\ ) + (16.9 - 25.7)\ eV$$

and through dissociative electron capture

$$O^{6+} (1s^2)^1S + CO_2\ [X\,^1\Sigma_g^+] \rightarrow O^{5+}\ (n = 3) + \{CO_2^+ \Rightarrow (CO^+,O);\ (O^+, CO)\} + (26 - 31.8)\ eV$$
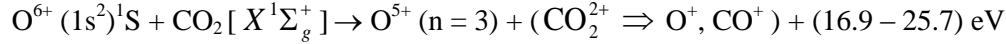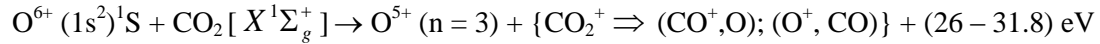
Similarly, for O^{6+} in CH_4, exothermic channels leading to CH_4^{2+}, which is known to break up into a number of possible fragments [46], can be correlated with O^{5+} (n = 3) formation as follows:

$$O^{6+} (1s^2)^1S + CH_4\ [X\,^1A_1] \rightarrow O^{5+}\ (n = 3) + (CH_4^{2+} \Rightarrow C^+, H^+, H, H_2) + (18 - 21.2)\ eV$$
$$O^{6+} (1s^2)^1S + CH_4\ [X\,^1A_1] \rightarrow O^{5+}\ (n = 3) + (CH_4^{2+} \Rightarrow C, H^+,\ H_3^+\ ) + (19.7 - 23.9)\ eV$$
$$O^{6+} (1s^2)^1S + CH_4\ [X\,^1A_1] \rightarrow O^{5+}\ (n = 3) + (CH_4^{2+} \Rightarrow C^+,\ H_2^+, H_2) + (20.0 - 24.2)\ eV$$
$$O^{6+} (1s^2)^1S + CH_4\ [X\,^1A_1] \rightarrow O^{5+}\ (n = 3) + (CH_4^{2+} \Rightarrow CH^+, H^+, H_2) + (21.1 - 25.3)\ eV$$
$$O^{6+} (1s^2)^1S + CH_4\ [X\,^1A_1] \rightarrow O^{5+}\ (n = 3) + (CH_4^{2+} \Rightarrow CH_3^+, H^+) + (21.8 - 26.0)\ eV$$
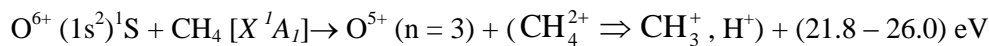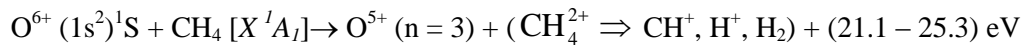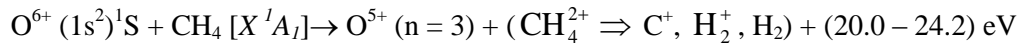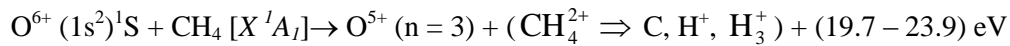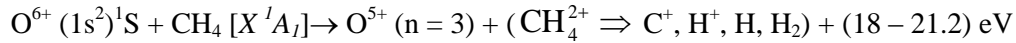
These product channels increase in relative importance as the energy increases.

Another common and surprising feature of the energy change spectra in Figure 22 is the significant contribution from highly endothermic channels. In the case of H_2O, the endothermic peak can be correlated with dissociative electron capture leading to O^{5+}(n = 4) formation:

$$O^{6+} (1s^2)^1S + H_2O\ [^1A_1] \rightarrow O^{5+}\ (n = 4) + \{H_2O^{2+} \Rightarrow (OH^+, H^+)\ (H^+, H^+, O)\} + (-5.9 - -11.5)\ eV$$
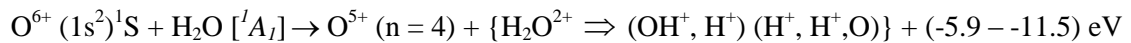
In CO_2 the corresponding channels are

$$O^{6+} (1s^2)^1S + CO_2\ [X\,^1\Sigma_g^+] \rightarrow O^{5+}\ (n = 4) + \{CO_2^{2+} \Rightarrow (O^+,CO^+);\ (C^+,O^+,O)\} + (-5.0 - -10.8)\ eV$$
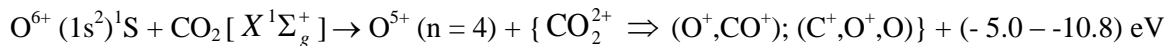
For O^{6+} ions in CH_4, the corresponding O^{5+} (n = 4) formation channels involve a greater number of possible fragmentation modes.

$$O^{6+} (1s^2)^1S + CH_4\,[X\,^1A_1] \rightarrow O^{5+}\ (n = 4) + (CH_4^{2+} \Rightarrow \{(CH^+, H_2^+, H);(CH_2, H^+, H^+);$$

$$(CH, H^+, H_2^+);\ (C, H_2^+, H_2^+\ )\} + (-4.6 - -8.1)\ eV$$
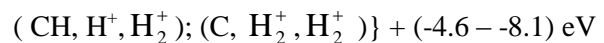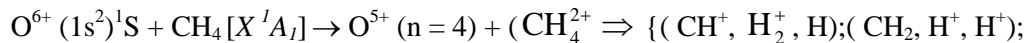
In the case of O^{6+} in CH_4 it was possible to analyse the energy change spectra shown in Figure 22 and obtain the separate contributions from the three main one-electron capture mechanisms. These are shown Figure 23.
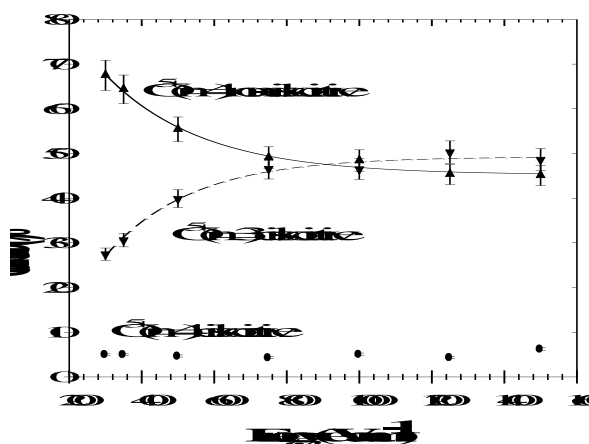
FIG. 23. Measured relative cross-sections for the main product states of O^{5+} formed in one-electron capture by O^{6+} ions in CH_4 (from [7]).
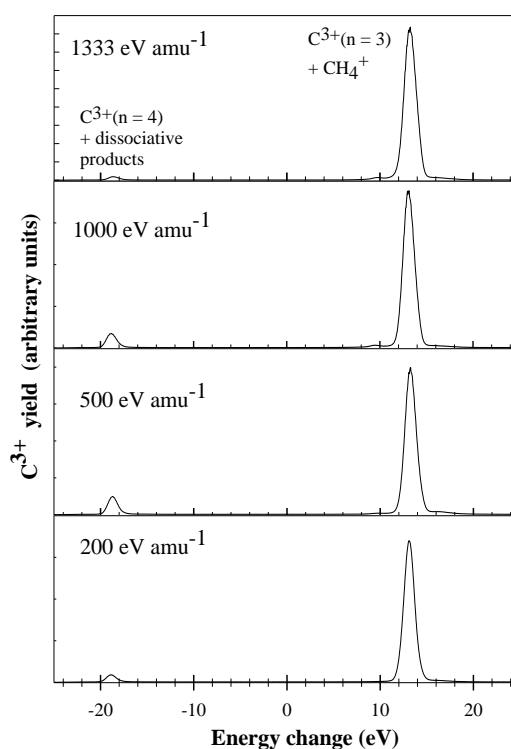
FIG. 24. Energy change spectra for one-electron capture by C^{4+} ions in CH_4 (from [7]).

Figure 24 shows energy change spectra [7] for 200 – 1333 eV amu^{-1} C^{4+} ions in CH_4 which allow an interesting comparison with the corresponding data for He-like O ions in CH_4. In this case, the spectra are clearly dominated by a well defined peak corresponding to $C^{3+}(n = 3)$ formation through the non-dissociative channels

$$C^{4+} (1s^2)^1S + CH_4 [X\,^1A_1] \rightarrow C^{3+}(n = 3) + CH_4^+\ [^1T_2] + (10.7 - 14.2)\ eV$$
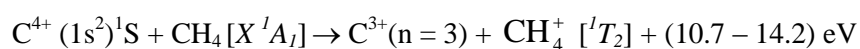
These spectra also exhibit small $C^{3+}(n = 4)$ contributions which can be correlated with the following highly endothermic dissociative product channels

125

$$C^{4+} (1s^2)^1S + CH_4 [X\ ^1A_1] \rightarrow C^{3+} (n = 4) + (CH_4^{2+} \Rightarrow CH_2^+, H^+, H) + (-18.6 - -19.7)\ eV$$

$$C^{4+} (1s^2)^1S + CH_4 [X\ ^1A_1] \rightarrow C^{3+} (n = 4) + (CH_4^{2+} \Rightarrow CH_3^+, H^+) + (-18.0 - -19.1)\ eV$$
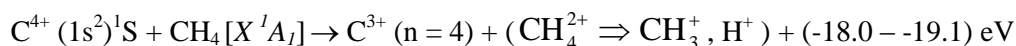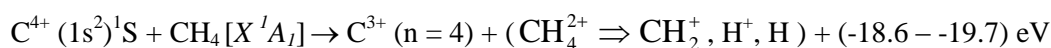
The separate contributions from the two observed one-electron capture mechanisms could be easily determined from an analysis of the energy change spectra and these relative cross-sections are shown in Figure 25.
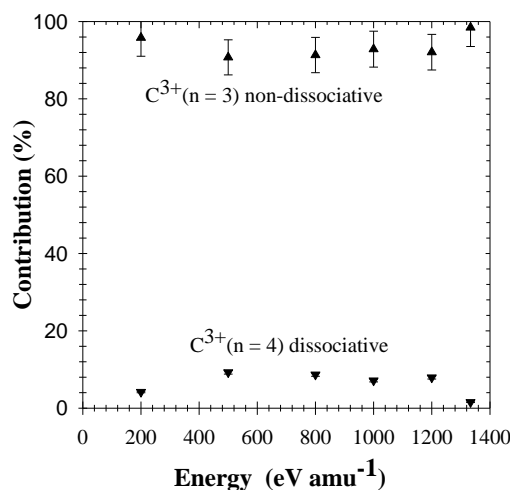
FIG. 25. *Measured relative cross-sections for the main product states of C^{3+} formed in one-electron capture by C^{4+} ions in CH_4 (from [7]).*

4. CONCLUSIONS

In TES studies of state-selective one-electron capture by H and He-like ions of C, N and O in H and H_2 within the range 250 – 900 eV amu^{-1} the main collision mechanisms leading to state-selective electron capture have been identified, their relative importance assessed and compared, where possible, with theoretical predictions and any previous measurements based on PES. For electron capture in H_2, striking differences between the main collision mechanisms have been observed. In the case of N^{5+} in H_2 both dissociative one-electron capture and two-electron autoionizing capture channels have been shown to be very important and increasing in relative importance with decreasing impact energy. However, non-dissociative electron capture is found to be dominant in the O^{6+} - H_2 and C^{4+} - H_2 collision systems. For H-like ions, in the O^{7+} - H_2 system non-dissociative and dissociative electron capture are found to be of about equal importance. However, for N^{6+} in H_2 there is no evidence of dissociative electron capture. In contrast, for C^{5+} in H_2 contributions from dissociative electron capture channels are substantial and increase in relative importance with decreasing energy when evidence of a two-electron autoionizing capture mechanism also appears.

TES measurements of one-electron capture by H and He-like C, N and O ions in atomic hydrogen at energies below 1000 eV amu^{-1} provide a valuable extension of previous measurements. In all the cases considered, as the impact energy decreases, electron capture becomes more selective until only a single *n* product channel is significant. These main product channels are well predicted by reaction windows calculated using a Landau-Zener approach. However, the same approach applied to the more complex energy change spectra in H_2 has been found to be less successful in predicting the main product channels.

Our TES studies of one-electron capture by 200 – 2000 eV amu^{-1} He^{2+} ions in CH_4, C_2H_4 and C_2H_6 have revealed significantly different patterns of behaviour. However, in spite of the large number of possible non-dissociative and dissociative product channels associated with a wide spread in energy

defects ΔE, all three cases confirm the highly selective nature of the electron capture process leading to a very limited number of product states $He^+(n, l)$. In the case of He^{2+} ions in CH_4, while non-dissociative electron capture into the $He^+(n = 2)$ state is dominant at the highest energies considered, at low energies $He^+(n = 1)$ formation through exothermic channels is dominant. This behavior is similar to our previous observations [2] of one-electron capture by slow He^{2+} ions in CO. TES results for He^{2+} ions in C_2H_4 exhibit a very different behaviour with $He^+(n = 2)$ as the main product ion arising through a variety of different dissociative and non-dissociative channels. Dissociative channels of small exothermicity are found to provide the main charge transfer contribution at the lowest energies. Our TES results for He^{2+} ions in C_2H_6 also identify $He^+(n = 2)$ as the main product ion. This arises from both dissociative and non-dissociative channels but, unlike C_2H_4, electron capture at low energies takes place predominantly through endothermic capture channels.

Studies of one-electron capture in collisions of $0.025–12$ keV amu^{-1} He^{2+} ions with H_2O molecules have been carried out in several laboratories using translational energy spectroscopy (TES), photon emission spectroscopy (PES) and fragment ion spectroscopy (FIS) to identify and quantify the collision mechanisms involved. Cross-sections for selective single electron capture into $n = 1, 2$ and 3 states of the He^+ ion have been obtained using TES while PES provided cross-sections for capture into the $He^+(2p)$ and $He^+(3p)$ states. Non-dissociative capture into the $n = 2$ states of He^+ is the dominant channel for collision energies above 250 eV amu^{-1} while dissociative transfer ionization leading to $He^+(n = 1)$ formation dominates at lower energies. Simple model calculations satisfactorily explain this behavior. Capture into $n = 3$ states of He^+ never accounts for more than a few percent of the total one-electron capture cross-section.

In the case of one-electron capture by $300 – 1500$ eV amu^{-1} O^{6+} ions in H_2O, CO_2 and CH_4 the TES studies have revealed very similar patterns of behaviour. In all three cases non-dissociative electron capture leading to $O^{5+}(4d)$ and a ground state molecular ion is a major charge transfer mechanism increasing in relative importance with decreasing energy. Dissociative capture into $O^{5+}(n = 3)$ states is also of major importance but decreasing with decreasing energy. Smaller contributions from dissociative capture into $O^{5+}(n = 4)$ states are also observed. Only in the case of $O^{6+} – CH_4$ collisions has our available energy resolution been adequate to numerically determine the relative contributions from these three electron capture mechanisms. The TES measurements for one-electron capture by C^{4+} in CH_4 collisions show that non-dissociative electron capture into $n = 3$ states of C^{3+} is dominant with a smaller but significant dissociative electron capture contribution associated with $C^{3+}(n = 4)$ formation arises from channels of high exothermicity.

ACKNOWLEDGEMENT

REFERENCES

[1]   HODGKINSON, J.M., McLAUGHLIN, T.K., McCULLOUGH, R.W., GEDDES, J., GILBODY, H.B., Importance of dissociative excitation by slow He2+ ions in one-electron capture collisions with H_2, J. Phys. B: At. Mol. Opt. Phys. **28** (1995) L393.

[2]   KEARNS, D.M., GILLEN, D.R., VOULOT, D., GREENWOOD, J.B., McCULLOUGH, R.W., GILBODY, H.B., The role of dissociative electron capture in collisions of slow He^{2+} ions with CO, J.Phys. B: At. Mol. Opt. Phys. **34** (2001) 3401.

[3]   KEARNS, D.M., McCULLOUGH, R.W., GILBODY, H.B., Experimental study of the collision mechanisms involved in one-electron capture by slow N^{5+} ions in atomic and molecular hydrogen, J. Phys B: At. Mol. Phys. **35** (2002) 4335.

[4]   KEARNS, D.M., McCULLOUGH, R.W., TRASSL, R., GILBODY, H.B., Collision mechanisms in one-electron capture by slow H and He-like ions of C, N and O in H and H_2, J. Phys B: At. Mol. Phys. **36** (2003) 3653.

[5]   SEREDYUK, B., McCULLOUGH, R.W., GILBODY H. B., Collision mechanisms in one-electron capture by He^{2+} ions in collisions with hydrocarbons, Phys. Rev. A **71** (2005) 022713.

[6]   SEREDYUK, B., et al., Charge exchange and dissociative processes in collisions of slow He^{2+} ions with H_2O molecules, Phys. Rev. A **71** (2005) 022705.

[7]   SEREDYUK, B., McCULLOUGH, R.W., GILBODY, H. B., to be published.

[8]   VOULOT, D., KEARNS, D.M., McCULLOUGH, R.W.,GILBODY, H.B., State-selective one-electron capture by slow state-prepared $N^{2+}(^2P)$ ground-state ions in collisions with hydrogen atoms, J. Phys. B: At. Mol. Phys. 34 (2001) 1039.

[9]   BASHKIN, S., STONER, J.O. Jr., Atomic Energy Levels and Grotrian Diagrams, Amsterdam: North Holland (1978).

[10]   SHARP, T. E., Potential-energy curves for molecular hydrogen and its ions, Atomic Data **2** (1971) 119.

[11]   BRUNDLE, C.R., ROBIN, M.B., Electronic Energies and Electronic Structures of the Fluoromethanes, J. Chem. Phys. **53** (1970) 2196.

[12]   DUJARDIN, G. WINKOUN, D., LEACH, S., Double photoionization of methane, Phys.Rev.A **31** (1985) 3027.

[13]   RABALAIS, J .W., BERGMARK, T. WERME, L. O., KARLSSON, L., SIEGBAHN, K., The Jahn-Teller Effect in the Electron Spectrum of Methane, Phys. Scr. **3** (1971) 13.

[14]   POLLARD, J.E., TREVOR, D.J., REUTT, J. E. LEE Y.T., SHIRLEY, D.A., Torsional potential and intramolecular dynamics in the $C_2H^+_4$ photoelectron spectra, J. Chem. Phys. **81** (1984) 5302.

[15]   MACKIE, R.A., et al., The molecular and dissociative photoionization of ethane in the inner and outer valence energy regions, J. Phys. B: At. Mol. Opt. Phys. **35** (2002) 1061.

[16]   REUTT, J.E., WANG, L.S. LEE, Y.T., SHIRLEY, D.Y. J., Molecular beam photoelectron spectroscopy and femtosecond intramolecular dynamics of H_2O^+ and D_2O^+, Chem. Phys. **85** (1986) 6928.

[17]   RICHARDSON, P. J., ELAND, J. H. D., FOURNIER, P. G., COOPER, D. L., Spectrum and decay of the doubly charged water ion, J. Chem. Phys. **84** (1986) 3189.

[18]   CORNAGGIA, C., HERING, Ph., Nonsequential double ionization of small molecules induced by a femtosecond laser field, Phys. Rev. A **62** (2000) 023403.

[19]   MASUOKA, T., NAKAMURA, E., HIRAYA, A., Kinetic-energy release in the dissociation of CO^{22+}, J. Chem. Phys. **104** (1996) 6200.

[20]   HANSSEN, J., GAYET. R., HAREL, C., SALIN, A., Electron capture by C^{4+}, $N^{5+}$and O^{6+} from atomic hydrogen in the keV amu^{-1} energy range, J. Phys. B: At. Mol. Opt. Phys. **17** (1984) L323.

[21]   DIJKKAMP, D., CIRIC, D., VLIEG, E., De BOER, A., De HEER, F.J., Subshell-selective electron capture in collisions of C^{4+}, N^{5+}, O^{6+} with H, H_2 and He, J. Phys. B: At. Mol. Phys. **18** (1985) 4763.

[22]   SHIMAKURA, N., KIMURA, M., Electron capture in collisions of N5+ ions with H atoms from the meV to keV energy regions, Phys. Rev. A **44** (1991) 1659.

[23]   BENDAHMAN, M., et al., Electron capture from atomic hydrogen by multiply charged ions in low energy collisions, J. Physique 46 (1985) 561.

[24]   HAVENER, C. C., HUQ, M. S., KRAUSE, N. F., SCHULZ, P. A., PHANEUF, R. A., Merged-beams measurements of electron-capture cross-sections for O5++H at electron-volt energies, Phys. Rev. A **39** (1989) 1725.

[25]   TSENG, H.C., LIN, C.D., Reevaluation of electron-capture cross-sections in C^{4+}+ H collisions, Phys. Rev. A. **58** (1998) 1966.

[26]   BORDENAVE-MONTESQUIEU, A., et al., Two-electron capture into autoionising configurations N^{4+}(1snln'l') with n=2, 3, 4 and n'≥n, observed by electron spectrometry in collisions of N^{6+}(1s) with He and H_2, at 4.2 keV amu^{-1}, J. Phys. B: At. Mol. Phys. **17** (1984) L223.

[27] SURAUD, M.G., HOEKSTRA, R., De HEER, F.J., BONNET, J.J., MORGENSTERN, R., State selective electron capture into nl subshells in slow collisions of C^{5+} and N^{6+} with He and H_2 studied by photon emission spectroscopy, J. Phys. B: At. Mol. Opt. Phys. **24** (1991) 2543.

[28] OKUNO, K. private communication (2002).

[29] KUMAR, A., SAHA, B.C., State-selective charge transfer in slow collisions of partially stripped He-like ions with H_2, Phys. Rev. A **59** (1999) 1273.

[30] GARGAUD, M., McCARROLL, R., Charge transfer in low-energy collisions of N^{3+}, C^{4+} and N^{5+} with H and H_2, J. Phys. B: Atom. Molec. Phys. **18** (1985) 463.

[31] ELIZAGA, D., et al, Calculations of Charge Transfer and Ionization Cross-sections for Ion - H_2 (D_2,DT,T_2) Collisions, Atom. Plasma-Mater. Interact. Data Fusion **9** (2001) 67 (IAEA Vienna).

[32] PANOV, M.P. N., BASALAEV, A.A., LOZHKIN, K.O., Interaction of Fully Stripped, Hydrogenlike and Heliumlike C, N, O, Ne and Ar Ions with H and He Atoms and H_2 Molecules, Phys. Scr. **T3** (1983) 124.

[33] HOEKSTRA, R., Kernfysisch Versneller Instituut, private communication (2002).

[34] LUBINSKI, G., JUHASZ, Z., MORGENSTERN, R., HOEKSTRA, R., State-selective electron-capture cross-section measurements for low-energy collisions of He-like ions on H_2, J. Phys.B: At. Mol. Opt. Phys. **33** (2000) 5275.

[35] MÉNDEZ, L., private communication (2002).

[36] McLAUGHLIN, T.K., McCULLOUGH, R.W., GILBODY, H.B., State-selective electron capture by slow C^{4+} ions in collisions with H_2 and O_2, J. Phys. B: At. Mol. Opt. Phys. **25** (1992) 1257.

[37] HOEKSTRA, R., BEIJERS, J.P.M., SCHLATMANN, A.R., MORGENSTERN, R., State-selective charge transfer in slow collisions of C^{4+} with H and H_2, Phys. Rev. A. **41**(1990) 4800.

[38] TAULBJERG, K., Reaction windows for electron capture by highly charged ions, J. Phys.B: At. Mol. Phys. **19** (1986) L367.

[39] KIMURA, M., et al., Landau-Zener Model Calculations of One-Electron Capture from He Atoms by Highly Stripped Ions at Low Energies, J. Phys. Soc. Japan. **53** (1984) 2224.

[40] McCULLOUGH, R. W., WILSON, S. M., GILBODY, H. B., State-selective capture by slow Ar^{4+}, Ar^{5+} and Ar^{6+} recoil ions in H, H_2 and He, J. Phys. B: At. Mol. Phys. **20** (1987) 2031.

[41] NIEHAUS, A., A classical model for multiple-electron capture in slow collisions of highly charged ions with atoms, J. Phys.B: At. Mol. Phys. 19 (1985) 2925.

[42] HOEKSTRA, R. Kernfysisch Versneller Instituut, private communication (2004).

[43] ABU-HAIJA, O., KAMBER, E.Y., FERGUSON, S.M., Single-electron capture by He^{2+} ions from triatomic molecules, Nuc. Instr. Methods in Phys. Res. B. **205** (2003) 634.

[44] GREENWOOD, J.B., et al., The Contribution of Charge Exchange to Extreme Ultra-Violet and X-ray Astronomy, Phys. Scr. T **110** (2004) 358.

[45] RUDD, M. E., GOFFE, T. V., ITOH, A. Ionization cross-sections for 10–300-keV/u and electron-capture cross-sections for 5–150-keV/u $^3He^{2+}$ ions in gases, Phys. Rev. A **32** (1985) 2128.

[46] DUJARDIN, G., WINKOUN, D., LEACH, S., Double photoionization of methane, Phys. Rev. A **31** (1985) 3027.

SURVIVAL PROBABILITIES OF SLOW IONS IN COLLISIONS WITH ROOM-TEMPERATURE AND HEATED SURFACES OF CARBON, TUNGSTEN AND BERYLLIUM

Z. HERMAN

V. Čermák Laboratory, J. Heyrovský Institute of Physical Chemistry, v.v.i.,
Academy of Sciences of the Czech Republic,
Dolejškova 3, 182 23 Prague 8, Czech Republic

Abstract

Survival probabilities S_a(%) of hydrocarbon ions C1, C2, and C3 and several non-hydrocarbon ions (Ar^+, N_2^+, CO_2^+) on room-temperature (hydrocarbon-covered) and heated (600^0C) surfaces of carbon (HOPG), tungsten, and beryllium were experimentally determined using the ion-surface scattering method for several incident energies from a few eV up to about 50 eV and for an incident angle of 30^0 (with respect to the surface). The plot of the survival probabilities (S_a) vs. the ionization energy (IE) of the incident species for room-temperature carbon showed a sharp decrease (from about 10 % to less than a percent) at about IE = 9.5 eV, close to the IE of alkanes C7 – C11, expected to be present in the hydrocarbon surface coverage. The semi-logarithmic plot of S_a vs. IE (data at 31 eV) for all studied surfaces was linear and could be fitted by an empirical equation log $S_a = a - b$(IE). The values of the parameters a and b were determined for all studied room-temperature and heated surfaces and can be used to estimate unknown survival probabilities of ions on these surfaces.

1. INTRODUCTION

The main process in the interaction of a projectile ion and a surface is neutralization of the projectile, as shown by numerous studies [1]. The neutralization rate or, vice versa, the percentage of ions surviving a collision of a slow ion incident on the surface, the survival probability, is one of the basic characteristics of ion-surface interactions.

Ejection of electrons from metals by slow ions and ion neutralization in interaction with metal surfaces was treated in a classical paper by Hagstrum [2]. Processes of electron transfer in hydrocarbon collisions with surfaces were treated theoretically by Janev and Krstic [3]. These authors also developed a general analytic expression for the resonant neutralization (RN) transition rate of ions at surfaces, $\omega^{RN}(R)$, in the form $\omega^{RN}(R) = A^{RN}R^\alpha \exp(-2\gamma R)$, where A^{RN} and α are constants depending on γ, $\gamma^2/2$ is the electron binding energy, and R the distance between the surface and the incident particle.

In this paper we concentrate on recent experimental data on ion survival probabilities as obtained in our laboratory over several years and on more general conclusions resulting from them that, hopefully, make it possible to estimate ion survival probabilities from ionization energies of projectile ions incident with a specified energy and under a specified angle on a particular surface. As a part of systematic scattering studies of interactions of slow hydrocarbon ions with surfaces relevant to fusion research, we determined the survival probabilities of projectile ions incident with energies from a few eV to about 50 eV on room-temperature and heated (to 600^0C) surfaces of carbon (HOPG) [4,6,7,8,11,13], tungsten [12] and beryllium [14]. The ion-surface scattering method used and the procedure used to extract the absolute ion survival probabilities from the scattering data are described in the next sections.

The experiment showed that the surfaces kept at room-temperature were covered by a layer of hydrocarbons from backstreaming pump oil or its hydrocarbon cracked fragments. This universal surface coverage could be sensitively tested by the occurrence of chemical reactions of H-atom transfer between the hydrocarbons on the surface and incident radical cations, e.g. [4]

$$CD_4^{+\bullet} + CH_3\text{-}S \rightarrow CD_4H^+ + (^{\bullet}CH_2\text{-}S) \tag{1}$$

or [6]

$$C_2D_4^{+\bullet} + CH_3\text{-}S \rightarrow C_2D_4H^+ + (^{\bullet}CH_2\text{-}S) \tag{2}$$
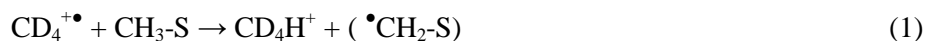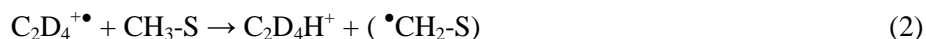
Heating the surface to about 600^0C or higher resulted in an effective removal of the hydrocarbon layer, as indicated by the absence of the H-atom transfer reactions [4,6,7,12]. Cooling the surface after heating to room-temperature led to re-establishing of the hydrocarbon layer on the surfaces within about an hour. Repeated heating and cooling the surface lead, within the experimental error, to the same scattering results (mass spectra of ion products of surface interactions, angular and translational energy of the ion products).

2. EXPERIMENTAL METHOD
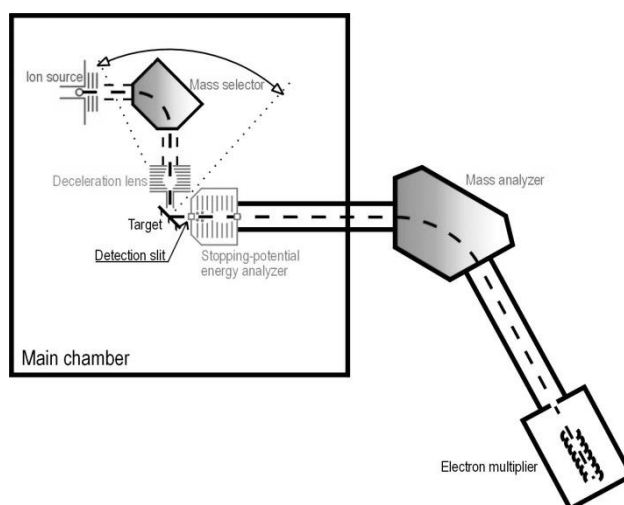
FIG. 1. Schematics of the apparatus EVA.

The experiments were carried out with the Prague beam scattering apparatus EVA II modified for ion-surface collision studies [4,7-9,11]. Projectile ions were formed by bombardment by 120 eV electrons of hydrocarbons or other gases (or their deuterated variants) at the ion source pressure of about 3.10^{-5} Torr. The ions were extracted, accelerated to about 150-200 eV, mass analyzed by a 90^0 permanent magnet, and decelerated to the required energy in a multi-element deceleration lens. The resulting beam had an energy spread of 0.2 eV, full-width-at-half-maximum (FWHM), angular spread of about 2^0, FWHM, and geometrical dimensions of 0.4x1.0 mm^2. The beam was directed towards the target surface under a pre-adjusted incident angle Φ_S (with respect to the surface). Ions scattered from the surface passed through a detection slit (0.4x1 mm^2), located 25 mm away from the target, into a stopping potential energy analyzer. After energy analysis the ions were focused and accelerated to 1000 eV into a detection mass spectrometer (a magnetic sector instrument), and detected with a Galileo channel multiplier. The primary beam exit slit, the target, and the detection slit were kept at the same potential during the experiments and this equi-potential region was carefully shielded by μ-metal sheets. The primary beam - target section could be rotated about the scattering center with respect to the detection slit to obtain angular distributions. The mass spectra of product ions were recorded with the stopping potential set at zero.

The energy of the projectile ions was measured by applying to the target a potential exceeding the nominal ion energy by about 10 eV. The target area then served as a crude ion deflector directing the projectile ions into the detection slit. Their energy could be determined with accuracy better than

about 0.2 eV. The incident angle of the projectile ions was adjusted before an experimental series by a laser beam reflection with a precision better than 1°. Incident (Φ_S) and scattering (Θ'_S) angles are given with respect to the surface plane.

The carbon surface target was a 5x5 mm sample of highly oriented pyrolytic graphite (HOPG) sample from which the surface layer was peeled-off immediately before placing it into vacuum. The sample was mounted into a stainless steel holder located 10 mm in front of the exit slit of the projectile ion deceleration system. The carbon target surfaces in the experiments were kept either at room temperature or at an elevated temperature of about 600^0 C. For this purpose, the carbon surface could be resistively heated up to about 1000 K and its temperature was measured by a thermocouple and by a pyrometer. Practical absence of chemical reactions with surface hydrocarbons indicated that heating the surface to 600^0C or higher decreased the concentration of hydrocarbons on the surface more that 100-times [4]. The temperature of 600^0 C was thus regarded as sufficiently high to essentially remove the hydrocarbon layer that covered the HOPG surface at room temperature and it was used in the present experiments (see also sections 3.3. and 3.4. further on). At higher temperatures an increasing emission of K^+ ions from the sample was observed.

The tungsten surface target [12] was a 99.9% tungsten sheet, 0.05 mm thick (Aldridge Chemical Comp.). Before placing it into vacuum, the surface was either mechanically or electrochemically polished. Electrolytic polishing followed the standard procedure of dipping the sample, as anode, for 30 seconds into a 20% solution of NaOH in water. The sample was mounted into a stainless steel holder located 10 mm in front of the exit slit of the projectile ion deceleration system. Similarly as with the carbon surface, at sample temperatures above about 500^0C, emission of K^+ ions from the sample, increasing with temperature, was observed. Ex situ XPS analysis of the W target after heating showed a sharp increase of tungsten carbides on the surface.

The scattering chamber of the apparatus was pumped by a 1380 l/s turbomolecular pump, and the detector by a 65 l/s turbomolecular pump; both pumps were backed by rotary vacuum pumps. The background pressure in the apparatus was about $5x10^{-7}$ Torr, during the experiments the pressure was about $5x10^{-6}$ Torr due to the leakage of the source gas into the scattering chamber.

3. ION SURVIVAL PROBABILITY: DETERMINATION FROM EXPERIMENTAL DATA

The ion survival probability S_a (percentage of ions surviving a surface collision) is defined as the sum of intensities of all product ions scattered from the target, ΣI_{PT}, to the intensity of the projectile reactant ions incident on the target, I_{RT}, $S_a = 100\ \Sigma I_{PT} / I_{RT}$ (here, $I_{RT} = I_{RTM} + \Sigma I_{PT}$, where I_{RTM} is the current of projectile ions actually measured on the target). While I_{RTM} was measured in the experiments reported here, ΣI_{PT} could not be directly determined and had to be estimated from the sum of intensities of product ion reaching the detector, ΣI_{PD}, taking into account the discrimination of the apparatus (D_A) and the angular discrimination of the scattering differential measurements ($D(\omega)$). A direct measurable quantity was the relative survival probability, $S_{eff} = \Sigma I_{PD} / I_{RT}$, related to S_a (expressed in percents) by $S_a = 100\ F\ S_{eff}$, where F summarizes the discrimination effects.

It holds for the intensity of the projectile (reactant) ion (R) registered on the detector (I_{RD}) and incident on the target (I_{RT})

$$I_{RD} = D_A\ D(\omega)_R\ I_{RT,} \tag{3}$$

and analogously for the scattered product ions (P)

$$I_{PD} = D_A\ D(\omega)_P\ I_{PT} \tag{4}$$

For the estimation of the angular discrimination of the reactant beam, $D(\omega)_R$, and the scattered product ion beam, $D(\omega)_P$, the following simplifications were made

1. The area of the detection slit (0.4×1.0 mm^2) was approximated by an aperture of the same area (diameter 0.72 mm, angular acceptance $\Theta_{ds} = 1.6^0$).
2. The angular distribution of the reactant beam was approximated by its full-width-at-half-maximum (FWHM), $\Theta_R(FWHM) = 2.0^{0.}$
3. The angular distribution of the scattered product beam was approximated by an average of FWHM of the product ion distributions, $\Theta_P(FWHM)$.
4. The angular discrimination was then approximately estimated as $D(\omega)_R = \Theta_{ds}^2 / \Theta_R^2 (FWHM)$ and $D(\omega)_P = \Theta_{ds}^2 / \Theta_P^2 (FWHM)$.

By putting a potential on the target (see above, section 2) one could deflect the reactant ion beam into the detection slit, measure its intensity entering the slit, I_{RS}, and its angular distribution, and register the ion current reaching the detector, I_{RD}. The discrimination of the apparatus was then $D_A = I_{RS} / I_{RD}$.

The angular discrimination factor, $D(\omega)_P / D(\omega)_R$, followed from the above approximations, $D(\omega)_P / D(\omega)_R = \Theta_P^2 (FWHM) / \Theta_R^2 (FWHM)$. The constant F was then $F = D_A [D(\omega)_P / D(\omega)_R]$. The values of D_A and $\Theta_P(FWHM)$ were determined for different sets of experiments and they were given in the published papers [4,6,7,8,11-13]. The values of the latter did not differ significantly. The values of $\Theta_R(FWHM)$ were obtained from specific measurements of angular distributions of the scattered product ions as reported in the published papers, too[4,6,7,8,11-13].

The absolute survival probability of incident ions, S_s, is related to the neutralization rate W_a (%) by $W_a = 1 - S_a$.

4. SURVIVAL PROBABILITIES OF HYDROCARBON AND OTHER IONS

The absolute survival probabilities of hydrocarbon and several other non-hydrocarbon ions as determined from the above mentioned experiments are summarized in Tables 1 – 5 for several incident energies between 15 eV and 46 eV. The incident angle was 30^0 (with respect to the surface) for all data in the Tables. Table 1 gives the survival probabilities of ions on room-temperature carbon (HOPG) surfaces. Under these conditions, the surfaces were covered by a layer of hydrocarbons, as indicated by the occurrence of chemical reactions (mainly H-atom transfer from the surface hydrocarbons to the open-shell projectile ions) at the surface [4-8,13]. Table 2 provides data on absolute survival probabilities of C1,C2 hydrocarbon ions and N_2^+ on carbon (HOPG) surfaces heated to 600^0C, where the surface hydrocarbon layer was effectively removed [4,6]. Table 3 and 4 contain analogous data for room-temperature and heated surfaces of tungsten (W), respectively [12]. Table 5 gives preliminary data obtained for room-temperature surfaces of beryllium (Be). References to data published earlier are given in the Tables. Some of the preliminary data on survival probabilities of C3 hydrocarbon ions on room-temperature carbon (HOPG) surfaces, included into our earlier review article [16], had to be corrected. A new careful recalibration of the discrimination factors required a correction of about 2 upwards [13]. The values in the Tables are mostly averages of measurements of many spectra and the error bars give the standard deviation for an average of a series of measured data. The S_a estimates may be influenced by the inaccuracy of the simplified evaluation of the discrimination factors.

The data on survival probabilities of ions in Tables 1-5 confirm that the main process in collisions of the ions with room-temperature and heated surfaces of carbon (HOPG), tungsten, and beryllium is ion neutralization. The data show a clear difference between survival probabilities of radical (odd-electron) ions and even-electron ions. While the survival probabilities of radical cations are about 2-1% or less, the survival probabilities of even-electron ions are in general larger (from several % to about 10-20%). For most projectile ions there was no systematic change with incident energy over the investigated incident energy range 15 eV to 46 eV.

TABLE 1. SURVIVAL PROBABILITY, Sa (%), OF CmHn+ and CmDn+ (m=1,2,3,7) HYDROCARBON AND SEVERAL NON-HYDROCARBON CATIONS AND DICATIONS ON ROOM TEMPERATURE CARBON (HOPG) SURFACES (INCIDENT ANGLE $\Phi S= 300$)

projectile ion	$E_{inc}= 16\pm 1$ eV S_a(%)	$E_{inc}=31\pm1$ eV S_a(%)	$E_{inc}=46\pm1$ eV S_a(%)	Ref.
CD_3^+	0.12 ± 0.03	0.22 ± 0.04	0.26 ± 0.16	[4]
CD_4^+	0.37 ± 0.06	0.34 ± 0.2	0.27 ± 0.26	[4]
CD_5^+	12.5 ± 5	12.0 ± 5	18 ± 7	[4]
$C_2H_2^+$	0.1 ± 0.03	0.1 ± 0.03	0.06 ± 0.01	[6]
$C_2D_2^+$			0.08 ± 0.02	[6]
$C_2H_3^+$	6.4 ± 0.4	4.1 ± 0.7	2.4 ± 0.5	[6]
$C_2H_4^+$	2.3 ± 0.6	1.2	0.7 ± 0.1	[6]
$C_2D_4^+$		1.0 ± 0.4	0.9 ± 0.2	[6]
$C_2H_5^+$	1.1 ± 0.03	1.0 ± 0.1	0.3 ± 0.03	[6]
$C_3H_2^+$ (1-propene)		1.7 ± 0.1	2.5	[13]
$C_3H_3^+$ (c-propane)		3.6 ± 0.3		[13]
$C_3H_3^+$ (1-propene)		7.8 ± 0.5		[13]
$C_3H_3^+$ (propane)	6.3	5.5 ± 0.3	3.9	[13]
$C_3H_4^+$ (c-propane)		2.3 ± 0.7	2.0 ± 0.7	[13]
$C_3H_4^+$ (1-propene)		1.8 ± 0.2		[13]
$C_3H_5^+$ (c-propane)		2.5 ± 0.2	2.0 ± 0.7	[13]
$C_3D_5^+$ (D-propane)		9.9 ± 1.4		[13]
$C_3H_5^+$ (propane)	11.2 ± 0.7	4.6 ± 0.2		[13]
$C_3H_6^+$ (c-propane)		1.8 ± 0.5	2.2 ± 0.1	[13]
$C_3D_6^+$ (D-propane)		4.8 ± 0.9		[13]
$C_3H_6^+$ (propane)	6.6 ± 0.9	7.2 ± 1.2	6.8 ± 2	[13]
$C_3D_7^+$ (D-propane)		20 ± 2.3	16 ± 3	[13]
$C_3H_7^+$ (propane)		11.9 ± 4	17 ± 6	[13]
$C_3D_8^+$ (D-propane)		1.4 ± 0.7		[13]
$C_3H_8^+$ (propane)	0.7 ± 0.3	2.7 ± 0.5	4.2 ± 2	[13]
$C_7H_7^+$ (toluene)		14.2 ± 4		[7]
$C_7H_8^+$ (toluene)		11.4 ± 2		[7]
Ar^+			0.005	[13]
CO_2^+			0.0035	[13]
CO_2^{2+}			0.05	[13]
$C_7H_7^{2+}$ (toluene)		23 ± 4		[7]
$C_7H_8^{2+}$ (toluene)		20 ± 7		[7]

However, investigation of survival probabilities of selected radical and even-electron hydrocarbon ions C1 and C2 on room-temperature carbon surfaces [8,16] at incident energies below 15 eV showed a continuous decrease towards zero (Figure 2).

The survival probabilities of the non-hydrocarbon ions Ar^+ and CO_2^+ were very small, up to two orders of magnitude smaller than for the listed hydrocarbon ions. The S_a value for the carbon dioxide dication CO_2^{2+} was more than ten times larger than for the singly-charged radical cation CO_2^+, in general agreement with earlier findings for hydrocarbon cations and dications [7].

Information on the survival probabilities of C1, C2, C3, and several other cations on a carbon (HOPG) surface covered at room temperature with hydrocarbons, as summarized in Table 1, provided sufficient data for an attempt to correlate the S_a values observed with a parameter characterizing the incident ions. An obvious characteristic is the recombination energy of these ions on this type of surface. Unfortunately, little is known about recombination energies of most ions in question.

Therefore, we tried to correlate the survival probability values with the ionization energies (IE) of the species in question, having in mind that the recombination energy may be in some cases somewhat different from the IE, mainly due to conformational changes in the ionization-recombination processes.

TABLE 2. SURVIVAL PROBABILITY, S_a (%), OF C1 AND C2 HYDROCARBON IONS ON CARBON (HOPG) SURFACES HEATED TO 600^0C (INCIDENT ANGLE $\Phi_S= 30^0$)

projectile ion	$E_{inc}= 16\pm 1$ eV S_a(%)	$E_{inc}=31\pm1$ eV S_a(%)	$E_{inc}=46\pm1$ eV S_a(%)	Ref.
CD_3^+	0.09		0.1	[4]
CD_4^+	(5)	0.23		[4]
		0.10 ± 0.025		[14]
CD_5^+			23	[4]
		27.3 ± 8		[14]
		35.2 ± 8		[14]
$C_2H_2^+$	0.1±0.04	0.1±0.04	0.36	[4]
		0.013± 0.013		[14]
$C_2D_2^+$		0.07±0.2		[4]
$C_2H_3^+$		3.6±0.2	5	[4]
		0.81 ± 0.11		[14]
$C_2H_4^+$		0.2±0.05	0.8±0.2	[4]
		0.06 ± 0.02		[14]
$C_2D_4^+$		0.4±0.05		[4]
$C_2H_5^+$		0.76 ± 0.11		[14]
N_2^+		0.0033 ± 0.0015		[14]
		0.0006 ± 0.0005		[14]

TABLE 3. SURVIVAL PROBABILITY S_a (%), OF C1, C2 AND C3 HYDROCARBON IONS AND SEVERAL NON-HYDROCARBON IONS ON ROOM TEMPERATURE TUNGSTEN (W) SURFACES (INCIDENT ANGLE $\Phi_S= 30^0$)

projectile ion	$E_{inc}= 16\pm 1$ eV S_a(%)	$E_{inc}=31\pm1$ eV S_a(%)	$E_{inc}=46\pm1$ eV S_a(%)	Ref.
CD_3^+		0.0185 ± 0.004		[14]
CD_4^+	0.03 ± 0.01	0.033 ± 0.01	0.12 ± 0.04	[12]
CD_5^+	4.7 ± 0.7	0.8 ± 0.1	1.2 ± 0.1	[12]
$C_2H_4^+$		0.10 ± 0.05		[14]
$C_2D_4^+$	0.17 ± 0.04	0.17 ± 0.04	0.19 ± 0.04	[12]
$C_2H_5^+$	2.7 ± 0.7	1.6 ± 0.5	0.85 ± 0.3	[12]
$C_3H_3^+$		1.05 ± 0.24		[14]
$C_3H_5^+$		0.8 ± 0.14		[14]
$C_3H_7^+$		2.16 ± 0.65		[14]
$C_3H_8^+$		0.19 ± 0.05		[14]
N_2^+		0.0015 ±0.0015		[14]
Ar^+		0.003 ± 0.002		[14]

TABLE 4. SURVIVAL PROBABILIY, S_a (%), OF C1 AND C2 HYDROCARBON IONS AND N_2^+ ON TUNGSTEN (W) SURFACES HEATED TO 600^0 C (INCIDENT ANGLE $\Phi_S= 30^0$)

projectile ion	$E_{inc}= 16\pm 1$ eV S_a(%)	$E_{inc}=31\pm1$ eV S_a(%)	$E_{inc}=46\pm1$ eV S_a(%)	Ref.
CD_4^+	0.03 ± 0.01	0.02 ± 0.007	0.02 ± 0.007	[12]
CD_5^+	1.1 ± 0.3	0.5 ± 0.04	0.5 ± 0.04	[12]
$C_2H_2^+$		0.007 ± 0.005		[14]
$C_2D_4^+$	0.16 ± 0.05	0.1 ± 0.03	0.14 ± 0.04	[12]
$C_2H_5^+$	0.58 ± 0.1	0.32 ± 0.1	0.24 ± 0.1	[12]
		0.34 ± 0.04		[14]
N_2^+		0.0005 ± 0.0005		[14]

TABLE 5. SURVIVAL PROBABILITY S_a (%), OF C1 AND C2 HYDROCARBON IONS ON ROOM TEMPERATURE BERYLLIUM (BE) SURFACES (INCIDENT ANGLE $\Phi_S= 30^0$)

projectile ion	$E_{inc}= 16\pm 1$ eV S_a(%)	$E_{inc}=31\pm1$ eV S_a(%)	$E_{inc}=46\pm1$ eV S_a(%)	Ref.
CD_4^+		0.047 ± 0.015	0.053 ± 0.015	[14]
CD_5^+	2.1 ± 0.5	2.2 ± 0.5	0.8 ± 0.2	[14]
$C_2D_4^+$	0.4 ± 0.1	0.9 ± 0.4		[14]
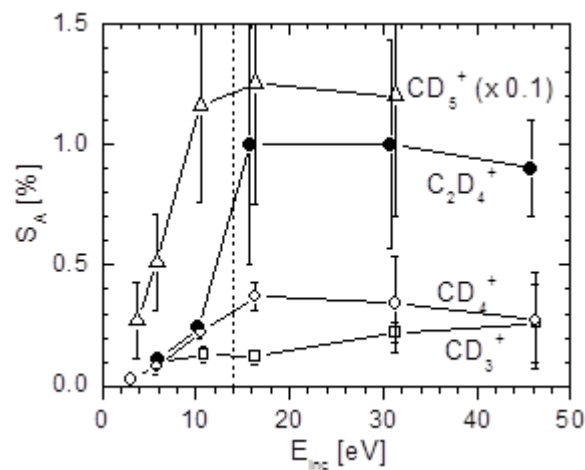
FIG. 2. S_a at low incident energies.
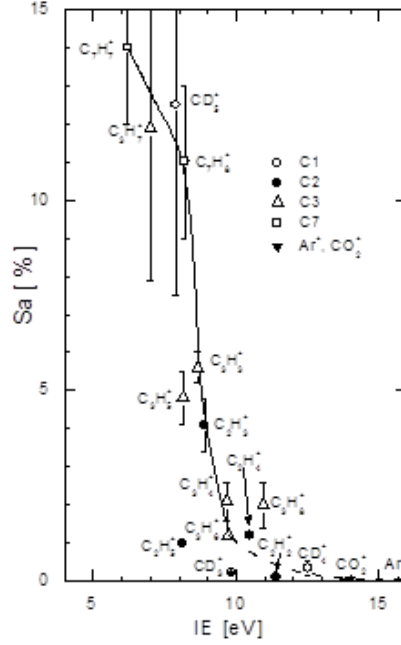
FIG. 3. Dependence S_a- IE for a room-temperature carbon (HOPG) surface.

TABLE 6. IONIZATION ENERGIES (IE) OF HYDROCARBON AND NON-HYDROCARBON SPECIES USED IN CORRELATIONS S_a – IE (DATA FROM REF. [17]

species	IE (eV)	species	IE(eV)
CH_3	9.84	C_3H_3	8.68
CH_4	12.51	C_3H_4	9.7
CH_5	7.92	C_3H_5	8.18
		C_3H_6	9.73
C_2H_2	11.40	C_3H_7	7.36
C_2H_3	8.9	C_3H_8	10.95
C_2H_4	10.51		
C_2H_5	8.13	CO_2	13.77
		N_2	15.58
C_7H_7	7.20	Ar	15.75
C_7H_8	8.82		

A plot S_a vs IE for the S_a values listed in Table 1 is shown in Figure 3. The data used were data at the incident energy of 31 eV and incident angle 30^0 (with respect to the surface). Tabulated values [17] of the ionization energies of the hydrocarbon particles in question have been used and the values are given in Table 6. For CD_5^+ the value used was assumed to be the energy release in the reaction $CD_5^+ + e \rightarrow CD_4 + D$ (7.9 eV). The Figure shows that the survival probability changes between about 8.5 eV and 9.5 eV from more than 10% to about 1% or less and it continues to decrease. An extrapolation of the steeply decreasing part of the curve goes to IE 9.5 eV. This value is close to the ionization energy of C7 – C11 alkanes ((9.56 – 9.92 eV [17]). If hydrocarbon chains analogous to C7-C11 alkanes are present as adsorbed hydrocarbons on the surface, the survival probability of the incident ions with IE higher than about 9.5 eV should lead to an effective charge transfer to the surface hydrocarbon and a strong decrease of the survival probability, while for the projectile ions of IE lower than that, charge transfer should be diminished and the survival probability correspondingly increased. Internal energy of incident ions may possibly affect this limit, but its role is at the moment not clear.

A very simple correlation between S_a and IE is the semi-logarithmic plot of these quantities, log S_a vs. IE, as shown in Figure 4. The dependence log S_a *vs* IE indicates an approximately linear decrease over the entire range of IEs of the studied incident ion species (7 – 16 eV). The least square fit of the data is described well by the equation $\log S_a = (3.9\pm0.5) – (0.39\pm0.04)$ x IE. Figure 5 shows an analogous semilogarithmic plot for the data on heated (600^0C) surfaces of carbon (HOPG), as given in Table 2. The straight line showing the least square fit of the data (solid line) is steeper than for the room-temperature carbon surfaces (dashed line from Figure 4 without experimental data).
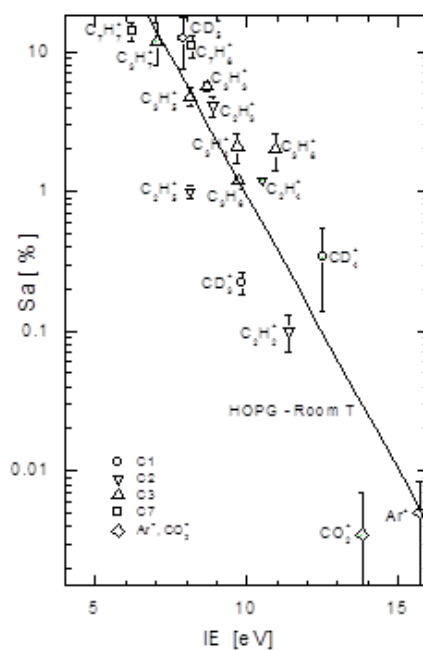
FIG. 4. Dependence S_a- IE in semi-log coordinates for a room-temperature carbon (HOPG) surface.
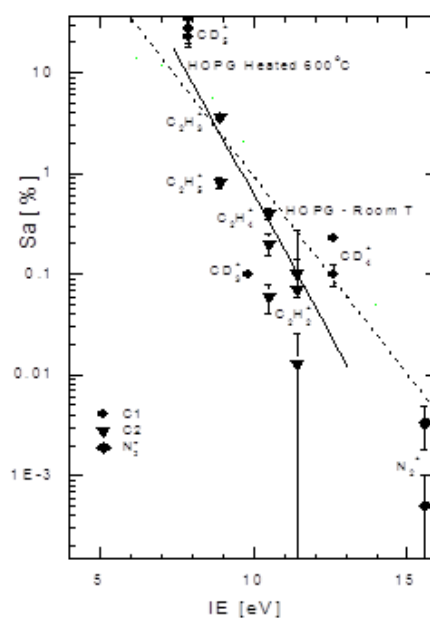
FIG. 5. Dependence S_a - IE in semi-log cooradinates for a heated carbon (HOPG) surface.

138
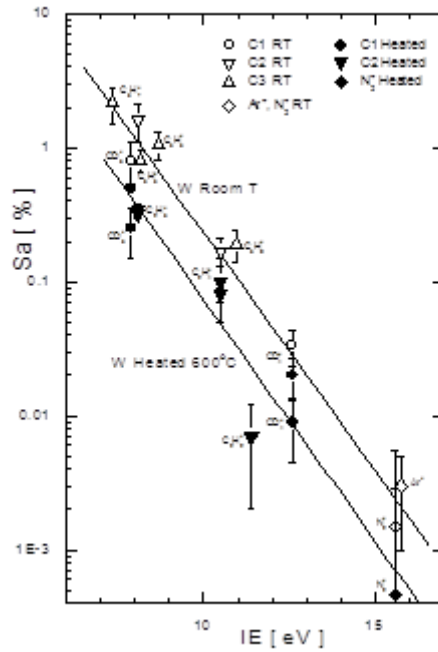
FIG. 6. Dependence of S_a- IE in semi-logarithmic coordinates for room-temperature and heated surfaces of tungsten.
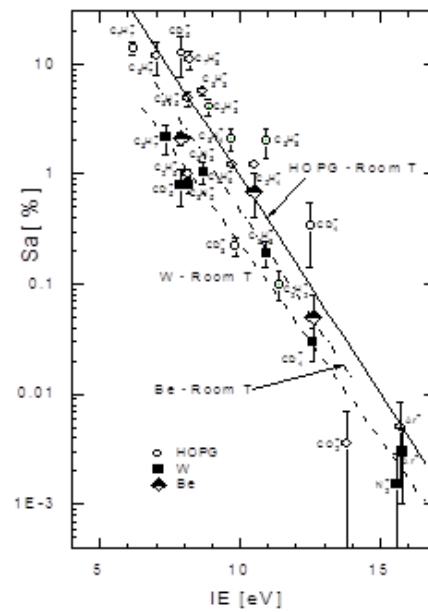
FIG. 7. Dependence log S_a- IE for room-temperature surfaces of carbon (HOPG), tungsten, and beryllium.

Figure 6 summarizes the data for survival probabilities of ions on room-temperature and heated surfaces of tungsten. The least square fit of the plots log S_a *vs.* IE leads to practically parallel lines, the one for heated surfaces at lower S_a values.

TABLE 7. VALUES OF PARAMETERS a AND b IN THE PLOTS LOG $S_a = a - b$(IE) FOR DIFFERENT SURFACES

surface	a	b
carbon(HOPG),RT	3.9 ± 0.5	0.39 ± 0.04
carbon (HOPG), H	5.4 ± 1.1	0.5 ± 0.1
tungsten, RT	2.9 ± 0.2	0.35 ± 0.02
tungsten, H	2.5 ± 0.4	0.35 ± 0.04
beryllium, RT	(3.9)	(0.39)

Note: RT – room-temperature, H- heated to 600^0 C

Figure 7 compares the semilogarithmic plots for survival probabilities of ions on different room-temperature (hydrocarbon-covered) surfaces of carbon (HOPG), tungsten, and beryllium. The available data for beryllium are only for three incident ions, CD_5^+, CD_4^+, and $C_2D_4^+$ (half-closed diamonds in Figure 7). The least square fits on data for carbon (HOPG) and tungsten are practically parallel lines mutually shifted in the ordinate scale. The available data for beryllium can be reasonably well fitted by a straight line parallel with that for carbon (HOPG) (see Figure 7).

In general, all semilogaritmic plots of survival probability vs. ionization energy of the projectiles in question, log S_a *vs.* IE, can be described by the empirical equation

$$\log S_a = a - b \text{ (IE)} \tag{5}$$

with different values of parameters a and b for different surfaces and their temperature. The values of parameters a and b for the investigated surfaces, as determined from the described experiments, are summarized in Table 7. The form of equation (5) is consistent with the general expression for the resonant neutralization transition rate of ions at surfaces developed by Janev and Krstic [3].

The values of the parameters b (slopes) for the room-temperature surfaces are practically the same. This similarity is evidently caused by the hydrocarbon coverage of the surfaces. The quality of the underlying surface is presumably reflected in the absolute value of S_a. For the heated carbon (HOPG) surface, practically devoid of surface hydrocarbons, both values of a and b are different.

The rough correlation between the logarithm of the survival probability and the ionization energy of the projectile ion as described by empirical relation (5) can be used in estimating the survival probability of any ion of known ionization energy on the particular surface, characterized by the parameters a and b. Though the error in the estimation may be rather large, equation (5) provides a new, quick way of its estimation for the purpose of plasma modeling.

ACKNOWLEDGMENTS

REFERENCES

[1] RABALAIS, J.W., Low Energy Ion-Surface Interactions, J. Wiley, New York, 1994.

[2] HAGSTRUM, H.D., Theory of Auger Ejection of Electrons from Metals by Ions, Phys. Rev. **96** (1954) 336.

[3] JANEV, R.K., KRSTIC, P.S., Determination of chemical composition and charge state distribution of chemical erosion hydrocarbon fluxes, Phys. Scr. **T124** (2006) 96.

[4] ROITHOVÁ, J., ŽABKA, J., DOLEJŠEK, Z., HERMAN, Z., Collisions of Slow Polyatomic Ions with Surfaces: Dissociation and Chemical Reactions of CD_5^+, CD_4^+, CD_3^+, and Their Isotopic Variants on Room-Temperature and Heated Carbon Surfaces, J. Phys. Chem. B, **106** (2002) 8293.

[5] ŽABKA, J., DOLEJŠEK, Z., ROITHOVÁ, J., GRILL, V., MÄRK, T.D., HERMAN, Z., Energy partitioning in collisions of slow polyatomic ions with carbon surfaces, Int. J. Mass spectrom. **213** (2002) 145.

[6] JAŠÍK, J., Collisions of Slow Polyatomic Ions with Surfaces: Dissociation and Chemical Reactions of $C_2H_2^+$, $C_2H_3^+$, $C_2H_4^+$, $C_2H_5^+$, and Their Deuterated Variants $C_2D_2^+$ and $C_2H_4^+$ on Room-Temperature and Heated Carbon Surfaces, J. Phys. Chem. A **109** (2005) 10208.

[7] JAŠÍK, J., et al., Surface-induced dissociation and reactions of dications and cations: Collisions of dications $C_7H_8^{2+}$, $C_7H_7^{2+}$, $C_7H_6^{2+}$ and a comparison with the respective cations $C_7D_8^+$ and $C_7H_7^+$, Int. J. Mass Spectrom. **249-250** (2006) 162.

[8] PYSANENKO, A., ŽABKA, J., ZAPPA, F., MÄRK, T.D., HERMAN, Z. Scattering of very slow (3–10 eV) hydrocarbon ions CD^{3+}, CD^{4+}, and CD^{5+} from room-temperature carbon (HOPG) surfaces, Int. J. Mass Spectrom. **273** (2008) 35.

[9] KUBIŠTA, J., DOLEJŠEK, Z., HERMAN, Z., Energy partitioning in collisions of slow polyatomic ions with surfaces: ethanol molecular ions on stainless steel surfaces, Eur. Mass Spectrom. **4** (1998) 311.

[10] ŽABKA, J., DOLEJŠEK, Z., HERMAN, Z., Energy Partitioning in Collisions of Slow Polyatomic Ions with Surfaces: Ethanol Molecular Ions on Surfaces Covered by Self-Assembled Monolayers (CF-SAM, CH-SAM, COOH-SAM), J. Phys. Chem. A **106** (2002) 10861.

[11] HERMAN, Z., Collisions of slow polyatomic ions with surfaces: The scattering method and results, J. Am. Soc. Mass Spectrom. **14** (2003) 1360.

[12] PYSANENKO, A., ŽABKA, J., MÄRK, T.D., HERMAN, Z., Collisions of slow hydrocarbon ions CD^{4+}, CD^{5+}, C_2D^{4+}, and C_2H^{5+} with room temperature and heated tungsten surfaces, Int. J. Mass Spectrom **277** (2008) 229.

[13] PYSANENKO, A., ŽABKA, J., FEKETEOVA, L., MÄRK, T.D., HERMAN, Z., Collisions of slow ions C_3H^{n+} and C_3D^{n+} (n = 2–8) with room temperature carbon surfaces: mass spectra of product ions and the ion survival probability, Eur. J. Mass Spectrom **14** (2008) 335.

[14] HERMAN, Z., ŽABKA, J., PYSANENKO, A., Correlations between survival probabilities and ionization energies of slow ions colliding with room-temperature and heated surfaces of carbon, tungsten, and beryllium, J. Phys. Chem. **113** (2009) 14838.

[15] HERMAN, Z., MÄRK, T.D. Collicions of Hydrocarbon Ions of Energies 10-50 eV with Carbon Surfaces: Ion Survival, Dissociation, Chemical Reactions, Scattering, Data for molecular processes in edge plasmas, Atom. Plasma-Mater. Interact. Data Fusion **14** (2007).

[16] PYSANENKO, A., ŽABKA, J., HERMAN, Scattering of Low-Energy (5-12 eV) $C_2D_4^+$ Ions from Room-Temperature Carbon Surfaces, Z. Collect. Czech Chem. Commun. **73** (2008) 755.

[17] LIAS, S.G., et al., Gas Phase Ion and Neutral Thermochemistry, J. Phys. Chem. Ref. Data, **17** (1988), Supplement 1.

ANALYTIC REPRESENTATION OF CROSS-SECTIONS FOR ELECTRON-IMPACT DISSOCIATIVE EXCITATION AND IONIZATION OF CH$_y^+$ (y = 1 – 4) IONS

R.K. JANEV[1,2], D. HUMBERT[3], R.E.H.CLARK[3], J. LECOINTRE[4,5], P. DEFRANCE[5], D. REITER[2]

[1]Macedonian Academy of Sciences and Arts,
1000 Skopje, Macedonia

[2]Institute for Energy Research – Plasma Physics, Forschungszentrum Jülich GmbH,
EURATOM Association, Trilateral Euregio Cluster,
D-52425 Jülich, Germany

[3]International Atomic Energy Agency,
A-1400 Vienna, Austria

[4]Department of Chemistry, Durham University,
Durham DH1 3LE, United Kingdom

[5]Department of Physics (PAMO), Catholic University of Louvain,
B-1348 Louvain-la-Neuve, Belgium

Abstract

The available experimental cross-section data on electron-impact dissociative excitation and ionization processes of methane family hydrocarbon molecular ions have been evaluated and represented by three-parameter analytic fit functions appropriate for use in plasma modeling codes. The accuracy of the fit functions is well within the uncertainties of experimental data.

1. INTRODUCTION

The hydrocarbon molecules enter the boundary regions of magnetically confined fusion plasma as result of the plasma interaction with carbon-containing plasma facing materials (e.g. divertor plates) of the fusion device. The chemical erosion of these materials is the main source of hydrocarbon species in the boundary plasma. The abundance of hydrocarbons is particularly high in the divertor region of toroidal fusion machines where the plasma temperature may be in the range from ~ 50 eV down to a few eVs (near the divertor walls). The chemical composition of hydrocarbons can range from CH to C$_3$H$_8$, including their singly charged ions. Collision processes of hydrocarbon species with plasma electrons, protons and hydrogenic neutrals (also abundant in the divertor region) strongly affect their transport inside the plasma [1], including their redeposition on divertor walls (usually at sites far away from those of their release) [2].

Methane (CH$_4$) is one of the major components of chemical erosion fluxes entering the plasma under most temperature conditions of the edge (divertor) plasma. Methane may also be deliberately introduced in the divertor region for plasma diagnostic and hydrocarbon transport studies. The CH$_4$ molecule is rapidly dissociated to a variety of neutral fragments in collisions with plasma electrons, and ionized (also dissociatively) in collisions with electrons and protons (via electron capture in the latter case), leading to generation of the entire spectrum of hydrocarbons of the methane family (CH$_y$, y = 1 – 4) along with their ions. The resulting hydrocarbon ions, CH$_y^+$, are subject to further fragmentation by electron-impact dissociative excitation, dissociative ionization and dissociative recombination processes. Obviously, the modeling of the fragmentation patterns of the methane family of hydrocarbons requires knowledge of the cross-sections for all these processes [3].

142

The cross-section information on hydrocarbon collision processes with electrons and protons, available as of 2002, has been collected and critically assessed in Ref [4]. After completion of that data assessment, a significant amount of new experimental cross-section information has become available for the hydrocarbon species of methane family, the overwhelming part of which concerns the electron-impact dissociative excitation (DE) and dissociative ionization (DI) processes of hydrocarbon ions CH_y^+, $y = 1 - 4$,

$$e + CH_y^+ \rightarrow A^+ + neutrals + e, \qquad (DE) \qquad (1)$$

$$\rightarrow A^+ + B^+ + neutrals + 2e, \quad (DI) \qquad (2)$$
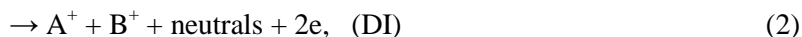
where A and B may be any of the constituents of CH_y^+. The DE process may occur by a direct transition to a dissociative excited state $CH_y^{+*(d)}$ (DDE), by a transition to a bound excited state $CH_y^{+*(b)}$ which is coupled by the nuclear kinetic energy operator with a dissociative excited state (predissociation, PDE),

$$e + CH_y^+ \rightarrow [CH_y^{+*(b)} \rightarrow CH_y^{+*(d)}] + e \rightarrow A^+ + neutrals + e, (PDE) \qquad (3)$$
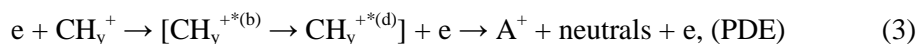
or by the resonant dissociative excitation (RDE) process

$$e + CH_y^+ \rightarrow (CH_y)^{**} \rightarrow A^+ + neutrals + e, \quad (RDE) \qquad (4)$$
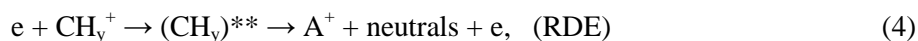
where $(CH_y)^{**}$ is a doubly excited autoionizing dissociative state. If the state $(CH_y)^{**}$ survives the autoionization region (lying above the potential energy surface of CH_y^+), then its dissociation leads to neutral products (dissociative recombination, DR). Normally, there is only one parent-ion excited state on which $(CH_y)^{**}$ is formed, implying that there is only one RDE channel, as opposed to the many possible DDE and PDE fragmentation channels.

The experimental measurements of electron-impact dissociative processes of CH_y^+ have been performed on storage rings [5,6] (for CH^+), [7] (for CH_2^+) and by using the crossed beams method at the Oak Ridge National Laboratory [8] (for CD_y^+, $y = 1 - 4$), [9] (for CH^+), [10] (for CH_2^+), [11] (for CH_3^+/CD_3^+) and at the Catholic University of Louvain [12-15] (for CD_y^+, $y = 1 - 4$). Deuterated hydrocarbon ions CD_y^+ have been studied in Refs. [8] and [12-15] in order to facilitate better collection of the light ion products D^+ and D_2^+ since the heavier fragments exhibit smaller energy spread. Isotopic effects in the DDE and DI cross-sections are not expected, but the RDE cross-section may show such an effect due to the mass dependence of the time the system spends in the autoionizing region, as observed in the DR cross-sections [16]. In all these experiments, the cross-sections for production of only one specific reaction product (ion or neutral) were measured; the observed cross-sections are therefore the sums of all possible DE and DI fragmentation channels producing that specific product. The observed products for which the total DE+DI cross-sections have been measured are given in Table 1, together with the incident electron energy range. We note, however, that in Refs. [12-15] the DI contribution to the total cross-section has been determined from the measured kinetic energy release (KER) distributions for a number of incident electron energies and from the knowledge of thermochemical dissociation energy limits for DI reaction channels.

It is important to note that in both the storage ring and crossed beam experiments the internal energy state of the target CH_y^+/CD_y^+ is not well specified. The hydrocarbon ions are known to have a number of long-lived metastable excited states above the ground state, which, even in the storage ring experiments, have not fully relaxed [5-7]. In the above mentioned crossed beams experiments the ions have been extracted from electron-cyclotron-resonance (ECR) sources with unknown temperature and, therefore, with an unknown level of vibrational excitation of their ground and possible metastable states in the interaction region. All this introduces significant differences in the measured cross-sections by different experimental groups which makes the comparison of observed cross-sections difficult, or even inappropriate. The difficulty of the interpretation of measured cross-sections comes

also from the lack of theoretical information about the potential energy surfaces of dissociative states of these ions and doubly excited states of their parent molecules (except for CH^+).

The objective of the present article is to analyze the currently available experimental information on dissociative processes of CH_y^+/CD_y^+ ions upon electron impact, to separate the DE and DI reaction channels to the extent currently possible (in view of the above mentioned lack of electronic structure information) and to present a selected set of DE and DI cross-sections, derived from the total DE+DI experimental ones, by a relatively simple analytic fit function appropriate for use in plasma application codes.

The analytic fit functions for DDE and DI reaction channels, the majority of which are believed to be mediated by dipole allowed transitions to certain dissociative state, are taken in Born-Bethe form, appropriately modified to describe the cross-section behaviour in the near-threshold region (we denote these functions F1-type fitting functions),

$$\sigma_{DDE,DI} = a\left(1 - \frac{E_{th}}{E}\right)^b \frac{1}{E} \ln\left(e + cE\right) \ (10^{-17} cm^2), \quad \text{(F1)} \tag{5}$$

where the electron energy, E, and the threshold energy, E_{th}, are expressed in eV units, $e = 2.71828\ldots$ is the base of natural logarithm and a, b, c are fitting parameters. The cross-sections for DE reaction channels mediated by an indirect mechanism (RDE or PDE) usually have a smaller threshold than the DDE reactions, a sharp increase after the threshold and fast decrease in the energy region beyond their maximum (due to their two-step character). We choose to describe the cross-sections of these indirect DE (IDE) channels by the fitting (type F2) functions of the form

$$\sigma_{IDE} = a\left(1 - \frac{E_{th}}{E}\right)^b \frac{1}{E^c} \ (10^{-17} cm^2). \quad \text{(F2)} \tag{6}$$

Although the analytic fit functions contain only three fitting parameters, they nevertheless represent the selected measured total cross-section data, well within their experimental uncertainties. The general accuracy of the fits is in the range 5-10%.

In the following sections we consider the DE and DI reaction channels for each target ion separately. In most of the experiments deuterated target ions were used and in the tables of reaction channels below we shall use the deuterated notation.

2. CH^+/CD^+ IONS

The dissociative excitation and ionization channels of CH^+/CD^+ ions upon electron impact are given in Table 2. In the same table the dissociation energy limits (for the ground states of target ion and dissociation products), D_0, for each channel, calculated using the NIST thermochemical tables [17], are also given, as well as the observed experimental threshold energies. For this diatomic hydrocarbon ion the potential energy curves of the lower bound and dissociative states are well known from quantum-chemistry calculations [18-20] and the theoretical thresholds for various dissociation channels (including excited products) are, therefore, also known and given in Table 2. This ion has a long-lived metastable state, $a^3\Pi$, lying 1.2 eV above the ground $X^1\Sigma^+$ state and may contaminate the CH^+/CD^+ ion beam. This circumstance, together with the possible vibrational excitation of ground-state CH^+/CD^+ beam ions, is reflected in the variety of experimentally observed threshold values for DE channels in Table 2 and their difference from theoretical ones. The small value of E_{th} (≈ 3 eV) for the C^++D DE channel observed in storage ring experiments indicates that the $a^3\Pi$ ions in the beam have been vibrationally excited. The observed E_{th} value (≈ 5 eV) for the D^++C DE channel in both storage ring [5] and crossed beams [12] experiments also indicates the presence of an $a^3\Pi$ metastable fraction, with the metastable ions vibrationally excited by 0.2 eV.

We should note that the threshold value of 5.1 eV for the D$^+$+C channel refers to the C atom in its ground ^{3}P state. The thresholds for production of excited C(^{1}D) and C(^{1}S) atoms in this fragmentation channel, calculated from the $a^3\Pi$ metastable state, are 5.3 eV and 7.0 eV, respectively. We finally note that the observed threshold value for the C$^+$+D$^+$ channel (22.1 eV) is consistent with the theoretical value of 22.9 eV for formation of the CD^{2+} ground state ion from the metastable state of CD$^+$ (see Table 2). This DI channel then results from the "Coulomb explosion" of the CD^{2+} ion formed by the CD$^+ \rightarrow$ CD^{2+}+e ionizing transition.

In Table 2 we include also the DI channel with C^{2+}+D products as the cross-section for production of C^{2+} has also been measured in Ref.[12]. The dissociation energy limit of this channel is 28.6 eV, about 1 eV below the observed threshold at 29.7 eV. The dissociation energy limit for the C^{2+}+D$^+$ dissociation would be 13.6 eV higher, far above the observed threshold for C^{2+} production. It is interesting to note that the Coulomb repulsive potential of C$^+$ and D$^+$ ions is just about 29 eV above the equilibrium distance of the CD$^+$ ground state ion. However, the mechanism of the process producing C^{2+}+D products is still unclear.

As mentioned in the introduction, all experiments measured the total particle (ion or neutral) production cross-sections (i.e. the sum of DE and DI). In the case of the CD$^+$ ion, however, the cross-section for the C$^+$+D$^+$ channel was also measured separately (albeit not by a coincident technique). This allows the determination of the DE channel cross-sections by subtracting the dissociative ionization from corresponding total ion production cross-section, since the contribution of the DI channel is the same in both C$^+$ and D$^+$ ion production cross-sections.

The cross-section for C$^+$ production of Ref.[12] has a threshold consistent with the theoretical value for the CD$^+$ ion in its ground state, and above ~15 eV it agrees with that of the storage ring experiment [6] in the overlapping energy range (up to 40 eV). On the other hand, the C$^+$ production cross-section of Ref.[9] at ~15 eV departs from the energy dependence of the other two measured cross-sections, reaching values that are lower by a factor 1.5 and 2 at 40 eV and 100 eV, respectively, with respect to the other two measurements. The cross-section for the C$^+$+D DE channel, obtained by subtracting the C$^+$+D$^+$ DI cross-section of Ref.[12] from the total C$^+$ production cross-section of the same source, has been fitted to the analytic function (5) and the fitting coefficients are given in Table 3.

In the case of D$^+$ ion production cross-section, the crossed beam data of Refs.[8] and [12] disagree markedly (by a factor of two) for energies above ~10 eV, those of Ref.[12] being smaller. On the other hand, the storage ring cross-section for production of C neutral (i.e. representing the D$^+$+C DE channel) of Ref.[5] agrees with the D$^+$ production cross-section of Ref.[8] (within their combined uncertainties) up to ~22-25 eV, where it starts to decrease with increasing energy, while that of Ref.[8] continues to increase due to the contribution of DI channel to the D$^+$ production. We note that the cross-section of Ref. [5] has its maximum at about 22 eV, exactly at the threshold of the DI channel (see Table 2). We have constructed the cross-section for the DE channel D$^+$+C by following the data of Ref.[5] up to 40 eV and extrapolating them further to 70 eV by the difference of the total DE + DI cross-section of Ref.[8] and DI cross-section of Ref. [12]. For energies above 70 eV, the cross-section already attains the Born-Bethe energy behaviour enshrined in Eq.(5). The coefficients of the analytic fit to this cross-section are given in Table 3 in the raw (A). In the raw (B) in the same table we give the values of fitting coefficients for the cross-section of this channel obtained when the C$^+$+D$^+$ DI cross-section is subtracted from the D$^+$ production cross-section of Ref.[12].

The coefficients of the analytic fits of the cross-sections for the C$^+$+D$^+$ and C^{2+}+D DI channels are also given in Table 3.

3. CH$_2^+$/CD$_2^+$ IONS

The dissociative reaction channels in e + CH$_2^+$/CD$_2^+$ collisions are shown in Table 4, together with the dissociation energy limits, D$_0$, and observed threshold energies. In the DI part of this table, the observed ion is the first listed. It should be mentioned that the CH$_2^+$ ion has a metastable a^4A$_2$ state

lying by 3.7 eV above the X^2A_1 ground state [21]. The D_0 values in Table 4 refer to the ground state of CH_2^+/CD_2^+ and of the products (except in the CD^{+*} +D case, where CD^{+*} is a metastable state).

The cross-sections for CH^+/CD^+ ion production of Refs.[10] and [13] show pronounced low-energy peaks with thresholds at about 3.5 eV and 4.5 eV, respectively, which, after the maximum (at about 8 eV), rapidly decrease. They are followed, however, by another smooth rise of the cross-section with an apparent threshold at 9.5 eV. The observed thresholds of these peaks are consistent with the thermochemical value of 4.48 for the $CD^+ + D$ channel with CD^+ being in its ground $X^1\Sigma^+$ state (and vibrationally excited in the case of Ref.[10] with the 3.5 eV threshold). It can be speculated that to the value of this peak some indirect DE mechanisms (PDE [10], or RDE [13]) might contribute. The second rise of the CD^+ production cross-section is most probably associated with the production of this ion in the $A^1\Pi$ and $b^3\Sigma^-$ excited states, when the D_0 values are 8.0 eV and 9.2 eV, respectively, (since with CD^+ in its metastable $a^3\Pi$ state D_0 would be 5.7 eV). It is also worthwhile to note that in Ref.[13] no signal was observed below 9.5eV for the C^+ production cross-section, while in Ref.[10] large values for this cross-section were observed down to ~3 eV (with an anticipated threshold around 1 eV). It has been argued in Ref.[10] that this part of the observed C^+ production cross-section could be due to an RDE mechanism. However, if the CH_2^+ target ion is assumed to be in its a^4A_2 state, then the D_0 value for this channel would be 0.6 eV. The threshold energies for the D^+ production cross-section in Refs.[7], [8] and [13] are close to each other and consistent with the D_0 values for the $D^+ + CD/(C+D)$ DE channels. We note that in Ref. [7] the production of $CD/(C+D)$ neutrals was measured so that the obtained cross-section represents the sum of $C^+ + CD$ and $C^+ + C + D$ DE channels. It is further worth noting in Table 4 that the thermochemical threshold for D_2^+ production is 11.18 eV, while the observed threshold is 7.0 eV. This indicates that the CD_2^+ ion beam contains a metastable (a^4A_2) fraction, even excited vibrationally by about 0.5 eV.

We now recall the fact that dissociative states of CD_y^{2+} energetically lie significantly above the excited dissociative states of CD_y^+. If for a given electron impact energy one measures the total kinetic energy spectra of released products, it is obvious that the products produced by the dissociative ionization will have total kinetic energy significantly higher than that of the products produced by dissociative excitation, i.e. they are separated on the energy scale of the products. Therefore, by measuring the kinetic energy release (KER) spectra associated with the production of a specific ion in the $e + CD^+$ collision, one can determine which part of the spectrum is due to the DE and which part of it is due to the DI processes. Moreover, since the KER spectrum for production of a specific ion at a given incident electron energy represents the differential cross-section for production of that ion in the collision, by integrating the DE and DI parts of the KER spectrum one can also determine the total DE and DI cross-section for that electron impact energy. While the threshold for the DE part of a specific ion production cross-section can be determined directly by the experiment, the threshold for the DI part can be determined from the thermochemical DI energy limit and the DI part of the KER spectrum. By using this procedure, the DE and DI components of the total ion production cross-section have been separated for all the singly charged ions that can be produced by dissociation of CD_y^+ (y = 2-4). Unfortunately, the number of electron impact energies for which the KER spectra have been measured was not very large (only 4 – 5) but this was found sufficient to adequately separate the DI component, σ_{DI}, from the total ion production cross-section, σ_{DE+DI}. The σ_{DE} component has then been obtained as the difference $\sigma_{DE} = \sigma_{DE+DI} - \sigma_{DI}$.

By applying this procedure for separation of the DE and DI contributions to the measured ion production cross-section, the determined σ_{DI} cross-section then represents a well defined DI reaction channel (with specified neutral products), only in a small number of cases. In most cases, particularly for the heavier CD_y^+ targets, σ_{DI} cross-sections include several channels that contain the measured ion. The σ_{DE} cross-sections, however, can be much better related to specific DE channels.

For the CD_2^+ target ion, such an analysis performed in Ref.[13] led to the DE and DI cross-sections listed in Table 5. In this table the coefficients of analytic fits of these cross-sections are given. As discussed earlier, the observed DE cross-section for CD^++D has contributions from two channels,

146

one associated with the ground state CD$^+$ ion (with threshold about 4.5 eV) and the other associated with production of CD$^+$ in its A$^1\Pi$ and $b^3\Sigma^-$ excited states (with threshold about 9.5 eV). The first contribution, well separated from the second one, was observed in both Refs.[10] and [13] and shows a sharp increase at the threshold and rapid decrease after its maximum around 8 eV. It has been fitted by the fit function F2, Eq.(6), using the data of Ref.[8]. We note that the maximum of this contribution in Ref.[10] is about two times larger than in Ref.[13]. For energies above 40 eV, the CD$^+$ ion production cross-sections of both Ref.[10] and Ref.[13] agree within their uncertainties.

The C$^+$ production cross-section of Ref.[13] has a threshold around 9.5 eV consistent with the thermochemical energy limit for the DE C$^+$+2D channel (see Table 4) increased by the observed mean KER. We believe that the large values of C$^+$ production cross-section (of about 5×10^{-17}cm^2) are due to the presence of a metastable (a^4A_2) in the CH$_2^+$ beam, absent in the experiment of Ref.[13]. Otherwise, a general physical mechanism, such as RDE, operating during the collision itself, would have to show itself in both experiments. At impact energies above ~25 eV, the C$^+$ production cross-sections of both experimental groups agree within their combined uncertainties, although for energies above 60 eV the data of Ref.[10] start to decrease while those of Ref.[13] continue to increase with increasing energy.

The D$^+$ production cross-section of Ref.[8] agrees well with the storage ring cross-section for production CD/(C+D) [7] performed up to 55 eV. As mentioned earlier, the cross-section of Ref. [7] represents the sum of the cross-sections for the DE channels D$^+$+CD and D$^+$+C+D. On the other hand, the D$^+$ production cross-section of Ref.[13], while showing approximately the same threshold as the other two cross-sections, starts to depart from them already at about 17 eV, and at 55 eV is about 35% smaller. Therefore, for the D$^+$+CD/(C+D) DE channels we have constructed a cross-section by using the data of Refs[7] up to 55 eV, the difference $\sigma_{DE+DI}([8]) - \sigma_{DI}([13])$ in the range $55 - 70$ eV, and for $E \geq 70$ eV we have extrapolated the obtained cross-section to obey the Born-Bethe high-energy behaviour. The coefficients of the analytic fit of this cross-section is given in Table 5 and labelled as (A). The fitting coefficients of the D$^+$+CD/(C+D) DE cross-section, obtained on the basis of the data of Ref.[13] are also given in Table 5, labelled as (B).

The DI cross-sections in Table 5 represent, in fact, the DI components of measured ion production cross-sections. The measured ion is the first listed one. Only in the cases of CD$^+$ and D$_2^+$ measured ions, is the other product known. As can be seen from Table 4, the DI component in the C$^+$ ion production cross-section is the sum of the cross-sections for D$_2^+$+C$^+$ and D$^+$+C$^+$+D DI channels, the first of which is known. From the difference $\sigma_{DI}(C^+ + ...) - \sigma_{DI}(D_2^+ + C^+)$ one can obtain the cross-section for the D$^+$+C$^+$+D DI channel. Similarly, $\sigma_{DI}(D^+....)$ represents the sum of the cross-sections for the CD$^+$+D$^+$, D$^+$+C$^+$+D and D$^+$+D$^+$+C DI channels. Since the cross-sections of the first two of these channels are already known, their sum subtracted from $\sigma_{DI}(D^+ + ...)$ will give the cross-section for the D$^+$+D$^+$+C DI channel. It is worth noting that the sum of DI cross-sections when CD$_x^+$ (x = 0,1) is the measured ion is equal to the sum of the DI cross-sections when D$_2^+$ and D$^+$ are the measured ions. In Refs. [12]-[15] this served as an additional criterion when determining the DI components of the total ion production cross-sections.

4. CH$_3^+$/CD$_3^+$ IONS

The dissociative excitation and ionization channel in e + CH$_3^+$/CD$_3^+$ collisions are shown in Table 6 together with the corresponding dissociation energies, D$_0$, and the observed energy thresholds. The values of D$_0$ have been calculated assuming that both the target ion and the dissociation products are in their ground states. The CD$_2^+$ ion production cross-sections of Refs. [14] and [11] show sharps peaks with onsets at 2.5 eV and 4.5 eV, respectively, significantly smaller than the dissociation energy limit of 5.41 eV for CD$_2^+$+D production. This indicates that either the CD$_3^+$ is vibrationally excited or in a metastable state, or else, the RDE mechanism is responsible for this part of the DE cross-section. The threshold value of 2.5 eV is consistent with the assumption that the ions beam contains a fraction of CD$_3^+$ ions in the $1^3A''$ metastable state that lies 3.56 eV above the ground state [22] and with the observed mean KER value of 0.5±0.1 eV [14]. The threshold value of 4.5 eV is consistent with the

assumption that CD_3^+ is vibrationally excited by about 1 eV. It is possible that the RDE mechanism also contributes to this part of the DE cross-section as the measured cross-section for the dissociative recombination of CH_3^+, competing with DE in the decay of CD_3^{**} doubly excited state, shows a sharp decrease just in the energy region $2 - 5$ eV [23]. Further, the CD_2^+ production cross-section of Ref.[14] exhibits a second rise at about 10 eV, indicating the opening of a new DE channel. This apparent threshold can be correlated with the formation of CD_2^+ in its a^4A_2 metastable state, possibly also vibrationally excited, which increases the D_0 value by the excitation energy ($= 3.7$ eV $+ E_{vib}$) of this state.

The observed threshold values for CD^+ ion production of ~6.2 eV [11]] and 7.0 eV [14] are consistent with the D_0 value for the CD^++D_2 DE channel and the observed mean KER of 1.5 ± 0.5 eV [14]. In the experiments of Ref.[14], the CD^+ product may also be vibrationally excited. The observed thresholds for C^+ production in Refs. [11] and [14] lie below the thermochemical dissociation limit 9.72 eV of the C^++D_2+D DE channel by 0.7 eV and 0.2 eV respectively, indicating that CD_3^+ ions must have been vibrationally excited in both experiments. The C^+ ion production cross-sections of both experiments show a sudden rise at about 15 eV, a clear indication of the opening of the C^++3D DE channel (see Table 6). The observed threshold for D_2^+ ion production (~11 eV) is consistent with the D_0 ($= 10.33$ eV) and mean KER ($= 1.3\pm0.1$ eV) values for the D_2^++CD DE channel, but in the case of D^+ ion production, the observed threshold (11.0 eV [8], 12.7 eV [14]) can be correlated with the small D_0 value of the D^++CD_2 DE channel (8.61 eV) only if it is assumed that the CD_2 product is formed in its a^4A_2 metastable state (possibly also vibrationally excited).

It should be noted that the CD_2^+ production cross-section of Ref. [11] is at least a factor of two smaller than that of Ref.[14] in the entire overlapping energy range (up to 100 eV). Its values in the energy region above ~40 eV are very close to the values of the DI cross-section of Ref.[14], which could be an indication that under the experimental conditions in Ref.[11] the DE channel $CD_2^+(a^4A_2)+D$ is not operative. We have, therefore, taken the data of Ref.[14] as a basis for our analytic fits and the fitting coefficients are given in Table 7.

The CD^+ and C^+ ion production cross-sections of Refs.[11] and [14] agree well in the overlapping energy range (up to 100 eV), with the exception of the low-energy peak of C^+ production cross-section which in Ref.[11] is about 50% higher than that of Ref.[14]. The coefficients of analytic fits for the DE and DI channel cross-sections, corresponding to the CD^+ and C^+ ion production cross-sections, are given in Table 7, with those for the C^++D_2+D channel determined from the data of Ref.[14] only.

In the case of D_2^+ and D^+ ion production cross-sections, the data of Ref.[8] and Ref.[14] differ significantly at energies above ~25 eV, those of Ref.[14] being smaller by 60-70%. Having in mind that in the case of CD^+ and CD_2^+ cases the D^+ ion production cross-sections in Ref [8] were in agreement with the storage ring data (in contrast to those of Refs.[12]and [13]), we have chosen to determine DE channel cross-sections corresponding to the D_2^+ and D^+ ion production by subtracting the pertinent DI cross-sections of Ref.[14] from the respective D_2^+ and D^+ ion production cross-section of Ref.[8] (up to 70 eV), and extrapolate them at energies above 70 eV to obey the Born-Bethe energy behaviour. The fitting coefficients of the DE cross-sections obtained in this manner are labelled by (A) in Table 7. The fitting coefficients for the cross-sections of the same DE channels, determined on the basis of the data of Ref.[14] alone are also given in Table 7 and labelled by (B).

The DI cross-sections in Table 7 represent the DI components of the total production cross-sections for the first listed ion (if more than one ion listed). The DI channel $CD^++D_2^+$ does not appear in this table because the sum of its D_0 value ($= 20.98$ eV, see Table 6) and the observed mean KER ($= 5.5$ eV, [14]) is below the estimated threshold of 29.2 eV. Similar considerations also eliminate the $C^++D^++D_2$ DI channel from the $\sigma_{DI}(C^+ +...)$ composite cross-section. With certain plausible assumptions on the contributions of DI channels in $\sigma_{DI}(C^+ +...)$ and $\sigma_{DI}(D_2^+ +...)$ composite cross-sections, one can achieve their complete decomposition, and thereby also the decomposition of the $\sigma_{DI}(D^+ +...)$ cross-section.

148

5. CH$_4^+$/CD$_4^+$ IONS

The complexity of CH$_4^+$/CD$_4^+$ target ions generates a large number of DE and DI reaction channels, shown in Table 8 together with their dissociation energies, D$_0$ (calculated under the assumption of ground states of the target ion and of the products). The observed threshold energies for a specific ion production and the estimated thresholds for the DI channels (taken from Ref.[15]) are also given in this table.

The observed ion production thresholds are consistent with the estimated thresholds (on the basis of D$_0$ values and the mean KER) for the DE channel with the smallest value of D$_0$ among those contributing to the same ion production cross-section. The exception is the DE channel D$^+$+CD$_3$, the estimated threshold for which is 6.6 eV (mean E$_{KER}$=1.2 eV [15]), while the observed one is 11.5 eV. This channel, therefore, does not contribute to the D$^+$ production cross-section. We also note that the observed thresholds for D$^+$ and D$_2^+$ production are consistent with those of Ref. [8]. We further note that some DI channels in Table 8, within a given ion production channel, do not contribute to the DI component of the corresponding ion production cross-section. This is the case, for instance with the CD$_2^+$+D$_2^+$ DI channel, where the estimated threshold 22.1 eV (mean E$_{KER}$ = 4,2 eV, [15]) lies significantly below the observed one (see table 8). For similar reasons, the DI channels CD$^+$+D$_2^+$+D and CD$^+$+D$^+$+D$_2$ do not contribute to the DI component of CD$^+$ ion production cross-sections, while the C$^+$+D$^+$+D$_2$+D and D$_2^+$+CD$_2^+$ DI channels do not contribute to the C$^+$ and D$_2^+$ ion production cross-sections, respectively.

In Table 9 we give the analytic fits of the cross-sections of decomposed DE and DI channels, except for the DI components of C$^+$, D$_2^+$ and D$^+$ ion production cross-sections. We note that apart from the 2.4 eV threshold, another apparent threshold is observed for the CD$_3^+$+D DE channel at about 17.5 eV (see Table 8). This may be related to the formation of the CD$_3^+$ ion in its excited ^{1}A$_2^{''}$ state which lies 17.4 eV above the ground state [24]. Therefore, the cross-section for this channel contains two components, both of which are shown in Table 9. We further note that the threshold of the first component (with E$_{th}$ = 2.4 eV) has an uncertainty of about ± 1 eV, because the lowest measured cross-section point is at the energy of 2.8 eV and its value is still very large, about 7×10^{-17}cm^2. It is possible that an indirect DE mechanism, with a threshold at much lower energy (perhaps below 1 eV), is contributing to this part of the cross-section, or that the CD$_4^+$ ion is significantly vibrationally excited. The low-energy part of the cross-section for this channel is best fitted by the analytic expression F2, Eq.(6).

The onsets and contributions of the CD$_2^+$+D$_2$ and CD$_2^+$+2D DE channels in CD$_2^+$ ion production cross-section are also well resolved in the experimental cross-section. The contribution of the CD$_2^+$+D$_2$ channel, however, shows a pronounced sharp peak at about 11 eV which may reflect a contribution from another channel in this energy region. The DE channels involving CD$_2^+$ and CD$^+$ ions are well separated and fitted individually (see Table 9), while the channels C$^+$+2D$_2$ and C$^+$+D$_2$+2D are jointly represented by one fit function. The DE components of D$_2^+$ and D$^+$ ion production cross-sections, given in Table 9, include all the DE channels listed in Table 8 for these ions, with the exception of the channel D$^+$+CD$_3$ for which the estimated threshold (6.6 eV, mean E$_{KER}$ = 1.2 eV, [15]) is considerably below the observed one (11.5 eV). For the inclusive D$_2^+$ and D$^+$ DE cross-sections, containing contributions from all the DE channels in which the D$_2^+$ and D$^+$ ions are respectively produced, two analytic fits are given in Table 9: one based on the data of Refs.[8] and [15], denoted by (A), and one based on the data of Ref.[15] only, represented by the sum of (B$_1$) and (B$_2$) fits of that table. The derivation of the cross-sections labelled by (A) for these two ions from the data of Refs.[8] and [15] has been done in the same way as in the case of CD$_3^+$, described in the previous section.

For the DI components of ion production cross-sections, only the specific DI channels for the CD$_3^+$, CD$_2^+$ and CD$^+$ ions could be clearly identified (see Table 9). For the C$^+$, D$_2^+$ and D$^+$ ions, the analytic fits in Table 9 give inclusive DI cross-sections for all the DI channels listed in Table 8 for

these ions, except for the channels $C^+ + D^+ + D_2 + D$ and $D_2^+ + CD_2^+$ that do not contribute to the corresponding inclusive cross-section for the reasons mentioned earlier.

6. CONCLUSIONS

In the present work we have analyzed the available experimental data for the dissociative excitation and ionization processes in electron collisions with the CH_y^+/CD_y^+ ($y = 1 - 4$) collisions. The storage ring data for the smaller hydrocarbons were found to be in good agreement with the crossed beams data. The ion production cross-sections from two experimental groups, Refs. [8-11] and Refs.[12-15] using crossed beams techniques are also found to agree (within their combined uncertainties) for the heavier product ions, but to disagree for the lighter ones, D_2^+ and D^+. These differences can be attributed to the differences in the ion source conditions that affect the internal energy state of extracted ions.

A complete separation of the contributions of DE and DI reaction channels to the total ion production cross-sections has been achieved for the CD^+ and CD_2^+ target ions, but for the CD_3^+ and CD_4^+ target ions this separation has been only partially achieved. The DE and DI channel (or group of channels) cross-sections, based on the ion production cross-section data of Refs.[8] and [12-15], have been fitted to three-parameter analytic functions having correct physical form both in the near-threshold and high-energy regions. The accuracy of the fits is in the range 5-10%, i.e. well within the experimental uncertainties of experimental data.

REFERENCES

[1]   STRAHAN, J.D., LIKONEN, J., COAD, P., et al., Modelling of carbon migration during JET ^{13}C injection experiments, Nucl. Fusion **48** (2008) 105002.
[2]   STANGEBY, P.C., et al., Measurements of the average energy of carbon atoms released from breakup of methane in the main SOL of DIII-D compared with DIVIMP code modelling, J. Nucl. Mater. **363-365** (2007) 201.
[3]   MATYASH, K. et al., Modeling of hydrocarbon species in ECR methane plasmas, J. Nucl. Mater. **313-316** (2003) 434.
[4]   JANEV, R.K., REITER, D., Collision processes of CH_y and CH_y^+ hydrocarbons with plasma electrons and protons Phys. Plasmas **9** (2002) 4071.
[5]   FORCK, P., PhD Thesis, Ruprecht-Karls-Universität Heidelberg, 1994.
[6]   AMITAY Z., et al., in Applications of Accelerators in Research and Industry, (DUGGAN, J.L., MORGAN, I.L.), AIP Press, New-York (1997) 51.
[7]   LARSON, Å., et al., Branching Fractions in Dissociative Recombination of CH_2^+, Astrophys. J. **505** (1998) 459.
[8]   DJURIĆ, N., ZHOU, S., DUNN, G.H., BANNISTER, M.E., Electron-impact dissociative excitation of CD_n^+ (n=2-5): Detection of light fragment ions D^+ and D_2^+, Phys. Rev. A **58** (1998) 304.
[9]   BANNISTER, M.E., et al., Electron-impact dissociation of CH^+ ions: Measurement of C^+ fragment ions, Phys. Rev. A **68** (2003) 042714.
[10]   VANE, C.R., BAHATI, E.M., BANNISTER, M.E., THOMAS, R.D., Electron-impact dissociation of CH_2^+ ions: Measurement of CH^+ and C^+ fragment ions, Phys. Rev. A **75** (2007) 052715.
[11]   BAHATI, E.M., et al., Electron-impact dissociation of CD_3^+ and CH_3^+ ions producing CD_2^+, CH^+, and C^+ fragment ions, Phys. Rev. A **79** (2009) 52703, see also: BANNISTER, M.E., SCHULTZ, D.R., this volume.
[12]   LECOINTRE, J., et al., Absolute cross-sections and kinetic energy release distributions for electron impact ionization and dissociation of CD^+, J. Phys. B: At. Mol. Opt. Phys. **40** (2007) 2201.
[13]   LECOINTRE, J., BELIC, D.S., JURETA, J.J., JANEV, R.K., DEFRANCE, P., Absolute cross-sections and kinetic-energy-release distributions for electron-impact ionization and dissociation of CD_2^+, Eur. Phys. J. D **55** (2009) 557, see also: DEFRANCE, P., et al., this volume.

[14] LECOINTRE, J., BELIC, D.S., JURETA, J.J., JANEV, R.K., DEFRANCE, P., Absolute cross-sections and kinetic-energy-release distributions for electron-impact ionization and dissociation of CD_3^+, Eur. Phys. J. D **55** (2009) 569; see also: DEFRANCE, P., et al., this volume.

[15] LECOINTRE, J., BELIC, D.S., JURETA, J.J., JANEV, R.K., DEFRANCE, P., Absolute cross-sections and kinetic energy release distributions for electron-impact ionization and dissociation of CD_4^+, Eur. Phys. J. D **50** (2008) 265.

[16] FLORESCU-MITCHELL, A.I., MITCHELL, J.B.H., Dissociative recombination, Phys. Rep. **430** (2006) 277.

[17] NIST Chemistry WebBook, http://webbook.nist.gov.

[18] LORQUET, A.J., Excited States of Gaseous Ions. II. Metastable Decomposition and Predissociation of the CH^+ Ion, J. Chem. Phys. **55** (1971) 4053.

[19] GREEN, S., et al., Calculated Potential-Energy Curves for CH^+, Phys. Rev. A **5** (1972) 1614.

[20] SAXON, R.P., LIU, B., Ab initio potential curve for the $b\,^3\Sigma^-$ state of CH+, J.Chem. Phys. **78** (1983) 1344.

[21] BRINKMANN, N.R., RICHARDSON, N.A., WESOLOWSKI, S.S., YAMAGUCHI, Y., SCHAEFER III, H.F., Characterization of the $\tilde{X}^2A_1$ and $\tilde{a}^4A_2$ electronic states of CH_2^+ Chem. Phys. Lett. **352** (2002) 505.

[22] XI, H.W., HUANG, M.-B., CHEN, B.-Z., LI, W.-Z., F-Loss and H-Loss Dissociations in Low-Lying Electronic States of the CH_3F^+ Ion Studied Using Multiconfiguration Second-Order Perturbation Theory, J. Phys. Chem. A **109** (2005) 9149.

[23] VEJBY-CHRISTENSEN, L., ANDERSEN, L.H., HEBER, O., KELLA, D., PEDERSEN, H.B., Complete Branching Ratios for the Dissociative Recombination of H_2O^+, H_3O^+, and CH_3^+, Astrophys. J. **483** (1997) 531.

[24] BLINT, R.J., MARSHALL, R.F., WATSON, W.D., Calculations of the lower electronic states of CH^{3+} - A postulated intermediate in interstellar reactions, Astrophys. J. **206** (1976) 627.

TABLE 1. MEASURED PARTICLE (ION OR NEUTRAL) PRODUCTION CROSS-SECTIONS IN DISSOCIATIVE ELECTRON – CH_y^+/CD_y^+ COLLISIONS

Ion	Ref.	Method	Measured product	Energy region	Accuracy
CH^+/CD^+	[5]	SR*	C,C$^+$,D	≤ 40 eV	50%
	[6]	SR	C$^+$	≤ 40 eV	50%
	[8]	CB**	D$^+$	≤ 70 eV	$\pm$ 15%
	[9]	CB	C$^+$	≤ 100 eV	$\pm$ (10-25)%
	[12]	CB	D$^+$,C$^+$	≤ 2500 eV	$\pm$ (15-25)%
CH_2^+/CD_2^+	[7]	SR	CH	≤ 55 eV	$\pm$ 25%
	[8]	CB	D$^+$	≤ 70 eV	$\pm$ 15%
	[10]	CB	CH$^+$,C$^+$	≤ 100 eV	$\pm$ (10-25)%
	[13]	CB	CD$^+$,C$^+$,D$_2^+$,D$^+$	≤ 2500 eV	$\pm$ 15%
CH_3^+/CD_3^+	[8]	CB	D$_2^+$,D$^+$	≤ 70 eV	$\pm$ 15%
	[11]	CB	CD$_2^+$,CH$^+$,C$^+$	≤ 100 eV	$\pm$ (10-50)%
	[14]	CB	CD$_2^+$,CH$^+$,C$^+$,D$_2^+$,D$^+$	≤ 2500 eV	$\pm$ 15%
CD_4^+	[8]	CB	D$_2^+$,D$^+$	≤ 70 eV	$\pm$ (10-15)%
	[15]	CB	CD$_3^+$,CD$_2^+$,CD$^+$,C$^+$,D$_2^+$,D$^+$	≤ 2500 eV	$\pm$ (10-15)%

    * Storage ring experiment
    ** Crossed beams experiment

TABLE 2. DISSOCIATIVE REACTION CHANNELS IN e+CH$^+$/CD$^+$ COLLISIONS, DISSOCIATION ENERGY LIMITS (D$_o$) AND OBSERVED (E_{th}^{obs}) AND THEORETICAL (E_{th}^{theor}) THRESHOLDS

Type of process	Reaction channel*	D$_o$(eV)	E_{th}^{obs} (eV)	E_{th}^{theor} (eV)
DE	C$^+$+D	4.17	3.0 [6,9] 5.5 [12]	5.6 (4.4)#
	D$^+$+C	6.51	5.0 [5] 5.1 [12] ~4.0 [8]	6.5 (5.3)
DI	C$^+$+D$^+$	17.77	22.1 [12]	24.1 (22.9)
	C^{2+}+D	28.6	29.7 [12]	–

    * Written for CD$^+$ only.
    # The values in parentheses are calculated from the $a^3\Pi$ metastable level.

TABLE 3. VALUES OF COEFFICIENTS a, b, c IN THE FITTING FUNCTION F1, EQ.(5), FOR DE AND DI CROSS-SECTIONS IN e+CH$^+$/CD$^+$ COLLISIONS

Type of process	Reaction products[*]	E_{th}(eV)	a	b	c	Data source
DE	C$^+$+D	5.5	586.0	3.0	0.07	[12]
	(A) D$^+$+C	5.1	267.5	2.5	0.9	[5,8,12]
	(B)	5.1	88.0	2.4	0.85	[12]
DI	C$^+$+D$^+$	22.1	550.0	1.8	0.04	[12]
	C^{2+}+D	29.7	56.6	1.9	0.51	[12]

* Written for CD$^+$ only.

TABLE 4. DISSOCIATIVE REACTION CHANNELS IN e+ CH$_2^+$/CD$_2^+$ COLLISIONS, DISSOCIATION ENERGY LIMITS, (D$_o$) AND OBSERVED THRESHOLDS (E$_{th}$)

Type of process	Reaction channels[*]	D_o(eV)	E_{th}(eV)
DE	CD$^+$+D	4.48	4.5 [13], 3.5 [10]
	CD^{+*}+D	8.0(A$^1\Pi$) 9.2(b$^3\sum^-$)	9.5 [13]
	C$^+$+D$_2$	4.31	<3.0 [10]
	C$^+$+2D	8.85	9.5 [13]
	D$_2^+$+C	11.18	7.0 [13]
	D$^+$+CD	8.47	8.8 [8, 13]
	D$^+$+C+D	7.63	10 [7]
DI	CD$^+$+D$^+$	18.08	25 [13]
	C$^+$+D$_2^+$	19.73	25.5 [13]
	C$^+$+D$^+$+D	22.44	
	D$_2^+$+C$^+$	19.79	26.0 [13]
	D$^+$+D$^+$+C	24.79	23.0 [13]
	D$^+$+ C$^+$+D	22.44	

* Written for CD$_2^+$ only.

TABLE 5. VALUES OF COEFFICIENTS a, b, c IN THE FITTING FUNCTIONS (5) (F1) AND (6) (F2) FOR DE AND DI CHANNEL CROSS-SECTIONS IN $e+CH_2^+/CD_2^+$ COLLISIONS

Type of process	Reaction products[*]	E_{th}(eV)	a	b	c	Fitting function	Data source
DE	CD^++D	4.5	3.55×10^6	3.92	5.0	F2	[13]
	$CD^{+*}+D$	9.5	187.0	2.38	0.037	F1	[13]
	C^++2D	9.5	285.0	2.59	0.043	F1	[13]
	D_2^++C	7.0	3.26	1.19	0.53	F1	[13]
	$D^++CD/C+D$	9.0	1260.0	2.912	7.37×10^{-3}	F1 (A)	[7,8,13]
		8.8	509.0	2.26	0.033	F1 (B)	[13]
DI	CD^++D^+	25.0	143.0	2.60	0.94	F1	[13]
	$C^++…$	25.5	119.0	3.57	0.86	F1	[13]
	$D_2^++C^+$	26.0	4.70	2.90	0.55	F1	[13]
	$D^++…$	23.0	454.0	2.24	0.15	F1	[13]

[*] Written for CD_2^+ only.

TABLE 6. DISSOCIATIVE REACTION CHANNELS IN e+ CH_3^+/CD_3^+ COLLISIONS, DISSOCIATION ENERGY LIMITS (D_0) AND OBSERVED THRESHOLDS (E_{th})

Type of process	Reaction channels[*]	D_o(eV)	E_{th}(eV)
DE	CD_2^++D	5.41	2.5 [14], 4.5 [11], (10) [14]
	CD^++D_2	5.55	6.2 [11], 7.0 [14]
	CD^++2D	10.09	
	C^++D_2+D	9.72	9.0 [11], 9.5 [14] (15.0) [14]
	C^++3D	14.27	
	D_2^++CD	10.33	11.0 [8,14]
	D_2^++C+D	13.88	
	D^++CD_2	8.61	11.0 [8], 12.7 [14]
	D^++C+D_2	12.05	
	D^++CD+D	13.04	
	D^++C+2D	16.59	
DI	CD_2^++D^+	19.01	25.5 [14]
	CD^++D_2^+	20.98	29.2 [14]
	CD^++D^++D	23.69	
	C^++D_2^++D	25.15	29.4 [14]
	C^++D^++D_2	23.32	
	C^++D^++2D	27.87	
	D_2^++D^++C	27.48	28.0 [14]
	D^++D^++CD	26.64	24.6 [14]
	D^++D^++C+D	30.19	

* Written for CD_3^+ only.

TABLE 7. VALUES OF COEFFICIENTS a, b, c IN THE FITTING FUNCTIONS (5) (F1) AND (6) (F2) FOR DE AND DI CHANNEL CROSS-SECTIONS IN e+CH_3^+/CD_3^+ COLLISIONS

Type of process	Reaction products[*]	E_{th}(eV)	a	b	c	Fitting function	Data source
DE	CD_2^++D	2.5	$8.90×10^3$	5.30	2.29	F2	[14]
		10.0	762	5.48	0.038	F1	[14]
	CD^++D_2/2D	7.0	275.0	2.20	0.001	F1	[11,14]
	C^++D_2+D	9.5	71.8	2.05	0.01	F1	[14]
	C^++3D	15.0	34.3	1.99	0.25	F1	[11,14]
	D_2^++CD/C+D	11.3	100.0	1.994	$4.9×10^{-3}$	F1(A)	[8,14]
		11.0	59.9	2.01	0.012	F1(B)	[14]
	D^++C+D_2/2D	11.0	1076.0	2.902	$5.60×10^{-3}$	F1(A)	[8,14]
	D^++CD+D	12.7	459.0	1.69	0.009	F1(B)	[14]
DI	CD_2^++D^+	25.5	187.0	1.55	0.76	F1	[14]
	CD^++D^++D	29.2	194.0	2.22	0.85	F1	[14]
	C^++…	29.4	78.8	2.31	0.88	F1	[14]
	D_2^++…	28.0	27.1	3.23	0.74	F1	[14]
	D^++…	24.6	460.0	2.50	0.86	F1	[14]

* Written for CD_3^+ target ion only.

156

TABLE 8. DISSOCIATIVE REACTION CHANNELS IN e+ CH_4^+/CD_4^+ COLLISIONS, DISSOCIATION ENERGY LIMITS (D_0) AND OBSERVED THRESHOLDS (E_{th})

Type of process	Reaction channels[*]	D_o(eV)	E_{th}(eV) [15]
DE	$CD_3^+ + D$	1.62	2.4 (17.5)
	$CD_2^+ + D_2$	2.49	3.7
	$CD_2^+ + 2D$	7.03	(8.2)
	$CD^+ + D_2 + D$	7.07	8.0
	$CD^+ + 3D$	11.7	(12.5)
	$C^+ + D_2 + D_2$	6.79	7.5
	$C^+ + D_2 + 2D$	11.34	
	$C^+ + 4D$	15.88	(16.5)
	$D_2^+ + CD_2$	7.93	9.5
	$D_2^+ + C + D_2$	10.96	
	$D_2^+ + CD + D$	10.49	
	$D_2^+ + C + 2D$	15.5	
	$D^+ + CD_3$	5.37	11.5
	$D^+ + CD_2 + D$	10.22	
	$D^+ + CD + D_2$	10.12	
	$D^+ + CD + 2D$	14.67	
	$D^+ + C + D + D_2$	13.67	
DI	$CD_3^+ + D^+$	15.22	19.2
	$CD_2^+ + D_2^+$	17.92	24.7
	$CD_2^+ + D^+ + D$	20.63	
	$CD^+ + D^+ + D_2$	20.79	29.0
	$CD^+ + D_2^+ + D$	22.50	
	$CD^+ + D^+ + 2D$	25.31	
	$C^+ + D_2^+ + 2D$	26.77	30.0
	$C^+ + D^+ + D_2 + D$	24.94	
	$C^+ + D^+ + 3D$	29.48	
	$D_2^+ + CD_2^+$	17.91	28.5
	$D_2^+ + C^+ + D_2$	22.22	
	$D_2^+ + C^+ + 2D$	26.76	
	$D_2^+ + D_2^+ + C$	24.39	
	$D_2^+ + D^+ + CD$	25.55	
	$D_2^+ + D^+ + C + D$	29.08	

TABLE 8. (CONT'D.)

Type of process	Reaction channels*	D_o(eV)	E_{th}(eV) [15]
DI	$D^+ + CD_2^+ + D$	20.79	26.5
	$D^+ + D^+ + CD_2$	23.82	
	$D^+ + D_2^+ + CD$	25.55	
	$D^+ + CD^+ + 2D$	25.31	
	$D^+ + C^+ + D + D_2$	24.93	
	$D^+ + D^+ + C + D_2$	27.26	

* Written for CD_4^+ only.

TABLE 9. VALUES OF COEFFICIENTS a, b, c IN THE FITTING FUNCTIONS (5) (F1) AND (6) (F2) FOR DE AND DI CHANNEL CROSS-SECTIONS IN $E+CD_4^+$ COLLISIONS

Type of process	Reaction products	E_{th}(eV	a	b	c	Fitting function	Data source
DE	$CD_3^+ + D$	2.4	3.54×10^4	4.55	3.0	F2	[15]
		17.5	335.0	1.23	0.074	F1	[15]
	$CD_2^+ + D_2$	3.7	212.0	2.77	0.001	F1	[15]
	$CD_2^+ + 2D$	8.2	400.0	7.38	0.013	F1	[15]
	$CD^+ + D_2 + D$	8.0	406.0	2.07	0.01	F1	[15]
	$CD^+ + 3D$	12.5	188.0	7.31	0.23	F1	[15]
	$C^+ + 2D_2$	7.5	157.0	2.60	0.01	F1	[15]
	$C^+ + 4D$	16.5	93.2	4.43	0.13	F1	[15]
	$D_2^+ + \ldots$	9.5	213.7	2.907	3.75×10^{-5}	F1(A)	[8,15]
		9.3	1.40×10^6	5.36	3.53	F2(B_1)	[15][§]
		17.0	156.0	3.95	0.006	F1(B_2)	[15][§]
	$D^+ + \ldots$	9.0	1795.8	3.6905	3.33×10^{-5}	F1(A)	[8,15]
		11.5	463	2.37	0.005	F1(B)	[15]
DI	$CD_3^+ + D^+$	19.2	131.0	3.07	1.05	F1	[15]
	$CD_2^+ + D^+ + D$	24.7	71.0	1.95	0.90	F1	[15]
	$CD^+ + D^+ + 2D$	29.0	106.0	2.46	0.52	F1	[15]
	$C_2^+ + \ldots$	30.0	28.0	1.68	0.85	F1	[15]
	$D_2^+ + \ldots$	28.5	26.0	1.47	0.94	F1	[15]
	$D^+ + \ldots$	26.5	368.0	2.46	0.50	F1	[15]

§ The total $\sigma_{DE}(D_2^+)$ cross-section in Ref. [15] is B_1+B_2.

DISSOCIATIVE RECOMBINATION OF HYDROCARBON MOLECULAR IONS AND BeH$^+$

M. LARSSON

Department of Physics, AlbaNova University Center,
Stockholm University, SE-10691 Stockholm, Sweden

Abstract

The dissociative recombination of hydrocarbon molecular ions with electrons has been studied in the ion storage ring CRYRING at Stockholm University. Absolute dissociative recombination cross-sections and recombination end products (branching ratios) have been measured, and from the measured cross-sections thermal rate constants have been obtained. Most of the data have been obtained for ions of type $C_xH_y{}^+$ ($x \leq 4$), which are the most relevant for the divertor and edge plasmas in fusion devices. An attempt has been made to find trends in the measured end products. The dissociative recombination cross-section of BeH$^+$ was calculated by ab initio methods. Because of the toxicity of Be, no experimental study of this ion has been performed with respect to its recombination cross-section.

1. INTRODUCTION

In thermonuclear fusion reactors with highly exposed carbon-based divertor plate segments of the vacuum chamber, C_xH_y hydrocarbons are released into the plasma. These hydrocarbon molecules are ionized and dissociated, leading to the formation of a broad range of hydrocarbon molecular ions (Janev & Reiter 2002, 2004). Low-energy electrons present in the plasma will dissociatively recombine with the hydrocarbon molecular ions, which leads to the formation of neutral atoms, molecules and free radicals:

$$C_xH_y{}^+ + e \rightarrow \text{neutral atoms, molecules and free radicals} \qquad (1)$$
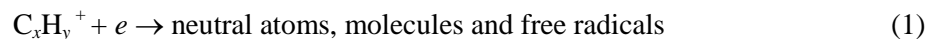
In order to accurately modelling the divertor and edge plasmas, the cross-sections, rate constants, and product branching ratios for the dissociative recombination process are required. Ab initio calculations of these quantities for hydrocarbon molecular ions are presently impracticable, and statistical methods are too unreliable, leaving experimental measurements as the only option. Whereas rate constants, in addition to being extracted from measured cross-sections, can be measured in plasma afterglow experiments (Mitchell & Rebrion-Rowe 1997, Florescu-Mitchell & Mitchell 2006), product branching ratios for hydrocarbon molecular ions are obtained in merged-beam ion storage ring experiments (Viggiano et al. 2005). The data presented in this article were obtained at the ion storage ring CRYRING, which is located at the Manne Siegbahn Laboratory, an accelerator laboratory at Stockholm University.

Beryllium is a possible candidate as plasma facing material in ITER because of its low erosion and atomic number. Hence the collisional properties of hydrides formed by the chemical bonding of Be- and H-atoms are relevant to study. However, because of the toxicity of beryllium, experiment with Be-containing molecules are rare. Dissociative recombination of BeH$^+$ has never been studied experimentally, and, more surprisingly, not theoretically either. This gap has now been filled and the calculation will be reported here (Roos et al. 2009).

A definitive review theory, experiment and applications of dissociative recombination was recently published by the present author and Ann Orel (Larsson & Orel 2008).

2. EXPERIMENTS

The cross-section for dissociative recombination is approximately proportional to the inverse of the electron energy. Applying beams of electrons and ions to induce collisions, the merged-beam configuration is clearly the best since it gives access to very low-energy collisions. In this geometry the beams are superimposed at an angle of 0^0. A comprehensive review of the application of merged beams appeared ten years ago (Phaneuf et al. 1999).

In the experiments used to study the hydrocarbon molecular ions the beams of ions electrons are merged in one straight section of the ion storage ring CRYRING. Figure 1 show a layout of the ion storage ring facility CRYRING.
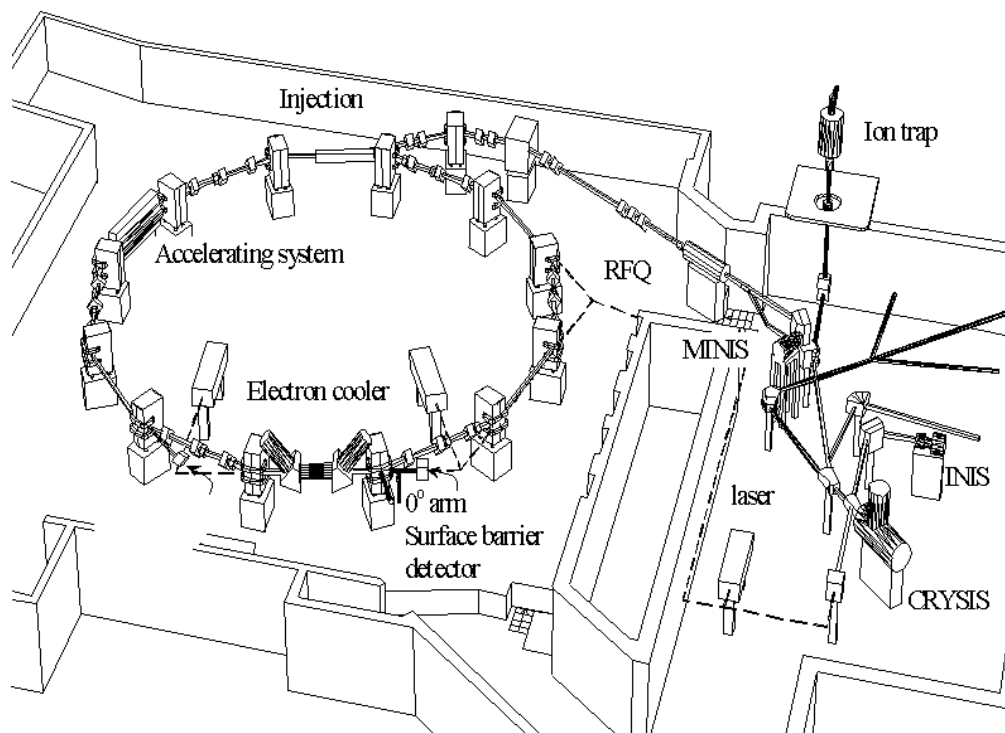
FIG. 1. Schematic view of CRYRING. Molecular ions are created in the ion source MINIS, accelerated and mass selected. In some cases they are further accelerated by the Radio Frequency Quadrupole (RFQ), and injected into the ring. The interaction region, i.e. the region in the electron cooler where the ion and electron beams are merged, is 85 cm. The ring is 52 m in circumference and its vacuum system kept at a pressure below 10^{-11} torr.

The molecular ions are produced in the ion source labelled MINIS in Figure 1, which is a hot filament Penning discharge source. The appriopriate chemical is fed into the ion source, where electrons present in the plasma will ionize and sometimes dissociate the parent molecules that molecular ions are formed. The ion source is kept at a platform voltage of 40 kV, so that the ions have a total energy of 40 keV when they are exctrated from the source. A magnetic mass selector is positioned just after the ion source, and serves the important task of selecting the correct ions from the source. Typical currents after mass selection fall in the nA to μA range. The section that follows the analyzing magnet, labelled RFQ, does not serve any purpose for the relatively heavy hydrocarbon ions; for ions with a charge-to-mass ratio larger than or equal to 0.25 the RFQ can act as an accelerator device, but few molecular ions fall in this category.

160

The injection phase is the next critical phase. In CRYRING multiturn injection is applied, which involves a the application of a time-dependent deformation of the main orbit in the ring, so that several orbits are stored side by side until the horizontal acceptance of the ring is filled (very much like winding a thread on a spool). Once the ring has been filled it is important to increase the beam energy promptly. The beam energy is 40 keV when the ring has been filled and this energy is by far too low to be useful for experiments. The accelerating system, occupying one straight section of the CRYRING, as shown in Figure 1, increases the beam energy in about one second to the maximum energy that the dipole magnets can keep in closed orbits. This is set by the magnetic rigidity, which is a product of the maximum magnetic field of the dipole magnets (1.2 T) and the radius of curvature (1.2 m). Having a magnetic rigidity of 1.44 Tm, the maximum beam energy for a singly charged ion in CRYRING is $96/A$ MeV, where A is the ion mass given in atomic mass units.

Having reached its maximum energy in about a second, the ion beam is then left to freely circulate in the ring for a few seconds. During this time the ions undergo vibrational and rotational relaxation by emission of infrared radiation. In principle the ions can also be phase-space cooled by the electron beam in the electron cooler device in Figure 1, but for the purpose of the experiments described here the electron cooling is not of critical importance. After a few to ten seconds, the data taking starts; neutral particles produced by dissocitive recombination and by collisions with residual gas molecules present in the electron-ion interaction. The particles are detected by an ion-implanted silicon crystal surface barrier detector. Figure 2 shows a pulse height spectrum recorded by such detector in an experiment with $^{13}CO^+$.

An energetic particle impinging on the surface barrier detector gives rise to a pulse with a height proportional to the amount of kinetic energy carried by the particle. In Figure 2 the peak at 3.4 MeV (i.e., corresponding to the full beam energy) derives from dissociative recombination of $^{13}CO^+$, which results in two atoms (C-atom and O-atom) arriving essentially simultaneous to the detector. Neutralizing collisions with residual gas molecules also leads to C+O-atoms or stable CO-molecules, but the contribution from this background is small at 3.4 MeV. The response time of the detector is too slow to make a distinction between the arrival of two separate atoms or a molecule. The pulse height spectrum in Figure 2 was recorded when the ion and electron beams had matching velocities, where the cross-section has a maximum. (Strictly speaking, it is the rate constant in the electron cooler which has a maximum at zero relative velocity.) By changing the relative velocity between the ions and electrons, a broad range of collsion energies (E) is accessed:

$$E = (E_i - E_e)^{1/2} \qquad (2)$$

where E_i is the ion beam energy and E_e is the electron beam energy. Figure 3 is an illustration of the raw data coming from such measurement.

In order to reduce the raw data shown in Figure 3 to an absolute cross-section, the number of ions and electrons present in the interaction region and the overlap factor (form factor) must be known. The electron beam is larger than the ion beam and approximately homogeneous, which reduces the form factor trivially to the area of the electron beam (Larsson & Orel 2008). The rate of interaction in the merged beam section can then be expressed as:

$$R = \frac{v_r \sigma n_e I_i l}{e v_i} \qquad (3)$$

where v_r is the relative velocity between electrons and ions, v_i is the ion velocity, I_i is the ion current, σ is the cross-section, n_e is the electron density, and l is the length of the interaction region. The ion current makes the sternest demand on the experimentalist since the current of a circulating beam must be measured. This is done with an ac transformer (Paal et al. 2003), which can meaure circulating beams of a few nanoamperes. Figure 4 show the cross-section obtained from the raw data in Figure 3. The uncertainty in the length of the interaction region is about 10%, the uncertainty in the electron current, and hence electron density, is about 2%, whereas the uncertainty in the ion current depends on

the number of stored ions. Typical values are 5-10%, but it can also be larger. This gives total systematic uncertainties of about 15−20%.
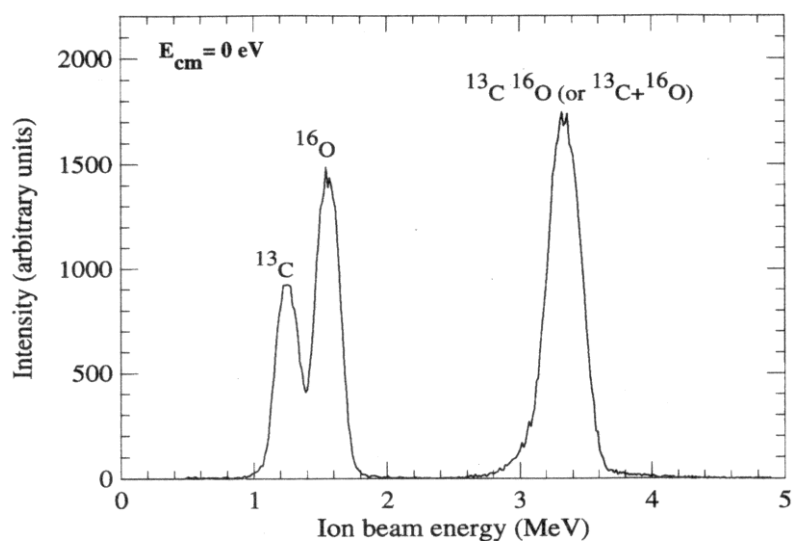
FIG. 2. Pulse height spectrum taken recorded at CRYRING in a study of $^{13}CO+$. The C and O peaks derive from collisions of CO+ with residual gas molecules, whereas the peak at C + O is totally dominated (>95%) by dissociative recombination events. It occurs at an energy corresponding to the full beam energy of 3.4 MeV (reprinted from Rosén et al. 1998).
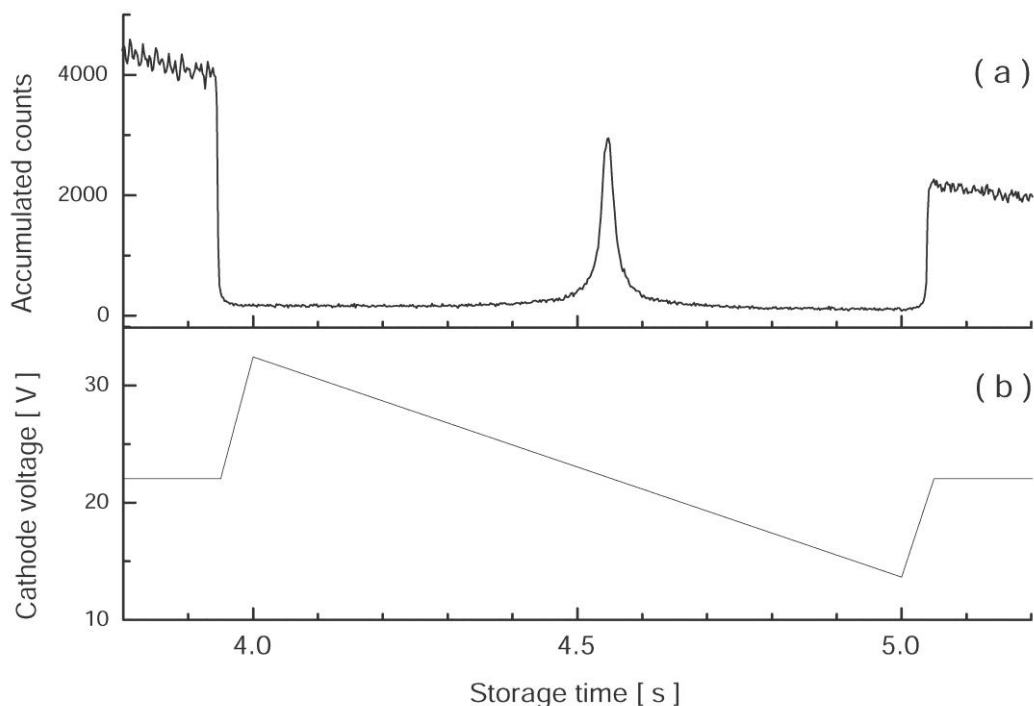
FIG. 3. Measurement of the dissociative recombination cross-section of $C_4D_2^+$. (a) The total number of counts in the pulse height spectrum peak corresponding to mass 76 amu (C_4D_2) from the surface barrier detetector accumulated over 1020 injection cycles. (b) The electron gun cathode voltage as a funtion of time during the cross-section measurement. When the cathode voltage is set at 22 V, the electron beam velocity matches that of the ion beam (reprinted from Danielsson et al. 2008).

162

$$7.5 \cdot 10^{-16} \cdot E^{-1.29}$$
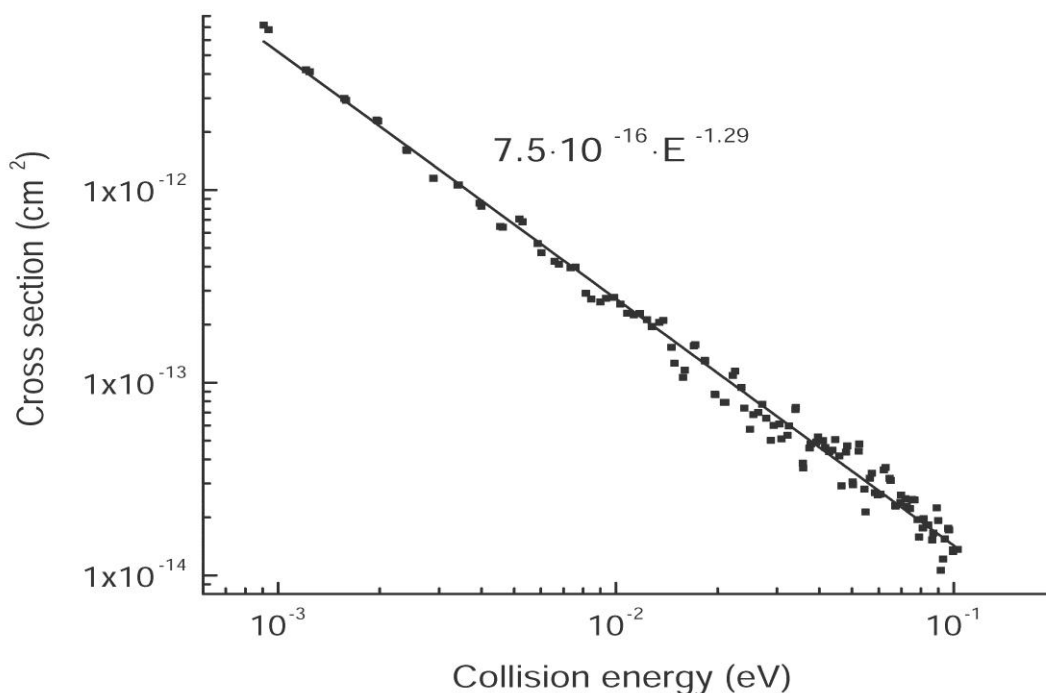
FIG. 4. The energy-dependent cross-section of the dissociative recombination of the diacetylene cation $C_4D_2^+$. The straight line gives the the fit of the cross-section between 1 and 100 meV collision energy (reprinted from Danielsson et al. 2008).

The inability of the surface barrier detector to discriminating between different combinations of particles arriving simultaneously makes it impracticable to use the detector alone for the determination of dissociative recombination end products. Instead a grid technique has been developed, which allows the separation of the different decay channels in the recombination of polyatomic ions (Larsson & Thomas 2001). If a grid with a known transmission (a stainless steal plate with a large number of small holes) is inserted in front of the surface barrier detector when dissociative recombination of the generic molecule ABC$^+$ is studied, the grid will block some recombination products while others will go through one of the holes and hit the detector. For example, if A is blocked and BC hits the detector for the reaction channel A + BC, a pulse will occur at $(m_{BC}/m_{ABC}) \times$ (full beam energy). If the grid transmission is labeled T, the probability for the combination A blocked *and* BC transmitted is $T(1-T)$. The decay channel A + B + C can also make a contribution to the pulse, but for this to happen, two independent particles, B and C, must go through holes while A is blocked. The probability for this is $T^2(1-T)$. The relative contribution to the $(m_{BC}/m_{ABC}) \times$ (full beam energy) pulse will depend on the branching ratios for A + BC and A + B + C. The argument can be generalized to all peaks in the pulse height spectrum, and the complete branching ratios can be obtained by relating the branching ratios to the measured pulse height spectrum via the transmission probabilities (Larsson & Thomas 2001, Larsson & Orel 2008).

The measurements of product branching ratios are ususally done at $E = 0$ eV, where the cross-section for recombination peaks.

3. THEORY

Only one theoretical project was carried out, namely a theoretical study of the dissociative recombination of BeH^+. The potential energy curves of the electronic states relevant for dissociative recombination of BeH^+ were determined by combining structure calculations with electron scattering calculations. For the structure calculations, the Multi-Reference Configuration Interaction (MRCI) technique was used to determine the neutral electronically bound adiabatic states situated below the potential energy curve of the ground state ($X\ ^1\Sigma^+$) of the BeH^+ ion. In a quasidiabatic representation, some of these neutral states will cross the ionic ground state and become resonant states, i.e., they will couple to the ionization continuum and have a finite probability for autoionization. In order to determine the energies and autoionization widths of the resonant states, the Complex Kohn Variational method (Rescigno et al. 1995) was used. In order to obtain the quasidiabatic potentials, the scattering data is combined with a diabatization procedure of the electronically bound states. Finally, the calculated potential energy curves, autoionization widths and electronic couplings between the neutral states can be used in order to carry out calculations on the nuclear dynamics.

The adiabatic potential energy curve of the BeH^+ ground state ($X\ ^1\Sigma^+$) as well as several excited states of BeH of $^2\Sigma^+$, $^2\Pi$, and $^2\Delta$ symmetries were calculated using the MRCI technique. For both the structure and scattering calculations, natural orbitals were used. The natural orbitals were determined using a MRCI calculation on the BeH+ ground state. In this calculation, the reference space consisted of the $1\sigma,\ 2\sigma,\ 3\sigma,\ 1\pi,\ 4\sigma$ orbitals and single and double excitations from the reference configurations into the virtual orbitals were included. The natural orbitals were calculated using a basis set for the H atom of $(4s,1p)$ contracted to $[3s,1p]$, while for Be, a basis set of $(10s,6p,1d)$ contracted into $[3s,3p,1d]$ was used. The natural orbitals were then further expanded with diffuse orbitals in order to accurately describe the Rydberg character of some of the electronic states. The H-orbitals are augmented with $(2s,2p,1d)$ orbitals, and the Be-orbitals with $(4s,1p,1d)$.

The MRCI calculations on the ionic and neutral excited electronic states were carried out using a reference space consisting of the $1\sigma,\ 2\sigma,\ 3\sigma,\ 1\pi,\ 4\sigma,\ 5\sigma$ orbitals. These natural orbitals all have an occupation number greater than approximatly 0.002.

Figure 5 shows the adiabatic potential energy curves of neutral BeH situated below the ionic ground state.

4. RESULTS

4.1. Product branching ratios, cross-sections and rate constants

The following ions were studied experimentally during the contract period: $C_3H_4^+$ (Geppert et al. 2004), $C_3D_7^+$, $C_4D_9^+$ (Larsson et al. 2005), $C_4D_2^+$ (Danielsson et al. 2008), D_2H^+ (Zhaunerchyk et al. 2008). The D_2H^+ isotopolog of H_3^+ was included in this report since it is of relevance in fusion research. The results agree well with the results from the TSR in Heidelberg (Lammich et al. 2003), but less well with theoretical results (Kokoouline & Greene 2005) for reasons that are not known.

The detailed results are given in Table 1. Here it is also pertinent to identify trends in the results.

Viggiano et al. (2005) considered the complete product distributions for the dissociative recombination of $C_2H_n^+$ ($n = 1-5$). They considered the enthalpy changes, ΔH, in the exothermic recombination processes and looked for correlations between single H atom loss and C−C cleavage, and the branching ratios for these channels. Figure 6 shows the result of this analysis.
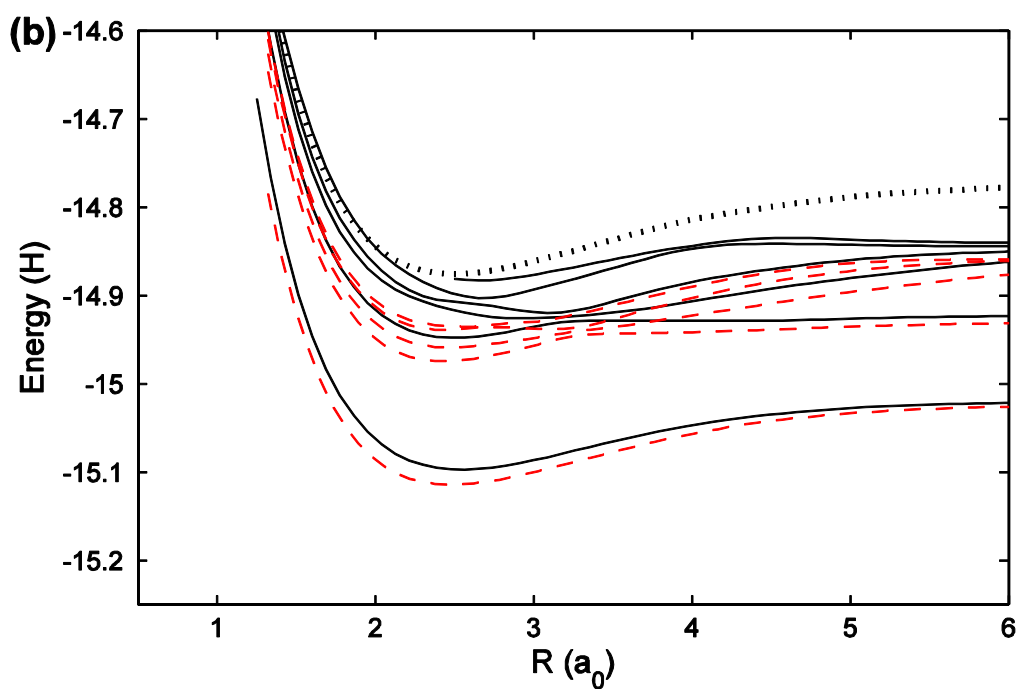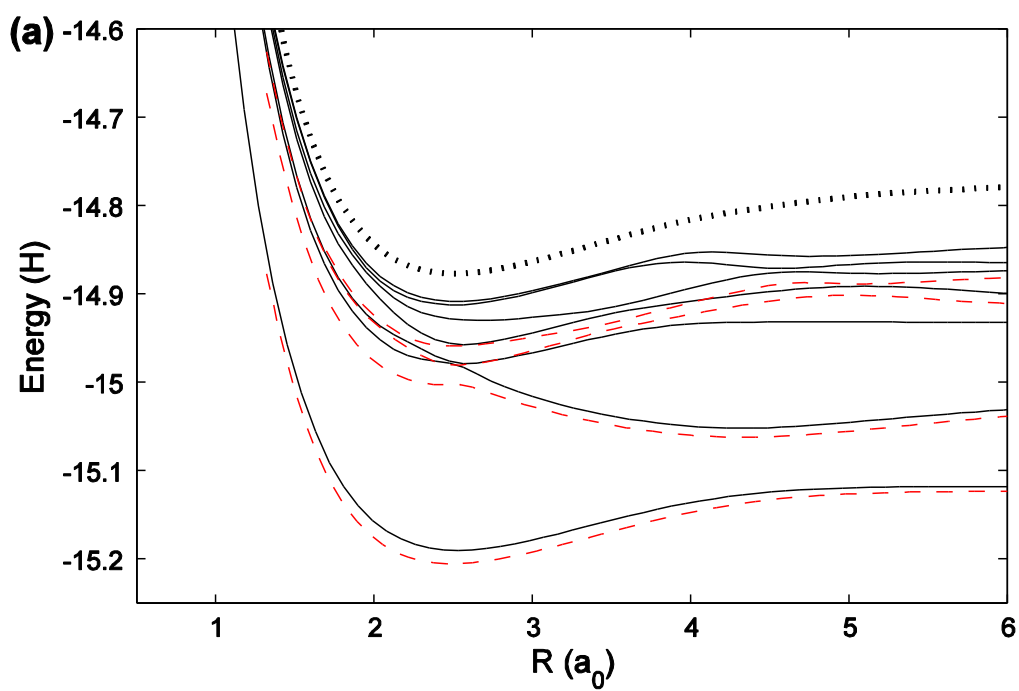
FIG. 5. Adiabatic potential energy curves of BeH of (a) $^2\Sigma^+$ symmetry, and (b) $^2\Pi$ symmetry. The black dotted curve is the ground state (X $^1\Sigma^+$) of the BeH$^+$ ion. The black full curves are the potentials calculated here, while the dashed (red) curves are potentials calculated by Pitarch-Ruiz et al. (2008). (Reprinted from Roos et al. 2009)
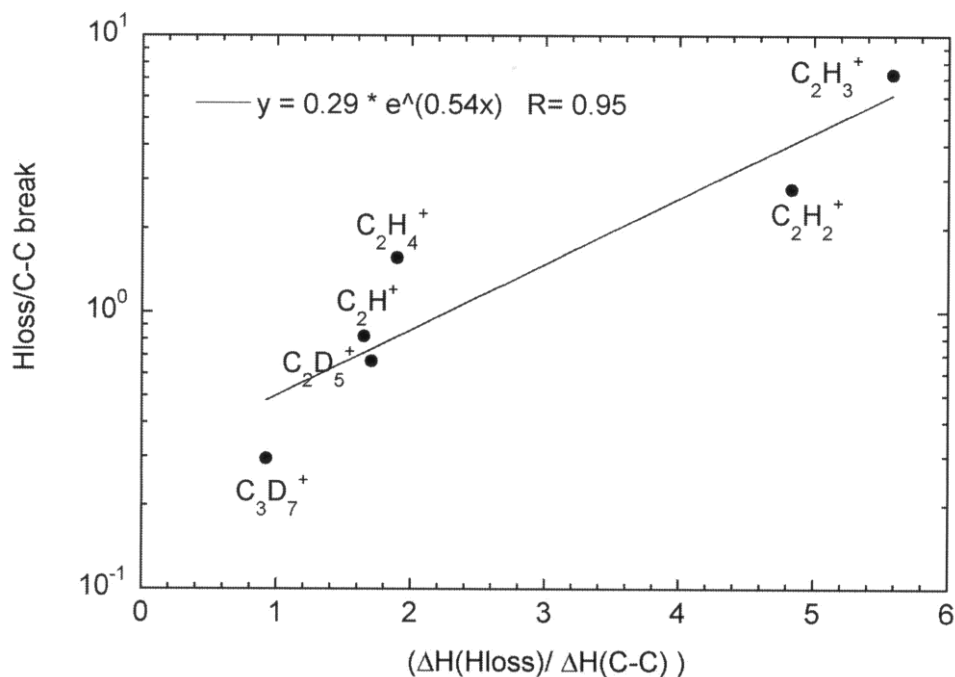
FIG. 6. The ratio of the branching ratio for single H-atom loss to that of C–C cleavage vs. the exothermicities for the two processes. The exothermicity for C–C cleavage is the one involving no rearrangement or H-atom loss. The branching ratio for the C–C cleavage, however, is the one obtained by summation of all C–C bond breaking channels. (Reproduced from Viggiano et al. 2005)

Dissociative recombination of $C_4D_2^+$ leads to 75% $C_4D + D$ and 25% $C_2D + C_2D$, which together with a enthalpy ratio of 1.75 gives a point in fairly good agreement with the straight line in Figure 6. The resolution was not sufficient to do the same analysis for $C_4D_9^+$, but for $C_3H_4^+$ it is clear that the correlation is very weak. Whereas the enthalpy ratio is close to unity, the end products $C_3H_3 + H$ completely dominates (88%), which gives a point far from the line. The reason for this is unknown and shows that this enthalpy based analysis does not always work.

The product branching ratios measured in this project and given in Table 1 can be compared with the estimates listed by Janev and Reiter (2004). The agreement for $C_3H_4^+$ is not good since the measured value for the H-atom extraction is 0.88 (Geppert et al. 2004) whereas 0.30 is listed by Janev and Reiter. Their estimated branching ratio for the $C_3H_2 + H + H$ is 0.55 whereas the measured value is less than 0.05. Since $C_3H_4^+$ did not fit well with the line in Figure 6, the difficulty in estimating the branching ratios is not surprising. The estimate is somewhat better for $C_3H_7^+$ (the experiment was done for $C_3D_7^+$); the dominant channel $C_3H_5 + H + H$ was estimated by Janev and Reiter (2004) to be 0.55 and measured by Larsson et al. (2005) to be 0.22. C_4H_x ions were not included in the compilations by Janev and Reiter (2004), and there are no other estimates to compare the results measured by Danielsson et al. (2008) and Larsson et al. (2005) with.

4.2. Results for BeH$^+$

The cross-sections for the dissociative recombination of BeH$^+$ and BeD$^+$ were calculated with a wave packet technique and are shown in Figure 7. The oscillations are due to the electronic couplings between the different neutral states shown in Figure 5 that drive the recombination process.

166
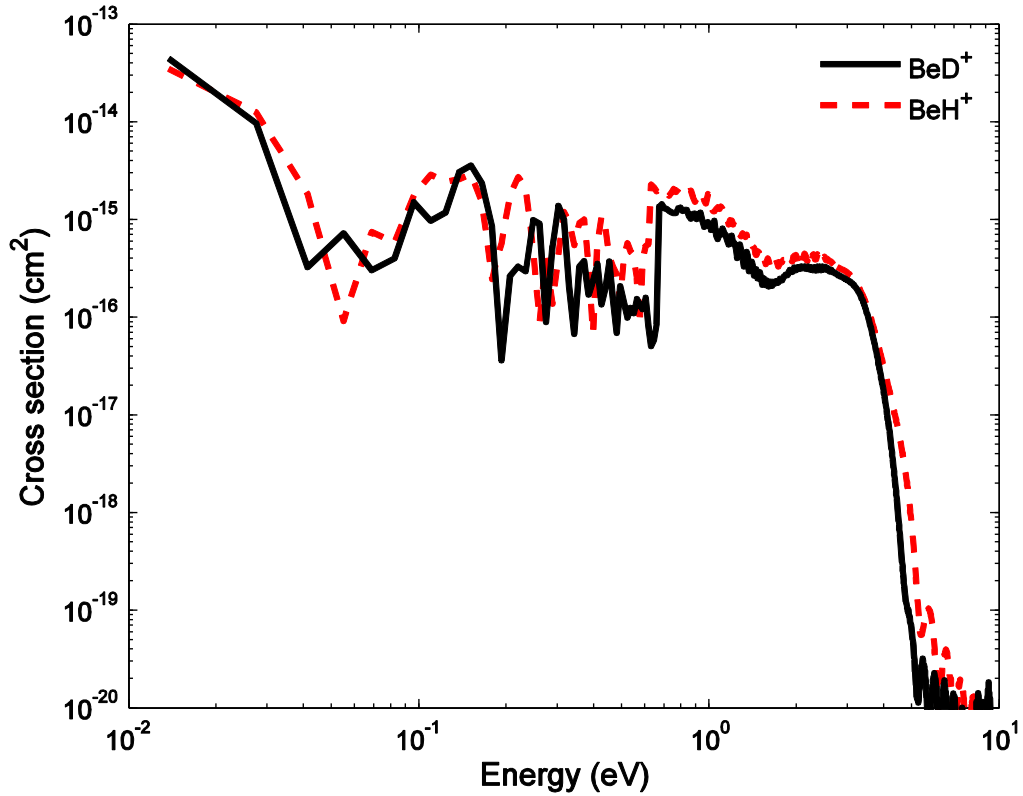
FIG. 7. Total cross-section for dissociative recombination of BeH$^+$ and BeD$^+$ in their lowest vibrational levels (v = 0). (Reproduced from Roos et al. 2009)

To simplify the use of the calculated cross-sections in modelling of the fusion plasmas, the cross-sections have been fitted to analytical forms. The cross-sections calculated using uncoupled potentials (no oscillations) have been used for the fitting. These cross-sections show a smooth energy dependence at collision energies below about 0.3 eV that easily can be fitted to functions of the form

$$\sigma(E) = \frac{\sigma_0}{E^b} \tag{4}$$

The parameters for BeH$^+$ and BeD$^+$ in both $v = 0$ and 1 are given in Table 2. It is clear that in the absence of the resonances, which do not make much of a contribution to the absolute level of the cross-section, the cross-sections have a close to $1/E$ variation.

TABLE 1. BRANCHING RATIOS AND CROSS-SECTIONS FOR POLYATOMIC IONS MEASURED IN CRYRING[1]

Ion	Branching ratio	Cross-section $\sigma(E)$ (in cm^2) and rate constant $k(T)$ (in cm^{3}s^{-1})	Reference
$C_3H_4^+$	C_3H_3 + H 0.87 C_3H_2 + H_2 $\leq$0.02 C_2H_3 + CH 0.01 C_2H_2 + CH_2 0.06 C_2H + CH_3 0.01 C_3H_2 + 2H $\leq$0.05	$\sigma(E) = 5.5 \times 10^{-15} \times E^{-1.01}$ $k(T) = 2.95 \times 10^{-6} \times (T/300)^{-0.67}$	Geppert et al. 2004
$C_4D_2^+$	C_4D + D 0.75 C_2D + C_2D 0.25	$\sigma(E) = 7.5 \times 10^{-16} \times E^{-1.29}$ $k(T) = 1.10 \times 10^{-6} \times (T/300)^{-0.79}$	Danielsson et al. 2008
C_3D_7	C_3D_6 + D 0.13 C_3D_5 + D_2 0.12 C_3D_5 + D + D 0.22 C_3D_4 + D_2 + D 0.09 C_2D_4 + CD_3 0.03 C_2D_3 + CD_4 0.02 C_2D_3 + CD_3 + D 0.15 C_2D_2 + CD_4 + D 0.03 C_2D_2 + CD_3 + D_2 0.21 Total C−C breaking: 0.44	$k(T) = 2.3 \times 10^{-7} \times (T/300)^{-0.73}$	Larsson et al. 2005
$C_4D_9^+$	C_3D_7 + CD_2 0.39 C−C preserved 0.61	$k(T) = 5.8 \times 10^{-7} \times (T/300)^{-0.59}$	Larsson et al. 2005
D_2H^+	D + D + H 0.76 D_2 + H 0.10 DH + D 0.14	$k(T = 300 \text{ K}) = 9 \times 10^{-7}$	Zhaurenchyk et al. 2008[2]

TABLE 2. PARAMETERS FOR THE FITTED FORM OF THE DISSOCIATIVE RECOMBINATION CROSS-SECTIONS AT LOW COLLISION ENERGIES

Ion	Vibrational level	$\sigma_0(10^{-16}$ cm$^2 \times eV^b)$	b
BeH^+	$v = 0$	3.10	0.99
BeH^+	$v = 1$	6.90	0.93
BeD^+	$v = 0$	3.32	1.02
BeD^+	$v = 1$	4.72	1.05

---

[1] The detailed error bars are given in the original articles, but left out here for space reasons.
[2] The same rate constant was deduced from the cross-section obtained by Lammich et al.

5. CONCLUSIONS

In this report we have reviewed work on hydrocarbon ions, D_2H^+ and BeH^+, which has been part of the Coordinated Research Project "Atomic and Molecular Data for Plasma Processing". The experimental work was carried out at the ion storage ring CRYING in Stockholm.

Product branching ratios for the dissociative recombination of hydrocarbon ions with electrons must be measured experimentally. Theoretical methods cannot yet handle systems of this complexity. The attempts by Viggiano et al. (2005) to find trends in the recombination end products, and the procedure by Janev and Reiter (2004) to make extrapolations are useful but cannot replace experiments.

The experimental results for D_2H^+ are completely consistent (Lammich et al. 2003, Zhaurenchyk et al. 2008), but do not agree with theoretical calculations (Kokoouline & Greene 2005). Since there is good agreement between experiment and theory for the other isotopologs (see Larsson & Orel 2008), this disagreement remains unexplained.

The results for BeH^+ and BeD^+ are new, there are no previous experimental or theoretical efforts to obtain the dissociative recombination cross-section for these ions.

ACKNOWLEDGEMENT

REFERENCES

[1]   DANIELSSON, M., et al., The cross-section and branching fractions for dissociative recombination of the diacetylene cation $C_4D_2^+$, Int. J. Mass Spectrom **273** (2008) 111.
[2]   FLORESCU-MITCHELL, A.I., MITCHELL, J.B.H., Dissociative recombination, Phys. Rep. **430** (2006) 277.
[3]   GEPPERT, W.D., THOMAS, R., EHLERDING, A., et al., Dissociative recombination of $C_3H_4^+$: preferential formation of the C_3H_3 radical, Int. J. Mass Spectrom. **237** (2004) 25.
[4]   JANEV, R.K., REITER, D., Collision processes of CH_y and CH_y^+ hydrocarbons with plasma electron and protons, Phys. Plasma **9** (2002) 4071−4081.
[5]   JANEV, R.K., REITER, D., Collision processes of $C_{2,3}H_y$ and $C_{2,3}H_y^+$ hydrocarbons with plasma electron and protons, Phys. Plasma **11** (2004) 780.
[6]   KOKOOULINE, V., GREENE, C.H., Theoretical study of C_{2v} triatomic ions: Application to H_2D^+ and D_2H^+, Phys. Rev. A **72** (2005) 022712.
[7]   LAMMICH, L., et al., Evidence for subthermal rotational populations in stored molecular ions through state-dependent dissociative recombination, Phys. Rev. Lett. **91** (2003)143201.
[8]   LARSSON, M., OREL, A.E., Dissociative Recombination of Molecular Ions, Cambridge University Press, Cambridge (2008) 380.
[9]   LARSSON, M., THOMAS, R., Three-body reaction dynamics in electron−ion dissociative recombination, Phys. Chem. Chem. Phys. **3** (2001) 4471.
[10]   LARSSON, M., et al., Rate constant and branching ratios for the dissociative recombination of $C_3D_7^+$ and $C_4D_9^+$, J. Chem. Phys. **122** (2005)156101.
[11]   MITCHELL, J.B.A., REBRION-ROWE, C., The recombination of electrons with complex molecular ions, Int. Rev. Phys. Chem. **16** (1997).
[12]   PAAL, A., SIMONSSON, A., KÄLLBERG, A., DIETRICH, J., MOHOS, I., "Current measurements of low-intensity beams at CRYRING", DIPAC 2003 Proceedings, Mainz, Germany (2003) 240.
[13]   PHANEUF, R.A., HAVENER, C.C., DUNN, G.H., MÜLLER, A. Merged-beams experiments in atomic and molecular physics, Rep. Prog. Phys. **62** (1999) 1143.

[14] PITARCH-RUIZ, J., SÁNCHEZ-MARIN, J., VELASCO, A.M., MARTIN, I., Full configuration interaction calculation of BeH adiabatic states, J. Chem. Phys. **129** (2008) 054310.

[15] RESCIGNO, T.N., MCCURDY, C.W., OREL, A.E. & LENGSFIELD, B.H., "The Complex Kohn variational method", in Computational Methods for Electron Molecule Collisions, (HUO, W.M., GIANTURCO, W.M., Eds.) Plenum: New York (1995) 1.

[16] ROSÉN, S., et al. Absolute cross-sections and final state distributions for dissociative recombination and excitation of CO^+ (v=0) using an ion storage ring, Phys. Rev. A **57** (1998) 4462.

[17] VIGGIANO, A.A., EHLERDING, A., ARNOLD, S.T., LARSSON, M., Dissociative recombination of hydrocarbon ions, J. Phys.: Conf. Ser. **4** (2005) 191−197.

[18] ZHAUNERCHYK, V., Dissociative recombination of D_2H^+ at the storage ring CRYRING, Phys. Rev. A **77** (2008) 034701.

ELECTRON IMPACT IONIZATION OF THE EDGE PLASMA CONSTITUENTS: PARTIAL CROSS-SECTIONS

D. KUBALA, J. KOČÍŠEK, S. DENIFL[1], F. ZAPPA[1], S. MATEJČÍK

Department of Experimental Physics, Comenius University Bratislava,
Mlynska dolina F2, 84248 Bratislava, Slovakia

[1]Permanent address: Institut für Ionenphysik, Leopold Franzens Universität,
 Technikerstr. 25,A-6020, Innsbruck, Austria

Abstract

The partial cross-section for positive ions formed via electron impact ionization (EII) to methane (CH_3D and CD_4), deuterated ethane (C_2D_6) and propane (C_3H_8) have been measured in a crossed electron/neutral beams apparatus with mass spectrometric analysis of the ions. The partial cross-sections of the ions formed via electron impact ionization to these molecules were determined at low temperature (approximately 300 K and 370 K in the case of propane) and at elevated temperature (approximately 700 K). Gas temperature induced differences in the partial cross-sections have been observed. Additionally, the effect of the isotopic composition of a molecules on the partial cross-sections for EII have been observed.

1. INTRODUCTION

Cross-section data for collision processes involving electron impact with small hydrocarbons are necessary for understanding and modelling plasma in the diverter region of the fusion reactor in the case of carbon facing components (e.g., Janev [1, 2, 3]). For this purpose it is essential to possess detailed quantitative data which characterise the elementary processes in the plasma (ionization energies, cross-sections, reaction rate coefficients etc). Due to the relatively low temperature in the plasma edge the plasma contains (in addition to electrons and atomic ions) also a significant amount of molecules and radicals as impurities [2,3] which are released due to chemical erosion caused by plasma-wall interaction. In the case of carbon covered surfaces, these molecules are small hydrocarbons C_xH_y (e.g. CH_4, C_2H_6, C_2H_4, C_2H_2, C_3H_8, and C_3H_6).

This paper presents a summary of the experimental studies of electron impact ionization (EII) reactions to selected hydrocarbon molecules (CD_4, CH_3D, C_2D_6 and C_3H_8) carried out at Comenius University in Bratislava. The partial cross-sections for electron impact ionization (1) and dissociative electron impact ionization (2) reactions:

$$e + M \rightarrow M^+ + 2e \qquad (1)$$

$$e + M \rightarrow (M\text{-}X)^+ + 2e \qquad (2)$$

have been measured as a function of the electron energy. The experiments have been carried out using crossed beams apparatus equipped with high resolutions electron beam source. The partial cross-sections for EII were measured at two different gas temperatures. The aim of the work was to study the influence of the gas temperature on the partial cross-sections for EII. Additionally we were also interested on the influence of the isotopic composition of the molecules on the kinetic parameters of the electron impact ionization of the molecules.

So far there exist only very little knowledge about the temperature dependence of the EII reactions. In our former studies [4,5,6] we have investigated the influence of the gas temperature on the values of the ionization energies of the molecules and the values of the appearance energies of fragment positive ions. It has been shown that with increasing gas temperature the ionization energies of the molecules and the appearance energies of the molecules slightly decreases due to increase of the internal rotational and vibrational energy of the molecules. Additionally to the temperature studies we

have measured also isotopic effects in the case of the ionization and appearance energies of selected molecules. In the monograph edited by Märk and Dunn [7] only few remarks on temperature dependence of the EII partial cross-sections are made and the situation has not improved since then.

2. EXPERIMENTAL SETUP

The experimental setup used for the present measurements consists of a crossed electron/molecule beams apparatus combined with a quadrupole mass spectrometer. A schematic view of the setup is shown in Figure 1. More detailed description can be found in [8]. The molecular beam is formed in a temperature controlled effusive molecular beam source (EMBS) which can be heated resistively up to 700 K. The molecules leaving the EMBS are in the thermal equilibrium with the walls of the EMBS, i.e., the molecules effusing from the EMBS through a hole with 0.5 mm have the same temperature as the EMBS. The neutral molecules interact in the reaction region of the trochoidal electron monochromator (TEM) with the electrons. The maximum electron energy resolution of the TEM is about 30 meV, however, in the present measurements we have worked with the energy resolution of 140 meV in order to achieve higher electron current and thus higher detection efficiency of the apparatus. The ions formed in the reaction region are extracted into a quadrupole mass spectrometer (QMS) by a weak electric field and collected by a secondary electron multiplier. Using this method the ion efficiency curves for selected ions were measured as a function of the electron energy. It must be noted that using this technique the doubly charged fragment cations appearing on even masses may be also formed but they cannot be distinguished from singly charged fragments appearing at the same mass by the mass spectroscopic technique.

The electron energy scale was calibrated using the ionization threshold of argon (15.76 eV) [9] measured under same conditions as the measured molecules. For the determination of the threshold energy a fitting procedure based on the Wannier threshold law [10] was used. The calibration of the partial cross-sections has been carried out using neon and argon as a calibration gases. Neon as a calibration gas has been chosen due the mass of the atom which is close to the mass of the CD_4 and CH_3D and C_2D_6 thus is more suitable for calibration than argon. In the present experiment we estimate a relative accuracy of the cross-sections of about 30%.

The absolute pressure in the molecular beam source was measured using a MKS Baratron capacitance manometer. The ion yields for fragment ions formed upon electron impact ionization of propane could be then transformed into an absolute cross-section scale. In the case of CH_3D and C_2D_6, this was done by measuring the cross-sections up to 150 eV and calibrating the intensity scale with the absolute ionization cross-section value of neon at 70 eV ($4.75 \times 10^{-17} cm^2$) reported by Rejoub et al [11]. The partial cross-sections for CD_4 were calibrated using absolute partial cross-sections measured by Tarnovsky et al. [12]. The partial cross-section for EII of C_3H_8 were calibrated using the partial cross-sections published in the paper Grill et al. [13].
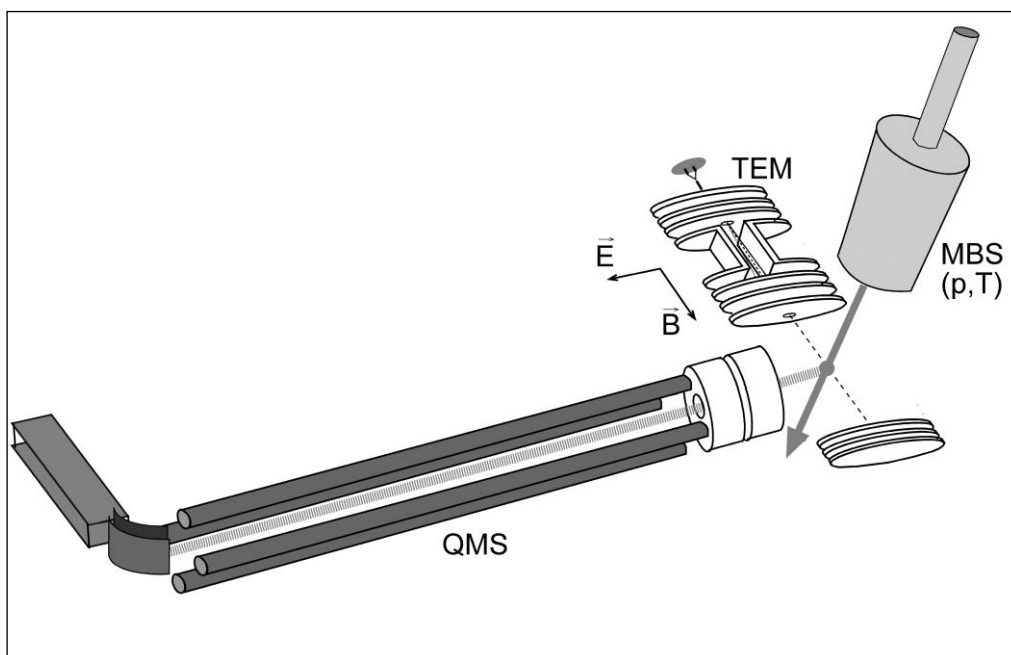
FIG. 1. Schematic view of the experimental setup showing the Effusive Molecular Beam Source (EMBS), Trochoidal Electron Monochromator (TEM) and Quadrupole Mass Spectrometer (QMS).
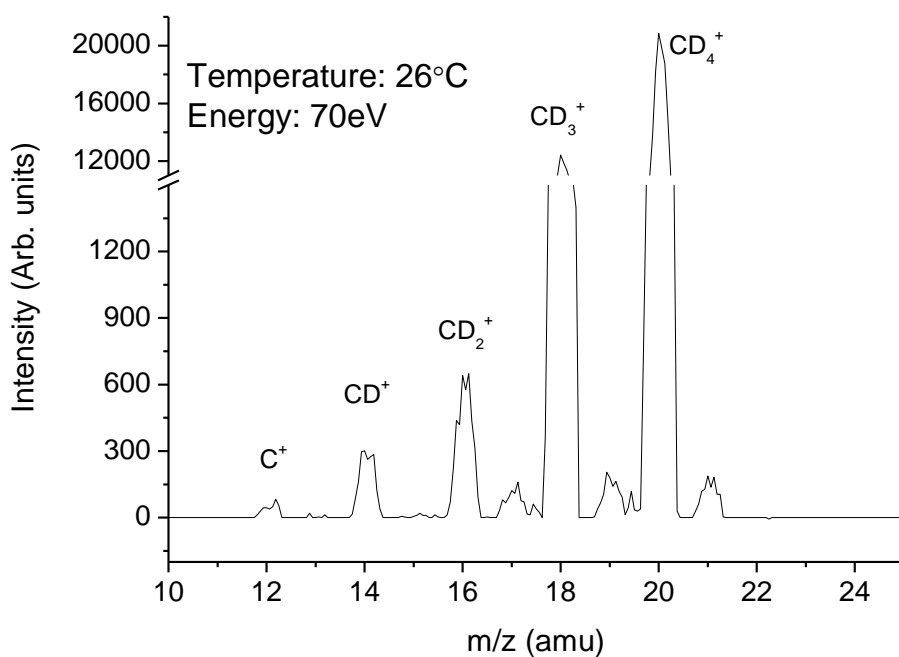
FIG. 2. Mass spectrum of CD_4 measured at the gas temperature of 303K and the electron energy of 70 eV.

3. RESULTS AND DISCUSSION

3.1. CD$_4$

Figure 2 shows the positive ion mass spectrum of CD$_4$ measured at an electron energy of 70 eV and the gas temperature of 303 K. The pressure in the main chamber was 1×10^{-7} mbar. The five most abundant positive ions formed upon the electron impact ionization of propane are CD$_4^+$ (m/z 20), CD$_3^+$ (m/z 18), CD$_2^+$ (m/z 16), CD$^+$ (m/z 14) and C$^+$ (m/z 12). For these ions the cross-sections as a function of the electron energy have been measured. We were not able to measure formation of D$_n^+$ (n=1,2) ion due to mass spectrometer limitation.

The absolute partial cross-sections for electron impact ionization of CD$_4$ were measured by Tarnovsky et al. [12] using a fast neutral beam technique. This technique is very reliable so we decided to calibrate our partial cross-sections using these data. These data were the only EII partial cross-section found for CD$_4$ in the literature. There exists good agreement in the shape of the cross-sections in present and the former experiment [12]. However, the present data exhibit more pronounced structures in the cross-sections in the low energy range (from threshold to approximatelly 50 eV). The reason could be that the present data were obtained in experiment with better electron energy resolution and the intensity of the signal was much better than in the fast beam experiment of Tarnovsky et al. [12]. We were also able to measure partial cross-section for the ion C$^+$ which was not measured by Tarnovsky et al. [12].

In the Figures 3 - 5 we present the partial cross-sections for EII to CD$_4$ measured at room temperature (303 K) and at elevated temperature of 683 K. The present cross-sections are compared with the cross-sections measured by Tarnovsky at al. [12]. These cross-sections were also used to calibrate the present low temperature cross-sections. The high temperature cross-sections are relative to the low temperature ones. The total cross-section (in the present case it represents sum of all measured partial cross-sections) is practically independent of the temperature for electrons greater than 80 eV. However, in the energy range from threshold to 80 eV we see pronounced changes in the shape of the cross-section and decrease of the total cross-section with increasing temperature. This feature we observe also in partial cross-sections for formation of CD$_4^+$ and CD$_3^+$. It seems that in this energy range indirect processes (autoionization) may occur, which depend strongly on the internal energy of the molecule, because the depletion of the cross-sections in this energy range is relatively strong.
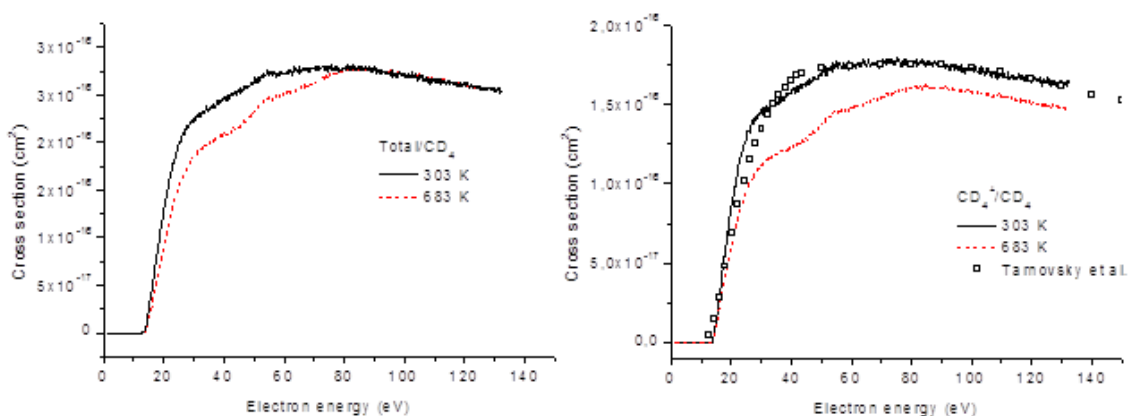
FIG. 3. Total cross-section for electron impact ionization (does not include D$^+$, D$_2^+$ contribution) of CD$_4$ and partial ionization cross-sections CD$_4^+$/CD$_4$ measured at the gas temperature 303 K and 683 K.

174

FIG. 4. Partial ionization cross-sections for electron impact ionization of CD_3^+/CD_4 and CD_2^+/CD_4 measured at the gas temperature of 303K and 683 K.
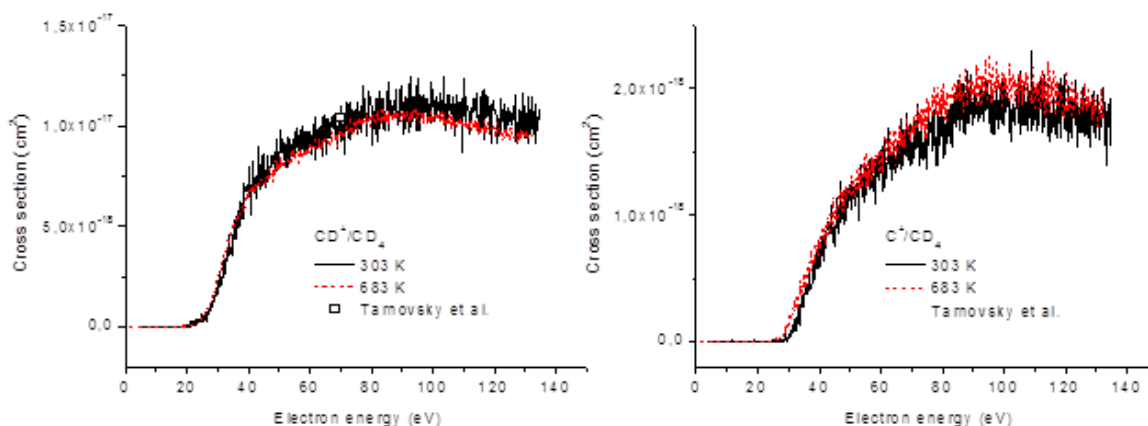
FIG. 5. Partial ionization cross-sections for electron impact ionization of CD^+/CD_4 and C^+/CD_4 measured at the gas temperature of 303 K and 683 K.

3.2. CH₃D

Figure 6 presents the mass spectrum of CH_3D measured at electron energy of 70 eV and the gas temperature of 299 K. The six most abundant positive ions formed upon the electron impact ionization of propane are CH_3D^+ (m/z 17), CH_2D^+ (m/z 16), CH_3^+ or CHD^+ (m/z 15), CD^+ or CH_2^+ (m/z 14), CH^+ (m/z 13) and C^+ (m/z 12). The ion m/z=20 is doubly charged ion Ar^{++}. The Ar was present in the gas sample for calibration purposes. For these ions the partial cross-sections as a function of the electron energy have been estimated. We were not able to measure formation of D^+ ion due to a mass spectrometer limitation.

In the case of electron impact ionization to CH_3D we were not able to find any partial cross-sections published in the literature. So we may only compare present measurements with CH_4 and CD_4 molecules. Generally, the value of the cross-sections for the parent ion is very similar to the values for CH_4 and CD_4 [12, 14]. The products of the dissociative reactions are, however, different due to the presence of two isotopes in the molecule, causing mixing between different fragment ions with identical mass (Figure 8).

175
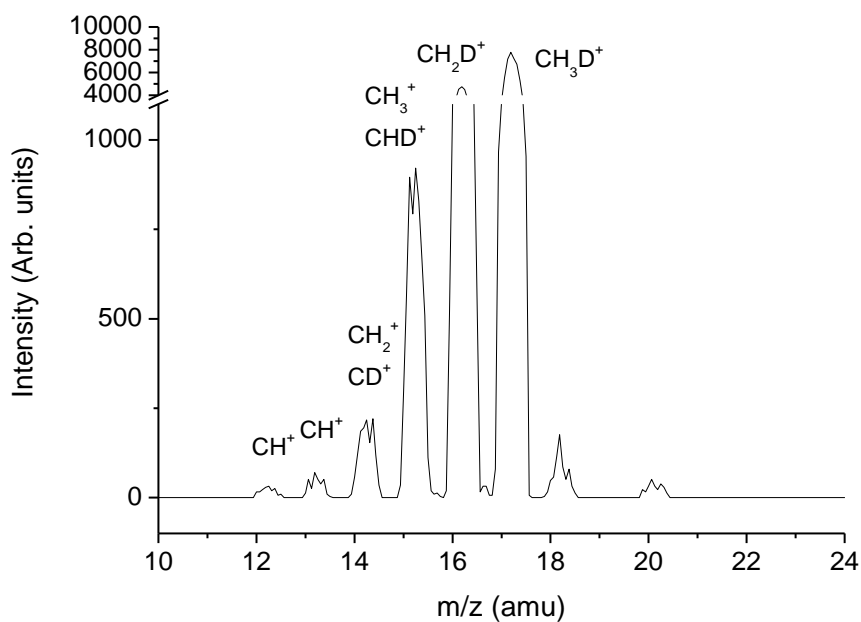
FIG. 6. Mass spectrum of CH₃D measured at the gas temperature of 26°C and the electron energy of 70 eV.

In the Figures 7- 9 we present the partial cross-sections for positive ion formation measured at low and high temperatures. The total ionization cross-section (in this case it represents again the sum of the all partial cross-sections) is practically independent of the temperature at electron energies over 80 eV, similar to the case of CD_4. In the total cross-section and also for CH_3D^+ and CH_2D^+ ions we see structures in the cross-sections which we attribute to some indirect processes in the EII (autoiionization). The temperature behaviour of the cross-sections is similar to CD_4. In the energy range from the threshold up to approximately 80 eV we see a decrease of the cross-section with elevated temperature. This decrease is observable in the electron energy range where indirect processes take place. The decrease we associate with the indirect processes and their dependence on the gas temperature. We are not able to distinguish the ions CHD^+ and CH_3^+, CD^+ and CH_2^+ mass spectrometrically. The cross-sections for these ions show weak increase with the increasing gas temperature, a situation similar to that of the case of C^+ ion.
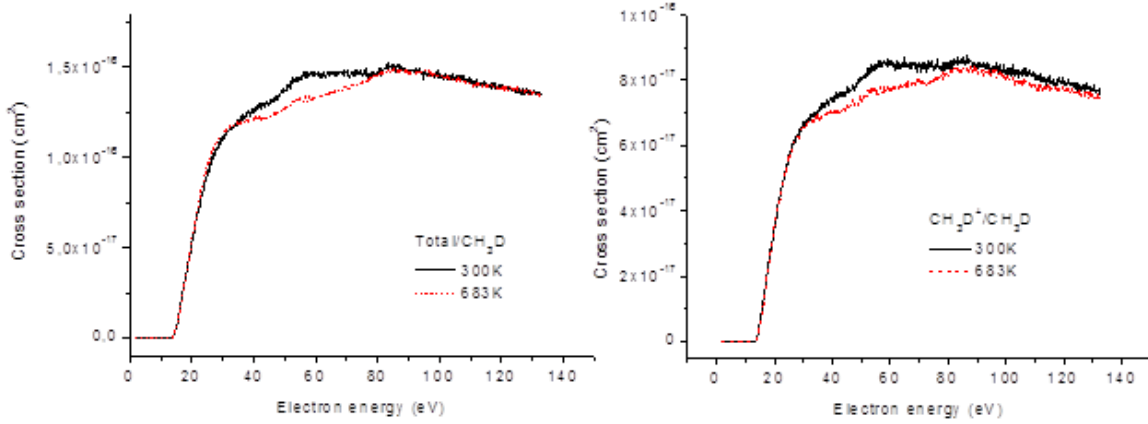
176

FIG. 7. Total cross-section for electron impact ionization of CH₃D and partial ionization cross-sections CH₃D⁺/CH₄D measured at the gas temperature of 300 K and 683 K.

FIG. 7. Total cross-section for electron impact ionization of CH_3D and partial ionization cross-sections CH_3D^+/CH_4D measured at the gas temperature of 300 K and 683 K.
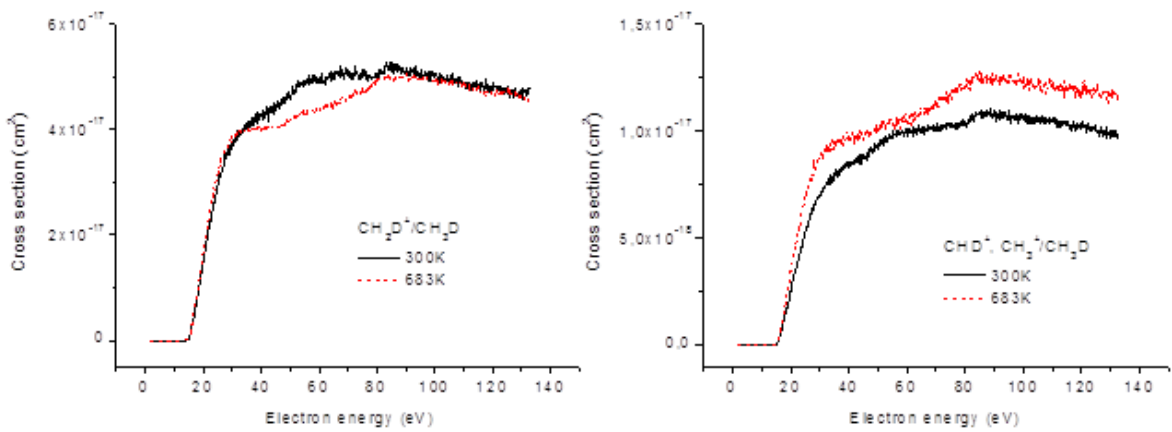
FIG. 8. Partial ionization cross-sections for electron impact ionization of CH_2D^+/CH_4D and CHD^+ or CH_3^+/CH_4D measured at the gas temperature of 300 K and 683 K.
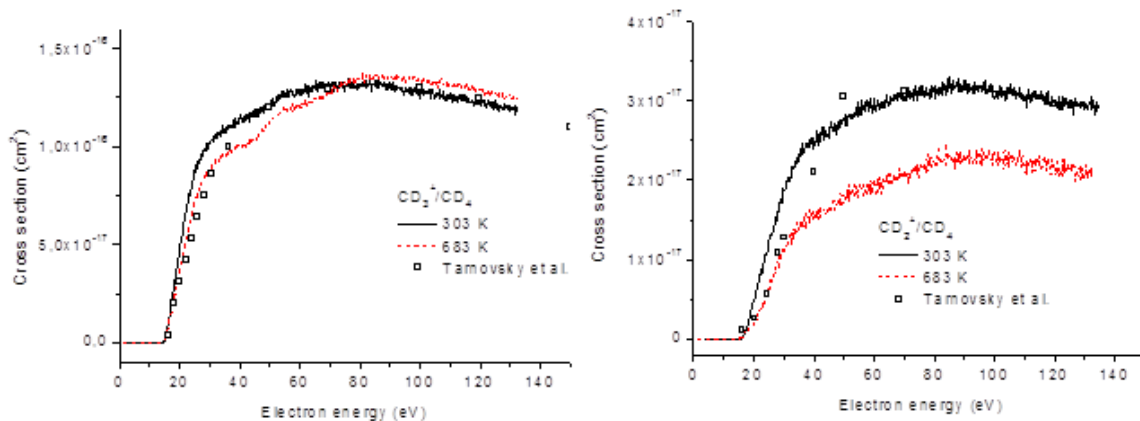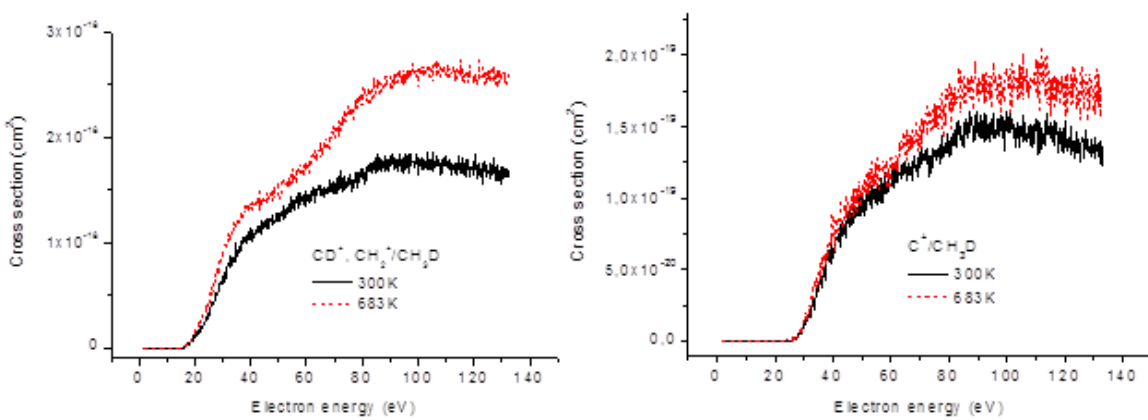

FIG. 9. Partial ionization cross-sections for electron impact ionization of CD^+ or CH_2^+/CH_4D and C^+/CH_4D measured at the gas temperature of 300 K and 683 K.

177

3.3. C_2D_6

Figure 10 presents the mass spectrum of C_2D_6 measured at electron energy of 70 eV and the gas temperature of 373 K. We have measured the absolute partial cross-section for the most intense ions at two different temperatures 373 K and 693 K.\
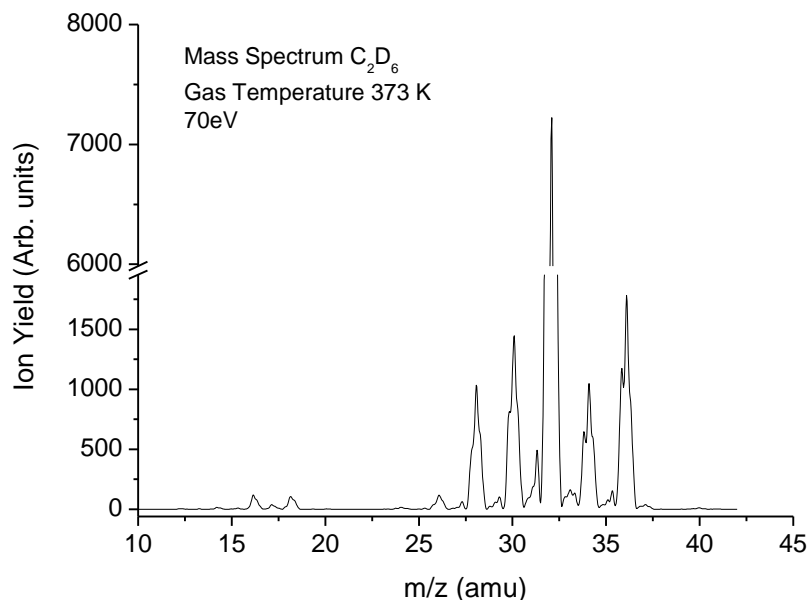
FIG. 10. shows the mass spectrum of C_2D_6 measured at electron energy of 70 eV and a gas temperature of 373 K.

Besides the dominant positive ions $C_2D_6^+$, $C_2D_5^+$, $C_2D_4^+$, $C_2D_3^+$, $C_2D_2^+$, also peaks at mass 26 amu, 24 amu, 18 amu, 17 amu 16 amu are visible in the mass spectrum, which can be assigned to C_2D^+, C_2^+, CD_3^+, $C_2D_5^{++}$, CD_2^+, respectively. However, it must be noted that some trace gases are present in the C_2D_6 sample (e.g., C_2D_4, C_2D_2 and CD_4) and thus some artifact in the ions yields may result from this. All ionization cross-sections as a function of the electron energy shown in the present report are background corrected if possible.

In the Figure 11 the absolute cross-sections for EII of deuterated ethane are displayed as a function of the electron energy (in the energy range from 0 to 150 eV) measured at two different temperatures. Within the precision of the present experiment we may conclude, that there is no change observed in the magnitude of the total absolute cross-section with the gas temperature. This observation is according to our expectation. The next Figure represents the absolute partial cross-section for formation of the parent molecular ions $C_2D_6^+$.

The cross-section for formation of the parent molecular ion decreases with the increasing gas temperature. Due to the increase of the internal energy of the molecule with the increasing gas temperature we expect increase in the decomposition rate of the molecular ion. Similar situation is also in case of the $C_2D_5^+$ ion (Figure 17), which cross-section decreases with the gas temperature. The most stable product ion $C_2D_4^+$ (Figure 17) does not change the magnitude with the temperature. Figure 18 presents the cross-sections for the formation of the ions $C_2D_3^+$ and $C_2D_2^+$ as a function of the gas temperature. The cross-sections of these two ions increase with the gas temperature.
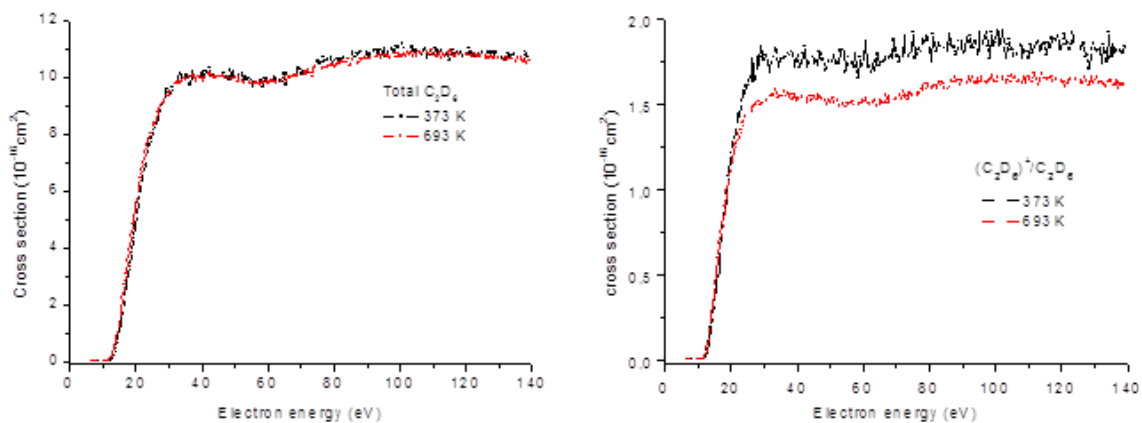
FIG. 11. Absolute total ionization cross-sections formed upon electron impact ionization of C_2D_6 and partial ionization cross-sections for formation of $C_2D_6^+ / C_2D_6$ measured at the gas temperature of 373 K and 693K without the contribution of D^+ and D_2^+ ions.
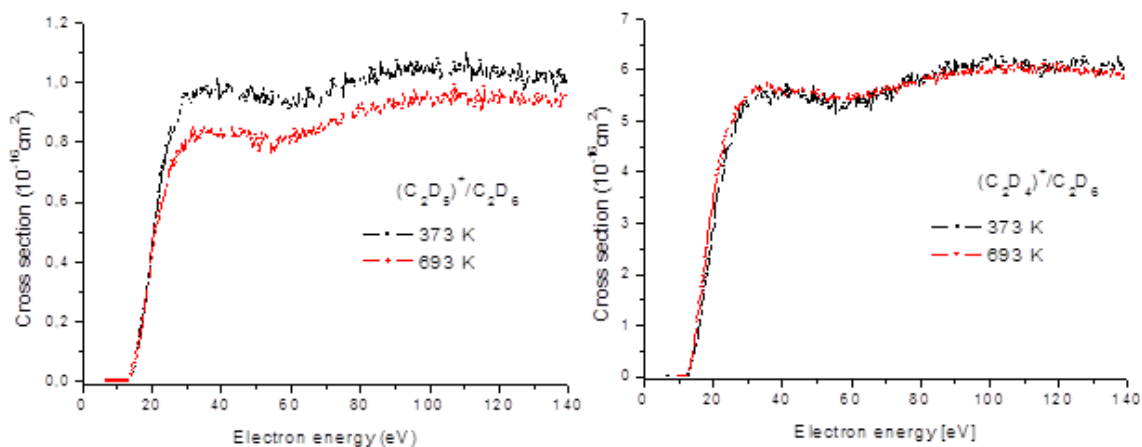
FIG. 17. Absolute partial ionization cross-sections for formation of $C_2D_5^+ / C_2D_6$ and $C_2D_4^+ / C_2D_6$ measured at the gas temperature of 373 Kand 693K.
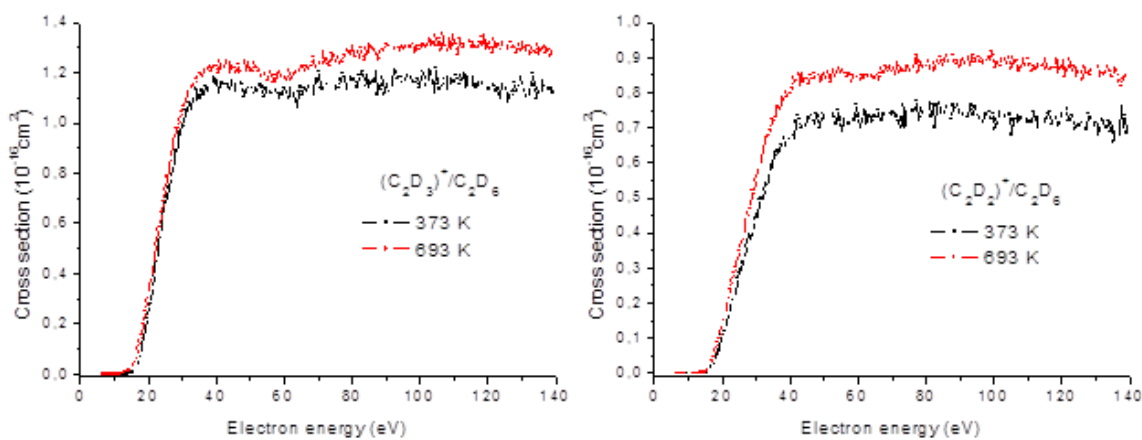
FIG. 18. Absolute partial ionization cross-sections for formation of $C_2D_3^+ / C_2D_6$ and $C_2D_2^+ / C_2D_6$ measured at the gas temperature of 373 Kand 693K.

179

3.4. C_3H_8

Figure 19 shows the mass spectrum of C_3H_8 measured at an electron energy of 75 eV and the gas temperature of 373 K. The pressure in the main chamber was 1×10^{-7} mbar. The most abundant cations formed upon the electron impact ionization of propane are $C_3H_8^+$ (m/z 44), $C_3H_7^+$ (m/z 43), $C_3H_5^+$ (m/z 41), $C_3H_3^+$ (m/z 39), $C_3H_2^+$ (m/z 38), $C_2H_5^+$ (m/z 29), $C_2H_4^+$ (m/z 28), $C_2H_3^+$ (m/z 27), and $C_2H_2^+$ (m/z 26). For these ions we have measured the cross-sections as a function of the electron energy and the gas temperature. The present partial cross-sections (measured at 370 K) were calibrated to absolute values using the values of the particular partial cross-sections from Grill et al. [13]. The high temperature cross-sections are relative to the 370 K cross-sections.
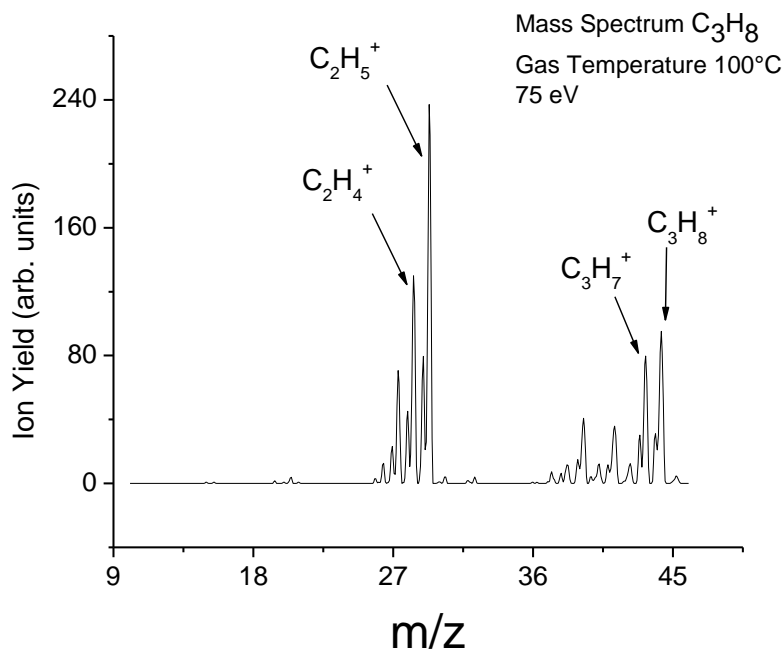
FIG. 19. Mass spectrum of C_3H_8 measured at the gas temperature of 100°C and the electron energy of 75 eV. The four most abundant peaks are assigned to the corresponding cations.

The EII partial cross-sections for C_3H_8 exhibit structures in the electron energy range 20-40 eV which we attribute to the indirect processes (autoionization). Similar, however, less pronounced structures are present also the partial cross-sections in Grill et al. [13]. The enhancement of these structures in present experiment could be associated with enhanced sensitivity of present setup to the slow ions.

In the case of EII of C_3H_8 we do not present total cross-section as in present work we have measured only most important dissociative ionization channels and many reaction channels which still could contribute to the total cross-section were omitted. In the Figures 20 to 24 we present the partial cross-sections for EII to C_3H_8 as measured at two different temperatures in present experiment (370 an 680 K). For comparison we present also the partial cross-sections measured by Grill et al [13]. The main difference between present data and those of Grill et al. [13] is in the shape of the cross-section in the energy range 20 to 40 eV. In the high electron energy range the shape of the present cross-sections are consistent with that of Grill et al. [13]. The influence of the gas temperature on the partial cross-sections in EII to C_3H_8 is relatively weak as it can be deduced from the Figures 20 to 24. The temperature variation is at the level of the precision of the experiment.
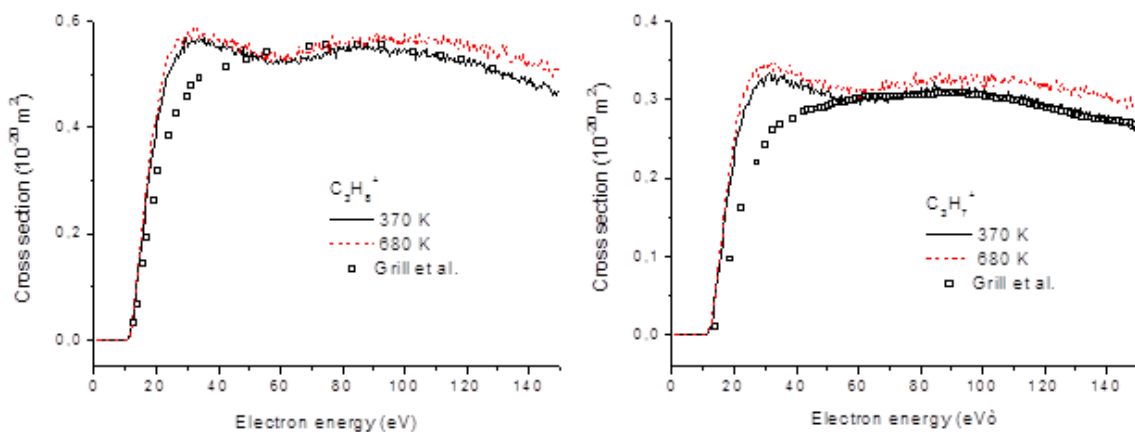
FIG. 20. Absolute partial ionization cross-sections for formation of $C_3H_8^+$ / C_3H_8 and $C_3H_7^+$ / C_3H_8 measured at the gas temperatures of 370 K and 680 K.
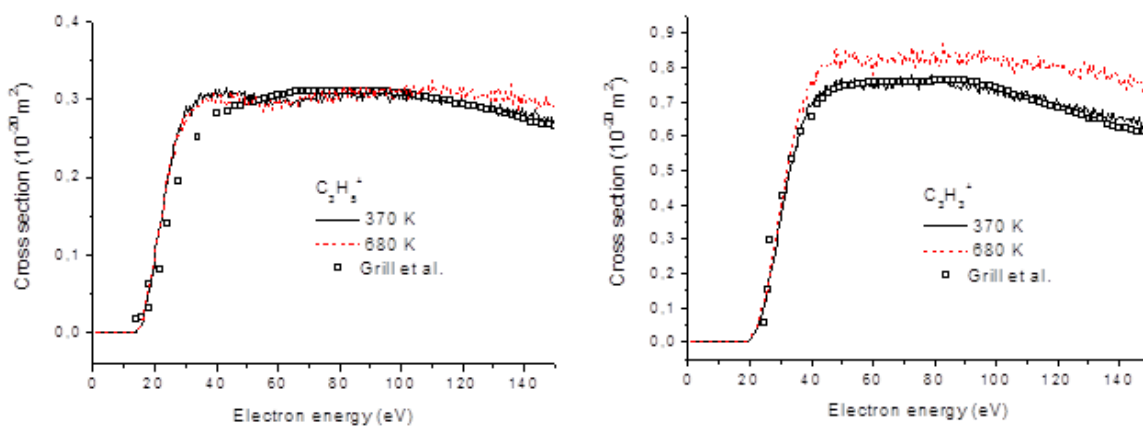
FIG. 21. Absolute partial ionization cross-sections for formation of $C_3H_5^+$ / C_3H_8 and $C_3H_3^+$ / C_3H_8 measured at the gas temperatures of 370 K and 680 K.
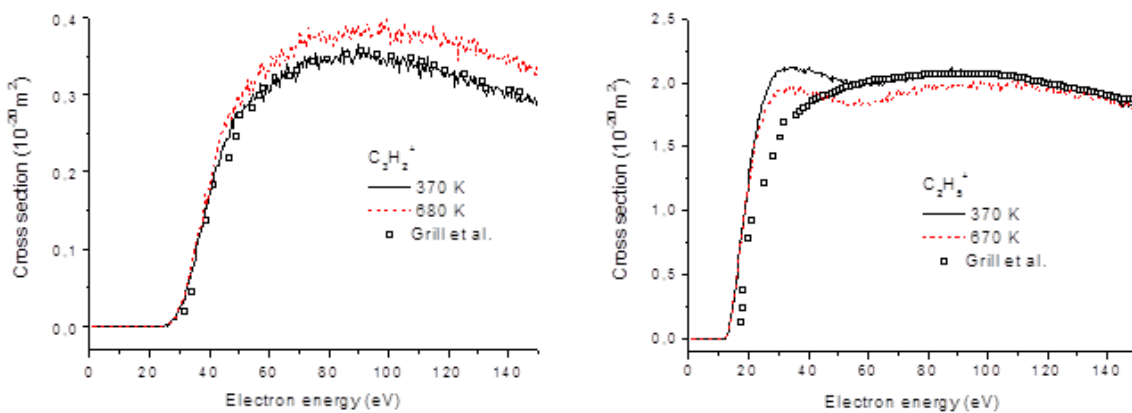
FIG. 22. Absolute partial ionization cross-sections for formation of $C_3H_2^+$ / C_3H_8 and $C_2H_5^+$ / C_3H_8 measured at the gas temperatures of 370 K and 680 K.
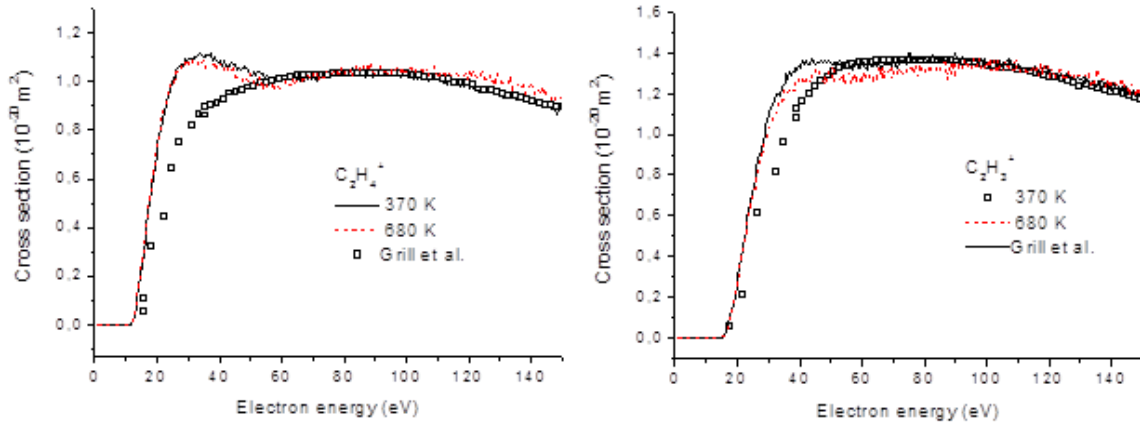
FIG. 23. *Absolute partial ionization cross-sections for formation of $C_2H_4^+/ C_3H_8$ and $C_2H_3^+/ C_3H_8$ measured at the gas temperatures of 370 K and 680 K.*
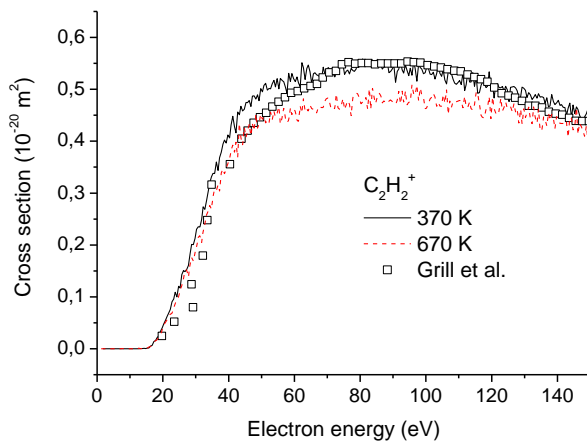
FIG. 24. *Absolute partial ionization cross-sections for formation of $C_2H_4^+/ C_3H_8$ and $C_2H_3^+/ C_3H_8$ measured at the gas temperatures of 370 K and 680 K.*

4. CONCLUSIONS

The objective of the work was to measure the partial cross-sections for electron impact ionization to selected hydrocarbons relevant to the edge of the fusion plasma (e.g., C_3H_8, CH_3D and CD_4) at room (~300K) and at high temperatures (~700K) with improved energy resolution of the electron beam and with an focus on the threshold region of the cross-sections. The aim was to evaluate the influence of the increasing gas temperature on the partial cross-section for EII.

Present study indicates that there exist gas temperature effects on partial cross-sections for EII. Some reaction channels in the EII were found to be temperature independent (at least in the measured gas temperature range). Other channels have shown strong change in the shape of the EII cross-sections with gas temperature in certain electron energy ranges. We associate these changes with indirect processes (autoionization). The problem of the temperature dependence of the autoionization processes on the gas temperature should be studied in more detail in the future. We see changes in the partial cross-sections also in the case of direct ionization; however, the observed differences are relatively low.

182

On the basis of present work we conclude that the partial cross-sections for EII depend relatively weakly on the gas temperature. The application of the cross-sections obtained at low temperature to high temperature plasma (gas temperature of 700K) could be acceptable for plasma modelling.

ACKNOWLEDGMENT

REFERENCES

[1]   Atomic and Molecular Processes in Fusion Plasmas, (JANEV, R.K., ed.) Plenum, New York (1995).

[2]   TAWARA, H., "Electron Collision Processes Involving Hydrocarbons", Atomic and Molecular Processes in Fusion Edge Plasmas, (JANEV, R.K., ed.), Plenum Press, New York (1995).

[3]   Physical Processes of Interaction of Fusion Plasmas with Solids, (HOFER,W.O., ROTH, E., Eds), Academic Press, San Diego (1996).

[4]   DENIFL, S., et al. Electron impact ionization of C_3H_8: appearance energies and temperature effects, Chem. Phys. Lett. **402** (2005) 80.

[5]   STANO, M., MATEJCIK, S., SKALNY, J.D., MÄRK, T.D.,Electron impact ionization of CH_4: ionization energies and temperature effects, J. Phys. B: At. Mol. Opt. Phys. **36** (2003) 261.

[6]   VAŠEKOVÁ, E., Electron impact ionization of C_2H_6: ionization energies and temperature effects, Int. J. Mass Spectrom. **235** (2004) 155.

[7]   Electron Impact Ionization, (MÄRK, T. D., DUNN, G. H., ed.)Springer-Verlag (1985).

[8]   MATEJCIK, S., FOLTIN, V., STANO, M., SKALNY, J.D., Temperature dependencies in dissociative electron attachment to CCl_4, CCl_2F_2, $CHCl_3$ and $CHBr_3$, Int. J. Mass Spect. **223–224** (2003) 9.

[9]   AFEEFY, H.Y., LIEBMAN, J.F., STEIN, S.E., Neutral Thermochemical Data in NIST Chemistry WebBook, NIST Standard Reference Database Number 69 (LINSTROM, P.J., MALLARD, W.G., Eds.)National Institute of Standards and Technology, Gaithersburg MD (2003).

[10]   WANNIER, G. H., The Threshold Law for Single Ionization of Atoms or Ions by Electrons, Phys. Rev. **90** (1953) 817.

[11]   REJOUB, R., LINDSAY, B.G., STEBBINGS, R.F., Determination of the absolute partial and total cross-sections for electron-impact ionization of the rare gases, Phys. Rev. A **65** (2002) 042713.

[12]   TARNOVSKY, V., LEVINY, A., DEUTSCH, H., BECKER, K., Electron impact ionization of CD_x (x = 1 - 4) J. Phys. B: At. Mol. Opt. Phys. **29** (1996) 139.

[13]   GRILL, V., et al., Absolute partial and total electron impact ionization cross-sections for C3H8 from threshold up to 950 eV, z. Phys. D **25** (1993) 217.

[14]   TIAN, C., VIDAL, C.R., Electron impact dissociative ionization and the subsequent ion-molecule reactions in a methane beam, Chem. Phys. **222** (1997) 105.

HYDROCARBON COLLISION DATABASE: REVISIONS, UPGRADES AND EXTENSIONS

D. REITER, B. KÜPPERS, R. K. JANEV

Institut für Energieforschung - Plasmaphysik, Forschungszentrum Jülich GmbH,
EURATOM-Association, Trilateral Euregio Cluster, D-52425 Jülich, Germany

E-mail: d.reiter@fz-juelich.de

Abstract

Kinetic analysis of the behaviour of hydrocarbons in fusion plasmas requires knowledge of cross-sections for their most relevant collision processes. Upgrades and extensions of the HYDKIN (HYDride KINetics) online cross-section database and analysis toolbox for collisions of hydrocarbons with electrons and protons in relevant fusion plasma conditions are presented.

1. INTRODUCTION

Magnetically confined fusion plasmas have meanwhile not only provided significant fusion power (of the same order of magnitude as the heating power), but they have also become powerful enough to threaten the integrity of the exposed vessel components [1,2]. This has become particularly clear during the design phase of the first thermonuclear burning fusion plasma device ITER (500 MW fusion power, loc.cit.), which is under construction currently in Cadarache, France.

Therefore fusion plasma physics focuses not only on typical high temperature plasma aspects (such as turbulent transport in confining magnetic fields, heating of plasmas by fusion alpha-particles, etc...), but more and more also on typical low temperature plasma physics aspects, including plasma surface interaction (erosion, re-deposition) and plasma chemical (molecular) processes in the edge region of fusion devices. Only these processes, through their plasma cooling and friction effects, provide access to tolerable operational regimes for the solid plasma container, loc.cit. and [3].

Plasma conditions near exposed components (divertor targets) of tokamaks are characterized by a low temperature (≈ 1 eV), high density (10^{20} - 10^{21} m^{-3}) and chemically rich self-sustained hydrogen plasma. For the high heat flux components carbon-based materials are often preferred. Erosion, transport and also molecular processes involving hydrocarbons and their ions then become relevant for quantifying plasma surface interaction in fusion devices.

Carbon based materials are widely used for plasma facing components, because carbon seems to be the most forgiving material in the harsh environment of fusion edge plasmas, and, by a considerable margin, also the best understood in magnetic fusion applications.

Chemical sputtering of plasma-facing graphite is then an important process in fusion plasmas, and leads to production of complex hydrocarbons, probably up to propane: C_3H_8. These molecules are dissociated in the plasma edge by collisions with electrons and protons, and produce simpler species, most of which are unsuitable for visible spectroscopy. An exception is CD, which radiates in the violet, and can be spectroscopically determined. The relationship between the observed CD spectrum and its precursor hydrocarbons is an object of many studies in fusion edge plasma science [4,5]. These studies are usually based upon transport calculations (often on a kinetic Monte Carlo level) for hydrocarbons in divertors and near limiter targets.

The purpose of these calculations is to relate the light emission from CD (or CH) to the total C_xD_y particle influx due to erosion processes, and hence to verify and validate predictive numerical

models describing plasma surface interaction and edge plasma transport in the boundary region of future fusion devices [6].

With respect to hydrocarbon transport in divertors still crude assumptions are typically made in integrated edge transport modelling, usually neglecting the breakup-chain altogether and treating only the final C and H atoms. The most recent hydrocarbon cross-section compilations [7,8,9,10], established in 2002 - 2004, provided a first comprehensive database, up to propane, C_3H_8, based on recent experimental and theoretical data, on thermo-chemical data and on physically motivated cross-section scaling relationships. The full database is available online, under http://www.hydkin.de [11] and first results of the accompanying online database analysis toolbox (e.g., for spectral analysis of chemical time-scales, or sensitivity analysis) have been given in [12,13].

In this present work we upgrade this cross-section database, in particular with respect to the dissociative recombination processes, for which a large number of newer results have become available in recent years, and which are particularly important in the low temperature divertor plasma conditions mentioned above. Also the cross-section database for dissociative ionization has been significantly revised, where this above mentioned previous database still suffered from poor quality of cross-section fits near the threshold regions of the various process channels. For the methane family (CH_y, y = 1…4) also recent experimental data for dissociative excitation and dissociative ionization of hydrocarbon ions have been included in this present upgrade. This latter group of processes is relevant for hydrocarbon chemistry in fusion plasmas only in rather hot, "ionizing" edge plasmas ($T_e \approx T_p \geq 30$ eV), as typically encountered for example in limiter plasmas or main chamber components.

1.1. Outline of the present paper

On order to discuss the outline of the present paper, we first recall here the terminology for the system of classes of collision processes for hydrocarbons in fusion edge plasmas:

The following categories of collision processes have also been already introduced in [7,8,9,10] for collision processes with electrons "e" or protons "*p*":

Direct- and dissociative ionization of neutral molecules (I-DI):

$$e + C_xH_y \rightarrow 2e + A^+ + B_1 + B_2 +.... \qquad (1)$$

where A^+ is an atomic or molecular ion, and B_1, B_2 ... (if any) are neutral fragments. Double ionization, leading directly to A^{++} or to two ionic fragments A_1^+, A_2^+, are typically ignorable in fusion edge plasmas.

In Section 2 below we revise the database of this category of processes, for the methane and ethane families of hydrocarbons. This is done by i) revision the data fitting procedure in particular near the threshold region and ii) a revision of process channels, ionization and appearance potentials. The high energy part (above about 100 - 200 eV) of the revised cross-sections mostly remains based upon the data from [7,8,9,10], only some spurious fits to cross-sections with incorrect asymptotical behaviour at large energies have been corrected. A corresponding revision/upgrading for the propane family has not yet been carried out.

Dissociative excitation of neutral molecules (DE):

$$e + C_xH_y \rightarrow e + B_1 + B_2 +.... \qquad (2)$$

i.e., all fragments B_1, B_2 ... are neutral. Only quite few new data regarding to this category of processes have become available since the previous database was published, and only for the methane family (CH_y, y = 1… 4). The revisions carried out since the first publication of the database (loc.cit.) are discussed in Section 3. One significant improvement of the database, relevant for all *DE*, *DE⁺*, *DI⁺*

processes and all hydrocarbons up to propane, was a new formulation of the energy dependent channel branching ratios $R(E)$, discussed here in the first part 3.1 of Section 3. This energy dependence in the branching ratios is needed to properly account for different threshold energies for the various partial cross-sections, which add up to one total cross-section. The original suggestions given in [7,8,9,10] to modify the branching ratios R for reaction channels contributing to one total cross-section had, under certain particular conditions, led to unsatisfactory partial channel cross-sections in the near threshold region.

Dissociative ionization of molecular ions (DI$^+$):

$$e + C_xH_y^+ \rightarrow 2e + A_1^+ + A_2^+ + B_1 + B_2 +.... \tag{3}$$
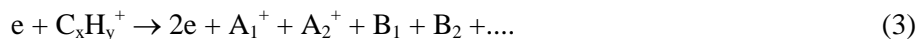
where A_1^+, A_2^+ are two ionic fragments, and B_1, B_2 ... (if any) are neutral fragments.

Dissociative excitation of molecular ions (DE$^+$):

$$e + C_xH_y^+ \rightarrow 2e + A^+ + B_1 + B_2 +.... \tag{4}$$

where A^+ is an atomic or molecular ion, and B_1, B_2 ... are neutral fragments.

New experimental cross-section data, for these two related classes of processes and for the methane family (CH_y^+, y = 1… 4), have recently become available from the group of P. Defrance (University of Louvain-la-Neuve, Belgium). These new data are currently in the process of publication (for references: see below). They have been kindly provided by the authors for implementation into the HYDKIN database prior to publication and are described in Section 4 here.

Dissociative recombination of molecular ions (DR):

$$e + C_xH_y^+ \rightarrow B_1 + B_2 +.... \tag{5}$$

where B_1, B_2... are two (or more) neutral fragments.

A large number of new process channels, as well as much better experimental information regarding the branching ratios, have become available since the first publication of the database. These processes, together with the charge exchange and particle re-arrangement processes, see below, are particularly important in the low plasma temperature regime of current detached or semi-detached divertors. This divertor operation condition is characterized by a chemically rich plasma state, in which the plasma is partially recombining in the volume rather than at the divertor targets. Therefore, in Section 5, we describe the corresponding upgrade of the HYDKIN database for this category of processes, for the methane-, ethane- and propane families.

Charge exchange and particle re-arrangement of neutral molecules (CX, PR):

$$p + C_xH_y \rightarrow C_xH_y^+ + H$$

$$p + C_xH_y \rightarrow A^+ + B_1 + B_2 + … \tag{6}$$

where B_1, B_2... are two (or more) neutral fragments. No revision of the database with respect to this group of processes has been carried out until now, except for a slight modification (unification) of the format of fit expressions, but based upon the same original data as before. We note, however, that in particular this class of processes is most relevant for fusion applications, because, as has been shown in [13], fragmentation of hydrocarbons in the most relevant low temperature "detached" divertor conditions proceeds primarily via a chain of DR and CX processes. We recommend giving a revision of this group of processes a highest priority. This includes not only reaction cross-sections but also information regarding collision kinetics (i.e., differential cross-sections, or equivalent information).

2. REVISED CROSS-SECTIONS FOR I-DI PROCESSES

In this section we carry out a revision of the cross-section database for ionization and dissociative ionization processes, for the methane (CH_y) and ethane (C_2H_y) families. In the next sub-section 2.1 we first discuss the fitting procedure used in the previous database, its shortcomings and provide a new, more robust fitting algorithm in particular for the near threshold region. In the second sub-section 2.2 we then compile the most recent new information on ionization potentials, appearance potentials (i.e., on the threshold energies of the various process channels), reaction energetics such as electron energy losses and kinetic energy releases. We then provide new tables of fit coefficients for expression (7) [see below] for these classes of processes. These tables are also implemented in the latest revision of the HYDKIN online database. A similar updating and revision of the database for the propane family C_3H_y is still missing.

2.1. Re-fitting of I-DI cross-sections

The cross-sections for the I-DI processes in the HYDKIN database [7,8,9,10] had been adopted from the earlier data collection [14]. There the following quite popular fitting expression for ionization processes had been used:

$$\sigma_{ion} = \frac{10^{-13}}{E \cdot I_c}\left[A_1 \ln\left(\frac{E}{I_c}\right) + \sum_{j=2}^{N} A_j\left(1 - \frac{I_c}{E}\right)^{(j-1)}\right] \quad (cm^2) \tag{7}$$

where I_c has a value close (or equal) to the ionization- or appearance potential (expressed in eV), E is the collision energy (expressed in eV) and A_j (j = 1, ..., N) are fitting parameters. The number of fitting parameters N was determined from the condition that the r.m.s. of the fit is not larger than 2-3%, typically $N \approx 6$. The term $ln(E/I_c)$ in expression indicates that dipole-allowed transitions are involved in I-DI processes.

For the total and partial ionization cross-sections of the $e + C_xH_y$ (x = 1,2,3; y ≤ 2x+2) collision systems, the values of I_c and A_j have been given the Appendix of [7] and in Table 7 of the report for the methane family [8], Table XVIII in [9] and in Appendix A.1 [10] for the ethane-family, and in Table XIX and Appendix A.2 [9,10], respectively, for the propane-family. These tables are revised and extended in sub-section 2.2 below.

Expression (7), with appropriate choices of the fitting coefficients A_j, can provide the proper physical behaviour in the threshold and asymptotic regions. In contrast to this, for example, the analytic expressions used in [15] have a fixed $(E - E_{th})^2$ behaviour in the threshold region, and an exponential decay behaviour ($\sim \exp(-aE)$) in the high-energy region (beyond the cross-section maximum). Such asymptotic behaviour of ionization cross-sections is completely un-physical. Of course also formula (7) gives physically correct asymptotic behaviour only if certain additional conditions for the fitting coefficients are imposed.

We start by discussing the necessary conditions for the fitting parameters A_j to provide the desired physically correct asymptotic behaviour, and we then correct (and upgrade, when new data are available), the fits from [7,8,9,10,14] in the next sub-section 2.2. For convenience we introduce the new independent variable x ("reduced energy") defined by $x = E / I_c$, so that the fitting function (7) then reads:

$$F(x) = C \frac{1}{x}\left[A_1 \ln(x) + \sum_{j=2}^{N} A_j\left(1 - \frac{1}{x}\right)^{(j-1)}\right] \quad (cm^2) \tag{8}$$

with $1.0 \leq x < \infty$ and $C = 10^{-13}/ I_c^2$, with I_c expressed in eV.

2.1.1. Near threshold behaviour

Below energies of 20-30 eV, the ionization cross-sections considered here are predominantly determined by their threshold behaviour,

$$\sigma_{ion} \sim (1 - E_{th} / E)^{\alpha} \quad \text{for } E_{th,1} \leq E \tag{9}$$

or, more generally, if more than one reaction channel contributes to a "total" cross-section:

$$\begin{aligned}
\sigma_{ion} = d_1 \cdot \left(1 - E_{th_1} / E\right)^{\alpha_1} & \quad \text{for } E_{th,1} \leq E \leq E_{th,2} \\
d_1 \cdot \left(1 - E_{th_1} / E\right)^{\alpha_1} + d_2 \cdot \left(1 - E_{th_2} / E\right)^{\alpha_2} & \quad \text{for } E_{th,2} \leq E \\
\ldots &
\end{aligned} \tag{10}$$

to account for different internal states (vibrational, rotational, electronic excitation), which can be involved. The correct treatment of multiple channel cross-sections, each with different threshold energy, via energy dependent branching ratios $R(E)$ is discussed in Section 3.1 below. The parameter I_c in   plays the role of the threshold energy E_{th}: $\sigma_{ion}(E = I_c) = 0$ and we require, of course:

$$\sigma_{ion}(E) \geq 0 \quad \text{for } I_c \leq E < \infty \tag{11}$$

i.e., for function $F(x)$ defined in (8) we require $dF(x) / dx \geq 0$ at x=1, necessarily.

The Taylor expansion of $F(x)$ at $x = 1$ reads:

$$\begin{aligned}
F_{Taylor}(x) = F(1) + \\
\left(A_1 + A_2\right)(x - 1) + \\
\left(-3/2\, A_1 - 2A_2 + A_3\right)(x - 1)^2 + \\
\left(11/6\, A_1 + 3A_2 - 3A_3 + A_4\right)(x - 1)^3 + \\
O\!\left((x - 1)^4\right)
\end{aligned} \tag{12}$$

The available experimental total ionization cross-sections show that the parameter α determining the near-threshold cross-section behaviour for this process has the value $\alpha \cong 3.0$. In view of the similarity of ionization mechanism for all hydrocarbon molecules, it can be safely assumed that the value $\alpha \cong 3.0$ characterizes the near-threshold cross-section behaviour also for the other molecules C_xH_y, x = 1, 2, 3; $1 \leq y \leq 2x+2$ of the methane, ethane and propane families, respectively.

Comparing (11) and (12), and with $F(1) = 0$ by definition, we see that necessarily:

Condition Th1: $A_1 + A_2 \geq 0$

Indeed, all cross-section fits from [14] (repeated in [7,8,9,10]) which violate this condition, start un-physically with negative values as the collision energy E increases from the threshold parameter I_c. These "cross-sections" return only later to positive values and then start to approximate the experimental and/or theoretical data. Typically in most cases only minor errors resulted, e.g., after Maxwellian averaging. An extreme example of such an erroneous behaviour is shown in FIG. 1 and FIG. 2, for the double ionization process $e + C_2H_2 \rightarrow C_2H_2^{2+} + 3e$, I-DI process for C_2H_2. For most other processes with this deficit in the fitting expressions the range of negative cross-section values was much narrower, fortunately.

Because of the value of $\alpha \cong 3.0$ in the near threshold scaling (, the first two derivatives of $\sigma(E)$ at $E = E_{th}$ can also expected to be zero. We therefore require in the new fits that also the second derivative near the threshold should, at least, not be negative.

188

Condition Th2: $-3/2A_1 - 2A_2 + A_3 \geq 0$

$$e + C_2H_2 \rightarrow C_2H_2{}^{2+} + 3e$$
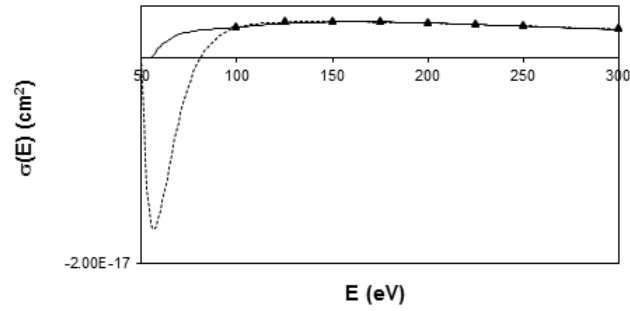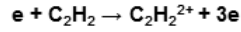
FIG. 1. Example of negative slope of cross-section, vs. electron energy, at threshold in original database, shown for double ionization of C_2H_2, with $E_{th}=I_p=53.4$ eV. Triangles: original data, from [14]. dotted line: original fit, loc.cit., solid line: corrected fit according to procedure described in text.

$$e + C_2H_2 \rightarrow C_2H_2{}^{2+} + 3e$$
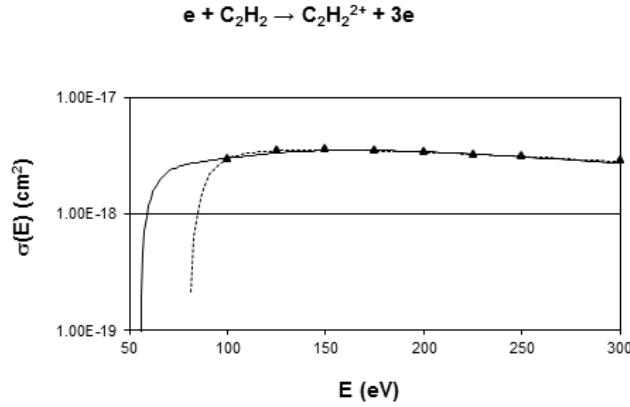
FIG. 2. same as Figure 1, but logarithmic scale for cross-section.

2.1.2. High energy asymptotic behaviour

As pointed out in [14] the attractive feature of (7) is that at asymptotically large collision energies it reduces to the Bethe-Born form for the ionization cross-section:

$$\sigma_{B-B,i} = \frac{4\pi a_0^2 Ry}{E} M_i^2 \ln(E \cdot C_i), \qquad C_i > 0 \tag{13}$$

with $Ry = 13.605$ *eV* being the Rydberg energy, $a_0 = 0.529 \times 10^{-8}$ *cm* the Bohr radius, and some constants M_i (related to the oscillator strength) and C_i, and hence:

$$\sigma_{B-B} = \frac{10^{-13}}{E \cdot I_c} \left[B_1 \ln\left(\frac{E}{I_c}\right) + B_0 \right] \qquad (cm^2), \qquad B_1 > 0 \tag{14}$$

189

$$e + C_3H_8 \rightarrow C_3H_4^{2+} + 2H_2 + 3e, \; E_{th} = 34.51$$
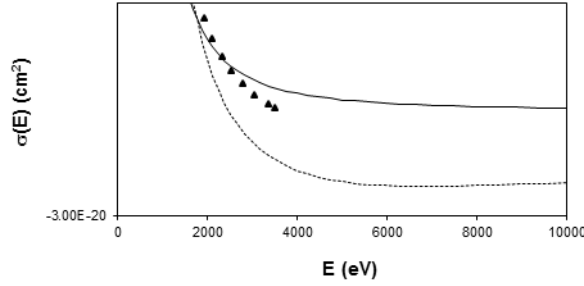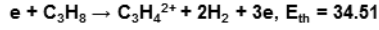
FIG. 3. Example of negative cross-sections at large electron energies in original database, shown here for double ionization of C_3H_8. Triangles: original data, from [14]. dotted line: original fit, loc.cit., solid line: corrected fit according to procedure described in text.
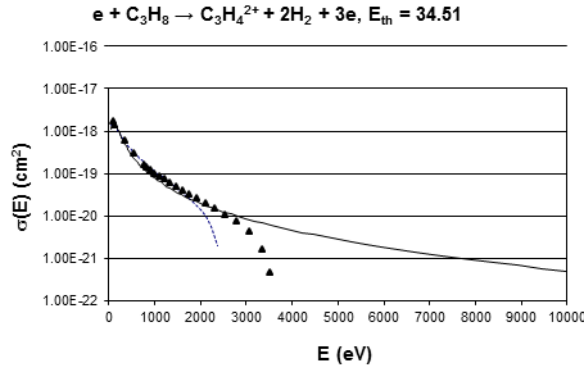
FIG. 4. same as Figure 3, but logarithmic scale for cross-section.

The asymptotic form of $F(x)$ (8) for large x values reads:

$$F_{\lim}(x) = \frac{C}{x}\left(A_1 \ln(x) + A_2 + A_3 + A_4 + \ldots\right) + O\left(\frac{1}{x^2}\right) \qquad (15)$$

with $C > 0$. It follows that necessarily

Condition H1: $A_1 > 0$

has to be fulfilled *at least* to provide the proper asymptotic behaviour at high energies. One can easily check that all cross-section fits in the database [14] with $A_1 < 0$ do, indeed, NOT have the proper asymptotic behaviour at high energies, but, instead, turn negative at some energy E_a (in the present database often around $E_a \approx 2000$ eV) and then approach zero from below with a positive slope at high energies, see figure 3 and figure 4 for an example from the previous database.

2.1.3. New fitting procedure

Based upon the same raw data as in [14] the fits for all direct ionization and dissociative ionization cross-sections have been revisited, retaining the fit formula (7) with N=6. The threshold parameter I_c has now been fixed to the "true" threshold energy $I_p = E_{th}$, or $A_p = E_{th}$ of each reaction channel, as determined either accurately experimentally or from thermo-chemical tables (previously it was treated as a variable fit parameter). For the total cross-sections, I_p is set now consistently to the minimum of all threshold energies $E_{th,i}$ values for the partial cross-sections contributing to the total.

Conditions Th1, Th2 and H1 have then been enforced. In cases in which the lack of raw data in the near threshold energy region did not allow such fits to be obtained without unphysical oscillations, near threshold data have been added before fitting according to

$$\sigma(E) = a\left(1 - \frac{E_{th}}{E}\right)^{\alpha} \quad , \quad or \tag{16}$$

$$\sigma(E) = a\left(1 - \frac{E_{th}}{E}\right)^{\alpha} \frac{1}{E}\ln(e + cE) \quad E_{th} \leq E \leq E_{th}(1 + \varepsilon) \tag{17}$$

whichever is more appropriate, with $\alpha = 3$, $c = 0.09$ and with ε a small number between 0 and 1 determined by the availability of reliable raw experimental data in the near threshold region.

2.2. Revised I-DI cross-section database

The rather poor quality of some of the previous ionization and dissociative ionization cross-sections in the near threshold region has now been considerably improved by a complete revision of these data sets, according to the procedure described in the previous sub-section. For the entire methane and ethane families a new compilation of threshold energies (ionization and appearance potentials) has been carried out, and all cross-sections have been refitted, using the same fit expression (7) as in the previous database, however now also taking into account the necessary conditions constraining the fitting coefficients A_i. Furthermore the threshold energy E_{th} is not a fitting parameter anymore, but fixed at either the ionization (I_p) or appearance potential (A_p). This removes a further slight inconsistency from the previous database, namely now the threshold energy for the total cross-section is always identical to the minimum threshold energy of all contributing channels.

A typical example for a revised fit is shown in figure 5. In this particular case $e + C_2H_6 \rightarrow C_2H_2^+ + ...$, and also in some other cases as well, in addition to the revised threshold energies and branching ratios also new, more recent cross-section data for the total cross-section in the intermediate energy range from about $2 \times E_{th}$ to $(5 - 10) \times E_{th}$ have been added from [23], see Section 2.4.

$$e + C_2H_6 \rightarrow C_2H_2^+ + ..., \ E_{th} = 15.3$$
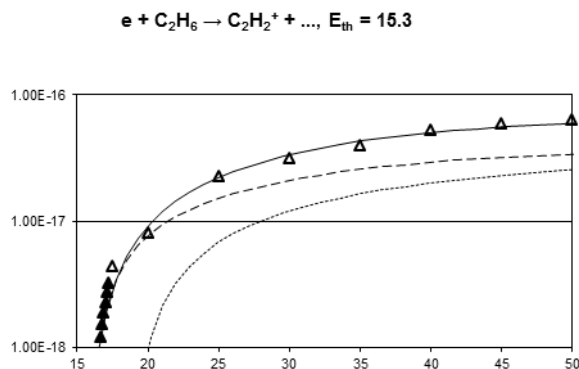
FIG. 5. Revised cross-section for DI process vs. electron energy (eV): Solid line: total $C_2H_6 \rightarrow C_2H_2^+$ + ... cross-section, fit (7) with threshold 15.3 eV, dashed line: $2H_2 + ...$ channel, same threshold, dotted line: $H_2 + 2H + ...$ channel, $E_{th} = 18.26$ eV, open triangles: cross-section data from [23] for total $C_2H_2^+ + ...$ cross-section, black triangles: near threshold data added according to (10) to avoid oscillations of fitting curve near threshold.

2.3. CH$_y$, y = 1 … 4 (methane family)

In the present upgrade new revised ionization (I_p) and appearance (A_p) potentials, as well as average electron energy loss and kinetic energy release estimates are given for CH_y, $y=1…4$.

The appearance potential, A_p, is the thermo-chemical threshold (dissociation limit) for the DI reaction, calculated with CH_y and the products in their ground states. When the experimental threshold $A_{p,exp}$ is different from A_p, it is given in brackets. The experimental thresholds are taken from Straub et al. [16] and from the cross-sections analysis of Lin and Shemansky [17].

The average electron energy loss, $\overline{E_{el}^{(-)}}$ is calculated as $\overline{E_{el}^{(-)}} = A_p + \overline{E_K}$ (or $= A_{p,exp} + \overline{E_K}$). The mean kinetic energy release $\overline{E_K}$ is taken to be the energy where the differential cross-section $\partial\sigma_{ion}(\rightarrow A^+ + ...) / \partial E_K$ has its maximum. The total mean kinetic energy $\overline{E_K}$ of reaction products is obtained from the experimental data of Gulch et al., [18] on $\overline{E_K}$ distributions under the assumption of binary initial fragmentation of the parent ion.

The branching ratios R_{DI} refer to the energy region well above all reaction channel thresholds (E > 100-150 eV), where they do not vary appreciably with the energy. In determining the contribution of $A^+ + B^+ +$ neutrals channels in the total $A^+ + ...$ (measured) cross-sections the branching ratios given at E = 200 eV by Wang et al.,[19] and the measured cross-sections for the ion pair production channels: $\rightarrow CH_2^+ + H^+ + ..., \rightarrow CH^+ + H^+ + ..., \rightarrow C^+ + H^+ + ...$ of Lindsay et al. [20], were used. The partial cross-sections for channels contributing to a total cross-sections have then been derived using these branching ratios and the procedure described in Section 3.1 below to obtain energy dependent branching ratios $R(E)$ from them for the near threshold region.

2.3.1. CH_4

Table 1 replaces and extends the corresponding data for CH_4 of Table 1 and I, from [7] and [8], respectively.

TABLE 1. IONIZATION (I_p) / APPEARANCE (A_p) POTENTIALS, REACTION ENERGETICS AND BRANCHING RATIO AT LARGE ENERGIES R_{DI} FOR e + CH_4 I-DI COLLISIONS

Reaction: e + $CH_4 \rightarrow$	I_p, A_p (eV)	$\overline{E_{el}^{(-)}}$ (eV)	$\overline{E_K}$ (eV)	R_{DI}	Notes
$CH_4^+ + 2e$	12.618	12.618	---	1.0	
$CH_3^+ + H + 2e$	14.323	15.1 ± 0.1	0.8 ± 0.1	1.0	(a)
$CH_2^+ + H_2 + 2e$	15.19	15.4 ± 0.2	1.2 ± 0.2	0.3 ± 0.1	(b), (c)
$CH_2^+ + 2H + 2e$	19.72 [20.5]	21.7 +. 0.2	1.2 ± 0.2	0.7 ∓ 0.1	
$CH^+ + H_2 + H + 2e$	19.87 [22.58]	23.3 ± 0.1	0.7 ± 0.1	0.45 ± 0.05	(b), (d)
$CH^+ + 3H + 2e$	22.41 [22.58]	23.3 ± 0.1	0.7 ± 0.1	0.55 ∓ 0.05	
$C^+ + H_2 + 2H + 2e$	24.04 [27.0]	27.6 ± 0.1	0.6 ± 0.1	0.8 ± 0.1	(b), (e)
$C^+ + 4H + 2e$	28.56 [27.0]	27.6 ± 0.1	0.6 ± 0.1	0.2 ∓ 0.1	
$C^+ + 2H_2 + 2e$	19.6	21.64	2.04	0	(*)
$H_2^+ + C + H_2 + 2e$	23.49 [28.9]	30.3 ± 0.2	1.4 ± 0.2	0.04	(f)
$H_2^+ + C + 2H + 2e$	27.98 [28.9]	30.3 ± 0.2	1.4 ± 0.2	0.67	
$H_2^+ + CH + H + 2e$	24.50 [28.9]	30.3 ± 0.2	1.4 ± 0.2	0.04	
$H_2^+ + CH_2^+ + 3e$	30.61 [45.0]	51.0 ± 0.2	6.0 ± 0.2	0.25	(g)
$H_2^+ + CH_2 + 2e$	20.1	22.36	2.26	0	(*)
$H^+ + CH + H_2 + 2e$	22.83 [22.88]	23.30 ± 0.05	0.42 ± 0.05	0.34	(h)
$H^+ + CH_2 + H + 2e$	22.93 [22.88]	23.30 ± 0.05	0.42 ± 0.05	0.34	
$H^+ + CH_3 + 2e$	18.0	19.91	1.91	0	(*)
$H^+ + CH + 2H + 2e$	27.36 [27.5]	27.92 ± 0.05	0.42 ± 0.05	0.22	
$H^+ + CH_2^+ + H + 3e$	33.34 [45.0]	50.0 ± 0.2	5.0 ± 0.2	0.055	(i), (j)
$H^+ + CH^+ + H_2 + 3e$	33.47 [35.2]	40.2 ± 0.2	5.0 ± 0.2	0.03	
$H^+ + C^+ + H_2 + H + 3e$	37.64 [38.0]	43.0 ± 0.2	5.0 ± 0.2	0.015	

Notes:

(a) P. Wang and C. R. Vidal (loc. cit.) report a 2.7% contribution of the ion pair channel $CH_3^+ + H^+ + 3e$ in the cross-section $\sigma_{ion}(CH_3^+ + ...)$ at $E = 200$ eV, but B. G. Lindsay et al (loc. cit.) failed to observe this channel. K. Gulch et al (loc. cit.) also failed to observe a contribution from the $CH_3^+ + H^+$ channel in the kinetic energy distribution of CH_3^+, which would have been characterized by a total average kinetic energy release $\overline{E_K}$ of about 6 eV.

(b) From the total cross-sections $\sigma_{ion} (\to CH_2^+ + ...)$, $\sigma_{ion} (\to CH^+ + ...)$ and $\sigma_{ion} (\to C^+ + ...)$ we have subtracted the contributions of ion pair formation channels $CH_2^+ + H^+$, $CH^+ + H^+$, $C^+ + H^+$, respectively, by using the experimental cross-sections of B. G. Lindsay et al (loc. cit.). These ion pair formation processes are accounted for in the total $\sigma_{ion} (\to H^+ + ...)$ cross-section.

(c) The reaction channel $CH_2^+ + 2H + 2e$, with $A_p = 19.72$ eV was not observed in the threshold analysis of Stano et al. [21]. However, the experimental cross-section $\sigma_{ion} (CH_2^+ + ...)$ of H. C. Straub et al. (loc. cit.) indicates a sharp increase of $\sigma_{ion} (\to CH_2^+ + ...)$ for $E > 20.5$ eV. The increase of the threshold from 19.72 eV to 20.5 eV may be an indication that CH_2^+ is vibrationally excited.

(d) If CH^+ in the reaction channel $CH^+ + H_2 + H$ is assumed to be in its meta-stable state, $CH^+(a^3\Pi)$, having an excitation energy $\cong 1.25$ eV, and H_2 is vibrationally excited in its $v = 3$ level, then the appearance potential for this reaction channel would be 22.58 eV. If CH^+ is formed in its $A^1\Pi$ excited state ($E_{exc} \cong 3.2$ eV) and H_2 is in its $v = 0$ vibrational ground state, then A_p for this reaction channel would be $\cong 23.07$ eV. In the reaction channel $CH^+ + 3H$, a vibrational excitation of CH^+ of 0.17 eV is sufficient to obtain the threshold value 22.58 eV.

(e) The reaction channel $C^+ + 2H_2 + 2e$, with $A_p = 19.56$ eV, gives a negligible contribution to $\sigma_{ion} (\to C^+ + ...)$. The appearance potential of the $C^+ + H_2 + 2H + 2e$ channel can become closer to the observed C^+ production threshold if either H_2 is highly vibrationally excited or C^+ is excited. M. Stano et al. (loc. cit.) as well as other authors [22] have observed a second threshold for this reaction channel at $E \cong 25 \pm 0.1$ eV that coincides with the value for $A_p = 25.04$ eV for $C^+ + H_2(v = 2) + 2H$.

(f) The reaction channel $H_2^+ + CH_2 + 2e$, with $A_p = 20.17$ eV, does not contribute to $\sigma_{ion} (\to H_2^+ + ...)$ [see also: X. Lin and D. E. Shemansky (loc. cit.)]. To become closer to the observed H_2^+ ion production threshold, the reaction channels $H_2^+ + C + H_2$ and $H_2^+ + CH + H$ require significant excitation of their products. When the products in these reaction channels are in their ground states, then the total contribution of these two channels to the cross-section $\sigma_{ion} (\to H_2^+ + neutrals)$ is about 10% [X. Lin and D. E. Shemansky (loc. cit.)]. H_2^+ in the dominant $H_2^+ + C + 2H$ channel is apparently vibrationally excited (at least up to the $v = 4$ level).

(g) The $H_2^+ + CH_2^+ + 3e$ channel is by far the dominant positive ion pair channel contributing to the cross-section $\sigma_{ion} (\to H_2^+ + A^+ + ...)$. The combined contribution of $H_2^+ + CH^+ + H$, $H_2^+ + H^+ + CH$ and $H_2^+ + H_2^+ + C$ channels to $\sigma_{ion} (H_2^+ + A^+ + ...)$ is about 25%. [P. Wang and C. R. Vidal, (loc. cit.)]. Since the $H_2^+ + ...$ ion production channel contributes only about 0.6% to the total dissociative ionization of CH_4 (at $E = 200$ eV), the $H_2^+ + A^+ + ...$ channels other than $H_2^+ + CH_2^+ + 3e$ are neglected. The threshold energy of 45.2 eV for $H_2^+ + CH_2^+$ ion pair channel is taken from X. Lin and D. E. Schemansky (loc. cit.).

(h) The reaction channel $H^+ + CH_3 + 2e$, with $A_p = 18.08$ eV, does not contribute to $\sigma_{ion} (\to H^+ + neutrals)$. The channels $H^+ + CH + H_2$ and $H^+ + CH_2 + H$ have an experimental joint threshold at $E \cong 22.9$ eV and give a small ($\approx 10\%$) contribution to the total $\sigma_{ion} (\to H^+ + ...)$ cross-section when the reaction products are in their ground states.

(i) The cross-section for ion pair production channels $H^+ + CH_2^+ + ...$, $H^+ + CH^+ + ...$ and $H^+ + C^+ + ...$ have been measured (B. G. Lindsay et al., loc. cit.) and their threshold energies are taken from that reference. The branching ratios for these channels were determined from the measured values of their cross-sections at $E \cong 100$ eV and the total experimental cross-section for H^+ production of H. C. Straub et al. (loc. cit.).

(j) The cross-sections for reaction channels $H^+ + CH^+ + H_2 + 3e$ and $H^+ + C^+ + H_2 + H + 3e$ include also the contributions when H_2 is dissociated to 2H. The H_2/2H sub-channels share the corresponding cross-section equally.

(*) These channels from the previous database [7,8] have been removed now ($R_{DI} = 0$), see notes (f), (h). C^+, H^+ and H_2^+ production from CH_4, respectively, is specified now by many new fragmentation channels, based upon much more detailed experimental information.

The revised threshold energies $E_{th} = I_p$ and fit coefficients A_i, i=1…6 for the ionization and dissociative ionization processes of CH_4 for fit expression (7) are given in the following two tables:

(a) Total ionization

process	I_p	A_i, i=1-3 A_i, i=4-6		
e + CH_4 → total ionization	1.26180E+01	2.49224E+00	-2.49224E+00	-1.24612E+00
		8.06114E+00	-2.08112E+01	1.85141E+01

(b) Partial cross-sections

process	I_p	A_i, i=1-3 A_i, i=4-6		
e + CH_4 → CH_4^+ + 2e	1.26180E+01	1.37567E+00	-1.37567E+00	-6.87833E-01
		7.22367E+00	-1.62101E+01	1.07413E+01
e + CH_4 → CH_3^+ + H + 2e	1.43230E+01	1.67087E+00	-1.50198E+00	-4.71225E-01
		4.26285E-01	1.76465E-03	-8.89114E-02
e + CH_4 → CH_2^+ total	1.51900E+01	1.70627E-01	-1.70627E-01	6.16491E-02
		-7.77480E-01	2.07542E+00	-8.03623E-01
e + CH_4 → CH_2^+ + H_2 + 2e	1.51900E+01	7.10123E-02	-6.19493E-02	-1.73801E-02
		1.05256E-01	3.49250E-01	-2.57176E-01
e + CH_4 → CH_2^+ + 2H + 2e	1.97200E+01	1.43321E-01	-1.26091E-01	-3.72000E-02
		1.09358E-01	8.58465E-01	-4.40669E-01
e + CH_4 → CH^+ total	1.98700E+01	7.94035E-03	-7.83510E-03	1.59367E-02
		4.36962E-01	6.01173E-01	-4.57163E-01
e + CH_4 → CH^+ + H_2 + H + 2e	1.98700E+01	8.75914E-05	-8.75914E-05	4.88367E-02
		3.19826E-01	-2.76811E-02	-4.20847E-02
e + CH_4 → CH^+ + 3H + 2e	2.24100E+01	6.48017E-03	-6.48017E-03	4.31887E-02
		3.26757E-01	1.64748E-01	-1.88793E-01
e + CH_4 → C^+ total	2.40400E+01	3.97508E-31	4.78842E-04	2.32334E-01
		-7.40873E-01	1.87218E+00	-1.08652E+00
e + CH_4 → C^+ + H_2 + 2H + 2e	2.40400E+01	9.46861E-31	1.00801E-02	1.28266E-01
		-3.73438E-01	1.23720E+00	-7.72898E-01
e + CH_4 → C^+ + 4H + 2e	2.85600E+01	2.69945E-30	1.42494E-03	3.85295E-02
		-1.16253E-01	3.36014E-01	-2.03466E-01
e + CH_4 → H_2^+ total	2.34900E+01	4.15934E-03	-4.15934E-03	-2.07967E-03
		5.27460E-02	5.27987E-01	-4.39476E-01
e + CH_4 → H_2^+ + C + H_2 + 2e	2.34900E+01	1.24563E-15	1.01999E-04	5.11410E-03
		4.52978E-02	-9.11785E-02	4.91998E-02
e + CH_4 → H_2^+ + C + 2H + 2e	2.79800E+01	5.15946E-25	5.87642E-15	9.60209E-02
		6.58415E-02	1.01720E-01	-1.42420E-01
e + CH_4 → H_2^+ + CH + H + 2e	2.45000E+01	7.87275E-04	-7.87275E-04	2.19765E-02
		-5.80286E-02	8.60985E-02	-4.52294E-02
e + CH_4 → H_2^+ + CH_2^+ + 3e	3.06100E+01	2.85449E-17	-2.23807E-17	1.37359E-02
		8.41534E-02	-1.78079E-02	-3.47136E-02
e + CH_4 → H^+ total	2.28300E+01	2.19305E-02	8.09278E-02	8.84135E-01
		-5.48659E+00	1.63963E+01	-9.58429E+00
e + CH_4 → H^+ + CH + H_2 + 2e	2.28300E+01	5.41343E-02	1.35252E-02	1.08252E-01
		-1.53107E+00	5.90053E+00	-3.87381E+00
e + CH_4 → H^+ + CH_2 + H + 2e	2.29300E+01	5.17759E-02	1.16952E-02	1.01054E-01
		-1.40466E+00	5.62420E+00	-3.70544E+00
e + CH_4 → H^+ + CH + 2H + 2e	2.73600E+01	2.09129E-02	2.11271E-02	7.36234E-02
		-8.93844E-01	3.50788E+00	-2.25108E+00
e + CH_4 → H^+ + CH_2^+ + H + 3e	3.33400E+01	1.99943E-03	8.33729E-03	1.96737E-02
		-2.16841E-01	8.45347E-01	-5.29540E-01
e + CH_4 → H^+ + CH^+ + H_2 + 3e	3.34700E+01	4.60218E-05	5.23336E-03	1.05358E-02

		-1.07195E-01	4.37392E-01	-2.73080E-01
e + CH$_4$ → H$^+$ + C$^+$ + H$_2$ + H + 3e	3.76400E+01	1.07227E-16	1.49688E-14	6.15155E-03
		2.03189E-02	1.53995E-02	-9.43320E-04

2.3.2. CH$_3$

Table 2 replaces and extends the corresponding data of Table 1 and I from [7] and [8], respectively, for e + CH$_3$ collisions. In this table the ionization (I_p) and appearance (A_p) potentials for CH$_3$, as well as the mean electron energy losses $\overline{E_{el}^{(-)}}$ have been determined exactly in the same way as for CH$_4$ in the previous paragraph.

The mean kinetic energy release $\overline{E_K}$ carried by the fragments was taken from the experimental data on E_K distributions of the products from the process $e + CD_3 \rightarrow A^+$ + neutrals, (D: deuteron) provided by P. Defrance (University of Louvain-la-Neuve, Belgium, 2008).

The values of the branching ratios R_{DI} have been assigned by taking into account the inverse dependence of inelastic cross-sections on the threshold energy (to a certain power). The analogy with the similar reaction channels in the e + CH$_4$ case also used as guidance.

TABLE 2. SAME AS Table 1, FOR e + CH$_3$ I-DI COLLISIONS

Reaction: e + CH$_3$ →	I_p, A_p (eV)	$\overline{E_{el}^{(-)}}$ (eV)	$\overline{E_K}$ (eV)	R_{DI}	Notes
CH$_3^+$ + 2e	9.84	9.84	---	1.0	
CH$_2^+$ + H + 2e	15.25	15.60 18.05 ± 0.1	0.35, E ≤ 30 eV 2.8 ± 0.1, E > 30 eV	1.0	
CH$^+$ + H$_2$ + 2e CH$^+$ + 2H + 2e	15.39 19.93	15.84 ± 0.05 21.4 ± 0.1	0.45 ± 0.05 1.5 ± 0.1	0.8 ± 0.1 0.2 ∓ 0.1	(a)
C$^+$ + H$_2$ + H + 2e C$^+$ + 3H + 2e	19.55 24.09	20.1 ± 0.1 24.6 ± 0.1	0.5 ± 0.1 0.5 ± 0.1	0.8 ± 0.1 0.2 ∓ 0.1	(a)
H$_2^+$ + CH + 2e H$_2^+$ + C + H + 2e	20.17 23.72	21.5 ± 0.1	1.3 ± 0.1 1.3 ± 0.1	0.7 ± 0.1 0.3 ∓ 0.1	(a)
H$^+$ + CH$_2$ + 2e	18.45	20.4, E < 35 eV 19.0, E ≥ 35 eV	1.8, E < 35 eV 0.4, E ≥ 35 eV	0.1	(b)
H$^+$ + C + H$_2$ + 2e	21.90	23.7, E < 35 eV 22.3, E ≥ 35 eV	1.8, E < 35 eV 0.4, E ≥ 35 eV	0.45	
H$^+$ + CH + H + 2e	22.89	24.7, E < 35 eV 23.3, E ≥ 35 eV	1.8, E < 35 eV 0.4, E ≥ 35 eV	0.36	
H$^+$ + CH$_2^+$ + 3e	28.85 [35.0]	40.6 ± 0.2	5.6 ± 0.2	0.06	(c), (d)
H$^+$ + CH$^+$ + H + 3e	33.53 [40.0]	45.6 ± 0.2	5.6 ± 0.2	0.03	

Notes:
(a) The assigned uncertainties to R_{DI} for this channel are probably only the lower limit.
(b) The channel $e + CH_3 \rightarrow H^+ + CH_2 + 2e$ is analogous to the channel $e + CH_4 \rightarrow H^+ + CH_3 + 2e$ that has a negligible contribution to the total H$^+$ production cross-section in that collision system. The assigned $R_{DI} = 0.1$ value for this channel is probably an upper limit.
(c) A total branching ratio of 0.09 was assigned to the ion pair channels $H^+ + CH_2^+$ and $H^+ + CH^+ + H$ in analogy with the total weight (of 0.10) of the ion pair production channels in the total $\sigma_{ion}(H^+ + ...)$ for the $e + CH_4$ case.
(d) The threshold energies for ion pair production channels $H^+ + CH_2^+$ and $H^+ + CH^+ + H$ where assigned in analogy with the corresponding threshold values of the analogous channels in the $e + CH_4$ case.

The revised threshold energies $E_{th} = I_p$ and fit coefficients A_i, $i = 1\ldots6$ for the ionization and dissociative ionization processes of CH_3 for fit expression (7) are given in the following two tables:

(a) Total ionization

process	I_p	A_i, i=1-3 A_i, i=4-6		
e + CH$_3$ → total ionization	9.84000E+00	7.13782E-01	-7.09869E-01	-3.49066E-01
		3.92425E-01	-2.12799E+00	6.18459E+00

(b) Partial cross-sections

process	I_p	A_i, i=1-3 A_i, i=4-6		
e + CH$_3$ → CH$_3^+$ + 2e	9.84000E+00	4.23837E-31	2.49612E-13	4.99224E-13
		1.18334E+00	-2.40188E+00	4.38422E+00
e + CH$_3$ → CH$_2^+$ + H + 2e	1.52500E+01	1.35877E+00	-1.35877E+00	9.14938E-01
		-8.88169E-01	-3.17873E+00	3.60415E+00
e + CH$_3$ → CH$^+$ total	1.53900E+01	9.87159E-02	-6.67243E-02	1.15464E+00
		-1.63359E+00	5.46943E-01	5.66797E-01
e + CH$_3$ → CH$^+$ + H$_2$ + 2e	1.53900E+01	1.05825E-01	-7.40998E-02	1.43605E+00
		-3.47516E+00	3.59484E+00	-1.10764E+00
e + CH$_3$ → CH$^+$ + 2H + 2e	1.99300E+01	2.78047E-02	-1.52763E-02	3.07354E-01
		-7.49147E-01	8.07913E-01	-2.58219E-01
e + CH$_3$ → C$^+$ total	1.95500E+01	1.83371E-02	-1.67758E-02	4.98321E-02
		-2.03752E-01	4.36853E-01	-1.57007E-01
e + CH$_3$ → C$^+$ + H$_2$ + H + 2e	1.95500E+01	1.63127E-02	-1.38517E-02	4.25139E-02
		-1.73675E-01	3.92583E-01	-1.59477E-01
e + CH$_3$ → C$^+$ + 3H + 2e	2.40900E+01	4.04307E-03	-3.25378E-03	8.69115E-03
		-3.87929E-02	9.33567E-02	-3.76597E-02
e + CH$_3$ → H$_2^+$ total	2.01700E+01	1.38133E-03	-8.87287E-04	2.50599E-02
		-1.78755E-03	-2.11499E-02	7.72218E-02
e + CH$_3$ → H$_2^+$ + CH + 2e	2.01700E+01	1.46025E-03	-1.17876E-03	3.19181E-02
		-5.34705E-02	6.28191E-02	1.50488E-02
e + CH$_3$ → H$_2^+$ + C + H + 2e	2.37200E+01	1.39457E-05	5.88377E-04	6.31599E-03
		8.11671E-03	-1.80087E-02	2.96730E-02
e + CH$_3$ → H$^+$ total	1.84500E+01	7.04746E-02	-7.04746E-02	4.32389E-02
		-2.98157E-01	8.94543E-01	-2.71915E-01
e + CH$_3$ → H$^+$ + CH$_2$ + 2e	1.84500E+01	1.33294E-02	-1.15746E-02	5.73934E-02
		-2.21078E-01	3.98837E-01	-2.05472E-01
e + CH$_3$ → H$^+$ + C + H$_2$ + 2e	2.19000E+01	3.71283E-02	-2.51346E-02	5.42324E-03
		1.23439E-01	1.12242E-01	-3.27727E-02
e + CH$_3$ → H$^+$ + CH + H + 2e	2.28900E+01	2.96443E-02	-2.11177E-02	2.23099E-03
		9.16179E-02	1.05386E-01	-3.24418E-02
e + CH$_3$ → H$^+$ + CH$_2^+$ + 3e	2.88500E+01	4.87473E-03	-3.97012E-03	-6.28145E-04
		9.43461E-03	2.79683E-02	-8.81358E-03
e + CH$_3$ → H$^+$ + CH$^+$ + H + 3e	3.35300E+01	2.14368E-03	-1.88039E-03	-5.45256E-04
		6.64177E-03	8.96215E-03	-2.47192E-04

2.3.3. CH$_2$, CH

Table 3 below replaces and extends the corresponding data for CH_2 and CH of Table I and 1 from [7] and [8] for $e + CH_2$ and $e + CH$ I-DI collisions.

196

The ionization (I_p) and appearance (A_p) potentials for CH_y ($y = 1, 2$) have been determined exactly in the same way as for CH_4. The thresholds in brackets {...} are equal to the mean electron energy loss $\overline{E_{el}^{(-)}}$. Those electron energy losses have also been determined in the same way as for CH_4; The mean kinetic energy releases $\overline{E_K}$ in the fragments have been determined as for CH_3, except for the $CH_3 \rightarrow CH_2$ and $CH_3 \rightarrow CH$ channels; The high energy branching ratios R_{DI} have been determined in the same way as for CH_3, except for the $CH_3 \rightarrow CH_2$ and $CH_3 \rightarrow CH$ channels.

TABLE 3. SAME AS Table 1, FOR e + CH_2 AND e + CH I-DI COLLISIONS

Reaction: e + $CH_2 \rightarrow$	I_p, A_p (eV)	$\overline{E_{el}^{(-)}}$ (eV)	$\overline{E_K}$ (eV)	R_{DI}	Notes
$CH_2^+ + 2e$	10.40	10.40	---	-	
$CH^+ + H + 2e$	15.08 {15.53}	15.53 ± 0.05	0.45 ± 0.05	-	
$C^+ + H_2 + 2e$	14.71 {15.2}	15.2 ± 0.1	0.5 ± 0.1	0.8 ± 0.1	
$C^+ + 2H + 2e$	19.24 {20.7}	20.74 ± 0.1	1.5 ± 0.1	0.2 ∓ 0.1	
$H^+ + CH + 2e$	18.04 {20.2}	20.24 ± 0.1	2.2 ± 0.1	0.8 ± 0.1	
$H^+ + C + H + 2e$	21.59 {24.0}	24.0 ± 0.1	2.4 ± 0.1	0.2 ∓ 0.1	
$H_2^+ + C + 2e$	18.87 {21.1}	21.1 ± 0.1	2.2 ± 0.1	1.0	
Reaction: e + CH $\rightarrow$					
$CH^+ + 2e$	10.63	11.30	---	1.0	
$C^+ + H + 2e$	14.81 {15.4}	15.4 22.0	1.6 7.2	0.25 ± 0.05 0.75 ∓ 0.05	(a)
$H^+ + C + 2e$	17.15	17.15 20.75	$\cong 0.1$ 3.6	0.15 ± 0.05 0.85 ∓ 0.05	(b)

Notes:
(a) The asymptotic state $C^+ + H$ can be reached either with a transition from CH to the state $CH^+(b^3\Sigma^-; v \geq 4)$ and this state then pre-dissociates to the dissociative state ($c^3\Sigma^+$) producing $C^+(^2P)$ and $H(^2S)$, or by a direct transition to the repulsive ($c^3\Sigma^+$) state. The corresponding $\overline{E_K}$ values from these transitions are 1.6 eV and 7.2 eV, as obtained from the potential energy curves for the CH^+ ion (Refs. [26] - [29] of JUEL-3966 Report [8]). It was assumed that CH is in its ground state.
(b) The asymptotic state $H^+ + C$ can be reached either with a transition from CH to the dissociative continuum of the $CH^+(b^3\Sigma)$ state, or to the dissociative $d^3\Pi$ state. The corresponding $\overline{E_K}$ values were obtained from the known potential energy curves of CH^+ (Refs. [26] - [29] of JUEL-3966 Report [8]).

The revised threshold energies $E_{th} = I_p$ and fit coefficients A_i, $i = 1...6$ for the ionization and dissociative ionization processes of CH_2 for fit expression(7) are given in the following tables:

e + CH$_2$

(a) Total ionization

process	I_p	A_i, i=1-3		
		A_i, i=4-6		
e + CH$_2$ → total ionization	1.04000E+01	2.44327E+00	-2.42224E+00	-1.17957E+00
		-4.56208E-01	-3.39693E-01	5.25298E-01

(b) Partial cross-sections

process	I_p	A_i, i=1-3		
		A_i, i=4-6		
e + CH$_2$ → CH$_2^+$ + 2e	1.04000E+01	1.16739E+00	-1.16739E+00	-5.83695E-01
		4.03027E+00	-1.10429E+01	8.16400E+00
e + CH$_2$ → CH$^+$ + H + 2e	1.50800E+01	7.96738E-01	-7.71019E-01	-1.43112E-01
		1.70895E+00	-4.12643E+00	2.83648E+00
e + CH$_2$ → C$^+$ total	1.47100E+01	4.17172E-02	-4.16279E-02	-2.06800E-02
		7.82342E-02	-2.19067E-01	3.28366E-01
e + CH$_2$ → C$^+$ + H$_2$ + 2e	1.47100E+01	4.44393E-02	-4.44393E-02	-2.22197E-02
		9.13071E-02	-1.73910E-01	2.29748E-01
e + CH$_2$ → C$^+$ + 2H + 2e	1.92400E+01	1.12275E-02	-1.12275E-02	-5.61375E-03
		1.97377E-02	-3.87536E-02	5.54721E-02
e + CH$_2$ → H$^+$ total	1.80400E+01	1.47516E-30	6.83567E-15	3.48178E-02
		-1.64395E-01	6.56239E-01	-2.50896E-01
e + CH$_2$ → H$^+$ + CH + 2e	1.80400E+01	9.25493E-04	-8.72261E-04	2.29696E-02
		-8.81371E-02	4.96552E-01	-2.06097E-01
e + CH$_2$ → H$^+$ + C + H + 2e	2.15900E+01	2.96064E-05	7.19407E-05	4.80918E-03
		-1.96108E-02	1.19876E-01	-4.81104E-02
e + CH$_2$ → H$_2^+$ + C + 2e	1.88700E+01	6.10570E-02	-6.10570E-02	-3.05285E-02
		1.72513E-01	-5.75088E-02	2.40555E-01

e + CH

(a) Total ionization

process	I_p	A_i, i=1-3		
		A_i, i=4-6		
e + CH → total ionization	1.06300E+01	2.31210E-01	-2.31210E-01	-1.15605E-01
		2.43804E+00	-7.38100E+00	8.61860E+00

(b) Partial cross-sections

process	I_p	A_i, i=1-3		
		A_i, i=4-6		
e + CH → CH$^+$ + 2e	1.06300E+01	1.53221E+00	-1.53221E+00	-7.65190E-01
		1.74903E+00	-3.91512E+00	2.06772E+00
e + CH → C$^+$ + H + 2e	1.48100E+01	4.74030E-01	-4.74030E-01	-2.37015E-01
		1.40756E+00	-2.77123E+00	1.91361E+00
e + CH → C + H$^+$ + 2e	1.71500E+01	8.99620E-02	-8.99620E-02	-4.49810E-02
		5.91504E-01	-1.42054E+00	1.28884E+00

2.4. C$_2$H$_6$

Table 4 replaces the corresponding tables IV and 4 of [9,10], respectively, for I-DI processes e + C$_2$H$_6$ $\rightarrow$ .... The revised threshold energies (E_{th}) for the ethane ionization and dissociative ionization cross-sections of the reaction channels are taken as the experimental appearance potentials for the corresponding ion-production cross-sections of [23]. The values in parenthesis are threshold energies for the sub-channels obtained as $A_p^{th} + \overline{E_K}$, where A_p^{th} is the thermo-chemical appearance potential for the considered sub-channel and $\overline{E_K}$ is the mean total kinetic energy for that sub-channel obtained from the measured ion kinetic energy spectra of Tian and Vidal (loc. cit.). The neutral fragmentation channels within a given ion-production channel are determined from the condition that the sum of their thermo-chemical appearance potential (A_p^{th}) and one of the peaks in the E_K spectrum obtained from the measured ion kinetic energy spectrum (by assuming sequential binary fragmentation) coincides with (or is somewhat above) the experimental threshold.

The average electron energy loss, $\overline{E_{el}^{(-)}}$ coincides with (or is somewhat larger than) the threshold energy for the considered channel.

The mean total energy of reaction products is obtained from the measured spectra $E_{K,j}$ for the ion "j" by using the relation $\overline{E_K}$ = $1/\mu \, M_j \, E_{K,j}$ where M_j is the mass of the ion "j", and $1/\mu = 1/M_j + 1/M_n$, M_n being the total mass of all other neutral fragments ("successive binary fragmentation").

TABLE 4. SAME AS Table 1, FOR e + C_2H_6 I-DI COLLISIONS. ADDITIONALLY: VIBRATIONALLY (v) AND ELECTRONICALLY (*) EXCITED STATES OF PRODUCTS INFERRED FROM COLLISION KINETICS

Reaction: e + $C_2H_6 \rightarrow$	I_p, A_p (eV)	$\overline{E_{el}^{(-)}}$ (eV)	$\overline{E_K}$ (eV)	R_{DI}	Notes (excited states)
$C_2H_6^+ + 2e$	1.15200E+01	11.52	-	-	
$C_2H_5^+ + H + 2e$	1.28000E+01	13.7	1.2	-	
$C_2H_4^+ + H_2 + 2e$	1.27000E+01	13.4	1.5	-	
$C_2H_3^+ + H_2 + H + 2e$	1.54000E+01	15.8	1.3	-	
$C_2H_2^+ + 2H_2 + 2e$	1.53000E+01	15.33	0.68	0.45	(a)
$C_2H_2^+ + H_2 + 2H + 2e$	(1.82600E+01)	18.26	1.35	0.55	
$C_2H^+ + H_2(v) + 3H + 2e$	2.88000E+01	28.8	2.1	-	(b), v= ~ 3-4
$C_2^+ + H_2^* + 2H_2 + 2e$	3.40000E+01	34.0	1.1	0.33	(c), (^{3}a, ^{3}c)
$C_2^+ + H_2^* + 2H_2 + 2e$	3.40000E+01	34.1	1.8	0.33	(^{1}B)
$C_2^+ + H_2(v) + 4H + 2e$	3.40000E+01	34.1	2.6	0.34	v=3
$CH_3^+ + CH_3(v) + 2e$	1.40000E+01	14.0	0.25	0.84	(d), v=1
$CH_3^+ + CH_2 + H + 2e$	(2.09000E+01)	20.9	2.4	0.06	
$CH_3^+ + CH + H_2 + 2e$	(2.07000E+01)	20.7	2.4	0.06	
$CH_3^+(v) + CH_3^+(v) + 3e$	(3.20000E+01)	32.0	6.6	0.04	$E_v^{tot} = $ ~ 2 eV
$CH_2^+ + CH_3^* + H + 2e$	(2.49000E+01)	24.9	0.19	0.15	(e), (3s ^{2}A$_1$';v=0)
$CH_2^+ + CH_3^* + H + 2e$	(2.55000E+01)	25.5	0.75	0.15	(3s ^{2}A$_1$' ;v=1)
$CH_2^+ + CH_3^* + H + 2e$	2.58000E+01	26.0	1.31	0.33	(3s ^{2}A$_1$' ;v=2)
$CH_2^+ + CH_2 + 2H + 2e$	2.58000E+01	26.0	2.06	0.33	
$CH_2^+ + CH_3^+ + H + 3e$	(3.80000E+01)	38.0	7.0	0.02	
$CH_2^+(v) + CH_2^+(v) + H_2 + 3e$	(3.80000E+01)	38.0	7.0	0.02	
$CH^+ + CH_3^* + 2H + 2e$	3.00000E+01	30.17	0.79	0.64	(f), (3s ^{2}A$_1$')
$CH^+ + CH_3^* + H_2 + 2e$	3.00000E+01	30.03	2.65	0.03	(3d ^{2}A$_1$')
$CH^+ + CH_3^* + H_2 + 2e$	3.00000E+01	30.0	2.65	0.03	(3d ^{2}E")
$CH^+ + CH_2 + H_2 + H + 2e$	3.00000E+01	30.1	1.6	0.30	
$C^+ + CH_3^* + H_2(v) + H + 2e$	3.20000E+01	32.0	1.0	0.10	(g), (3s ^{2}A$_1$'), $v=4$
$C^+ + CH_3^* + H_2 + H + 2e$	3.20000E+01	32.03	0.5	0.23	(3d ^{2}E")
$C^+ + CH_3^* + H_2 + H + 2e$	3.20000E+01	32.06	0.5	0.22	(3d ^{2}A$_1$')
$C^+ + CH_2^* + 2H_2 + 2e$	3.20000E+01	32.85	0.5	0.15	(3d ^{3}A$_2$)
$C^+ + CH_2 + 2H_2 + 2e$	3.20000E+01	32.88	0.5	0.15	(C)
$C^+ + CH_2 + 2H_2 + 2e$	3.20000E+01	32.97	0.5	0.15	(D)
$C_2H_5^{2+} + H + 3e$	3.36100E+01	-	-	-	
$H^+ + C_2H_4 + H + 2e$	2.05000E+01	20.5	0.9	0.65	(h)
$H^+ + C_2H_3 + H_2 + 2e$	2.05000E+01	20.5	1.4	0.35	
$H_2^+ + C_2H_4 + 2e$	1.80000E+01	18.0	1.15	-	(h)
H_3^+ (total)	3.32000E+01	-	-	-	

Notes:

(a) The values of branching ratios R_{DI} for these two channels have been determined from the relative size of the corresponding peaks in the E_K spectrum.

(b) The energy threshold for this channel, in conjunction with the observed $\overline{E_K}$ value, can be obtained only if H_2 is vibrationally excited to $v \cong 3\text{-}4$ levels.

(c) The experimental threshold for the C_2^+ ion production channel, in conjunction with the observed E_K spectrum, requires that the H_2 product be electronically or vibrationally excited to the indicated states. The values of R_{DI} are determined on the basis of relative height of the corresponding peaks in the E_K spectrum.

(d) The vibrational quantum in CH_3 is assumed to be about 0.24 eV. The thermo-chemical appearance potentials for the $CH_3^+ + CH_2 + H$ and $CH_3^+ + CH + H_2$ channels are 18.48 eV and 18.32 eV, respectively, and are not separated in the E_K spectrum. Their joint size is about 16% of the E_K peak corresponding to the $CH_3^+ + CH_3$ channel.

(e) Although energy thresholds for the $CH_2^+ + CH_3$ $(3s^2A_1';$ $v = 0, 1) + H$ reaction channels are below the value of 25.8 eV observed in the experiment of Tian and Vidal [23], it is taken that they nevertheless contribute to the CH_2^+ production cross-section since in another $e + C_2H_6$ experiment the CH_2^+ appearance potential was observed at 25.0 eV [24]. While for E < 25.8 eV their contribution to $\sigma_{ion}(CH_2^+ + ...)$ may be negligible, for energies well above the 25.8 eV their contribution may be up to 30%, as indicated by their peaks in the E_K spectrum. The vibrational quantum in $CH_3(3s^2A_1')$ excited state is about 0.56 eV. The excited $CH_3(3s^2A_1')$ state rapidly decays radiatively to the ground electronic state of CH_3.

(f) The listed neutral fragmentation channels are consistent with the observed CH^+ appearance potential and the observed E_K spectrum. The electronically excited CH_3 state decays radiatively to the ground state of CH_3. The values of R_{DI} are determined from the relative size of the corresponding peaks in the E_K spectrum.

(g) The E_K spectrum related to C^+ production is rather broad in the region 0.3 - 1.5 eV and may include many neutral fragmentation channels. Consistent with this spectrum and with the observed C^+ ion production threshold are the channels that involve the indicated electronically excited states of CH_3 and CH_2. All these states are radiatively coupled with the corresponding ground electronic states. The uniformity of R_{DI} values for all the neutral fragmentation channels reflects the broad (almost peak-less) structure of the E_K spectrum.

(h) E_K spectra for H_2^+ and H^+ ion production channels were not reported by Tian and Vidal [23]. The mean energy $\overline{E_K}$ for the neutral fragmentation channels where determined as $\overline{E_K} = E_{th} - A_p^{th}$, where E_{th} is the experimental threshold and A_p^{th} is the calculated thermo-chemical appearance potential. The suggested R_{DI} values for the $H^+ + C_2H_4 + H$ and $H^+ + C_2H_3 + H_2$ channels are based on the probabilities for breaking one or two C-H bonds.

The threshold energies $E_{th} = I_p$ (or $E_{th} = A_p$, whichever is appropriate) and fitting parameters A_i for I and DI cross-sections of the ethane family C_2H_y of hydrocarbon molecules for fit expression (7) are given in the following tables.

For the smaller molecules of this family: C_2H_y, y=0...5, the relevant information on threshold energies and branching ratios is kept the same as in the previous database, only the fitting procedure has been revised as described above, with the following exceptions:

i) The $e + C_2$ I-DI data have been missing in [9,10], and are added here for completeness.
ii) The threshold energies for the double ionization processes have been revised according to data given in chapter 20 in [2].

Note that in some cases in the tables below certain processes seem to appear twice, sometimes even with identical threshold energy and fit coefficients. This is a consequence of the explicit distinction of processes in Table 4 by the excited state of products.

e + C$_2$

(a) Total ionization

process	I$_p$	A$_i$, i=1-3 A$_i$, i=4-6		
e + C$_2$ → total ionization	1.14100E+01	3.11536E+00 1.92410E+00	-3.11536E+00 -2.69722E+00	-1.55768E+00 3.94953E+00

(b) Partial cross-sections

process	I$_p$	A$_i$, i=1-3 A$_i$, i=4-6		
e + C$_2$ → C$_2^+$ + 2e	1.14100E+01	2.18010E+00 2.06587E+00	-2.18010E+00 -8.26403E-01	-1.09005E+00 1.00656E+00
e + C$_2$ → C + C$^+$ + 2e	1.74400E+01	1.45920E+00 1.61867E+00	-1.45920E+00 -8.15502E-01	-7.29598E-01 1.13449E+00

e + C$_2$H

(a) Total ionization

process	I$_p$	A$_i$, i=1-3 A$_i$, i=4-6		
e + C$_2$H → total ionization	1.16100E+01	3.36862E+00 1.18982E+01	-3.27340E+00 -3.49587E+01	-8.60684E-01 2.98085E+01

(b) Partial cross-sections

process	I$_p$	A$_i$, i=1-3 A$_i$, i=4-6		
e + C$_2$H → C$_2$H$^+$ + 2e	1.16100E+01	3.00833E+00 1.03762E+01	-2.97506E+00 -3.26757E+01	-9.68937E-02 2.69854E+01
e + C$_2$H → C$_2^+$ + H + 2e	1.74300E+01	2.27368E-01 -7.30431E-01	-1.54393E-01 3.43064E-02	7.05112E-01 1.00471E+00
e + C$_2$H → CH$^+$ + C + 2e	1.92900E+01	1.47591E-01 9.65153E-03	-1.40935E-01 1.38787E+00	-4.25405E-02 -8.87944E-01
e + C$_2$H → C$^+$ + CH + 2e	1.99200E+01	5.13887E-02 3.72725E-01	-5.13887E-02 1.08120E-02	-1.61369E-02 -1.48563E-02
e + C$_2$H → C$_2$ + H$^+$ + 2e	1.96200E+01	1.12449E-01 9.45741E-01	-1.12449E-01 -1.10189E+00	4.19456E-02 7.56711E-01

e + C$_2$H$_2$

(a) Total ionization

process	I$_p$	A$_i$, i=1-3		
		A$_i$, i=4-6		
e + C$_2$H$_2$ → total ionization	1.14000E+01	5.05929E+00	-5.05929E+00	-1.68643E+00
		-4.84899E+00	1.30678E+01	-6.42704E+00

(b) Partial cross-sections

process	I$_p$	A$_i$, i=1-3		
		A$_i$, i=4-6		
e + C$_2$H$_2$ → C$_2$H$_2^+$ + 2e	1.14000E+01	4.20012E+00	-4.20012E+00	-2.10006E+00
		9.37225E-01	4.72060E+00	-5.94119E+00
e + C$_2$H$_2$ → C$_2$H$^+$ + H + 2e	1.64800E+01	6.28673E-01	-6.28673E-01	-2.09558E-01
		6.44489E+00	-1.34565E+01	8.93182E+00
e + C$_2$H$_2$ → C$_2^+$ + H$_2$ + 2e	1.77600E+01	7.84877E-02	-7.84877E-02	-2.61626E-02
		1.32154E-01	1.35897E+00	-8.90799E-01
e + C$_2$H$_2$ → CH$^+$ + CH + 2e	2.06100E+01	3.62698E-12	-3.62698E-12	4.88943E-02
		5.88615E-01	2.74283E+00	-1.93746E+00
e + C$_2$H$_2$ → C$^+$ + CH$_2$ + 2e	2.03500E+01	1.63264E-02	-1.63264E-02	-5.44213E-03
		1.45098E-01	7.25255E-01	7.12582E-02
e + C$_2$H$_2$ → H$^+$ + C$_2$H + 2e	1.84600E+01	1.14922E-01	-1.14922E-01	-3.83072E-02
		-9.26343E-02	2.87976E+00	-1.61432E+00
e + C$_2$H$_2$ → C$_2$H$_2^{2+}$ + 3e	3.27000E+01	2.32153E-30	3.57101E-13	4.25719E-03
		1.98005E-02	4.49789E-01	-9.50067E-02
e + C$_2$H$_2$ → C$_2$H^{2+} + H + 3e	3.72000E+01	2.75133E-05	-2.75133E-05	9.94734E-05
		-1.12833E-03	1.42337E-02	-1.16847E-02

e + C₂H₃

(a) Total ionization

process	I_p	A_i, i=1-3 A_i, i=4-6		
e + C₂H₃ → total ionization	8.25000E+00	2.84993E+00 -1.50243E+00	-2.84993E+00 -3.30255E+00	-9.49978E-01 6.24375E+00

(b) Partial cross-sections

process	I_p	A_i, i=1-3 A_i, i=4-6		
e + C₂H₃ → C₂H₃⁺ + 2e	8.25000E+00	1.35968E+00 -5.34213E-01	-1.35968E+00 -3.57649E-01	-4.53225E-01 1.78776E+00
e + C₂H₃ → C₂H₂⁺ + H + 2e	1.29200E+01	1.22933E+00 4.45256E-02	-1.22933E+00 3.27236E-01	-6.14663E-01 6.43250E-01
e + C₂H₃ → C₂H⁺ (total)	1.42300E+01	7.11659E-01 2.35496E-01	-7.11523E-01 1.28577E+00	-3.55558E-01 -7.16912E-01
e + C₂H₃ → C₂H⁺ + H₂ + 2e	1.42300E+01	6.38574E-01 2.11251E-01	-6.38453E-01 1.13942E+00	-3.19045E-01 -5.93711E-01
e + C₂H₃ → C₂H⁺ + 2H + 2e	1.60200E+01	8.34433E-02 5.86261E-02	-8.34367E-02 2.17040E-01	-4.17084E-02 -2.19713E-01
e + C₂H₃ → C₂⁺ + H₂ + H + 2e	1.97800E+01	6.95930E-02 1.32248E-01	-6.95930E-02 4.13481E-01	-2.31977E-02 -3.25042E-01
e + C₂H₃ → CH₂⁺ + CH + 2e	1.74100E+01	4.24043E-02 6.61934E-02	-4.24043E-02 5.52132E-02	-2.12021E-02 -4.24751E-02
e + C₂H₃ → CH⁺ + CH₂ + 2e	1.82400E+01	6.41536E-18 1.76402E-01	4.36739E-13 5.75007E-01	4.36744E-13 -4.10556E-02
e + C₂H₃ → C⁺ + CH₃ + 2e	1.70400E+01	8.40370E-02 -1.07918E-01	-8.40370E-02 7.09169E-01	-2.80123E-02 -3.23944E-01
e + C₂H₃ → H⁺ + C₂H₂ + 2e	1.51200E+01	6.65734E-02 -5.15841E-02	-6.65734E-02 2.52867E-01	-2.21911E-02 1.28546E-01

e + C$_2$H$_4$

(a) Total ionization

process	I$_p$	A$_i$, i=1-3 A$_i$, i=4-6		
e + C$_2$H$_4$ → total ionization	1.05100E+01	4.71486E+00 -3.30967E+00	-4.71486E+00 -5.97955E-01	-1.57162E+00 7.07765E+00

(b) Partial cross-sections

process	I$_p$	A$_i$, i=1-3 A$_i$, i=4-6		
e + C$_2$H$_4$ → C$_2$H$_4^+$ + 2e	1.05100E+01	2.74595E+00 1.77227E+00	-2.74595E+00 -4.80076E+00	-1.37297E+00 3.15670E+00
e + C$_2$H$_4$ → C$_2$H$_3^+$ + H + 2e	1.30900E+01	1.46480E+00 -1.58756E+00	-1.46480E+00 4.48597E+00	-4.88266E-01 -1.65638E+00
e + C$_2$H$_4$ → C$_2$H$_2^+$ (total)	1.32300E+01	5.10398E-01 -6.71375E-01	-5.10398E-01 2.66035E+00	-1.70133E-01 8.20013E-01
e + C$_2$H$_4$ → C$_2$H$_2^+$ + H$_2$ + 2e	1.32300E+01	3.24396E-01 -3.28628E-01	-3.24396E-01 2.29104E+00	-1.08132E-01 4.43669E-01
e + C$_2$H$_4$ → C$_2$H$_2^+$ + 2H + 2e	1.77600E+01	2.89452E-01 -2.96633E-01	-2.89452E-01 1.54699E+00	-9.64841E-02 -7.56145E-01
e + C$_2$H$_4$ → C$_2$H$^+$ + H$_2$ + H + 2e	1.90600E+01	3.91392E-24 2.07210E-01	4.48729E-16 -3.31355E-01	4.48729E-16 1.88288E+00
e + C$_2$H$_4$ → C$_2^+$ + 2H$_2$ + 2e	2.00900E+01	1.92537E-03 6.65171E-02	-1.92537E-03 1.55755E-01	-6.41790E-04 5.16633E-02
e + C$_2$H$_4$ → CH$_3^+$ + CH + 2e	1.69400E+01	8.49862E-03 7.05858E-02	-8.49862E-03 1.06500E-02	-2.83287E-03 3.50546E-01
e + C$_2$H$_4$ → CH$_2^+$ + CH$_2$ + 2e	1.79400E+01	9.74673E-02 -1.20248E-01	-9.74673E-02 6.82582E-01	-3.24891E-02 -3.78335E-01
e + C$_2$H$_4$ → CH$^+$ + CH$_3$ + 2e	1.82000E+01	9.66541E-05 4.45046E-02	-9.66541E-05 1.72261E-02	-3.22180E-05 1.29673E-01
e + C$_2$H$_4$ → C$^+$ (total)	1.89400E+01	3.11841E-03 1.86251E-02	-3.11841E-03 2.82313E-02	-1.03947E-03 6.25788E-02
e + C$_2$H$_4$ → C$^+$ + CH$_2$ + H$_2$ + 2e	2.22200E+01	8.96970E-04 1.18413E-02	-8.96970E-04 8.37422E-03	1.69086E-04 1.55720E-02
e + C$_2$H$_4$ → C$^+$ + CH$_3$ + H + 2e	2.18700E+01	9.40427E-04 1.20556E-02	-9.40427E-04 8.05675E-03	1.74842E-04 1.55757E-02
e + C$_2$H$_4$ → C$^+$ + CH$_4$ + 2e	1.89400E+01	8.44042E-04 2.58120E-02	-8.44042E-04 -7.83623E-03	7.21730E-05 3.09890E-02

e + C_2H_5

(a) Total ionization

process	I_p	A_i, i=1-3 A_i, i=4-6		
e + C_2H_5 → total ionization	8.12000E+00	1.33352E+00 -3.67560E-01	-1.33352E+00 -5.51379E+00	-4.44507E-01 1.14150E+01

(b) Partial cross-sections

process	I_p	A_i, i=1-3 A_i, i=4-6		
e + C_2H_5 → $C_2H_5^+$ + 2e	8.12000E+00	1.21203E+00 -1.34263E+00	-1.21203E+00 2.33610E+00	-4.04008E-01 -1.43938E+00
e + C_2H_5 → $C_2H_4^+$ + H + 2e	1.21000E+01	8.56906E-01 -9.27824E-01	-8.56906E-01 2.34436E+00	-2.85635E-01 -4.10607E-01
e + C_2H_5 → $C_2H_3^+$ (total)	1.01400E+01	3.76758E-01 -3.80929E-01	-3.76758E-01 8.75378E-01	-1.25586E-01 2.62832E+00
e + C_2H_5 → $C_2H_3^+$ + H_2 + 2e	1.01400E+01	7.69159E-01 -6.89728E-01	-7.69159E-01 1.77793E+00	-2.56386E-01 2.09499E-01
e + C_2H_5 → $C_2H_3^+$ + 2H + 2e	1.46700E+01	3.18788E-01 -6.06895E-01	-3.18788E-01 2.25302E+00	-1.06263E-01 -1.29900E+00
e + C_2H_5 → $C_2H_2^+$ + H_2 + H + 2e	1.48100E+01	5.00145E-01 -3.40942E-01	-5.00145E-01 2.49594E+00	-1.66715E-01 -8.73536E-01
e + C_2H_5 → C_2H^+ + $2H_2$ + 2e	1.53500E+01	1.89802E-01 -2.27074E-01	-1.89802E-01 1.18216E+00	-6.32673E-02 -3.61848E-01
e + C_2H_5 → CH_3^+ + CH_2 + 2e	1.40400E+01	1.32814E-01 -1.65898E-01	-1.32814E-01 6.18695E-01	-4.42714E-02 -2.48978E-01
e + C_2H_5 → CH_2^+ + CH_3 + 2e	1.46000E+01	4.23322E-02 2.84318E-02	-4.23322E-02 -8.60992E-02	-1.41107E-02 3.96179E-01
e + C_2H_5 → CH^+ + CH_4 + 2e	1.47900E+01	9.45209E-03 3.84480E-02	-9.45209E-03 -9.13083E-02	-3.15070E-03 2.76908E-01
e + C_2H_5 → C^+ (total)	1.89200E+01	1.86754E-02 9.36246E-03	-1.86754E-02 1.19453E-01	-6.22513E-03 7.51163E-03
e + C_2H_5 → C^+ + CH_4 + H + 2e	1.89700E+01	9.35050E-03 4.97272E-03	-9.34666E-03 5.95339E-02	-3.08773E-03 3.72478E-03
e + C_2H_5 → C^+ + CH_3 + H_2 + 2e	1.89200E+01	9.34975E-03 4.99393E-03	-9.34541E-03 5.94993E-02	-3.09196E-03 3.74416E-03

e + C_2H_6

(a) Total ionization

process	I_p	A_i, i=1-3		
		A_i, i=4-6		
e + C_2H_6 → total ionization	1.15200E+01	6.03747E+00	-5.99052E+00	-2.92484E+00
		-4.11754E+00	2.70115E+00	5.24993E+00

(b) Partial cross-sections

process	I_p	A_i, i=1-3		
		A_i, i=4-6		
e + C_2H_6 → $C_2H_6^+$ + 2e	1.15200E+01	1.05038E+00	-1.05038E+00	-5.10091E-01
		-4.66191E-01	1.70296E+00	-1.41227E+00
e + C_2H_6 → $C_2H_5^+$ + H + 2e	1.28000E+01	1.03160E+00	-1.03160E+00	-5.14175E-01
		5.32943E-02	1.10906E+00	-1.45837E+00
e + C_2H_6 → $C_2H_4^+$ + H_2 + 2e	1.27000E+01	3.76101E+00	-3.76095E+00	-1.88038E+00
		5.10189E-01	3.54312E+00	-4.25086E+00
e + C_2H_6 → $C_2H_3^+$ + H_2 + H + 2e	1.54000E+01	1.09952E+00	-1.09952E+00	1.24478E-01
		7.48572E-01	-1.50798E+00	1.24606E+00
e + C_2H_6 → $C_2H_2^+$ (total)	1.53000E+01	8.69981E-02	-8.69981E-02	3.95639E-01
		4.05974E-01	-1.19644E+00	2.29092E+00
e + C_2H_6 → $C_2H_2^+$ + $2H_2$ + 2e	1.53000E+01	4.15609E-02	-4.15609E-02	5.96632E-01
		-1.17613E+00	1.41082E+00	1.05087E-01
e + C_2H_6 → $C_2H_2^+$ + H_2 + 2H + 2e	1.82600E+01	5.80287E-02	-5.80287E-02	5.20093E-01
		-7.51220E-01	8.95693E-01	4.57642E-01
e + C_2H_6 → C_2H^+ + H_2 + 3H + 2e	2.88000E+01	3.90590E-12	-3.90590E-12	1.19233E+00
		-3.33147E+00	7.33891E+00	-4.74566E+00
e + C_2H_6 → CH_3^+ (total)	1.40000E+01	2.81446E-31	3.10222E-13	6.20444E-13
		8.69726E-01	-2.64912E+00	2.78810E+00
e + C_2H_6 → CH_3^+ + CH_3 + 2e	1.40000E+01	2.29000E-31	4.91249E-15	2.54178E-02
		6.35589E-01	-2.03902E+00	2.29509E+00
e + C_2H_6 → CH_3^+ + CH_2 + H + 2e	2.09000E+01	4.10434E-15	-4.10427E-15	3.51478E-03
		3.61554E-02	-1.31095E-01	1.56347E-01
e + C_2H_6 → CH_3^+ + CH + H_2 + 2e	2.07000E+01	3.35323E-13	-3.34453E-13	2.25174E-04
		5.69573E-02	-1.69919E-01	1.78245E-01
e + C_2H_6 → CH_3^+ + CH_3^+ + 3e	3.20000E+01	1.37001E-24	1.58796E-16	1.54345E-03
		2.90615E-02	-9.71548E-02	1.09742E-01
e + C_2H_6 → CH_2^+ (total)	2.49000E+01	3.06854E-02	-3.06854E-02	1.03558E+00
		-4.84574E+00	1.07546E+01	-6.48771E+00
e + C_2H_6 → CH_2^+ + CH_3 + H + 2e	2.49000E+01	3.25275E-03	1.43717E-02	3.36224E-02
		-2.69667E-01	1.05181E+00	-7.40178E-01
e + C_2H_6 → CH_2^+ + CH_3 + H + 2e	2.55000E+01	1.59194E-02	-8.32014E-03	1.31234E-01
		-7.29984E-01	1.76792E+00	-1.13423E+00
e + C_2H_6 → CH_2^+ + CH_3 + H + 2e	2.58000E+01	1.56100E-02	3.82984E-03	2.27000E-01
		-1.16939E+00	3.07510E+00	-1.99260E+00
e + C_2H_6 → CH_2^+ + CH_2 + 2H + 2e	2.58000E+01	1.56100E-02	3.82984E-03	2.27000E-01
		-1.16939E+00	3.07510E+00	-1.99260E+00
e + C_2H_6 → CH_2^+ + CH_3^+ + H + 3e	3.80000E+01	1.71574E-03	-1.71574E-03	2.39205E-02
		-1.15520E-01	2.50105E-01	-1.52348E-01
e + C_2H_6 → CH_2^+ + CH_2^+ + H2 + 3e	3.80000E+01	1.71574E-03	-1.71574E-03	2.39205E-02
		-1.15520E-01	2.50105E-01	-1.52348E-01
e + C_2H_6 → CH^+ (total)	3.00000E+01	1.63352E-02	-1.63352E-02	2.54519E-01

		-9.39489E-01	3.55719E+00	-2.76437E+00
e + $C_2H_6 \rightarrow CH^+ + CH_3 + 2H + 2e$	3.00000E+01	1.04545E-02	-1.04545E-02	1.62892E-01
		-6.01273E-01	2.27660E+00	-1.76920E+00
e + $C_2H_6 \rightarrow CH^+ + CH_3 + H_2 + 2e$	3.00000E+01	4.90056E-04	-4.90056E-04	7.63557E-03
		-2.81847E-02	1.06716E-01	-8.29311E-02
e + $C_2H_6 \rightarrow CH^+ + CH_3 + H_2 + 2e$	3.00000E+01	4.90056E-04	-4.90056E-04	7.63557E-03
		-2.81847E-02	1.06716E-01	-8.29311E-02
e + $C_2H_6 \rightarrow CH^+ + CH_2 + H_2 + H + 2e$	3.00000E+01	4.90056E-03	-4.90056E-03	7.63557E-02
		-2.81847E-01	1.06716E+00	-8.29311E-01
e + $C_2H_6 \rightarrow C_2^+$ (total)	3.40000E+01	3.90899E-13	-3.90899E-13	4.71799E-01
		-2.43404E+00	5.41610E+00	-3.36446E+00
e + $C_2H_6 \rightarrow C_2^+ + 3H_2 + 2e$	3.40000E+01	1.28997E-13	-1.28997E-13	1.55694E-01
		-8.03233E-01	1.78731E+00	-1.11027E+00
e + $C_2H_6 \rightarrow C_2^+ + 3H_2 + 2e$	3.40000E+01	1.28997E-13	-1.28997E-13	1.55694E-01
		-8.03233E-01	1.78731E+00	-1.11027E+00
e + $C_2H_6 \rightarrow C_2^+ + H_2 + 4H + 2e$	3.40000E+01	1.32906E-13	-1.32906E-13	1.60412E-01
		-8.27573E-01	1.84147E+00	-1.14392E+00
e + $C_2H_6 \rightarrow C^+$ (total)	3.20000E+01	2.30089E-13	-2.30089E-13	2.30943E-01
		-1.28702E+00	3.31825E+00	-2.15011E+00
e + $C_2H_6 \rightarrow C^+ + CH_3 + H_2 + H + 2e$	3.20000E+01	2.30089E-14	-2.30089E-14	2.30943E-02
		-1.28702E-01	3.31825E-01	-2.15011E-01
e + $C_2H_6 \rightarrow C^+ + CH_3 + H_2 + H + 2e$	3.20000E+01	5.29204E-14	-5.29204E-14	5.31168E-02
		-2.96014E-01	7.63197E-01	-4.94525E-01
e + $C_2H_6 \rightarrow C^+ + CH_3 + H_2 + H + 2e$	3.20000E+01	5.06195E-14	-5.06195E-14	5.08074E-02
		-2.83143E-01	7.30015E-01	-4.73024E-01
e + $C_2H_6 \rightarrow C^+ + CH_2 + 2H_2 + 2e$	3.20000E+01	3.45133E-14	-3.45133E-14	3.46414E-02
		-1.93052E-01	4.97737E-01	-3.22516E-01
e + $C_2H_6 \rightarrow C^+ + CH_2 + 2H_2 + 2e$	3.20000E+01	3.45133E-14	-3.45133E-14	3.46414E-02
		-1.93052E-01	4.97737E-01	-3.22516E-01
e + $C_2H_6 \rightarrow C^+ + CH_2 + 2H_2 + 2e$	3.20000E+01	3.45133E-14	-3.45133E-14	3.46414E-02
		-1.93052E-01	4.97737E-01	-3.22516E-01
e + $C_2H_6 \rightarrow C_2H_5^{2+} + H + 3e$	3.36100E+01	7.11311E-04	-7.11311E-04	-2.37104E-04
		2.56826E-01	-3.60794E-01	1.32105E-01
e + $C_2H_6 \rightarrow H^+$ (total)	2.05000E+01	2.82314E-11	-2.82314E-11	2.64194E-01
		-1.18196E+00	2.92576E+00	3.39427E-01
e + $C_2H_6 \rightarrow H^+ + C_2H_4 + H + 2e$	2.05000E+01	1.83504E-11	-1.83504E-11	1.71726E-01
		-7.68273E-01	1.90174E+00	2.20628E-01
e + $C_2H_6 \rightarrow H^+ + C_2H_3 + H_2 + 2e$	2.05000E+01	9.88099E-12	-9.88099E-12	9.24680E-02
		-4.13685E-01	1.02402E+00	1.18799E-01
e + $C_2H_6 \rightarrow H_2^+ + C_2H_4 + 2e$	1.80000E+01	6.52632E-19	1.89252E-14	3.78513E-14
		5.90472E-02	-1.26149E-01	4.28668E-01
e + $C_2H_6 \rightarrow H_3^+$ (total)	3.32000E+01	4.66489E-13	2.72250E-02	5.44500E-02
		8.25000E-01	-1.07000E+00	4.02000E-01

3. DE ON CH$_4$

For C$_x$H$_y$, (and also for SiH$_y$) molecules, fits for the total cross-sections $\sigma^{tot}(E)$ for dissociative excitation (of neutrals: DE, and of ions: DE$^+$) but also for other electron impact collision processes (e.g. dissociative ionization of molecular ions: DI$^+$) in the databases [7,8,9,10] and in a similar database for Silane (see [11]) have been given in the following generic form:

$$\sigma_\lambda^{tot}\left(MH_y\right) = A_0 F_M^\lambda(y)\left(1 - \frac{E_{th}}{E}\right)^{\alpha_\lambda} \frac{1}{E}\ln(e + cE) \quad \left(\times 10^{-16} cm^2\right) \qquad (18)$$

with A_0, α_λ and c constants, $F_M^\lambda(y)$ a "structural" function of y, the number of hydrogen atoms in the hydride molecule. M stands for C, C$_2$, C$_3$, Si and λ labels the type of process, such as dissociative excitation, dissociative ionization, etc. (DE, I-DI, DE$^+$ and DI$^+$), loc.cit.

Most studied electron impact collision processes in these databases have many reaction channels, all of which [except the direct ionization and the pure electron capture] are related to the molecular dissociation. The total cross-section of a given type of process for a given MH$_y$ molecule is the sum of partial cross-sections of individual reaction channels of that process for the considered molecule. The contribution of a particular reaction channel j to the total cross-section σ_λ^{tot} of the process λ at a given collision energy E, is given by the branching ratio

$$R_j^\lambda(E) = \frac{\sigma_j^\lambda(E)}{\sigma_\lambda^{tot}(E)}, \qquad (19)$$

where $\sigma_j^\lambda(E)$ is the partial cross-section of channel j. Obviously, this relation can be used to determine $\sigma_j^\lambda(E)$ when $\sigma_\lambda^{tot}(E)$ and $R_j^\lambda(E)$ are known.

3.1. R(E): energy dependent branching ratios

However, the formulas for $R_j^\lambda(E)$ proposed in the previous database have had significant shortcomings and could, under certain conditions, even lead to negative cross-sections in the near threshold region. For this reason the online database HYDKIN only used constant branching ratios rather than these energy dependent functions. However the precision of the partial cross-sections near their threshold energies was unnecessarily reduced by this. In this Section we provide new formulas for the branching ratios which do not suffer from the defects, and which have been implemented in HYDKIN in January 2007.

As pointed out in the references [7,8,9,10] it was shown experimentally that the cross-section branching ratios R_j^λ for these molecules remain the same in the entire energy region above ~ 20 - 30 eV (within the uncertainties of the data, 8-10%). The observed energy invariance of channel branching ratios for these processes indicates that the basic dynamical mechanism for all reaction channels is the same, and the differences in the values of R_j^λ are related to structural factors.

Hence the assumption of energy independence of all R_j^λ is a highly plausible first approximation. The resulting unitarity relation for the branching ratios,

$$\sum_j R_j^\lambda = 1 \quad , \qquad (20)$$

has then been used together with an ordering of partial processes according to the reaction thresholds

$$E_{th,1} < E_{th,2} < E_{th,3} < \dots E_{th,k} < \dots \tag{21}$$

in the following arguments:

- It is obvious that in the energy region $E_{th,1} < E \le E_{th,2}$, when only the channel with lowest threshold is open, R_1^{λ} should be one, while (20) gives a smaller value.
- The partial cross-section $\sigma_1^{\lambda}(E)$ calculated as $R_1^{\lambda} \cdot \sigma_{\lambda}^{tot}(E)$ will be reduced. More generally, in any part of the energy region when not all reaction channels are open, the true unitarity condition

$$\sum_{all\,k} \sigma_k^{\lambda}(E) = \sigma_{\lambda}^{tot}(E) \tag{22}$$

for the cross-sections themselves (not just for the R_j^{λ}) is not satisfied.
- In order to satisfy the unitarity condition at any collision energy, the factors R_k^{λ} have to be modified. This translates into a requirement that R_k^{λ} depend on energy.

To describe the new option for energy dependent branching ratios we start by noting that E_{th} in (18) for the total cross-section is always the minimum of all $E_{th,j}$, i.e., $E_{th} = E_{th,1}$ of the partial reaction channels according to relation (21). Furthermore we note that when evaluating the partial cross-section of channel j, the E_{th} in (18) should be replaced by the proper $E_{th,j}$ for that channel in order to provide proper threshold behavior for each partial cross-section as well.

Hence, instead of the definition (19) we will define the new energy dependent branching ratios as

$$\sigma_j(E) = \hat{R}_j(E) \cdot \sigma(E, E_{th,j})$$

with $\sigma(E, E_{th,j})$ defined as the total cross-section (18) but with E_{th} replaced by the individual channel threshold $E_{th,j}$.

Consequently the fit expressions for the partials have different energy dependencies already before multiplication with a branching ratio. Hence unitarity relation (20) for the branching ratios is not applicable and only the unitarity relation for the cross-sections themselves, (22) , needs to be fulfilled. We now define the energy dependent branching ratios [still assuming the ordering (21)] in the following way: In a first step we produce energy dependent branching ratios $\hat{R}_k(E)$ according to

$$\begin{aligned}
\hat{R}_1(E) &= \quad 0 \quad \text{for } E < E_1 \\
\hat{R}_1(E) &= \quad 1 \quad \text{for } E \ge E_1 \\
&\quad\vdots \\
\hat{R}_k(E) &= \quad 0 \quad \text{for } E < E_k \\
\hat{R}_k(E) &= \quad R_k/R_1 \quad \text{for } E \ge E_k
\end{aligned} \tag{23}$$

with R_j being the (energy independent) branching ratios given e.g., in the database [7,8,9,10] or in Table 5 below. In a second step we apply a common normalizing function $\alpha(E)$ which is the same for all channels j, and which will be determined from the cross-section unitarity relation (22). Hence the normalizing function $\alpha(E)$ is defined as:

$$\alpha(E) = \frac{\sigma^{tot}(E)}{\sum_j \hat{\sigma}_j(E)} \tag{24}$$

where $\hat{\sigma}_j$ is evaluated according to [compare with (18)]:

210

$$\hat{\sigma}_j(e) = \hat{R}_j(E) \cdot \sigma(E, E_{th,j})$$

$$= \hat{R}_j(E) \cdot A_0 F_M^\lambda(y) \left(1 - \frac{E_{th,j}}{E}\right)^{\alpha_\lambda} \frac{1}{E} \ln(e + cE) \quad (\times 10^{-16} cm^2) \tag{25}$$

with the same constants A_0, α_λ, c as for the corresponding total cross-section, and with $\hat{R}_j(E)$ according to (23). Finally the partial cross-section for channel j is given as:

$$\sigma_j(MH_y) = \alpha(E) \cdot \hat{\sigma}_j(E) = \hat{R}_j(E) \cdot \sigma(E, E_{th,j}) \tag{26}$$

Hence we have automatically fulfilled the unitarity relation (22), the correct near threshold behavior for each partial and total cross-section, and, furthermore,

$$\frac{\tilde{R}_i(E)}{\tilde{R}_j(E)} = \frac{\hat{R}_i(E) \cdot \alpha(E)}{\hat{R}_j(E) \cdot \alpha(E)} = \frac{\hat{R}_i(E)}{\hat{R}_j(E)} = \frac{R_i}{R_j} \tag{27}$$

at **all** energies E at which the partial channels i,j are both open.

3.2. New data for DE: methane family

New information regarding the DE processes for the molecules of the methane family, collected since the first publication of the database [7,8] are compiled in the Table 5. These data replace those from Table II in [7] and Table 2 in [8]. In particular the threshold energies, E_{th}, the branching ratios R_{DE} at high energies, mean electron energy loss, $\overline{E_{el}^{(-)}}$ and the mean total kinetic energy of the products, $\overline{E_K}$ have been upgraded. Note that even for the unmodified data, which are also still available as option in the online database HYDKIN for reproducibility, the resulting cross-sections may be different from those found earlier with this online tool in the near threshold regions, unless the new energy dependent branching ratio option (previous sub-section) is not de-activated.

The branching ratios R_{DE} for CH$_y$, $y = 3, 4$ where slightly modified with respect to the values in the earlier database [7,8] due to the introduction of new reaction channels. In the earlier database the R_{DE} values for dominant $CH_3 + H$ and $CH_2 + H$ dissociative excitation channels in CH$_4$ and CH$_3$ were comprising the contributions for some H-producing channels that are now explicitly included in the lists of reactions.

The threshold energy E_{th} is generally determined by $E_{th} = D_0 + \overline{E_K}$, where D_0 is the dissociation energy for a given channel. For the channel $CH_4 \rightarrow CH_3 + H$ the threshold energy $E_{th} = 8.8$ eV is the experimental value [25]. For CH dissociation channels, E_{th} is the vertical transition energy from the CH ground state to the corresponding dissociative or pre-dissociative state calculated in [26].

The values of $\overline{E_K}$ (the mean total kinetic energy of the products) is obtained by using the relation $\overline{E_K} = \kappa D_0$, where D_0 is the dissociation energy for a given channel. For the dominant channels ($CH_y \rightarrow CH_{y-1} + H$, $CH_{y-2} + H_2$) the value $\kappa = 0.7$-0.8 has been chosen as suggested by the known values of $\overline{E_K}$ for $CH_4 \rightarrow CH_3 + H$ and dominant dissociation channels of CH. For the "weak" reaction channels, having large values of D_0, the value of κ was chosen such that the calculated E_{th} does not exceed (or exceeds only slightly) the ionization limit of CH$_y$. For the dissociation channels of CH, $\overline{E_K}$ was calculated from the known E_{th} and D_0 values.

TABLE 5. NEUTRAL DISSOCIATIVE CHANNELS OF CH_y: BRANCHING RATIOS, R_{DE}, THRESHOLD ENERGIES, E_{th}, MEAN ELECTRON ENERGY LOSS, $\overline{E_{el}^{(-)}}$, AND MEAN TOTAL KINETIC ENERGY OF PRODUCTS, $\overline{E_K}$

Reaction channel		R_{DE}	$E_{th} = \overline{E_{el}^{(-)}}$ (eV)	$\overline{E_K}$ (products) (eV)	Notes
$e + CH_4$	$\rightarrow CH_3 + H + e$	0.70	8.8	4.3	[27]
	$\rightarrow CH_2 + H_2 + e$	0.14	8.6 ± 0.2	3.8 ± 0.2	(a)
	$\rightarrow CH_2 + 2H + e$	0.06	11.5 ± 0.2	2.2 ± 0.2	(b)
	$\rightarrow CH + H_2 + H + e$	0.07	11.0 ± 0.2	1.8 ± 0.2	
	$\rightarrow C + 2H_2 + e$	0.02	10.4 ± 0.3	2.2 ± 0.3	
	$\rightarrow C + H_2 + 2H + e$	0.01	13.8 ± 0.5	1.0 ± 0.5	
$e + CH_3$	$\rightarrow CH_2 + H + e$	0.79	8.2 ± 0.2	3.4 ± 0.2	[27]
	$\rightarrow CH + H_2 + e$	0.14	7.7 ± 0.2	3.0 ± 0.2	
	$\rightarrow CH + 2H + e$	0.03	10.5 ± 0.5	1.2 ± 0.5	
	$\rightarrow C + H_2 + H + e$	0.04	9.7 ± 0.2	1.4 ± 0.2	
$e + CH_2$	$\rightarrow CH + H + e$	0.90	7.5 ± 0.2	2.9 ± 0.2	[27],(c)
	$\rightarrow C + H_2 + e$	0.08	6.0 ± 0.2	2.6 ± 0.2	
	$\rightarrow C + 2H + e$	0.02	9.2 ± 0.5	1.2 ± 0.5	
$e + CH$	$\rightarrow C(^3P) + H + e$	0.04	3.46 ± 0.3	± 0.3	[27], (d)
		0.08	4.02	0.56	(e)
		0.35	7.55	4.09	(f)
	$\rightarrow C(^1D) + H + e$	0.35	7.7 ± 0.3	3.0 ± 0.3	(g)
	$\rightarrow C(^1S) + H + e$	0.18	6.39	0.25	(h), (i)

[27]: Reaction channels included in the database of Ref. [27].

Notes:

(a) $\overline{E_K} = 4.3$ eV for $CH_4 \rightarrow CH_3 + H$ channel is the difference E_{th} - D_0 where $D_0 = 4.48$ eV.

(b) The assigned uncertainties to $\overline{E_K}$ are perhaps the lower limits.

(c) The threshold energy of the $CH_2 \rightarrow CH(A^2\Delta) + H$ channel is about 10.2 eV, i.e., about 0.2 eV below the CH ionization limit, and can contribute to the $CH + H$ dissociation by 5-10%.

(d) This channel proceeds via excitation of the $CH(B^2\Sigma^-)$ state that pre-dissociates (by tunneling) to $C(^3P) + H$ products. Its potential well has a depth of about 0.3 eV [26].

(e) This channel is activated by excitation of the $C^2\Sigma^+$ state of CH that pre-dissociates to $B^2\Sigma^-$, to produce $C(^3P)$ and H.

(f) This channel proceeds by excitation of the purely repulsive state $1^4\Pi$ of CH

(g) This channel proceeds by excitation of the close lying $2^2\Pi$, $3^2\Pi$ and $4^2\Pi$ states with vertical transition energies ranging from 7.43 ($2^2\Pi$) to 8.05 ($4^2\Pi$). The $2^2\Pi$ state is pre-dissociative (by tunneling), while $3^2\Pi$ and $4^2\Pi$ pre-dissociate to $2^2\Pi$ by radial coupling.

(h) This channel proceeds by excitation of the dissociative $2\Sigma^+$ state of CH.

(i) The relative weights of dissociation channels proceeding via excitation of a doublet state were taken from their contribution to the total photo-ionization cross-section [26]. Here it was assumed that in electron-impact dissociation of CH the $1^4\Pi$ channel is as strong as the dissociation via the $2,3,4^2\Pi$ group of pre-dissociating states.

4. NEW DATA FOR DE$^+$ AND DI$^+$ FOR CH$_y^+$ (METHANE FAMILY)

Recently, experimental data have become available for the total ion production cross-section of dissociative excitation (DE$^+$) and dissociative ionization (DI$^+$) of CD$_y^+$ ions from the methane family (y = 1 - 4) by electron impact (where D is the deuteron) from the group of P. Defrance at the Catholic University of Louvain-la-Neuve (Belgium), see also Janev et al, in this present volume, [28]. The measured cross-sections are the sum $\sigma_{tot}(DE^+ + DI^+)$ for a given ion production. Only in the case of D$^+$ production additionally also the dissociative ionization cross-section $\sigma_{tot}(DI^+)$ has been measured separately for each value of y = 1 - 4. Besides the above total ion production cross-sections also the total kinetic energy release (KER) was measured at a number of electron impact energies. The experimental results for CD$^+$ have been published [29], for the ions CD$_2^+$ and CD$_3^+$ they are in press [30], and for CD$_4^+$ see [31]. The energy range covered by these measurements extends from the threshold up to 2.8 keV.

An analysis of the $\sigma_{tot}(DE^+ + DI^+)$ and $\sigma_{tot}(DI^+)$ (for D$^+$ only) ion production cross-sections and the corresponding KER spectra was performed to determine the individual $\sigma(DE^+)$ and $\sigma(DI^+)$ cross-sections for
a) specific (A^+ + *neutrals*) reaction channels, $\sigma(DE^+; A^+ + ...)$ contributing to $\sigma_{tot}(DE^+; A^+)$
and for
b) specific (A^+ + *ion* + *neutrals*) reaction channels, $\sigma(DI^+; A^+ + ion + ...)$ contributing to $\sigma_{tot}(DI^+; A^+)$.

The thermo-chemical dissociation energies (D$_0$) for any DE$^+$ or DI$^+$ reaction channel can be calculated from the thermo-chemical data available in the literature (e.g., the NIST Chemistry Web book). Using such values of D$_0$ and the experimentally observed KER spectra it was possible to determine the energy thresholds for different *ion* + *neutrals* (for DE$^+$) and *ion* + *ion* + *neutrals* (for DI$^+$) reaction channels. The KER spectra, representing in fact differential cross-sections (in energy), have been used to determine the values of the total cross-section for the identified reaction channel at the electron energies for which the KER was measured. This information was sufficient to derive the cross-sections for the most important *ion* + *neutrals* (in the case of DE$^+$) and *ion* + *ion* + *neutral* (in the case of DI$^+$) reactions. The derived channel cross-sections have been checked against the fulfilment of the "sum rules", i.e., their sum has to be equal to the corresponding measured total ion production cross-section (consistency check).

The DE$^+$ and DI$^+$ channel cross-sections have been fitted to analytic expressions of the form:

$$\sigma_{DE^+} = \sigma_{DE^+}^{(a)} + \sigma_{DE^+}^{(b)}$$ (a)

$$\sigma_{DE^+}^{(a)} = a_1 \left(1 - \frac{E_{th}}{E}\right)^{a_2} \frac{1}{E}\ln(e + a_3 E) \quad \left(\times 10^{-16} cm^2\right)$$ (b)

$$\sigma_{DE^+}^{(b)} = b_1 \left(1 - \frac{E_{th}}{E}\right)^{b_2} \frac{1}{E^{b_3}} \quad \left(\times 10^{-16} cm^2\right)$$ (c) (28)

and

$$\sigma_{DI^+} = c_1 \left(1 - \frac{E_{th}}{E}\right)^{c_2} \frac{1}{E}\ln(e + c_3 E) \quad \left(\times 10^{-16} cm^2\right)$$ (29)

where E_{th} is the threshold energy, e = 2.71828..., and a_i, b_i, c_i are the fitting parameters. E and E_{th} are expressed in eV units. The two parts in σ_{DE+} in (28) reflect the two peak structure in some of the DE$^+$ cross-sections. The specific DE$^+$ and DI$^+$ channels are characterized by their threshold energies and their branching ratios (R_{DE+} and R_{DI+}), respectively, at high energies. Examples of these cross-sections, for $e + CH_3^+$ collisions, are shown in FIG. 6 and Figure 7. In the present HYDKIN database the LLN data (see Tables below) are used for both the DE$^+$ and DI$^+$ channels. The DE$^+$ data labled "ORNL" in

Figure 6 are obtained by taking the experimental (DE[+] + DI[+]) cross-sections from ORNL and subtracting the LLN DI[+] cross-sections.
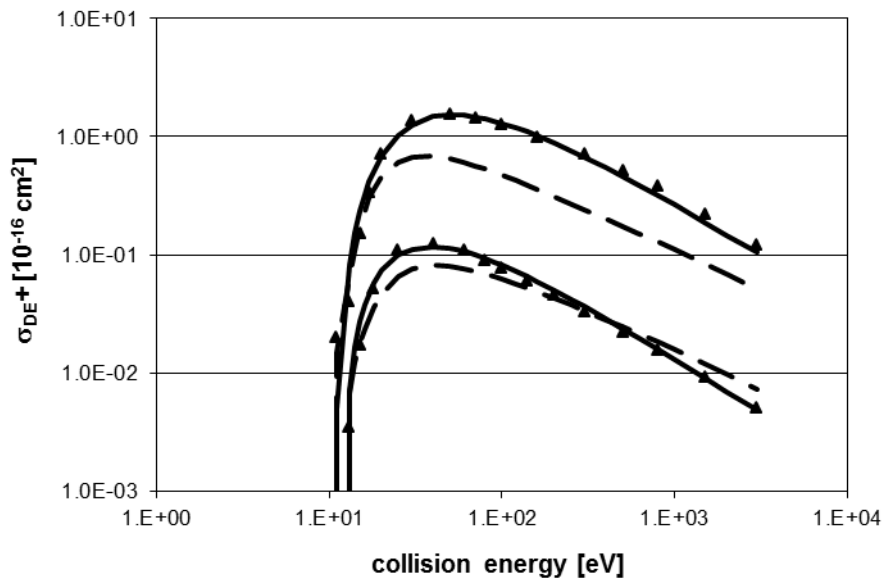
FIG. 6. *Dissociative excitation cross-section (in units of 10^{-16} cm^2) of CH$_3^+$ ions by electron impact, vs. electron energy (eV). Total H$^+$ (upper curves) and H$_2^+$ (lower curves) production channels Triangles: ORNL data. Solid lines: fit to expression (28), ORNL, see text. Dashed lines: fit to LLN data, see Table 7.*
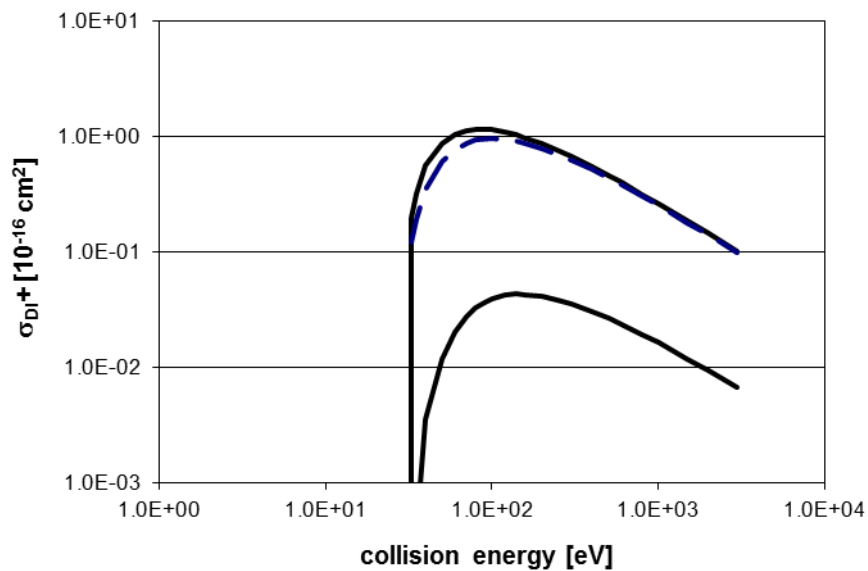
FIG. 7. *same as Figure 6, but for dissociative ionization of CH3+ ions. Solid lines: fit to expression (28). Total H+ and H2+ production rates derived from Table 11. Dashed line: [30]. Only LLN data are available.*

214

4.1. DE⁺ for methane family

Revised data for dissociative excitation of CH_y^+ (DE⁺): Louvain-la-Neuve University data (LLN data) are summarized in Table 6, Table 7, Table 8 and Table 9. These tables replace table III in [7] and Table 3 in [8]. In the hydrocarbon ions the H atoms are taken to be equivalent to D atoms, for which most of these experiments have been carried out. The new fitting coefficients a_i, b_i are also given in these tables. Equation (28) with these fitting coefficients replaces Equation (14) in [7].

TABLE 6. DISSOCIATIVE EXCITATION CHANNELS OF CH_4^+: BRANCHING RATIOS R_{DE+}, THRESHOLD ENERGIES E_{th}, AND MEAN TOTAL KINETIC ENERGY OF PRODUCTS $\overline{E_K}$. FITTING COEFFICIENTS a_i AND b_i FOR FIT EXPRESSION (28)

$CH_4^+ \rightarrow \ldots$	E_{th} (eV)	$\overline{E_K}$ (eV)	b_1 / a_1	b_2 / a_2	b_3 / a_3	Type	R_{DE+}	Note
$CH_3^+ + H$	2.4 *	0.8	3.54×10^3	4.55	3.0	b_i	1	(a)
$CH_3^{+*} + H$	17.5	0.8	33.5	1.23	0.075	a_i	1	(b)
$CH_2^+ + H_2$	3.7 *	1.2	6.26×10^4	7.24	3.44	b_i	1	
$CH_2^+ + 2H$	8.2	1.2	24.2	5.82	0.211	a_i	1	
$CH^+ + H_2 + H$	8.0 *	0.7	8.66×10^7	5.60	5.33	b_i	1	
$CH^+ + 3H$	12.5	0.7	34.8	2.53	0.13	a_i	1	(a)
$C^+ + 2H_2$	<u>9.0</u> *	0.6					0.55	
$C^+ + H_2 + 2H$	12.0	0.6	2.51×10^5	3.94	3.83	b_i	0.45	
$C^+ + 4H$	<u>16.5</u>	0.6	11.0	2.73	0.69	a_i	1	
$H_3^+ + CH$	9.5 *	0.8	0.0974	0.86	0.015	a_i	1	
$H_2^+ + CH_2$	<u>9.3</u> *	1.4					0.33	
$H_2^+ + CH + H$	12.0	1.4	1.4×10^5	5.36	3.53	b_i	0.33	(a)
$H_2^+ + C + H_2$	12.4	1.4					0.33	§
$H_2^+ + C + 2H$	<u>17.0</u>	1.4	15.6	3.95	0.0055	a_i	1	
$H^+ + CH_3$	7.3	1.0					0.1	(c),
$H^+ + CH_2 + H$	<u>11.5</u> *	1.0	46.3	2.37	0.005	a_i	0.4	(d),
$H^+ + CH + H_2$	<u>11.5</u> *	1.0					0.5	§

Notes:

* Observed threshold. It is normally used in (28b) or (28c). If the formula (b) or (c) refers to more than one channel, the threshold value to be used in the formula is underlined

§ Significant disagreement in measured $\sigma_{DE+ + DI+}(A^+ + \ldots)$ between these present LLN data and the ORNL database [28]

(a) The values R_{DE+} are related to the total $\sigma_{DE+}(A^+ + \ldots)$ cross-section in [31], when these channels have been further splitted into subchannels in this present report.

(b) With respect to the collision kinetics the CH_3^{+*} and CH_3^+ ions may be considered as being the same (CH_3^+) ion.

(c) The threshold of 7.3 eV for the $H^+ + CH_3$ channel has not been observed clearly.

(d) Theoretical thresholds for $H^+ + CH_2 + H$ and $H^+ + CH + H_2$ channels are 11.2 eV and 11.1 eV respectively.

TABLE 7. DISSOCIATIVE EXCITATION CHANNELS OF CH_3^+: BRANCHING RATIOS R_{DE+}, THRESHOLD ENERGIES E_{th}, AND MEAN TOTAL KINETIC ENERGY OF PRODUCTS $\overline{E_\kappa}$. FITTING COEFFICIENTS a_i and b_i FOR FIT EXPRESSION (28)

$CH_3^+ \rightarrow \ldots$	E_{th} (eV)	$\overline{E_\kappa}$ (eV)	b_1 / a_1	b_2 / a_2	b_3 / a_3	Type	R_{DE+}	Note
$CH_2^+ + H$ (from CH_3^{+*})	2.5 *	0.3	8.90×10^2	5.3	2.29	b_i	1	(a)
$CH_2^+ + H$	<u>10.0</u>	3.0	76.2	5.48	0.038	a_i	1	(b)
$CH^+ + H_2$		0.4					0.3	
$CH^+ + 2H$	8.5 *	1.6	17.3	1.35	0.034	a_i	0.7	(c)
$C^+ + H_2 + H$	9.5 *	0.5	4×10^4	4.79	3.21	b_i	1	
$C^+ + 3H$	<u>15.0</u>	0.5	6.5	3.87	0.9	a_i	1	(d)
$H_2^+ + CH$	<u>11.0</u> *	1.3					0.6	
$H_2^+ + C + H$	15.2	1.3	5.99	2.01	0.012	a_i	0.4	
$H^+ + CH_2$	10.0 *	0.6					0.2	
$H^+ + C + H_2$	<u>12.65</u> *	0.6	45.9	1.69	0.009	a_i	0.4	(e), §
$H^+ + CH + H$	14.0	0.6					0.4	

Notes:

* Observed threshold. If the formula for $\sigma_{DE+}^{(b)}$ (A^+) or $\sigma_{DE+}^{(a)}$ (A^+) refers to more than one channel, the threshold energy to be used in the formula is underlined.

§ Significant disagreement of LLN and ORNL data for $\sigma_{DE+ + DI+}$ (H^+) is observed [28].

(a) The threshold of 2.5 eV for the $CH_2^+ + H$ channel indicates that the parent CH_3^+ ion is in an excited metastable state, CH_3^{+*}. This channel can be treated individually or ignored.

(b) The threshold of 10.0 eV for $CH_2^+ + H$ is calculated assuming CH_3^+ is in its ground state.

(c) The theoretical threshold for the $CH^+ + H_2$ channel is 6.0 eV. It has been observed, but the steep rise of the cross-section starts at 8.5 eV, the threshold (also theoretical) for the $CH^+ + 2H$ channel.

(d) The values R_{DE+} are related to the total $\sigma_{DE+}(A^+ + \ldots)$ cross-section in [30], when these channels have been further splitted into subchannels in this present report.

(e) The theoretical threshold of 10.0 eV for the $H^+ + CH_2$ channel has been observed, but the steep rise of the cross-section starts at 12.65 eV, the theoretical threshold of the $H^+ + C + H_2$ channel.

TABLE 8. DISSOCIATIVE EXCITATION CHANNELS OF CH_2^+: BRANCHING RATIOS R_{DE+}, THRESHOLD ENERGIES E_{th}, AND MEAN TOTAL KINETIC ENERGY OF PRODUCTS $\overline{E_K}$. FITTING COEFFICIENTS a_i AND b_i FOR FIT EXPRESSION (28)

$CH_2^+ \rightarrow \ldots$	E_{th} (eV)	$\overline{E_K}$ (eV)	b_1 / a_1	b_2 / a_2	b_3 / a_3	Type	R_{DE+}	Note
$CH^+ + H$	4.5 *	0.5	3.55×10^5	3.92	5.0	b_i	1	(a)
$CH^+* + H$	<u>9.5</u>	1.8	18.7	2.38	0.037	a_i	1	(b)
$C^+ + H_2$	5.5 *	0.55					0.15	
$C^+ + 2H$	<u>9.5</u>	0.55	28.5	2.59	0.043	a_i	0.85	(c)
$H_2^+ + C$	7.0 *	2.3	0.323	1.19	0.544	a_i	1	(d)
$H^+ + CH$	<u>8.8</u> *	2.5					0.45	(e),
$H^+ + C + H$	13.7	2.5	50.9	2.26	0.033	a_i	0.55	§

Notes:

* Observed threshold, but not necessarily used in (28b) or (28c) if the steep rise of the cross-section starts from the (theoretical) threshold for another channel for A^+ production; see (c) below.

§ Significant disagreement of LLN ($H^+ \equiv D^+$) and ORNL ($H^+ \equiv H^+$) data for $\sigma_{DE+ \, + \, DI+}$ is observed [28].

(a) The values R_{DE+} are related to the total $\sigma_{DE+}(A^+ + \ldots)$ cross-section in [30], when these channels have been further splitted into subchannels in this present report.

(b) The theoretical threshold for $CH^+ + H$ is $\cong$ 5.0 eV. The theoretical thresholds for $CH^{+*}(a^3\Pi) + H$ and $CH^+*(A^1\Pi) + H$ channels are 7.5 eV and 9.8 eV, respectively. The value of 9.5 eV used in (28b) is a weighted average.

(c) The theoretical threshold of 5.5 * eV for $C^+ + H_2$ is observed, but the steep rise of the cross-section starts only at 9.5 eV, close to the theoretical threshold of 9.7 eV for the $C^+ + 2H$ channel. The value of 9.5 eV is used in (28b).

(d) The theoretical threshold for the $H_2^+ + C$ channel is $\cong$ 10.8 eV. The experimentally observed threshold at $\cong$ 7.0 eV indicates that the parent CH_2^+ ion is in a metastable or vibrationally excited state with excitation energy of about 3.8 eV. Above 10.8 eV the observed cross-section has a steep rise, indicating that the contribution of metastable CH_2^+ ion to measured cross-section is small, perhaps < 5.0%.

(e) The theoretical threshold of $H^+ + CH$ channel is $\cong$ 10 eV. The observed value of $\cong$ 8.8 eV indicates that the initial CH_2^+ ion is vibrationally excited.

TABLE 9. DISSOCIATIVE EXCITATION CHANNELS OF CH⁺: BRANCHING RATIOS R_{DE+}, THRESHOLD ENERGIES E_{th}, AND MEAN TOTAL KINETIC ENERGY OF PRODUCTS $\overline{E_K}$. FITTING COEFFICIENTS a_i AND b_i FOR FIT EXPRESSION (28)

$CH^+ \to \dots$	E_{th} (eV)	$\overline{E_K}$ (eV)	b_1 / a_1	b_2 / a_2	b_3 / a_3	Type	R_{DE+}	Note
$H^+ + C$ (^3P)	5.1 *	0.1					0.6	(a), §
$H^+ + C$ (^1D)	8.2	1.2	8.85	2.4	0.85	a_i	0.3	(b)
$H^+ + C$ (^1S)	12.5	3.7					0.1	(c)
$C^+ + H$	5.5 *						0.45	
$C^+ + H$	9.0		58.6	3.0	0.073	a_i	0.55	(d)

Notes:

* Observed threshold, but not necessarily used in (28b) or (28c) if the steep rise of the cross-section starts from the (theoretical) threshold for another channel for A⁺ production; see (c) below.

§ Significant disagreement of LLN ($H^+ \equiv D^+$) and ORNL ($H^+ \equiv H^+$) data for $\sigma_{DE+ + DI+}$ is observed, see [28].

The values R_{DE+} are related to the total $\sigma_{DE+}(A^+ + \dots)$ cross-section in [29], when these channels have been further splitted into subchannels in this present report.

(a) The observed threshold of 5.1 eV is close to the theoretical threshold of 5.2 eV for the $H^+ + C(^3P)$ channel obtained if the parent CH⁺ ion is in its metastable $CH^{+*}(a^3\Pi)$ state (with a transition to the $b^3\Sigma^-$ $(v \geq 10)$ states).

C(^3P) is also produced by a transition from the ground CH⁺ state to its $d^3\Pi$ dissociative state with a threshold of 8.8 eV. The weight of this channel in the total C(^3P) production may be about 70%. C(^3P) is also produced from $CH^{+*}(a^3\Pi)$ by transition to $d^3\Pi$ dissociative state with a threshold of 7.2 eV.

(b) Production of C(^1D) may be due to transition from ground CH⁺ state to the $2^1\Sigma$ excited state (with threshold of 8.2 eV) and to $2^1\Pi$ state ($E_{th} = 12.7$ eV). If CH⁺ is in its $a^3\Pi$ metastable state, these thresholds are for 1.2 eV smaller.

(c) C(^1S) is produced from the ground CH⁺ state by a transition to $3^1\Sigma^+$ excited state.

(d) The C⁺ + H channel with $E_{th} = 5.5$ eV corresponds to transition from ground CH⁺ state to the $b^3\Sigma^-$ excited state with vibrational levels v ≥ 4 ($E_{th} = 5.6$ eV) followed by pre-dissociation to the $c^3\Sigma^+$ dissociative state. The $C^+ + H$ channel with $E_{th} = 9.0$ eV corresponds to the direct transitions from the ground CH⁺ state to its dissociative excited state $c^3\Sigma^+$.

4.2. DI$^+$ for methane family

Revised data for dissociative ionization of CH$_y^+$ (DI$^+$): Louvan-la-Neuve University data (LLN data) are summarized in Table 10, Table 11, Table 12 and Table 13. These tables replace Table IV in [7] and Table 4 in [8]. In the hydrocarbon ions the H atoms are taken to be equivalent to D atoms, for which most of these experiments have been carried out. The new fitting coefficients c_i are also given in these tables. Equation (29) with these fitting coefficients replaces Equation (17) in [7]. The mean electron energy loss $\overline{E_{el}^{(-)}}$ is equal to E_{th}.

TABLE 10. MAIN REACTION CHANNELS IN DISSOCIATIVE IONIZATION OF CH$_4^+$: BRANCHING RATIOS, R_{DI+}, THRESHOLD ENERGIES E_{th} , AND MEAN TOTAL KINETIC ENERGY OF IONIC PRODUCTS, $\overline{E_K}$ = $\overline{E_K^+}$. THE MEAN KINETIC ENERGY $\overline{E_K^0}$ OF NEUTRAL PRODUCTS IS =0 (ZERO). FITTING COEFFICIENTS c_i FOR FIT EXPRESSION (29)

$CH_4^+ \rightarrow \dots$	E_{th} (eV)	$\overline{E_K}$ (eV)	c_1	c_2	c_3	R_{DI+}	Note
$CH_3^+ + H^+ + e$	19.2	4.0	7.55	3.27	46.7	1.0	
$CH_2^+ + H_2^+ + e$						0.1	§
$CH_2^+ + H^+ + H + e$	24.7	4.1	4.19	2.12	29.9	0.9	(a)
$CH^+ + H_2^+ + H + e$						0.1	
$CH^+ + H^+ + H_2 + e$	29.0	3.6	10.6	2.46	0.523	0.1	(b)
$CH^+ + H^+ + 2H + e$						0.8	
$C^+ + H_2^+ + H_2 + e$						0.1	
$C^+ + H_2^+ + 2H + e$	<u>30.0</u>	3.2	1.42	1.75	50.0	0.1	(c),
$C^+ + H^+ + H_2 + H + e$						0.3	(d)
$C^+ + H^+ + 3H + e$	32.7					0.5	
$H_3^+ + CH^+ + e$	21.0	6.2	0.104	3.64	10.0	1.0	
$H_2^+ + H^+ + CH + e$	<u>28.5</u>	3.0				0.8	
$H_2^+ + H_2^+ + C + e$	30.4	6.0	0.402	1.62	13.0	0.2	(e)
$H^+ + H^+ + CH_2 + e$	<u>29.0</u>					0.8	
$H^+ + H^+ + H + CH + e$	32.0	5.0	1.80	2.52	14.2	0.2	
$CH_4^{2+} + e$	14.0	-	0.437	4.24	0.0235	1.0	(f)

Notes:

§   The values R$_{DI+}$ are related to the total σ_{DI+}(A^+ + …) cross-section in [31], when these channels have been further splitted into subchannels in this present report.

(a)   With the observed $\overline{E_K}$ = 4.1 eV, the theoretical threshold of the $CH_2^+ + H_2^+$ channel is 22.0 eV, while for the $CH_2^+ + H^+ + H$ channel it is 24.7 eV. Change of the slope of observed $\sigma_{DE+ + DI+}$ takes place at E $\cong$ 24.7 eV, an evidence of the dominance of $CH_2^+ + H^+ + H$ channel in DI$^+$.

(b)   With observed $\overline{E_K}$ = 3.6 eV, theoretical thresholds of $CH^+ + H_2^+ + H$, $CH^+ + H^+ + H_2$ and $CH^+ + H^+ + 2H$ channels are 26.1 eV, 24.3 eV and 29.0 eV, respectively. Evidence of apperance of DI$^+$ in $\sigma_{DE+ + DI+}$ can be seen at $E \cong$ 20.0 eV.

(c)   Theoretical thresholds for C$^+$ + ion + neutrals channels are: E_{th} ($C^+ + H_2^+ + H_2$) = 28.3 eV, E_{th} ($C^+ + H_2^+ + 2H$) = 30.0 eV, E_{th} ($C^+ + H^+ + H_2 + H$) = 28.5 eV and E_{th} ($C^+ + H^+ + 3H$) = 32.7 eV.
For the first three channels an effective threshold of $\cong$ 30.0 eV was chosen.
A slightly different value c_1 = 1.51 is quoted in [31] for C$^+$ production channels.

(d)   When more than one threshold energy is quoted, the underlined one is used in the formula for σ_{DI+}.

(e)   The value c_1 = 1.75 for H$_2^+$ production quoted in [31] for this fit comprises all fracmentations producing H$_2^+$ in this table, e.g. double counting this 2H$_2^+$ channel.

(f)   Single, non-dissociative ionization.

TABLE 11. MAIN REACTION CHANNELS IN DISSOCIATIVE IONIZATION OF CH_3^+: BRANCHING RATIOS, R_{DI+}, THRESHOLD ENERGIES E_{th}, AND MEAN TOTAL KINETIC ENERGY OF IONIC PRODUCTS, $\overline{E_K} = \overline{E_K^+}$. THE MEAN KINETIC ENERGY $\overline{E_K^o}$ OF NEUTRAL PRODUCTS IS =0 (ZERO). FITTING COEFFICIENTS c_i FOR FIT EXPRESSION (29)

$CH_3^+ \rightarrow \ldots$	E_{th} (eV)	$\overline{E_K}$ (eV)	c_1	c_2	c_3	R_{DI+}	Note
$CH_2^+ + H^+ + e$	25.5	6.3	12.5	1.74	10.0	1	§
$CH^+ + H + H^+ + e$	29.2	5.5	8.6	1.59	9.0	1	(a)
$C^+ + H^+ + H_2 + e$						0.2	
$C^+ + H^+ + 2H + e$	29.4	1.5	5.0	2.5	11.0	0.8	(b)
$H_2^+ + C^+ + H + e$	<u>28.0</u>					0.5	
$H_2^+ + H^+ + C + e$	30.3	2.8	2.52	3.29	1.17	0.5	(c)
$H^+ + H^+ + CH + e$	<u>32.2</u>					0.8	
$H^+ + H^+ + C + H + e$	35.5	5.5	1.40	1.29	10.0	0.2	

Notes:
§ The values R_{DI+} are related to the total $\sigma_{DI+}(A^+ + \ldots)$ cross-section in [30], when these channels have been further splitted into subchannels in this present report.
(a) The channel $CH^+ + H_2^+$ has a theoretical threshold at 26.4 eV, but no change of the slope of experimental $\sigma_{DE+ + DI+}$ is observed at this energy. Therefore, the contribution of this channel to CH^+ production has been neglected.
(b) The theoretical threshold of the $C^+ + H^+ + H_2$ channel is about 25.0 eV but it is not seen as change in the slope of experimental $\sigma_{DE+ + DI+}$. $E_{th} = 29.4$ eV is the threshold of the $C^+ + H^+ + 2H$ channel.
(c) When two threshold values are listed for production of a given ion, the underlined one is used in the formula for σ_{DI+}.

TABLE 12. MAIN REACTION CHANNELS IN DISSOCIATIVE IONIZATION OF CH_2^+: BRANCHING RATIOS, R_{DI+}, THRESHOLD ENERGIES E_{th}, AND MEAN TOTAL KINETIC ENERGY OF IONIC PRODUCTS, $\overline{E_K} = \overline{E_K^+}$. THE MEAN KINETIC ENERGY $\overline{E_K^o}$ OF NEUTRAL PRODUCTS IS =0 (ZERO). FITTING COEFFICIENTS c_i FOR FIT EXPRESSION (29)

$CH_2^+ \rightarrow \ldots$	E_{th} (eV)	$\overline{E_K}$ (eV)	c_1	c_2	c_3	R_{DI+}	Note
$CH^+ + H^+ + e$	25.0	3.7	8.3	3.0	62.8	1	(a)
$C^+ + H_2^+ + e$	26.0	5.8	0.188	3.21	45.0	1	
$C^+ + H^+ + H + e$	28.0	5.6	7.6	3.55	47.9	1	
$H^+ + H^+ + C + e$	30.6	5.8	8.5	1.15	3.8	1	
$CH_2^{2+} + e$	21.0	-	13.7	2.23	0.021	1	(b)

Notes:
(a) The "observed" threshold (change of the slope of $\sigma_{DE+ + DI+}$) of $\cong 25.0$ eV is about 3 eV above the theoretical one, 21.8 eV, calculated with the observed $\overline{E_K} \cong 3.7$ eV. This indicates that the product ion CH^+ is in its $A^2\Pi$ excited state with a weight (perhaps) higher than ~ 60%.
(b) Single, non-dissociative ionization.

TABLE 13. MAIN REACTION CHANNELS IN DISSOCIATIVE IONIZATION OF CH^+: BRANCHING RATIOS, R_{DI+}, THRESHOLD ENERGIES E_{th} , AND MEAN TOTAL KINETIC ENERGY OF IONIC PRODUCTS, $\overline{E_\kappa} = \overline{E_\kappa^+}$. THE MEAN KINETIC ENERGY $\overline{E_\kappa^o}$ OF NEUTRAL PRODUCTS IS =0 (ZERO). FITTING COEFFICIENTS C_I FOR FIT EXPRESSION (29)

$CH^+ \rightarrow \dots$	E_{th} (eV)	$\overline{E_\kappa}$ (eV)	c_1	c_2	c_3	R_{DI+}	Note
$C^+ + H^+ + e$	22.1	6.4	48.3	1.79	0.06	1	(a)
$C^{2+} + H + e$	25.5	4.5	5.03	2.71	1.32	1	(b)

Notes:

(a) This DI^+ cross-section has been measured directly. The theoretical threshold for $C^+ + H^+$ production from the ground state CH^+ ion is 24.1 eV. The observed threshold of 22.1 eV indicates that the initial state of CH^+ ion has been either vibrationally excited or in its $a^3\Pi$ metastable state. For the $a^3\Pi$ state the theoretical threshold would be 22.9 eV, which is within the experimental uncertainty of observed E_{th} = 22.1 eV and the $\overline{E_\kappa}$ = 6.4 eV value.

(b) This is a rare example of charge asymmetric DI^+ process.

5. DISSOCIATIVE RECOMBINATION

After first publication of the ethane and propane databases [7,8,9,10] in 2002-2004 a number of new experimental results on dissociative recombination of hydrocarbon ions have become available, even new reaction channels have been identified. In the second sub-section 5.2 below we update and revise the corresponding tables VI and 6 (for methane) and tables VIII and 15 for the ethane and propane families in those references, respectively, for branching ratios and kinetic energy of products. Before doing so we first provide new fit coefficients for the total dissociative recombination cross-sections. This now leads to a unified full cross-section database format for all DR data. This format was derived by combining the fit expressions for cross-section (for methane family molecular ions, [7.8]) and the fit expressions for Maxwellian rate coefficient (for the higher hydrocarbon ions) given in the original works [9,10]. The rate coefficients have been converted back into cross-sections by a conventional implicit non-linear fitting algorithm. This often ill-conditioned problem (inverse Laplace transformation) of deriving cross-sections from rate coefficients can be solved in the present case very accurately by making the (reasonable) additional assumption that the form of the cross-section fit expression for higher hydrocarbons is the same as that of the simple total cross-sections fits for the methane DR channels.

5.1. Total dissociative recombination cross-section database

Total dissociative recombination cross-sections for the methane family of electrons with CH_y^+ (y = 1 - 4) ions have been derived in [7,8] from most recent available experimental information. In the energy region above ~ 1-2 eV, the total recombination cross-sections $\sigma_{DR}^{tot}(CH_y^+)$ show resonant structures, pronounced particularly in the energy region around 5-10 eV where the thresholds of competing dissociative excitation processes lie (see Section 4). After averaging over these resonances, the cross-sections $\sigma_{DR}^{tot}(CH_y^+)$ (y = 1 - 4) can all be represented in the form

$$\sigma_{DR}^{tot}(CH_y) = \frac{A}{E^\alpha(1+aE)^\beta}\left(\times 10^{-16}\,cm^2\right) \tag{30}$$

where the fitting parameters A, α, a and β are given in Table 14 and E is expressed in eV units. The value of parameters α is close (or equal) to one, in accordance with the Wigner's law for break-up reactions.

TABLE 14. FITTING COEFFICIENTS A, a, α AND β FOR TOTAL DISSOCIATIVE RECOMBINATION CROSS-SECTIONS, IN FIT EXPRESSION (30)

Collision System	A	a	α	β
$e + CH_4^+$	3.00	0.10	1.25	1.00
$e + CH_3^+$	4.80	0.80	1.10	0.50
$e + CH_2^+$	6.70	1.20	1.15	0.50
$e + CH^+$	3.16	0.13	0.75	1.00
$e + C_2H_6^+$	13.98	0.19	1.06	0.47
$e + C_2H_5^+$	12.28	0.19	1.06	0.47
$e + C_2H_4^+$	10.58	0.19	1.06	0.47
$e + C_2H_3^+$	8.88	0.19	1.06	0.47
$e + C_2H_2^+$	7.18	0.19	1.06	0.47
$e + C_2H^+$	5.48	0.19	1.06	0.47
$e + C_2^+$	2.28	0.19	1.06	0.47
$e + C_3H_8^+$	18.31	0.19	1.06	0.47
$e + C_3H_7^+$	17.06	0.19	1.06	0.47
$e + C_3H_6^+$	15.81	0.19	1.06	0.47
$e + C_3H_5^+$	14.57	0.19	1.06	0.47
$e + C_3H_4^+$	13.32	0.19	1.06	0.47
$e + C_3H_3^+$	12.07	0.19	1.06	0.47
$e + C_3H_2^+$	10.82	0.19	1.06	0.47
$e + C_3H^+$	9.57	0.19	1.06	0.47
$e + C_3^+$	3.41	0.19	1.06	0.47

As described in [9,10] total thermal rate coefficients $\langle\sigma v\rangle_{DR}^{tot}$ for molecular ions of the ethane family have been measured for $C_2H_3^+$, $C_2H_5^+$ and $C_2H_7^+$. From these and also from analogy to dissociative recombination of molecular ions of the methane family the following expression for total dissociative recombination rate coefficients was deduced:

$$\langle\sigma v\rangle_{DR}^{tot}\left(C_2H_y^+\right)= \frac{F_2^{DR}(y)}{T^{1/2}\left(1+0.27\,T^{0.55}\right)}\left(\times 10^{-8}\,cm^3/s\right) \quad , \tag{31}$$

where T is expressed in eV, and the scale factor 10^{-8} gives the typical magnitude of DR rate coefficients at T ~ 1 eV. The "structural" function $F_2^{DR}(y)$ can easily be obtained from the available experimental values of $\langle\sigma v\rangle_{DR}^{tot}(C_2H_y^+)$ at thermal temperatures, and its form is

$$F_2^{DR}(y) = 3.105\,(1 + 0.45y) \tag{32}$$

This linearity is broken only for the $y = 0$ case (C_2^+ ion), when $F_2^{DR}(C_2^+) \cong 1.87$, loc. cit.

A very similar analysis has led to the same expression for total dissociative recombination rate coefficients of molecular ions from the propane family $\langle\sigma v\rangle_{DR}^{tot}$ ($C_3H_y^+$):

$$\langle\sigma v\rangle_{DR}^{tot}\left(C_3H_y^+\right)= \frac{F_3^{DR}(y)}{T^{1/2}\left(1+0.27\,T^{0.55}\right)}\left(\times 10^{-8}\,cm^3/s\right) \quad , \tag{33}$$

As discussed in [9,10] the "structural" function $F_3^{DR}(y)$ can be determined from the available thermal $\langle\sigma v\rangle_{DR}^{tot}$ data for $C_3H_2^+$, $C_3H_3^+$, $C_3H_5^+$ and $C_3H_7^+$ ions. The linear fit of this data gives

$$F_3^{DR}(y) = 6.84\ (1 + 0.15y) \tag{34}$$

Compared with (32) for $F_2^{DR}(y)$, (34) shows that $F_3^{DR}(y)$ increases with increasing number of hydrogen y three times more slowly than $F_2^{DR}(y)$. This reflects the experimentally observed fact that the thermal values of $\langle\sigma v\rangle_{DR}^{tot}$ ($C_xH_y^+$) tend to saturate both with increasing x and y, loc.cit.

We also note that for the $e + C_3^+$ system a value $F_3^{DR}(y{=}0) = 2.80$ was suggested. The validity of temperature dependence (31), (33) of $\langle\sigma v\rangle_{DR}^{tot}$ can be extended up to 20 - 30 eV, where the DR process becomes already insignificant relative to the competing DE$^+$ process.

The rate coefficient for an individual DR channel $e + C_xH_y^+ \rightarrow A + B^* + ...$ is given by

$$\langle\sigma v\rangle_{DR}^{tot}\left(A, B^*/C_xH_y^+\right) = R_{DR}\left(A, B^*/C_xH_y^+\right)\langle\sigma v\rangle_{DR}^{tot}\left(C_xH_y^+\right), \quad x = 1,2,3 \tag{35}$$

where $R_{DR}(A,B^*/C_xH_y^+)$ is the corresponding branching ratio. The recent revisions regarding these branching ratios and other information on particular DR channels for a given molecular ion are discussed in the next sub-section 5.2.

In order to arrive at cross-section fits of the same form as for the methane family (3) we first note that Maxwellian rate coefficients are always related to the cross-section by the Laplace transformation. The inverse problem to derive a cross-section from a rate coefficient, i.e., an inverse Laplace transformation, is often ill conditioned. The method of steepest decent has, for example, successfully been applied in [32] for a special class of processes. In the present case, however, in which a fitting expression for the cross-section is already given, this inverse problem reduces to a simple implicit non-linear least squares problem. We have used a 64-point Gauss-Laguerre integration scheme for the Maxwellian rate coefficient for cross-sections of the form (30) and a standard implicit orthogonal distance regression algorithm. The resulting fitting coefficients for the DR cross-sections for the ethane and propane families are also given in Table 14. The maximum error, when comparing the original rate coefficients with those obtained by numerical integration using the newly derived cross-sections is below 1% in the entire relevant temperature range of 0 - 20 eV. Clearly, the fitting coefficients a, α and β are all the same for the ethane and propane families, because the temperature dependence of the rate coefficients was the same for all these ions.

5.2. New DR Tables

In this section the revised data are given, respectively, for branching ratios R_{DR} and kinetic energy of products $E_K^{(0)}$ in their ground states and for zero electron impact energy. Also included in these tables are the possible excited products. "Possible" here means only "energetically possible", which does not mean that it is really possible from the point of view of collision dynamics (i.e. availability of appropriate couplings) and symmetry considerations. The excited species in these tables are determined from the value of $E_K^{(0)}$ and the values of excitation energies of the reaction products given in Table III of [10], because $E_K^{(0)}$ is given in the corresponding tables for the ground state products.

5.2.1. DR for methane family

This Table 15 is essentially identical to the one from the original methane family database, [7,8], however the list of possible excited states has now been added. In particular direct CH(A) production might be an important additional contribution to Gerö band emission at low plasma temperatures (below 2-3 eV), when hydrocarbon fragmentation proceeds predominantly via pathways involving DR processes.

TABLE 15. MAIN DISSOCIATIVE RECOMBINATION CHANNELS OF CH_y^+, THEIR CROSS-SECTION BRANCHING RATIOS (R_{DR}), TOTAL KINETIC ENERGY OF PRODUCTS ($E_K^{(0)}$) IN THEIR GROUND STATES AND FOR ZERO ELECTRON IMPACT ENERGY, AND POSSIBLE EXCITED PRODUCTS. THIS TABLE REPLACES TABLE VI (AND TABLE 6) OF THE ORIGINAL DATABASE REF. [7] (AND [8]), RESPECTIVELY

Reaction channel		R_{DR}	$E_K^{(0)}$(eV)	Excited products for $E < 1$ eV	Notes
$e + CH_4^+$	$\rightarrow CH_3 + H$	0.21	8.13	CH_3 ($^2A_1'$; $^2A_2''$)	(a), [27]
	$\rightarrow CH_2 + H_2$	0.09	7.82	CH_2 (a, b, c)	
	$\rightarrow CH_2 + H + H$	0.43	3.28	CH_2 (*a, b*)	[27]
	$\rightarrow CH + H_2 + H$	0.25	3.39	CH(*B*), CH(*A*, -0.24 eV; *C*, -0.55 eV)	(b)
	$\rightarrow C + H_2 + H_2$	0.02	4.38	C($^1D_2$; $^1S_0$; $^5S_2^0$)	
$e + CH_3^+$	$\rightarrow CH_2 + H$	0.40	4.99	CH_2 (a, b, c)	[27]
	$\rightarrow CH + H_2$	0.14	5.09	CH (a; A, B, C)	
	$\rightarrow CH + H + H$	0.16	0.56	CH (*a*)	
	$\rightarrow C + H_2 + H$	0.30	1.55	C ($^1D_2$)	
$e + CH_2^+$	$\rightarrow CH + H$	0.25	5.96	CH (a; A, B, C)	(c), [27]
	$\rightarrow C + H_2$	0.12	6.95	C ($^1D_2$; $^1S_0$; $^5S_2^0$)	
	$\rightarrow C + H + H$	0.29	2.42	C (^3P) + 2H(^2S)	(d)
		0.34	1.16	C (^1D) + 2H(^2S)	(d)
$e + CH^+$	$\rightarrow C + H$	1.0	7.10		[27]

for $E_{el} \leq 0.9$ eV

$e + CH^+$	$\rightarrow C + H$	0.75	5.84	C (^1D) + H(^2S)	
		0.25	4.42	C (^1S) + H(^2S)	

for $E_{el} = 0.9 - 9$ eV

$e + CH+$	$\rightarrow C + H$	0.075	5.84	C (^1D) + H(^2S)	
		0.025	4.42	C (^1S) + H(^2S)	
		0.25	-0.38	C ($^3P^0$) + H(^2S)	
		0.20	-0.58	C ($^1P^0$) + H(^2S)	
		0.45	-0.84	C ($^3D^0$) + H(^2S)	

[27]: Channels included in Ref. [27]

Notes:

(a) The excited species in this table have not been given in [7,8], the relevant values of excitation energies of the reaction products have only been published later in the ethane and propane database [7,8] and therefore may have been unnoticed by readers only interested in methane family DR processes.

(b) The 0.24 eV and 0.55 eV endothermicities can be compensated if the initial ion is vibrationally excited.

(c) This is the most probable source for direct production of CH(*A*) (the upper level of the spectroscopically important Gerö band emission). The possible resonant dissociative excitation mechanisms in DE^+ reactions, which correlate with this DR channel, are discussed in Section 4 and in more detail in the contribution by Janev at al. in this same volume.

(d) In original database [7,8] this was one single channel, with $R_{DR} = 0.63$. The new data for revision 2007 are taken from [33].

5.2.2. DR for ethane family

The following Table 16 lists the main dissociative recombination channels of $C_2H_y^+$, their cross-section branching ratios (R_{DR}), total kinetic energy of products ($E_K^{(0)}$) in their ground states and for

zero electron impact energy, and possible excited products. This table replaces Table VIII (and Table 8) of the original database [9] (and [10]), respectively.

TABLE 16. MAIN DISSOCIATIVE RECOMBINATION CHANNELS OF $C_2H_y^+$, THEIR CROSS-SECTION BRANCHING RATIOS (R_{DR}), TOTAL KINETIC ENERGY OF PRODUCTS ($E_K^{(0)}$) IN THEIR GROUND STATES AND FOR ZERO ELECTRON IMPACT ENERGY, AND POSSIBLE EXCITED PRODUCTS

Reaction channel		R_{DR}	$E_K^{(0)}$(eV)	Excited products for E<1 eV	Notes
$e + C_2^+$	$\rightarrow C + C$	1.0	5.18	$C(^1D)$, $C(^1S)$	
$e + C_2H^+$	$\rightarrow C_2 + H$	0.43	5.64	C_2 (a; b; A; c; d; C)	[34]
	$\rightarrow CH + C$	0.39	2.96	$CH(A; a)$, $C(^1D; {}^1S)$	
	$\rightarrow C + H + C$	0.18	-0.58		(a), (b)
$e + C_2H_2^+$	$\rightarrow C_2H + H$	0.50	6.53	$C_2H(A; B^1; B)$	[35]
	$\rightarrow C_2 + H + H$	0.30	0.57	C_2 (a; b)	
	$\rightarrow CH + CH$	0.13	1.43	$CH(a; A)$	
	$\rightarrow CH_2 + C$	0.05	2.32	$C(^1D; {}^1S)$	
	$\rightarrow C_2 + H_2$	0.02	5.11	C_2 (a; b; A; c; d; c)	
$e + C_2H_3^+$	$\rightarrow C_2H_2 + H$	0.29	6.72		[36]
	$\rightarrow C_2H + H + H$	0.59	1.85		
	$\rightarrow C_2H + H_2$	0.06	6.39	$C_2H(A; B; B^1)$	
	$\rightarrow CH_2 + CH$	0.03	1.18	CH_2 (a; b;), $CH(A; a)$	
	$\rightarrow C_2 + H_2 + H$	0.024	0.43	C_2 (a; b; A)	
	$\rightarrow CH_3 + C$	0.006	2.49	$C(^1D; {}^1S)$	
$e + C_2H_4^+$	$\rightarrow C_2H_3 + H$	0.11	5.67	C_2H_3 (A; B)	[34]
	$\rightarrow C_2H_2 + H + H$	0.66	4.15		
	$\rightarrow C_2H_2 + H_2$	0.06	8.68		
	$\rightarrow C_2H + H + H_2$	0.10	3.82	$C_2H(A; B'; B; C)$	
	$\rightarrow CH_2 + CH_2$	0.04	3.04	CH_2 (a; b)	
	$\rightarrow CH_3 + CH$	0.02	3.44	$CH(a; A; B)$	
	$\rightarrow CH_4 + C$	0.01	4.40	$C(^1D; {}^1S)$	
$e + C_2H_5^+$	$\rightarrow C_2H_4 + H$	(0.12)	6.53		
	$\rightarrow C_2H_3 + H + H$	(0.47)	1.69	C_2H_3 (A)	
	$\rightarrow C_2H_3 + H_2$	(0.06)	6.23	C_2H_3 (A; B)	
	$\rightarrow C_2H_2 + H_2 + H$	(0.12)	4.70		
	$\rightarrow C_2H_2 + 3H$	(0.06)	0.17		(a)
	$\rightarrow CH_4 + CH$	0.02	3.97	$CH(A; a; B)$	
	$\rightarrow CH_3 + CH_2$	0.15	3.92	CH_2 (a; b; c)	
$e + C_2H_6^+$	$\rightarrow C_2H_5 + H$	(0.16)	7.14	C_2H_5 (3s; 3p)	(c)
	$\rightarrow C_2H_4 + H + H$	(0.38)	5.55		
	$\rightarrow C_2H_4 + H_2$	(0.06)	10.09	H_2 (B)	
	$\rightarrow C_2H_3 + H_2 + H$	(0.18)	5.26	C_2H_3 (A;B)	
	$\rightarrow CH_4 + CH_2$	(0.04)	7.43	CH_2 (C; 3p)	
	$\rightarrow CH_3 + CH_3$	(0.09)	7.79	CH_3 (3s; 3p; 3d)	
	$\rightarrow CH_3 + CH_2 + H$	(0.05)	2.17	CH_2 (a;b)	(a)
	$\rightarrow CH_2 + CH_2 + H_2$	(0.04)	1.86	CH_2 (a;b)	(a)
$e + C_2D_5^+$	$\rightarrow C_2D_4 + D$	0.12	6.53		[37],(a),(d)
	$\rightarrow C_2D_3 + D + D$	0.28	1.69	C_2D_3 (A)	(a)
	$\rightarrow C_2D_2 + D_2 + D$	0.30	4.70		(a)
	$\rightarrow C_2D_2 + 3D$	0.13	0.25		(a)
	$\rightarrow CD_3 + CD_2$	0.17	3.92	CD_2 (a; b; c)	(a)

(a) new channels, added to original database [9,10] during revision 2007

(b) For $E < 0.58$ eV this channel is not open and the assumed branching ratios for $C_2 + H$ and $CH + C$ channels are 0.55 and 0.45, respectively.

(c) The suggested branching ratios for $C_2H_6^+$ are in accordance with the experimental finding in [38] that the total branching ratio of all C_2-containing channels is 0.78, and that for CX+CY+... channels is 0.22. However, for the individual channels the suggested branching ratios within these two groups are fairly uncertain and are determined following the trends of R_{DR} in other CH_y^+-cases.

(d) The presented branching ratios are for $C_2D_5^+$ from [37]. The branching ratios for $C_2H_5^+$ may be significantly different from the analogous channels in $C_2D_5^+$ as shown experimentally for the $C_3H_7^+$ and $C_3D_7^+$ DR in [39,40]. These are the channels when DR proceeds via a doubly excited state.

5.2.3. DR for propane family

Main dissociative recombination channels of $C_3H_y^+$, their cross-section branching ratios (R_{DR}), total kinetic energy of dissociation products ($E_K^{(0)}$) in their ground state and for zero electron impact energy, and possible excited products for $E < 1$ eV. This new Table 17 replaces Table XV (and Table 15) of the original database [9] (and [10]), respectively.

The values of R_{DR} given in parentheses are suggested by using the trend of R_{DR} for the analogous DR channels in systems where R_{DR} have been measured at $E \cong 0$ eV ($C_3H_4^+$, $C_3H_7^+$), as well as some other physical considerations. The assigned values for R_{DR}, however, satisfy the experimental findings for the weights of $[C_3^+]$ and $[C_2] + [C]$ in the total DR of [38].

TABLE 17. MAIN DISSOCIATIVE RECOMBINATION CHANNELS OF $C_3H_y^+$, THEIR CROSS-SECTION BRANCHING RATIOS (R_{DR}), TOTAL KINETIC ENERGY OF PRODUCTS ($E_K^{(0)}$) IN THEIR GROUND STATES AND FOR ZERO ELECTRON IMPACT ENERGY, AND POSSIBLE EXCITED PRODUCTS

Reaction channel		R_{DR}	$E_K^{(0)}$ (eV)	Excited products for $E < 1$ eV	Notes
$e + C_3^+$	$\rightarrow C_2 + C$	1.0	5.04	C (^{1}D; ^{1}S; ^{5}S$_2^0$), C$_2$ (a; b; A; c; d; C; e)	
$e + C_3H^+$	$\rightarrow C_3 + H$	0.66	6.32	C$_3$ (a; b; A; B; ^{1}S$_u^+$)	
	$\rightarrow C_2H + C$	0.31	4.70	C (^{1}D; ^{1}S; ^{5}S$_2^0$), C$_2$H(A, B^1, B)	
	$\rightarrow C_2 + CH$	0.03	2.31	C$_2$ (a; b; A; c; d), CH (a, A)	
$e + C_3H_2^+$	$\rightarrow C_3H + H$	(0.78)	9.15	H ($n = 2$)	
	$\rightarrow C_3 + H + H$	(0.07)	2.78	C$_3$ (a; b)	
	$\rightarrow C_3 + H_2$	(0.02)	7.31	C$_3$ (a; b; A; B; ^{1}S$_u^+$)	
	$\rightarrow C_2H_2 + C$	(0.05)	6.05	C (^{1}D; ^{1}S; ^{5}S$_2^0$)	
	$\rightarrow C_2H + CH$	(0.06)	4.73	CH (a; A; B; C), C$_2$H(A; B^1; B)	
	$\rightarrow C_2 + CH_2$	(0.02)	3.20	C$_2$ (a; b; A; c; d), CH$_2$ (a; b; c)	
$e + C_3H_3^+$	$\rightarrow C_3H_2 + H$	(0.82)	3.38	C$_3$H$_2$ (A; B)	
	$\rightarrow C_3H + H + H$	(0.06)	2.10		
	$\rightarrow C_3H + H_2$	(0.03)	6.64		
	$\rightarrow C_3 + H_2 + H$	0.00	---		(a)
	$\rightarrow C_2H_2 + CH$	(0.04)	2.55	CH (a; A)	
	$\rightarrow C_2 + CH_3$	(0.01)	1.00	C$_2$ (a; b; A)	
	$\rightarrow C_2H + CH_2$	(0.04)	2.11	CH$_2$ (a; b)	
$e + C_3H_4$	$\rightarrow C_3H_3 + H$	0.87	7.28		[41]
	$\rightarrow C_3H_2 + H + H$	0.04	2.32	C$_3$H$_2$ (A; B)	
	$\rightarrow C_3H_2 + H_2$	0.01	6.86	C$_3$H$_2$ (A; B; C)	
	$\rightarrow C_3H + H_2 + H$	0.00	---		(a)
	$\rightarrow C_2 + CH_4$	0.00	---	C$_2$ (a; b; A; c; d; C)	(a)
	$\rightarrow C + C_2H_4$	0.00	---	C (^{1}D; ^{1}S)	(a)
	$\rightarrow C_2H_3 + CH$	0.01	3.02	CH (a; A; B)	(b)

226

	$\rightarrow C_2H_2 + CH_2$	0.06	5.93	CH_2 (a; b; c)	(b)
	$\rightarrow C_2H + CH_3$	0.01	5.91	$C_2H(A; B^1; C)$, CH_3 (A_1')	(b)
$e + C_3H_5^+$	$\rightarrow C_3H_4 + H$	(0.72)	5.70		
	$\rightarrow C_3H_3 + H + H$	(0.06)	2.63		
	$\rightarrow C_3H_3 + H_2$	(0.03)	7.16		(c)
	$\rightarrow C_3H_2 + H_2 + H$	(0.06)	2.21	C_3H_2 (A; B)	
	$\rightarrow C_2H + CH_4$	(0.02)	5.73	C_2H (A; B^1; B)	
	$\rightarrow C_2H + CH_3 + H$	(0.02)	1.25		(b)
	$\rightarrow C_2H_4 + CH$	(0.03)	3.20	CH (a; A; B)	
	$\rightarrow C_2H_3 + CH_2$	(0.02)	2.80	C_2H_3 (A), CH_2 (a; b; c)	
	$\rightarrow C_2H_2 + CH_3$	(0.03)	6.12	CH_3 (3s)	
	$\rightarrow C_2H_2 + CH_2 + H$	(0.01)	1.27	CH_2 (a; b)	(b)
$e + C_3H_6^+$	$\rightarrow C_3H_5 + H$	(0.53)	5.90	C_3H_5 (A; B; C; 3d)	
	$\rightarrow C_3H_4 + H + H$	(0.06)	3.47		
	$\rightarrow C_3H_4 + H_2$	(0.04)	8.01		(c)
	$\rightarrow C_3H_3 + H_2 + H$	(0.06)	4.94		
	$\rightarrow C_2H_5 + CH$	(0.04)	2.56	CH (a; A)	
	$\rightarrow C_2H_4 + CH_2$	(0.06)	5.40	CH_2 (a; b; c)	
	$\rightarrow C_2H_3 + CH_3$	(0.09)	5.42	C_2H_3 (A; B), CH_3 (3s)	
	$\rightarrow C_2H_2 + CH_4$	(0.04)	8.93		(b)
	$\rightarrow C_2H_2 + CH_3 + H$	(0.08)	3.89		(b)
$e + C_3H_7^+$	$\rightarrow C_3H_6 + H$	0.42	5.97		
	$\rightarrow C_3H_5 + H + H$	0.08	2.15	C_3H_5 (A)	(d)
	$\rightarrow C_3H_5 + H_2$	0.04	6.69	C_3H_5 (A; B; C; 3d; 4s)	(d)
	$\rightarrow C_3H_4 + H_2 + H$	0.09	4.27		
	$\rightarrow C_2H_6 + CH$	(0.01)	3.19	CH (a; A; B)	(e)
	$\rightarrow C_2H_5 + CH_2$	(0.01)	3.24	CH_2 (a; b; c)	(e)
	$\rightarrow C_2H_4 + CH_3$	0.04	6.51	CH_3 (3s; 3p)	(f)
	$\rightarrow C_2H_3 + CH_4$	0.04	5.95	C_2H_3 (A; B)	(d)
	$\rightarrow C_2H_3 + CH_3 + H$	0.15	1.67	C_2H_3 (A)	(d),(b)
	$\rightarrow C_2H_2 + CH_4 + H$	(0.01)	4.62		(b),(e)
	$\rightarrow C_2H_2 + CH_3 + H_2$	0.11	4.68		(b),(e)
$e + C_3H_8^+$	$\rightarrow C_3H_7 + H$	(0.46)	6.67	C_3H_7 (3s; 3p; 3d)	
	$\rightarrow C_3H_6 + H + H$	(0.09)	5.10		
	$\rightarrow C_3H_6 + H_2$	(0.05)	9.63	H_2 (B)	
	$\rightarrow C_3H_5 + H_2 + H$	(0.08)	5.82	C_3H_5 (A; B; C; 3d)	
	$\rightarrow C_2H_6 + CH_2$	(0.07)	6.74	CH_2 (a; b; c)	
	$\rightarrow C_2H_5 + CH_3$	(0.06)	7.22	CH_3 (3s; 3p), C_2H_5 (3s; 3p)	
	$\rightarrow C_2H_4 + CH_4$	(0.01)	10.11		(b)
	$\rightarrow C_2H_4 + CH_3 + H$	(0.08)	5.63	CH_3 (3s)	(b)
	$\rightarrow C_2H_3 + CH_4 + H$	(0.03)	5.28	C_2H_3 (A; B)	(b)
	$\rightarrow C_2H_3 + CH_3 + H_2$	(0.06)	5.33	CH_3 (3s); C_2H_3 (A; B)	(b)
	$\rightarrow C_2H_2 + CH_4 + H_2$	(0.01)	8.28		(b)

(a) channel removed from database [9,10], during revision 2007
(b) new channel, added to original database [9,10] during revision 2007
(c) This channel is only open for $E > 1$ eV.
(d) The measured combined branching ratio for these reactions [37] was partitioned among them in accordance with the weights of branching ratios of analogous reactions in the $C_3D_7^+$ case [39].
(e) The combined branching ratio for these reactions was found to be < 0.05 in [37]. In the $C_3D_7^+$ case the DR channels $C_2D_2 + CD$ and $C_2D_5 + CD_2$ have not been detected [39].
(f) It is possible that the $C_2H_4 + CH_2 + H$ channel contributes to the R_{DR} value by 0.01 or less. This channel, however, has not been detected in the $C_3D_7^+$ case [39].

6. CONCLUSIONS

The HYDKIN online databases for the cross-sections for the I-DI, DE, DE$^+$ and DR classes of hydrocarbon collisions processes in fusion edge plasmas have been updated. For DR processes all channels up to dissociative recombination of the propane ion ($C_3H_8{}^+$) have been revisited. For I-DI the present revision has been carried out for the methane and ethane family, i.e., up to C_2H_6. For DE (neutral molecules) and DE$^+$ as well as DI$^+$ (molecular ions) only the database for the methane family has been updated. No new data, as compared to those already contained in the database [7,9] already, are known to us regarding the charge exchange and particle re-arrangement (CX-PR) categories. These latter processes are, however, particularly important in combination with dissociative recombination as providing the main fragmentation pathways for hydrocarbons at low plasma temperatures (1-2 eV).

Probably the additional CX-type collision processes, which are still missing in the HYDKIN database (and absent on other databases as well) involving H$_2$ (e.g., CX and PR of $C_xH_y{}^+$ with H$_2$), and H$_2{}^+$ (with C_xH_y) could be relevant at low plasma temperatures (a few eV). Given the high molecular hydrogen density typically encountered in so called "detached" divertor plasmas of tokamaks in the plasma temperature region below a few eV, adding these processes could potentially improve the sometimes still poor agreement between experimentally observed and theoretically estimated molecular CH and CH$^+$ band emission resulting from hydrocarbon sources at low plasma temperatures.

Another significant upgrade and extension of the present database could also be with regard to growth processes, i.e., formation of larger hydrocarbons from smaller ones in divertor plasma conditions, if conditions can be identified in which those become really competitive despite the very intense hydrogen-electron components in fusion plasmas.

REFERENCES

[1] LOARTE, A. et al. in Progress in the ITER Physics Basis, Chapter 4, Nuclear Fusion, **47** (2007) 203.

[2] Nuclear Fusion Research, Springer Series in Chem. Phys. **78**, (CLARK, R., REITER, D. Eds), Springer, Berlin Heidelberg (2005).

[3] STANGEBY, P.C., The Plasma Boundary of Magnetic Fusion Devices, Institute of Physics Publishing (2000).

[4] POSPIESZCZYK, A. et al., Determination of Rate Coefficients for Atoms and Molecules (Hydrocarbons and Hydrogen with its Isotopes) by Measurement and Modelling in the Boundary Plasma of TEXTOR, Atom. Plasma-Mater. Interact. Data Fusion **13** (2007).

[5] FANTZ, U. et al., Correlation of the intensity ratio of C$_2$/CH molecular bands with the flux ratio of C$_2$H$_y$/CH$_4$ particles , J. Nucl. Mat. **337-339** (2005) 1087.

[6] BREZINSEK, S., et al., Determination of photon efficiencies and hydrocarbon influxes in the detached outer divertor plasma of ASDEX Upgrade, Phys. Scr. **T128** (2007) 40.

[7] JANEV, R.K., REITER, D., Collision processes of CH$_y$ and CH$_y{}^+$ hydrocarbons with plasma electrons and protons Phys. Plasmas **9** (2002) 4071.

[8] JANEV, R.K., REITER, D., Collision Processes of Hydrocarbon Species in Hydrogen Plasmas I, Report **JUEL-3966** (2002).

[9] JANEV, R.K., REITER, D., Phys. Plasmas **11** (2004) 780.

[10] JANEV, R.K., REITER, D., Collision Processes of Hydrocarbon Species in Hydrogen Plasmas II. The ethane and propane families, Report **JUEL-4005** (2002).

[11] REITER, D., KÜPPERS, B., http://www.hydkin.de (2008).

[12] REITER, D., et al., Detailed atomic, molecular and radiation kinetics in current 2D and 3D edge plasma fluid codes, J. Nucl. Mat. **363–365** (2007) 649.

[13] REITER, D., KÜPPERS, B., JANEV, R.K., "Hydrocarbon chemistry in fusion edge plasmas: a sensitivity analysis", 12th International Workshop on Plasma-Facing Materials and Components for Fusion Applications, Forschungszentrum Jülich. (2009) Accepted for publication in: Physica Scripta.

[14] JANEV, R.K., WANG, J.G., MURAKAMI, I., KATO, T., Cross-sections and Rate Coefficients for Electron-Impact Ionization of Hydrocarbon Molecules, Res. Report NIFS-DATA-68, National Institute for Fusion Science, Toki, Japan (2001).

[15] ALMAN, D.A., RUZIC, D.N., A hydrocarbon reaction model for low temperature hydrogen plasmas and an application to the Joint European Torus, Phys. Plasmas **7** (2000) 1421.

[16] STRAUB, H.C., LIN, D., LINDSAY, B.G., SMITH, K.A., STEBBINGS, R.F., Absolute partial cross-sections for electron-impact ionization of CH_4 from threshold to 1000 eV, J. Chem. Phys. **106** (1997) 4430.

[17] LIU, X., SHEMANSKY, D.E., Analysis of electron impact ionization properties of methane, J. Geophys. Res. **111** (2006) A04303.

[18] GULCH, K., et al., Cross-sections and ion kinetic energies for electron impact ionization of CH_4, Int. J. Mass Spectrom. **228** (2003) 307.

[19] WANG, P., VIDAL, C. R., Dissociation of multiply ionized alkanes from methane to n-butane due to electron impact, J. Chem. Phys. **280** (2002) 309.

[20] LINDSAY, B.G. REJONS, R., STEBBINGS, R.F., Production of positive ion pairs by electron-impact ionization of CH_4, J. Chem. Phys, **114** (2001) 10225.

[21] STANO, M., MATEJCIK, S., SKALNY, J.D., MÄRK, T.D.,Electron impact ionization of CH_4: ionization energies and temperature effects, J. Phys. B: At. Mol. Opt. Phys. **36** (2003) 261.

[22] MORRISON, J.D., TRAEGER, J.C., Ionization and dissociation by electron impact III. CH_4 and SiH_4, Int. J. Mass Spectrom. Ion Phys. **11** (1973) 289, MATHUR, D., Collisions of slow electrons with methane: ionization, fragmentation and resonances, J. Phys. B **13** (1980) 4703.

[23] TIAN, C., VIDAL, C.R., Electron impact dissociative ionization of ethane: Cross-sections, appearance potentials, and dissociation pathways, J. Chem. Phys. **109** (1998)1704.

[24] AU, J.W., COOPER, G., BRION, C.E., The molecular and dissociative photoionization of ethane, propane, and n-butane: absolute oscillator strengths (10–80 eV) and breakdown pathways, Chem. Phys. **173** (1993) 241.

[25] BRONGERSMA, H.H., OOSTERHOFF, L.J., Singlet-triplet excitation of saturated hydrocarbons by low-energy electron impact, Chem. Phys. Lett. **3** (1969) 437.

[26] VAN DISHOECK, E.F., Photodissociation processes in the CH molecule, J. Chem. Phys. **86** (1987)196.

[27] ERHARDT, A.B., LANGER, W.D., Collisional Processes of Hydrocarbons in Hydrogen Plasmas, Report **PPPL-2477,** Princeton Plasma Physics Laboratory, Princeton USA (1987).

[28] JANEV, R.K., et al., Analytic representation of cross-sections for electron-impact dissociative excitation and ionization of CH_y^+ (y = 1 − 4) ions, Atom. Plasma-Mater. Interact. Data Fusion **16** (2009).

[29] LECOINTRE, J., et al., Absolute cross-sections and kinetic energy release distributions for electron impact ionization and dissociation of CD^+, J. Phys. B: At. Mol. Opt. Phys. **40** (2007) 2201.

[30] LECOINTRE, J., BELIC, D.S., JURETA, J.J., JANEV, R.K., DEFRANCE, P., Absolute cross-sections and kinetic-energy-release distributions for electron-impact ionization and dissociation of CD_2^+, Eur. Phys. J. D **55** (2009) 557; LECOINTRE, J., BELIC, D.S., JURETA, J.J., JANEV, R.K., DEFRANCE, P., Absolute cross-sections and kinetic-energy-release distributions for electron-impact ionization and dissociation of CD_3^+, Eur. Phys. J. D **55** (2009) 569.

[31] LECOINTRE, J., BELIC, D.S., JURETA, J.J., JANEV, R.K., DEFRANCE, P., Absolute cross-sections and kinetic energy release distributions for electron-impact ionization and dissociation of CD_4^+, Eur. Phys. J. D **50** (2008) 265.

[32] LIN, H. S., EYRING, H., Calculation of the Reaction Cross-section from a Rate Constant by the Method of Steepest-Descent, Proc. of the National Academy of Sciences, **68** (1971) 402.

[33] THOMAS, R.D., et al., Three-body fragmentation dynamics of amidogen and methylene radicals via dissociative recombination, Phys. Rev. A **71** (2005) 032711.

[34] EHLERDING, A., et al., Phys. Chem. Lett. **6** (2004) 949.

[35] DERKATCH, A.M., et al., Branching ratios in dissociative recombination of the $C_2H_2^+$ molecular ion , J. Phys. B **32** (1999) 3391.

[36] KALHORI, S., et al., Dissociative recombination of $C_2H_3^+$, Astron. Astrophys. **391** (2002) 1159

[37] GEPPERT, W., et al., Phys. Rev. Lett. **93** (2004) 153201.

[38] ANGELOVA, G., et al., Branching ratios for the dissociative recombination of hydrocarbon ions: III: the cases of $C_3H_n^+$ (n=1–8), Int. J. Mass Spectrom. **235** (2004) 7.

[39] EHLERDING, A., et al., Rates and Products of the Dissociative Recombination of $C_3H_7^+$ in Low-Energy Electron Collisions, J. Phys. Chem. A **107** (2003) 2179.

[40] LARSSON, M., et al., Rate constants and branching ratios for the dissociative recombination of $C_3D_7^+$ and $C_4D_9^+$, J. Chem. Phys. **122** (2005) 156101.

[41] GEPPERT, W., et al., Dissociative recombination of $C_3H_4^+$: preferential formation of the C_3H_3 radical, Int. J. Mass Spectrom. **237** (2004) 25.

ELECTRON COLLISION CROSS-SECTIONS OF POLYATOMIC MOLECULES RELEVANT TO PLASMA-MODELING

M. HOSHINO[1], M. J. BRUNGER[2], C. MAKOCHEKANWA[3], S. J. BUCKMAN[3], H. CHO[4], H. TANAKA[1]

[1]Department of Physics, Sophia University,
 Tokyo 102-8554, Japan

[2]Centre for Antimatter-Matter Studies, Flinders University,
 Adelaide SA 5001, Australia

[3]Centre for Antimatter-Matter Studies, Australian National University,
 Canberra ACT 0200, Australia

[4]Department of Physics, Chungnam National University, Daejeon 305-764, Republic of Korea

Abstract

Under the IAEA's Coordinated Research Program (CRP) on "Atomic and Molecular Data for Plasma Modeling (Research Coordination Meeting: RCM, 2005-2008)", 1) electron collision cross-sections have been provided for polyatomic molecules relevant to plasma-modeling. The energy range is covered from ~ 1 eV to ~100 eV for the scattering angles of 20° to 130°. The cross-sections include the elastic scattering, vibrational excitation, electronic excitation, electron attachment, and dissociation processes. In addition, 2) data compilation in printed form has been performed for: a) Elastic Differential Cross-sections for Electron Collisions with Polyatomic Molecules, b) Cross-sections of Electron-induced Resonant Vibrational Excitations in Polyatomic Molecules, and c) Electron-impact Excitation Cross-sections of Electronic States in Polyatomic Molecules. We conclude our report by examining new electron collision experimental setups installed to carry out these objectives as well as the on-going measurements currently being undertaken.

1. INTRODUCTION

With the review article on "Needs for Cross-sections in Fusion Plasma Research" by Summers [1] as a guide, atomic and molecular species relevant to fusion plasma research are summarized as follows. In the fusion reactor design, it has become an urgent and important issue that impurities sourced from the vessel walls and plasma contact points hugely influence the plasma behaviour. Needless to say, the primary reactants and spent fuel, ^2D, ^3T and ^4He together with ^7Li used for tritium breeding, are principally to be considered in the design. In the next generation Tokamaks (ITER), as materials for the boundary surfaces, plans are now afoot to use C, boronised C (giving results similar to Be) and Be for the high-heat load divertor and wall plates, due to their good thermal properties and low atomic number. Furthermore, the use of High Z metals such as Mo and W are suggested in divertors and divertor simulators.

1.1. Need for cross-section data in fusion plasmas

Impurities will always inevitably be present in a fusion plasma. These include wall-material impurities which will also always be, to a certain degree, present in the fusion plasma, particularly at its edge or divertor regions. However, their specific chemical composition will depend on the used wall materials. The second source of impurities are those species deliberately introduced into the plasma (core or edge) for reasons including diagnosis, radiative cooling, suppressing chemical erosion, or other purposes. Common impurities found in fusion plasmas include atomic (e.g. H, He, Li, Be, B, C, O, Si, Ti, Cr, Fe, Ni, Mo, W) and their isotopomic (e.g. ^1H, ^2D, ^3T, ^3He, ^4He 7Li) species. For the edge plasma as well as for the central plasma probes, metastable rich He and many other heavy elements, Ne, Ar, Kr, and still others are introduced as the puffing gases.

To understand the role of impurities with the help of cross-section data, the fusion plasma is divided into three regions: the high-temperature confined plasma core, the plasma penetrated by most neutral beams, and the edge and scrape-off layer (SOL) and divertor plasma. Although the collision community traditionally paid their attention to electron-ion collisions and ion-atom collisions, divertors are considered to have more difficult environments. For example, chemical sputtering, which is strongly dependant on the dump plats and throat materials (though it remains undecided at the present between Be and C for the ITER), also needs consideration in that environment.

The divertors serve to channel the SOL plasma away from the main plasma chamber in order to separate that chamber from a cold plasma (low temperature: T_e ~100 - 102 eV) leading to more complicated surface interactions and impurity problems [2]. Most of the H ions arriving at the divertor plates are eventually desorbed in the form of H_2. In the cold divertor plasmas H_2 can play some role as a source and a sink of hydrogen (H) ions, where the H ion flux reduction might be attributed to molecular assisted recombination (MAR) [3], [4]: $H_2(v) + H^+ \rightarrow H_2^+ + H$ and $H_2(v)^+ + e \rightarrow H + H$; $H_2(v) + e \rightarrow H^- + H$ and $H^- + H^+ \rightarrow H + H$. The MAR rate coefficients are estimated to be higher than that for the ion-electron recombination. These rate coefficients depend strongly on the vibrational excitation of the ground electronic state ($X^1\Sigma_g+$). Therefore, measurements of the H_2 density and vibrational population are necessary for understanding the role of H_2 in the plasma.

Furthermore, in the cold divertor plasmas near the C-materials used in the present and next generation Tokamaks, although the physical sputtering can be suppressed, the chemical sputtering leading to production of hydrocarbon molecules (C_mH_n/C_mD_n) cannot be suppressed. Erosion and reproduction of carbon materials is essential for long operation of next generation Tokamaks. In most Tokamak experiments, the production, fragmentation and ionization pathways of both CH_n/CD_n (n ≤ 4) and C_2H_n/C_2D_n (n ≤ 6) need to be understood qualitatively [2]. Thus, reliable data for all relevant hydrocarbon molecules and their fragments are required.

1.2. Overview of data compilations for electron-molecule collisions

To understand the particle behaviour in the cold divertor plasma as mentioned above, the plasma parameters are initially deduced from an analysis of the radiation spectra of the molecules populated in the particular states. For example, radiative electron capture populates preferentially the low-lying levels of Li-like ions, whereas the collisional (three-body) recombination populates preferentially the highly excited Rydberg levels. Radiative and/or collisionally induced transitions between all the levels occur continuously. A method commonly used to estimate the population densities of the different ionic levels in the plasma is the so-called collisional-radiative (C-R) model [5, 6].

Another area of interest is the use negative ions for heating purposes in plasma neutral beam injectors. The negative ions H^-/D^- are typically produced efficiently via dissociative attachment of vibrationally excited H_2/D_2 molecules within the discharge plasma [7]. Thus, reliable electron collision data have been demanded for all the possible processes: rotational, vibrational and electronic states, dissociation, dissociative attachment and inoization of the relevant molecules. In this report, the work addressed under the IAEA-CRP is described as follows: 1) providing electron collision cross-sections for the C-H polyatomic molecules relevant to plasma-modeling [8, 9,10], 2) installing new electron collision experimental-setups to carry out these objectives [8] and 3) compiling a) Elastic Differential Cross-sections for Electron Collisions with Polyatomic Molecules [11], b) Cross-sections of Electron-induced Resonant Vibrational Excitations in Polyatomic Molecules [12], and c) Electron-impact Excitation Cross-sections of Electronic States in Polyatomic Molecules [13], respectively, in printed form. Target species also include other polyatomic molecules related to plasma processing as well as to environmental issues, because of the similar discharge phenomena involving the relevant atomic and molecular collision processes. This is well summarized in the review paper under the collaborative work of Australia, Korea, and Japan [14].

2. PROVIDING ELECTRON COLLISION CROSS-SECTIONS [11], [15]

Overviews of the available electron collision cross-sections are presented for H_2 [16] and CH_4 [17] in Figs 1(a) and (b) as representative cases.
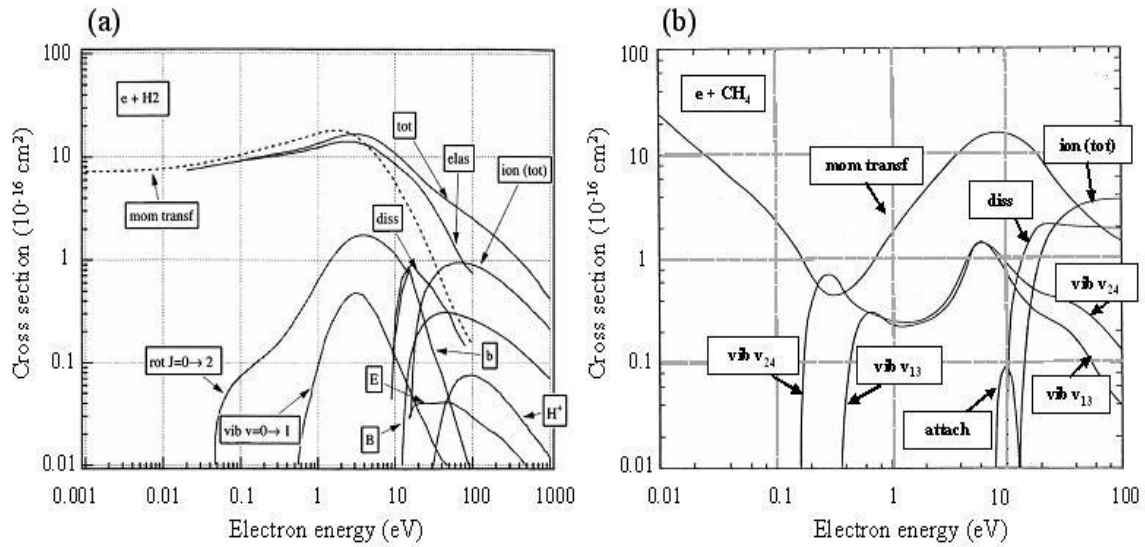

FIG. 1. Electron impact collision cross-sections for (a) H_2 and (b) CH_4 molecules.

2.1. Definition of cross-sections

In what follows we shall concentrate first on a single collision between an electron and an atom or molecule. We first classify collisions into two kinds, namely, elastic and inelastic. In an elastic collision, the internal energy of an atom or molecule is unchanged. However a part (ΔE) of the electron energy E_0 is transferred to the atom or a molecule as given by $\Delta E / E_0 \approx m/M \approx 10^{-4}$, where m is the electron mass and M is the mass of the atom or molecule. In an inelastic collision, there is a change in the internal energy, which leads to one or more of rotational, vibrational, or electronic excitation, dissociation, ionization, or attachment of an electron to a molecule. For an atom, electronic excitation and ionization are the only possibilities. The energy transfer to rotational, vibrational, and electronic degrees of freedom is roughly in order of the ratios $(m/M)^{1/2} : (m/M)^{1/4} : 1 \approx 10^{-3} : 10^{-1} : 10$.

The probability of an inelastic collision is expressed in terms of the cross-section defined as follows. Suppose that I_0 electrons of energy E_0 per unit area are incident on a gas consisting of N atoms or molecules per unit volume. The number of electrons scattered into the solid angular element $d\Omega$ in the direction Ω (θ, ϕ), measured from the polar axis taken along the direction of electron incidence, can be written as:

$$I_{0n} (\Omega) = N I_0 \, d\sigma_{0n} (E_0, \Omega) / d\Omega. \tag{1}$$

The subscript $0n$ indicates a transition from the ground state 0 to an excited or ionized state n. One calls the quantity $d\sigma_{0n} (E_0, \Omega) / d\Omega$ the differential cross-section (DCS) for the excitation $0 \rightarrow n$.

Theoretically, the differential cross-section is expressed in terms of the scattering amplitude f_{0n} (E_0, Ω), which is determined from the asymptotic behaviour of the electron wave function, in the form:

$$d\sigma_{0n}(E_0, \Omega)/d\Omega = (k_n/k_0) \, | f_{0n}(E_0, \Omega)|^2, \tag{2}$$

233

where k_0 is the magnitude of the electron momentum before the collision and k_n the same after the collision.

The integral of the differential cross-section over all scattering angles, viz. ,:

$$q_{0n}(E_0) = \int \int d\sigma_{0n}(E_0, \Omega)/d\Omega . \sin\theta \, d\theta \, d\phi \qquad (3)$$

is called the (integral) cross-section (TCS) for the excitation $0 \to n$. Note that the full angular range is preferably covered when measuring the DCS e.i. from 0° to 180°, in determining an integral cross-section experimentally.

The elastic-scattering cross-section q_0 (E_0) is defined similarly, by replacing the final state n by the ground state 0 in Eqs. (1) - (3). To discuss effects of elastic scattering on electron transport phenomena, it is more important to consider the momentum-transfer cross-section (q_{0M}) defined by:

$$q_{0M}(E_0) = \int \int d\sigma_0 (E_0, \Omega)/d\Omega . (1 - \cos\theta) \sin\theta \, d\theta \, d\phi . \qquad (4)$$

The sum of the cross-sections given by Eq. (3) over all possible kinds of excitation (including the elastic-scattering cross-section), viz.,

$$Q (E_0) = q_0(E_0) + \sum q_{0n}(E_0) \qquad (5)$$

is called the total cross-section (TCS).

If the distribution of particle speeds v is given by $F(v)$, then the reaction rate constant for a process with cross-section q_n is calculated as:

$$\kappa_n = \int q_n F(v) \, v \, dv \qquad (6)$$

2.2. Overview of electron beam-molecular beam scattering experiments

2.2.1. Instrumentation

A typical electron spectrometer [18] is shown in Figure 2 consists of an electron gun with a hemispherical monochromator, a molecular beam, and a rotatable detector (θ: the scattering from 10° to around 130°) with a hemispherical analyzer, all contained in a vacuum chamber. A beam of molecules is produced by effusing the target through a nozzle with an internal diameter of, for example 0.3 mm, and a long length to ensure a high aspect ratio. The spectrometer and the nozzle can also be heated to a temperature of about 50°C to reduce the possibility of contamination during the measurements. The molecular beam is crossed with a monoenergetic beam of electrons of fixed incident energy. At a particular scattering angle, scattered electrons are detected. A number of lenses in the spectrometer are used for imaging and energy control of the incident and scattered electron beam, whose characteristics are carefully modeled by electron trajectory calculations. The ideal molecular beam has a small size and a uniform high density. As far as this molecular beam remains within the view cone angle of the electron analyzer, the detection probability for scattered electrons should be uniform and the measured scattering intensities are directly proportional to the scattering cross-sections.

In some systems, both the monochromator and analyzer are enclosed in differentially pumped boxes in order to reduce the effect of background gases and to minimize any stray electron background. The magnetic field in the chamber should be kept to as low as a few milli-Gauss. Overall energy resolution varies typically from around 20 to 80 meV (FWHM). The angular scale is accurate to about ±1.5°, as determined by noting the symmetry of the elastic scattering about the true zero-degree point.
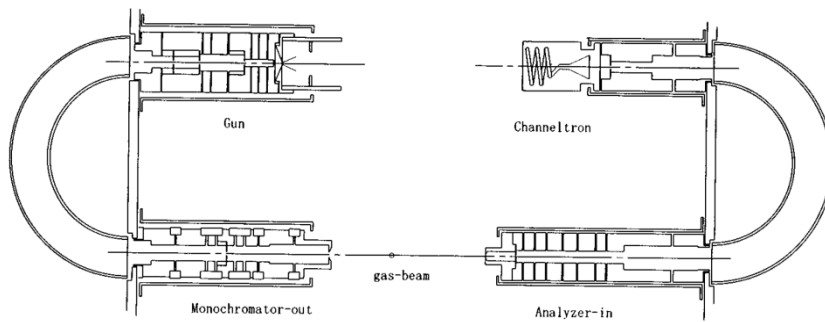
234

FIG. 2. Schematic diagram of the electron spectrometer at Sophia University.

However, this conventional spectrometer is only capable of differential scattering measurements over an angular range typically from 10° to around 130°. This is because of the mechanical restriction imposed by the size of some of the elements in the electron spectrometer. To overcome this limitation, an electron spectrometer with a magnetic-angle changing device has been developed to measure electron scattering cross-sections at backward angles up to 180° [19]. This technique involves the production of a magnetic field, localized in the vicinity of the interaction region, to change the trajectories of the incident and scattered electrons, such that one can effectively rotate the scattering geometry. The use of two concentric coils, producing opposed but coaxial magnetic fields, ensures that the electron beam passes through the common centres of the coils and thus crosses with the target molecular beam. The arrangement of the coils and their currents is such as to cancel the dipole and the octupole moments of the magnetic field outside the solenoids and so have a minimal effect on the effective operation of the electrostatic spectrometer. This technique has been used in measuring some of the elastic differential cross-sections presented later, with detailed descriptions being found in earlier publications [20, 21].

2.2.2. Normalization and energy calibration

Relative measurements of the angular distribution are placed on an absolute scale by use of the relative flow technique [22]. This technique relies on measurements of the ratio of scattered electron intensities for the gas of interest relative to that for a standard gas. To establish the correct flow conditions, in particular that the mean-free-paths for the two gases are identical in the capillary needle, the driving pressures for the two gases must be set very carefully. In other words, the densities of the two gases are set to be identical by adjusting the pressure behind the nozzle so as to maintain approximately equal gas Knudsen numbers. The ratio of the driving pressures is determined from values of the molecular diameters of the standard gas and the target molecules. Full details on the conditions that need to be fulfilled to properly conduct a relative flow experiment have been discussed by Gibson [23] and references therein.

Providing the above conditions are satisfied, the ratio of the two cross-sections σ_x and σ_h (x for the target gas of interest, h for the helium standard) can be determined from the following equation:

$$\frac{\sigma_x}{\sigma_h} = \frac{I_x P_h}{I_h P_x} \tag{7}$$

where I_x and I_h are the scattered electron intensities, and P_x and P_h are the corresponding driving pressures for the two gases respectively.

For most of the elastic differential cross-section measurements presented here, the following standard helium cross-sections were used: Boesten and Tanaka [24] or Nesbet [25] for energies below

20 eV, and Brunger *et al* [26] at higher energies. Boesten and Tanaka (1992) have accumulated a large data base and calculated rational function fits for a representative set of elastic, non-resonant *e* + He differential cross-sections (DCS) comprising (1) the variational DCS of Nesbet (1979), (2) the eikonal DCS of Byron and Joachain (27) and the experimental data of Wagenaar *et al*. [28], Register *et al*.[29], Bromberg [30], and Jansen et al [31], with the arranged priorities in the order given. The fits, expressed as functions of the scattering angle with the impact energy as the parameter, form smooth functions at sufficiently closely spaced intervals to allow for easy first- or second-order interpolation over angles θ from 0° to 180° and energies E_0 from 0.1 to 1000 eV. Maximum deviation from the data set is 10.4% for experiments and 20% for theory at low angles smaller or equal to 10°, where theory deviates from the experiments.

The absolute electron energy scale is calibrated by observing either the position of the second quasi-vibrational resonance peak of the N_2^- $^2\Pi_g$ resonance, at the energy of 2.198 eV for a scattering angle of 60° [32], or the position of the He$^-$ $1s^2 2s^2$ 2S resonance at 19.367 eV [33].

2.3. Illustrative examples for electron collision cross-sections

As pointed out above, electron collisions with atoms and molecules are of general importance in the initiation of discharges and plasmas. Our research program is based on three major objectives, achieved experimentally by studies of electron-molecule collision mechanisms under: (1) Elastic Scattering, (2) Excitation Processes (vibrational and electronic) and (3) Dissociation, Attachment and Scattering from Excited Molecules. Three broad classes of polyatomic molecular targets have been studied: Hydrocarbon- Molecules, Fluorocarbon-Molecules and Environmental-Molecules. Hence a *systematic* measurement of absolute DCSs for electron scattering by these molecules has been performed within an impact energy range from 1.5 to 100 eV and scattering angles between 10° and normally around 130°. However for a few molecules this is even up to 180°.

2.3.1. Elastic electron scattering

As shown in Figs. 1(a) and (b), elastic scattering is important in all collisions and generally its cross-sections are much larger than those of inelastic scattering. It is therefore much easier to obtain their absolute cross-sections, for example with the relative flow method just described. Fortunately, as long as the transmission efficiency of the electrostatic lens system is guaranteed for the electron beam, the elastic cross-sections can be measured simultaneously with the corresponding inelastic cross-sections. They thus can serve as a calibration standard for absolute determination of the inelastic DCS.

Along with our current program to determine the absolute elastic cross-sections for electron collisions with the C-H polyatomic and C-F polyatomic molecules, we also have a long history of producing experimental results that are relevant to the themes of this report. But, in this section, we will restrict our report mainly to these C-H polyatomic molecules measured since this project started in 2005. Other fusion relevant C-H molecules are summarized in three compilations of numerical electron collision cross-section databases as discussed later. These are as follows.

(a) C_3H_6 (the isomers propene (C_3H_6) and cyclopropane (c-C_3H_6)) [34]

This is a study in which electron-scattering DCS have been measured for 1.5-100 eV and the angular range of 20° -130° as shown in Figure 3. Included also is a theoretical calculation using the Schwinger multichannel (SMC) method of pseudopotentials which has been carried out for the elastic DCS, integral elastic cross-sections (ECS), and momentum-transfer cross-sections (MTCS) for the energy range of 2.0 to 40 eV and an angular range of 0° − 180°. The resembleance of the π* shape resonance in these cross-sections, observed at 1.5 − 2.0 eV for propene, to similar structures in C_2H_4 and C_2F_4 clearly points to the effect of the molecular double bond for these molecules. In addition, below 60 eV, we observed clear differences in the peak positions and magnitudes between the DCS, ECS, and MTCS for C_3H_6 and c-C_3H_6, which we view as an isomer effect. Full details of this work can be found in the paper [34].
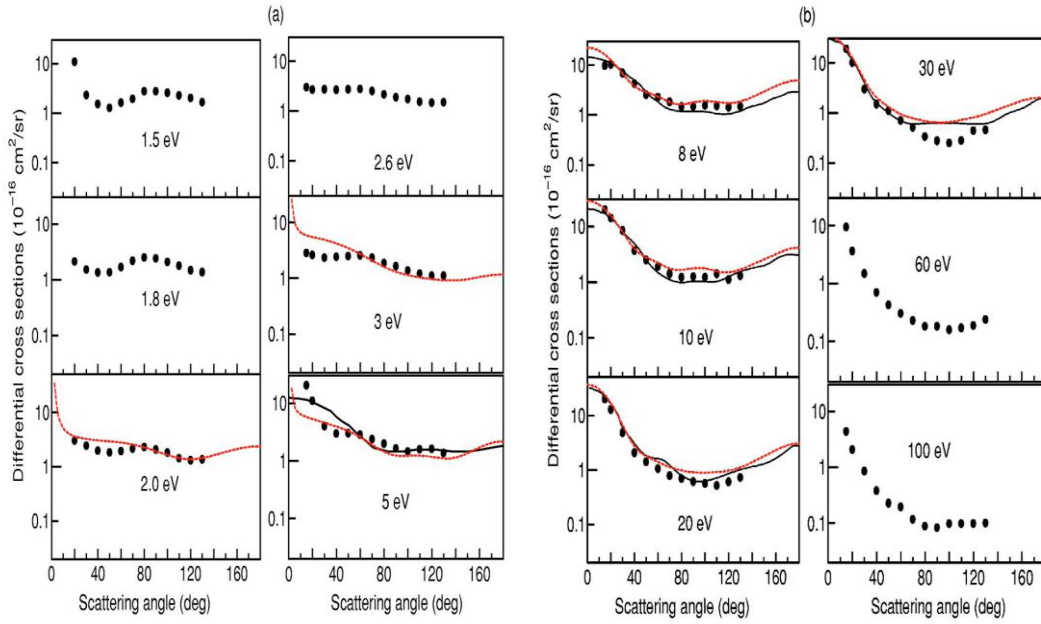
FIG. 3. Electron-impact C_3H_6 experimental (circles) and theoretical (lines) elastic DCSs as functions of the scattering angles in the energy range of (a) 1.5 – 5 eV and (b) 8 – 100 eV Also included in some panels are the only available DCS results of Winstead et al. (black solid lines). References are in the original paper [34].
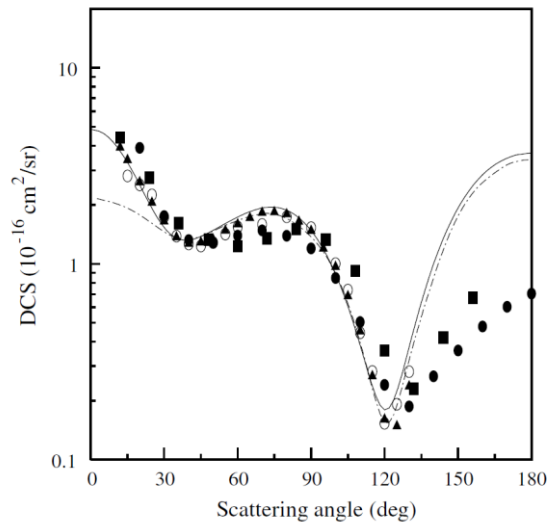

FIG. 4. DCS for elastic e^- – CH_4 scattering at 5 eV. Full line, theoretical data; dot-dashed line, theoretical results of Bettega et al; full circles, present experimental data; full squares, experimental data of Shyn and Cravens; open circles, experimental data of Boesten and Tanaka; full triangles, experimental data of Bundschu. References are in the original paper [35].

(b) CH$_4$ [35]:

Absolute DCS for elastic scattering by CH$_4$ have been measured at six incident electron energies between 5 to 100 eV and over the scattering angles between 10° to 180°, using a crossed-beam electron spectrometer combined with a magnetic angle-changing device to extend the measurements to backward angles (125 - 180). DCS, ECS, MTCS are also calculated by employing the iterative Schwinger variational method with a complex optical potential as well as by combining the distorted-wave approximation. As shown in Figure 4, the comparison between two approaches successfully revised the previous ECS and MTCS due to the limitations of the earlier DCS measurements with the scattering angles covered up to 130°. Full details of this work can be found in the paper [35].

2.3.2. Electron –induced resonant vibrational excitation

When an electron approaches a molecule, the electron exerts a torque on the molecule leading to rotational excitation. Molecules in plasma are mostly in rotationally excited states, and the distribution over the rotational states is expected to play a role in chemical reactions. Unfortunately, the electron-beam method is currently incapable of resolving individual rotational energy levels (except for hydrogen and hydride molecules). Therefore, measurements so far have dealt with an envelope of rotational structure in an energy-loss spectrum, giving only gross information. An electron approaching a molecule exerts not only a torque but also a force that causes changes in molecular internuclear distances. This, of course, leads to vibrational excitation. Recent relevant examples of our work in this area, again for the isomers cycropropane and propene, are given in Figs. 5 and 6, respectively. Full details of this work, including a discussion of the resonance features observed, is given in the paper [36].

(a) C$_3$H$_6$ (the isomers propene (C$_3$H$_6$) and cyclopropane (c-C$_3$H$_6$)) [36]

The vibrational excitation experimental results for these molecules are shown in Figs. 5 and 6. For both molecules the bending and stretching vibrational modes are studied at loss enegies 0.12 eV and 0.37 eV, respectively, for propene, and 0.13 and 0.37 eV, respectively, for cyclo-propane, at the scattering angle of 90° and impact energy range 1 - 16 eV. For C = C double bond containing propene molecules, the peak observed at about 2 eV is a π* shape resonance. This vibrational excitation channel proceeds via formation of the transient $C_3H_6^-$ ion due to the incident electron being trapped temporarily into valance orbitals with the C = C antibonding character, i.e. the lowest unoccupied molecular orbital (LUMO). In addition, peaks observed in the corresponding electron impact TCS at 2.2 and 9.5 eV for propene and 1.5, 6 and 9.5 eV for cyclo-propene were concluded to be resonant in nature and to have significant origins in the vibrational excitation.
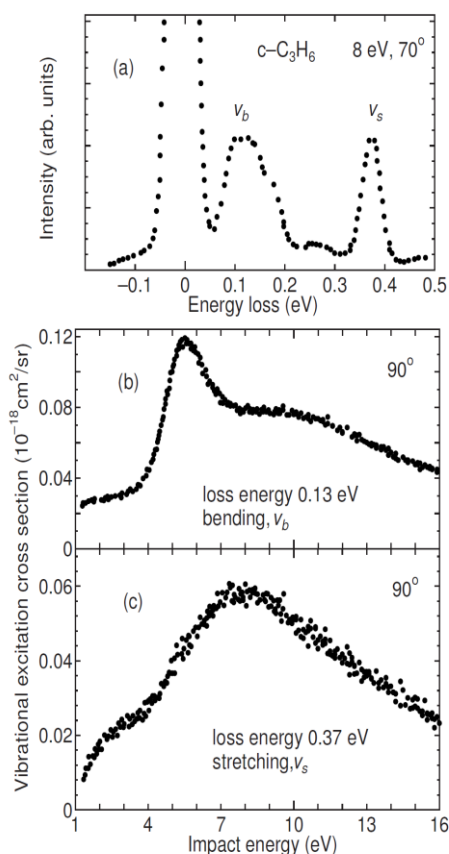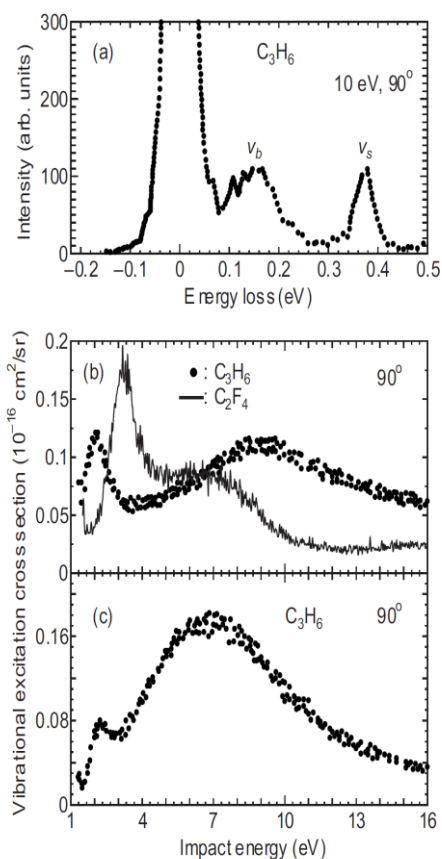
FIG. 5. c-C₃H₆ electron impact. (a) Energy loss spectrum at 8 eV and a scattering angle of 70°, and vibrational excitation cross-sections for the (b) bending v_b mode, and (c) C-C stretching v_s mode.

FIG. 6. C₃H₆ electron impact. (a) Energy loss spectrum at 10 eV and a scattering angle of 90°, and vibrational excitation cross-sections for the (b) bending v_b mode, and (c) C-C stretching v_s mode.

2.3.3. Electronic excitation dissociation

In general, numerous electronically excited states contribute to the cross-sections for electronic excitation, dissociation and dissociative ionization. It is well known that after dissociation, those intrinsically energetic fragments play a leading role in the plasma, especially in the reactive low temperature plasma. Also subsequent light emissions, i.e. from a glow discharge plasma, provides information about the formation of the electronically excited dissociation fragments. The cross-sections and appearance potentials for the various optical emissions can thus be studied in many ways useful for plasma diagnostics.

(a) CH₄ [37]:

It is, in general, held that all the electronic excitation states of CH_4 are repulsive states, leading to dissociation channels. This implies that in any plasma containing CH_4, either chemically active neutral molecules or radicals will be formed with high efficiency. Amongst these species are also neutral, non-emitting radicals (i.e. radicals in the ground electronic state: CH_3, CH_2, and CH), and ionized fragments, all with rather important roles in plasma physics. However, it is very difficult to

measure their concentration in operating plasma because of their non-emitting nature. An apparatus combining the crossed-beam and threshold-ionization techniques has therefore been used to measure absolute cross-sections for electron impact CH_3 radical production, with full details being given in Ref. [37]. In Figure 7 we illustrate some of the experimental results from this work.
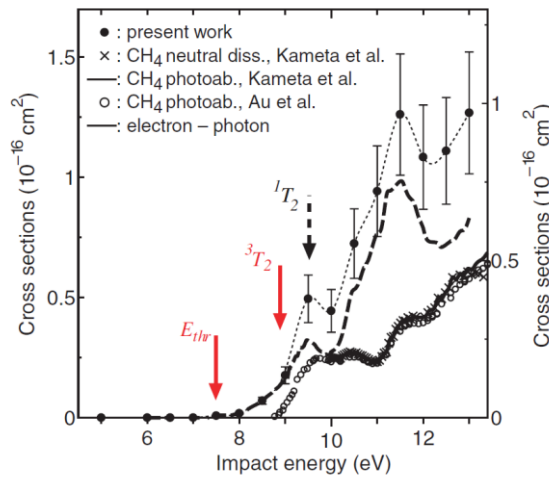

FIG. 7. Absolute cross-sections for CH_3 radical production. Also included are the photon impact results from literature. The arrows show the threshold energy E_{thr} and the $^3T_2$ and $^1T_2$ state peaks. The dashed curve is the difference between the current neutral CH_3 and the photon impact total neutral dissociation cross-sections. For detailed information, reference should be made to Ref. [37].

(b) H_2 [38]:

Differential and integral cross-sections for electron-impact excitation of the dipole-allowed $B^1\Sigma+_u$ and $C^1\Pi_u$ electronic states of molecular hydrogen have recently been measured. The differential cross-sections were determined by analysis of normalized energy-loss spectra obtained using a crossed-beam apparatus at the electron-impact energies of 40, 100, and 200 eV. Integral cross-sections were subsequently derived from these data. That work was undertaken in order to investigate some ambiguities between earlier experimental data and recent BEF-scaled cross-sections, as defined and by Kim [39] and also to extend the energy range of the available data. The major results from that work, along a comparison to earlier work, can be found in Figure 8. Optical oscillator strengths, also determined as a part of this investigation, were found to be in fair accord with previous measurements and some calculations. Please consult the following paper more details:
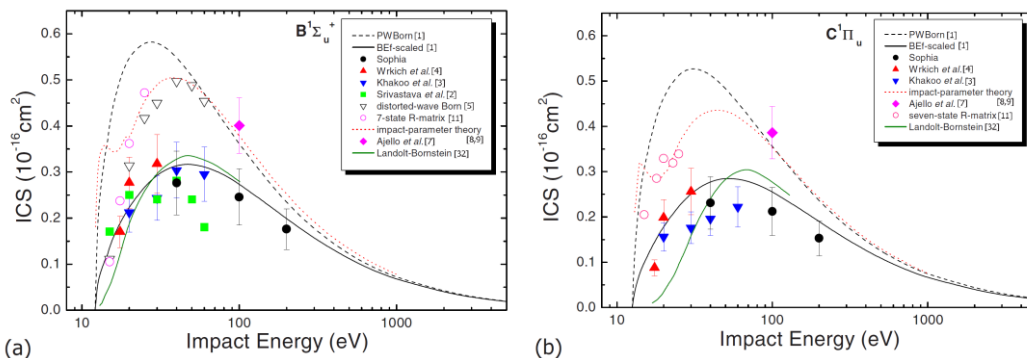

FIG. 8. Integral cross-sections of electronic excitations (10^{-16} cm^2) plotted for the (a) $B^1\Sigma_u+$ and (b) $C^1\Pi_u$ electronic states. For detailed information, reference should be made to Ref. [39].

240

2.3.4. Electron attachment

Electron impact excitation, fragmentation and ionization of methane (CH_4), silane (SiH_4) and germane (GeH_4) are processes that have invited a lot of research interest, owing to their widespread use in chemical vapour deposition (CVD) and etching. In particular, fragmentation becomes the most important channel. This is because electron impact, unlike photon collisions limited by dipole interaction rules, can excite any dissociative state of a molecule leading to fragmentation. This is thus a key mechanism by which radicals and molecular ions are produced in various fields of industrial applications, including aspects of atmospheric and space science.

(a). XH_4 (X=C, Si, Ge) [40]:

Low-energy electron impact induced fragment negative ion formation from CH_4, SiH_4 and GeH_4 has been studied using a quadrupole mass spectrometer. Relative cross-sections are determined for all three molecules for the X^-, XH^-, XH_2^- and XH_3^- ions over the energy range 4 - 20 eV. The most dominant negative ion fragment is CH_2^- in CH_4, SiH_3^- in SiH_4 and a combination of GeH_3^- and GeH_2^- in GeH_4, with peaks at 11.5 eV, 8.8 eV and an average of 8.6 eV, respectively. Fragmentation into these negative ions is attributed to resonant dissociative electron attachment processes. Having successfully carried out experiments investigating electron impact CH_3 neutral radical formation from CH_4 [37], we took particular interest in probing the correlation, if at all, between production of this neutral radical and its corresponding negative ion (CH_3^-). Full details of this work will be given in Ref. [40].

2.3.5. Electron scattering from excited molecules [41]

It is well known that vibrational/rotational (hot) and electronic excitation of molecules play an important role in electron attachment processes. The need for such knowledge in order to model plasmas, discharges, and so on is also recognized. Although electron attachment to hot molecules has been relatively well studied, little is known experimentally about the scattering of slow electrons from vibrationally excited species. The main reasons may be due to the difficulties in producing excited target molecules in sufficient number densities and then properly characterizing them. Theoretical work on this problem has also been limited, although a number of calculations have been performed by Capitelli et al. [4] on H_2.

(a) CO_2 [42]:

Inelastic and superelastic excitation function measurements have been performed for electron scattering from the ground vibrational quantum (000), the bending vibrational quantum (010) and the unresolved first bending overtone (020) and symmetric stretch (100) modes of the ground electronic state in hot (700 K) carbon dioxide (CO_2) molecules. The incident electron energy range of these measurements was 1–9 eV, with the relevant excitation functions being measured at the respective electron scattering angles of 30°, 60°, 90°, and 120°. Where possible, comparison was made to the often quite limited earlier data with satisfactory agreement typically being found to within the cited experimental errors. Examples of results from this study are given in Figure 9, with a full description of this work found in Ref. [42].
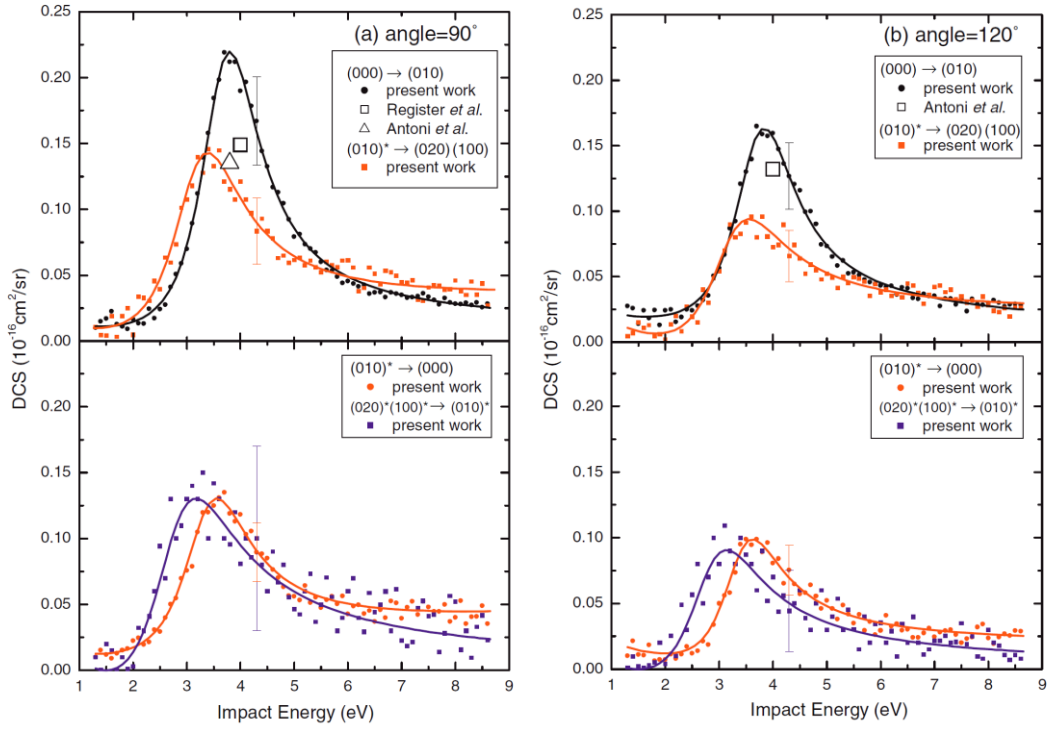
241

FIG. 9. Vibrational excitation functions for the inelastic (000)→(010) and (010)*→(020)(100) transitions and (010)*→(000) and (020)*(100)*→(010)* superelastic transitions of CO_2 at impact energies of 1–9 eV and at scattering angles of (a) 90° and (b)120°. For detailed information, reference should be made to Ref. [42].

(b) H_2 [43]:

As mentioned earlier, in the cold divertor plasmas, H_2 can play some role as both a source and a sink of hydrogen ions. In the MAR, the rate coefficients depend strongly on the vibrational excitation of the H_2 ground state ($X^1\Sigma_g+$). Therefore, measurements of the H_2 density and vibrational population distribution are necessary for understanding the role of H_2 here. Although this was one of our most important issues to for experiments under this project, the Jet Propulsion Laboratory (JPL) group, fortunately, has already succeeded to do the experiments on electron collisions with hot H_2 with examples of their data being given in Ref. [43]. Nevertheless, in all physics, it is critical for cross-check measurements to be made for data more reliably. Thus we will revert to this project at later time. Figure 10 shows the results published by the JPL group.
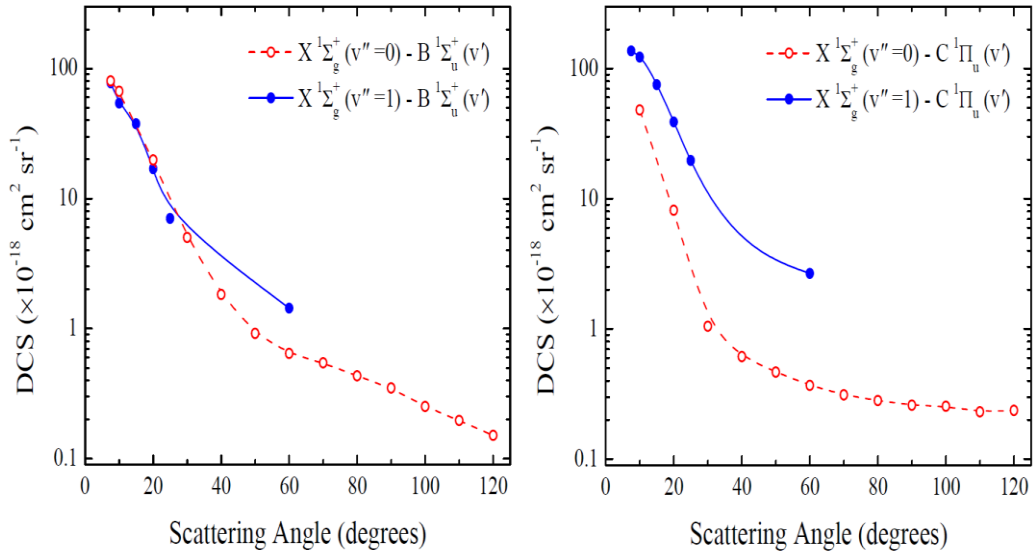
FIG. 10. DCS for excitation of the B $^1\Sigma_u^+$ (v') and C $^1\Pi_u$ (v') states from the X $^1\Sigma_g^+$ (0) and X $^1\Sigma_g^+$ (1) ground state levels of H_2 at an impact energy of 40 eV. For detailed information, reference should be made to Ref. [43].

3. INSTALLATION OF NEW EXPERIMENTAL SETUPS FOR CROSS-SECTION MEASUREMENTS

In order to determine electron impact cross-sections with more accuracy, as well as over a wider energy-range, the following two methods have been introduced to complement the existing electron energy loss spectroscopy (EELS) method.

3.1. Time-of-flight spectrometer (TOF) [44]

In general, as shown in Figs 1(a) and (b), electron impact cross-sections reveal their maxima near the threshold of the opening inelastic channels for optically forbidden transitions. In order to measure the inelastic DCSs in the energy range extending from threshold to several eV above the threshold of the inelastic channel, a time-of-flight apparatus is suggested for use in acquiring qualitative DCS. One reason for this suggestion may be that the TOF approach eliminates the need for the complicated calibration procedures required when using conventional electrostatic EELS at these low energies. The new TOF experimental setups have been successfully installed at Sophia University and the Australian National University (which is already in the full operation [44]).

3.2. Cold collisions of electrons with molecules [45]

Cold electron collisions are those in which the de Broglie wavelength of the electron is very much greater than the dimensions of the molecular target (an electron of energy 10 meV for a corresponding wavelength of 12.2 nm). One can thus expect to make quantum scattering phenomena more apparent in these very low energy ranges. Furthermore, in their practical application in weakly ionized plasmas, cold collisions dominate in the lower end of the thermal energy range and play an important role in systems such as the cold plasma in the divertor and RF plasmas in processing. Therefore, there is a considerable practical interest in acquiring cross-sections for cold electron-molecule collisions.

Following the experimental technique at the Institute for Strorage Ring Facilities, University of Aarhus, a new project has been started under the collaboration of Tokyo Institute of Technology and the Photon Factory, KEK, in Japan. By using synchrotron radiation, photo-ionized electrons from 2P$_{3/2}$ Ar$^+$ at 15.759 eV are employed in the energy range from $\sim$ 2.6 meV above the ionization energy

threshold. A new experimental setup has been installed and is now in operation. An earlier reference to this is given below from the work of Field et al. [45].

The above two approaches appear very promising in our efforts to produce more reliable electron collision cross-sections for atom and molecules related to fusion plasmas. This is particularly the case for studying near-threshold data.

4. COMPILING NUMERICAL ELECTRON COLLISION CROSS-SECTION DATABASES

For discharges occurring in the cold plasma near the divertor region, the most significant electron collision processes occur in the electron energy range less than 100 eV. The generic primary processes are elastic and inelastic electron scattering (rotational, vibrational, and electronic excitations), electron impact ionization, electron-impact dissociation and attachment. However, the many possible excitation processes arising from the many degrees of freedom available within molecules make the study of electron-molecule collisions extremely complex. Comprehensive sets of electron-molecule collision cross-section data are, therefore, only limited to the simplest of diatomics (e.g. H_2, N_2 [46], CO_2) and a few polyatomics (e.g. CH_4, CF_4 [47], SiH_4 and SF_6 [48]). Three reports have been prepared for the Numerical Electron Collision Cross-section Databases as follows:

4.1. Elastic DCS [11]

Elastic differential cross-sections for electron collisions with polyatomic molecules

Experimental data for electron-polyatomic molecule collisions are reviewed in connection with fusion and processing plasmas, as well as with the associated environmental issues. The electron scattering experiments for differential cross-section (DCS) measurements for various processes, such as elastic scattering, have been performed across a broad range of energies (1-100 eV), mainly, at Sophia University since 1978, and some were also done under collaboration with the Australian National University, Flinders University and the Chungnam National University. As a benchmark cross-section, elastic data are essential for the absolute scale conversion of inelastic DCS, as well as for testing computational methods. The need for cross-section data for a wide variety of molecular species is also discussed, because there is an urgent need to develop an international program to provide the scientific and technological communities with authoritative cross-sections for electron-molecule interactions. Note that the detailed comparison with other data available is not given here. Rather, other available data can be found in the references we cite. This course of action was adopted to keep this report to a sensible length, so that only our numerical data is given.

4.2. Vibrational excitation [12]

Electron-induced resonant vibrational excitations in polyatomic molecules

We continue our review of experimental data for electron-polyatomic molecule collisions in connection with fusion and processing plasmas, as well as with the associated environmental issues. In this case we focus on vibrational excitation processes, in particular what vibrational modes can be identified in electron energy loss experiments and which of these modes are resonantly enhanced due to the temporary capture of the incident electron by the species in question. In this latter respect we report indicative excitation function data, all of which were originally measured at Sophia University and for which the differential cross-section, for excitation of the relevant mode, is studied as a function of the incident electron energy at a fixed scattered electron angle. Unlike our previous compilation (NIFS–DATA–101) for elastic scattering, which was conducted over a broad range of energies (1–100 eV), vibrational excitation cross-sections usually only become significant when the resonance enhancement process occurs. As a consequence, this survey encompasses incident electron energies between 1–30 eV. Consistent with our first report, no detailed comparison is made here with any other data that might be available in the literature. This course of action was once again adopted in order to keep this report to a sensible length.

4.3. Electronic excitations [13]

Electron-impact excitation of electronic states in polyatomic molecules
-Application Examples of the BEB- scaling model in Optically-allowed Transitions-

Integral cross-sections for the optically allowed electronic excitations by electron impact are reviewed for polyatomic molecules, by applying the Binary-Encounter-Bethe (*BEB*) oscillator strength (*f*) scaling model (*BEf*-scaling). Following the context of the previous reviews, the scaling model originally proposed by Yong-Ki Kim to determine the electron-impact cross-sections for ionization of atoms and molecules is also summarized briefly because of its wide range of applications [Electron-Impact Cross-section Database, NIST, Y.-Ki Kim]. The present report not only focuses on the need for the this type of cross-section data, but also elucidates the verification of the scaling model in the general application for atoms and particularly polyatomic molecules.

Other relevant review articles that date from post-1990 are listed below. Note also that those review articles for electron collision cross-sections in general after 1990 are well summarized in "Molecular Processes in a Plasma" as recently published by Itikawa [16].

1. International Bulletin on Atomic and Molecular Data for Fusion, **42** (1992) - **58** (2000) published by IAEA
2. Collision Data Involving Hydro-Carbon Molecules, H. Tawara, Y. Itikawa, H. Nishimura, H. Tanaka, and Y. Nakamura, *NIFS-DATA-6* July (1990)
3. Cross-section Data, ed M. Inokuti, *Adv. At. Mol. Opt. Phys.* **33** (1994)
4. Atomic Data and Nuclear Data Tables **76** (2000) 1
5. One Century of Experiments on Electron-Atom and Molecule Scattering: a Critical
   Review of Integral Cross-sections for Polyatomic Molecules, Hydrocarbons and
   Halides, G. P. Karwasz, R. S. Brusa, and A. Zecca, *La Rivista del Nuvo Cimento* 24 (1) (4) (2001)
6. Electron-Molecule Scattering Cross-Sections. I. Experimental Techniques and Data for Diatomic Molecules, M. J. Brunger and S. J. Brunger, *Phys. Report* **357** (2002) 217
7. Analytic Cross-sections for Electron Collisions with Hydrocarbons: CH_4, C_2H_6, C_2H_4, C_2H_2, C_3H_8, and C_3H_6, T. Shirai, T. Tabata, H. Tawara, and Y. Itikawa, *Atomic Data and Nuclear Data Tables* **80**, (2002) 147
8. Interaction of Photons and Electrons with Molecules, M.J.Brunger and S.J.Buckman,
   Photon and Electron Interactions with Atoms, Molecules, and Ions, vilI/17, sub-volume C ed Y. Itikawa, Landorf-Beurnstein (2003, Berlin: Springer) p6
9. Collision Processes of C_2, $3H_y$ and C_2, $3H_y$ Hydrocarbons with electrons and Protons, R. K .Janev and D. Reiter, *Phys. Plasma* **11** (2004) 780
10. Vibrational Excitation of Polyatomic Molecules by Electron Collisions
    Y. Itikawa, J. Phys. B: At. Mol. Opt. Phys **37** (2004) R1

5. CONCLUSIONS

As mentioned in abstract, under the IAEA's Co-ordinated Research Program on" Atomic and Molecular Data for Plasma Modeling" (2005-2008), we have provided the Electron Collision Cross-sections for Polyatomic Molecules relevant to Plasma-modeling. Those cross-sections include the elastic scattering, vibrational excitation, electronic excitation, electron attachment, and dissociation processes. Three database in printed form has been compiled as follows, a) Elastic Differential Cross-sections for Electron Collisions with Polyatomic Molecules, b) Cross-sections of Electron-induced Resonant Vibrational Excitations in Polyatomic Molecules, c) Electron-impact Excitation Cross-sections of Electronic States in Polyatomic Molecules. Target Molecules are classified into H-C Molecules produced from the internal wall materials of fusion chambers, H-C & C-F Molecules for plasma processing, and environmental issues. New Electron Collision Experimental-setups have been installed in order to extend our projects further. The project has been performed under the international collaboration among Japan, Australia, and Korea, which has been extending to organize the *Asian-Pacific Atomic-data Network (APAN)* since 2008.

ACKNOWLEDGEMENT

REFERENCES

[1]   SUMMERS, H. P., "Need for Cross-sections in Fusion Plasma Research", Cross-section Data, Vol. 33 (Inokuti, M., Bederson, B. Walter, H., Eds) Academic Press, San Diego and London (1994) 275.

[2]   BREZINSEK, S., et al., Hydrocarbon injection for quantification of chemical erosion yields in tokamaks. Journal of Nuclear Materials, J. Nucl. Mater. **363 - 365** (2007) 1119.

[3]   JANEV, R.K., et al., Survey of atomic processes in edge plasmas, J. Nucl. Mater. **121** (1984) 10.

[4]   KRASHENINNIKOV, S.I., PIGAROV, A.YU., SIGMAR, D.I., Plasma recombination and divertor detachment, Phys. Lett. A **214** (1996) 285.

[5]   KLISNICK, A., SUREAU, A., GUENNOU, H., MÖLLER, C., VIRMONT, J., Effective rates for li-like ions; calculated XUV gains in Al^{10+}, Appl. Phys. B **50** (1990) 153.

[6]   JANEV, R.K., REITER, D., Collision processes of $C_{2,3}H_y$ and $C_{2,3}H_y^+$ hydrocarbons with plasma electron and protons, Phys. Plasma **11** (2004) 780.

[7]   OHARA, Y., OKUMURA, Y., Negative ion based neutral beam injectors, Nucl. Fusion **32** (1992) 1679.

[8]   TANAKA, H., "Atomic and Molecular Data for Plasma Modeling", Report INDC (NDS)-0482, Vienna (2005).

[9]   TANAKA, H., "Atomic and Molecular Data for Plasma Modeling", Report INDC (NDS)-0482, Vienna (2007).

[10] TANAKA, H., "Atomic and Molecular Data for Plasma Modeling", Report INDC (NDS)-0482, Vienna (2008).

[11] HOSHINO, M., et al., Research Report NIFS-Data Series (ISSN 0915-6364) NIFS-DATA-101 (2008).

[12] KATO, H., et al., Research Report NIFS-Data Series, to be published (2009).

[13] KAWAHARA, T., et al., Research Report NIFS-Data Series, to be published (2009).

[14] BRUNGER, M.J., CHO, H., TANAKA, H., BUCKMAN, S.J., Measurements of Electron Collision Cross-sections of Relevance to Plasma and Gas Discharge Physics, Japanese J. Applied Physics **45** (2006) 8183.

[15] TANAKA, H., SUEOKA, O., Mechanisms of electron transport in electrical discharges and electron collision cross-sections, Adv. At. Mol. Opt. Phys, **44** (2001) 1.

[16] ITIKAWA, Y., Molecular Processes in Plasma, Springer, Verlag Berlin Heidelberg (2007) 172.

[17] KURACHI, M., NAKAMURA, Y., in Proceedings of the Thirteenth Symposium Ion Sources and Ion-Assisted Technology (TAKAGI, T., Ed), (1990) 205.

[18] TANAKA, H., BOESTEN, L., MATSUNAGA, D., KUDO, T., Differential elastic electron scattering cross-sections for ethane in the energy range from 2 to 100 eV, J, Phys. B: At. Mol. Phys. **21** (1988) 1255.

[19] READ, F.H., CHANNING, J.M., Production and optical properties of an unscreened but localized magnetic field, Rev. Sci. Instrum. **67** (1996) 2372.

[20] CHO, H., GULLEY, R.J., TRANTHAM, K.W., UHLMANN, L.J., DEDMAN, C.J., BUCKMAN, S.J., Elastic electron scattering from sulfur hexafluoride, J. Phys. B: At. Mol. Phys. **33** (2000) 3531.

[21] CHO, H., LEE, H., PARK, Y.S., J. Korean Phys. Soc. **43** (2003) 40.

[22] SRIVASTAVA, S., CHUTJIAN, A., TRAJMAR, S., Absolute elastic differential electron scattering cross-sections in the intermediate energy region. I. H_2, J. Chem. Phys. **63** (1975) 2659.

[23] GIBSON, J. C., GREEN, M. A., TRANTHAM, K. W., BUCKMAN, S. J., TEUBNER, P. J. O., BRUNGER, M. J., Elastic electron scattering from CO_2, J. Phys. B: At. Mol. Opt. Phys. **32** (1999) 213.

[24] BOESTEN, L., TANAKA, H., Rational function fits to the nonresonant elastic differential cross-sections (DCS) for e + He collisions, 0°-180°, 0.1 to 1000 eV, At. Data Nucl. Data Tables **52** (1992) 25.

[25] NESBET, R.K., 1979. Variational calculations of accurate e^- - He cross-sections below 19 eV, Phys. Rev. A **20** (1979) 58.

[26] BRUNGER, M.J., BUCKMAN, S.J., ALLEN, L.J., MCCARTHY, I.E., RATNAVELU, K., Elastic electron scattering from helium: absolute experimental cross-sections, theory and derived interaction potentials, M. J. Brunger, S. J. Buckman, L. J. Allen, I. E. McCarthy, K. Ratnavelu, J. Phys. B: At. Mol. Opt. Phys. **25** (1992) 1823.

[27] BYRON, F.W., JOACHAIN, C., Elastic scattering of electrons and positrons by complex atoms at intermediate energies, Phys. Rev. A **15** (1977) 128.

[28] WAGENAAR, R.W., DE BOER, A., VAN TUBERGEN, T., LOS, DE HEER, F.J., Absolute differential cross-sections for elastic scattering of electrons over small angles from noble-gas atoms, J. Phys. B: At. Mol. Phys. **19** (1986) 3124.

[29] REGISTER, D.F., TRAJMAR, S., SRIVASTAVA, S.K., Absolute elastic differential electron scattering cross-sections for he: A proposed calibration standard from 5 to 200 eV, Phys. Rev. A **21** (1980) 1134.

[30] BROMBERG, P., Absolute differential cross-sections of electrons elastically scattered by the rare gases. i. small angle scattering between 200 and 700 eV, J. Chem. Phys. **61** (1974) 963.

[31] JANSEN, R.J.H., DE HEER, F.J., LUYKEN, H.J., VAN WINGERDEN, B., BLAAUW, H.J., Absolute differential cross-sections for elastic scattering of electrons by helium, neon, argon and molecular nitrogen, J. Phys. B: At. Mol. Phys. **9** (1976) 185.

[32] ROHR, K., N_2- resonance at 2 eV as an energy standard in low-energy electron scattering experiments, J. Phys. B: At. Mol. Phys. **10** (1977) 2215.

[33] BRUNT, J.N.H., KING, G.C., READ, F.H., Resonance structure in elastic electron scattering from helium, neon and argon, J. Phys. B: At. Mol. Phys. **10** (1977) 1289.

[34] MAKOCHEKANWA, C., et al., Experimental and theoretical elastic cross-sections for electron collisions with the C_3H_6 isomers, J. Chem. Phys. **124** (2006) 024323.

[35] CHO, H., et al., A comparative experimental and theoretical study on elastic electron scattering by methane, J. Phys. B: At. Mol. Opt. Phys. **41** (2008) 045203.

[36] MAKOCHEKANWA, C., et al., Electron and positron scattering cross-sections for propene and cyclopropane., Phys. Rev. A **77** (2008) 042717.

[37] MAKOCHEKANWA, C., et al., Experimental observation of neutral radical formation from CH_4 by electron impact in the threshold region, Phys. Rev. A **74** (2006) 042704.

[38] KATO, H., et al., Electron-impact excitation of the B $^1\Sigma_u^+$ and C $^1\Pi_u$ electronic states of H_2, Phys. Rev. A **77** (2008) 062708.

[39] KIM, Y., Scaled born cross-sections for excitations of H_2 by electron impact, J. Chem. Phys. **126** (2007) 064305.

[40] HOSHINO, M., et al., in preparation (2009).

[41] CHRISTOPHOROU, L.G., OLTHOFF, J.K., Electron interactions with excited atoms and molecules, Adv. At. Mol. Opt. Phys, **44** (2001) 155.

[42] KATO, H., et al., Vibrational excitation functions for inelastic and superelastic electron scattering from the ground-electronic state in hot CO_2, Chem. Phys. Lett. **465** (2008) 31.

[43] JOHNSON, P.V., MALONE1, C.P., KHAKOO, M.A., MCCONKEY, J.W., KANIK, I., Electron collisions with constituents of planetary atmospheres, J. Phys: Conference Series **88** (2007) 012069.

[44] LANGE, M., MATSUMOTO, J., SETIAWAN, A., PANAJOTOVIĆ, R., HARRISON, J., LOWER, J. C.A., NEWMAN, D.S., MONDAL, S., BUCKMAN, S.J., Angle-resolving time-of-flight electron spectrometer for near-threshold precision measurements of differential cross-sections of electron-impact excitation of atoms and molecules., Rev. Sci. Instrum. **79** (2008) 043105.

[45] FIELD, D., LUNT, S., JONES, N., ZIESEL, J-P., Photonic, Electronic and Atomic Collisions, Proceedings on XXIII International Conference (BURGDOERGER, J., COHEN, J.S., DATZ, S., VANE, C.R., Eds) (2001) 263.

[46] ITIKAWA, Y.J., Cross-sections for Electron Collisions with Nitrogen Molecules, Phys. Chem. Ref. Data, **35** (2006) 31.

[47] CHRISTOPHOROU, L.G., OLTHOFF, J,K., Electron Interactions With Plasma Processing Gases: An Update for CF_4, CHF_3, C_2F_6, and C_3F_8, J. Phys. Chem. Ref. Data, **28** (1999) 967.

[48] PHELPS, A.V., VAN BRUNT, R.J., Electron-transport, ionization, attachment, and dissociation coefficients in SF_6 and its mixtures, J. Appl. Phys. **64** (1988) 4269.

R-MATRIX CALCULATIONS OF ELECTRON MOLECULE COLLISION DATA

J. TENNYSON

Department of Physics and Astronomy, University College London,
Gower St., London WC1E 6BT, UK

Abstract

Results for R-matrix calculations performed during the Coordinated Research Project (CRP) on Atomic and Molecular Data for Plasma Modelling are discussed. Electron collision problems studied include collisions with various carbon containing molecules including C_2, HCCH, CH_4, $C_2 H_6$ and $C_3 H_8$.

1. INTRODUCTION

The R-matrix method provides a powerful and flexible method of calculating cross-sections and rates for a variety of electron collision processes. Although there are a number of numerical implementations of the method for electron – molecule collisions, the UK molecular R-matrix codes [1, 2] provide the most general and flexible implementation available, particularly in the polyatomic version of the code which is designed to work with Gaussian Type Orbitals (GTOs) [3]. An expert system, Quantemol-N, has recently been developed for running which greatly simplifies the running of the polyatomic version of the codes [4].

2. THE R-MATRIX METHOD

The basic step in the R-matrix method is the division of configuration space into two regions [5]. A sphere centred at the molecular centre of mass is used define the inner region. For the method to be successful this sphere must contain the electronic wave function of the entire N-electron target; for small molecules sphere of radius of about 10 a_0 is usually sufficient although radii significantly larger than this have been used on occasion [6, 7].

In this inner region, the wave function of the $(N + 1)$-electron system (target plus scattering electron) is given by

$$\Psi_k = \mathcal{A} \sum_{i,j} a_{i,j,k} \Phi_i(1,\ldots,N) F_{i,j}(N+1) + \sum_i b_{i,k} \chi_i(1,\ldots,N+1) , \qquad (1)$$

where $\mathcal{A}$ is the antisymmetrization operator, $F_{i,j}$ are continuum orbitals and χ_i are two-centre L^2 functions constructed from N-electron target orbitals.

In eq. (1), Φ_i is the wave function of the ith target state. Electron-correlation effects can be included efficiently in these target wave functions via configuration interaction (CI) expansions [8]. It is the choice of this CI expansion which largely determines which L^2 functions are included in the wave function; the standard choice is to use a complete active space valence CI ie to freeze the core electrons and to allow the valence electrons to move freely within both the occupied and valence orbitals [9].

The inclusion of polarization effects in low-energy electron-molecule collision calculations, even when close-coupling expansions such as eq. (1) are employed, presents a difficult problem [10]. Recently Gorfinkiel and Tennyson developed a molecular R-matrix with pseudostates (MRMPS) method [11, 12] which uses large numbers of states in the close-coupling expansion, many of which are not true physical states of the system. This procedure was originally designed to treat electron impact ionization, a process surprisingly well described by cruder semi-empirical methods [13]. The

MRMPS method is indeed successful at giving near-threshold ionization cross-sections [14], but is probably of greater use in fully converging polarization potentials [7, 15].

3. RESULTS

3.1. Carbon dimer

Carbon dimers, the C_2 molecule, can easily form in fusion plasmas that use graphite walls. Indeed C_2 electronic emission spectra have been monitored as part of the ASDEX experiments [16, 17] using the Swan band. The Swan band involves emissions from the d $^3\Pi_u$ state to the a $^3\Pi_u$ state, which is a very low-lying excited state of the system. Given that these are triplet states and the ground state of C_2 is of $^1\Sigma^+$ symmetry the most likely excitation route is via electron collisions.

Halmova *et al* [18] used the R-matrix method to study a variety of processes involving low-energy collisions with C_2. As part of their study Halmova *et al* calculated a comprehensive set of potential energy curves for C_2 which formed not only important input to their R-matrix electron scattering calculations but also can be used for interpreting or simulating electron spectra of C_2. I therefore note that subsequent to this work a comprehensive set of potential energy curves C_2 have been computed as part of detailed new studies of the electronic spectrum of C_2 [19, 20].

Halmova *et al*'s electron impact excitation cross-sections are summarised in Figure 1 which, in particular, details separately excitation to the d $^3\Pi_u$ state from both the ground state and the low-lying metastable state. Neither of these cross-sections are particularly big although excitation from the metastable state actually gives a significantly larger cross-section. The reader is referred to the original paper for further details.

It is worth noting that Halmova *et al* used their study on electron collisions with C_2 as the starting point for a series of calculations on electron collisions with C_2^- with special emphasis on the electron impact electron detachment cross-section [14,15]. These studies, which used the MRMPS method discussed above, successfully reproduced the rather unexpected resonance structure ob-served in this process [21] and the total cross-section. They demonstrated that while the resonances were essentially short-range in nature, the remainder of the cross-section could calculated using a Born model which considered simply the dipole coupling between the target anion and the continuum (or their case the pseudo-continuum).

3.2. Hydrocarbons

Hydrocarbons are considered to be an important contaminant in fusion plasmas [25,26]. Electron collisions with hydrocarbons have been extensively studied experimentally by Tanaka and co-workers [23, 27], as discussed elsewhere in this volume, and others [10, 24, 28, 29].

My group has undertaken a number of electron collision studies with hydrocarbon species including acetylene [30] and the alkanes methane, ethane and propane [22]. Cross-sections for electron collisions with these systems are given in the cited papers where comparisons with measurements and other theoretical studies can also be found.

Figure 2 gives differential cross-sections for electron collisions with methane at 5 eV. This Figure compares the R-matrix calculations of Varambhia *et al* [22] with measurements due to Tanaka *et al* [23] and Sohn *et al* [24]; the agreement is good. I note that there are other experimental [29] and theoretical [28, 29] studies of this process and comparisons with these generally give a similar level of agreement.

Varambhia *et al* [22] found that by including a significant number of coupled states in their CC expansion they were able to get good results for electron – methane cross-section, including correctly reproducing the Ramsauer mini-mum in the elastic scattering channel. However, their results are less

satisfactory for the higher alkanes as it proved harder to completely include polarization effects in these systems. It would seem likely that it will be necessary to use the MRMPS method to get completely satisfactory results for these systems. However MRMPS calculations are very computationally demanding; at the moment the largest MRMPS calculation is the one for C_2 discussed above. New MRMPS calculations for small hydrocarbons are now underway in my group; such calculations should be extendable to the alkanes in the near future.
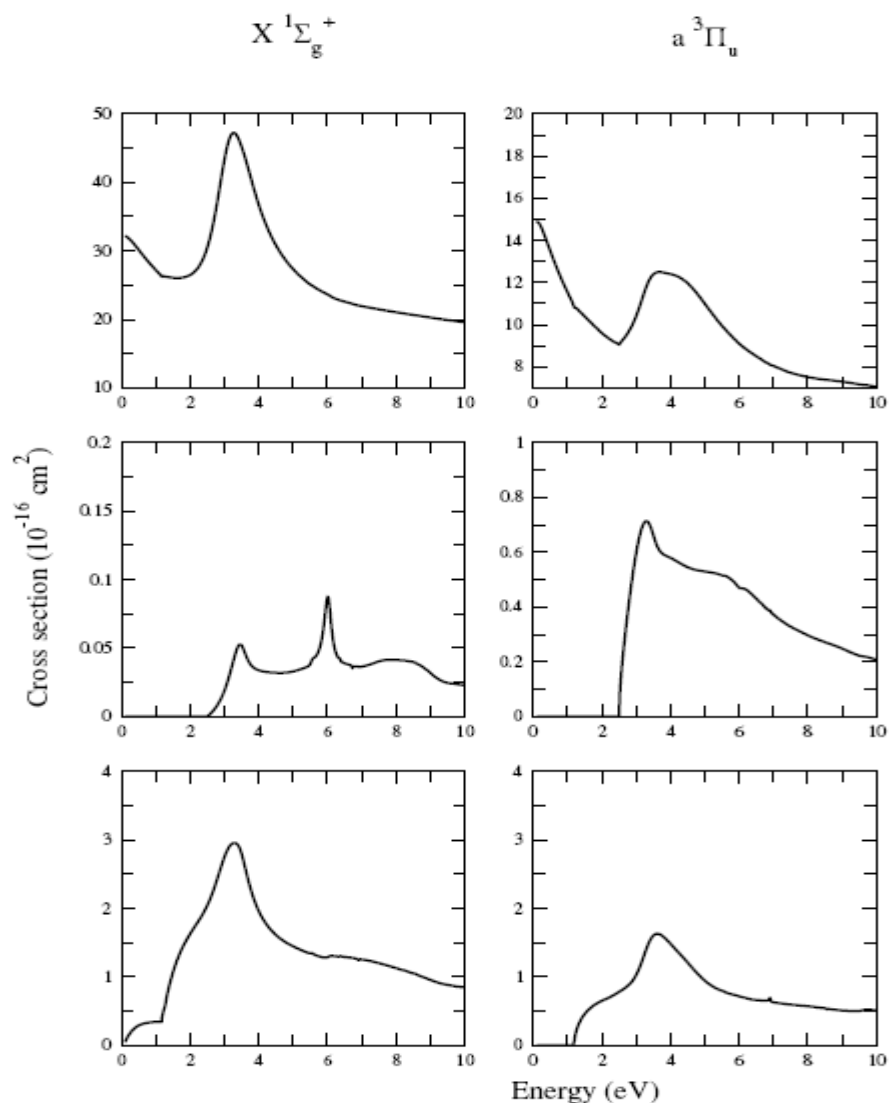

FIG. 1. Electron impact cross-sections for the C_2 molecule at its equilibrium geometry as calculated by Halmova et al [18]. The left hand panels are for molecules starting in the $X^1\Sigma_g^+$ ground state and the right hand panels are for molecules starting in the low-lying $a^3\Pi_u$ metastable state. The top row is the total cross-section as a function of energy. The second row is for excitation to the $d^3\Pi_u$ state and the lower panels are for excitation to all other states.
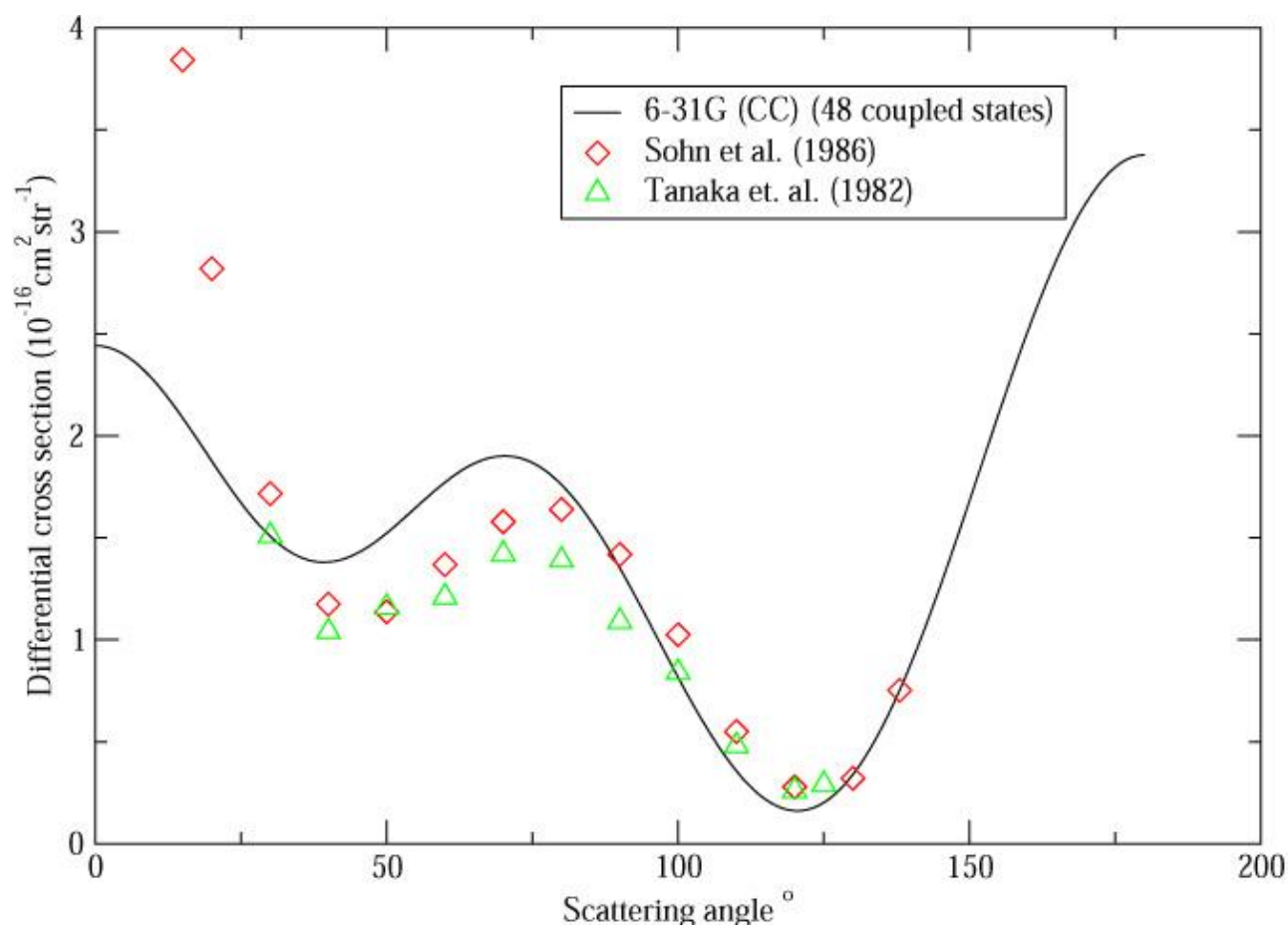
FIG. 2. Differential cross-sections for electron collisions with methane at 5 eV: results of an R-matrix study with 48 coupled states [22] is compared the measurements of Tanaka et al [23] and Sohn et al [24].

This work has been done in part as a contribution to the IAEA Coordinated Research Project (CRP) on Atomic and Molecular Data for Plasma Modelling. The author thanks those colleagues whose work he has quoted freely from in the cited publications.

REFERENCES

[1]   MORGAN, L., TENNYSON, J., GILLAN, C., The UK molecular R-matrix codes, Computer Phys. Comms. **114** (1998) 120.
[2]   BURKE, P.G., TENNYSON, J., R-matrix theory of electron molecule scattering. Molecular Physics: An International Journal at the Interface Between Chemistry and Physic, Mol. Phys. **103** (2005) 2537.
[3]   MORGAN, L. A., GILLAN, C. J., TENNYSON, J., CHEN, X., R-matrix calculations for polyatomic molecules: electron scattering by N_2O, Phys. B: At. Mol. Opt. Phys. **30** (1997) 4087.
[4]   TENNYSON, J., BROWN, D., MUNRO, J., ROZUM, I., VARAMBHIA, H., VINCI, N., Quantemol-N: an expert system for performing electron molecule collision calculations using the r-matrix method, J. Phys. Conf. Series **86** (2007) 012001.
[5]   BURKE, P.G., BERRINGTON, K.A., Atomic and Molecular Processes: an R-matrix Approach. Institute of Physics Publishing, Bristol (1993).
[6]   BRANCHETT, S.E., TENNYSON, J., MORGAN, L.A., Electronic excitation of molecular hydrogen using the r-matrix method, J. Phys. B: At. Mol. Opt. Phys. **23** (1990) 4625.

[7] TARANA, M., TENNYSON, J., Polarization effects in electron collisions with Li_2: application of the molecular r-matrix method with pseudostates, J. Phys. B: At. Mol. Opt. Phys. **41** (2008) 205204.

[8] TENNYSON, J., A new algorithm for hamiltonian matrix construction in electron - molecule collision calculations, J. Phys. B: At. Mol. Opt. Phys. **29** (1996) 1817.

[9] TENNYSON, J., R-matrix calculation of Rydberg states of CO, J. Phys. B: At. Mol. Opt. Phys. **29** (1996) 6185.

[10] GIL, T., LENGSFIELD, B., MCCURDY, W., RESCIGNO, T., Ab initio complex kohn calculations of dissociative excitation of methane: Close-coupling convergence studies Phys. Rev. A **49** (1994) 2551.

[11] GORFINKIEL, J.D., TENNYSON, J.,. Electron and H^{+3} collisions at intermediate energies, J. Phys. B: At. Mol. Opt. Phys. **37** (2004) L343.

[12] GORFINKIEL, J.D., TENNYSON, J., Electron impact ionization of small molecules at intermediate energies: the molecular r-matrix with pseudostates method, J. Phys. B: At. Mol. Opt. Phys. **38** (2005) 1607.

[13] KIM, Y.K., RUDD, M.E., Binary-encounter-dipole model for electron-impact ionization, Phys. Rev. A **50** (1994) 3954.

[14] HALMOVÁ, G., TENNYSON, J., Resonances in electron-impact electron detachment of C_2^-, Phys. Rev. Lett. **100** (2008) 213202.

[15] HALMOVÁ, G., GORFINKIEL, J.D., TENNYSON, J., Low and intermediate energy electron collisions with the C_2^- molecular anion, J. Phys. B: At. Mol. Opt. Phys. **41** (2008) 155201.

[16] STARKE, P., FANTZ, U., BALDEN, M., Investigations of chemical erosion of carbon materials in hydrogen and deuterium low pressure plasmas, J. Nucl. Mater. **337-339** (2005) 1005.

[17] FANTZ, U., MEIR, S., MAR. AND ASDEX UPGRADE TEAM, Correlation of the intensity ratio of C_2/CH molecular bands with the flux ratio of C_2H_y/CH_4 particles, J. Nucl. Mater. **337-339** (2005) 1087.

[18] HALMOVÁ, G., GORFINKIEL, J.D., TENNYSON, J., Low-energy electron collisions with C_2 using the R-matrix method, J. Phys. B: At. Mol. Opt. Phys. **39** (2006) 2849.

[19] KOKKIN, D.L., BACSKAY, G.B., SCHMIDT, T.W., Oscillator strengths and radiative lifetimes for C_2: Swan, Ballik-Ramsay, Phillips, and $d^3\Pi_g \leftarrow c^3\Sigma_u^+$ systems, J. Chem. Phys. **126** (2007) 084302.

[20] SCHMIDT, T.W., BACSKAY, G.B., Oscillator strengths of the Mulliken, Swan, Ballik-Ramsay, Phillips, and $d^3\Pi_g \leftarrow c^3\Sigma_u^+$ systems of C_2 calculated by MRCI methods utilizing a biorthogonal transformation of CASSCF orbitals, J. Chem. Phys. **127** (2007) 234310.

[21] PEDERSEN, H.B., DJURIĆ, N., JENSEN, M.J., KELLA, D., SAFVAN, C.P., CHRISTENSEN, V., ANDERSEN, L.H., Doubly charged negative ions of B_2 and C_2, Phys. Rev. Lett. **81** (1998) 5302.

[22] VARAMBHIA, H., MUNRO, J., TENNYSON, J., R-matrix calculations of low-energy electron alkane collisions, Int. J. Mass Spectrometry **271** (2008) 1.

[23] TANAKA, H., ET AL., Differential cross-sections for elastic scattering of electrons by CH_4 in the energy range of 3 to 20 eV, J. Phys. B: At. Mol. Phys. **15** (1982) 3305.

[24] SOHN, W., et al.,. Elastic electron scattering from CH_4 for collision energies between 0.2 and 5 eV, J. Phys. B: At. Mol. Opt. Phys. **19** (1986) 3625.

[25] JANEV, R.K., REITER, D., "Collision processes of hydrocarbon species in hydrogen plasmas 2. The ethane and propane families", Berichte des Forschungszentrums Jlich **JUEL-4005**, Forschungszentrum Jlich, Zentralbibliothek, Verlag (2003).

[26] DAUWE, A., TYTGADT, M., REITER, D., BAELMANS, M., "Automatic reduction of the hydrocarbon reaction mechanisms in fusion edge plasmas", Berichte des Forschungszentrums Jlich **JUEL-4229**, Forschungszentrum Jlich, Zentralbibliothek, Verlag (2006).

[27] MAKOCHEKANWA, C., et al., Electron and positron scattering cross-sections for propene and cyclopropane, Phys. Rev. A, **74** (2006) 042704.

[28] LENGSFIELD, B.H., RESCIGNO, T.N., MCCURDY, C.W., Ab initio study of low-energy electron-methane scattering, Phys. Rev. A **44** (1991) 4296.

[29] CHO, H., et al., A comparative experimental and theoretical study on elastic electron scattering by methane. J. Phys. B: At. Mol. Opt. Phys. **41** (2008) 045203.

[30] FRANZ, J., et al., Correlation and polarization effects in electron/positron scattering from acetylene: A comparison of computational models. Nucl. Instr. Meths. Phys. Res. B **266** (2008) 425.

254